INTERNATIONAL DOCTORAL
SCHOOL OF THE USC

María
Lago Silva

PhD Thesis

Covalent and Supramolecular Helical Polymers Based on Axially Chiral Allenes

Santiago de Compostela, 2024

Doctoral Programme in Chemical Science and Technology

ESCOLA DE DOUTORAMENTO
INTERNACIONAL DA USC

DOCTORAL THESIS

COVALENT AND SUPRAMOLECULAR HELICAL POLYMERS BASED ON AXIALLY CHIRAL ALLENES

Author

María Lago Silva

Supervisors: Emilio Quiñoá Cabana and Félix Freire Iribarne

Tutor: Emilio Quiñoá Cabana

PHD PROGRAMME IN CHEMICAL SCIENCE AND TECHNOLOGY

SANTIAGO DE COMPOSTELA

2024

Abbreviations and Acronyms

α	Optical Rotation
Å	Angstrom
A	area
Aib	α-Aminoisobutyric Acid
AFM	Atomic Force Microscopy
ap	antiperiplanar
AT	Active Template
b	optical path
BTA	benzene-1,3,5-tricarboxamide
bipy	bipyridine
c	concentration
°C	Degree Celsius
c-c	*cis-cisoidal*
c-t	*cis-transoidal*
calc.	calculated
CIP	Cahn-Ingold-Prelog priority rules
CP	Circularly Polarized
CSP	Chiral Stationary Phase
CuAAC	copper-catalyzed azide–alkyne cycloaddition
CyD	cyclodextrin
δ	chemical shift
1,2-DCE	1,2-dichloroethane
DCM	dichloromethane
DEA	1,3-di-*tert*-butyl-diethynylallene
DFT	Density Function Theory
ΔE_{bind}	Binding energy
ΔH_{elo}	Elongation Enthalpy
ΔH_{np}	Nucleation Penalty

ΔH_{nuc}	Nucleation Enthalpy
DIPA	di*iso*propylamine
DIPEA	*N,N*-di*iso*propiletilamina
DMAP	*N,N*-dimethylpyridin-4-amine
DMF	*N,N*-dimethylformamide
DMSO	dimethylsulfoxide
DNA	Deoxyribonucleic Acid
Đ	dispersity
DSC	Differential Scanning Calorimetry
ΔS_{elo}	Elongation Entropy
ΔS_{nuc}	Nucleation Entropy
ε	dielectric constant
ε	extinction coefficient
ee	Enantiomeric Excess
e.g.	Latin expression “exempli gratia”; for example
equiv	equivalents
ESI	Electrospray Ionization
FG	Functional Group
FWHM	Full Width at Half-Maximum
g	gram
g_{abs}	anisotropy or dissymmetry factor
GFN2-xTB	Grimme’s extended semiempirical tight-binding method
GPC	Gel Performance Chromatography
GPCRs	G-protein Coupled Receptors
HOPG	Highly Oriented Pyrolytic Graphite
HPLC	High-Performance Liquid Chromatography
Θ	tilting degree
i.e.	Latin expression “id est”; it is
IR	Infrared Spectroscopy
K	Kelvin
K_{eq}	Equilibrium constant

K_{elo}	Elongation constant
K_{nuc}	Nucleation constant
λ	Wavelength
l	Cell length
LB	Langmuir-Blodgett
LS	Langmuir-Schaefer
m	multiplet
m-	*meta*-position
M	*minus;* counterclockwise
M	molarity
MB	Mass Balance model
MCH	methylcyclohexane
MeCN	acetonitrile
mdeg	millidegree
mg	milligram
MHz	Megahertz
min	minutes
mL	milliliter
MM	Molecular Mechanics
μM	micromolar
mM	millimolar
mmol	millimol
Mn	Number Average Molecular Weight
MOF	Metal-Organic Framework
MPA	α-methoxyphenylacetic acid
m.r.u.	Monomer Repeating Unit
MTPA	α-methoxy-α-trifluoromethylphenylacetic acid
Mw	Weight Average Molecular Weight
Mz	Z Average
ν	Wavenumber
nbd	2,5-norbadiene

NMR	Nuclear Magnetic Resonance
nm	nanometer
NOESY	Nuclear Overhauser Effect Spectroscopy
o-	*ortho*-position
OPE	oligo(phenyleneethylene)
OR	Optical Rotation
P	*plus*; clockwise
p-	*para*-position
PA	poly(acetylene)
PAEPA	poly[(allenylethynylenephenylene)acetylene
PBI	perylenebisimide
PG	protecting group
PLA	poly(lactic)
PMMA	poly(methylmethacrylate)
PPA	poly(phenylacetylene)
ppm	Parts Per Million
R	*Rectus,* Latin for right
ROA	Raman Optical Activity
ROESY	Rotating Frame Overhauser Enhancement Spectroscopy
rt	room temperature
σ	Cooperativity Factor
s	Singlet
S	*Sinister*, Latin for left
SaS	Sergeants and Soldiers
SCXRD	Single-crystal X-ray diffraction
Sp	*syn*periplanar
SP	Supramolecular Polymer
STD	Saturation-Transfer Difference
T	temperature
t	triplet
t-c	*trans-cisoidal*

t-t	*trans-transoidal*
TBAF	tetrabutylammonium fluoride
TBAX	tetrabutylammonium salt
TD	Time-Dependent
TFA	trifluoroacetic acid
TGA	Thermogravimetric Analysis
THF	tetrahydrofuran
TIPS	tri-*iso*-propylsilyl
TMS	trimethylsilyl
UV-vis	Ultraviolet-visible
VCD	Vibrational Circular Dichroism
VT	variable temperature
ω_1	dihedral angle

Index

Summary

Summary

Chirality has inspired important advances in many areas of research, including chemistry, given its impact on nature. In this sense, supramolecular chiral detection can profoundly affect the nature of one or more parts, or even the whole, of a system of greater complexity. For example, this phenomenon can be found in many natural systems such as the α-helix of proteins or the double helix that makes up the DNA. Thus, chirality is involved in vital functions such as the storage of genetic information and recognition processes.

Axial chirality is also present in helical systems, named helical chirality, which arises from the arrangement of part or all of a molecule or assembly under a chiral influence that eliminates any element of symmetry. This type of chirality is one of the structural motifs most present in natural systems with important biological functions, such as the aforementioned DNA or proteins, among others. The scientific community, inspired by the close structure-function relationship observed in these diverse biomacromolecules, focused great efforts on the preparation of new synthetic materials in an attempt to mimic their properties. As a result of these efforts, the field of non-natural helical polymers has developed a wide range of chiral polymers with a high variability of functionalities and applications.

In the field of covalent helical polymers, one of the most relevant families is the family of polyphenylacetylenes (PPAs), which are characterized by their highly dynamic character. The high dynamism of these polymers allows them to modulate their structure (helical sense and/or elongation) in response to different external stimuli (temperature, metal ions, solvent properties, pH, light, etc.), thus acting as sensors. Consequently, unraveling the communication mechanisms that generate these structural changes provides a better understanding of the recognition processes that operate in more complex systems, facilitating the rational design of new systems that mimic the complex gears that govern nature.

On the other hand, supramolecular helical polymers, which are composed of monomeric units with the ability to self-assemble through weak supramolecular interactions, are worth mentioning. Unlike the case of covalent helical polymers, the polymerization process is reversible and the molecular aggregates that form them are

only generated under favorable conditions and the alteration of which results in the loss of self-assembly. Therefore, the design of the monomeric units is crucial to increase the stability and application of these materials. One of the most interesting properties of these materials is chirality amplification, initially described for covalent polymers and now extended to all types of polymers. Furthermore, other related phenomena of interest include helicity induction.

This thesis, entitled: "Covalent and Supramolecular Helical Polymers Based on Axially Chiral Allenes", comprises four research projects, which focus on the study of the structure and properties of helical polymers, both covalent and supramolecular, using axially chiral allenes as a source of chirality. The following presents the most significant results from each chapter.

Chapter 3.1. Dynamic Axial-to-Helical Communication Mechanism in Poly[(allenylethynylenephenylene)acetylene]s under External Stimuli

The rational design of polymeric helical structures that respond selectively to stimuli is one of the greatest challenges facing the scientific community nowadays. For this purpose, it is necessary to elucidate both their secondary structure and the mechanism of transmission of the chiral information that governs them. There are several examples in the literature in which it is possible to effectively control the final helix adopted by the polymer through the application of external stimuli, leading to a specific helical sense and elongation degree. Most of the structures described so far are composed of monomeric units with conformational freedom and a chiral center as a source of chirality. In this way, external stimuli that induce conformational changes in the monomeric units change the orientation of the source of chirality, whose information is transmitted to the polyene backbone by various mechanisms, resulting in a change in the overall helical structure.

This chapter describes a novel mechanism of chiral communication in PPA-derived polymers, using for the first time an axially chiral allene as a source of chirality, whose structural features mean that monomer units exhibit no conformational variability. This gives rise to a new family of helical polymers, called poly[(alenylethynylenylphenylenephenylene)acetylene]s (PAEPAs), in which the axial chirality is transmitted through space from the allene units to the polyene backbone by an axial-to-helical mechanism. The rigid allenic structure of the monomeric units, which

place their substituents in two perpendicular planes, results in quasi-static helical polymers.

Therefore, the helical sense in a PAEPA is determined by the allene substituent with the optimal distance/size ratio relative to the polyene backbone. Nevertheless, by altering the priority of such substituents through the activation or deactivation of supramolecular interactions through suitable external stimuli, such as amines, it became possible to modify the helical sense of the polymer. The external stimulus interaction with the isopropyl group present on one of the allene substituents transforms the so-called quasi-static polymers into dynamic helical polymers.

The dynamic mechanism from axial to helical was demonstrated by ^{14}N-NMR. Moreover, the supramolecular interaction was further confirmed by the protection of the isopropyl group involved in the interaction with the external stimulus, highlighting the crucial role of the activation of these supramolecular interactions in the helix inversion process.

The secondary structure of the polymer was further elucidated through a combination of various experimental techniques (AFM, DSC), supported by theoretical calculations. These studies suggested a *cis-transoidal* conformation for the polymer scaffold, consisting of an internal and external helix with opposite screw senses.

These results open a new horizon both in the design of stimuli-responsive materials and in the development of new methods of chiral communication in macromolecules.

Chapter 3.2. *P/M* Macromolecular Switch Based on Conformational Control Exerted by an Achiral Side Chain within an Axially Chiral Locked Pendant

Molecular and macromolecular switches are mechanisms used by nature in sensing and transport processes. Therefore, the interaction of such molecular switches with different stimuli, such as pH, ions, and light, often leads to an equilibrium between two functionally relevant conformational states (ON/OFF). In general, the inherent complexity of these systems makes it difficult to elucidate the mechanisms of conformational control in large biomacromolecules. To gain knowledge in this area, the scientific community has carried out extensive work over the past decades to develop simple and easily tunable molecular and macromolecular switches.

In this line, dynamic helical polymers are macromolecular switches in which the control of the *P/M* helix direction is achieved by means of different helix induction mechanisms. These mechanisms arise from conformational changes within the monomeric repeating units induced by interactions with various external stimuli. Hence, the information can be transmitted from the chiral center to the polymer backbone following different mechanisms, either directly through space by tele-induction or in several steps, so that the information is first transmitted to an achiral spacer in the monomer unit and then collected by the polyene backbone (chiral harvesting).

In this work, we describe a novel macromolecular helical switch based on a chiral monomer that bears a flexible achiral arm within its structure to control the *P*- and *M*-helical directions of a macromolecular gear without altering the chiral information in the monomeric repeating units. To this end, and considering the results obtained for PAEPAs (Chapter 3.1.), whose preferred helical direction is determined by the axial conformational stability of a chiral allene, we again selected a tetrasubstituted allene. In this case, the allene moiety incorporates an achiral arm with conformational variability at one of its substituents. Therefore, control over the extended/bent conformational composition of the flexible achiral arm is the only requirement to induce helix inversion in the macromolecular polymeric structure. A (dimethyl)methyl-*p*-tolylsulfonamide group was selected as the achiral arm on one of the allene substituents, since this group can readily form hydrogen bonds with solvents or anions. Thus, *P* and *M* enantiomers of the previously designed monomers (mono-**1**) were synthesized, and their behavior in different solvents was studied. ECD studies revealed, as expected, that the axial *P* or *M* chirality of the allenic moiety remains unchanged due to its stable configuration. However, NMR studies (^{1}H and NOESY) for mono-(*P*)-**1** showed that the substituent bearing the sulfonamide group can adopt two different conformations: extended (c-I), in Lewis base solvents (THF, DMF, DMSO); and bent (c-II), in non-Lewis base solvents ($CHCl_3$, DCM, 1,2-DCE).

In light of the results obtained with the monomers, similar studies were carried out for the corresponding polymers (poly-(*P*)-**1** and poly-(*M*)-**2**). ECD studies in Lewis base solvents, where the N – H of the sulfonamide group can form hydrogen bond interactions with the solvent, showed that the polymers adopted a *P* helix for poly-(*P*)-**1** and an *M* helix for poly-(*M*)-**1**. In contrast, ECD studies in non-Lewis based solvents, such as DCM or 1,2-DCE, suggested structural changes in the polymers towards the opposite helical

senses. An in-depth analysis of the data obtained by ECD, supported by IR studies, showed that the structural changes produced are due to the different Lewis-base character of the solvents that induce conformational changes in the substituent containing the sulfonamide group. Furthermore, STD and NOESY NMR experiments showed that in Lewis-based solvents the *p*-tolyl-sulfonamide group adopts an extended conformation (c-I) and is therefore placed away from the polyene backbone. Thus, the extended conformation avoids the interference of this group with the helix induction command ordered by the closet allene substituent. On the contrary, a bent conformation (c-II) is favored in non-Lewis base solvents, which places the bent arm close to the backbone, surpassing the command given by any other substituent and inducing an opposite helical sense. As a result, a helical inversion mechanism of a dynamic helical polymer based on the conformational control of a flexible achiral arm is presented. Furthermore, low-temperature ECD studies revealed that multi-chiral helical structures containing up to five axial motifs — the two coaxial helices (internal and external), the chiral allene, and two extra-chiral axial motifs described by the aryl-ethynyl-allene matrix — can be prepared by combining rigid chiral allenes with helical polymers such as PPAs. Finally, ECD, DSC, AFM, and theoretical calculations were combined to obtain relevant structural parameters related to their secondary structure for both helical senses. These results show that the combination of molecular switches, supramolecular chemistry, and polymers can lead to different mechanisms of helical induction through complex structures, allowing a better understanding of how information can be transferred across different levels of complexity.

Chapter 3.3. Mechanically Interlocked Macromolecular Gears: Elongation and Helical Sense Control of a Helical Polymer by Acting on a Chiral Rotaxane Used as Pendant Group

The bottom-up approach is used by nature to create complex systems in which a small fragment of a macromolecule is usually involved in a stimulus-response process, often resulting in a change in the conformational composition of the entire macromolecule. In dynamic helical polymers, such as PPAs, conformational changes of a chiral pendant group induced by external stimuli are efficiently transmitted through space to the polyene backbone, mirroring processes observed in nature.

Inspired by this information and given the results obtained in the studies of the axial-to-helical communication mechanism of PAEPAs (Chapters 3.1. and 3.2.), we designed

a sophisticated macromolecular gear combining mechanically interlocked molecules, i.e. a rotaxane, and dynamic helical polymers (PPAs). A PPA derivative with a chiral rotaxane as the monomer unit was synthesized. A chiral allene was selected as the thread of the rotaxane due to its axial chirality and restricted conformational composition. This thread was then combined with a small macrocycle as a wheel to compose the final rotaxane. The piroueting of the wheel was intended to change the relative volume of the substituents to the thread (allene), ultimately altering their steric effects on the polyene backbone. This, in turn, would induce a conformational change in the entire macromolecule.

Therefore, a triazole group was introduced onto one of the substituents of the allene to form the rotaxane. The triazole group acts as a link between the thread and the macrocycle, functionalized with a bipyridine group. Thus, the donor nitrogens of the bipyridine form a hydrogen bond with the C–H of the triazole group, stabilizing a specific co-conformation within the rotaxane structure. The previously designed rotaxane was synthesized with a very good yield. ROESY NMR studies and the resolution of its X-ray crystal structure confirmed the arrangement of the wheel in a preferred co-conformation stabilized by the bipyridine-triazole hydrogen bond. Stimulus-response studies were then carried out by adding external stimuli that could alter the hydrogen bond, leading to a co-conformational change in the rotaxane. A protic acid (formic acid) and a copper salt with weak ligands [$Cu(MeCN)_4BF_4$] was used. ECD, UV-vis, and NMR studies revealed two different co-conformations of the wheel to the chiral axis, depending on the stimulus used. Subsequently, similar studies were conducted on the corresponding polymer. The results showed a sophisticated multi-switch system that allows alternation among three distinct helical conformations (*P* helix and stretched *P* and *M* helices), depending on the stimulus applied and in a reversible manner.

This novel system demonstrates the ability to achieve three different helical conformations by controlling the relative orientation of the wheel, i.e. the rotaxane co-coformation, without altering the chiral moiety. The chiral allene will always have the same relative orientation of its substituents, showing a quasi-static behavior due to its locked conformational composition. Nevertheless, the modification of the wheel orientation leads to a change in the relative position of the wheel substituents with respect to the helical backbone, which in turn results in a different command dictated by the new arrangement.

Finally, AFM images of the polymer provided information about its secondary structure, such as the helical pitch and the screw sense of the external helix, revealing a *cis-transoidal* polyene backbone.

Therefore, this work shows how small structural changes in a mechanically interlocked molecule can be amplified when incorporated into a macromolecule as a monomeric unit of a dynamic polymeric helix. Efforts in these lines are currently ongoing to increase the functionality and complexity of the system.

Chapter 3.4. Axially-Chiral Allene-Based Supramolecular Polymers

Supramolecular polymers are characterized by their dynamic and reversible nature. These properties, inherent to this type of polymers, are conferred by the non-covalent nature of the bonds linking the monomeric units, which allows their application in various scientific fields. In general, the monomeric units are usually composed of planar π-conjugated cores, allowing π-π interactions between them, functionalized with paraffinic or glycol side chains, which ensure the stability of the supramolecular polymer in the desired aggregation medium. Other weak interactions that often contribute to the stabilization of these structures are hydrogen bonds or van der Waals interactions. The introduction of chirality in the above-mentioned side chains often favors the adoption of supramolecular helical structures. Thus, the induction of asymmetry is classically achieved by introducing point chirality in the solubilizing side chains.

An under-explored strategy for obtaining chiral supramolecular polymers is the polymerization of three-dimensional non-planar units, especially those with axial or helical chirality. These chiral molecules have a very distorted and rather rigid three-dimensional structure, which does not facilitate their assembly. However, this strategy has been on the rise in recent years to increase the diversity of chiral building blocks for the construction of new supramolecular materials. Although chiral allenes have been successfully used in the construction of functional chiral materials, they have not been studied in supramolecular polymers.

This chapter describes the supramolecular polymerization of axially chiral allenes, which favors their self-assembly by introducing into their substituents aggregating groups based on ethylene diamides bearing a gallic wedge with paraffinic chains. These groups stabilize the supramolecular aggregates by providing additional interactions such as hydrogen bonds, π-π and van der Waals interactions.

Studies carried out with different techniques (ECD, UV-vis, IR, NMR, AFM, and computational studies) using a solvent that favors the dissolved state ($CHCl_3$) and a solvent that favors the aggregated state (MCH), showed results indicative of the formation of a supramolecular chiral aggregate in MCH. Furthermore, in these studies, the aggregates were observed to have a chirality opposite to the axial chirality of the allene — (*P*)-allene, (*M*)-aggregate; (*M*)-allene, (*P*)-aggregate —. Parallel self-assembly and interdigitation of single molecule fibers, generate larger fiber-like aggregates. In these aggregates, the chirality of the fiber is dictated by the axial chirality of the allene used as a central core of the building block. To further elucidate the mechanism governing their supramolecular polymerization, ECD experiments were performed at variable temperatures. These experimental studies revealed that the supramolecular polymerization followed a cooperative mechanism.

Therefore, this work deals with an appealing mechanism for the induction of axial-to-axial supramolecular helices by self-assembly of non-planar building blocks. These results open new horizons in the design of chiral supramolecular materials, expanding the diversity of chiral building blocks and consequently enhancing the properties associated with the aggregate.

Resumo

Resumo

A quiralidade inspirou importantes avances en moitas áreas da investigación, entre elas cabe descatar na química, dada a súa repercusión na natureza. Nesta liña, un proceso de detección supramolecular quiral pode afectar profundamente á natureza dunha parte, ou de varias partes, ou incluso á totalidade dun sistema de maior complexidade. Por exemplo, este fenómeno pode atoparse na estrutura de moitos sistemas naturais como na α-hélice das proteínas ou na dobre hélice que conforma o ADN. Polo tanto, a quiralidade está presente en funcións vitais tan importantes como son o almacenamento de información xenética e os procesos de recoñecemento, entre outros.

En sistemas moleculares a quiralidade pode emerxer de diferentes tipos de unidades que comprenden motivos axiais, helicoidais e planares, ademais de centros de asimetría. Neste traballo centrámonos na quiralidade axial, a cal xorde pola presenza dun eixe quiral que dispón nunha molécula catro grupos en dous planos perpendiculares por parellas onde a rotación está restrinxida ou bloqueada. Un dos grupos máis amplamente empregados como fonte de quiralidade axial son os alenos. As características estruturais destes motivos axialmente quirais convérteos en atractivos bloques de construción quirais para formar sistemas de maior complexidade. Aínda que ditos bloques de construción foron incorporados con éxito en diversos materiais quirais, apenas foron empregados na formación de estruturas macromoleculares.

A quiralidade axial tamén está presente en sistemas helicoidais, denominándose quiralidade helicoidal, a cal emerxe pola disposición dunha parte ou da totalidade dunha molécula ou conxunto baixo influenza quiral que elimina calquera elemento de simetría. Este tipo de quiralidade é un dos motivos estruturais máis amplamente presente en sistemas naturais con importantes función biolóxicas, como os previamente citados ADN ou proteínas, entre outros. A comunidade científica, inspirada na estreita relación estrutura–función observada nestas diversas bio-macromoléculas, centrou grandes esforzos na preparación de novos materiais sintéticos tratando de imitar as súas propiedades. Ditos esforzos deron lugar a que o campo dos polímeros helicoidais non naturais, desenvolvera unha ampla gama de polímeros quirais cunha gran variabilidade de funcionalidades e aplicacións.

No ámbito dos polímeros helicoidais covalentes, unha das familias máis relevantes son os poli(fenilacetileno)s (PPAs), dos cales destacan o seu gran carácter dinámico. O gran dinamismo destes polímeros permite modular a súa estrutura (sentido de xiro e/ou elongación) mediante diversos estímulos externos (temperatura, ións metálicos, propiedades do disolvente, pH, luz, etc.) actuando deste xeito como sensores. Polo tanto, elucidar os mecanismos de comunicación que xeran ditos cambios estruturais, arroxa unha maior comprensión dos procesos de recoñecemento que teñen lugar en sistemas de maior complexidade, facilitando o deseño racional de novos sistemas que imitan os complexos engrenaxes que gobernan na natureza.

Por outro lado, cabe destacar os polímeros helicoidais supramoleculares, os cales están compostos por unidades monoméricas coa capacidade de autoensamblaxe mediante interaccións supramoleculares débiles. Ao contrario que no caso dos polímeros helicoidais covalentes, o proceso de polimerización é reversible e os agregados moleculares que os conforman só se xeran en condición favorables, cuxa alteración resulta na perda do autoensamblaxe. Polo tanto, o deseño das unidades monoméricas é crucial para aumentar a estabilidade e aplicación destes materiais. Unha das propiedades máis interesantes destes materiais é a da amplificación de quiralidade, descrita por primeira vez para polímeros covalentes e estendida hoxe en día a todo tipo de polímeros. Ademais, relacionado con este fenómeno atópanse outras propiedades de gran interese como a indución da helicidade.

Esta tese titulada: “Polímeros Helicoidais Covalentes e Supramoleculares baseados en Alenos Axialmente Quirais”, inclúe catro proxectos de investigación nos que se abordarán o estudo da estrutura e do comportamento de polímeros helicoidais, tanto covalentes coma supramoleculares, nos que se empregan como fonte de quiralidade alenos axialmente quirais. A continuación expoñeranse os resultados máis relevantes de cada capítulo.

Capítulo 3.1. Mecanismo de Comunicación Dinámico de Axial a Helicoidal en Poli[(aleniletinilenfenileno)acetileno]s Baixo Estímulos Externos

O deseño racional de estruturas helicoidais poliméricas que respondan selectivamente a estímulos é un dos grandes retos da comunidade científica hoxe en día. Para isto é necesario coñecer tanto a estrutura secundaria dos mesmos como o

mecanismo de transmisión da información quiral que os gobernan. Na bibliografía atópanse diferentes exemplos nos que é posible controlar de maneira eficaz a hélice final adoptada polo polímero a través da aplicación de estímulos externos, obtendo así un sentido de xiro específico. A maioría das estruturas descritas están compostas por unidades monoméricas con liberdade conformacional e que contan cun centro quiral como fonte de quiralidade. De esta maneira, estímulos externos que xeran cambios conformacionais nas unidades monoméricas, cambian a orientación da fonte de quiralidade, cuxa información é transmitida mediante diferentes mecanismos ao esqueleto poliénico, xerando un cambio no conxunto da estrutura helicoidal.

Neste capítulo descríbese un novo mecanismo de comunicación quiral en polímeros derivados de PPAs, no cal emprégase como fonte de quiralidade por primeira vez un aleno axialmente quiral, cuxas características estruturais fan que as unidades monoméricas non presenten variabilidade conformacional. Deste xeito, emerxe unha nova familia de polímeros helicoidais, denominada poli[(aleniletinilenfenileno)acetileno]s (PAEPAs), na que a quiralidade axial transmítese das unidades alénicas ao esqueleto poliénico a través do espazo mediante un mecanismo de axial a helicoidal. A ríxida estrutura alénica das unidades monoméricas, a cal dispón aos seus substituíntes en dous planos perpendiculares, da lugar a polímeros helicoidais practicamente estáticos. Polo tanto, o sentido de xiro preferente nun PAEPA está determinado polo substituínte do aleno coa óptima relación distancia/tamaño ao esqueleto poliénico. Con todo, modificando a prioridade de ditos substituíentes mediante a activación ou desactivación de interaccións supramoleculares a través dos estímulos externos adecuados, como aminas, foi posible modificar o sentido de xiro do polímero ao interaccionar cun grupo isopropilo presente nun dos substituíntes do fragmento alénico, transformado así ditos polímeros cuasiestáticos en polímeros helicoidais dinámicos. Este mecanismo dinámico de axial a helicoidal foi demostrado por ^{14}N-RMN. Dita interación tamén se corroborou trala protección do grupo isopropilo implicado na interacción co estímulo externo, o cal mostra o papel clave da activación das interaccións supramoleculares no proceso de inversión da hélice.

Así mesmo, elucidouse a estrutura secundaria dos polímeros sintetizados mediante a combinación de diversas técnicas experimentais (AFM, DSC) apoiadas por cálculos teóricos. Estes estudos suxiren unha conformación *cis-transoide* para a cadea polimérica, formada por unha hélice interna e externa con sentidos de xiro opostos.

Estes estudos abren un novo horizonte tanto no deseño de materiais sensibles a estímulos, como no desenvolvemento de novos métodos de comunicación quiral en macromoléculas.

Capítulo 3.2. Interruptor Macromolecular *P/M* baseado no Control Conformacional Exercido por unha Cadea Lateral Aquiral dentro dun Colgante Quiral Bloqueado Axialmente

Os interruptores moleculares e macromoleculares son mecanismos utilizados pola natureza en procesos de sinalización ou transporte. Así, a interacción dos interruptores bio-moleculares con diferentes estímulos como o pH, os ións e a luz, levou con frecuencia a un equilibrio entre dous estados conformacionais funcionalmente relevantes (ON/OFF). En xeral, a elucidación dos mecanismos que rexen o control conformacional en grandes bio-macromoléculas vese obstaculizada pola complexidade dos sistemas. Para adquirir coñecementos neste campo, a comunidade científica realizou un traballo exhaustivo durante as últimas décadas para desenvolver interruptores moleculares ou macromoleculares sinxelos e facilmente sintonizables. Nesta liña, os polímeros helicoidais dinámicos son interruptores macromoleculares nos que o control do sentido do xiro *P/M* consíguese recorrendo a diferentes mecanismos de indución da hélice, que xorden da manipulación conformacional das unidades de repetición monoméricas debido ás interaccións cos diferentes estímulos. Así, pódese transmitir información desde o centro quiral ata a cadea principal do polímero seguindo diferentes mecanismos, tanto directamente a través do espazo mediante tele-indución, como en varios pasos de maneira que a información transmítese primeiro a un espaciador aquiral na unidade monomérica, e despois recóllese pola columna vertebral do polieno (colleita quiral).

Neste traballo, descríbese un novidoso interruptor helicoidal macromolecular baseado nun monómero quiral que posúe un brazo flexible aquiral dentro da súa estrutura, co obxectivo de controlar os sentidos helicoidais *P* e *M* dunha engrenaxe macromolecular sen alterar a información quiral nas unidades de repetición monoméricas. Para elo, tendo en conta os resultados obtidos para os PAEPAs (Capítulo 3.1.), cuxo sentido preferente de xiro está determinado pola estabilidade conformacional axial dun aleno quiral, seleccionamos de novo un aleno tetrasubstituído. Neste caso o aleno presenta nun dos seus substituíntes un brazo aquiral con variabilidade conformacional. Desta maneira, o control sobre a composición conformacional

estendida/dobrada do brazo flexible aquiral é o único requisito necesario para inducir unha inversión de hélice na estrutura do polímero macromolecular. Para elo, empregouse como brazo aquiral un grupo (dimetil)metil-*p*-tolilsulfonamida como un dos substituíntes do aleno, xa que dito grupo pode formar facilmente enlaces de hidróxeno con disolventes ou anións.

Polo tanto, sintetizáronse os enantiómeros *P* e *M* dos monómeros previamente deseñados (mono-**1**) e, a continuación, estudouse o seu comportamento en diferentes disolventes. Os estudos de ECD mostraron, como era de esperar, que a quiralidade axial *P* ou *M* do fragmento alénico permanece inalterada debido á súa configuración restrinxida. Non obstante, mediante estudos de RMN (^{1}H e NOESY) púidose deducir que o substituínte que leva o grupo sulfonamida de mono-(*P*)-**1** pode adoptar dúas conformacións diferentes: estendida (c-I) en disolventes base de Lewis (THF, DMF, DMSO) e dobrada (c-II) en disolventes non base de Lewis ($CHCl_3$, DCM, 1,2-DCE).

Á vista dos resultados obtidos cos monómeros realizáronse os mesmos estudos para os correspondentes polímeros (poli-(*P*)-**1** e poli-(*M*)-**2**). Os estudos de ECD en disolventes de base de Lewis, onde o N–H do grupo sulfonamida pode establecer interaccións mediante enlaces de hidróxeno co disolvente, mostran que os polímeros adoptan unha hélice *P* para poli-(*P*)-**1** e unha *M* para poli-(*M*)-**1**. Por outra parte, nas disolucións dos polímeros en disolventes non base de Lewis, como DCM ou 1,2-DCE, obsérvanse cambios estruturais nos polímeros cara ás estruturas de sentido helicoidal opostos. O análise en profundidade dos datos obtidos por ECD, xunto con estudos de IR, amosaron que os cambios estruturais producidos débense ao diferente carácter de base de Lewis dos disolventes que provocan os cambios conformacionais no substituínte que contén o grupo sulfonamida. Ademais, experimentos de STD e NOESY por RMN demostraron que o grupo *p*-tolil-sulfonamida adopta unha conformación estendida (c-I) en disolventes de base de Lewis e, polo tanto, atópase afastado do esqueleto do polieno, polo que non interfire no comando de indución da hélice ordenado polo substituínte do aleno máis próximo. Por outro lado, no caso dos disolventes non base de Lewis favorécese unha conformación dobrada (c-II), o que sitúa ao brazo dobrado preto do esqueleto, de maneira que dobrega a orde dada por calquera outro substituínte, inducindo un sentido de xiro oposto. Como resultado, preséntase un mecanismo de inversión de hélice dun polímero helicoidal dinámico baseado no control conformacional dun brazo aquiral flexible. Ademais, a partir de estudos de ECD a baixa

temperatura tamén descubrimos que as estruturas helicoidais multiquirais, que comprenden ata cinco motivos axiais —as dúas hélices coaxiais (interna e externa), o aleno quiral e dous motivos axiais adicionais quirais descritos pola matriz aril-etinil-aleno— pódense preparar combinando alenos quirais ríxidos con polímeros helicoidales como PPA. Por último, mediante estudos de ECD, DSC, AFM e cálculos teóricos, puidéronse obter importantes parámetros estruturais relacionados coa súa estrutura secundaria para ambos sentidos de xiro. Estes resultados indican que a combinación de interruptores moleculares, química supramolecular e polímeros pode dar lugar a diferentes mecanismos de indución helicoidal a través de estruturas complexas, o que permite unha mellor comprensión de como se pode transferir a información a través de diferentes niveis de complexidade.

Capítulo 3.3. Engrenaxes Macromoleculares Entrelazadas Mecánicamente: Control da Elongación e Sentido Helicoidal dun Polímero Helicoidal Actuando sobre un Rotaxano Quiral Usado como Grupo Colgante

A natureza utiliza o denominado "bottom-up approach", é dicir, aproximación ascendente, para crear sistemas complexos nos que un pequeno fragmento dunha macromolécula adoita estar implicado nun proceso estímulo-resposta que moitas veces resulta nun cambio na composición conformacional da macromolécula en conxunto. Nos polímeros helicoidais dinámicos, como os PPA, os cambios conformacionais nun grupo colgante quiral inducidos por estímulos externos transmítense de forma eficiente a través do espazo ata a columna vertebral do polieno, analogamente ao que ocorre na natureza.

Inspirados nesta información e á vista dos resultados obtidos a partir dos estudos do mecanismo de comunicación axial a helicoidal dos PAEPA (Capítulos 3.1. e 3.2.), deseñamos un sofisticado engrenaxe macromolecular que combina moléculas entrelazadas mecánicamente, é dicir, un rotaxano, e polímeros helicoidais dinámicos (PPAs). Para iso, sintetizouse un derivado de PPA cun rotaxano quiral como unidade monomérica. Seleccionouse un aleno quiral como eixe do rotaxano debido a súa quiralidade axial e a súa composición conformacionalmente restrinxida. Por último, dito eixe combinouse cun pequeno macrociclo como roda para construír o rotaxano final. Con este deseño buscábase analizar o efecto sobre a orientación relativa da roda con

respecto ao eixe quiral mediante estímulos externos, xa que a rotación da roda permitiría cambiar o volume relativo dos substituíntes respecto do eixe (aleno), para finalmente variar os seus efectos estéricos respecto ao esqueleto poliénico, ocasionando así un cambio conformacional no conxunto da macromolécula. Con este obxectivo, introduciuse un grupo triazol nun dos substituíntes do aleno ao formar o rotaxano que serve de punto de unión entre o eixe e o macrociclo, o cal está funcionalizado cunha bipiridina, cuxos nitróxenos dadores forman un enlace de hidróxeno co C–H do grupo triazol.

O rotaxano obxectivo sintetizouse cun moi bo rendemento e estudos de ROESY-RMN, xunto ca resolución da súa estrutura cristalina por raios X, permitiu confirmar a disposición da roda nunha conformación preferente estabilizada mediante o enlace de hidróxeno bipiridina-triazol. A continuación, procedeuse a estudos estímulo-resposta mediante a adición de estímulos externos que puideran romper dito enlace de hidróxeno conducindo a un cambio co-conformacional no rotaxano. Para elo empregáronse un ácido prótico (ácido fórmico) e unha sal de cobre con ligandos débiles [$Cu(MeCN)_4BF_4$]. Estudos de ECD, UV-vis e RMN permitiron elucidar dúas orientacións diferentes da roda con respecto ao eixe quiral dependendo do estímulo empregado, é dicir, dúas co-conformacións distintas. A continuación, leváronse a cabo os mesmos estudos no correspondente polímero. Os resultados amosan un sofisticado sistema de conmutación múltiple que permite alternar entre tres conformacións diferentes para a hélice (hélice *P* e hélices estiradas *P* e *M*), en función do estímulo aplicado e de maneira reversible. Polo tanto, este sistema demostra a capacidade de acadar tres conformacións helicoidais diferentes controlando a orientación da roda do rotaxano sen alterar o fragmento quiral. O aleno quiral terá sempre a mesma orientación relativa dos seus substituíntes, mostrando un comportamento cuasiestático debido á súa estabilidade conformacional. Non obstante, a introdución dun macrociclo para formar o rotaxano nun dos substituíntes do aleno altera a prioridade da orde de indución da hélice debido á propiedade dos subcompoñentes do rotaxano de moverse entre si, concretamente en canto á orientación da roda respecto ao eixe. Polo tanto, ó alterar esta orientación, a posición relativa dos substituíntes da roda con respecto á columna vertebral helicoidal cambia, dando lugar a unha orde diferente ditada pola nova disposición. Por último, imaxes de AFM do polímero permitiron obter información acerca da estrutura secundaria do

mesmo, como o paso de hélice e o sentido de xiro da hélice externa, revelando unha conformación *cis-transoide* do esqueleto poliénico.

Polo tanto, este traballo mostra como os pequenos cambios estruturais nunha molécula entrelazada mecanicamente pódense amplificar ao ser incorporados nunha macromolécula como unidade monomérica dunha hélice polimérica dinámica. Continúanse realizando esforzos nesta liña co fin de incrementar a funcionalidade e complexidade do sistema.

Capítulo 3.4. Polímeros Supramoleculares baseados en Alenos Axialmente Quirais

Os polímeros supramoleculares caracterízanse por posuír un carácter dinámico e reversible. Estas propiedades, inherentes a este tipo de polímeros, sonlle conferidas pola natureza non covalente dos enlaces que unen as unidades monoméricas, o que permite aplicalos en diversos campos científicos. En xeral, as unidades monoméricas adoitan estar compostas por núcleos planos π-conxugados, que permiten interaccións π-π entre eles, funcionalizados con cadeas laterais parafínicas ou glicoladas, que aseguran a estabilidade do polímero supramolecular no medio de agregación desexado. Outras das interaccións débiles que adoitan contribuír na estabilización destas estruturas son os enlaces de hidróxeno ou as interaccións de Van der Waals. A introdución da quiralidade nas cadeas laterais xeralmente promove a adopción de armazóns helicoidais supramoleculares. Concretamente, a estratexia mais amplamente empregada para a indución da asimetría consistiu clasicamente na introdución de quiralidade puntual nas cadeas laterais solubilizantes.

Unha estratexia pouco explorada para a obtención de polímeros supramoleculares quirais é a polimerización de unidades tridimensionais non planas, especialmente aquelas con quiralidade axial ou helicoidal. Estas moléculas quirais teñen unha estrutura tridimensional moi distorsionada e bastante ríxida que non facilita o seu ensamblado. Non obstante, nos últimos anos esta estratexia está emerxendo co obxectivo de aumentar a diversidade dos bloques de construción quirais para a construción de novos materiais supramoleculares. Os alenos quirais, pese a que foron exitosamente empregados na construción de materiais quirais funcionais, non foron estudados en polímeros supramoleculares.

Neste capítulo abórdase a polimerización supramolecular de alenos axialmente quirais favorecendo o seu autoensamblaxe mediante a introdución de grupos agregantes baseados en etilendiamidas conectadas mediante un grupo gálico a cadeas parafínicas. Estes grupos estabilizan os agregados supramoleculares ao proporcionar interaccións adicionais como enlaces de hidróxeno, π-π e Van der Waals.

Estudos mediante diferentes técnicas (ECD, UV-vis, IR, NMR, AFM e estudos computacionais) empregando un disolvente que favorece o estado disolto ($CHCl_3$) e un disolvente que promove o estado agregado (MCH), amosaron resultados que son indicativos da formación dun agregado quiral supramolecular en MCH. Ademais, nestes estudos observouse que os agregados presentan unha quiralidade que se opón á quiralidade axial do aleno — (*P*)-aleno, (*M*)-agregado; (*M*)-aleno, (*P*)-agregado—. En cambio, a autoensamblaxe e a interdixitación paralela dos agregados xera estruturas máis grandes similares a fibras. Nestes agregados, a quiralidade da fibra está ditada pola quiralidade axial do aleno, empregado como núcleo central do bloque de construción. Finalmente, co obxectivo de elucidar o mecanismo de polimerización supramolecular, realizáronse experimentos de ECD a temperatura variable. Ditos estudos experimentais, permitiron concluír que o mecanismo de polimerización seguido polo sistema supramolecular é un mecanismo cooperativo.

Polo tanto, este traballo aborda un interesante mecanismo de indución de hélices supramoleculares de axial a axial mediante a autoensamblaxe de bloques de construción non planos, que abre un novo horizonte no deseño de materiais supramoleculares quirais, aumentando a diversidade de bloques de construción quirais e, polo tanto, as propiedades do agregado asociado ao bloque de construción.

Chapter 1. Introduction

Chapter 1. Introduction

Section 1.6.1. of this chapter is reproduced with the permission of RSC from the following Chemical Society Reviews publication:

María Lago-Silva,[a] Manuel Fernández-Míguez,[a] Rafael Rodríguez,[a] Emilio Quiñoá,[a] Félix Freire,[a]* Stimuli-responsive synthetic helical polymers, *Chem. Soc. Rev.* **2024**, *53*, 793 – 852. DOI: 10.1039/D3CS00952A.

Affiliations

[a]Centro Singular de Investigación en Química Biolóxica e Materiais, Moleculares (CiQUS) and Departamento de Química Orgánica, Universidade de Santiago de Compostela E-15782 Santiago de Compostela (Spain)

1.1. Chirality

Chirality is a property that describes the asymmetry of those objects that are non-superimposable with their mirror images, called enantiomers. Molecules and molecular systems can be chiral by asymmetrically arranging atoms in space around a center, an axis, or a plane, leading to point, axial, and planar chirality, respectively. Not only covalently bonded molecules with defined configuration and conformation but also non-covalently interacting supramolecular assemblies with conformational flexibilities and even transient molecular conformations can form chiral structures or architectures.

1.1.2. Chirality in nature

Chirality is present in artificial constructions and utensils, such as spiral staircases or simple screws. However, chirality is a natural property, and it is present in living beings, such as some plants (Figure 1a), the shells of many animals (Figure 1b) or our own hands and feet. The modern relevance of chiral molecules stems predominantly from the presence of homochirality in biological systems. In this sense, a chiral supramolecular sensing event may deeply affect the nature of one part, or several parts, or even the whole of a multicomponent assembly. This interesting phenomenon can be found in many natural systems, such as the α-helix structure of proteins[1] and in the DNA double helix[2]. The helicity of these biomolecules is imposed by the homochiral nature of their constitutive *L*-aminoacids (proteins) or *D*-carbohydrates (DNA).[3] Moreover, these helical structures can assemble into superstructures in living organisms (coiled-coil helix bundle proteins, DNA superhelices, or protein-DNA hybrid superstructures)(Figure 1c,d), [4,5] which are responsible for vital functions such as genetic information storage, replication, ion transport, recognition processes, or asymmetric chemical transformations

[1] L. Pauling; R. B. Corey, H. R. Branson, *Proc. Natl. Acad. Sci.* **1951**, *37*, 205–211.

[2] J. D. Watson, F. H. C. Crick, *Nature* **1953**, *171*, 737–738.

[3] Y. Dorca, E. E. Greciano, J. S. Valera, R. Gómez, L. Sánchez, *Chem. Eur. J.* **2019**, *25*, 5848–5864.

[4] W. W. C.Topley, G. S. Wilson, L. H. Collier, A. Balows, M. Sussman, *Topley & Wilson's Microbiology and Microbial Infections: Systematic Bacteriology*; A Hodder Arnold Publication: Arnold, **1998**.

[5] J. R. Schnell, J. J. Chou, *Nature* **2008**, *451*, 591–595.

among others.[6],[7],[8] This has led to the need to produce molecules in enantiopure form for biological applications.

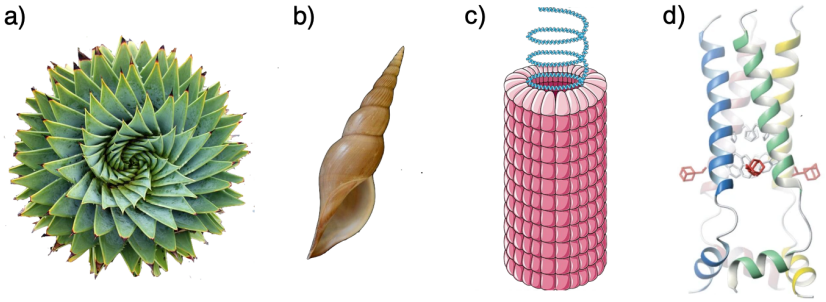

Figure 1. (a) Aloe polyphylla . (b) Molusc shell. (c) Cartoon representation of helical capsid of the tobacco virus. (d) Structure of the M2 trans-membrane protein (reproduced from ref. 5 with permission from Springer Nature, copyright 2008).

Chirality also led to development of theories of chemical structure. For instance, Pasteur's discovery of the optical activity of sodium ammonium tartrate crystals[9,10] triggered the independent recognition by Le Bel and Van't Hoff that the constituents surrounding a tetravalent carbon center are located at the corners of a tetrahedron.[11,12] Since then, the chiral covalent stereogenic units covering axial, planar and helical motifs, as well as stereogenic centers, have been extensively studied.[13] However, the origin of homochirality in nature remains partially unknown at present. It is unclear whether this feature serves a specific purpose, although some theories suggest a connection to information storage.[14] An alternative hypothesis is based on the observation that the creation of highly organized and substantial molecules lowers entropy barriers. This

[6] B. Alberts, A. Johnson, J. Lewis, D. Morgan, M. Raff, K. Roberts, P. Walter, *Molecular Biology of the Cell*, 6th ed.; Garland Science: New York, **2014**.

[7] W. Saenger, *Principles of Nucleic Acid Structure*, 1st ed.; Springer-Verlag: New York, **1984**, p 556.

[8] G. E. Schulz, R. H. Schrimer, *Principles of Protein Structure*, 1st ed.; Springer-Verlag: New York, **1979**.

[9] L. Pasteur, *Ann. Chim. Phys. Sér.* **1848**, *24*, 442–459.

[10] J. Gal, *Nat. Chem.* **2017**, *9*, 604–605.

[11] J. H. Van't Hoff , *Arch. Need. Sci. Exactes Nat.*,**1874**, *9*, 445-454.

[12] J. A. Le Bel, *Bull. Soc. Chim. Fr.* **1874**, *22*, 337.

[13] G. A. Hembury, V. V. Borovkov, Y. Inoue, *Chem. Rev.* **2008**, *108*, 1–73.

[14] J. D. Carroll, *Chirality* **2009**, *21*, 354–358.

phenomenon has been confirmed empirically with amino acids, which tend to form larger aggregates from enantiopure substrates than racemic mixtures.[15]

1.1.3. Sources of Chirality

In molecular systems, chirality can arise from chiral covalent stereogenic units comprising axial, planar and helical motifs, in addition to stereogenic centers[16] (Figure 2). The absolute stereochemistry of all these motifs (except for the helical) is assigned using variations of the systems originally developed by Cahn, Ingold and Prelog[17].

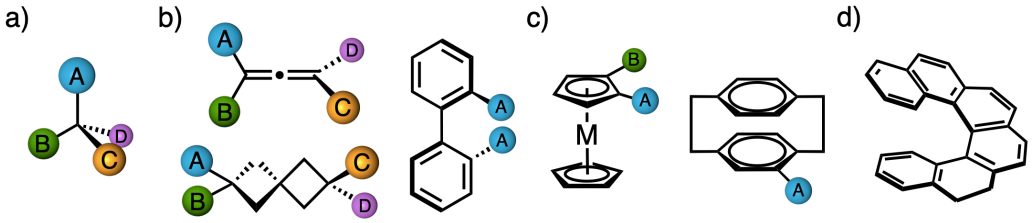

Figure 2. Schematic representation of molecules containing different chiral motifs. (a) chiral point, (b) chiral axes (substituents not all necessaryly different), (c) chiral planes and (d) helical stereogenic elements.

1.1.3.1. Point Chirality

Point chirality is usually considered the most fundamental form of chirality. In this case, the chirality arises from the different substituents attached three-dimensionally to a central atom giving rise to a C_1 symmetry for the whole molecule (for example, four different substituents around a sp^3 carbon atom). The relative spatial arrangement of these substituents, according to the Cahn-Ingold-Prelog priority rule system (CIP rules) for the assignment of absolute configurations, can result either in a clockwise spatial order or in an anticlockwise spatial order. These correspond to the *R* (*Rectus*, Latin for right) and *S* (*Sinister*, Latin for left) enantiomers, respectively, which allow us to name and distinguish both enantiomers of non-superimposable mirror images of a chiral molecule. Moreover, the presence of more than one chiral center in the same molecule can give place to diastereoisomers (Figure 3).

[15] R. R. Julian, S. Myung, D. E. Clemmer, *J. Phys. Chem. B* **2005**, *109*, 440–444.

[16] E. Eliel, S. H. Wilen, L. Mander, *Stereochemistry of Organic Compounds*, John Wiley and Sons, Inc., New York, **1994**.

[17] R. S. Cahn, C. Ingold, V. Prelog, *Angew. Chem. Int. Ed. Engl.* **1966**, *5*, 385–415.

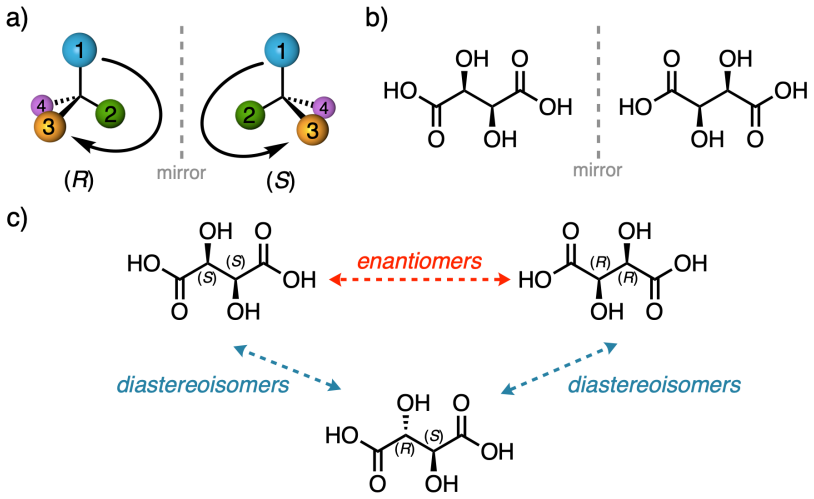

Figure 3. (a) Chiral center representation and sssignment of chirality according to the CIP rules: colors mean different substituents. (b) Chemical structure of tartaric acid enantiomers. (c) Stereoisomers of tartaric acid, showing both enantiomers and diastereoisomers.

1.1.3.2. Axial Chirality

Axial chirality emerges from the presence of a chiral axis, which is a physical or imaginary line in a molecule containing four groups located in two different planes in pairs where rotation is restricted or locked (Figure 4).

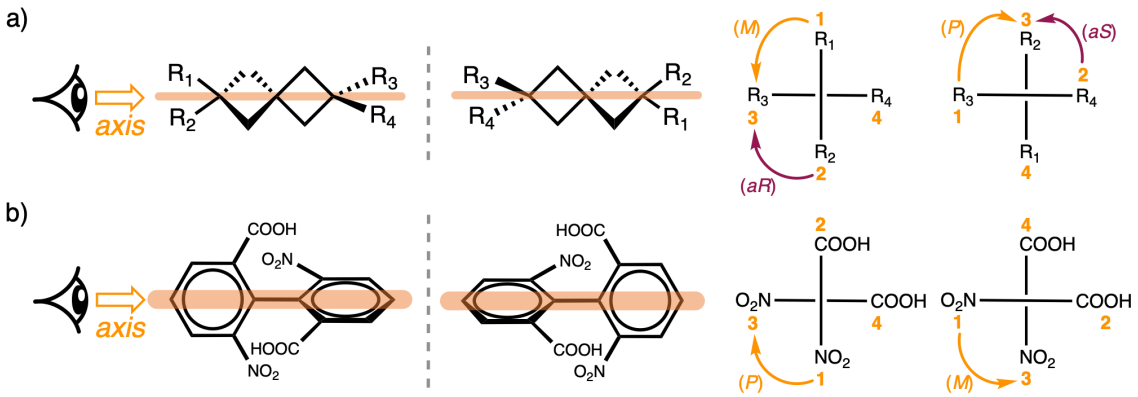

Figure 4. Examples of axially chiral structures and their respective projections along the chiral axis with priority number and corresponding chirality assignment: (a) a chiral spiro-compound and (b) a chiral biphenyl.

Axial chirality is also present in helical molecules, known as helical chirality. The helix is present in natural systems with important biological functions, such as DNA, [18]

[18] P. L. Privalov, C. Crane-Robinson, *Prog. Biophys. Mol. Biol.* **2018**, *135*, 30–48.

the α-helix of proteins and polysaccharides[19]. This structural motif is also present in artificial systems like foldamers, supramolecular polymers,[20] covalent polymers,[21] and non-planar single molecules (e.g., helicenes) (Figure 5). Here, the chirality arises from the unidirectional nature of the twist propagation along the long axis of the molecule or assembly.[13] Therefore, a clear distinction must be made between configurational and conformational chirality. The latter arises from the arrangement of part or all molecule or assembly under a chiral influence that removes any element of symmetry from it. In this case, the direction of rotation is determined by looking from either end along the helical axis; it is called *P* helicity if the rotation is clockwise and *M* helicity if the rotation is counterclockwise (Figure 5, bottom-right).

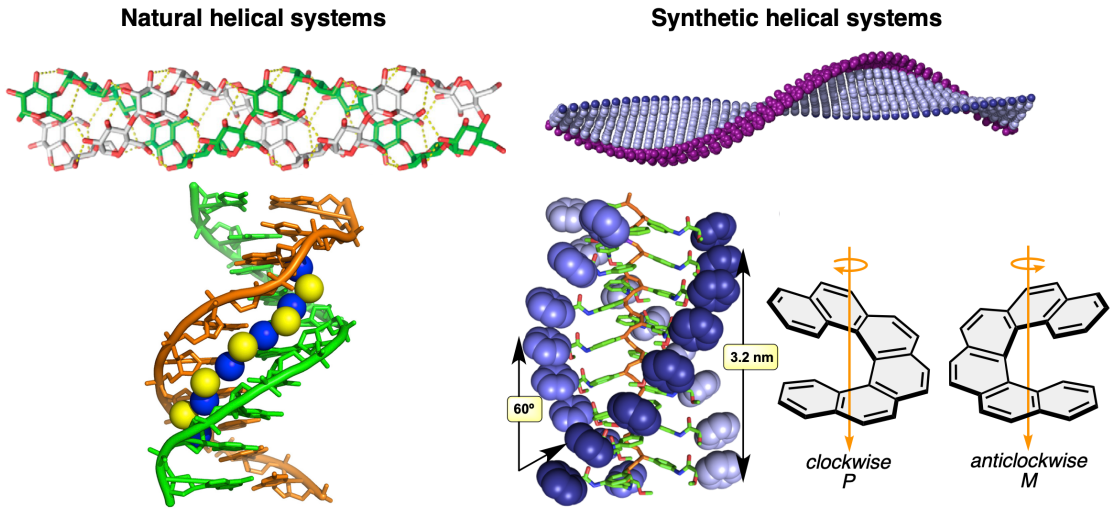

Figure 5. Examples of natural and synthetic helical systems. Left, from the top to the bottom, A-amylose polysaccharide (top-left; reproduced from ref. 19 with permission from Elsevier, copyright 2019) and DNA dodecamerfragments interact with water molecules (bottom-left; reproduced from ref. 18 with permission from Elsevier, copyright 2018). Right, supramolecular synthetic polymer (top-right; reproduced from ref. 20 with permission from John Wiley and Sons, copyright 2021), covalent synthetic polymer (bottom-right; reproduced from ref. 21 with permission from American Chemical Society, copyright 2016), and hexahelicene enantiomers (bottom right).

[19] V. V. Vu, J. A. Hangasky, T. C. Detomasi, S. J. W. Henry, S. T. Ngo, E. A. Span, M. A. Marletta, *J. Biol. Chem* **2019**, *294*, 12157–12166.

[20] Z. Fernández, B. Fernández, E. Quiñoá, F. Freire, *Angew. Chem. Int. Ed*. **2021**, *60*, 9919–9924.

[21] R. Rodríguez, E. Quiñoá, R. Riguera, F. Freire, *J. Am. Chem. Soc*. **2016**, *138*, 9620–9628.

1.1.3.2.1. Allenes

One of the best-known axially chiral building blocks is the allene group, the common name given to hydrocarbons containing two consecutive double bonds (Figure 6a), being the smallest members of the family of cumulenes.[22] In 1875, Van't Hoff predicted that the substituents of allenes must be placed in two perpendicular planes, whose hypothesis was experimentally confirmed by Maitland and Milss in 1935. The presence of this 90º twist around the central *sp*-hybridized carbon atom (Figure 6b), allenes are axially chiral when appropriately substituted. That is, if the substituents of each pair are different from each other, two non-superimposible mirror images are possible and, therefore, two enantiomers can be identified (Figure 6a). In this sense, CIP rules are used to assign priority to the substituents giving preference to the substituents in front respect to the rear substituents.[23] To determine the turning sense, 1-2-3 pathway is followed. If the sense is clockwise the enantiomer is assigned as *aR* and if it is anticlockwise the enantiomer is *aS*. Axially chiral enantiomers can also be assigned by the descriptors *P* (plus) to clockwise sense, and *M* (minus) to anticlockwise sense. In this case, the rotating sense is determined by going from the most priority substituent in front to the most priority substituent on the back, omitting the lower priority substituents in both pairs (Figure 6c).

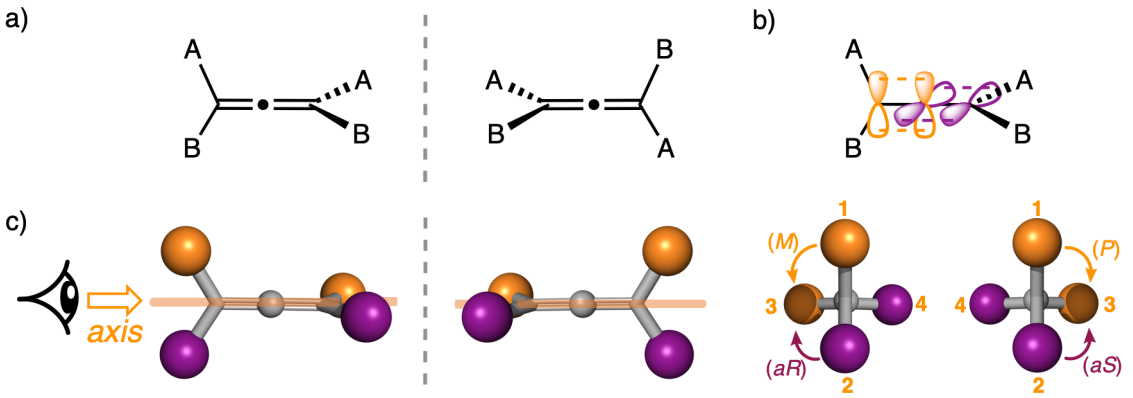

Figure 6. (a) Structure of a pair of enantiomers of a chiral allene. (b) Classical orbital description of allenes. (c) Descriptors for axial chirality of a pair of enantiomers of a chiral allene.

[22] G. P. Moss, P. A. S. Smith, D. Tavernier, *Pure Appl. Chem*. **1995**, *67*, 1307–1375.
[23] V. Prelog, G. Helmchen, *Angew. Chem. Int. Ed. Engl*. **1982**, *21*, 567–583.

The structural features of allenes make them attractive shape-persistent chiral scaffolds to build up chiral compounds of higher complexity. Nevertheless, the inherent instability of allenes makes them initially poorly suited for synthesis. However, in recent decades, the development of stable allenic building blocks has made them very versatile intermediates in organic chemistry.[24] The most popular methods for preparing substituted allenes are metal-catalyzed syntheses. Among them, SN2' reactions of propargylic electrophiles, 1,4-addition to enynes, and 1,6-addition to acceptor-substituted enynes stand out.[25]

In 1988, Alberts and Wynberg reported the isolation of a trimethylsilyl-protected 1,1,3-triethynylallene.[26] However, it was not until a decade later, after intense synthetic effort[27] that Diederich and co-workers described the synthesis of the first stable 1,3-diethynylallene (**DEA**).[28] These **DEA**s were prepared through a palladium-mediated SN2' regioselective type reaction between the (±)-bispropargylic precursor and triisopropylsilylacetylene (Figure 7). Futhermore, the most convenient method to resolve enantiomers of **DEA** was to use High Performance Liquid Chromatography (HPLC) and a chiral stationary phase (CSP), that requires fewer synthetic operations.[29]

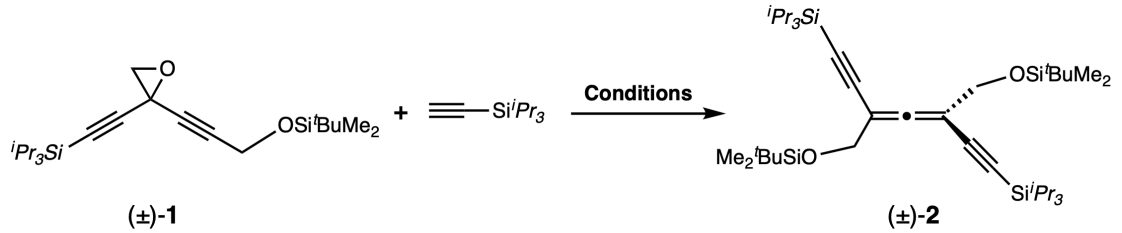

(±)-**1** (±)-**2**

Figure 7. Synthesis of the first stable DEA ((±)-**2**). Conditions: 1.[Pd(PPh$_3$)$_4$], CuI, DIPA, DCM, 25 ºC; 2. ^{t}BuMe$_2$SiCl, imidazole, DMAP, 25ºC (52%). DIPA = HN^{i}Pr$_2$; DMAP = 4-(dimethylamino)pyridine. Reproduced from ref. 28 with permission from John Wiley and Sons, copyright 2001.

The wide tolerance of **DEA**s to different substituents led to the synthesis of several stable **DEA**s during the following years.[24] The key point to improve the stability of the

[24] P. Rivera-Fuentes, F. Diederich, *Angew. Chem. Int. Ed.* **2012**, *51*, 2818–2828.

[25] N. Krause, A. Hoffmann-Röder, *Tetrahedron* **2004**, *60*, 11671–11694.

[26] A. H. Alberts, H. Wynberg, *J. Chem. Soc., Chem. Commun*. **1988**, 748-749.

[27] T. Lange, J. D. van Loon, R. R. Tykwinski, M. Schreiber, F. Diederich, *Synthesis* **1996**, 537–550.

[28] R. C. Livingston, L. R. Cox, V. Gramlich, F. Diederich, *Angew. Chem. Int. Ed*. **2001**, *40*, 2334–2337.

[29] J. L. Alonso-Gómez, P. Schanen, P. Rivera-Fuentes, P. Seiler, F. Diederich, *Chem. Eur. J.* **2008**, *14*, 10564–10568.

allenes is the introduction of two bulky substituents, often *tert*butyl groups, at both ends of the allene (Figure 8). Such bulky substituents protect the highly reactive cummulenic carbon from nucleophilic attacks and prevent interaction with other molecules. Thus, this design solved the major instability problem that allenes had presented up to that time. In addition, the two *tert*butyl groups also improved the solubility of the derived compounds in organic solvents, which had been another problem encountered.

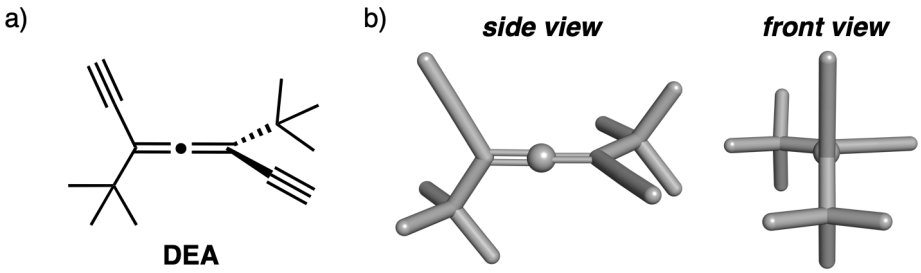

Figure 8. (a) Chemical structure and (b) 3D representation of 1,3-di-*tert*-butyl-diethynylallene.

Since the first successful report of the synthesis and chiral separation of enantiopure **DEA**s, derivatizations of these allenes have been increasingly used as all-carbon building blocks with high configurational stability and unique chiroptical properties.[30] Following the construction and study of homochiral macrocycles, molecular cages and acyclic oligomers,[31-35] **DEA**s were also introduced into more complex supramolecular assemblies (Figure 9).[36, 37] Moreover, the pronounced chiral

[30] R. Livingston, L. R. Cox, S. Odermatt, F. Diederich, *Helv. Chim. Acta* **2002**, *85*, 3052–3077.

[31] J. L. Alonso-Gómez, P. Rivera-Fuentes, N. Harada, N. Berova, F. Diederich, *Angew. Chem. Int. Ed*. **2009**, *48*, 5545–5548.

[32] S. Castro-Fernández, I. R. Lahoz, A. L. Llamas-Saiz, J. L. Alonso-Gómez, M.-M. Cid, A. Navarro-Vázquez, *Org. Lett.* **2014**, *16*, 1136–1139.

[33] S. Castro-Fernández, J. Álvarez-García, L. García-Río, C. Silva-López, M. M. Cid, *Org. Lett.* **2019**, *21*, 5898–5902.

[34] S. Míguez-Lago, B. D. Gliemann, M. Kivala, M. M. Cid, *Chem. Eur. J.* **2021**, *27*,13352–13357.

[35] P. Rivera-Fuentes, J. L. Alonso-Gómez, A. G. Petrovic, F. Santoro, N. Harada, N. Berova, F. Diederich, *Angew. Chem. Int. Ed.* **2010**, *49*, 2247–2250.

[36] O. Gidron, M. Ebert, N. Trapp, F. Diederich, *Angew. Chem. Int. Ed.* **2014**, *53*, 13614–13618.

[37] O. Gidron, M. Jirásek, N. Trapp, M.-O. Ebert, X. Zhang, F. Diederich, *J. Am. Chem. Soc*. **2015**, *137*, 12502–12505.

characteristics of enantiopure alleno-acetylenes led to combine them with receptor motifs to develop chiral chemosensors.[38, 39]

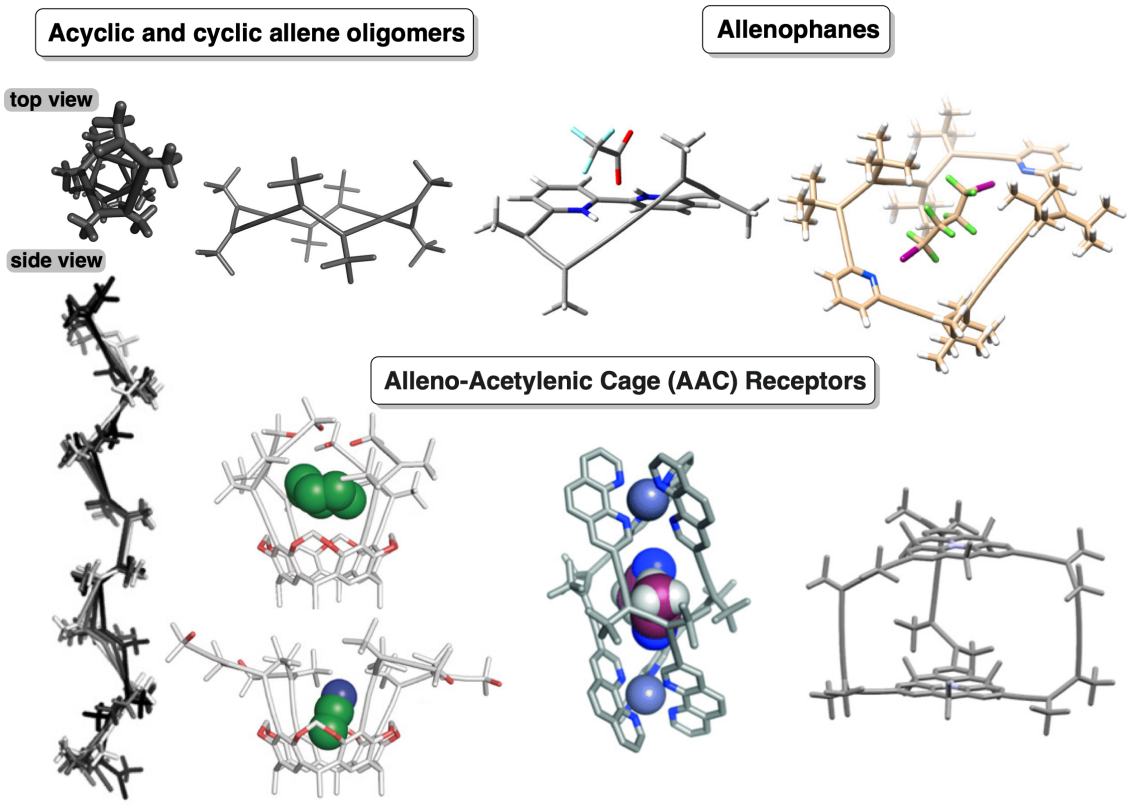

Figure 9. Top-left: Acyclic and cyclic allene oligomers (reproduced from ref. 35 with permission from John Wiley and Sons, copyright 2010; and reproduced from ref. 31 with permission from John Wiley and Sons, copyright 2009). Top-right: double protonation of [14$_2$]-bipyridoallenophane with TFA acid and X-ray crystal structure of [14$_1$]-pyridoallenophane forming an inclusion complex with $C_4F_8I_2$ (reproduced from ref. 33 with permission from American Chemical Society, copyright 2019; and reproduced from ref. 32 with permission from American Chemical Society, copyright 2014; respectively). Bottom-left: X-ray crystal structure of (*P*)$_4$-allenoacetylenic cages with closed (top) and open (bottom) configurations for molecular recognition (reproduced from ref. 38 with permission from John Wiley and Sons, copyright 2016). Bottom-center: metallorganic cage (reproduced from ref. 36 with permission from John Wiley and Sons, copyright 2014). Bottom right: a chiral alleno-acetylenic molecular cage (reproduced from ref. 34 with permission from John Wiley and Sons, copyright 2021).

[38] C. Gropp, N. Trapp, F. Diederich, *Angew. Chem. Int. Ed.* **2016**, *55*, 14444–14449.

[39] C. Gropp, S. Fischer, T. Husch, N. Trapp, E. M. Carreira, F. Diederich, *J. Am. Chem. Soc.* **2020**, *142*, 4749–4755.

1.1.3.3. Planar Chirality

Planar chirality is the chirality resulting from the arrangement of out-of-plane groups with respect to a relevance plane, named “chiral plane”.[16] Initially, molecules with planar chirality were considered a chemical curiosity and strategies for their asymmetric synthesis were uncommon. However, their presence in biologically active molecules (Figure 10a-c) and the discovery of their optoelectronic properties, together with the development of efficient and high-yielding synthetic methods to generate chiral derivatives (Figure 10e), are expanding the field and the area is still in the early stages of development.[40] The assignment of absolute configurations in planar-chiral molecules is based on the application of the standard CIP nomenclature rules[17] (Figure 5, bottom-right). The nomenclature of ‘(*Rp*)-isomer’ means that the *R* absolute configuration is based on ‘planar’ chirality (Figure 10b).

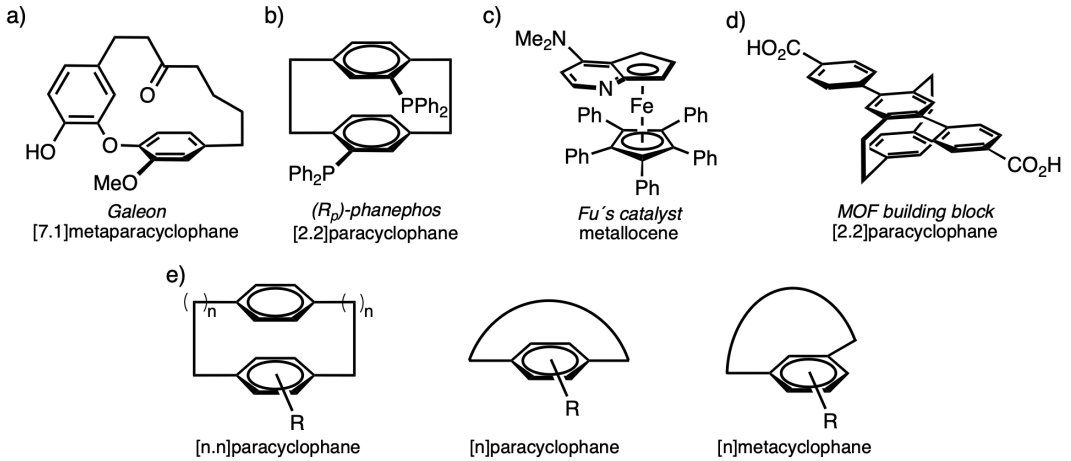

Figure 10. Selected examples of natural and artificial molecules exhibiting planar chirality only: (a) Galeon,[41] (b) (R_p)-phanaphos,[42] (c) Fu’s catalyst,[43] (d) MOF precursor;[44] and (e) frecuent cyclophanes prototypes with planar chirality. Reproduced from ref. 30 with permission from John Wiley and Sons, copyright 2022.

[40] R. López, C. Palomo, *Angew. Chem. Int. Ed.* **2022**, *61*, e202113504.

[41] K. E. Malterud, T. Anthonsen, J. Hjortås, *Tetrahedron Lett.* **1976**, *17*, 3069–3072.

[42] P. J. Pye, K. Rossen, R. A. Reamer, N. N. Tsou, R. P. Volante, P. J. Reider, *J. Am. Chem. Soc*. **1997**, *119*, 6207–6208.

[43] J. C. Ruble, H. A. Latham, G. C. Fu, *J. Am. Chem. Soc*. **1997**, *119*, 1492–1493.

[44] M. Cakici, Z.-G. Gu, M. Nieger, J. Bürck, L. Heinke, S. Bräse, *Chem. Commun.* **2015**, *51*, 4796–4798.

1.1.3.4. Mechanical Chirality

1.1.3.4.1. Mechanically Interlocked Molecules

Mechanically interlocked molecules (MIMs) are characterized by an entanglement in space between molecules or molecular parts. This entanglement can be present as a *mechanical bond* that links two or more molecular components, which cannot be separated without breaking or distorting the chemical bonds between atoms. The union of *n* subunits by mechanical bonds gives rise to the corresponding [n]catenanes, molecule with two or more interlocking ring-shaped component parts (Figure 11a); or [n]rotaxanes, molecules consisting of stoppered axle(s) components threaded through one or more macrocycles (Figure 11b).[45]

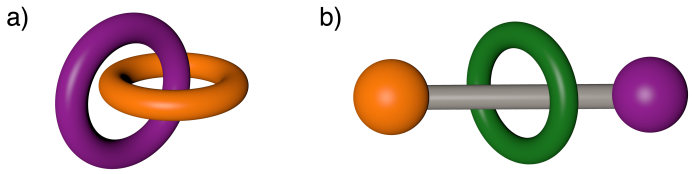

Figure 11. Examples of mechanically interlocked molecules: (a) [2]catenane; (b) [2]rotaxane.

A catenane or rotaxane may be chiral by the inclusion of a classical chiral motif, such as a chiral center, axis, or plane. However, chirality may arise as a direct result of the mechanical bond, even when the interlocked components are themselves achiral.[46,47] This may be described as “mechanical chirality”, a term recently defined by Bruns and Stoddart as “a non-classical form of chirality resulting from the spatial arrangements of component parts connected by mechanical bonds”.[45]

Thus, mechanical chirality can arise in [2]catenanes due to facially unsymmetric rings (Figure 12a) or in directionality in both rings (Figure 12b). Also, catenanes that have directionality in both rings can be referred to as topologically chiral.[45]

Mechanical chirality can appear in [2]rotaxanes from both the axle and the macrocycle, which are directional (Figure 12c). Moreover, mechanical motion can give rise to co-conformational chirality; the position of one component relative to the other (their co-conformation) can lead to desymmetrization of the molecule.[45] For example, a

[45] C. J. Bruns, J. F. Stoddart, *The Nature of the Mechanical Bond: From Molecules to Machines*; J. Wiley and Sons: Hoboken, NJ, **2016**.

[46] J. Niemeyer, N. Pairault, *Synlett* **2018**, *29*, 689–698.

[47] R. J. Bordoli, S. M. Goldup, *J. Am. Chem. Soc.* **2014**, *136*, 4817–4820.

macrocycle can be trapped on one side of the non-interlocked axle component where there would be a prochiral center, a form of atroposiomerism as shown in Figure 12d.

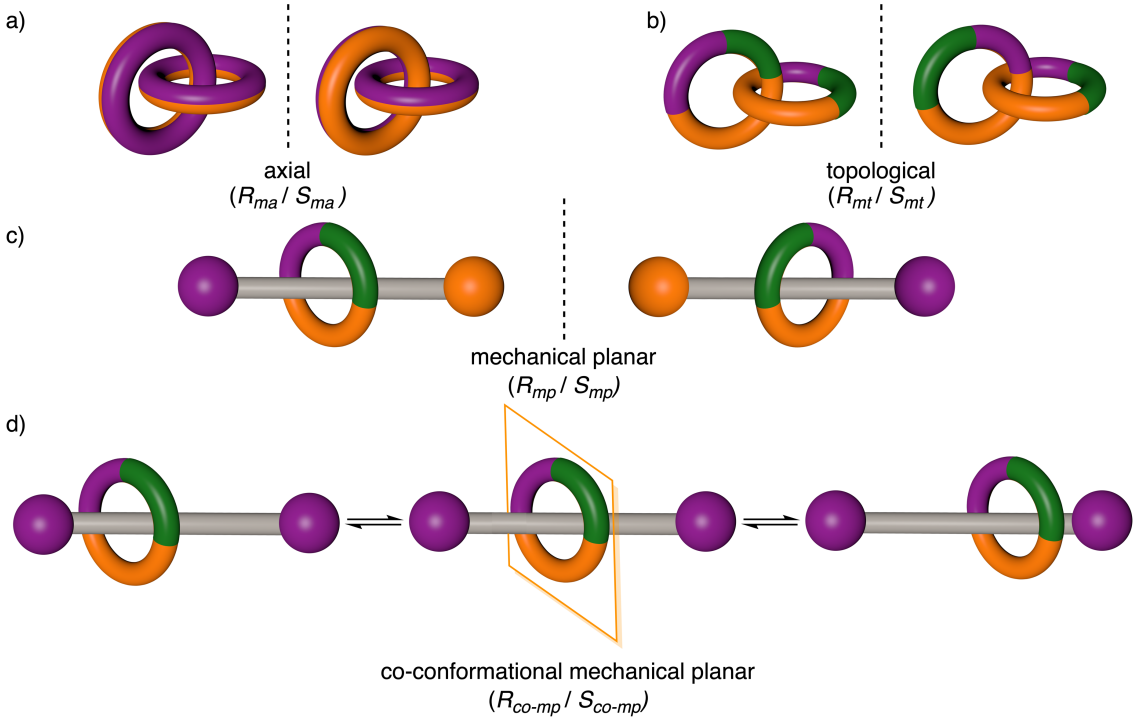

Figure 12. Schematic representations of enantiomers of [2]catenanes and [2]rotaxanes arising as aconsequence of the mechanical bond: (a) [2]catenane consisting of facially unsymmetric rings; (b) [2]catenane consisting of two directional rings; (c) [2]rotaxane consisting of directional ring and axle components and (d) [2]rotaxanes consisting of a ring trapped on one side of what would be a prochiral centre of the non-interlocked axle component.

Furthermore, the chiroptical properties of chiral interlocked molecules, which are in many cases distinct from those of the constituent subcomponents, are readily studied and provide not only an insight into their structures but also the opportunity to generate systems with switchable optical properties for materials applications.[48,49]

[48] E. M. G. Jamieson, F. Modicom, S. M. Goldup, *Chem. Soc. Rev*. **2018**, *47*, 5266–5311.

[49] A. H. G. David, R. Casares, J. M. Cuerva, A. G. Campaña, V. Blanco, *J. Am. Chem. Soc.* **2019**, *141*, 18064–18074.

1.1.3.4.1.1. Templated synthesis approach to Mechanically Interlocked Molecules

The synthesis of MIMs has progressed a long way since the development of template-directed methods,[50] pioneered by Sauvage[51] and Stoddart.[52] In these methods, the precursors to the interlocked structure are organized in relation to one another in space through non-covalent interactions such that, when a final covalent bond is formed, the components become permanently entangled, resulting in a mechanical bond. Thus, this approach relies on the formation of a thermodynamically stable, suitably pre-organized complex between the covalent components (Figure 13a, intermediate III). The interlocked architecture is then captured by a final covalent bond-forming reaction (the stoppering process) that is, to a first approximation, independent of the threading state of the molecule. This previously "passive" template approach has been expanded into an "active" form in which the functionality of a macrocycle is able to mediate the formation of a new covalent bond. Since bond formation takes place more rapidly through the ring cavity than elsewhere in the solution, this "active template" (AT)[53-55] results in threaded products and thus can be used for mechanical bond formation under kinetic control (Figure 13b).

[50] J. E. M. Lewis, P. D. Beer, S. J. Loeb, S. M. Goldup, *Chem. Soc. Rev*. **2017**, *46*, 2577–2591.

[51] C. O. Dietrich-Buchecker, J. P. Sauvage, J. P. Kintzinger, *Tetrahedron Letters* **1983**, *24*, 5095–5098.

[52] P. R. Ashton, T. T. Goodnow, A. E. Kaifer, M. V. Reddington, A. M. Z. Slawin, N. Spencer, J. F. Stoddart, C. Vicent, D. J. Williams, *Angew. Chem. Int. Ed. Engl*. **1989**, *28*, 1396–1399.

[53] J. D. Crowley, S. M. Goldup, A.-L. Lee, D. A. Leigh, R. T. McBurney, *Chem. Soc. Rev*. **2009**, *38*, 1530.

[54] M. Denis, S. M. Goldup, *Nat. Rev. Chem*. **2017**, *1*, 0061.

[55] J. E. M. Lewis, R. J. Bordoli, M. Denis, C. J. Fletcher, M. Galli, E. A. Neal, E. M. Rochette, S. M. Goldup, *Chem. Sci.* **2016**, *7*, 3154–3161.

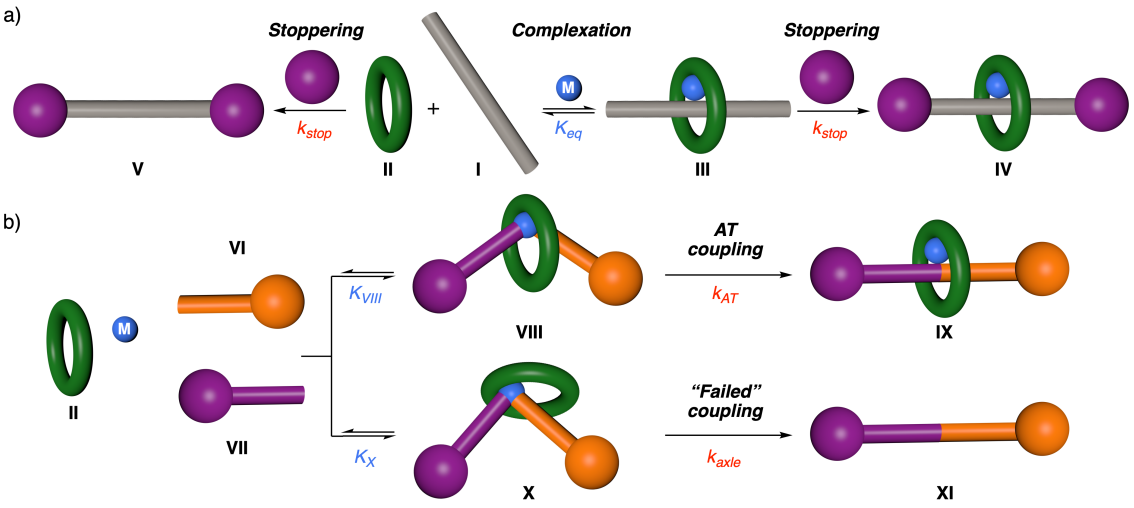

Figure 13. (a) Schematic representation of the metal ion [M]-directed passive template approach to rotaxanes by stoppering, showing the key steps that determine selectivity. K_{eq} is the equilibrium constant for the complexation between unthreaded pre-axle I, macrocycle II and M; and k_{stop} is the rate constant for the stoppering of intermediate III to form product IV. (b) Schematic representation of the AT approach to rotaxanes showing the key steps that determine selectivity. K_{VIII} is the equilibrium constant for the formation of VIII; k_{AT} is the rate constant for the conversion of VIII to IX; K_X is the equilibrium constant for the formation of X; and k_{axle} is the rate constant for the conversion of X to XI. Reproduced from ref. 54 with permission from Springer Nature, copyright 2017.

Looked at in this way, the active template phenomenon is kinetically driven, with the selectivity for the threaded product depending on the same factors that determine selectivity in catalytic processes: the position of the pre-equilibrium between the starting materials and activated complexes (for example, figure 13b VIII and X), the relative rates with which these complexes progress towards the products and any background reactions that compete with the desired bond formation.

The active template approach to interlocked molecules is, potentially, much more tolerant to modifications of the macrocycle structure than approaches based on thermodynamically stable complexes (Figure 13).[53-55] Bipyridine macrocycles are particularly effective in this approach, and for this reason Goldup and coworkers have developed an optimized, flexible synthesis of these building blocks that can be readily scaled to produce gram quantities of these useful starting materials.[55] Given the scalability of both the synthesis of this family of macrocycles and the mechanical bond formation step, combined with the potential to extend the application to more complex molecules, the active template reaction mediated by bipyridine macrocycles clearly has

a promising future in the synthesis of interlocked architectures for a wide variety of applications.[54]

1.2. Molecular and Macromolecular Switches

The complexity of biosystems has inspired the scientific community to develop molecular systems with increasing complexity to generate more elaborate stimuli-responsive materials,[56] such as those seen in living matter. Vital processes, such as metabolism, mutation, and even reproduction, occur through situations of disequilibrium that, at some point, require and produce a directed molecular movement carried out by the participation of biomolecular machinery.[57] Thus, various stimuli-responsive molecules and artificial materials undergo a change in their self-organization or assembly by the presence or absence of stimuli, and eventually, this leads to a change in their function and properties.[58] Therefore, the design and construction of individual molecules that change their conformation in a predictable manner in response to an external stimulus offers the opportunity to have control over a sub-nanometer scale world.[45]

A molecular switch simply changes (co-)conformations in response stimuli. So that, if the stimulus-response function is reversible, the function is called a "switch" and can produce a reversible change in functionality or property, rendering functionally “on” and “off” conformational states. However, machines and motors perform mechanical work. They move a system uphill in an energetic landscape. Accomplishing work in the molecular world is far from trivial and remains a contemporary challenge for chemistry. The mechanical bond is likely to play a fundamental role in molecular machines that convert heat, light, electricity, etc. into mechanical energy in the form of motion.[45]

Over the last decade, the field has flourished with the development of molecular and macromolecular switches that respond to stimuli as varied as ions,[59] light,[60,61] and redox

---

[56] E. R. Kay, D. A. Leigh, F. Zerbetto, *Angew. Chem. Int. Ed*. **2007**, *46*, 72–191.

[57] P. Luisi, Self-organization. *In The Emergence of Life: From Chemical Origins to Synthetic Biology*, Cambridge: Cambridge University Press, **2006**, 85–111.

[58] K. Kinbara, T. Aida, *Chem. Rev*. **2005**, *105*, 1377–1400.

[59] P. C. Knipe, S. Thompson, A. D. Hamilton, *Chem. Sci*. **2015**, *6*, 1630–1639.

[60] Y. Yu, M. Nakano, T. Ikeda, *Nature*, **2003**, *425*, 145.

[61] R. Klajn, *Chem. Soc. Rev*. **2014**, *43*, 148–184.

processes.[62] Potential applications for such systems include a wide variety of scenarios, such as catalysis,[63] organic light-emitting diodes,[64] receptors, drug delivery,[65] and others.

An interesting family of molecular switches are the so called "molecular torsion balance", which are simpler model compounds that provide information to rationalize conformational behavior.[66] The ability to alternate between two main relevant states in response to a stimulus provides a means of measuring intra- and inter- molecular forces, desolvatation and solvophofic effects by comparing different equilibrium positions (Figure 14).[67]

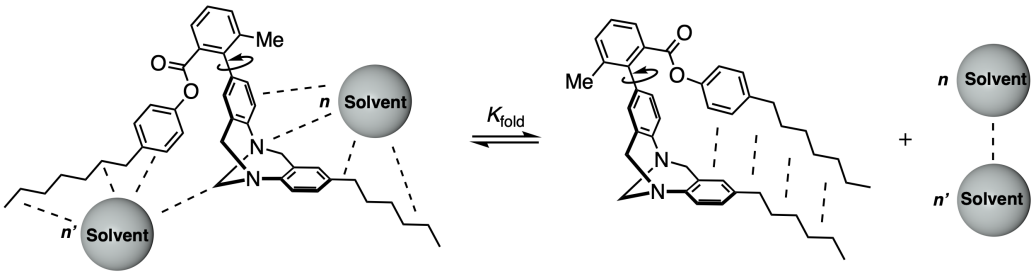

Figure 14. Folding equilibrium for molecular balance in solution. Reproduced from ref. 52 with permission from Springer Nature, copyright 2013.

1.2.1. Mechanically Interlocked Switches

A powerful family of molecular switches is one of MIMs, such as rotaxanes since the freedom of mobility of the sub-components is comparable to that of supramolecular systems. However, it is not possible to break the mechanical bond to release its components, unless the energy applied is high enough to break a covalent bond.[45] Thus, in addition to the structural characteristics, the stability of rotaxanes is remarkably high.

[62] I. Jones, P. Knipe, T. Michaelos, S. Thompson, A. Hamilton, *Molecules* **2014**, *19*, 11316–11332.

[63] B. M. Neilson, C. W. Bielawski, *ACS Catal*. **2013**, *3*, 1874–1885.

[64] X. Su, S. Voskian, R. P. Hughes, I. Aprahamian, *Angew. Chem. Int. Ed*. **2013**, *125*, 10934–10939.

[65] Y. B. Zheng, B. Kiraly, T. J. Huang, *Nanomedicine* **2010**, *5*, 1309–1312.

[66] S. Paliwal, S. Geib, C. S. Wilcox, *J. Am. Chem. Soc*. **1994**, *116*, 4497–4498.

[67] L. Yang, C. Adam, G. S. Nichol, S. L. Cockroft, *Nat. Chem.* **2013**, *5*, 1006–1010.

So far, various rotaxane molecular switches have been reported.[68-70] One of the most enticing properties of rotaxanes is the ability of their subcomponents to move relative to each other. Both translational (shuttling) and rotational (pirouetting) motion have been exploited in the functioning of molecular switches based on MIMs.[71-74] Figure 15 shows the work of Leigh and co-workers in which they prepared a simple two-station molecular shuttle consisting of one axle component bearing two stations with different levels of attractive interactions with the wheel component. Each attractive interaction must be strong enough to fix the position of the wheel component at the respective station, but this can be modulated by the appropriate stimulus to realize the shuttling (Figure 15a). Perturbation of the binding energies of any of the stations results in the redistribution of the macrocycle toward a new equilibrium state, as driven by thermal motion. Changing the position of the macrocycle in a well-determined way is possible, by making the binding affinity of the less occupied station more favorable (Figure 15b, transformation of station B to B'), or by destabilizing the interaction between the most occupied station and the macrocycle (Figure 15b, transformation of station A to A').[71]

[68] J. F. Stoddart, *Angew. Chem. Int. Ed*. **2014**, *53*, 11102–11104.

[69] A. Caballero, F. Zapata, P. D. Beer, *Coord. Chem. Rev*. **2013**, *257*, 2434–2455.

[70] D. Dattler, G. Fuks, J. Heiser, E. Moulin, A. Perrot, X. Yao, N. Giuseppone, *Chem. Rev*. **2019**, *120*, 310–433.

[71] S. Erbas-Cakmak, D. A. Leigh, C. T. McTernan, A. L. Nussbaumer, *Chem. Rev*. **2015**, *115*, 10081–10206.

[72] C. Pezzato, C. Cheng, J. F. Stoddart, R. D. Astumian, *Chem. Soc. Rev*. **2017**, *46*, 5491–5507.

[73] L. Zhang, V. Marcos, D. A. Leigh, *Proc. Natl. Acad. Sci. U.S.A*. **2018**, *115*, 9397–9404

[74] A. W. Heard, S. M. Goldup, *ACS Cent. Sci*. **2020**, *6*, 117–128.

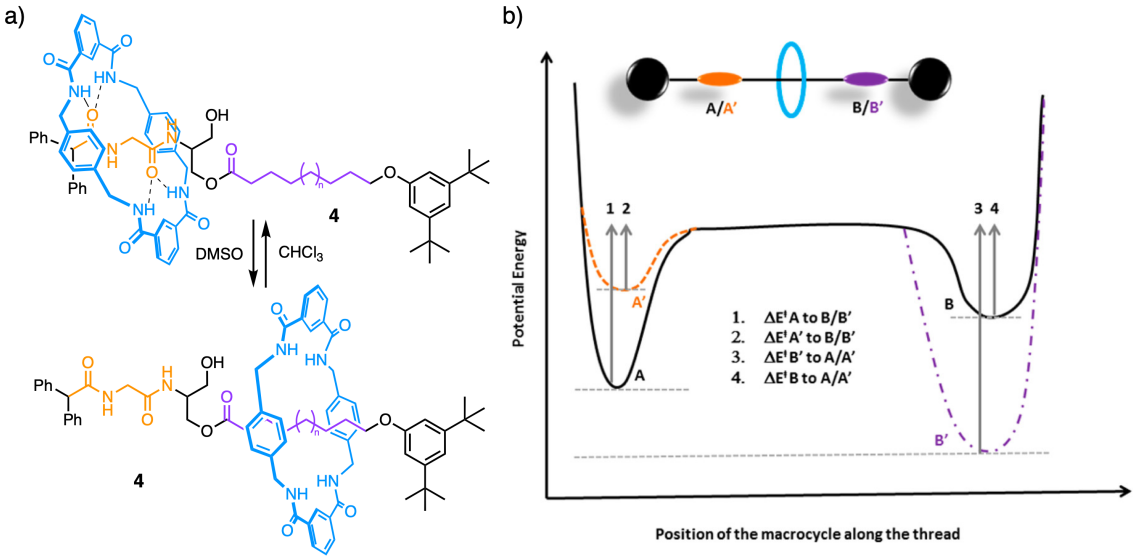

Figure 15. (a) Solvent-dependent shuttling in a [2]rotaxane (**4**). (b) Potencial energy diagram of a rotaxane-based bistable molecular shuttle. Reproduced from ref. 71 with permission from American Chemical Society, copyright 2015.

Molecules containing rotaxane-linked units frequently exhibit unique properties that have not been previously reported. Among them, the most illustrative example may be the "molecular elevator" developed by Stoddart and coworkers.[75,76] By combining three rotaxane units consisting of crown ether wheels and sec-ammonium shafts with additional bipyridinium stations, the acid/base treatment produces an elevator-like motion through efficient switching of the three rotaxane units (Figure 16).

[75] J. D. Badjić, V. Balzani, A. Credi, S. Silvi, J. F. Stoddart, *Science* **2004**, *303*, 1845–1849.

[76] J. D. Badjic, C. M. Ronconi, J. F. Stoddart, V. Balzani, S. Silvi, A. Credi, *J. Am. Chem. Soc.* **2006**, *128*, 1489–1499.

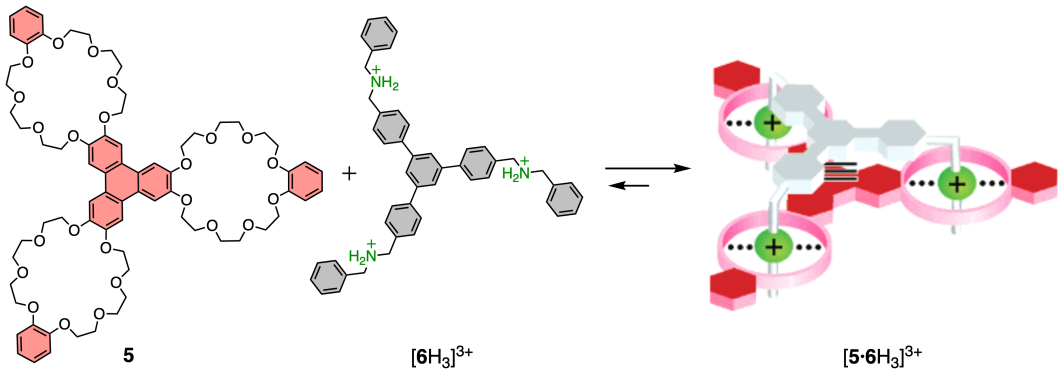

Figure 16. Chemical structure of the molecular elevator components: tris-crown ether **5** and the tris-ammonium ion [**6**H$_3$]$^{+3}$ and and the equilibrium between the components and the superbundle [**5**·**6**H$_3$]$^{3+}$, which lies to the right in favor of the superbundle in solvents. Reproduced from ref. 76 with permission from American Chemical Society, copyright 2006.

1.2.2. Switchable Polymeric Materials

Polymeric systems that are characterized by a reversible change in the secondary structure of the polymer and are accompanied by a change in chirality (e.g., helical inversion) can be classified as molecular switches. The chiral columns developed by Freire, Maeda, Yashima, and their colleagues are an outstanding example of macromolecular switches whose functionality can be altered by inverting the helical structure of the polymer.[77,78] They found that adding a metal cation (stimulus) to the mobile phase, the secondary structure of the polymer used a stationary phase column is inverted, affecting drastically to its affinity towards a pair of enantiomers (Figure 17). This novel design represents remarkable progress in the fabrication of modulable columns for enantiomeric resolution.

[77] K. Shimomura, T. Ikai, S. Kanoh, E. Yashima, K. Maeda, *Nat. Chem.* **2014**, *6*, 429–434.
[78] D. Hirose, A. Isobe, E. Quiñoá, F. Freire, K. Maeda, *J. Am. Chem. Soc.* **2019**, *141*, 8592–8598.

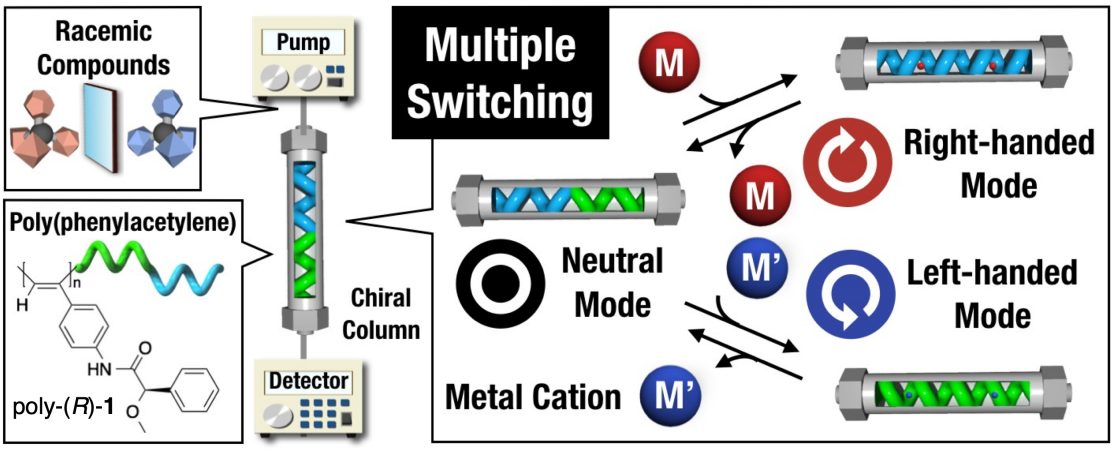

Figure 17. Application of poly-(*R*)-**1**/M^{n+} as multiple-switch chiral stationary phase. Reproduced from ref. 78 with permission from American Chemical Society, copyright 2019.

Another outstanding example of switchable polymeric material is the polymer-based highly enantioselective organocatalysts developed by Yashima and co-workers.[79] They described several catalysts for asymmetric synthesis based on the macromolecular optically activity of dynamic PPA derivatives. Thus, they synthesized a series of poly-(biarylylacetylene) composed of axially chiral but racemic 2-arylpyridyl-*N*-oxide monomeric units with *N*-oxide moieties close to the polymer backbone. The resulting PPA (poly-**2**) is enantioselective deracemized with a chiral alcohol [(*R*)- or (*S*)-1-phenylethane-1,2-diol (**7**)] that induces a preferred helical sense. This effect is maintained by the memory effect after the stimulus removal and is also accompanied by a chiral amplification phenomenon. Finally, the resulting helicity-memorized poly-**2** showed high enantioselectivity for the asymmetric allylation of benzaldehyde (Figure 18).

[79] T. Ikai, M. Ando, M. Ito, R. Ishidate, N. Suzuki, K. Maeda, E. Yashima, *J. Am. Chem. Soc.* **2021**, *143*, 12725–12735.

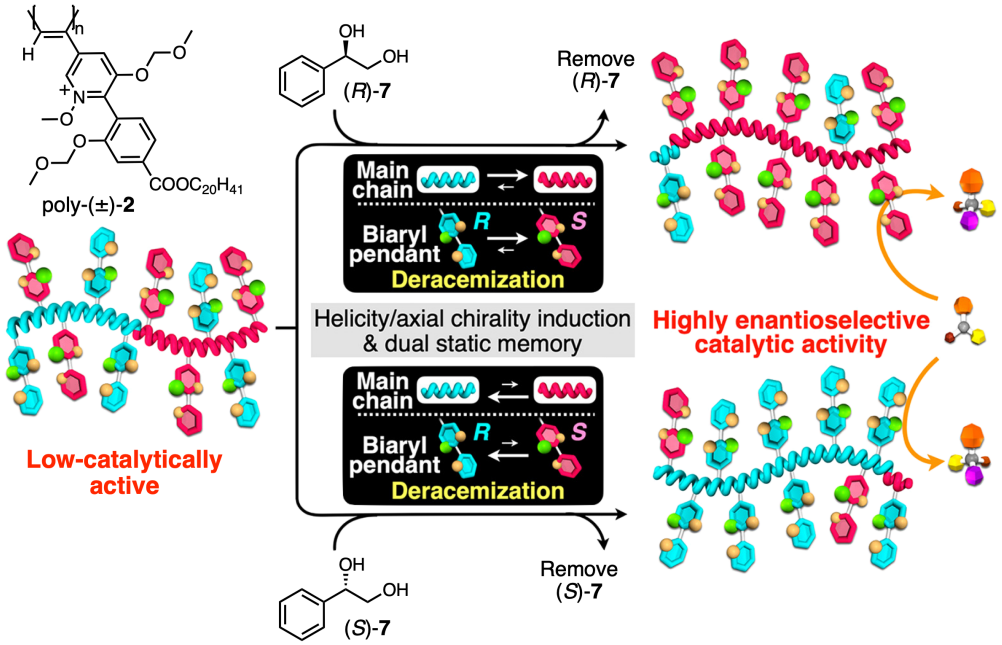

Figure 18. Structure of racemic poly-(±)-**2** and schematic illustration of its emergent highly enantioselective catalytic activity. Reproduced from ref. 79 with permission from American Chemical Society, copyright 2021.

1.2.2.1. Mechanically Interlocked Polymers (MIPs)

As a result of the combination of dynamic polymers with MIMs, mechanically interlocked polymers (MIPs) emerge to exploit their collective mechanical performance by properly integrating them into responsive materials for use in various applications. [80-84] Therefore, polyrotaxanes and polycatenanes have attracted interest in the polymer chemistry field because of the potential benefit of the large ranges of motion allowed by mechanically bonded components.[85,86] Especially, polyrotaxanes are of particular interest as they are synthetically more accessible than polycatenanes.[84]

Various topologies of polyrotaxanes have been described. As shown in Figure 19, main-chain polyrotaxanes may consist of (a) a polymeric shaft with multiple threaded

[80] A. Tamura, N. Yui, *Polym. J.* **2017**, *49*, 527–534.
[81] Y. Arisaka, N. Yui, *J. Mater. Chem. B* **2019**, *7*, 2123–2129.
[82] Y. Cho, J. Kim, A. Elabd, S. Choi, K. Park, T. Kwon, J. Lee, K. Char, A. Coskun, J. W. Choi, *Adv. Mater.* **2019**, *31*, 1905048.
[83] P. Ding, L. Wu, Z. Lin, C. Lou, M. Tang, X. Guo, H. Guo, Y. Wang, H. Yu, *J. Am. Chem. Soc.* **2023**, *145*, 1548–1556.
[84] T. Takata, *ACS Cent. Sci.* **2020**, *6*, 129–143.
[85] N. Hoyas Pérez, J. E. M. Lewis, *Org. Biomol. Chem.* **2020**, *18*, 6757–6780.
[86] S. Mena-Hernando, E. M. Pérez, *Chem. Soc. Rev.* **2019**, *48*, 5016–5032.

macrocycles, (b) a [2]rotaxane polymerized through the macrocycle, (c) a [3]rotaxane polymerized through both macrocycles, or (d) a [2]rotaxane polymerized through both the macrocycle and the shaft. Alternatively, sidechain polyrotaxanes in which (e) the backbone or (f) macrocycle components are pendants of the polymer chain.

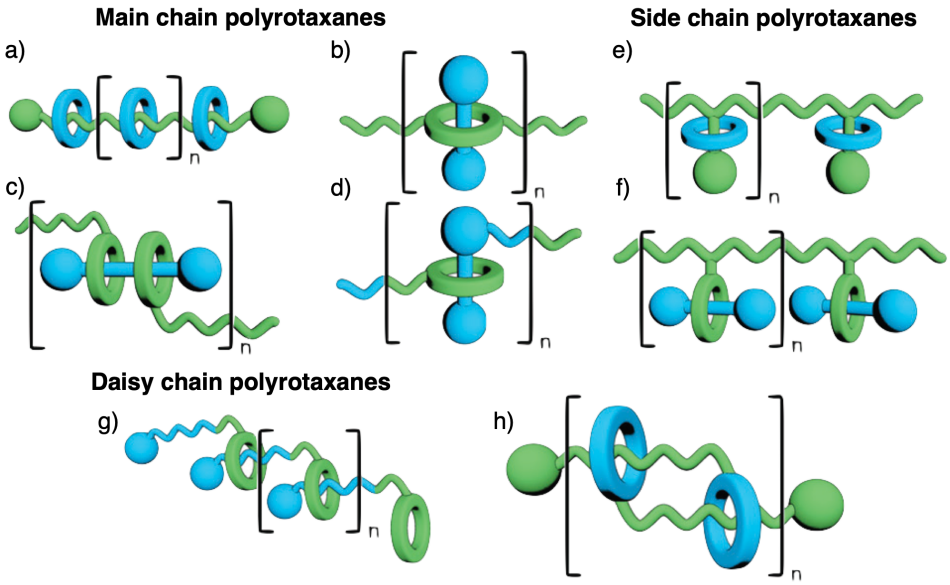

Figure 19. Cartoon diagrams of various polymeric rotaxanes and catenanes. Reproduced from ref. 85 with permission from the Royal Society of Chemistry, copyright 2020.

There are two main ways to prepare these materials: by forming mechanical bonds on a pre-formed polymer or by polymerizing a monomeric (pseudo)cross-linked unit. Polymerization of MIMs incorporating reactive functionalities suitable for polymerization reactions is ostensibly the simplest methodology. Numerous efficient templates for the synthesis of MIMs have been developed over the last decades, allowing access to a wide range of structures.[71, 87, 88] Therefore, the use of polymerizable monomers in which the mechanical bond is kinetically stable ensures that the precise ratio of monomer units and MIMs incorporated in the resulting polymer is known.

For example, Osakada and coworkers in 2009 reported a [2]rotaxane based on a dibenzo[24]crown-8-ether (DB24C8) with an acrylamide moiety added to one of the

[87] J. E. Beves, B. A. Blight, C. J. Campbell, D. A. Leigh, R. T. McBurney, *Angew. Chem. Int. Ed.* **2011**, *50*, 9260–9327.
[88] J. E. M. Lewis, P. D. Beer, S. J. Loeb, S. M. Goldup, *Chem. Soc. Rev.* **2017**, *46*, 2577–2591.

stoppers (Figure 20a).[89] Copolymerization with a range of substituted styrenes led to the successful formation of side-chain poly[n]rotaxanes in which the number of interlocked units could be effectively controlled by varying the ratio of rotaxane and styrene-monomers. However, homo-polymerization of this rotaxane was unsuccessful, likely due to the steric bulk of the macrocycle.

Sometime later, Takata and co-workers supported this approach as they were able to polymerize a switchable molecular shuttle in a helical polyacetylene if the macrocycle was located remotely from the polymerizable group.[90,91] Thus, they reported for the first time the control of the helical sense of polyacetylene by a molecular shuttle, i.e., a chiral [2]rotaxane monomer (Figure 20b).

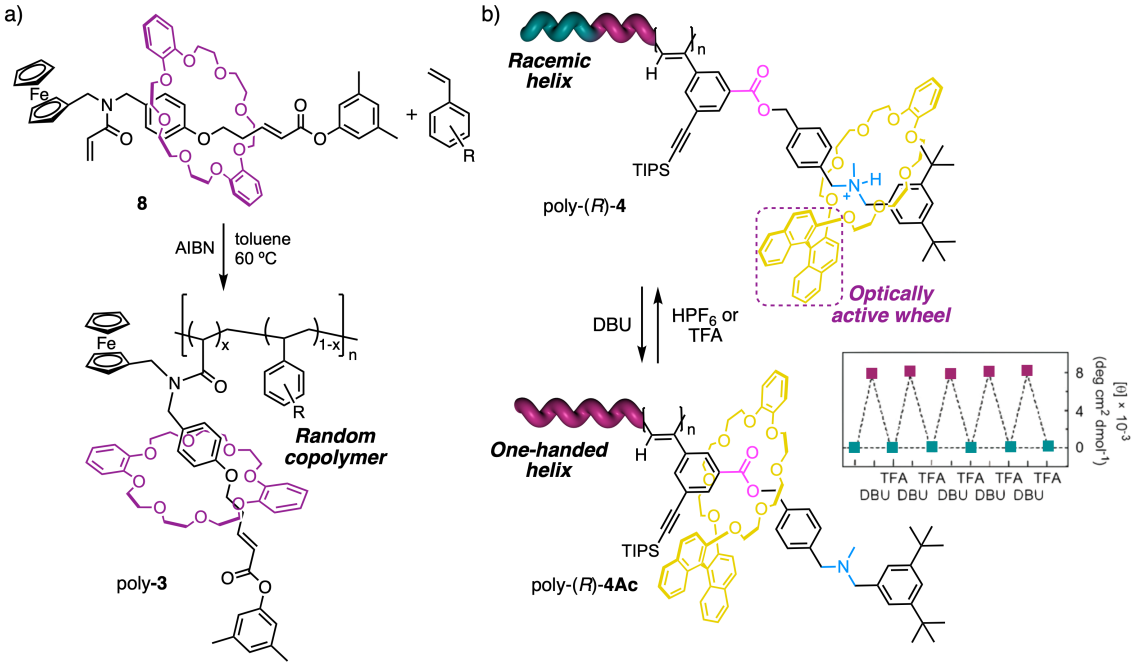

Figure 20. (a) Copolymerization of Osakada's acrylamide [2]rotaxane monomer with a range of substituted styrenes. (b) Helical control over a poly[2]rotaxane based on an acid/base switchable rotaxane with a chiral crown ether macrocycle based on BINOL. Reproduced from ref. 91 with permission from the Royal Society of Chemistry, copyright 2011.

In the protonated state, the macrocycle bearing the stereogenic binaphthyl unit occupies the ammonium station far from the polymer backbone due to H-bonding

[89] Y. Suzaki, S. Murata, K. Osakada, *Chem. Lett.* **2009**, *38*, 356–357.

[90] F. Ishiwari, K. Fukasawa, T. Sato, K. Nakazono, Y. Koyama, T. Takata, *Chem. Eur. J.* **2011**, *17*, 12067–12075.

[91] F. Ishiwari, K. Nakazono, Y. Koyama, T. Takata, *Chem. Commun.* **2011**, *47*, 11739–11741.

interactions, and the polymer chain adopts a random conformation (Figure 20b, top). As a result, no significant ECD signal is observed attributable to the polymer chain. Deprotonation of the ammonium unit results in the net displacement of the macrocycle towards the polymer backbone. This leads to an increased influence of the stereogenic unit in the macrocycle on the conformation of the polymer backbone and the appearance of a ECD signal associated with the polyacetylene moiety as it adopts a predominantly single-handed helical conformation (Figure 20b, bottom).

1.3. Helical Polymers

As mentioned earlier, helices are one of the most repeated structural motifs in nature and play a key role related to their inherent chirality. Thus, the helical structure found in biomacromolecules, such as DNA, peptides, or polysaccharides, is directly related to their important biological functions.[92-94]

Inspired by the natural helical systems, scientists have made a great effort to mimic the structures of biological helices and their functions. Non-natural helical polymers including supramolecular[95-98] and covalent helical

[92] E. Kervio, A. Hochgesand, U. E. Steiner, C. Richert, *Proc. Natl. Acad. Sci. U.S.A*. **2010**, *107*, 12074–12079.

[93] A. Brewer, A. P. Davis, *Nat. Chem*. **2014**, *6*, 569–574.

[94] B. Liu, C. G. Pappas, J. Ottelé, G. Schaeffer, C. Jurissek, P. F. Pieters, M. Altay, I. Marić, M. C. A. Stuart, S. Otto, *J. Am. Chem. Soc*. **2020**, *142*, 4184–4192.

[95] F. García, R. Gómez, L. Sánchez, *Chem. Soc. Rev*. **2023**, *52*, 7524–7548.

[96] E. Yashima, N. Ousaka, D. Taura, K. Shimomura, T. Ikai, K. Maeda, *Chem. Rev*. **2016**, *116*, 13752−13990.

[97] O. J. G. M. Goor, S. I. S. Hendrikse, P. Y. W. Dankers, E. W. Meijer, *Chem. Soc. Rev*. **2017**, *46*, 6621–6637.

[98] T. Aida, E. W. Meijer, S. I. Stupp, *Science* **2012**, *335*, 813–817.

polymers,[99-110] have been extensively studied during the last decades due to the possibility of creating a large variability of helical scaffolds with different functionalities by rational design. Thus, while the building blocks used by nature are limited, chemistry offers a wide range of chemical structures with different functionalities limited mainly by the creativity of the scientist.

Early examples in the birth of the field include the work reported by Nata et al. in 1955 in which he described the first synthetic helical polymer.[111] More in detail, he reported the helical structure in the solid state of an isotactic poly(propylene) (poly-**5**, Figure 21). This polymer showed equal populations of right and left-handed helices in the solid state, but once the polymer was dissolved, this helical structure disappeared and became random coil.

Inspired by this finding, Pino et al. developed in the 1960s a new series of poly(vinyl) (poly-**6**, Figure 21) polymers by polymerization of different chiral vinyl monomers,[112] where the inclusion of the chiral center in the monomer unit promoted for the first time the adoption of a helix with a predominant screw sense excess, which was determined by optical rotation.

---

[99] E. Schwartz, M. Koepf, H. J. Kitto, R. J. M. Nolte, A. E. Rowan, *Polym. Chem*. **2011**, *2*, 33–47.

[100] E. Yashima, K. Maeda, H. Iida, Y. Furusho, K. Nagai*, Chem. Rev*. **2009**, *109*, 6102–6211.

[101] J. Liu, J. W. Y. Lam, B. Z. Tang, *Chem. Rev*. **2009**, *109*, 5799–5867.

[102] B. M. Rosen, C. J. Wilson, D. A. Wilson, M. Peterca, M. R. Imam, V. Percec, *Chem. Rev.* **2009**, *109*, 6275–6540.

[103] E. Yashima, K. Maeda, Y. Furusho, *Acc. Chem. Res*. **2008**, *41*, 1166–1180.

[104] J. G. Rudick, V. Percec, *Acc. Chem. Res*. **2008**, *41*, 1641–1652.

[105] T. Nakano, Y. Okamoto, *Chem. Rev*. **2001**, *101*, 4013–4038.

[106] N. Liu, L. Zhou, Z.-Q. Wu, *Acc. Chem. Res*. **2021**, *54*, 3953–3967.

[107] Y. Nagata, R. Takeda, M. Suginome, *ACS Cent. Sci*. **2019**, *5*, 1235–1240.

[108] F. Freire, E. Quiñoá, R. Riguera, *Chem. Rev*. **2016**, *116*,1242–1271.

[109] Y. Wang, T. Harada, L. Q. Phuong, Y. Kanemitsu and T. Nakano, *Macromolecules* **2018**, *51*, 6865–6877

[110] J. J. L. M. Cornelissen, A. E. Rowan, R. J. M. Nolte, N. A. J. M. Sommerdijk, *Chem. Rev*. **2001**, *101*, 4039–4070.

[111] G. Natta, P. Pino, P. Corradini, F. Danusso, E. Mantica, G. Mazzanti, G. J. Moraglio, *J. Am. Chem. Soc*. **1955**, *77*, 1708–1710.

[112] P. Pino, G. P. Lorenzi, *J. Am. Chem. Soc*. **1960**, *82*, 4745–4747.

The breakthrough came in the 1970s when many research groups started working in the field of helical polymers. In 1974, Nolte et al. applied chiral stationary phase high-performance liquid chromatography (CSP-HPLC) for the first time to resolve poly(*tert*-butyl isocyanide) (poly-**7**, Figure 21) into left- and right-handed helices.[113] Later, in 1979, Okamoto et al. were the first to report the helix sense selective polymerization using achiral monomeric units and a chiral catalyst. Notably, this optically active polymer, derived from the triphenylmethyl metacrylate (TrMA) (poly-**8**, Figure 21), showed high specific rotation and was able to maintain its helical conformation in solution. Moreover, it showed relevant chiral recognition ability for racemic compounds, which allowed them to apply these polymeric materials as CSP for HPLC.[114]

Some years later, in 1988, Green and coworkers reported a new family of helical polymers, the poly(isocyanate)s (poly-**9**, Figure 21).[115] These new materials showed a structure composed of right-handed and left-handed helical conformations, connected by helical reversals, which could be modified by external stimuli through covalent or non-covalent interactions. This discovery triggered the study of a new family of polymers, the "dynamic helical polymers".

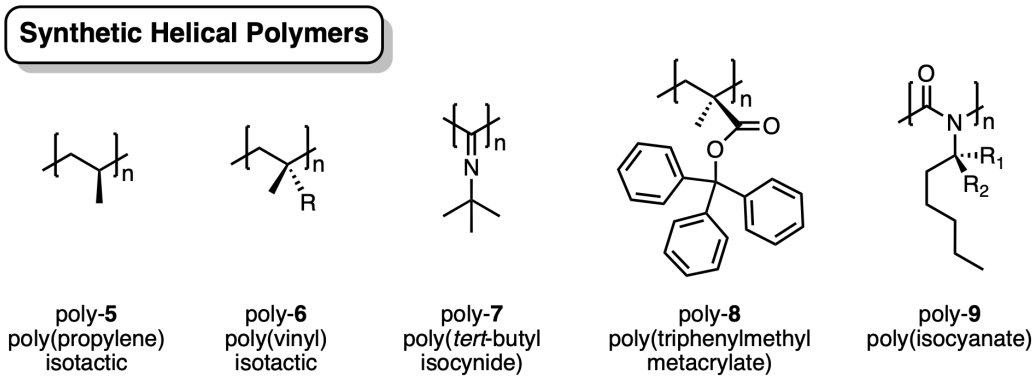

Figure 21. Structure of some of the earliest examples of synthetic helical polymers.

1.3.1. Classification of Helical Polymers

Helical polymers can be classified according to the interconversion energy barrier between the *P* and *M* helices into two main groups: static and dynamic helical polymers.

[113] R. J. M. Nolte, A. J. M., Van Beijnen, W. Drenth, *J. Am. Chem. Soc*. **1974**, *96*, 5932–5933.

[114] Y. Okamoto, K. Suzuki, K. Ohta, K. Hatada, H. Yuki, *J. Am. Chem. Soc.* **1979**, *101*, 4763–4765.

[115] M. M. Green, C. Andreola, B. Munoz, M. P. Reidy, K. Zero, *J. Am. Chem. Soc.* **1988**, *110*, 4063–4065.

In static helical polymers, a high helix inversion energy barrier leads to the formation of the polymer under kinetic conditions, and the incorporation of the monomer unit is blocked once it is added to the growing polymer chain. In contrast, dynamic helical polymers have a low interconversion energy barrier. Therefore, the helical sense can be modulated from *P* to *M*, or vice versa, by external stimuli.[100,110]

1.3.1.1. Static Helical Polymers

This class of polymers shows a preferred helical direction which is defined during the polymerization process. Thereby, optically active static helical polymers can be obtained by polymerizing optically active monomers or by using a chiral initiator or catalyst to polymerize an achiral or prochiral monomer (helical selective polymerization method).[116] The structural parameters of this family of polymers (helical sense and helical pitch) are determined by the chiral substituents covalently attached to the polymer main chain or by the chiral initiators or catalysts. Therefore, the resulting helical conformations cannot be modified and are stable even in solution. These polymers generally have bulky substituents with low conformational freedom. Representative examples are poly(methacrylate)s (poly-**10**), poly(methylacrylamide)s (poly-**11**) poly(quinoxaline-2,3-dyl)s (poly-**12**) or poly(guanidine)s (poly-**13**) (Figure 22).

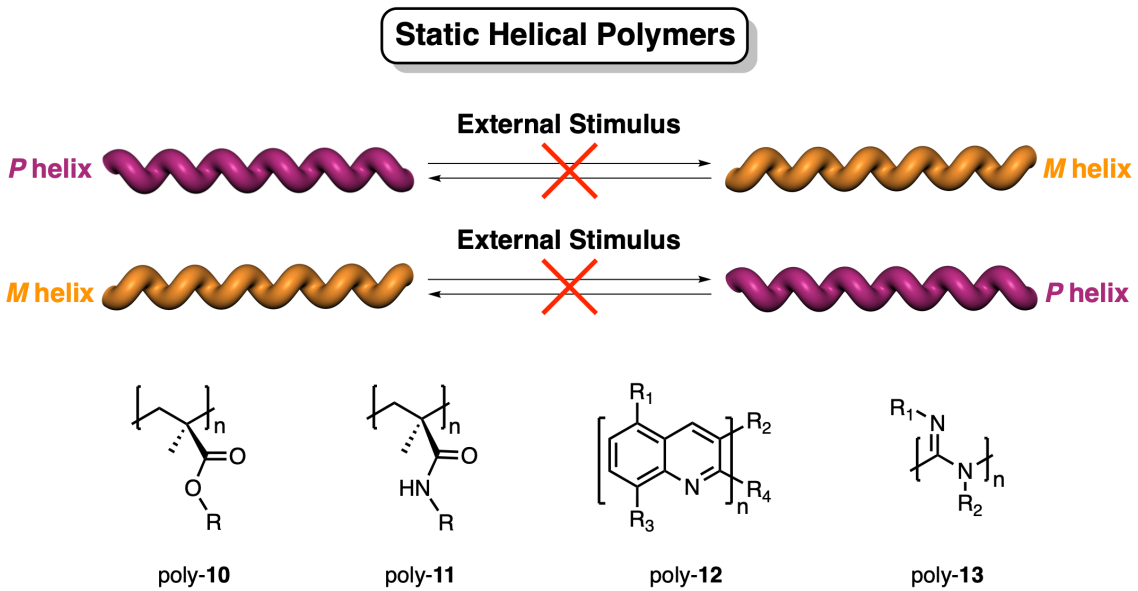

Figure 22. Conceptual representation and some representative scaffolds of static helical polymers.

[116] Y. Okamoto, T. Nakano, *Chem. Rev*. **1994**, *94*, 349–372.

1.3.1.2. Dynamic Helical Polymers

Dynamic helical polymers possess a low interconversion energy barrier, allowing the coexistence of two helical orientations within the polymer chain (*P* and *M*), separated by helical reversals. This equilibrium can be easily tuned by external stimuli, resulting in one-handed helical sense excess.

These polymers can be synthesized by polymerizing an optically active monomer[117] or by polymerizing an achiral monomer in the presence of a chiral solvent[118] or chiral additive.[119] This process results in a polymer with a dominant helical orientation, where the *P/M* equilibrium shifts toward the conformation that best accommodates the chiral inductor attached to the polymer. Some representative examples of this group are poly(isocyanate)s[100] (poly-**14**), poly(isocyanide)s[99] (poly-**15**), poly(silane)s[120-122] (poly-**16**), or poly(acetylene)s[123] (poly-**17**) (Figure 23).

[117] I. Louzao, J. M. Seco, E. Quiñoá, R. Riguera, *Angew. Chem. Int. Ed*. **2010**, *122*, 1472–1475.

[118] D. Lee, Y.-J. Jin, H. Kim, N. Suzuki, M. Fujiki, T. Sakaguchi, S. K. Kim, W.-E. Lee, G. Kwak, *Macromolecules* **2012**, *45*, 5379–5386.

[119] E. Yashima, K. Maeda, Y. Okamoto, *Nature* **1999**, *399*, 449–451.

[120] M. Fujiki, J. Organomet. Chem. **2003**, *685*, 15–34.

[121] M. Fujiki, *Macromol. Rapid Commun*. **2001**, *22*, 539–563.

[122] A. Ohira, M. Kunitake, M. Fujiki, M. Naito, A. Saxena, *Chem. Mater*. **2004**, *16*, 3919–3923.

[123] J. W. Y. Lam, B. Z. Tang, *Acc. Chem. Res*. **2005**, *38*, 745–754.

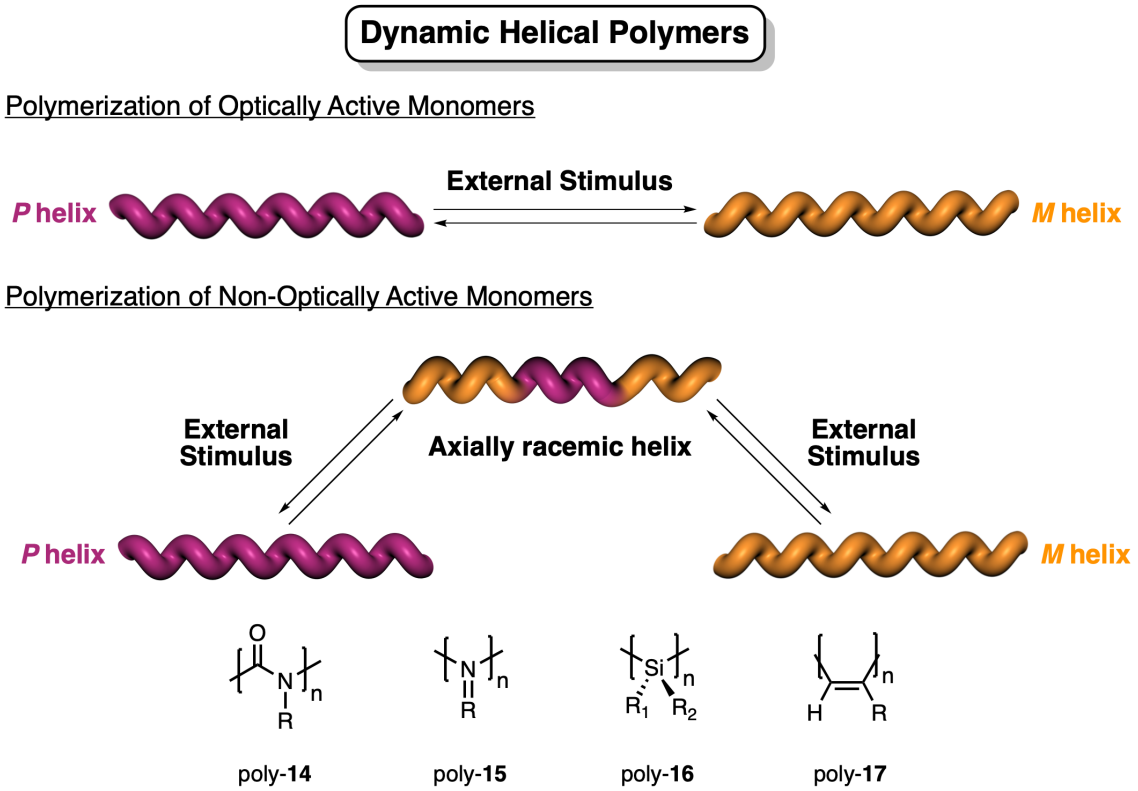

Figure 23. Conceptual representation and some representative scaffolds of the dynamic helical polymers.

1.4. Poly(phenylacetylene)s

Poly(phenylacetylene)s (PPAs) are one of the most studied dynamic helical polymers. They belong to the family of poly(acetylene)s (PAs), characterized by a π-conjugated backbone, whose pioneering application as conductive materials by Heeger, MacDiarmid, and Shirakawa was awarded the Nobel Prize in Chemistry in the year 2000.[124] Moreover, these materials are highly stable in solid state, as well as in solution, and can exhibit other unique optical and chiroptical properties, which make them suitable for applications such as CSP for HPLC,[77,78,125] sensors,[95-98,126] or asymmetric catalysts.[79,107,127]

[124] A. J. Heeger, *Rev. Mod. Phys.* **2001**, *73*, 681–700.

[125] Y. Zhou, C. Zhang, Q. Geng, L. Liu, H. Dong, T. Satoh, Y. Okamoto, *Polymer* **2017**, *131*, 17–24.

[126] S. Leiras, E. Suárez-Picado, E. Quiñoá, R. Riguera, F. Freire, *Giant* **2021**, *7*, 100068.

[127] Y. Nagata, T. Nishikawa, M. Suginome, *J. Am. Chem. Soc.* **2015**, *137*, 4070–4073.

PAs are easily prepared by polymerization of monomeric units having an alkyne moiety, including phenylacetylenes (**9**), propionic esters (**10**), propargyl esters (**11**), propargyl amides (**12**) or aliphatic acetylenes (**13**)(Figure 24a).[101] Among them, PPAs, that are derived from **9**, are the most studied due to their easy synthesis, high stereoregularity, and high molecular weight.[96]

In the polymerization process, the conjugated double bonds can adopt four possible configurations — *cis-cisoidal* (*c-c*), *cis-transoidal* (*c-t*), *trans-cisoidal* (*t-c*) or *trans-transoidal* (*t-t*) — (Figure 24b), but only *cis*- configurations will favor folding into the helical structure; otherwise, if the polymer adopts the *trans*- configurations, the helical scaffold cannot be formed.[128-130]

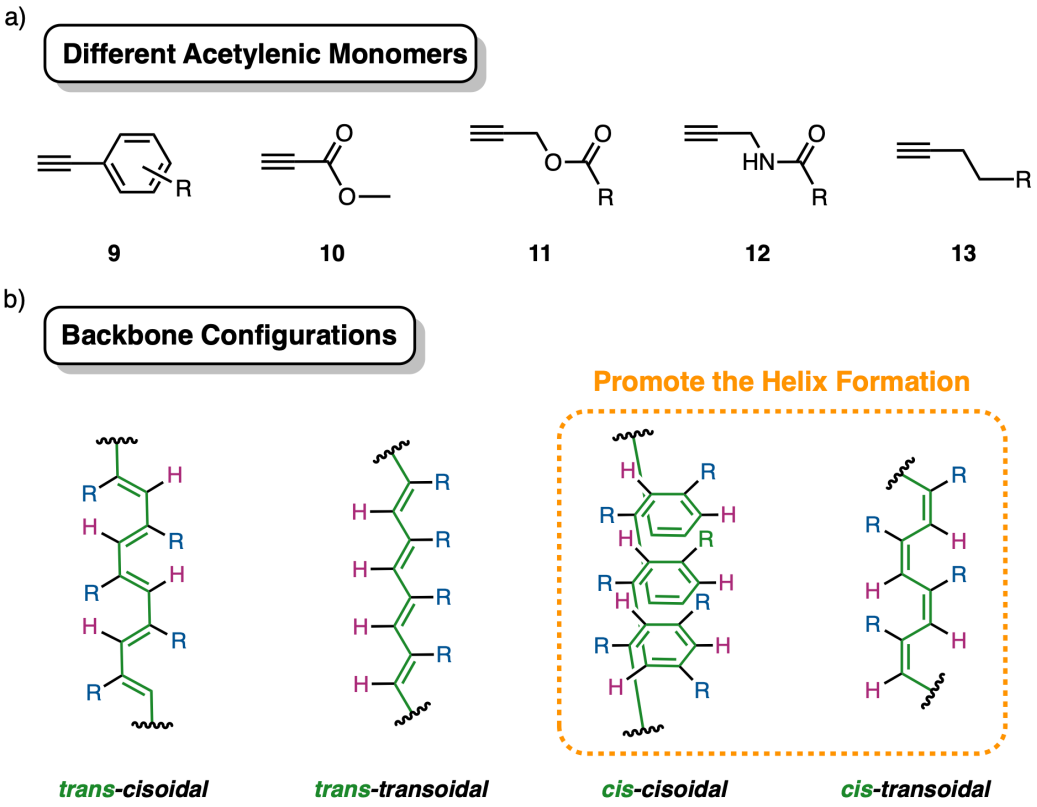

Figure 24. (a) Chemical structures of representative monomers of the PA family. (b) Possible configurations that the polyene backbone of the PAs can adopt.

[128] C. I. Simionescu, V. Percec, S. Dumitrescu, J. *Polym. Sci. Polym. Chem. Ed.*, **1977**, *15*, 2497–2509.

[129] C. I. Simionescu, V. Percec, *Prog. Polym. Sci.*, **1982**, *8*, 133–214.

[130] M. Tabata, T. Sone, Y. Sadahiro, *Macromol. Chem. Phys.* **1999**, *200*, 265–282.

In this sense, Noyori and coworkers developed powerful rhodium-based catalysts[131,132] that, through a stereospecific living polymerization, generate polymers in high yield, with low polydispersity and high content of *cis*- double bonds in the polyenic backbone. More specifically, the polymerization mechanism catalyzed by Rh(I) consists of a head-to-tail stereospecific and regioselective 2,1-insertion mechanism (Figure 25). This mechanism is produced by the steric repulsion between monomeric units, leading to a highly stereoregular polymer chain. More specifically, the polymerization mechanism catalyzed by Rh(I) consists of a head-to-tail stereospecific and regioselective 2,1-insertion mechanism. Different examples of these commercially available Rh(I) catalysts are $[Rh(nbd)Cl]_2$, $[Rh(cod)Cl]_2$, and $[Rh(cod)(BF_4)]$, among others, which are tolerant toward various functional groups and work well in a wide range of organic solvents and even in water.[133,134]

[131] Y. Kishimoto; P. Eckerle, T. Miyatake, T. Ikariya, R. Noyori, *J. Am. Chem. Soc.* **1994**, *116*, 12131–12132.
[132] K. Hirao, Y. Ishii, T. Terao, Y. Kishimoto, T. Miyatake, T. Ikariya, R. Noyori, *Macromolecules* **1998**, *31*, 3405–3408.

[133] Z. Ke, S. Abe, T. Ueno, K. Morokuma, *J. Am. Chem. Soc.* **2011**, *133*, 7926–7941.

[134] N. S. L. Tan, A. B. Lowe, *Angew. Chem. Int. Ed.* **2020**, *59*, 5008–5021.

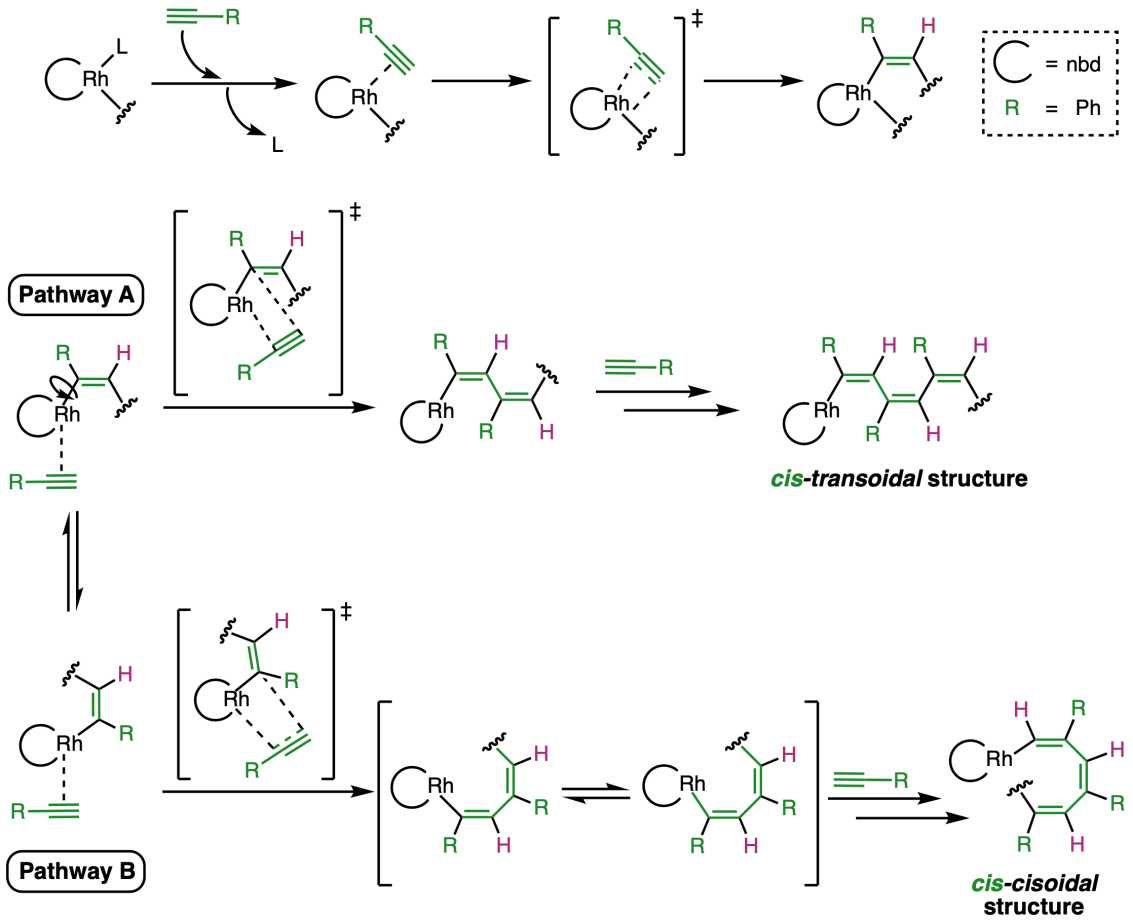

Figure 25. Proposed polimerization mechanism of the PPAs catalyzed by Rh(I). Reproduced from ref. 133 with permission from the American Chemical Society, copyright 2011.

Recently, Maeda and coworkers took a step forward in controlling the polymerization process of PPAs by means of a novel rhodium-based multicomponent catalytic system.[135] This catalytic system consists of commercially or readily available and laboratory-stable materials such as $[Rh(nbd)Cl]_2$, boronic acid derivatives, diphenylacetylene, 50% aqueous KOH and PPh_3. During the reaction, the boronic and diphenylacetylene components are introduced at the initiating end of the polymers, which provides a method to facilitate the synthesis of several end-functionalized PPAs with high *cis*-stereoregularity (Figure 26). In addition, the polymerization initiation efficiency is typically quantitative, and therefore the molecular weight of the polymers can be well controlled by the initial feed ratio ([monomer]/[Rh]). These synthetic breakthroughs pave

[135] T. Taniguchi, T. Yoshida, K. Echizen, K. Takayama, T. Nishimura, K. Maeda, *Angew. Chem. Int. Ed.* **2020**, *59*, 8670–8680.

the way towards fully controlled living polymerization, which is crucial for the application of developing polymers as highly sophisticated materials.

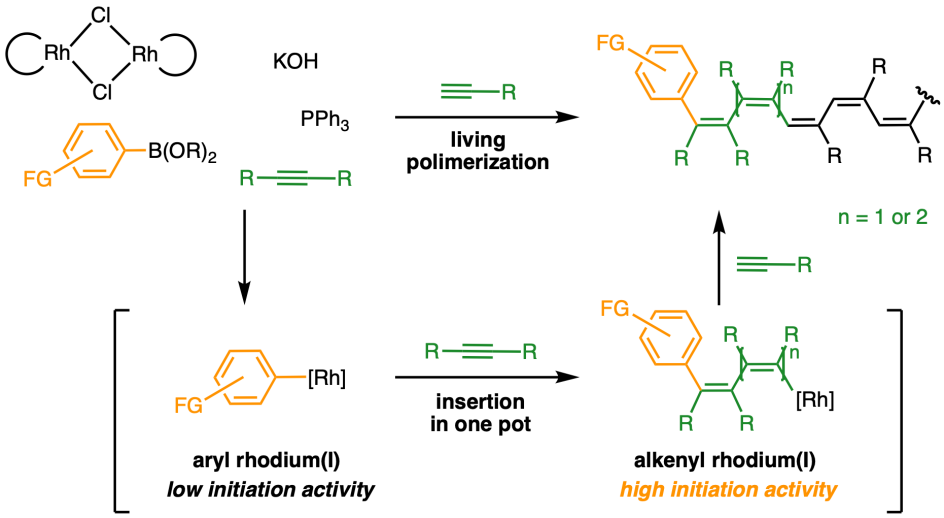

Figure 26. Living polymerization of phenyl acetylenes using a rhodium-based multicomponent catalytic system. FG = functional group. Reproduced from ref. 135 with permission from the John Wiley and Sons, copyright 2020.

1.5. Structural Elucidation of Poly(phenylacetylene)s

In a similar manner to natural helical macromolecules, the functionality of artificial helical polymers is closely linked to their secondary structure. Therefore, a structural understanding of polymers is essential to tailor them to specific applications. However, deciphering the secondary structure of artificial helical polymers is a current challenge in polymer chemistry. For this purpose, a combination of different techniques is necessary to obtain an approximate secondary structure of the macromolecule under study.

1.5.1. Determination of the Polyene Backbone Configuration

The polyene backbone of PPAs (internal helix) can adopt four possible configurations after polymerization: *c-c*, *c-t*, *t-c,* or *t-t*. As alluded to above, only the *cis*-scaffolds will promote the helix formation, whose elongation degree will depend on the dihedral angle between the conjugated double bonds (ω_1) —*c-c* ($\omega_1 < 90^o$); *c-t* ($\omega_1 > 90^o$)— (Figure 27a).

Percec and coworkers introduced ^{1}H NMR spectra to distinguish between the four possible configurations of the polyene backbone by combining theoretical and experimental studies.[128, 129, 136, 137] In *trans*-polyenes, the chemical shift of the vinylic proton varies between 6.20 – 7.20 ppm. Furthermore, one can distinguish between *t-c* and *t-t* scaffolds by carefully examining the ^{1}H NMR spectra. Specifically, in the former, all aromatic protons resonate together, while in the latter two aromatic protons are upfield shifted. However, *cis*-polyenes resonate around 5.60 – 5.80 ppm, and the aromatic protons also show a different splitting pattern depending on the *cisoidal* or *transoidal* configuration of *the cis*-polyene. Thus, in the ^{1}H NMR spectra of *c-c* scaffolds only one aromatic proton of the phenylacetylene monomer repeating unit is upfield shifted when compared to the other aromatic protons. On the contrary, in PPAs with *c-t* polyene backbone, two aromatic protons the phenylacetylene monomer repeating unit are shifted upfield. Moreover, in the case of *cis*-scaffolds, the chemical shift of the vinylic proton will also depend on the aromatic substitution pattern: 5.80 ppm for the *para*-substituted (*c-*

[136] C. I. Simionescu, V. Percec, *J. Polym. Sci. Polym. Chem. Ed*. **1980**, *18*, 147–155.
[137] C. I. Simionescu, V. Percec, *J. Polym. Sci. B Polym. Lett. Ed*. **1979**, *17*, 421–429.

c), 6.85 ppm for the meta- substituted (*c-t*) and 6.70 ppm for the ortho- substituted (*c-t*) polymers. From these studies was possible to propose an equation to determine the *cis*-content of double bonds in PPAs (Equation 1).

$$\%_{cis} = [A_{cis}/(A_{total} \cdot H_{total})] \cdot 100$$

Equation 1. Mathematical statement to calculate the *cis*-content of double bonds in PPAs. A_{cis} is the area of the vinylic proton peak (5.6 – 5.8 ppm), A_{total} is the total area of the observed ^{1}H NMR spectrum and H_{total} refers to the number of protons within the pendant.

Another helpful technique to elucidate the conformation of the polyene skeleton (Figure 27a) is Differential Scanning Calorimetry (DSC).[138-140] Sometimes it is not easy to distinguish *c-c* from *c-t* scaffolds in ^{1}H NMR spectra. DSC studies can help to solve this problem, where two different thermograms are found for both *c-c* and *c-t* scaffolds. Thus, the thermograms of *c-c* scaffolds show an exothermic peak around 200 ºC – 240 °C, corresponding to an isomerization process from *c-c* to *t-t* (Figure 27b). In contrast, *c-t* scaffolds display a thermogram with two exothermic peaks: the first one around 140 ºC and the second one around 240 ºC, related with the *c-t* to *c-c* and *c-c* to *t-t* isomerization processes, respectively (Figure 27c). However, depending on the pendant group used to functionalize the PPA, these thermograms can present additional exothermic peaks that make DSC studies useless to assign the configuration of a PPA backbone.

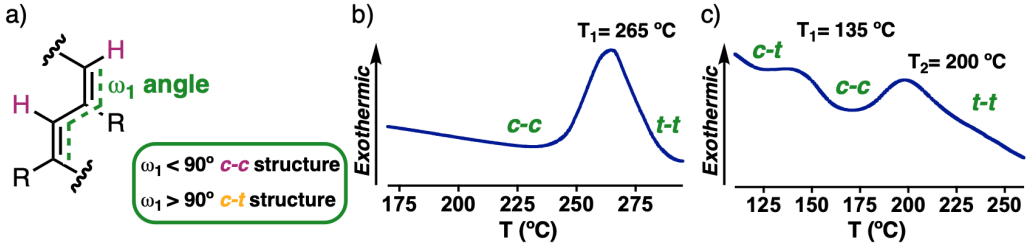

Figure 27. (a) Relationship of the ω_1 angle to the ultimate structure adopted by the internal helix. Representative DSC thermograms for (b) *c-c* and (c) *c-t* scaffolds.

[138] A. Motoshige, Y. Mawatari, Y. Yoshida, R. Motoshige, M. Tabata, *Polym. Chem.* **2014**, *5*, 971–978.

[139] A. Motoshige, Y. Mawatari, R. Motoshige, Y. Yoshida, M. Tabata, *J. Polym. Sci., Part A: Polym. Chem.* **2013**, *51*, 5177–5183.

[140] Y. Yoshida, Y. Mawatari, A. Motoshige, R. Motoshige, T. Hiraoki, M. Wagner, K. Müllen, M. Tabata, *J. Am. Chem. Soc.* **2013**, *135*, 4110–4116.

In order to solve this limitation, Raman spectroscopy is also a powerful technique to extract information about the PPA scaffold as the polyene backbone is active in Raman. Moreover, different Raman spectra were found for *cis*- and *trans*- polyene backbones. The characteristic resonance bands of the polyene backbone in a PPA with a *cis*-configuration are: C=C$_{cis}$ (ca. 1530 cm-1), C–C$_{cis}$ (ca. 1335 cm^{-1}) and C–H$_{cis}$ (ca. 956 cm^{-1}), while for the *trans*- configuration the characteristic bands are C=C$_{trans}$ (ca. 1475 cm^{-1}) and C–C$_{trans}$ (ca. 1200 cm^{-1}).[141,142] Additionally, it is possible to get information of *cis* and *trans* polyene backbones from FT-IR spectroscopy: C–H$_{trans}$ (1015 cm^{-1}) and C–H$_{cis}$ (740 cm^{-1}).[143,144]

Another spectroscopic technique that provides information about the backbone is UV-vis. However, this technique provides only information about the elongation of the polymer, and not about the configuration. Thus, if the backbone of the polyene is stretched, this structural change is accompanied by a bathochromic shift of the polyene band in the UV-vis spectrum. This bathochromic shift is produced due to an increase in the conjugation of double bonds in polyene main chain. Conversely, when the polyene backbone contracts, a hypochromic effect is observed, attributed to a reduction in the conjugation of the double bonds. Although UV-vis spectroscopy provides valuable information on modifications in the polymer scaffold caused by external stimuli, it cannot be used to distinguish between *c-c* and *c-t* configurations.[145-149]

---

141 A. Misayaka, T. Sone, Y. Mawatari, S. Setauesh, K. Müllen, M. Tabata, *Macromol. Chem. Phys.* **2006**, *207*, 1938–1944.

142 A. Miyasaka, Y. Mawatari, T. Sone, M. Tabata, *Polym. Degrad. Stab.* **2007**, *92*, 253–259.

143 H. Shirakawa, S. Ikeda, *Polym. J*. **1971**, *2*, 231–244.

144 T. Ito, H. Shirakawa, S. Ikeda, *J. Polym. Sci. Polym. Chem. Ed*. **1974**, *12*, 11–20.

145 A. Motoshige, Y. Mawatari, Y. Yoshida, C. Seki, H. Matsuyama, M. Tabata, *J. Polym. Sci. A Polym. Chem.* **2012**, *50*, 3008–3015.

146 V. Percec, M. Peterca, J. G. Rudick, E. Aqad, M. R. Imam, P. A. Heiney, *Chem. Eur. J.* **2007**, *13*, 9572–9581.

147 V. Percec, J. G. Rudick, M. Peterca, E. Aqad, M. R. Imam, P. A. Heiney, *J. Polym. Sci. A Polym. Chem*. **2007**, *45*, 4974–4987.

148 V. Percec, E. Aqad, M. Peterca, J. G. Rudick, L. Lemon, J. C. Ronda, B. B. De, P. A. Heiney, E. W. Meijer, *J. Am. Chem. Soc*. **2006**, *128*, 16365–16372.

149 V. Percec, J. G. Rudick, M. Peterca, M. Wagner, M. Obata, C. M. Mitchell, W.-D. Cho, V. S. K. Balagurusamy, P. A. Heiney, *J. Am. Chem. Soc*. **2005**, *127*, 15257–15264.

In addition, other methods rely on the reactivity of the polyene backbone to identify the configuration of the double bonds. For example, Kaneko and coworkers reported a methodology in the solid state based on light irradiation-induced isomerization that helps to distinguish between *c-c* and *c-t* scaffolds because it leads to a photocyclic aromatization reaction in the PPA backbone. Interestingly, this reaction only occurs with *c-c* structures, where the conjugated polyene backbone adopts the geometry required for the reaction to take place, leading to a 1,3,5-trisubstituted benzene derivative.[150]

1.5.2. Scaffolding the Helical Structure of PPAs

The macromolecular helical structure of PPAs is composed of two coaxial helices — the internal helix and the external helix — which can rotate in the same or opposite directions, depending on the scaffold adopted by the polymer (Figure 28). This structural feature is intrinsic to all the PPAs, independently of their helical sense or elongation degree.

The internal helix is defined by the conjugated polyene backbone, whose helical direction and elongation degree are determined by the dihedral angle between the conjugated double bonds (ω_1). The value of ω_1 angle, as discussed above (Figure 27a), dictates the configuration of the backbone in *c-c* or *c-t* scaffolds, which in turn determines the elongation degree. Moreover, the ω_1 sign is related to the helical sense of the internal helix: negative values of ω_1 give rise to a *M* internal helix, and positive values give rise to a *P* internal helix (Figure 28). Consequently, helical sense and elongation of the internal helix are easily determined by ECD spectroscopy.[151]

The second coaxial helix is the one defined by the pendant groups which are arrayed around a peripheral coaxial position around the internal helix. The helical direction of this helix can only be determined by AFM measurements, as well as the structural parameters (helical pitch and packing angle). As alluded to above, helical sense of the external helix depends on the internal scaffold adopted by the polymer (ω_1). Thus, if $\omega_1 < 90^o$, the polymer shows a *c-c* scaffold with three residues per turn (3/1 helix, compressed structure), where the internal and external helices rotate in the same

[150] L. Liu, T. Namikoshi, Y. Zang, T. Aoki, S. Hadano, Y. Abe, I. Wasuzu, T. Tsutsuba, M. Teraguchi, T. Kaneko, *J. Am. Chem. Soc.* **2013**, *135*, 602–605.

[151] B. Fernández, R. Rodríguez, E. Quiñoá, R. Riguera, F. Freire, *ACS Omega* **2019**, *4*, 5233–5240.

direction. On the other hand, if $\omega_1 > 90°$, the polymer presents a *c-t* scaffold with two residues per turn (2/1 helix, stretched structure), where both helices rotate in opposite directions (Figure 28).

Therefore, a combination of different techniques is needed to elucidate the secondary structure of a PPA. A detailed explanation of this process is discussed further below.

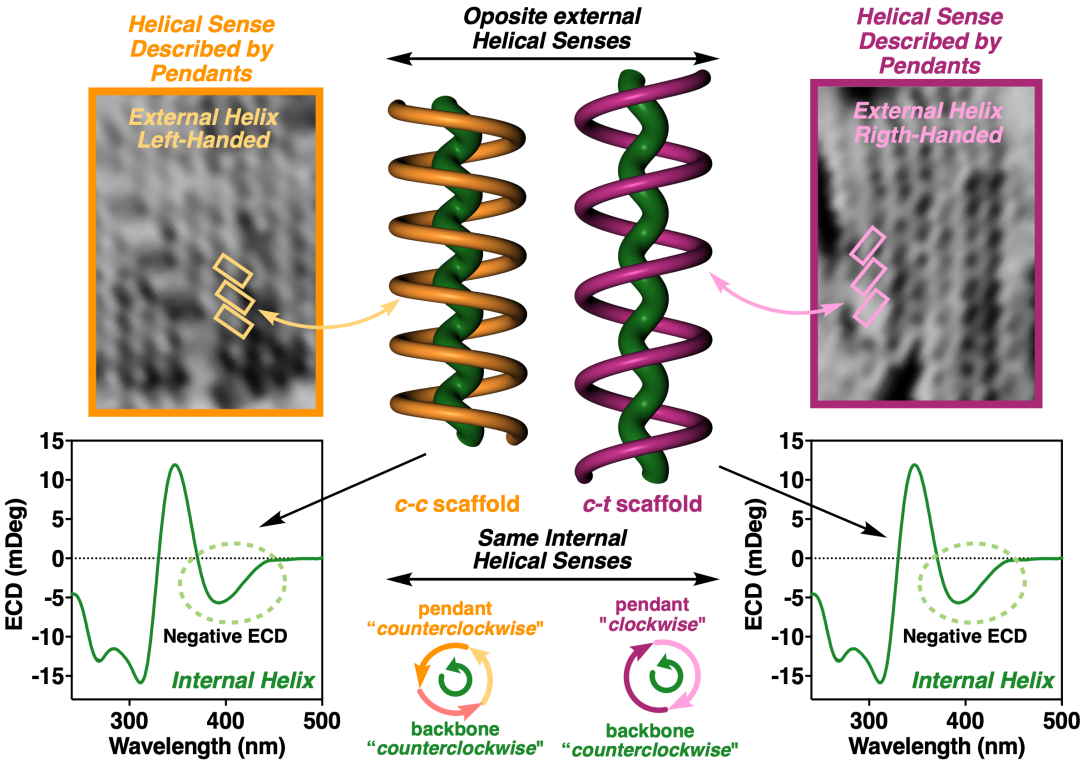

Figure 28. Schematic illustration of two possible scaffolds that a PPA can adopt and their relationship to ECD and AFM studies.

1.5.2.1. Chiroptical Spectroscopies

Chiroptical spectroscopic methodologies find extensive application in determining the absolute configuration, studying the conformational space, and determining the chiral strength of chiral molecules. The most frequently used methods are Optical Rotation (OR), Electronic Circular Dichroism (ECD), Vibrational Circular Dichroism (VCD), and Raman Optical Activity (ROA). In general, the data obtained by these techniques are

combined to evaluate and corroborate the results obtained, although their independent use is feasible depending on the specific objective pursued.[152]

The basis of all chiroptical spectroscopies is the same: the interaction of incident light with a chiral sample. This incident light can be linearly or circularly polarized. The linearly polarized light can be achieved as a summation of two left- and right-handed circularly polarized electrical components (E_L and E_R) with the same phase and magnitude.[153] However, when the components are out of phase and/or have different magnitudes, the resulting light is elliptically polarized, and if the phase shift is 90°, whereas the magnitude of the components is the same, then the resulting light is circularly polarized (Figure 29). A sample is said to be optically active when it interacts differently with both components of polarized light, being able to manifest itself in different ways.

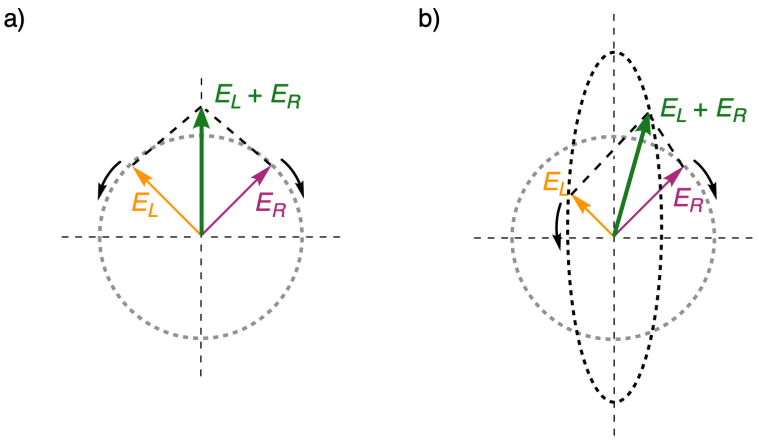

Figure 29. Frontal view of linearly polarized light (green arrow), as a summation of a left circularly polarized light (orange arrow) and a right circularly polarized light (purple), before (a) and after (b) passing through a chiral sample.

1.5.2.1.1. Optical rotation

The optical rotation (α) provides the degree of deviation of the polarized light as it travels through a solution of an optically active compound. It can be precisely defined as the angle between the major axis of the ellipse and the plane of polarization of the original linear polarized light. The phenomenon that causes this angle rotation is called

[152] K. Nakanishi, N. Berova, P. L. Polavarapu, and R. W. Woody, *Comprehensive Chiroptical Spectroscopy, Volume 1, Instrumentation, Methodologies, and Theoretical Simulations*, Wiley-VCH Verlag GmbH & Co. KGaA: Weinheim, Germany, **2013**.

[153] S. Allenmark, J. Gawronski, *Chirality* **2008**, *20*, 606–608.

birefringence, which is a consequence of the different speed/refractive index of left and right circularly polarized lights while traveling through the sample. The data obtained with this technique depends on the solvent used, the temperature, the concentration, and the cell length. Thus, the standardized data is expressed as specific rotation by applying Equation 2.[154]

$$[\alpha]_{\lambda}^{T} = \alpha_{obs}/c \cdot l$$

Equation 2. Mathematical statement to calculate the specific optical rotation. ***T*** indicates the temperature at which the measurement is perform, $\boldsymbol{\lambda}$ indicates the wavelength used; α_{obs} stands for the observed optical rotation (degrees) that the instrument provides; $\boldsymbol{c}$ is de concentration ($g \cdot mL^{-1}$) and $\boldsymbol{l}$ is the cell length (dm).

The main disadvantage of this technique is its low sensitivity and the large amount of sample required. In macromolecules such as polymers, the specific rotation value is typically one order magnitude higher than the one for the corresponding monomeric unit.

1.5.2.1.2. Electronic Circular Dichroism

One of the most useful techniques for determining the presence of a preferred helical sense in macromolecules, as well as a preferential conformation in discrete chiral molecules, is the Electronic Circular Dichroism (ECD). When a circularly polarized light passes through a chiral media, the resulting light can become an elliptically polarized light, due to the different absorption of the right and left circularly polarized light by the chiral medium (Figure 29b). This phenomenon is known as ECD.[155] The two circularly polarized lights are mirror images of each other, as are the enantiomers. When two enantiomers interact with linearly polarized light, they absorb opposite amounts of light circularly polarized to the right and the left, respectively. Thus, the ECD spectrum is experimentally obtained by measuring the differential absorption of the left- and right-handed circularly polarized light at each wavelength (Equation 3). By applying the Lambert-Beer law, a molar quantity, $\Delta\varepsilon$, is defined (Equation 4).

$$\mathrm{ECD} = \mathrm{A^l} - \mathrm{A^r}$$

Equation 3. Mathematical definition of ECD, where A^l is the absorption of the left circularly polarized light, A^r is the absorption of the right circularly polarized light.

[154] P. Vollhardt, N. Schore, *Organic Chemistry: Structure and Function,* 5th ed., Omega, **2008**.
[155] G. Pescitelli, L. Di Bari, N. Berova, *Chem. Soc. Rev*. **2011**, *40*, 4603–4625.

The application of the Lambert-Beer law allows the definition of a molar quantity, $\Delta\varepsilon$, as expressed in Equation 4.

$$\Delta\varepsilon = \varepsilon^{l} - \varepsilon^{r} = \frac{\mathrm{ECD}}{\mathrm{c.\,b}}$$

Equation 4. Mathematical definition of $\Delta\varepsilon$, where *c* and *b* are the sample concentration (mol·L^{-1}) and the optical path (cm), respectively.

Normally, the value given by a circular dichroism spectrophotometer is the ellipticity (θ, in mdeg), which is related with the ECD by the following equation:

$$\theta(\mathrm{mdeg}) = 32982 \cdot \mathrm{ECD}$$

Equation 5. Mathematical definition of ellipticity (θ).

The ECD is a signed parameter since A^l can be higher or smaller than A^r, and the resulting positive and negative bands are always exactly opposite spectra for the enantiomers. Each ECD band, called the Cotton effect, correlates with the UV-vis band corresponding to one or more electronic transitions. The ratio between $\Delta\varepsilon$ and ε is defined as the g_{abs} (Equation 6), also known as the anisotropy or dissymmetry factor. The g_{abs} is independent of concentration and path length and is often used to express the chiral power of a system.[152]

$$g_{\mathrm{abs}} = \frac{\Delta\varepsilon}{\varepsilon} = \frac{A^l - A^r}{A}$$

Equation 6. Mathematical definition of the g_{abs}.

The dissymmetry factor values are within the range −2 to +2. In the case of small organic molecules within an isotropic media, it is noteworthy that the absolute values of g_{abs} usually exhibit magnitudes smaller than 10^{-3}.[156]

This technique has been widely used in the analysis of the secondary structure of macromolecules, such as peptides, as it provides not only information about the chiral content but also about the folding. There are characteristic ECD spectra for the most common foldings: α-helix, β-sheet, β-turn or random coil. Moreover, the chiroptical response is a magnitude strongly dependent on the shape-persistency of the molecule,

[156] M. Wakabayashi, S. Yokojima, T. Fukaminato, K. Shiino, M. Irie, S. Nakamura, *J. Phys. Chem. A* **2014**, *118*, 5046–5057.

so any conformational change due to any change in the environmental conditions will be easily detected. Also, structural, thermodynamic, and kinetic parameters can be obtained. Therefore, the versatility to modify experimental parameters and the low amount of sample required have transformed ECD into a powerful technique to study stimuli-responsive chiral systems.

In the case of helical polymers, this technique facilitates the determination of both the single-handed helix excess and the assessment of helical changes through the analysis of the characteristic Cotton effect in the vinylic region. More specifically, this technique provides information about the helical direction described by the internal helix (polyene backbone). Recently, it has been reported that a positive Cotton band corresponds to an internal helix *P*, while a negative Cotton effect corresponds to a helix *M*. This correlation and the role of the main dihedral angles of the polymeric structure were determined by TD-DFT (Time-Dependent Density Function Theory) calculations.[157,158]

1.5.2.1.3. Theoretically Calculated Circular Dichroism

Technological advances and improvements in theoretical methods for calculating molecular properties have made quantum-chemical methods the most rigorous methodology for predicting chiroptical spectra. ECD calculations can be performed on large molecules, and the main challenge is the description of the excited states. Thus, to obtain reliable results, it is necessary to consider electron correlation, which implies the use of large basis sets. In this sense, TD-DFT methods are the most efficient as they offer the best compromise between accuracy and cost.[159,160]

There are other factors to consider when attempting to simulate an ECD spectrum. Since it is a very geometry-sensitive spectroscopy, the flexibility of the system must be taken into account.[161] Therefore, the first step before predicting or interpreting an ECD

[157] B. Fernández, R. Rodríguez, A. Rizzo, E. Quiñoá, R. Riguera, F. Freire, *Angew. Chem. Int. Ed*. **2018**, *57*, 3666–3670.

[158] B. Fernández, R. Rodríguez, E. Quiñoá, R. Riguera, F. Freire, *ACS Omega* **2019**, *4*, 5233–5240.

[159] J. Autschbach, *Chirality* **2009**, *21*, E116-E152.

[160] J. Autschbach, L. Nitsch-Velasquez, M. Rudolph, *Top. Curr. Chem*. **2011**, *298*, 1–98.

[161] M. Kwit, M. D. Rozwadowska, J. Gawroński, A. Grajewska, *J. Org. Chem*. **2009**, *74*, 8051–8063.

spectrum is to know the conformation or conformational distribution of the system, i.e. to identify which conformers have a significant population under the working conditions. Once the low-energy conformers are identified, ECD spectra must be calculated for each of them. The conformer populations must then be evaluated and the ECD spectra weighted according to their relative populations. The last stage consists of summing the acquired weighted spectra to generate the resulting spectrum of the system.

In the field of helical polymers, early examples using theoretical calculations to solve the polymeric structure applied semi-empirical methods, which are very costly in terms of time and computational resources. Nevertheless, Freire and co-workers described for the first time the correlation between the helical sense of the internal helix of a PPA and the sign of the ECD in the vinylic region (usually around 380 nm). They applied the TD-DFT method to a series of small oligomers of PPAs whose detailed structure was already known from experimental techniques.[157] In this way, they were able to demonstrate that the application of the DFT method in combination with a suitable functional (rCAM-B3LYP) and with a not very large computational basis (3-21G) in small PPA oligomers (*n* = 9-12) is a very useful tool to assign the internal helical direction in PPAs and to obtain information about the mains dihedral angles that build up the helical scaffold.[158]

1.5.2.2. X-ray diffraction

X-ray diffraction is a phenomenon in which atoms in a crystal produce an interference pattern from the waves present in an incoming X-ray beam.[162]

Regarding polymers, to obtain a diffraction pattern of these materials, it is essential to create an oriented film. I.e., it needs to have a rigid, rod-shaped structure that is prone to form liquid crystal phases. This requirement is particularly applicable to lipotropic or thermotropic liquid crystals, where films with a regular helical structure can be prepared through methods such as physical shearing or the application of electric or magnetic fields to the sample.[163] However, despite the insights provided by this technique into secondary structure parameters like helical pitch, helix width, and helix length, it does not provide information about the helical sense.[100]

---

[162] C. Hammond. *The Basics of Crystallography and Diffraction*, 4th ed., Oxford University Press: Oxford, UK, **2015**.

[163] E. Yashima, *Polym. J*. **2010**, *42*, 3–16.

1.5.2.3. Atomic Force Microscopy

The Atomic Force Microscopy (AFM) is a very-high-resolution type of scanning probe microscopy that acquires topographic data by scanning the sample's surface using a sharp AFM tip.[164] This process generates a three-dimensional topographic image of the surface, which is a powerful tool for studying various materials at the molecular or atomic level.

In the field of helical polymers, the application of AFM enables the acquisition of information regarding the secondary structure of the polymer. Thus, it provides useful information on the packing angle, helical pitch and, more importantly, on the helical sense of the secondary structure. However, sample preparation is not straightforward; only well-ordered, self-assembled monolayers will provide images with sufficient resolution to extract all the desired data. The key factors to consider in the sample preparation include the solvent used to dissolve the sample, the protocol of deposition (e.g., drop casting, spin coating, etc.), and the substrate used to support the monolayer. Specially, the selected substrate will be a crucial factor, as it can affect the intramolecular interactions between chains, as well as the helical conformation.[165]

Yashima and co-workers were pioneers in reporting the first approach to analyze by AFM the helical structure of a PPA copolymer, bearing an achiral bulky C_{60} and an optically active amine (Figure 30, poly-**18**).[166] They drop casted a diluted polymer solution on two different substrates: mica and highly oriented pyrolytic graphite (HOPG). This deposition protocol consists of settling a small amount of solution over a substrate, where the solvent is evaporated and settled the polymer on the surface (Figure 30a). Thus, they observed two different results, proving the key role of the substrate employed over the scaffold adopted (Figure 30b). The AFM images on mica showed isolated particles due to the repulsive interactions between the hydrophobic C_{60} and the hydrophilic mica substrate, forcing the polymer to aggregate. In contrast, the AFM

[164] G. Binnig, C. F. Quate, Ch. Gerber, *Phys. Rev. Lett.* **1986**, *56*, 930–933.

[165] J. Kumaki, S. -I. Sakurai, E. Yashima, *Chem. Soc. Rev.* **2009**, *38*, 737–746.

[166] T. Nishimura, K. Takatani, S. -I. Sakurai, K. Maeda, E. Yashima, *Angew. Chem. Int. Ed.* **2002**, *41*, 3602–3604.

images on HOPG revealed some extended and individual copolymer chains with isolated particles.

Later, this methodology was applied to different systems, such as for poly(4-carboxyphenylacetylene) (poly-**19**) complexed with (*R*)-naphtylethylamine and, also for its corresponding amide (poly-**20**) showed, in both cases, isolated helical chains (Figure 30c and 30d, respectively).[167] Thus, these results demonstrated the robustness of the methodology.

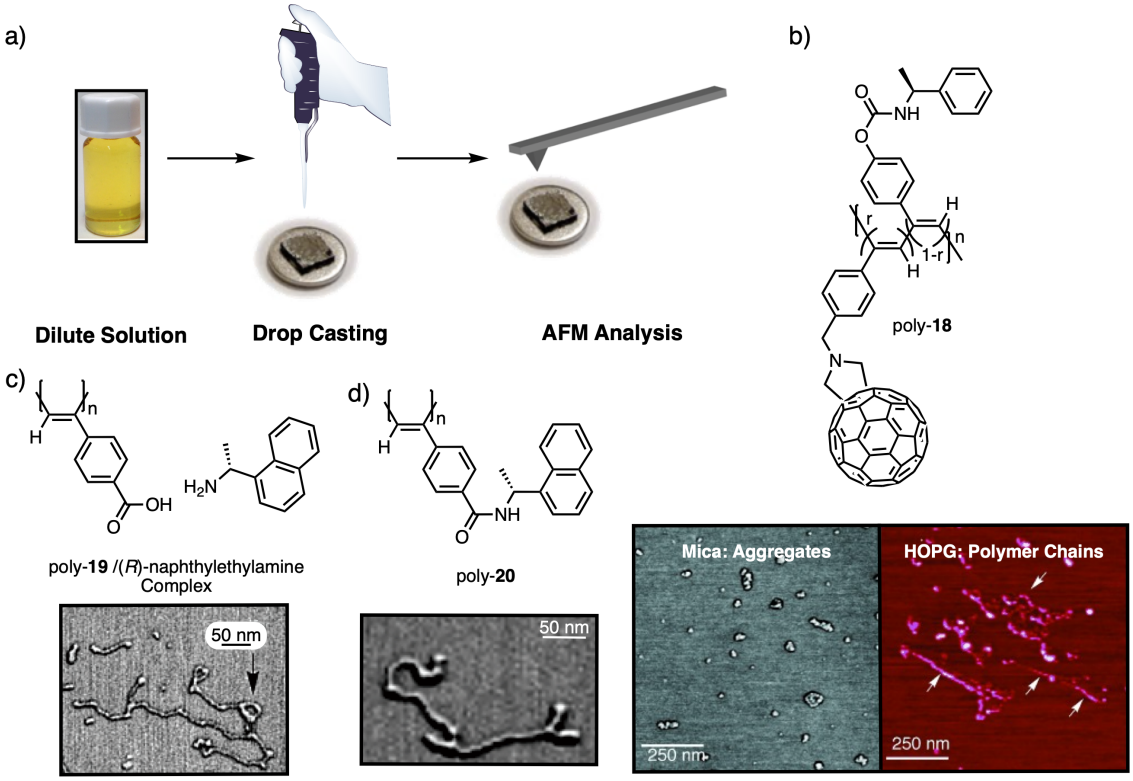

Figure 30. (a) Schematic representation of drop casting deposition technique. (b) Chemical structure and AFM image for poly-**18** after drop casting deposition on different substrates. Reproduced from ref. 166 with permission from the John Wiley and Sons, copyright 2002. (c) Chemical structure and AFM image for poly-**19**/(*R*)-naphthylethylamine complex after drop casting deposition on mica. (d) Chemical structure and AFM image for poly-**20** after drop casting deposition on mica. Reproduced (c,d) from ref. 165 with permission from the Royal Society of Chemistry, copyright 2009.

Inspired by these promising results, Yashima and co-workers devised a new strategy to promote the assembly of the polymer chains into well-defined 2D crystals.[165] They proposed to apply the spin coating as a deposition protocol, which consists of four

[167] S. -I. Sakurai, K. Kuroyanagi, K. Morino, M. Kunitake, E. Yashima, *Macromolecules* **2003**, *36*, 9670–9674.

steps: deposition, spin-up, spin-off, and evaporation (Figure 31a). The spin modes (speed and time), which influence the polymer-surface interactions and the solvent evaporation rate, can be controlled. Thus, this protocol facilitates the obtention of uniform monolayers with controlled thickness, as the solvent evaporation happens under more control at an air/solid interface.

Following this methodology, the authors prepared monolayers (on HOPG) of a PPA bearing pendants with long alkyl chains, that also promoted the self-assembly between polymeric strands by chain interdigitation.[168] After deposition, they kept the sample under solvent vapors overnight to allow the slow nucleation and growth of 2D crystals. They succeeded in the obtention of the corresponding monolayers for poly-(*L*)-**21** and poly-(*D*)-**21** (derived from *L*-alanine and *D*-alanine, respectively). The direct visualization of these AFM images allowed a detailed examination of the external helix of the polymer (Figure 30b). AFM images of poly-(*L*)-**21** unveiled the presence of *M*-helices described by pendant groups. Specifically, the helices showed a helical pitch of 2.34 nm and a packing angle of 40°, indicative of an 11/5 *c*-*t* helix (two residues per turn). As a *c*-*t* helix, it was expected that the internal and external helices would rotate in opposite directions, which confirmed by ECD showing the presence of a right-handed internal helix. Therefore, the combination of the information obtained from AFM, ECD, and other structural techniques such as X-ray, and NMR allowed them to elucidate the secondary structure of poly-**21**, an 11/5 helical structure with two residues per turn supported by an internal helix rotate in the opposite helical sense.

[168] S. -I. Sakurai, K. Okoshi, J. Kumaki, E. Yashima, *Angew. Chem. Int. Ed.* **2006**, *118*, 1267–1270.

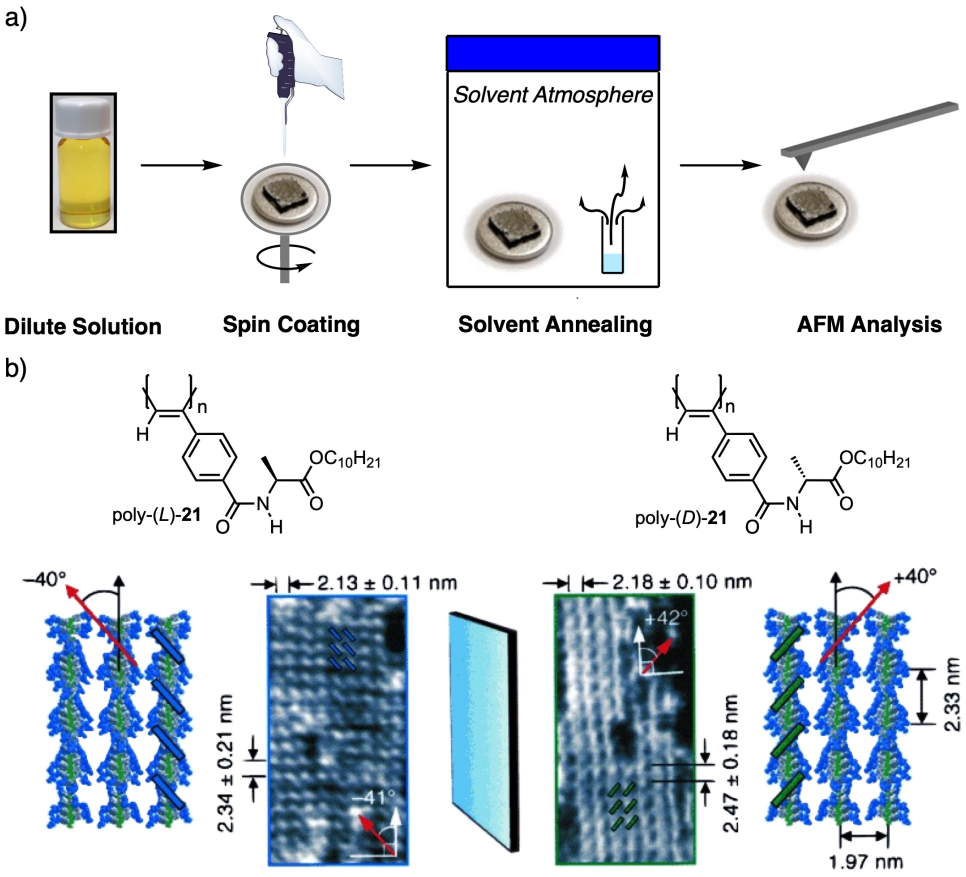

Figure 31. (a) Schematic illustration of the spin-coating and solvent exposure process. (b) Chemical strcuture of poly- **21** and schematic drawings of the mirror-image relationship of helical poly-(*L*)-**21** (left) and poly-(*D*)-**21** (right) constructured from their 2D crystals. Reproduced from ref. 168 with permission from the John Wiley and Sons, copyright 2006.

Furthermore, they study extended beyond solution analysis to investigate the dynamic behavior of poly-(*L*)-**21** in the solid state. Notably, alterations in the solvent polarity, employed for generating vapors overnight, resulted in the formation of 2D crystals for poly-(*D*)- **21**,[169] displaying an opposite helical sense.

[169] S. -I. Sakurai, K. Okoshi, J. Kumaki, E. Yashima, *J. Am. Chem. Soc.* **2006**, *128*, 5650–5651.

Over the last two decades, Yashima's protocol has been applied in a wide range of systems, such as polymers with pendants of different topologies,[108,165] copolymers,[170-172] and even complex polymer-metal systems.[173,174]

Alternative techniques to drop casting and spin coating have also been developed, such as Langmuir-Blodgett (LB) and Langmuir-Schaefer (LS).[175,176] The main difference between the methodologies described above and these is that, in the previous ones, the monolayer is formed at an air/solid interface, and in LB and LS methodologies, the monolayer formation occurs at an air/water interface when the solid support is introduced or approached to a pool of water. For example, LB can be the technique of choice for polymers with amphiphilic character, where the hydrophilic part attaches to the mica (hydrophilic support),[177,178] whereas by LS was able to obtain monolayers for PPAs with different substitution pattern on the aryl ring.[21, 179]

1.6. Helical Structure Control in Polymers

Since the discovery of dynamic synthetic helical polymers, one of the most ambitious goals has been to achieve total control over the helix, both in terms of rotational direction and length. The need to have a rational understanding of the behavior of the helical structure of polymers lies in its impact on their stimulus-response properties, which can

[170] S. Ohsawa, S. -I. Sakurai, K. Nagai, M. Banno, K. Maeda, J. Kumaki, E. Yashima, *J. Am. Chem. Soc.* **2010**, *133*, 108–114.

[171] S. Ohsawa, S. -I. Sakurai, K. Nagai, K. Maeda, J. Kumaki, E. Yashima, *Polym. J.* **2011**, *44*, 42–50.

[172] S. Arias, R. Rodríguez, E. Quiñoá, R. Riguera, F. Freire, *J. Am. Chem. Soc.* **2018**, *140*, 667–674.

[173] F. Freire, J. M. Seco, E. Quiñoá, R. Riguera, *Angew. Chem. Int. Ed*. **2011**, *50*, 11692–11696.

[174] S. Arias, F. Freire, E. Quiñoá, R. Riguera, *Polym. Chem*. **2015**, *6*, 4725–4733.

[175] G. G. Roberts, *Langmuir-Blodgett Films*, Plenum, New York, **1990**.

[176] A. Ulman, *An Introduction to Ultrathin, Organic Films-From Langmuir-Blodgett to Self-Assembly*, 1st ed.; Academic Press: New York, **1991**.

[177] B. S. Li, J. W. Y. Lam, Z.-Q. Yu, B. Z. Tang, *Langmuir* **2012**, *28*, 5770–5774.

[178] B. S. Li, S. Z. Kang, K. K. L. Cheuk, L. Wan, L. Ling, C. Bai, B. Z. Tang, *Langmuir* **2004**, *20*, 7598–7603.

[179] R. Rodríguez, J. Ignés-Mullol, F. Sagués, E. Quiñoá, R. Riguera, F. Freire, *Nanoscale* **2016**, *8*, 3362–3367.

be used in different applications such as sensing, molecular recognition, asymmetric synthesis, signaling, information storage, and so on.[96,180]

1.6.1. Helix Induction Mechanisms in Helical Polymers

In order to rationalize how the stimulus-response is produced in dynamic helical polymers, deciphering the operating mechanisms is of utmost importance.[180] In this sense, there are different ways to control the helical sense of a polymer that are described below.

1.6.1.1. Tele-induction Mechanism

Tele-induction is the most frequently helix induction mechanism that governs the screw sense excess adopted by chiral and achiral polymers. In general, the main chain of synthetic helical polymers is achiral. Thus, PPAs and their derivatives, whose backbone is achiral, can adopt a preferred helical sense due to the conformational composition adopted by the pendant group. Following this mechanism, changes in the spatial distribution of substituents in the chiral centers or in the species associated with the pendant groups result in stimuli being transmitted through space to the polymer backbones, which adopt specific conformations that lead to *P* or *M* helical structures (Figure 32).

In a polymer functionalized with a chiral pendant, such as a poly(phenylacetylene) (PPA) with the benzamide of (*S*)-phenylglycine methyl ester (poly-**22**),[117] the presence of a preferred conformation at the chiral center induces a specific helical direction in the polymer main chain. Moreover, variations in the conformational composition of the pendant group due to external stimuli, such as solvent effects or the addition of metal ions, can result in either helical sense enhancement or helical inversion effect (Figure 32a).

Nevertheless, if the helical polymer is achiral (equal population of left-handed and right-handed helices) a phenomenon of asymmetry amplification (helical induction) arises from interactions between the polymer and external chiral molecules used as external stimuli. For example, a PPA bearing a benzoic group as pendant (poly-**23**)

[180] M. Lago-Silva, M. Fernández-Míguez, R. Rodríguez, E. Quiñoá, F. Freire, *Chem. Soc. Rev*. **2024**, *53*, 793 – 852.

showing a random helix (null ECD signal),[119, 181] adopts a single helical sense after further addition of chiral amines (Figure 32b). This process is reversible and the addition of a stronger acid (e.g., trifluoroacetic acid) results into a disappearance of the induced helix. The same behavior was observed both in the solution and the solid state, in a gel state, and liquid crystalline phase.

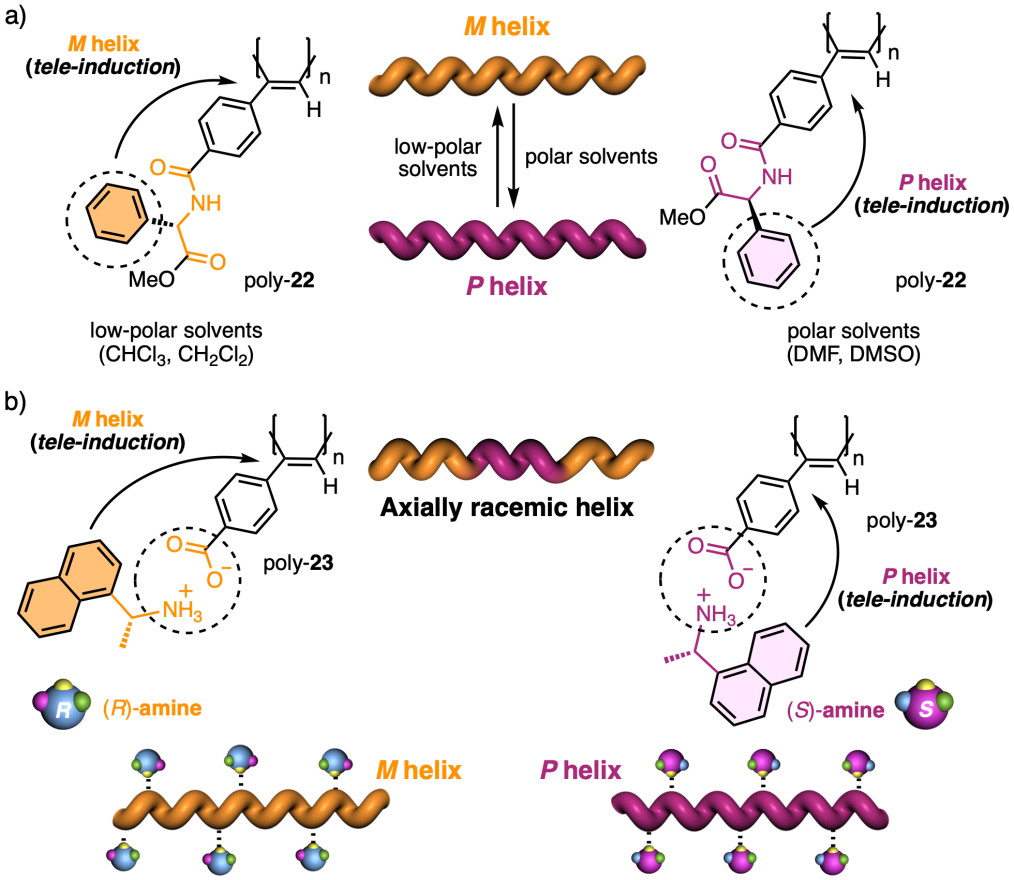

Figure 32. Schematic illustration of tele-induction mechanism in PPAs. (a) Helix inversion of a chiral PPA bearing 4-benzamide of (*S*)-phenylglycine methyl ester as pendant group (poly-**22**) by tuning its conformational composition using solvent polarity as external stimulus. (b) Chiral amplification of an achiral PPA bearing 4-benzoic acid as pendant (poly-**23**) using chiral amines as external stimuli. Reproduced from ref. 180 with permission from the Royal Society of Chemistry.

[181] E. Yashima, T. Matsushima, Y. Okamoto, *J. Am. Chem. Soc.* **1995**, *117*, 11596–11597.

1.6.1.2. Chiral Harvesting Mechanism

This mechanism relies on the introduction of a chiral source at a remote position, separated from the backbone by achiral spacers. In this scenario, the transmission of information can follow two different paths. The induction of: (i) a conformational change in the achiral spacer;[182,183] or (ii) a tilting degree in the supramolecular arrangement of the achiral spacers along the helix.[184] Both mechanisms are triggered by alterations in the conformational composition of a chiral group positioned remotely. These changes are subsequently communicated to the achiral spacer and picked up by the polymer backbone to adopt an excess *P*- or *M*-sense of the helix. Our research group has explored this mechanism using both strategies. For example, following the first approach, a PPA bearing an α-aminoisobutyric acid (Aib) peptide chain used as a flexible achiral spacer, and functionalized at their N-terminal end with a chiral center, such as (*R*)- or (*S*)-α-methoxy-α-trifluoromethylphenylacetic acid (MTPA, Mosher reagent)(poly-**24**) was prepared.[182] In this system, the conformational preference adopted by the chiral moiety is transmitted to the adjacent achiral residue by adopting a preferred *P*- or *M*-twisted conformer and propagated to the other achiral residues through a helical sense induction mechanism. This form of communication was demonstrated for residues of different lengths ((*R*)-MTPA-$(Aib)_n$-PPAs, n = 1, 2, 3). Furthermore, variations in the conformational composition of the chiral residue, or substitution of the chiral residue by its enantiomer, lead to the induction of the opposite helical direction, generating a dynamic helical folding (Figure 33).

[182] R. Rodríguez, E. Suárez-Picado, E. Quiñoá, R. Riguera, F. Freire, *Angew. Chem. Int. Ed*. **2020**, *59*, 8616–8622.

[183] R. Rodríguez, E. Quiñoá, R. Riguera, F. Freire, *Small*, **2019**, *15*, 1805413.

[184] J. J. L. M. Cornelissen, J. J. J. M. Donners, R. de Gelder, W. S. Graswinckel, G. A. Metselaar, A. E. Rowan, N. A. J. M. Sommerdijk, R. J. M. Nolte, *Science* **2001**, *293*, 676–680.

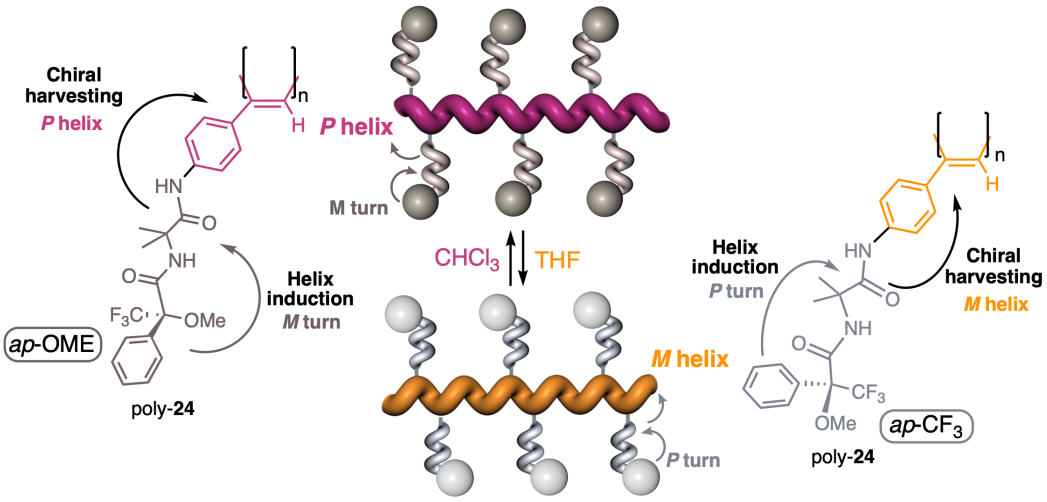

Figure 33. Screw sense induction of helical polymers through chiral harvesting using flexible achiral spacers. Reproduced from ref. 180 with permission from the Royal Society of Chemistry.

On the other hand, as already mentioned, the chiral information can be trasmited through the supramolecular arrangement of the achiral spacers along the helix. An illustrative example following this second approach was reported in a PPA bearing oligo(*p*-phenyleneethynylene)s (OPEs) as rigid achiral spacers and derivatized with chiral pendant groups.[185,186] Hence, the disposition of the chiral moiety affects the stacking of the OPE units within the helical structure, inducing a specific positive or negative tilting degree (θ), which is further harvested by the polyene backbone inducing either a *P* or *M* internal helix (Figure 34).

[185] Z. Fernández, B. Fernández, E. Quiñoá, R. Riguera, F. Freire, *Chem. Sci.* **2020**, *11*, 7182–7187.
[186] Z. Fernández, B. Fernández, E. Quiñoá, F. Freire, *J. Am. Chem. Soc.* **2021**, *143*, 20962–20969.

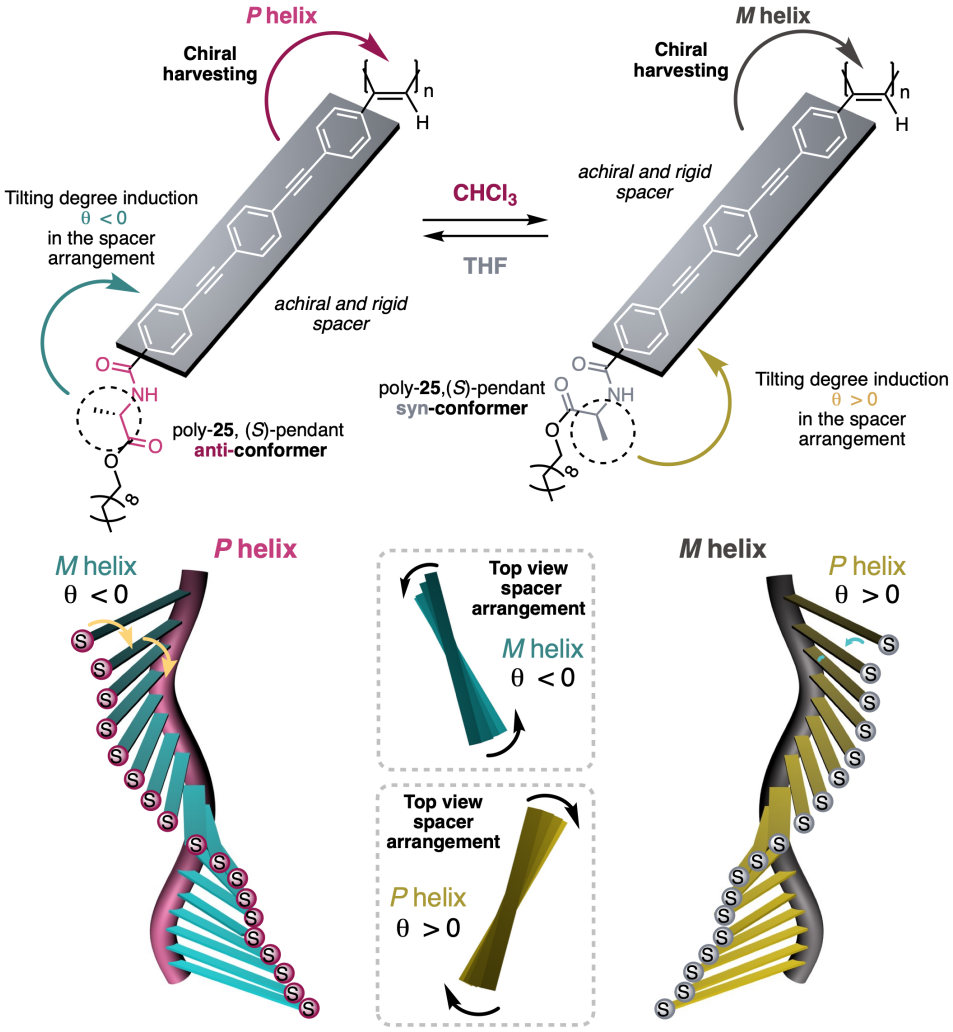

Figure 34. Screw sense induction of helical polymers through chiral harvesting using rigid achiral spacers. Reproduced from ref. 180 with permission from the Royal Society of Chemistry.

1.6.1.3. Chiral Overpass Mechanism

The modulation of the conformational composition of multichiral side chains of a helical polymer offers the possibility of inducing a unique phenomenon known as the chiral overpass effect.[187,188] Thus, in a helical polymer bearing a pendant composed of two or more chiral centers, the chiral center closest to the polymer backbone is more likely to control its handedness (tele-induction), whereas the other center has little to no impact on the structural characteristics of the helical structure. However, if a conformational change in the pendant places a second chiral residue near the backbone,

[187] E. Suárez-Picado, E. Quiñoá, R. Riguera, F. Freire, *Angew. Chem. Int. Ed.* **2020**, *59*, 4537–4543.
[188] R. Rodríguez, E. Rivadulla-Cendal, M. Fernández-Míguez, B. Fernández, K. Maeda, E. Quiñoá, F. Freire, *Angew. Chem. Int. Ed.* **2022**, *134*, e202209953.

it will command the screw direction preference. In other words, the second chiral center overrides the order of the first one.

For example, the chiral overpass mechanism is found in a polymer that carries the anilide of (*S*)-alanine-(*R*)-methoxyphenylacetate — (*S*)-Ala-(*R*)-MPA dimer — as a pendant (poly-**26**).[188] In this PPA, two different conformations can occur on the pendant moiety: extended and bent. If the dimer adopts an extended conformation, the (*S*)-alanine, located closer to the polyene backbone, commands a preferred macromolecular structure (screw-sense and elongation) in the PPA (*M* helix, Figure 35a). In contrast, by fixing a bent structure to the dimeric pendant, it is possible to place the second chiral residue close to the main chain, which is now responsible for the screw-sense preference adopted by the helical macromolecular structure (*P* helix, Figure 35a). Furthermore, if the (*S*)-Ala-(*S*)-MPA pendant is used, *M* helices are obtained in both extended and bent conformations (Figure 35b), corroborating the chiral overpass effect as a helical control mechanism.

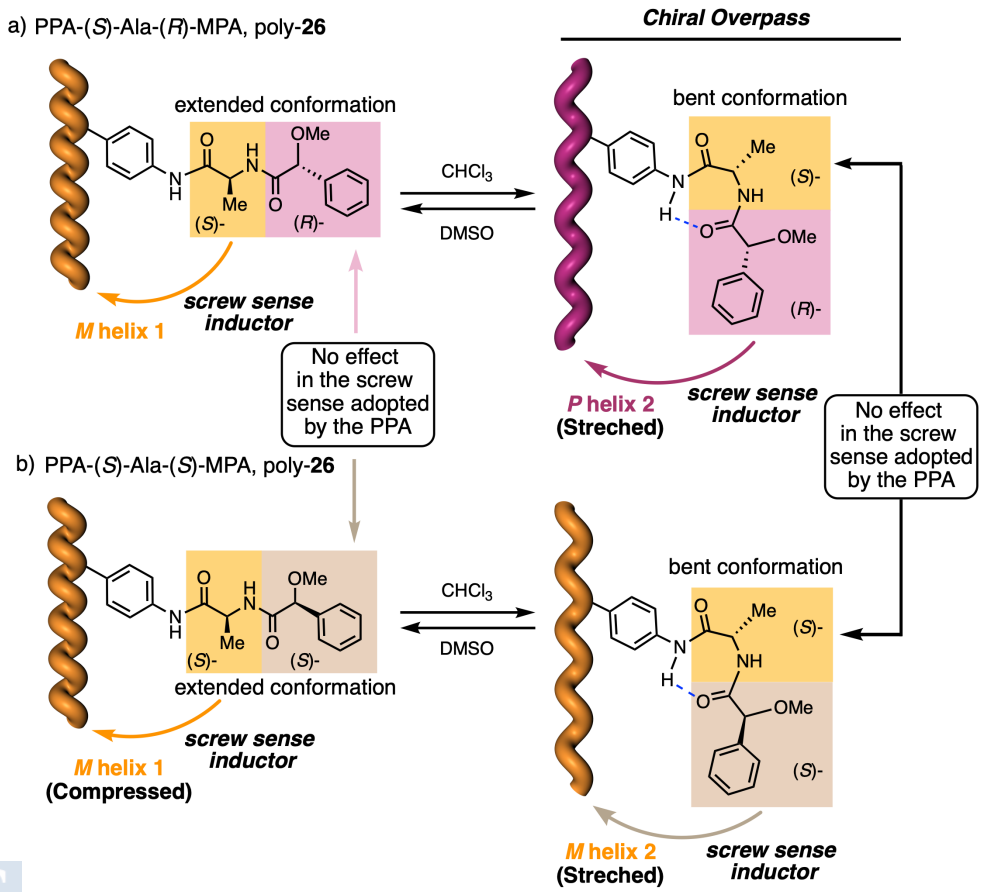

Figue 35. Schematic illustration of the chiral overpass effect in PPAs, controlling both stretching and handedness. Reproduced from ref. 180 with permission from the Royal Society of Chemistry.

1.6.2. Control over Polymer Chain Elongation in Helical Polymers

Once the mechanisms responsible for the induction of preferential handedness have been described, another factor that plays a key role is the degree of elongation of the helical scaffold (compression/stretching), given the impact that a small structural change can have on the properties of the macromolecules.

The degree of elongation in the helical scaffold depends on both the nature of the pendants[21] and the potential interactions they may form with other pendants[189,190] and external stimuli.[126,191-194] As mentioned in Section 5.1., this change can be easily monitored through UV-vis spectroscopy and, in some cases, even observed with the naked eye.[126,191] Therefore, helix stretching is associated with a red shift in the UV-vis spectrum (bathochromic shift) caused by increased conjugation of the polymer backbone (resulting in longer wavelengths), while helix compression corresponds to a hypsochromic shift.[145]

Early examples of PPAs with tunable degrees of elongation were reported by Yashima and co-workers. They described different PPAs bearing several cyclodextrins (CyD) (α, β and γ-CyD) as pendant groups (linked to the backbone by ester, ether, or amide connections).[192,193] For instance, poly-**27** adopts a compressed helix in alkaline water, whereas an increase in the DMSO content in the solvent mixture leads to a bathochromic shift in the corresponding band of the polyene by UV-vis, which is accompanied by a color change of the solution from yellow to red and an inversion of the helical sense, as deduced from the ECD studies (Figure 36a). These structural changes are the result of a different arrangement of the CyD units along the polymer chains in both solvents.[193]

---

[189] S. Arias, F. Freire, M. Calderón, J. Bergueiro, *Angew. Chem. Int. Ed*. **2017**, *56*, 11420–11425.

[190] S. Wang, S. Xie, H. Du, H. Zeng, J. Zhang, X. Wan, *Sci. China Chem*. **202**3, *66*, 887–895.

[191] R. Kakuchi, S. Nagata, R. Sakai, I. Otsuka, H. Nakade, T. Satoh, T. Kakuchi, *Chem. Eur. J*. **2008**, *14*, 10259–10266.

[192] E. Yashima, K. Maeda, O. Sato, *J. Am. Chem. Soc*. **2001**, *123*, 8159–8160.

[193] K. Maeda, H. Mochizuki, M. Watanabe, E. Yashima, *J. Am. Chem. Soc*. **2006**, *128*, 7639–7650.

[194] S. Leiras, F. Freire, E. Quiñoá, R. Riguera, *Chem. Sci*. **2015**, *6*, 246–253.

Later, Tabata and coworkers described a completely different approach for a polymer that showed fragments of stretched and compressed scaffolds coexisting on the same backbone.[130] A change in the temperature can also change the population of these fragments, resulting in a higher proportion of contracted helix with increasing temperature. They called this phenomenon the helix accordion-like oscillation helix effect, the "HELIOS effect" (Figure 36b).

Another relevant approach, reported by Takata, in which MIMs are used as pendants,[91,195] is worth mentioning. For instance, selective control over the position of the subcomponents of a rotaxane allowed them to control the degree of elongation of the polymer scaffold (poly-**28**) by moving the interlocked macrocycle closer or further away from the backbone not only in the solution state but also in the solid state (Figure 36c).[195]

[195] N. Zhu, K. Nakazono, T. Takata, *Chem. Commun*. **2016**, *52*, 3647–3649.

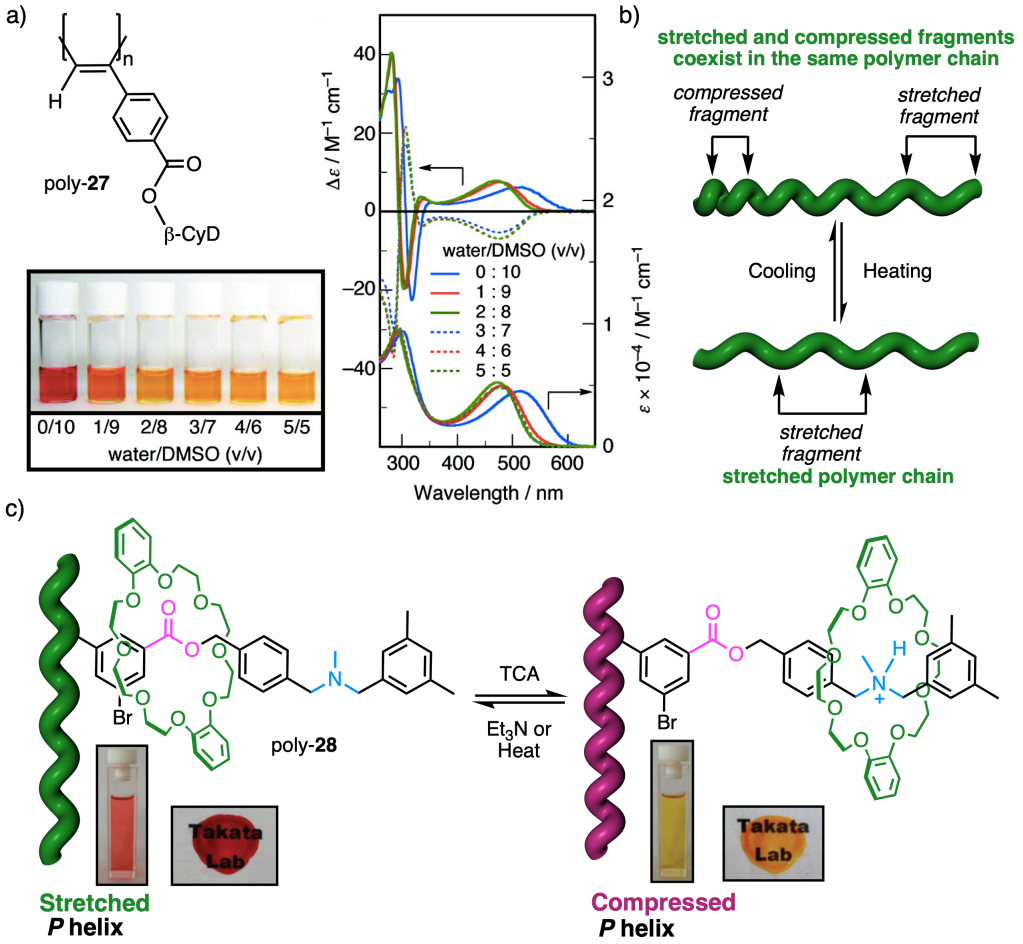

Figure 36. (a) Schematic illustration of the stretching process of poly-**27** by the change in the solvent composition (DMSO/water at different ratios). Reproduced from ref. 193 with permission from the American Chemical Society, copyright 2006. (b) Conceptual representation of the HELIOS effect within a polymer chain. (c) Schematic illustration of the acid-mediated control on the elongation of poly-**28** driven by the rotaxane molecular switch (TCA = trichloroacetic acid). Reproduced from ref. 195 with permission from the Royal Society of Chemistry, copyright 2016.

A relevant example showing the enormous impact of a conformational change in the elongation degree was developed by Freire and Riguera, who developed a PPA functionalized with MTPA as a pendant (poly-**29**) where the *cis/trans* conformational change in the amide (H–)N–C(=O) produces changes in the elongation of the polymer. Moreover, they described that *sp*/*ap* conformational change (O=)C–C(–O) could produce a helical inversion in the polymer due to a different spatial location of the substituents by tele-induction. Therefore, four different helical scaffolds were obtained for poly-(*R*)-**29**,

considering the donor character (compressed/stretched) and the polarity (*P*/*M*) of the solvent (Figure 37).[196]

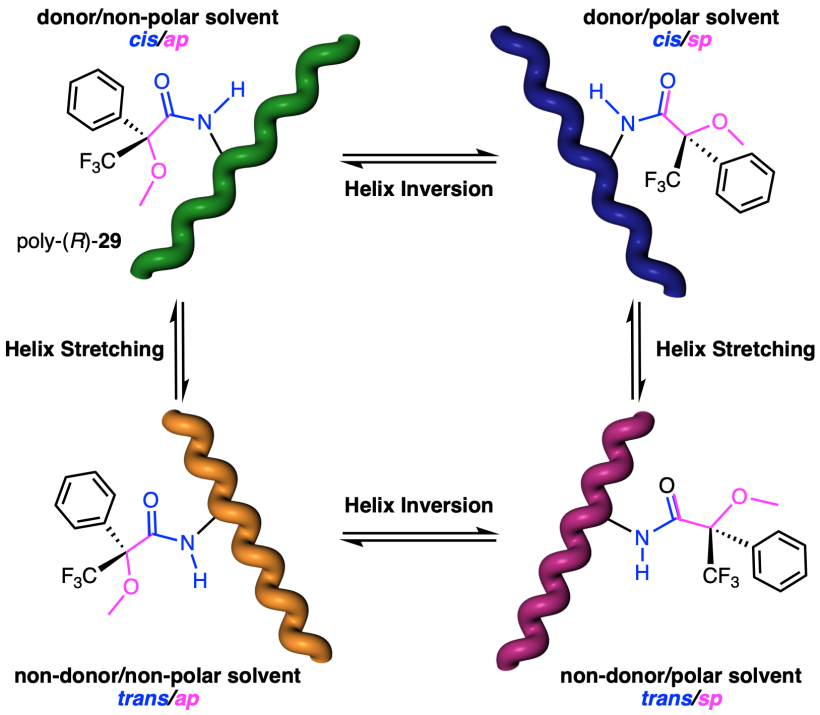

Figure 37. Correspondence between the four different structural states of poly-(*R*)-**29** and the polar/low-polar and donor/non-donor properties of the solvents. Reproduced from ref. 196 with permission from the Royal Society of Chemistry, copyright 2013.

Furthermore, our research group described the remarkable effect of the aromatic substitution pattern on the helical scaffold in PPAs.[21] *Para*-, *meta*- and *ortho*-substituted polymers derived from MPA were synthesized. The results showed differences in elongation and dynamic behavior due to the difficulties of the pendant groups to accommodate within the helical scaffold when approaching the backbone (Figure 38). Thus, the *para*-MPA (*p*-poly-**30**) presents a highly dynamic stretched helix, while the *ortho*-MPA (*o*-poly-**30**) is completely static and has an almost flat structure with a strong tendency to aggregate. Interestingly, the behavior of the meta-(*m*-poly-**30**) is in the middle of the previous two, i.e., it is not very dynamic, showing a weak response to external stimuli and exists as an equilibrium of two helices, one compressed and the other stretched.

[196] S. Leiras, F. Freire, J. M. Seco, E. Quiñoá, R. Riguera, *Chem. Sci.* **2013**, *4*, 2735–2743.

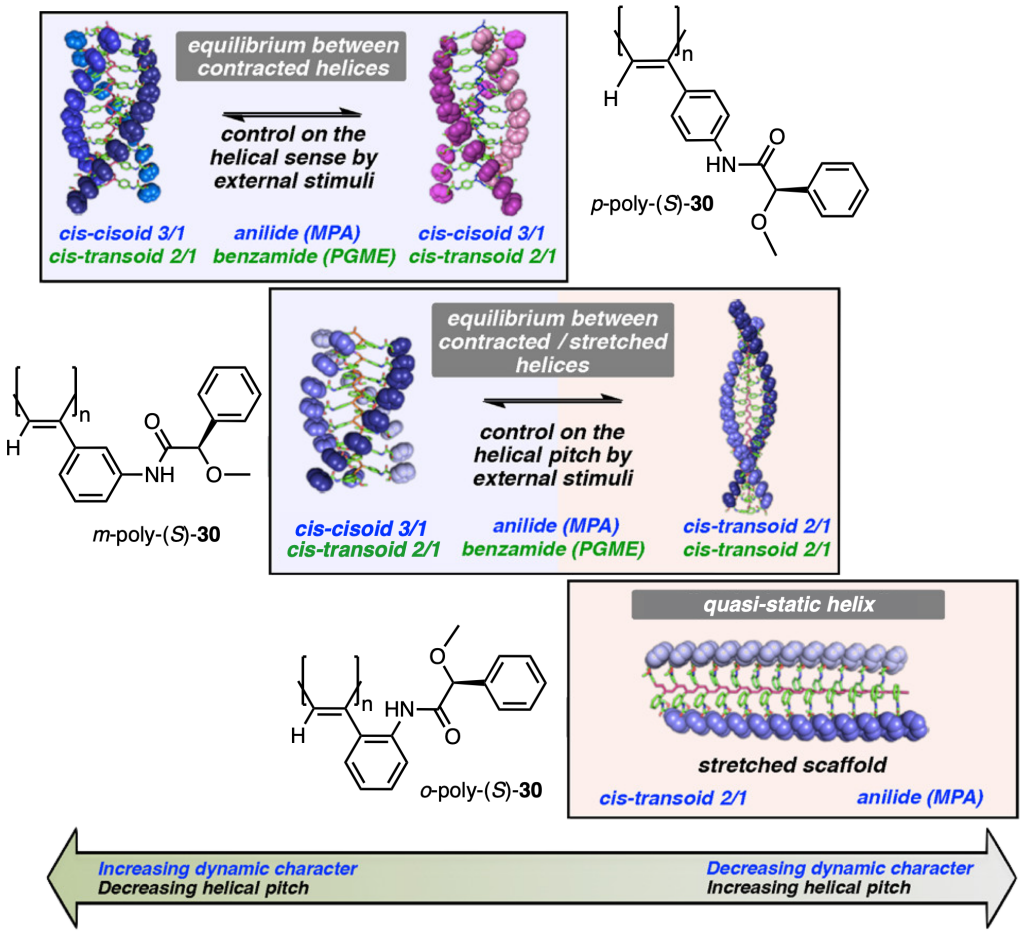

Figure 38. Schematic representation of the effect of the substitution pattern on the aryl ring has over the helical scaffold and the responsiveness towards external stimuli. Reproduced from ref. 21 with permission from American Chemical Society, copyright 2016.

1.7. Supramolecular Polymers

Over the last few decades, considering that the screw sense of helical structures is strongly influenced by non-covalent interactions between chiral entities, a new concept for helical polymers has emerged from the field of supramolecular chemistry. In good accordance with a covalent polymer, a supramolecular polymer can be defined as a macromolecule in which monomeric units are held together by non-covalent interactions (e.g., hydrogen bonding, π-π stacking and Van der Waal's forces).[95]

In recent years, this family of polymers has found applications in various scientific fields, such as optoelectronic devices,[197] biomedicine,[198] adhesives,[199] catalysis,[200,201] or even more sophisticated structures[202].

1.7.1. Classification of Supramolecular Polymers

Different approaches have been described to classify supramolecular polymers according to the nature of the self-assembling units or the non-covalent forces acting to build up the aggregate species. However, the most used feature to classify this type of polymers is the supramolecular polymerization mechanism. Such classification involves the evaluation of the Gibbs free energy of the polymer as a function of conversion (thermodynamic classification), and it is based on the classification made by Carothers for covalent polymers.[203] Hence, two supramolecular polymerization mechanisms have been described for supramolecular polymers: the *isodesmic* mechanism and the *cooperative* or *nucleation-elongation* mechanism (Figure 39a).[3]

In the isodesmic mechanism, comparable to step polymerization in covalent polymers, supramolecular polymerization is well-described by a single binding constant as the non-covalent interactions established among pendants remain unaffected by increasing the length chain. Therefore, each addition is equivalent (same equilibrium constant), and polymer growth will be favored by increasing the concentration of monomers in the solution or by decreasing the sample temperature.

---

[197] Y. Yamamoto, T. Fukushima, Y. Suna, N. Ishii, A. Saeki, S. Seki, S. Tagawa, M. Taniguchi, T. Kawai, T. Aida, *Science* **2006**, *314*, 1761–1764.

[198] Z. Álvarez, A. N. Kolberg-Edelbrock, I. R. Sasselli, J. A. Ortega, R. Qiu, Z. Syrgiannis, P. A. Mirau, F. Chen, S. M. Chin, S. Weigand, E. Kiskinis, S. I. Stupp, *Science* **2021**, *374*, 848–856.

[199] W. Zhao, J. Tropp, B. Qiao, M. Pink, J. D. Azoulay, A. H. Flood, *J. Am. Chem. Soc*. **2020**, *142*, 2579–2591.

[200] M. A. Martínez‐Aguirre, Y. Li, N. Vanthuyne, L. Bouteiller, M. Raynal, *Angew. Chem. Int. Ed*. **2020**, 133, 4229–4237.

[201] O. Dumele, L. Đorđević, H. Sai, T. J. Cotey, M. H. Sangji, K. Sato, A. J. Dannenhoffer, S. I. Stupp, *J. Am. Chem. Soc.* **2022**, *144*, 3127–3136.

[202] S. Datta, Y. Kato, S. Higashiharaguchi, K. Aratsu, A. Isobe, T. Saito, D. D. Prabhu, Y. Kitamoto, M. J. Hollamby, A. J. Smith, R. Dalgliesh, N. Mahmoudi, L. Pesce, C. Perego, G. M. Pavan, S. Yagai, *Nature* **2020**, *583*, 400–405.

[203] W. H. Carothers, *Chem. Rev*. **1931**, *8*, 353–426.

The cooperative mechanism, equivalent to the chain-growth covalent polymerization, involves two different regimes. The first one is the nucleation regime, which is a thermodynamically unfavorable initial step that yields nuclei. The latter is the elongation regime in which these nuclei grow up to form the final aggregated species. More concretely, the monomer first aggregates in a kinetically preferred structure that depolymerizes and subsequently polymerizes into the thermodynamically stable aggregate. Therefore, if the process is thermodynamically controlled, it will result in a single type of helical aggregate. However, if the process occurs under kinetic control, the structure of the final aggregate will depend on several variables, such as preparation method, temperature modulation, and so on.[204]

In broad terms, the cooperative mechanism is defined by two different binding constants — the nucleation K_n and the elongation K_e — and by the degree of cooperativity (σ), described as the quotient between K_n and K_e. As a result, the lower the value of σ, the higher the cooperativeness of the process.[205]

The self-assembly mechanism during supramolecular polymerization has been extensively studied by UV-vis and temperature-dependent ECD spectroscopy, which has allowed the definition of the mechanisms described above. Thus, by monitoring the variation of an intrinsic property (typically the spectroscopic signal normalized to a given wavelength) as a function of temperature, the cooling curve is obtained. If the resulting curve is sigmoidal, the polymerization will follow an isodesmic process, whereas if a hyperbole along an untangled slope is obtained, the polymerization will follow a cooperative process (Figure 39b). In both cases, it is worth considering that the cooling curves must be recorded at slow rates to avoid possible hysteresis and to ensure that the system remains in thermodynamic control.

[204] M. Wehner, F. Würthner, *Nat. Rev. Chem.* **2019**, *4*, 38–53.

[205] T. F. A. De Greef, M. M. J. Smulders, M. Wolffs, A. P. H. J. Schenning, R. P. Sijbesma, E. W. Meijer, *Chem. Rev.* **2009**, *109*, 5687–5754.

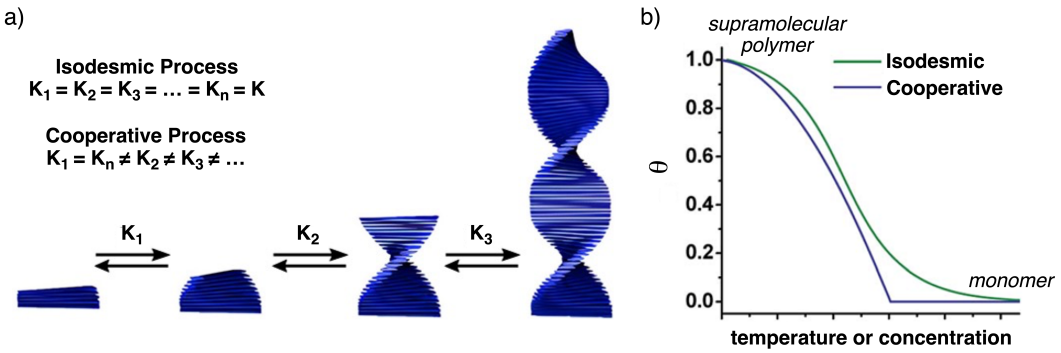

Figure 39. (a) Schematic representation of the isodesmic and cooperative mechanism of supramolecular polymerisation, showing the equality of K and the nucleation-elongation steps, respectively. (b) Fraction of aggregates versus concentration/ temperature for isodesmic and cooperative growth depicted by a sigmoidal and non-sigmoidal with critical nucleation step profile, respectively. Reproduced from ref. 205 with permission from American Chemical Society, copyright 2009.

The resulting cooling curves are usually fitted with the mathematical Mass Balance (MB) model. In this sense, the fraction of species added at different temperatures is simulated based on Mass Balance equations for different sets of thermodynamic parameters describing both the equilibrium in the nucleation phase (K_n, characterized by ΔH_n and ΔS_n) and the equilibrium in the elongation phase (K_e, characterized by ΔH_e and ΔS_e). Both phases are separated by the characteristic elongation temperature (T_e). Moreover, the accuracy of the obtained values is maintained by fitting the cooling curve to multiple concentrations.[206] Thus, the cooperativity of the process is quantified by the following equation.

$$\sigma = \frac{K_n}{K_e} = e^{\Delta H_{np}/R \cdot T}$$

Equation 7. Mathematical statement for determining the degree of cooperativity of the polymerization process.

In this approach, ΔS_e is considered the same as ΔS_n to simplify the fitting. Thus, a new expression is introduced: the nucleation penalty (ΔH_{np}), given by the difference of ΔH_e minus ΔH_n. The more negative ΔH_{np}, the lower σ and the higher the cooperativity

[206] C. Kulkarni, E. W. Meijer, A. R. A. Palmans, *Acc. Chem. Res.* **2017**, *50*, 1928–1936.

(σ < 0). In the case of $\Delta H_e = \Delta H_n$, σ = 1 and the system will follow an isodesmic process.[205]

1.7.2. Helical Supramolecular Polymers

The presence of stereogenic elements (point, axial or planar chiral motifs) in monomeric units that self-assemble to form supramolecular polymers has contributed to the development of this field, giving rise in many examples to more complex secondary structures in a controlled manner.[3, 96] The most relevant processes generally used to build up helical supramolecular polymers are asymmetry transfer, asymmetry amplification, and symmetry breaking.[95]

The asymmetry transfer process, which will be discussed in the following section (Section 7.2.1.), involves the use of chiral monomeric units to achieve the supramolecular level. However, asymmetry amplification is of growing interest as it implies the co-assembly between different monomers. Thus, the formation of supramolecular copolymers is a useful strategy to achieve complexity and functionality.[207]

The symmetry-breaking process is the less common strategy to achieve homochiral supramolecular polymers. This one implies the formation of enantiomeric excess from a racemic mixture by the application of an appropriate external stimulus (solvent, stirring, light, magnetic field, etc.).[208]

1.7.2.1. Asymmetry Transfer in Helical Supramolecular Polymers

The transfer of asymmetry process is the self-assembly mechanism that is influenced or determined by the chirality of the corresponding building blocks. Thus, during the non-covalent interaction of two chiral molecules to form a supramolecular dimer, the spatial constraints imposed by the inherent three-dimensional orientation of their constituent parts may favor only one of the possible stereochemical configurations. As more molecules are assembled to form first oligomers, and then supramolecular

[207] B. Adelizzi, N. J. Van Zee, L. N. J. de Windt, A. R. A. Palmans, E. W. Meijer, *J. Am. Chem. Soc*. **2019**, *141*, 6110–6121.

[208] A. Arango-Restrepo, O. Arteaga, D. Barragán, J. M. Rubi, *Phys. Chem. Chem. Phys*. **2023**, *25*, 9238–9248.

polymers, the preferred dimer orientation is transferred to the growing aggregate, resulting in the propagation of the preferred stereochemical outcome.[95]

The transfer of asymmetry depends on several factors, such as the distance between the chiral motif and the assembly site, the strength of the non-covalent interactions, the competition between chiral and achiral interactions, or even the nature of the solvent.[209-211] Another factor that largely determines the transferability of asymmetry is the type of supramolecular polymerization mechanism governing the self-assembly process. Most of the examples reported occur under cooperative supramolecular polymerization, where, usually, the involvement of two or more different types of directional non-covalent forces determines the stability of the final helical polymer.

One of the best-known examples of the formation of a helical supramolecular polymer showing asymmetry transfer, which also occurs under thermodynamic control, is the self-assembly of benzene-1,3,5-tricarboxamides (BTAs)(Figure 40a).[212, 213]

The three amide groups present in the monomer core form a triple array of hydrogen bonds, which allows the effective stacking of the aromatic nuclei, placing the adjacent molecules one on top of the other with a rotation angle of about 60º, following a highly cooperative supramolecular polymerization mechanism. The presence of stereocenters on the aliphatic chains determines the preferential *P* or *M* screw sense of the resulting supramolecular aggregate, which is confirmed by the appearance of a strong Cotton effect in the ECD spectrum (Figure 40b). For example, in the case of compounds such as **14** (Figure 40), the supramolecular polymerization happens in non-polar solvents, commonly methylcyclohexane (MCH), leading to helical aggregates with opposite helicity.[213] This result directly stems from the transfer of asymmetry from the peripheral chiral centers to the supramolecular level.

---

[209] O. Takahashi, Y. Kohno, M. Nishio, *Chem. Rev*. **2010**, *110*, 6049–6076.

[210] C. R. Martinez, B. L. Iverson, *Chem. Sci*. **2012**, *3*, 2191–2201.

[211] M. F. J. Mabesoone, A. R. A. Palmans, E. W. Meijer, *J. Am. Chem. Soc.* **2020**, *142*, 19781–19798.

[212] S. Cantekin, T. F. A. de Greef, A. R. A. Palmans, *Chem. Soc. Rev*. **2012**, *41*, 6125–6137.

[213] M. M. J. Smulders, A. P. H. J. Schenning, E. W. Meijer, *J. Am. Chem. Soc*. **2007**, *130*, 606–611.

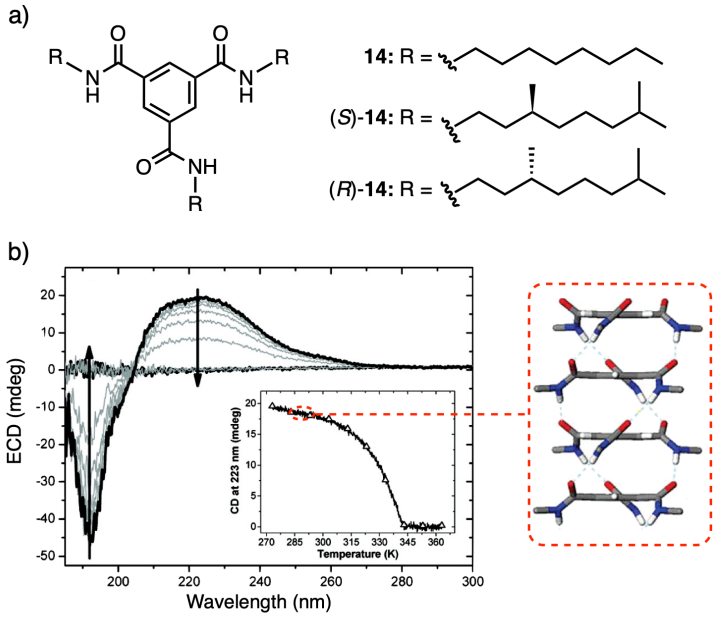

Figure 40. (a) Chemical structure of (*R*)-**14**. (b) ECD spectra in heptane ($1.4 \cdot 10^{-5}$ M) for (*R*)-**14**; the inset shows the decrease of ellipticity at 223 nm when increasing the temperature. Model of the right-handed helix proposed for (*R*)-**14** based. Reproduced from ref. 213 with permission from American Chemical Society, copyright 2007.

The cooperative self-assembly was also observed in BTAs bearing linear and branched alkyl chains as substituents,[213] as well as in BTAs with reversed amide linkage,[214] or even with thioamides.[215] This progress in BTAs derivatives has contributed significantly to a greater understanding of the practical and theoretical facets associated with supramolecular polymerization, which has been extrapolated to a broader spectrum of supramolecular motifs.

In view of these advances, Sánchez and coworkers developed a different approach, but also based on π-extended C_3-symmetries, incorporating chiral and achiral oligo(phenyleneethylene) (OPE) tricarboxyamides as substituents (Figure 41a).[216,217] Experimental and theoretical analyses of various monomers showed that, in most cases, self-assembly also occurs through a cooperative process (Figure 41b), with cooperativity

[214] P. J. M. Stals, J. C. Everts, R. de Bruijn, I. A. W. Filot, M. M. J. Smulders, R. Martín‐Rapún, E. A. Pidko, T. F. A. de Greef, A. R. A. Palmans, E. W. Meijer, *Chem. Eur. J.* **2010**, *16*, 810–821.

[215] T. Mes, S. Cantekin, D. W. R. Balkenende, M. M. M. Frissen, M. A. J. Gillissen, B. F. M. De Waal, I. K. Voets, E. W. Meijer, A. R. A. Palmans, *Chem. Eur. J.* **2013**, *19*, 8642–8649.

[216] F. García, P. M. Viruela, E. Matesanz, E. Ortí, L. Sánchez, *Chem. Eur. J.* **2011**, *17*, 7755–7759.

[217] F. García, P. A. Korevaar, A. Verlee, E. W. Meijer, A. R. A. Palmans, L. Sánchez, *Chem. Commun*. **2013**, 49, 8674–8676.

factor values comparable to those obtained for some BTAs derivatives. These aggregates are stabilized by a triple hydrogen bonding arrangement and π-π stacking of the aromatic rings.

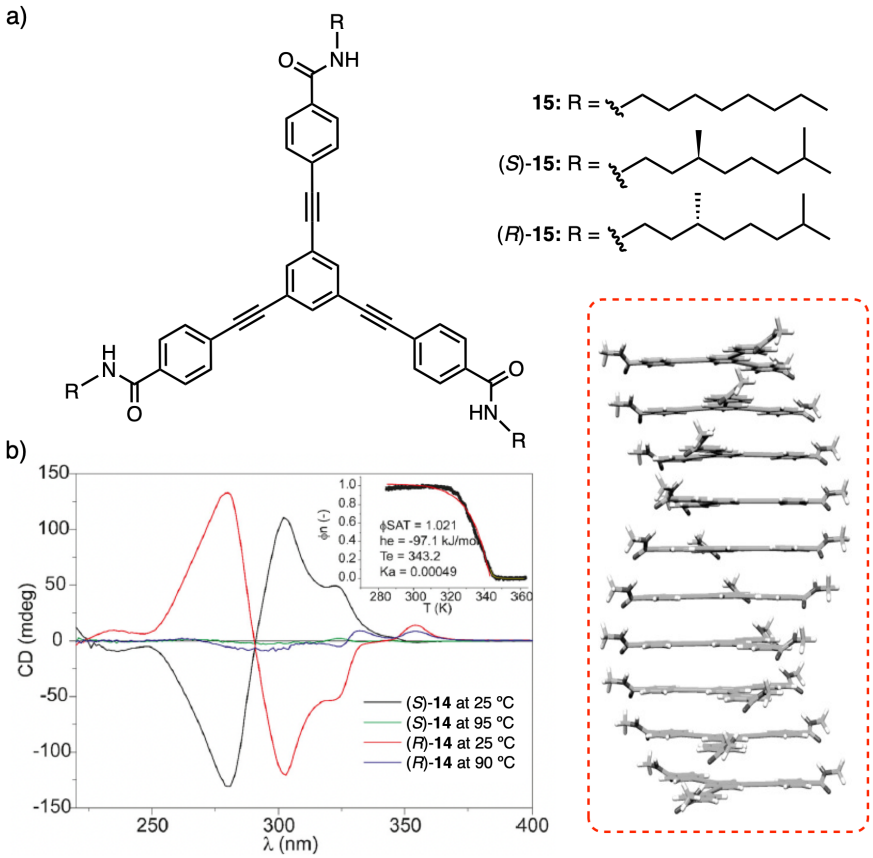

Figure 41. (a) Chemical structure of **15**. (b) Experimental ECD spectra of (*S*)-**15** and (*R*)-**15** in MCH at different temperatures. The inset shows the non-sigmoidal variation of the degree of aggregation (θ) versus the temperature, which demonstrates the cooperative character of the supramolecular polymerization of compound **15** with the corresponding fitting. Reproduced from ref. 216 with permission from the John Wiley and Sons, copyright 2011.

1.7.2.2. From Axial Chirality towards Supramolecular Helicity

An underexplored strategy to obtain chiral supramolecular polymers consists of the polymerization of three-dimensional non-planar units especially those involving axial or helical chirality.[218,219] These chiral molecules have a highly distorted and rather rigid three-dimensional structure that prevents easy self-assembly. Recently, Sánchez and

[218] Z. Xie, V. Stepanenko, K. Radacki, F. Würthner, *Chem. Eur. J.* **2012**, *18*, 7060–7070.
[219] J. Buendía, E. E. Greciano, L. Sánchez, *J. Org. Chem.* **2015**, *80*, 12444–12452.

co-workers have demonstrated the efficient formation of chiral supramolecular polymers based on a carbo[6]helicene scaffold.[220] For this purpose, they have introduced two peripheral *N*-(2-(2-(4-(4-ethynylbenzamido)ethyl)-3,4,5-tridecyloxybenzamides units to efficiently favor the supramolecular interaction of the [6]helicenes via a fourfold H-bonding array between the amides (Figure 42a).

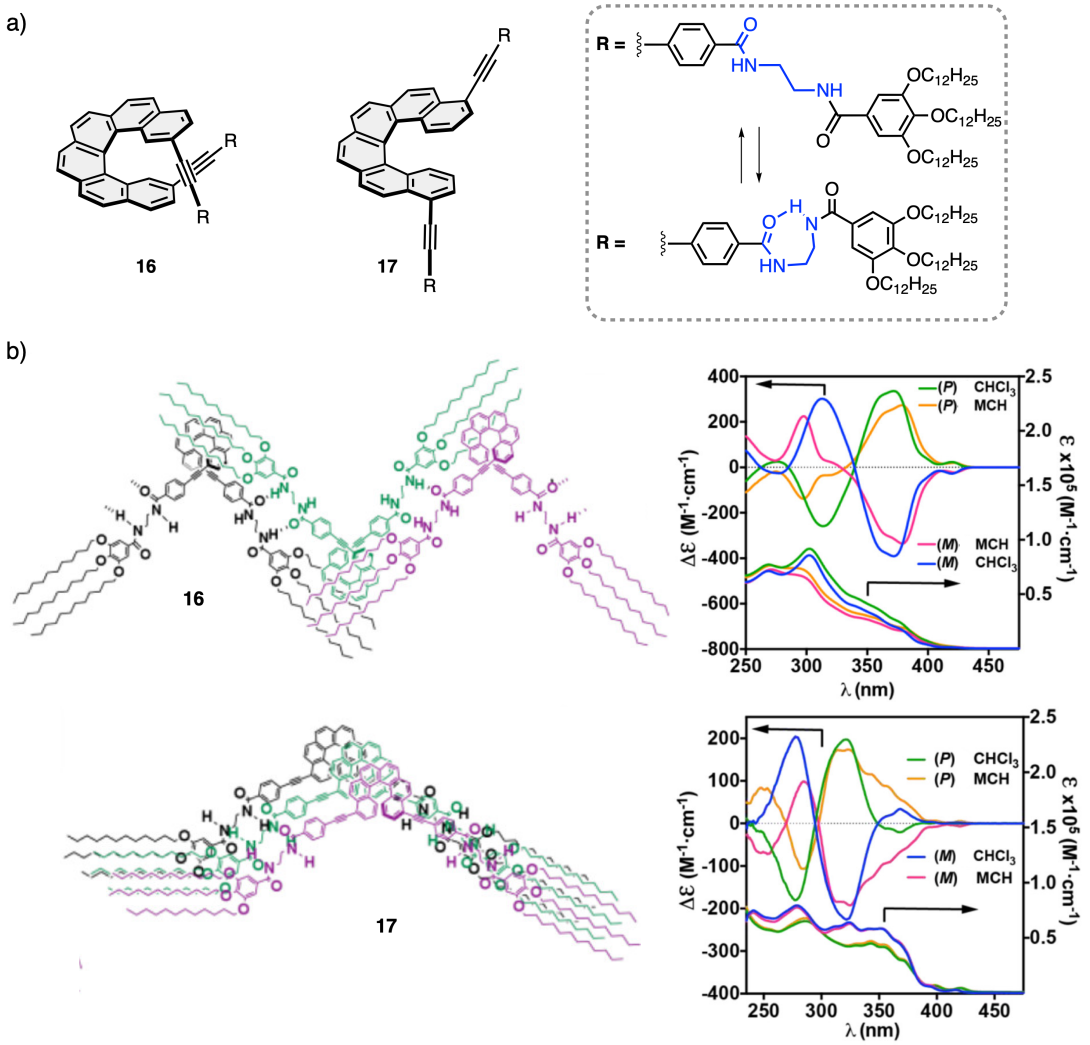

Figure 42. (a) Chemical structures of the helicene derivatives **16** and **17**. (b) Schematic illustration of head-tail self-assembly of **16**, the head-head self-assembly of **17** and and their respective ECD spectra. Reproduced from ref. 220 with permission from American Chemical Society, copyright 2022.

The resulting compounds showed different chiroptic responses due to the different substitution patterns (Figure 42b). Interestingly, the ECD spectra of (*P*)-**16** and (*P*)-**17** in

[220] R. Rodríguez, C. Naranjo, A. Kumar, P. Matozzo, T. K. Das, Q. Zhu, N. Vanthuyne, R. Gómez, R. Naaman, L. Sánchez, J. Crassous, *J. Am. Chem. Soc.* **2022**, *144*, 7709–7719.

MCH showed some modifications in comparison to those detected in $CHCl_3$ that could be indicative of an excitonic coupling of the aromatic units due to the efficient supramolecular polymerization (Figure 42b).

These aggregates showed stability and properties with great applicability, such as the high ability of these helicene derivatives to self-assemble on a (conducting) surface and the high chiroptic activity. Therefore, the field is still evolving, in which systems with increasing complexity are constantly emerging.

Chapter 2. Objectives

Chapter 2. Objectives

Helical polymers —covalent and supramolecular— have been extensively studied during the last decades due to their high structure/function relationship. As a result, helical polymers have been proposed to be useful in a wide range of fields, including materials science, catalysis, biology, and even as components of molecular gears. In all cases, the study of the secondary structure is key to the subsequent manipulation of the helix and to the rational design of its possible applications.

In this context, this Doctoral Thesis focuses on the development of novel chiral polymeric materials based on axially chiral allenes as a chiral source with potential applications in molecular recognition processes. Allenes are an enticing option for obtaining chiral compounds of greater complexity. Therefore, it will be necessary to understand the communication mechanisms that helical polymers may present to incorporate the allenes into novel macromolecular gears in the interplay between polymers, chirality, mechanically interlocked molecules, and supramolecular chemistry.

Dynamic Axial-to-Helical Communication Mechanism in Poly[(allenylethynylenephenylene)acetylene]s under External Stimuli

One of the most enticing properties of dynamic helical polymers, which has driven their development in recent decades, is their stimuli-responsive properties. These properties enable the modulation of both their helical sense and elongation. To rationalize how the stimulus-response is produced, deciphering the operating mechanisms is of utmost importance. In all the mechanisms described so far, modifications in the helical structure of the PPAs result from a conformational change in the pendants, which are then further harvested by the polymeric backbone.

The main aim of this project is to demonstrate a different chiral induction mechanism for polymers, based on modified poly(phenylacetyelene)s (PPAs) in which the pendant groups are conformationally locked chiral allenes, giving rise to poly[(allenylethynylenephenylene)acetylene]s (PAEPAs). As a result, the screw sense of a PAEPA will be determined by the allenyl substituent with the optimal size/distance relationship to the backbone. However, PAEPAs could be transformed into dynamic helical polymers by the on/off (activation/deactivation) of supramolecular interactions by an appropriate external stimulus. Herein, this project presents a novel approach to tame

the helices of chiral dynamic helical polymers and introduces a new dynamic mechanism of axial-to-helical communication.

Publication associated with this objective: M. Lago-Silva, M. M. Cid, E. Quiñoá, F. Freire, *Angew. Chem. Int. Ed*. **2023**, *62*, e202303329.

P/M **Macromolecular Switch Based on Conformational Control Exerted by an Achiral Side Chain within an Axially Chiral Locked Pendant**

Dynamic helical polymers are macromolecular switches in which the *P/M* screw sense control is achieved by relying on different helix induction mechanisms that arise from the conformational manipulation of a monomer repeating unit due to interactions with different stimuli.

In this work, our objective is to create a macromolecular helical switch based on a chiral pendant that possesses an achiral flexible arm within its structure. More specifically, we aim to control the *P* and *M* helical senses of a macromolecular gear without altering the chiral information of the pendant by using an allene moiety. Thus, the control over the extended/bent conformational composition of an achiral flexible arm is the only prerequisite necessary to induce a helix inversion in the macromolecular polymer structure.

Publication associated with this objective: M. Lago-Silva, M. M. Cid, E. Quiñoá, F. Freire, *J. Am. Chem. Soc*. **2024**, *146*, 752–759.

Mechanically Interlocked Macromolecular Gears: Elongation and Helical Sense Control of a Helical Polymer by Acting on a Chiral Rotaxane Used as Pendant Group

A bottom-up approach can be used to create complex macromolecular systems that act as macromolecular gears. Nature uses this approach to create complex systems in which a small fragment of a macromolecule is usually involved in a stimulus-response process that often changes the conformational composition of the whole macromolecule. This response is effectively transmitted to the rest of the complex system by a conformational communication mechanism. In dynamic helical polymers such as PPAs, conformational changes in a chiral pendant group induced by external stimuli are effectively transmitted through space to the polyene backbone.

We envisioned a sophisticated macromolecular gear combining mechanically interlocked molecules, i.e., a rotaxane, and dynamic helical polymers, i.e., a PPA. To this

end, we designed a PPA with a chiral rotaxane as the monomeric repeating unit. A chiral allene was chosen as the chiral thread due to its axial chirality and restricted conformational composition. It was combined with a small macrocycle as a wheel to construct the rotaxane. By controlling the relative orientation of the wheel to the chiral axis through external stimuli, we would be able to change the relative volume of the substituents to vary their steric effects. Consequently, the polyene backbone will amplify these structural changes by modifying the elongation and/or helical sense of the polymer scaffold. This novel approach aims to provide a better understanding of how information can be effectively transferred across different levels of complexity.

Axially-Chiral Allene-Based Supramolecular Polymers

Supramolecular helical polymers result from a delicate balance of non-covalent interactions among the building blocks. Typically, these building blocks for the construction of such macromolecular structures are usually based on flat aromatic cores functionalized with either paraffinic or glycolated side chains, which ensure the solubility of the supramolecular polymer in the desired aggregating media. The introduction of chirality in the aforementioned side chains generally promotes the adoption of supramolecular helical scaffolds. Asymmetry induction is classically achieved by introducing point chirality in the solubilizing side chains.

An underexplored strategy for obtaining chiral supramolecular polymers is the polymerization of three-dimensional non-planar monomeric units, especially those with axial or helical chirality. These chiral molecules have a highly distorted and rather rigid three-dimensional structure that prevents easy self-assembly. Aiming to increase the diversity of chiral building blocks for the construction of novel supramolecular materials and the potential applications thereof, we envisioned chiral allenes as building blocks for the preparation of helical supramolecular aggregates. In this context, their self-assembly could be favored by incorporating aggregating moieties. Thus, we propose the functionalization of tetrasubstituted allenes with two dendritic aggregating moieties based on ethylene diamides bearing a gallic wedge with paraffinic chains. This novel approach will allow the supramolecular polymerization of the chiral sterically constrained allene derivatives, leading to new types of chiral supramolecular polymers.

Chapter 3. Results

3.1. Dynamic Axial-to-Helical Communication Mechanism in Poly[(allenylethynylenephenylene)acetylene]s under External Stimuli

The results of this chapter have been published by Angewandte Chemie International Edition as:

María Lago-Silva,[a] María Magdalena Cid,[b] Emilio Quiñoá,[a] Félix Freire,*[a] Dynamic Axial-to-Helical Communication Mechanism in Poly[(allenylethynylenephenylene)acetylene]s under External Stimuli, *Angew. Chem. Int. Ed.* **2023**, *62*, e202303329. DOI: 10.1002/anie.202303329.

Affiliations

[a]Centro Singular de Investigación en Química Biolóxica e Materiais, Moleculares (CiQUS) and Departamento de Química Orgánica, Universidade de Santiago de Compostela E-15782 Santiago de Compostela (Spain)

[b]Departamento de Química Orgánica, Universidade de Vigo, 36310 Vigo (Spain)

Abstract: Helix inversion in chiral dynamic helical polymers is usually achieved by conformational changes at the pendant groups induced through external stimuli. Herein, a different mechanism of helix inversion in poly(phenylacetylene)s (PPAs) is presented, based on the activation/deactivation of supramolecular interactions. We prepared poly[(allenylethynylenephenylene)acetylene]s (PAEPAs) in which the pendant groups are conformationally locked chiral allenes. Therefore, their substituents are placed in specific spatial orientations. As a result, the screw sense of a PAEPA is fixed by the allenyl substituent with the optimal size/distance relationship to the backbone. This helical sense command can be surpassed by supramolecular interactions between another substituent on the allene and appropriate external stimuli, such as amines. So, a helix inversion occurs through a novel axial-to-helical communication mechanism, opening a new scenario for taming the helices of chiral dynamic helical polymers.

3.1.1. Precedents

Dynamic helical polymers have attracted the attention of the scientific community during the last decades due to their stimuli-responsive properties,[96,101,103,106,182,221,222] which allow tuning their helical sense[182,188,223] or elongation,[224-228] once they have been prepared, via external stimuli such as temperature, pH, chiral additives, cations, or anions among others.[126,187,189,229-235] Moreover, helical polymers find applications in other fields such as asymmetric synthesis,[79,236,237] or chiral stationary phases in High Performance Liquid Chromatography (HPLC),[78,238] due to their structure/function relationship. However, although the secondary structure adopted by a helical polymer is important to establish a correct structure/function relationship, its elucidation is extremely complicated.[186] The main limitation to obtain robust structural data is the presence of monomer repeating units along the polymeric chain, which makes powerful structural techniques such as Nuclear Magnetic Resonance (NMR) practically useless. To obtain an approximate 3D structure of a helical polymer, it is necessary to combine the information obtained from different structural techniques such as Electronic Circular Dichroism (ECD),[157,239] NMR[128,240] and Atomic Force Microscopy (AFM)[165,169,179,241-245] among others.[246] Furthermore, in these systems, chiral information is transmitted from the chiral pendant to the polymeric backbone, such that a handedness preference is induced. In order to rationalize how the stimulus-response is produced, deciphering the operating mechanisms is of utmost importance. In this sense, there are different ways to control the helical sense of a polymer. Thus, if the polymer is chiral, the presence of a preferred conformer at the chiral pendant group results in an induced helical sense that can be either *P* or *M*.[231, 247] Variations in the conformational composition of the pendant group result in either helical sense enhancement or helical inversion (Figure 43a).[21,110] On the other hand, if the helical polymer is achiral, amplification of asymmetry phenomena (helical induction) arise from interactions between the polymer and external chiral molecules used as external stimuli.[119] In chiral and achiral polymers, the changes produced in the helical structures are related to the spatial dispositions adopted by the substituents or associated species at the pendant groups. Interestingly, during the last years different mechanisms for the transmission of chiral information have been explored —for example, from the pendant to the

polyene backbone in poly(phenylacetylene)s (PPAs)— (Figure 43b).[172, 248, 249] In these studies, the chiral pendant group is placed at a remote position, separated from the polyene backbone by achiral spacers. Thus, the helical induction in the polymer can follow two different mechanisms: 1) inducing a conformational change in the achiral spacer[182, 250] or 2) inducing a tilting degree in the supramolecular arrangement of the achiral spacers along the helix (Figure 43b).[185] These structural changes produced in the spacer, or in the arrangement of the spacer along the polymer scaffold, are further harvested by the polyene backbone which induces a screw sense excess in the helical material.

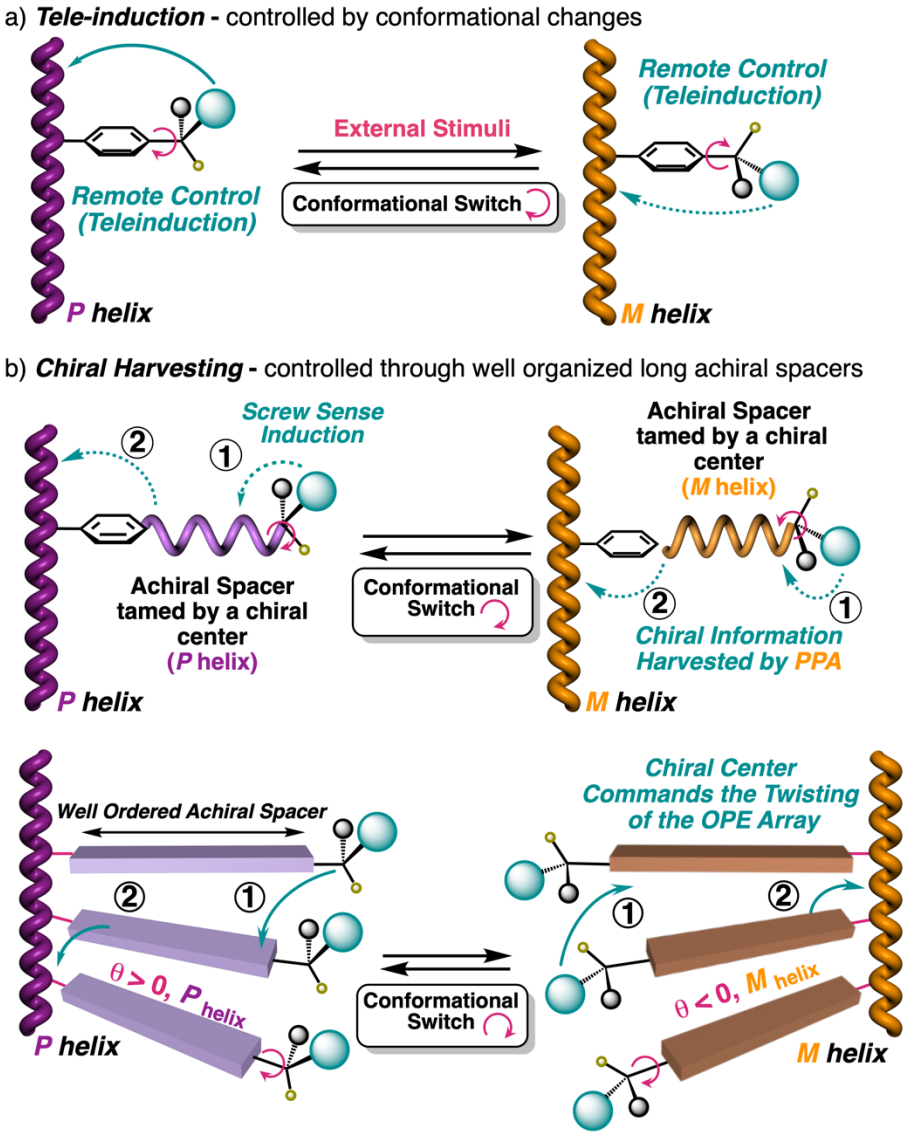

Figure 43. Conceptual representations of the chiral information transmission mechanisms from the pendant to the polyene backbone in PPAs. (a) *Chiral Tele-induction* mechanism. (b) *Chiral Harvesting* mechanism: by inducing a conformational change in the achiral spacer and through a tilting degree in the supramolecular arrangement of the achiral spacers along the helix.

Herein, we introduce a novel mechanism of chiral tele-induction by combining two concepts, chirality, and supramolecular chemistry to study the direct communication between the polymeric backbone and the chiral pendant. In our design, the idea is to prepare a chiral monomer with a restricted conformational space bearing functional groups that can be involved in supramolecular interactions, such as a properly substituted allenic motif. The restricted rotation in cumulated dienes prevents the relative spatial orientation between the allenic substituents from being altered. So, allenes can possess axial chirality since their four substituents lie in two perpendicular planes (Figure 44). The tunable relative size of the substituents by supramolecular interactions would eventually result in a specific helical handedness in the polymer without altering the conformational composition in the pendant group (Figure 44).

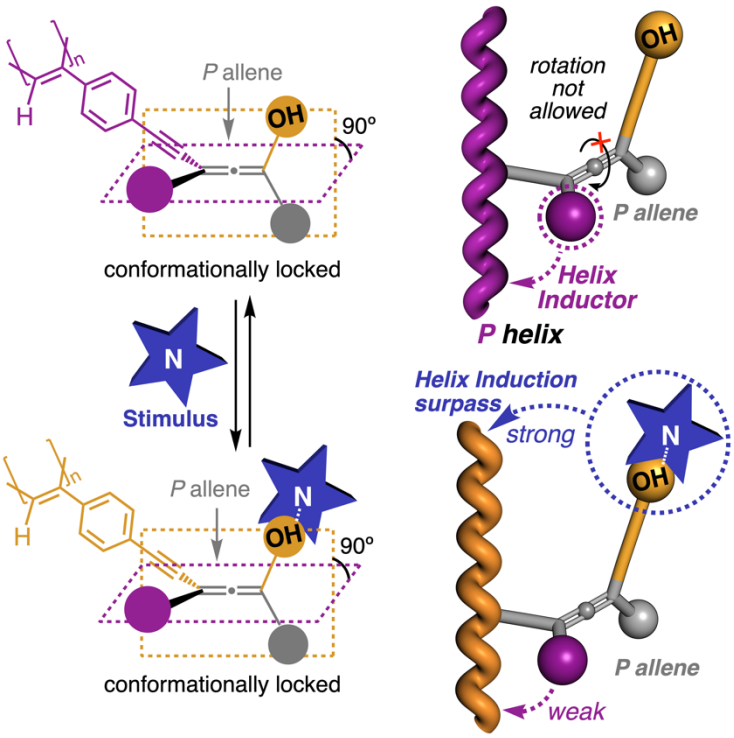

Figure 44. Conceptual view of the chiral information transmission mechanism from the allenic pendants to the polyene backbone via axial-to-helical communication.

3.1.2. Discussion

To perform these studies, we chose PPAs as helical polymers. The control of the helical sense in PPAs, as already described above, is usually achieved by introducing a chiral center in the monomer repeating unit, where the conformational composition and

the distance from the chiral center to the backbone of the polymer plays an important role. In this sense, the polymeric structure (elongation/sense) is related to the different spatial dispositions adopted by the substituents of the chiral pendant. In our design, we envisioned allenes with restricted conformational composition as suitable chiral pendant groups. As a result, the helix adopted by a modified PPA bearing chiral allenes as pendants (i.e., poly[(allenylethynylenephenylene)acetylenes, PAEPAs) should be inert to stimuli that are normally involved in altering the conformational composition of chiral pendants, such as solvent polarity. In this case, a helix inversion can be produced in the PAEPA by taking advantage of the rigidity of the relative spatial orientation between the allenic substituents. We expected that the helical sense of the PPA would be dictated by the relative size of the allenic substituents, with the one closest to the backbone being the key substituent (Figure 44). However, if the allene substituent in a remote position could be involved in supramolecular interactions with other molecules, their joint volume could become large enough to surpass the command of the proximal substituent and cause a helical handedness inversion in the polymer backbone (Figure 44). For this reason, we focused our attention on 1,3-diethynylallene [(*P*)-**DEA**, (*M*)-**DEA**][251] (Figure 45a). This chiral allene is a highly configurational and stable building block, which displayed outstanding chiroptical properties in the construction of allene-acetylenic oligomers, macrocycles, cages and supramolecular assemblies.[24, 31, 32, 34, 35, 38, 252]

Based on this information, we became interested in studying the effect of transferring the molecular properties of allene-acetylenes to the corresponding helical polymers (Figure 44) by exploring a new mechanism of helical induction based on supramolecular interactions between allene and achiral molecules. So, we envisioned phenylacetylene monomers bearing (*P*)- and (*M*)-**DEA** —i.e., (*P*)-**1** and (*M*)-**1**— (Figure 45a,b) as suitable building blocks. These allenes have, on the carbon located near the polymerizable terminal alkyne, the phenylacetylene group necessary to obtain the polymer and a *tert*-butyl group. These two groups form the first plane while, in the second perpendicular plane, the substituents are *tert*-butyl and 2-methylbut-3-yn-2-ol (Figure 45b). Looking at the structure and considering the rigidity of the chiral allenes used as pendants, one could synthesize a helical polymer (Figure 45c) with a screw sense preference that would be commanded by the *tert*-butyl group placed closest to the backbone (Figure 46a). The other *tert*-butyl and 2-methylbut-3-yn-2-ol substituents would be placed in a more remote position and therefore their helix-

inducing effects would be expected to be negligible. However, the hydroxy group in the pendant can establish supramolecular interactions with other molecules via hydrogen bonds, so that the size of the hydroxy-bearing substituent increases without altering its conformational composition. Therefore, this interaction could eventually result in a different helical sense preference with consequent helix inversion (Figure 44).

To test our hypothesis, (*P*)- and (*M*)-**1** monomers were prepared through a Sonogashira cross-coupling between the phenylacetylene derivative and the enantiomerically pure (*P*)- and (*M*)-**DEA** to yield monomers (*P*)-**1** and (*M*)-**1** in ca. 98% yield (Figure 45b) (**DEA** was prepared according to the literature, see Experimental Section Chapter 3.1.). Next, these monomers were submitted to polymerization using a Rh(I) catalyst (Figure 45c), which provided poly-(*P*)-**1** and poly-(*M*)-**1** in high yields (98%) and with high *cis* content of the double bonds[129] as inferred from ^{1}H-NMR and Raman spectra (see Experimental Section Chapter 3.1., Figures S6 and S8a).

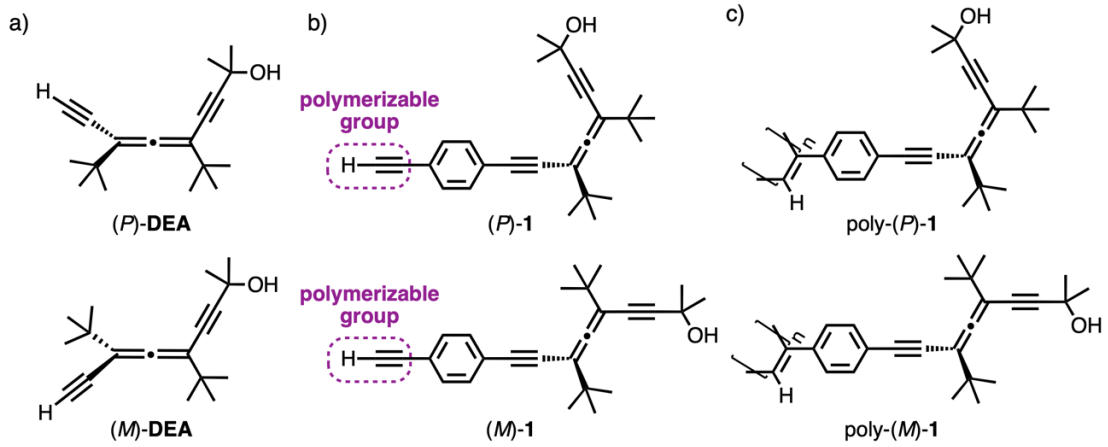

Figure 45. (a) Chemical structure of (*P*)-**DEA** and (*M*)-**DEA**. (b) Chemical structure of monomers (*P*)-**1** and (*M*)-**1**. (c) Chemical structure of polymers poly-(*P*)-**1** and poly-(*M*)-**1**.

ECD studies of the corresponding polymers in different solvents showed how the helical sense adopted by poly-(*P*)-**1** ($ECD_{390} > 0$, *P* helix) and poly-(*M*)-**1** ($ECD_{390} < 0$, *M* helix) remained unaltered regardless of the donor or polar character of the solvent used to dissolve the polymer (Figures 46b,c). Thus, in these polymers an axial-to-helical induction mechanism arises, where the axial chirality of the allene is transmitted to the polyene backbone through effective tele-induction (Figure 46b,c and see Experimental Section Chapter 3.1., Figures S12-S14). More precisely, the different

spatial orientations of the nearby *tert*-butyl group are those that govern the helical sense of the polymer (Figure 46a).

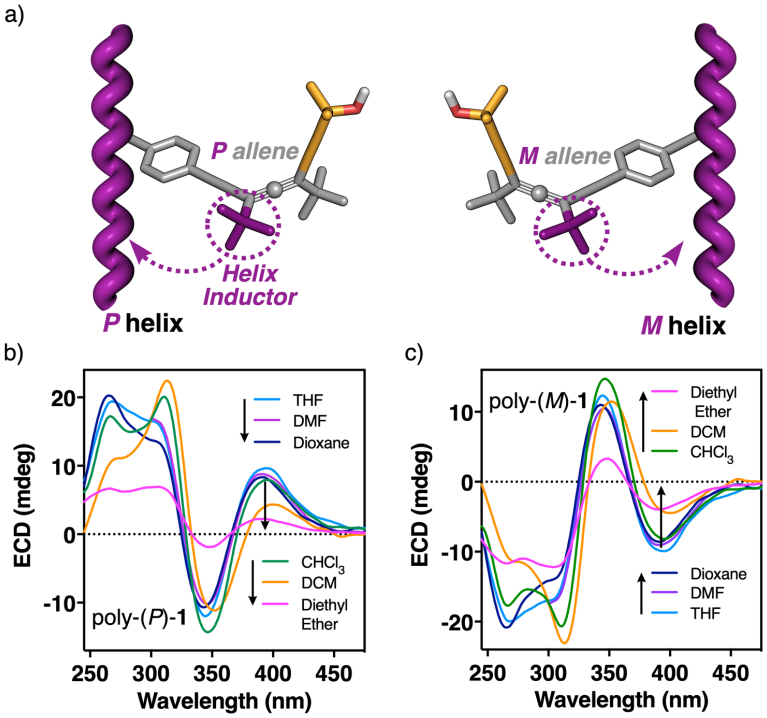

Figure 46. (a) Conceptual view of the chiral information transmission mechanism from the *tert*-butyl group of the allene positioned closest to the polyene backbone via axial-to-helical communication. ECD studies of (b) poly-(*P*)-**1** and (c) poly-(*M*)-**1** in different solvents (0.5 mM).

Next, to demonstrate the axial-to-helical tele-induction surpass mechanism in poly-**1**, we used the hydroxy group of the chiral allene to modify its spatial environment via supramolecular interactions with other molecules, such as amines. To perform these studies and considering the quasi-static behaviors of poly-(*P*)-**1** and poly-(*M*)-**1** in different solvents, diethyl ether was the solvent of choice to carry them out. In this solvent, poly-(*P*)-**1** and poly-(*M*)-**1** show the least screw sense excess, a fact that indicates a greater dynamic behavior and therefore better stimuli responsive properties (Figure 46b,c).

The addition of primary amines such as methylamine, propylamine, isopropylamine, or *tert*-butylamine did not produce helix inversion in poly-(*P*)-**1** (Figure 47a and see Experimental Section Chapter 3.1., Figure S16a), even when this PAEPA was dissolved in pure primary amines, where the interaction between poly-(*P*)-**1** and the primary amine was guaranteed (Figure 47b and see Experimental Section Chapter 3.1., Figure S15a). The existence of this supramolecular interaction poly-(*P*)-**1**/primary amine was demonstrated by 14N-NMR, where a shift

towards higher frequencies is observed for the N of the amine in a mixture of poly-(*P*)-**1**/ primary amine in 1/1 mol/mol ratio (see Figure 47c and see Experimental Section Chapter 3.1., Figure S23). Therefore, although the primary amine is attached to PAEPA, the bulkiness around the nitrogen atoms of the primary amines is not sufficient to overcome the effect of the proximal *tert*-butyl group and produce handedness inversion (Figure 47d).

Interestingly, when analogous experiments are performed with secondary [e.g., diethylamine, diisopropylamine (DIPA)] and tertiary amines [e.g., triethylamine, diisopropylethylamine (DIPEA)], a helix inversion occurs in poly-(*P*)-**1** (from *P* to *M*, Figure 47e-f and see Experimental Section Chapter 3.1., Figures S15b, S16b-d and S17). This helix inversion is not produced by a conformational change in the rigid pendant group, but rather by the supramolecular interaction between the hydroxy group and the amines. This interaction was demonstrated by ^{14}N-NMR (Figure 47g and see Experimental Section Chapter 3.1., Figures S24-S25). Thus, when the supramolecular interaction poly-(*P*)-**1**/amine (secondary or tertiary) takes place, the volume of the allene substituent that contains the hydroxy group increases and starts to command the helical sense of PAEPA, surpassing the order given by the *tert*-butyl group, which causes a helix inversion (Figure 47h).

As expected, similar results were obtained for poly-(*M*)-**1** due to the enantiomeric relationship, i.e., no response to the presence of primary amines and screw sense inversion from *M* to *P* when secondary or tertiary amines are added to a solution containing poly-(*M*)-**1** (see Experimental Section Chapter 3.1., Figures S19 and S20). Moreover, the helix inversion process is reversible, so that after carrying out a workup with aqueous media to remove the amines, the original helical sense is recovered (see Experimental Section Chapter 3.1., Figure S18).

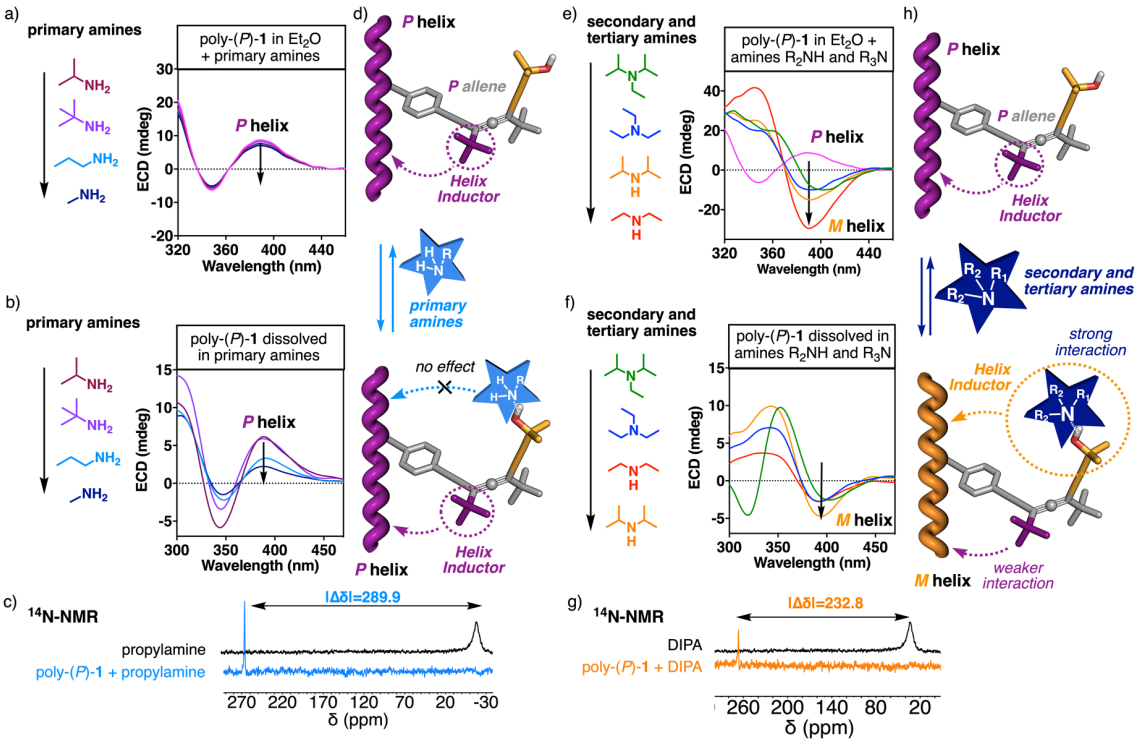

Figure 47. (a) ECD titration experiments of poly-(*P*)-**1** with primary amines in diethyl ether (1.0 mM). (b) ECD studies of poly-(*P*)-**1** dissolved in primary amines (0.3 mM). (c) Comparison of the ^{14}N-NMR spectra of methylamine and poly-(*P*)-**1**/methylamine in 1/1 mol/mol ratio (solvent: Et_2O). (d) Conceptual representation of the poly-(*P*)-**1**/primary amine interaction. (e) ECD titration experiments of poly-(*P*)-**1** with secondary and tertiary amines in diethyl ether (1.0 mM). (f) ECD studies of poly-(*P*)-**1** dissolved in secondary and tertiary amines (0.3 mM). (g) Comparison of the ^{14}N-NMR spectra of Et_3N and poly-(*P*)-**1**/Et_3N in a 1/1 mol/mol ratio (solvent: Et_2O). (h) Conceptual representation of the poly-(*P*)-**1**/secondary/tertiary amine interaction.

To further demonstrate the role of the hydroxy group in the amine/poly-(*P*)-**1** interaction, its acetylation with acetic anhydride yielded poly-(*P*)-**1-OAc** (Figure 48a). ECD studies in different solvents showed the same *P* helical sense (ECD_{390}> 0, *P* helix) as the one adopted by the parent poly-(*P*)-**1** (Figure 48b and see Experimental Section Chapter 3.1., Figure S21b). Again, the quasi-static *P* helix adopted by poly-(*P*)-**1-OAc** is attributed to the *P* axial chirality of the allene used as pendant. However, in this case, further addition of amines (primary, secondary, and tertiary) to a diethyl ether solution of poly-(*P*)-**1-OAc** did not produce any change in the screw sense preference of the polymer. We attributed this behavior to the lack of interactions between the amines and this PAEPA (Figure 48c and see Experimental Section Chapter 3.1., Figure S22). ^{14}N-NMR studies corroborate the absence of this supramolecular interaction since the N peak of the amines does not suffer any shift after the addition of poly-(*P*)-**1-OAc** (Figure 48d and see Experimental Section Chapter 3.1., Figure S26).

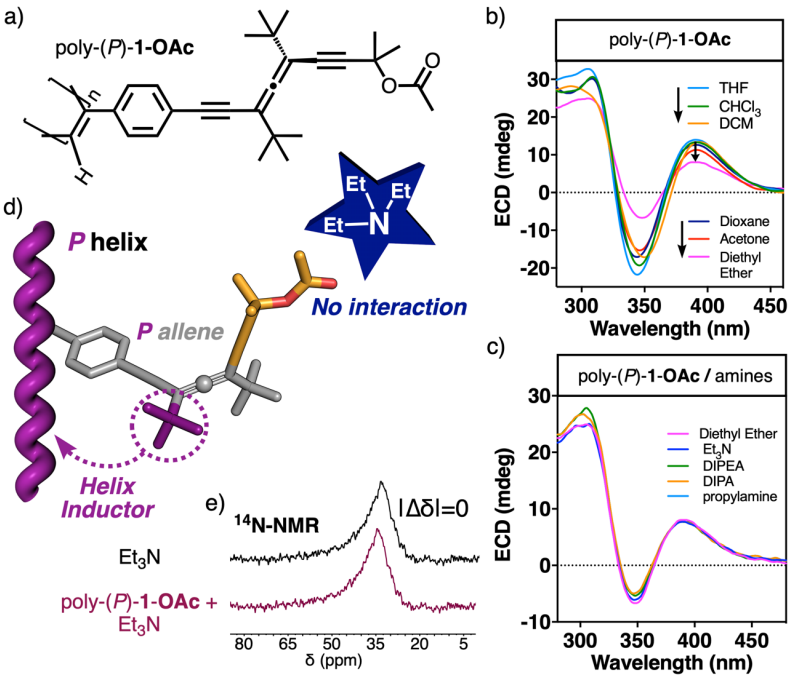

Figure 48. (a) Chemical structure of poly-(*P*)-**1**-**OAc**. (b) ECD studies of poly-(*P*)-**1**-**OAc** in different solvents (1.0 mM). (c) ECD studies of different poly-(*P*)-**1**-**OAc**/amine mixtures in diethyl ether (1.0 mM). (d) Conceptual representation of poly-(*P*)-**1**-**OAc** screw sense induction. (e) Comparison of the ^{14}N-NMR spectra of Et_3N and poly-(*P*)-**1**-**OAc**/Et_3N in a 1/1 mol/mol ratio (solvent: Et_2O).

Finally, we aimed to analyze the secondary structure of poly-(*P*)-**1**. Thus, structural studies such as AFM, DSC and computational calculations were carried out. To perform the AFM studies of poly-(*P*)-**1**, it was first necessary to prepare 2D-crystals of these polymers. These crystals were obtained using Yashima's protocol,[165,169,241] which consist in spin coat a dilute chloroform solution of the polymer onto highly oriented pyrolytic graphite (HOPG) and leaving it under a solvent atmosphere for a few hours. High-resolution AFM images of these crystals were obtained, allowing us to extract several key helical parameters, such as helix width (5 nm), helix pitch (3.7 nm) and the orientation of the external part of the helix (*M* helix) (Figure 49a and see Experimental Section Chapter 3.1., Figure S31). Therefore, poly-(*P*)-**1** adopts in chloroform a *cis-transoidal* helix where internal and external helices rotate in opposite directions (Figure 49b). In this case, the polyene backbone rotates clockwise —*P* helix, (ECD_{390}> 0)—, while the external helix rotates counterclockwise —*M* helix, AFM—. DSC studies corroborated the presence of a *cis-transoidal* polyene skeleton, since a trace with two exothermic peaks was found, typical of this helical scaffold (see Experimental Section Chapter 3.1., Figure S9). Combining all the data obtained from the different structural techniques, it was

possible to model an approximated 3D structure of poly-(*P*)-**1** (ω_1=158°) (Figure 49b and S32). In addition, TD-DFT (rCAM-B3LYP/3-21G)[151,253-255] computational studies were carried out for a short oligomer (n = 9) of poly-(*P*)-**1**, which allowed us to obtain a theoretical ECD spectrum that matches the experimental one (Figure 49c and see Experimental Section Chapter 3.1. for more detailed information). This fact indicates that the proposed structure is in good agreement with that adopted by poly-(*P*)-**1** in solution.

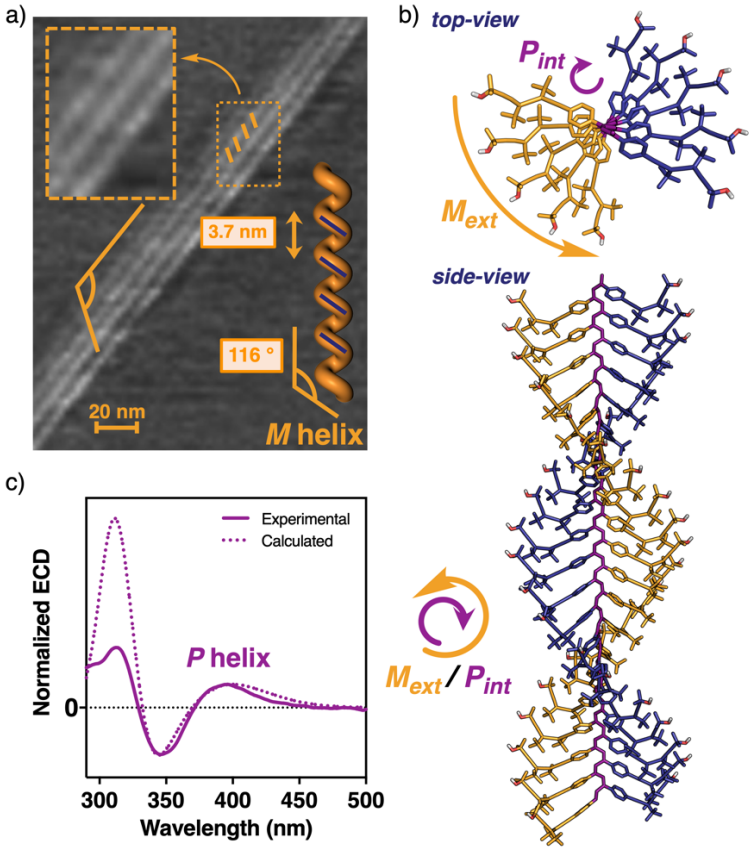

Figure 49. (a) AFM image obtained from a poly-(*P*)-**1** monolayer. (b) 3D model of poly-(*P*)-**1**. (c) ECD spectra of poly-(*P*)-**1** in $CHCl_3$ vs. calculated ECD spectra.

3.1.3. Conclusion

In conclusion, we have demonstrated that PAEPAs, which bear chiral and conformationally restricted pendant groups, behave as quasi-static helical polymers, and can be transformed into dynamic helical polymers by activation/deactivation supramolecular interactions. Thus, if we can vary the size of the substituents in a conformationally restricted pendant, the order it commands will depend on the activation/deactivation of this supramolecular interaction. This new dynamic mechanism

of chiral axial-to-helical communication was demonstrated using poly-(*P*)-**1**, in which a chiral allene with restricted conformational composition plays a key role. In poly-(*P*)-**1,** a *tert*-butyl group commands the helical sense due to its large size and proximity to the backbone. Additional supramolecular interactions between the hydroxy group of a remotely placed allenic substituent with secondary or tertiary amines result in helix inversion in poly-(*P*)-**1** because activation/deactivation of such interactions modifies the relative bulkiness of the dominant substituents. This dynamic axial-to-helical mechanism was demonstrated by ^{14}N-NMR, and by acetylation of the hydroxy group, showing the role of the alcohol/amine interaction on the helix inversion process. These studies open a new window in the design of stimuli-responsive materials, encouraging the scientific community to search for different ways to induce screw sense preferences in helical polymers, as well as to develop new methods of chiral communication in macromolecules.

3.2. *P/M* Macromolecular Switch Based on Conformational Control Exerted by an Achiral Side Chain within an Axially Chiral Locked Pendant

The results of this chapter have been published by Journal of American Chemical Society as:

María Lago-Silva,[a] María Magdalena Cid,[b] Emilio Quiñoá,[a] Félix Freire,*[a] *P/M* Macromolecular Switch Based on Conformational Control Exerted by an Achiral Side Chain within an Axially Chiral Locked Pendant, *J. Am. Chem. Soc*. **2024**,*146*, 752–759. DOI: 10.1021/jacs.3c10766.

Affiliations

[a]Centro Singular de Investigación en Química Biolóxica e Materiais, Moleculares (CiQUS) and Departamento de Química Orgánica, Universidade de Santiago de Compostela E-15782 Santiago de Compostela (Spain)

[b]Departamento de Química Orgánica, Universidade de Vigo, E-36310 Vigo (Spain)

Abstract: Molecular switches, supramolecular chemistry, and polymers can be combined to create stimuli-responsive multi-chiral materials. Therefore, by acting on the extended/bent conformational composition of an achiral arm, it is possible to create a macromolecular gear, where different supramolecular interactions can be activated/deactivated to control the helical sense of a polymer containing up to five different chiral axial motifs. For this, a chiral allene with a flexible achiral arm was introduced as a pendant in a poly(phenylacetylene). Through flexible arm control between extended and bent conformations, it is possible to selectively induce either a *P* or *M* helical sense in the polymer, while the relative spatial distribution of the substituents in the allene remains unaltered in two perpendicular planes (configurationally locked). These results show that complex dynamic multi-chiral materials can be obtained by polymerization of appropriate monomers that combine chirality, switching properties, and the ability to generate chiral supramolecular assemblies.

3.2.1. Precedents

Molecular and macromolecular switches are mechanisms used by nature for signaling or transport processes. Thus, the interaction of biomolecular switches with different stimuli such as pH, ions and light, frequently led to an equilibrium between two functionally (ON/OFF) relevant conformational states.[256-258] In general, elucidation of the mechanisms governing conformational control in large biomacromolecules is hampered by the complexity of the systems.[259] To gain knowledge in this field, the scientific community has done exhaustive work over the last few decades to develop simple and easily tunable molecular or macromolecular switches,[71, 84, 96, 259-264] where the knowledge gained is of great use for subsequent designs. The molecular torsion balances of Wilcox et al.[66] constitutes an interesting example. These systems inspired complex and sophisticated molecular machines such as the robotic arms developed by Leigh et al.[265]

Dynamic helical polymers are macromolecular switches[266-269] where the *P*/*M* screw sense control is achieved by resorting to different helix induction mechanisms that arise from the conformational manipulation of the pendant of a monomer repeating unit because of interactions with different stimuli. Thus, information from the chiral center to the main chain of the polymer can be transmitted directly, across space, through helical induction effects such as tele-induction,[21, 119, 196, 223, 227, 250, 271-278] chiral overpass,[187, 188] or substituent overpass,[279] or indirectly, in a two-step process, where information from a chiral group placed at a remote position on the pendant is first transmitted to an achiral spacer and then harvested by the polyene backbone (chiral harvesting).[182, 185, 186, 280] In copolymers, Zentel designed an isocyanate copolymer that shows reversible helix-inversion induced by isomerization of an azobenzene group.[268, 269]

In this work, our objective is to create a macromolecular helical switch based on a chiral pendant that possesses, within its structure, a molecular machine formed by an achiral molecular torsion balance. More precisely, our goal is to control the *P* and *M* helical senses of a macromolecular gear without altering the chiral information of the pendant, and where conformational changes of an achiral side chain are the only requirement necessary to induce a helix inversion in the macromolecular polymer structure. Therefore, this novel helix induction mechanism will show how conformational

changes in the achiral side chain of a chiral pendant result in helical sense control of the helix, without altering the chiral information of the pendant.

To achieve this goal, it is necessary to design a chiral and rigid pendant group that meets the following requirements (Figure 50): 1.- The relative spatial distribution between the different substituents (**a**, **b**, **c**), with respect to the chiral element of the pendant, must be locked. For instance, the four substituents of a chiral allene placed in two perpendicular planes, whose relative spatial distribution will always be the same due to the presence of two consecutive double bonds. 2.-The bulkiness of the different substituents (**a**, **b**, **c**) must be different to establish a well-defined hierarchical helix induction effect among them. It is necessary to also consider the distance from the substituents to the polymer main chain to control their helix induction effects.3.- One of these substituents, i.e., **c** in Figure 1, must show different conformations when playing with intramolecular and/or intermolecular forces that function similarly as a molecular torsion balance.

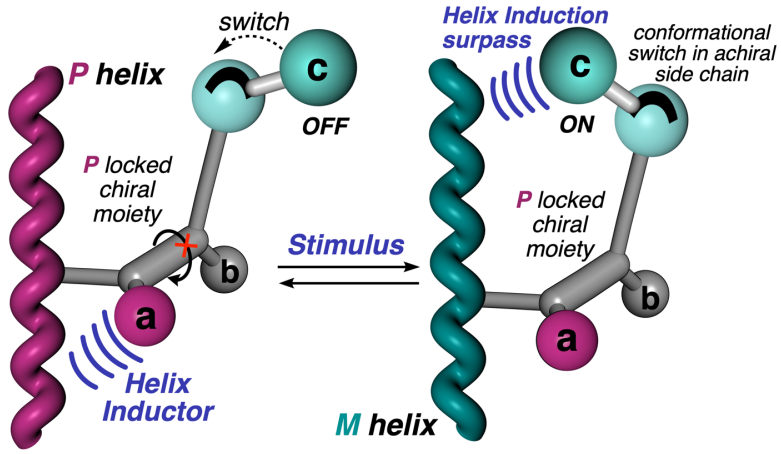

Figure 50. Conceptual view of a helix inversion process commanded by a mimetic molecular torsion balance as pendant.

Therefore, when this side chain adopts a conformation that places the bulky group remote from the backbone, the helix will be governed by a different substituent of the chiral pendant. However, by acting on the conformational composition of the molecular torsion balance mimetic side chain, this substituent will place its atoms close to the backbone, commanding a helix inversion of the polyene main chain. Therefore, our goal is to create a macromolecular gear where a conformational switch of an achiral side chain from a chiral pendant promotes a helix inversion of the polymer.

3.2.2. Discussion

In a recent work, we demonstrated that poly[(allenylethynylenephenylene)acetylene]s (PAEPAs) are helical polymers whose screw sense excess is determined by the axial conformational stability of the chiral allene.[279] Accordingly, PAEPAs comprise the two first requisites of the desired macromolecular gear, i.e., a unique spatial distribution of the different substituents in the two perpendicular planes of the allene. So, to complete our design, two *tert*-butyl groups were included in two perpendicular planes of the allene (side chains **a** and **b**) and a (dimethyl)methyl-*p*-tolyl-sulfonamide group in the last vacant position of the allene (side chain **c**), which can easily form hydrogen bonds with Lewis base solvents or anions[281] (Figure 51a). Therefore, monomers mono-(*P*)-**1** and mono-(*M*)-**1** were synthetized from previously reported allenes[251,279,282] by derivatizing the propargylic alcohol with a sulfonamide group using $FeCl_3$ as a catalyst (see Experimental Section Chapter 3.2., Section 5.2.2). ECD studies of both monomeric enantiomers in different solvents show, as expected, that the *P* or *M* axial chirality of the allene moiety remains unaltered due to restricted rotation along the two consecutive double bonds of the allene (Figure 51b). However, the substituent bearing the sulfonamide group of mono-(*P*)-**1** can adopt two different conformations —c-I and c-II (Figure 51c)— in Lewis base (c-I: THF, DMF, DMSO) and non-Lewis base solvents (c-II: $CHCl_3$, DCM, 1,2-DCE) as inferred from ^{1}H-NMR studies. In them, the protons of the two methyl groups ($H^{e,f}$) of the carbon linked to the sulfonamide group shift upfield when mono-(*P*)-**1** dissolves in Lewis base solvents (Figure 51d and see Experimental Section Chapter 3.2., Figure S12) due to the anisotropic effect of the *p*-tolyl group. This conformational change is produced by an H-bond interaction between the Lewis base solvents and the acidic proton (H^d) of the sulfonamide. Furthermore, to elucidate the most stable conformers adopted by mono-(*P*)-**1** in Lewis base and non-Lewis base solvents, NOESY experiments were carried out (Figure 51e,f, and see Experimental Section Chapter 3.2., Figures S13b,c and S14b). From these studies, it was possible to obtain the distance from the sulfonamide proton (H^d) to the two methyl groups of the carbon linked to the sulfonamide group, in addition to the distance from these two methyl groups to the *p*-tolyl group (see Experimental Section Chapter 3.2., Table S3). Thus, while in Lewis base solvents, the *p*-tolyl-sulfonamide group adopts an extended arrangement (conformer c-I), in non-Lewis base

solvents, a bent conformation is generated placing the *p*-tolyl-sulfonamide group closer to the alkyne (conformer c-II) (Figure 51c).

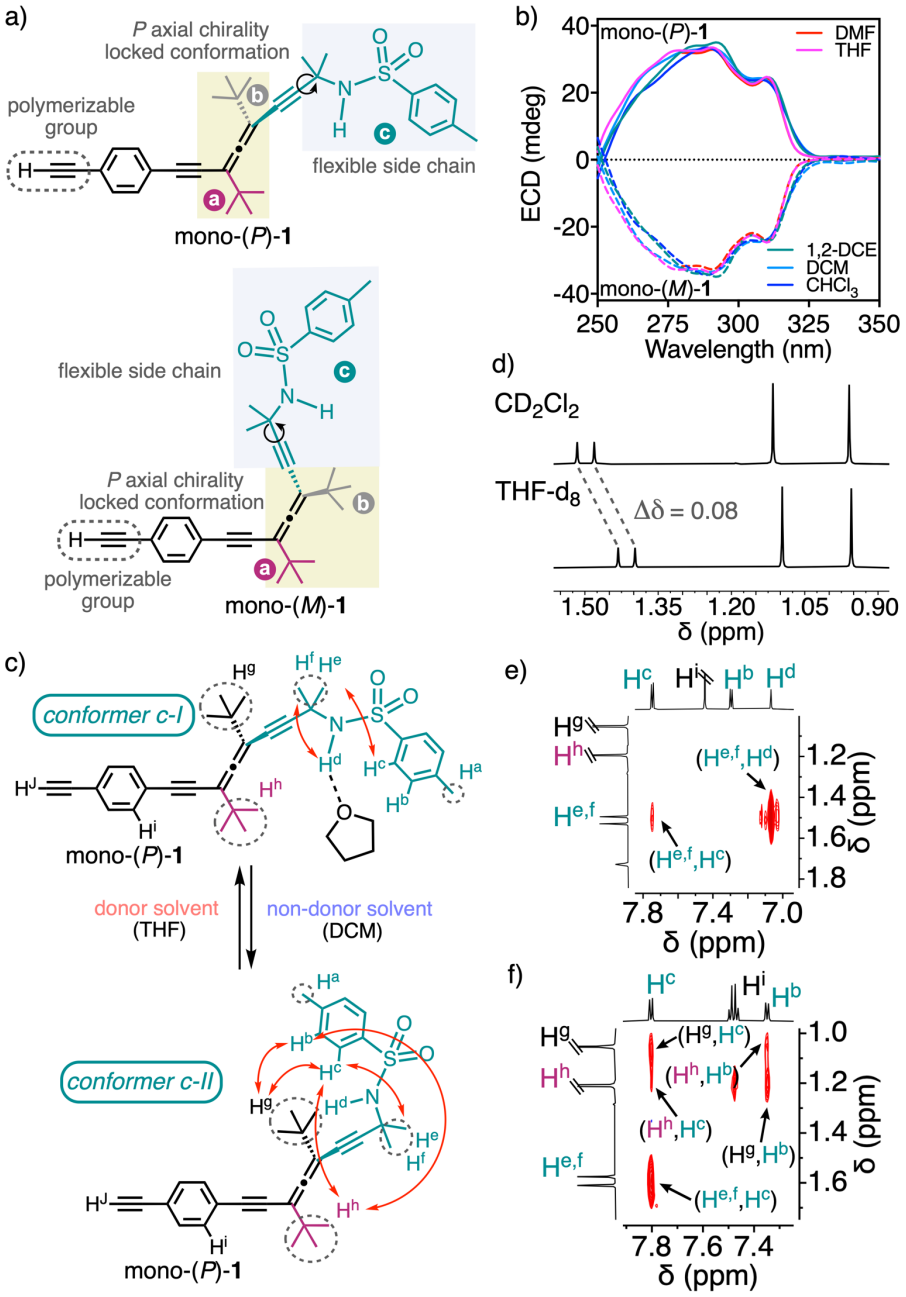

Figure 51. (a) Chemical structures of mono-(*P*)-**1** and mono-(*M*)-**1**. (b) ECD studies of mono-(*P*)-**1** and mono-(*M*)-**1** in different solvents (0.8 mM). (c) Conformational flexibility of the C—C—C—N bond (substituent c) (a-c labels are used to indicate substituents and do not refer to the priority of configuration) (red arrows indicate the most relevant protons showing NOESY signal). (d) ^{1}H-NMR zoomed area of the two methyl ($H^{e,f}$) and *tert*-butyl groups of mono-(*P*)-**1** in non-Lewis base (CD_2Cl_2) and Lewis base (THF-d_8) solvents. (e) NOESY zoomed area (THF-d_8, 278 K, 750 MHz). (f) NOESY zoomed area (CD_2Cl_2, 278 K, 750 MHz).

Next, monomers (*P*)-**1** and (*M*)-**1** were polymerized using $[Rh(nbd)Cl]_2$ as catalyst,[133,134] affording poly-(*P*)-**1** and poly-(*M*)-**1** (Figure 52a) in good yields (85 %), low polydispersity and with high contents of *cis* configuration of the double bonds as inferred from ^{1}H-NMR and Raman studies (see Experimental Section Chapter 3.2., Figures S6, S8).[128,283]

ECD and UV-vis studies were carried out for poly-(*P*)-**1** and poly-(*M*)-**1** dissolved in solvents with different polarity and Lewis base character (Figure 52b and see Experimental Section Chapter 3.2., Figures S15-S17), which allowed to determine their stimuli-responsive properties by controlling the conformational composition of the side chain containing the sulfonamide group (side chain **c**) (Figure 52a). So, ECD studies in Lewis base solvents such as DMF, DMSO or THF, where the N–H of the sulfonamide group can establish a hydrogen bond interaction with the solvent, show that the polymers adopt a *P* helix for poly-(*P*)-**1** and an *M* for poly-(*M*)-**1** with the classical three alternating Cotton bands [poly-(*P*)-**1** ECD(+/-/+); poly-(*M*)-**1** ECD(-/+/-)] (Figure 52b and see Experimental Section Chapter 3.2., Figures S15 and S16). On the other hand, when the polymers are dissolved in non-Lewis base solvents such as DCM or 1,2-DCE, structural changes are observed in the polymers towards the opposite helical sense structures. Thus, poly-(*P*)-**1** shows a first ECD band slightly negative ($ECD_{350} < 0$; *M* helix), while the other two are positive (-/+/+) (Figure 52b), whereas for poly-(*M*)-**1** the first ECD band becomes slightly positive ($ECD_{350} > 0$; *P* helix), and the other two are negative (+/-/-) (see Experimental Section Chapter 3.2., Figure S16). To demonstrate that these structural changes are attributed to the Lewis base character of the solvents and not to their polarity, the ECD response of poly-(*P*)-**1** was plotted against polarity and Lewis base/acceptor properties[196,284] of the solvents quantitatively represented by their dielectric constant (ε) and Gutmann's values (Figure 52c,d). Thus, by plotting the ECD signal at 350 nm *vs*. the solvent dielectric constant (ε), it is possible to observe how THF, with a polarity like DCM or DCE, produces an ECD spectrum with opposite sign (Figure 52c). On the other hand, when the ECD changes at 350 nm are plotted *vs*. the solvents Gutmann's values (DN-AN) (Figure 52d), it is possible to visualize how Lewis base solvents promote a negative Cotton band in this region ($ECD_{350} < 0$) whereas non-Lewis base solvents promote a positive Cotton band ($ECD_{350} > 0$). These studies show the structural changes produced in poly-(*P*)-**1** are due to the different Lewis base character of the solvents that cause the conformational changes in the allenic sulfonamide (chain

c). Analogous behavior was observed for poly-(*M*)-**1** (see Experimental Section Chapter 3.2., Figure S16a). This interaction was also inferred by IR studies where the frequency of the NH of the sulfonamide group of poly-(*P*)-**1** shows a $\Delta\nu = 31$ cm^{-1} in THF (3276 cm^{-1}) respect to the value obtained in 1,2-DCE (3245 cm^{-1}) due to its supramolecular interaction with the Lewis base solvent (see Experimental Section Chapter 3.2., Figure S19).

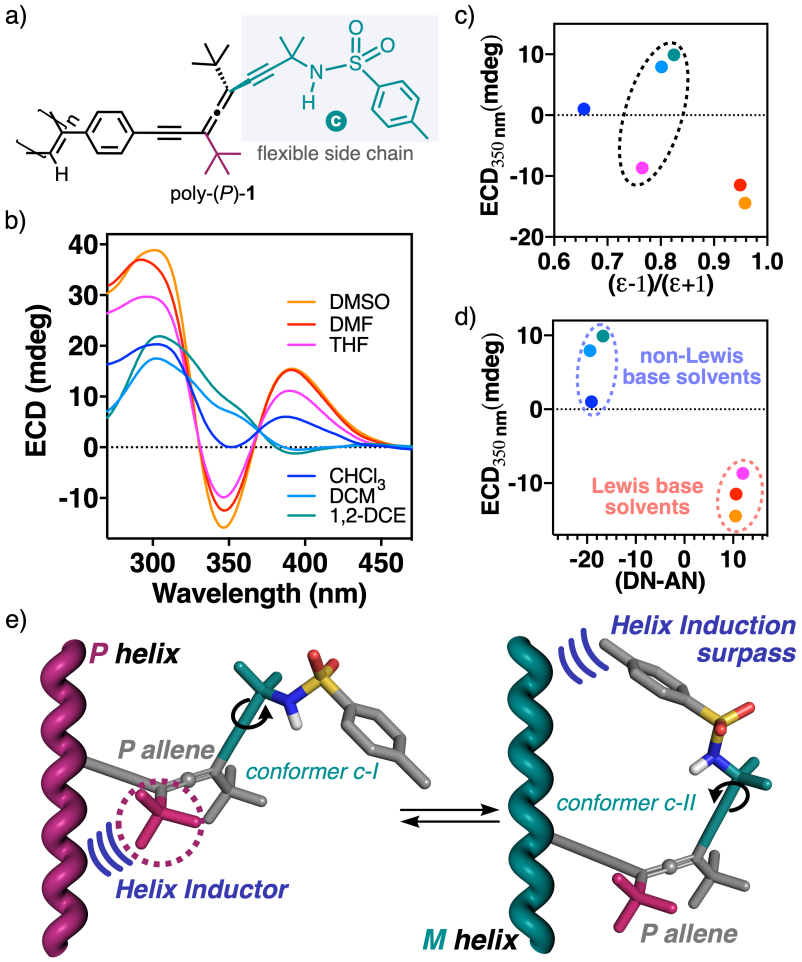

Figure 52. (a) Chemical structure of poly-(*P*)-**1**. (b) ECD studies of poly-(*P*)-**1** in different solvents (0.8 mM). (c) Graph showing the relationship between the ECD signal at 350 nm and the polarity of the solvent. (d) Graph indicating the relationship between the Lewis base/acceptor properties of the solvents and ECD signal at 350 nm. (e) Conceptual representation of the effect of a conformational change at the pendants by external stimuli.

To further corroborate these results, STD NMR experiments were carried out for solutions of poly-(*P*)-**1** in THF-d_8 and CD_2Cl_2, which revealed a poly-(*P*)-**1**/THF-d_8 supramolecular interaction (see Experimental Section Chapter 3.2., Figure S20), while no effects were observed in CD_2Cl_2 (see Experimental Section Chapter 3.2., Figure S21).

Moreover, NOESY NMR experiments for poly-(*P*)-**1** demonstrated that the *p*-tolyl-sulfonamide group adopts an extended conformation and therefore lies away from the polyene backbone (conformer c-I) in Lewis base solvents, whereas in non-Lewis base solvents a bent conformation is favored (conformer c-II) (Figure 52e and see Experimental Section Chapter 3.2., Figures S22 and S23).

UV-vis studies indicate that the diastereomeric *P* and *M* macromolecular helices obtained in Lewis base and non-Lewis base solvents at room temperature have similar scaffolds because no variations are observed in the conjugation of alternating double bonds (band at ca. 380 nm) due to stretching or compression of the polyene main chain (see Experimental Section Chapter 3.2., Figure S17b).

This macromolecular chirality switch (*P* to *M* or *M* to *P*) can be only attributed to the side chain of the chiral allene (Figure 52a) because it is the only flexible moiety in the pendant group. Thus, the conformational composition found in substituent **c** in the monomer also works in polymers (Figure 51c). These two conformers generate different steric effects when are placed within a PAEPA helical scaffold: while conformer c-I fits well into this helix due to an extended orientation of the pendant, conformer c-II exhibits more steric interactions due to its bent conformation, so poly-(*P*)-**1** is better folded in Lewis base than in non-Lewis base solvents (Figure 53a).

To stabilize, on the pendant group of poly-(*P*)-**1**, conformer c-I in Lewis base solvents and conformer c-II in non-Lewis base solvents, low temperature ECD studies were carried out at in 1,2-DCE and THF. When Lewis base solvents are used (*e.g.,* THF), no helical changes are observed at either high or low temperatures or at different heating/cooling rates, indicating a quasi-static thermal behavior of the polymer (see Experimental Section Chapter 3.2., Figure S24a and S25a). In this case, the rigidity of the allene pendant in combination with the adoption of a very stable extended conformer of the side chain **c** results in a well folded helix (Figure 53e). Conversely, when VT-ECD studies were carried out for poly-(*P*)-**1** in 1,2-DCE, a different thermal effect was observed depending on the cooling rate. Thus, when a cuvette containing the poly-(*P*)-**1** solution was placed directly in a cooled bath at 268 K, a magnification of the ECD trace was observed (Figure 53b and see Experimental Section Chapter 3.2., Figure S24c), indicating an enhancement of the *M* screw sense preference in the polymer due to a stabilization of the conformer c-II of side chain **c** at the pendant (*M* scaffold 1).

Intriguingly, when temperature of the 1,2-DCE solution was lowered by using a cooling rate (≤10 K·min^{-1}), a two-step helix induction process was obtained. In an initial stage, when the temperature was lowered to 278.5 K, a screw sense excess of the *M* helix adopted by poly-(*P*)-**1** was obtained, like when applying a fast cooling (Figure 53b and see Experimental Section Chapter 3.2., Figure S24c). However, when the temperature decreases from 278.5 K to 268.0 K, a second stretched *M* helix (*M* scaffold 2) is formed (Figure 53c and see Experimental Section Chapter 3.2., Figures S25c,d and S26). This structural change is fully reversible and when the temperature increases from 268 K to 278 K, the *M* scaffold 1 is recovered, indicating that to obtain the *M* scaffold 2 it is necessary to go through the *M* scaffold 1 (Figure 53e and see Experimental Section Chapter 3.2., Figure S27). Interestingly, by looking at the variation of the ECD trace during the cooling process (Figure 53c), it is possible to observe that the stretching of the polyene band (maximum absorbance of the ECD polyene band: 400 nm for *M* scaffold 1 and 420 nm for *M* scaffold 2) is accompanied by the emergence of an abnormally high positive exciton coupling band centered at 337 nm, which corresponds to the absorbance of the chiral allene pendant. Analogous results were also obtained for the enantiomer poly-(*M*)-**1** (see Experimental Section Chapter 3.2., Figure S29).

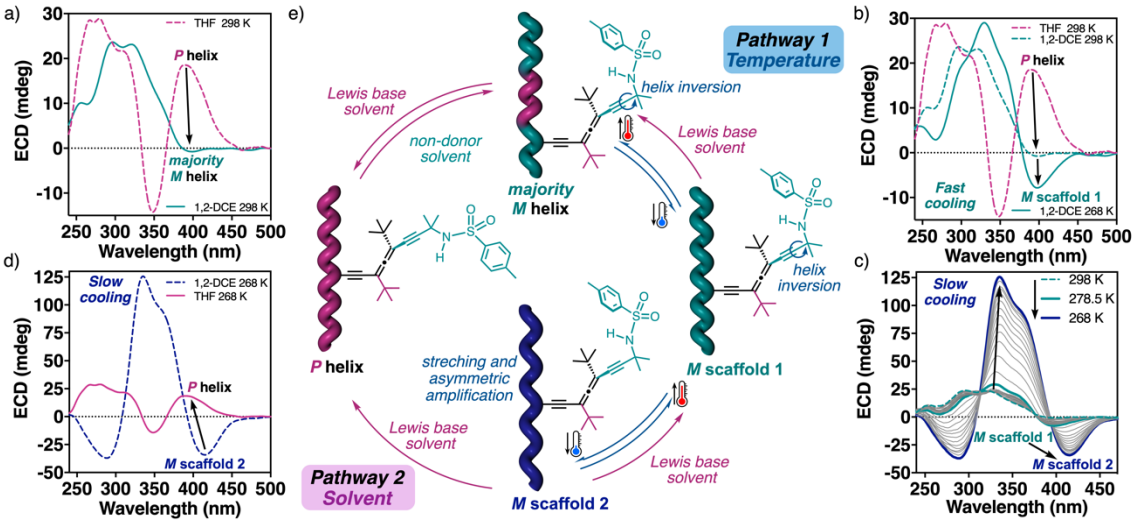

Figure 53. (a) Evolution of the ECD spectra of poly-(*P*)-**1** (1.6 mM) from THF to 1,2-DCE solutions at rt. (b) VT-ECD spectra of poly-(*P*)-**1** (1.6 mM in 1,2-DCE) after fast cooling. (c) VT-ECD spectra of poly-(*P*)-**1** (1.6 mM in 1,2-DCE) after slow cooling. (c) VT-ECD spectra of poly-(*P*)-**1** in 1,2-DCE (1.6 mM) after slow cooling followed by addition of 60 equiv of THF at 268 K. (e) Schematic representation of reversible tuning of the backbone scaffold under external stimuli.

To further demonstrate that conformational changes around the sulfonamide group are responsible for the helix inversion, monomer (*P*)-**1** was methylated at the sulfonamide group [(*P*)-**2**] (see Experimental Section Chapter 3.2.). As expected, poly-(*P*)-**2** adopts, in all solvents at 293K, a *P* screw sense excess commanded by the *P* chirality of the allene (see Experimental Section Chapter 3.2., Figure S18), which increases when the ECD spectra are measured at lower temperatures (see Experimental Section Chapter 3.2., Figures S30-S33).

Recently, our group reported that the use of rigid and planar spacers such as oligophenylenethynylenes (OPEs) or bispyridyldichlorido Pt(II) complexes between the polyene backbone and the chiral pendant[186, 280] can produce, in certain scaffolds, a new chiral axial arrangement of the spacers within the helical scaffold whose ECD pattern dominates the ECD spectra of the whole helical system. In these polymers, helix induction in the polyene backbone follows a chiral harvesting mechanism, where chiral information from the axial array of the spacer is harvested by the polyene backbone.

In this sense, when observing the 3D-structure of mono-(*P*)-**1**, an extended and rigid aryl-alkyne-allene fragment is found that could produce a novel axial chiral motif within the helical scaffold. To discern 3D structural parameters of poly-(*P*)-**1** in Lewis base and non-Lewis base solvents, AFM (Atomic Force Microscopy) studies were performed. Thus, 2D crystals of poly-(*P*)-**1** were prepared from THF and 1,2-DCE solutions following Yashima's protocol[165] and employing highly oriented pyrolytic graphite (HOPG) as substrate. High resolution images revealed the presence of well-ordered monolayers in both cases: external *M* helix (THF solution) and external *P* helix (1,2-DCE solution).

In addition, other important structural parameters were obtained, such as a helical pitch of 4.3 nm for the THF sample and a longer pitch (4.8 nm) for the 1,2-DCE sample (Figure 54a,b and see Experimental Section Chapter 3.2., Figures S34 and S35). DSC studies corroborated the presence of a *cis-transoidal* polyene skeleton (see Experimental Section Chapter 3.2., Figure S9). So, the combination of all the obtained data allowed to model an approximated 3D structure for poly-(*P*)-**1** in Lewis base (*P* internal helix, ω_1= 155°) and non-Lewis base solvents (*M* internal helix, ω_1= -165°) (Figure 54 and see Experimental Section Chapter 3.2., Section 15). Consequently, in the helical structure with ω_1= 155°, the two classical coaxial helices are found —internal polyene; external pendants— (Figure 5c). However, in the most stretched helix (ω_1=

165°), a new axial motif was disclosed by ECD. It is originated by a supramolecular chiral array of the allene groups (Figure 54d), forming a helix that rotates in the opposite direction to the polyene backbone, as shown by the negative Cotton effect at 420 nm. Furthermore, a positive exciton coupling band centered at 337 nm is indicative of a positive tilting degree in the axial array of the allene groups (see Experimental Section Chapter 3.2., Figure S38).

Thus, the allene group not only functions as a helix inductor due to its intrinsic chirality, but creates a supramolecular array within the helical scaffold of the polymer, generating yet another chiral motif, previously observed only for non-chiral planar spacers as OPEs or bispyridyldichlorido Pt(II) complexes.[186,280] Consequently, five different axial motifs are found in a PAEPA: the allene, the internal helix, the external helix and two allene axial arrays (P_{allene}, $M_{int}/P_{ext}/P_{axial\text{-}1}/P_{axial\text{-}2}$) (Figure 54d).

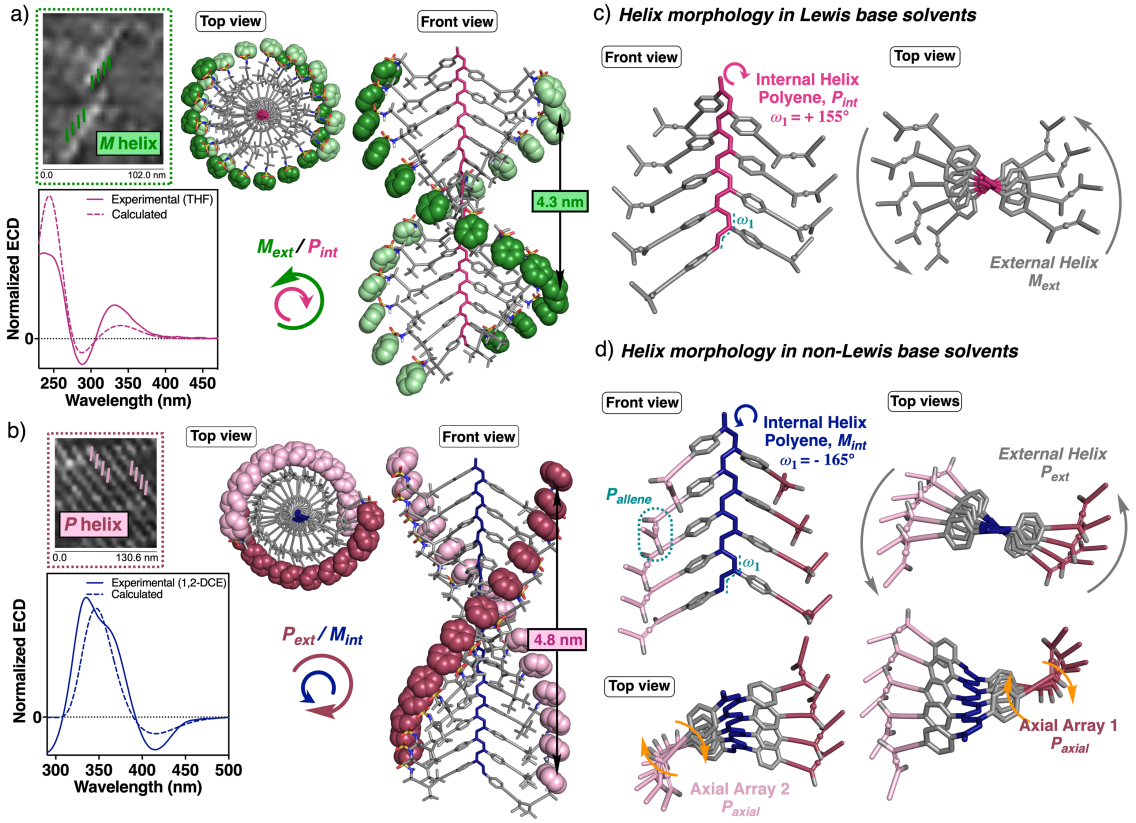

Figure 54. 3D model structures of poly-(*P*)-**1** obtained from AFM image of 2D crystals in (a) Lewis base and (b) non-Lewis base solvents. ECD spectra of poly-(*P*)-**1** in (a) THF and (b) 1,2-DCE *vs.* calculated spectra from the 3D structures obtained in both solvents. Axial motifs found in the helical structures adopted by poly-(*P*)-**1** in (c) Lewis base and (d) non-Lewis base solvents.

Finally, to further demonstrate that the dynamic behavior of poly-(*P*)-**1** is due to variations in the conformational composition of side chain **c** containing the sulfonamide

group, a titration with different anions such as N_3^-, CN^- and F^- (introduced as tetrabutylammonium salts: $TBAN_3$, TBACN, TBAF, 0.35 mM in MeCN) were added to 1,2-DCE solutions of poly-(*P*)-**1** slowly cooled at 268K whose side chain **c** adopted, consequently, a bent conformer (Figure 55 for $TBAN_3$ and see Experimental Section Chapter 3.2., Sections 5.2.16 and 5.2.17 for other salts).Thus, in the presence of 1 equiv of azide (Figure 55a), the stretched *M* helix (*M* scaffold 2) is transformed into a more compressed *M* helix (*M* scaffold 1), where an equilibrium between bent and extended structures at the side chain of the allene is present. The reversibility of the process was demonstrated by extraction with water of the anion salt ($TBAN_3$) (see Experimental Section Chapter 3.2., Figure S41). By increasing the amount of the azide anion (> 3 equiv) a helix inversion arises because of the adoption of an extended structure in substituent **c** (Figure 55b and see Experimental Section Chapter 3.2., S40a). Therefore, these results reveal the role of the sulfonamide group and the extended/bent orientation of substituent **c** in the helix inversion of poly-(*P*)-**1** (Figure 55c).

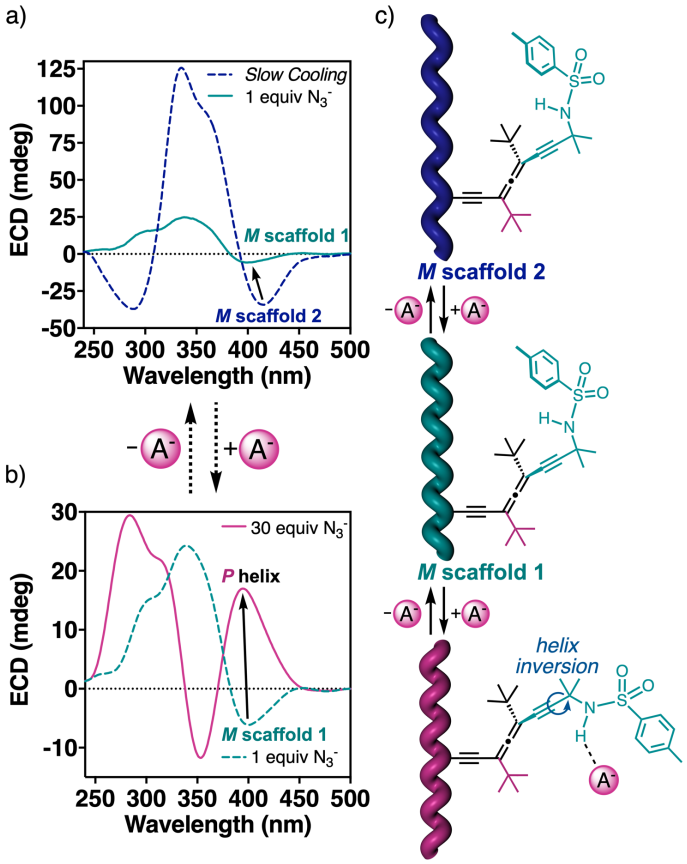

Figure 55. (a) ECD spectra of poly-(*P*)-**1** (1.6 mM in 1,2-DCE, 268 K) after slow cooling (dashed blue) and (b) after being titrated with azide ion [1 equiv (green) and 30 equiv (pink)]. (c) Schematic representation of the reversible switching of the helical sense of poly-(*P*)-**1** upon addition of azide ion.

3.2.3. Conclusion

In conclusion, we have demonstrated that the helical sense of a chiral helical polymer, such as a PAEPA, can be modulated by acting on the conformational composition of an achiral side chain without changing the relative spatial distribution of the substituents in an axial chiral allene group used as pendant. So, the chiral allene will always have the same relative orientation of its substituents, showing a quasi-static behavior due to its conformational stability. In this work, we managed to create a dynamic PAEPA by altering the priority of the helix induction order due the conformational control of an achiral side chain that works as a flexible arm. Thus, when this arm is extended, this substituent is placed away from the polyene backbone and does not interfere with the helix induction command ordered by the closer allene substituent. However, when the arm is bent, this substituent surpasses the order given by that substituent as it approaches the backbone, and thus commands the helical sense of the PPA. As a result, a helix inversion mechanism of a dynamic helical polymer based on the conformational control of a flexible arm is presented. Moreover, from these studies we also found that multi-chiral helical structures, which comprise five axial motifs —the two coaxial helices (internal and external), the chiral allene and two extra chiral axial motifs described by the aryl-ethynyl-allene array— can be prepared by combining rigid, extended and axially chiral allenes with helical polymers such as poly(phenylacetylene)s. These results indicate that the combination of information or ideas from molecular switches, supramolecular chemistry and polymers can give rise to different helical induction mechanisms through complex structures, allowing a better understanding of how information can be transferred at different levels of complexity.

3.3. Mechanically Interlocked Macromolecular Gears: Elongation and Helical Sense Control of a Helical Polymer by Acting on a Chiral Rotaxane Used as Pendant Group

Abstract: A bottom-up approach can be used to create complex macromolecular systems that act as macromolecular gears. Here we show that by combining mechanically interlocked molecules, such as a chiral rotaxane used as a pendant, with a helical polymer, such as a poly(phenylacetylene) (PPA), it is possible to create a macromolecular gear in which the motions in the mechanically interlocked macromolecules used as pendants are amplified by changes in the strain and/or screw sense of the helical polymer. Thus, controlling the position of an achiral wheel relative to the chiral axis allows us to play with a chiral substituent overpass mechanism of transmission of chiral information from the chiral rotaxane to the PPA. Therefore, this work shows how the fields of molecular machines, supramolecular chemistry, and polymers can work together to create complex systems where structural changes in a mechanically interlocked molecule are amplified by using it as a pendant group in a dynamic helical.

3.3.1. Precedents

Nature uses the bottom-up approach to create complex systems involved in processes such as signaling or transmission of chiral information.[285, 286] In those complex systems, a small fragment of a macromolecule usually participates in a stimulus-response process that often alters its conformational composition. This response is effectively transmitted through a conformational communication mechanism to the rest of the system, resulting in the signaling or transmission of information that is picked up by other complex systems.[287] For instance, opsin proteins translate light stimulus into nerve impulses,[288] or the G-protein coupled receptors (GPCRs) use extracellular signals to modulate intracellular processes.[289]

Screw sense control of dynamic chiral helical polymers is usually achieved by controlling the conformational composition of the chiral pendant present in the monomer repeating unit. Thus, the spatial chiral information of the pendant can be altered and transmitted to the polyene backbone by tele-induction, either by conformational [21, 146, 250, 272, 278, 290, 291] or by the chiral supramolecular arrangement of an achiral spacer used to connect the chiral center to the polyene main chain —chiral harvesting mechanism[182,183,185]—.

The most studied helix induction mechanism in dynamic chiral helical polymers is tele-induction,[180] where conformational changes in a chiral pendant group induced by external stimuli such as solvents,[193,196,291-293]pH,[294,295] anions,[281] or cations,[78,296] among others, are effectively transmitted through the space to the polyene backbone. Moreover, the chiral helix inductor can be either covalent[21,180,182,183,185,278,291]or supramolecular[276,297,298] linked to the backbone. During the last few years, our group has explored alternative helix induction mechanisms based on tele-induction, which differ from the classical one involving conformational changes in a short chiral pendant group. Thus, the *chiral overpass* or the *substituent overpass effect* were described. In the *chiral overpass effect*, the pendant of the PPA is a multi-chiral residue.[187, 188] Interestingly, by playing with the conformational composition of the pendant, it is possible to place the different chiral centers in different spatial orientations relative to the polyene backbone. As a result, the helical sense of the PPA can be selectively controlled by the different chiral residues of the pendant, with the helical sense induction coming from the chiral

center closest to the polyene backbone.[187] On the other hand, in the *substituent overpass effect*, the pendant group consists of a chiral fragment with restricted conformational flexibility. Therefore, the relative spatial distribution of the substituents in the chiral pendant will always be the same in the presence or absence of external stimuli. In this system, to play with the helical sense of the polymer, it is necessary to vary the relative volume of the substituents, which can be done by activating supramolecular interactions with other molecules[279] or by playing with the conformational composition of the achiral substituents (e.g., extended/bent conformers).[299] As a result, the relative volume of the substituents changes without changing their relative spatial distribution. This fact causes the volume/distance of the substituent relative to the polyene backbone to change, inducing changes in the elongation or the screw sense of the polymer without altering the chiral information of the pendant group.

In line with the mechanisms of helix induction based on tele-induction, and more specifically related to the substituent overpass effect, we envisioned a sophisticated macromolecular gear consisting of a PPA bearing a rotaxane (achiral wheel and chiral axle) as a substituent of a chiral allene used as a pendant group. The chiral allene, which possess axial chirality is conformationally locked, and therefore the relative spatial distribution of the substituents is not altered by external stimuli. As a result, the corresponding PPA will adopt a screw sense excess towards the *P* or *M* helix with a quasi-static behavior dictated by the axial chirality of the allene. The introduction of a macrocycle to create a rotaxane on one of the substituents of the allene will allow us to create a macromolecular gear that combines information from different fields, such as supramolecular chemistry, polymer chemistry, and molecular machines. One of the most enticing properties of rotaxanes is the ability of their sub-components to move relative to each other. Our aim is that by playing with the wheel position within the allene substituent, i.e., the co-conformation within the rotaxane, it is possible to change the relative volume of the substituents, leading to a substituent overpass effect. Thus, the presence of different stimuli used as INPUT will activate the macromolecular gear. The movement of the wheel in the rotaxane substituent will be transmitted to the polyene backbone, inducing a structural change (Figure 56), such as helix inversion, which may be accompanied by an elongation change (stretching/compression).

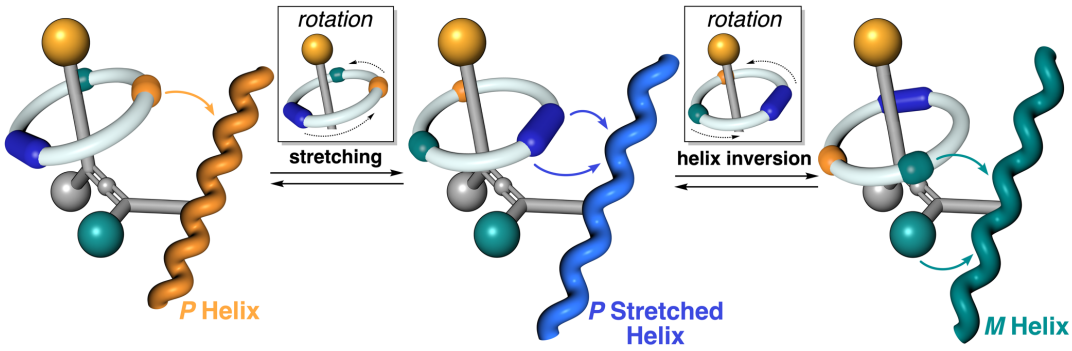

Figure 56. Conceptual view of the macromolecular helical structural changes commanded by the different positions of the wheel in a rotaxane with a chiral axis used as pendant.

Rotaxanes were previously introduced in the field of helical polymers as pendants groups by Takata and co-workers.[90, 91] However, in their designs, the source of chirality was introduced in the macrocycle but not in the linear axis. As a result, they were able to use a molecular shuttle to switch between an axially racemic polymer or one with a preferred handedness, depending on the distance of the chiral macrocycle relative to the polyene backbone. Herein, we aim to go one step further and create a highly dynamic side-chain helical polyrotaxane. To achieve this, it is necessary to effectively transmit the movements of the wheel (macrocycle) with respect to the chiral axis towards the polyene backbone, which will amplify these structural changes by modifying the elongation and/or the helical sense of the polymer scaffold.

3.3.2. Discussion

Recently, we reported that poly[(allenylethynylenephenylene)acetylene]s (PAEPAs) are helical polymers whose screw sense excess is determined by the axial conformational stability of the chiral allene.[279] The structural features of the allene group locate its four substituents in two perpendicular planes with a fixed spatial distribution. To induce structural changes in the helical polymer, it is necessary to manipulate the relative volume of the substituents to vary their steric effects and, consequently, their priority in the helix induction effect. Therefore, to complete our design, we incorporated two *tert*-butyl groups in two perpendicular planes of the allene (side chains **a** and **b**) and a 4-(3,5-di-*tert*-butylbenzyl)-1-ethynyl-1,2,3-triazole in the last vacant position of the allene (side chain **c**)(Figure 57).

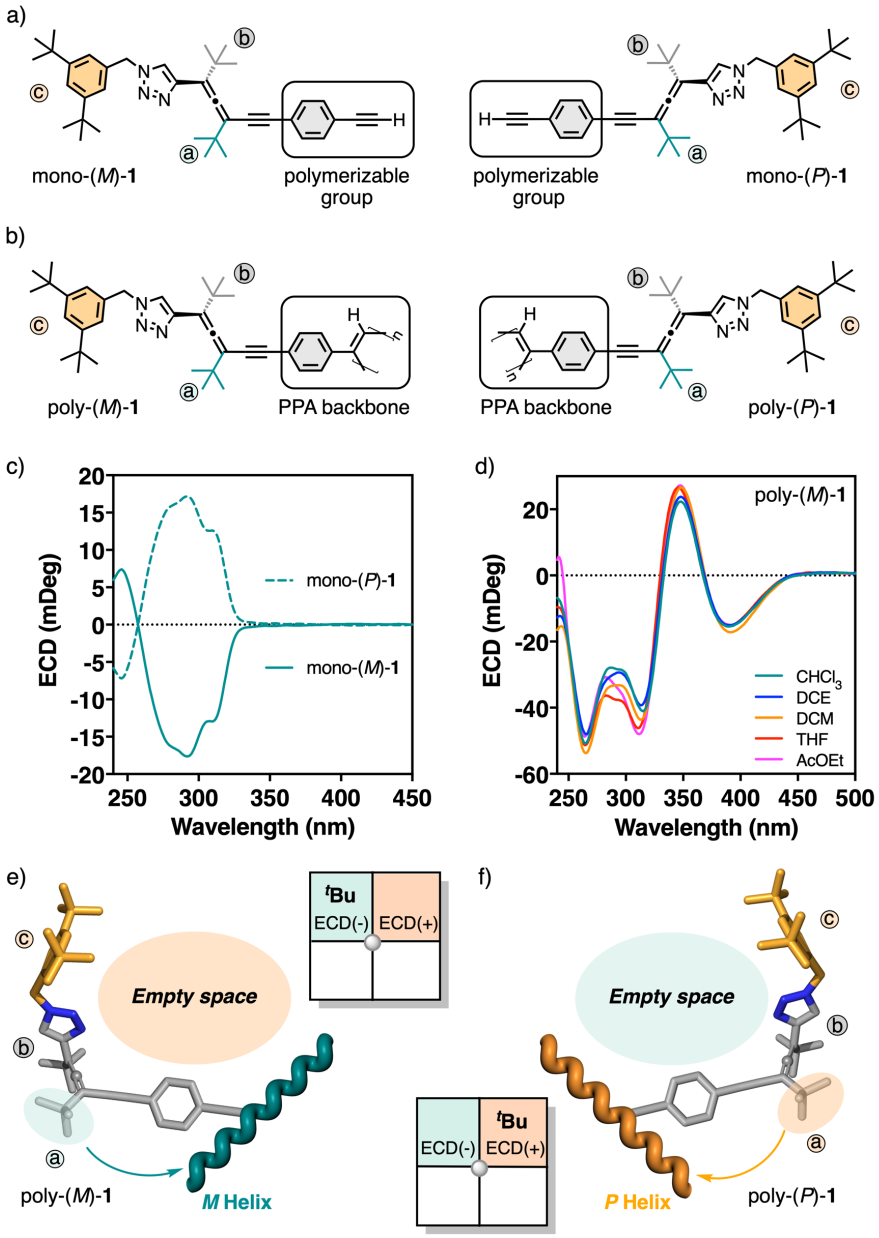

Figure 57. Chemical structure of (a) mono-(*M*)-**1** and mono-(*P*)-**1**, (b) poly-(*M*)-**1** and poly-(*P*)-**1**. ECD studies of (c) the abovementioned monomers (0.25 mM) and of (d) poly-(*M*)-**1** (0.50 mM) in different solvents. 3D model of the helix induction mechanism induced by substituent (a) in (e) poly-(*M*)-**1** and (f) poly-(*P*)-**1**, highlighting the empty area generated by the chiral allene pendant group.

Therefore, the monomers mono-(*M*)-**1** and mono-(*P*)-**1** were synthesized using a variation of previously reported synthetic protocols for allenes[251,279] (see Experimental Section Chapter 3.3., Section 5.3.2). ECD studies of both monomeric enantiomers show, as expected, spectra that are mirror images and with the same pattern as the axial chirality of the allene moiety remains unchanged due to their configurational stability (Figure 57c and see Experimental Section Chapter 3.3., Figure S22). Subsequently, mono-(*M*)-**1** and mono-(*P*)-**1** were polymerized using $[Rh(nbd)Cl]_2$

as a catalyst,[133] affording poly-(*M*)-1 and poly-(*P*)-**1** (Figures 57b and see Experimental Section Chapter 3.3., Table S2) in good yields (95%), low polydispersity and with high contents of *cis* configuration of the double bonds as inferred from ^{1}H-NMR and

Raman studies[128, 283] (see Experimental Section Chapter 3.3., Figures S17 and S19a). ECD and UV-vis studies of poly-(*M*)-**1** and poly-(*P*)-**1** solutions in solvents of different polarity and donor character (Figure 57d and see Experimental Section Chapter 3.3. S25 and S26) show the quasi-static behavior of these PAEPAs. In these polymers, the helical sense is dictated by the *tert*-butyl group located on the **a**-substituent of the allene, since it is the closest group to the backbone. As expected, the specific spatial arrangement of the allene substituents in two perpendicular planes generates an empty area on the opposite side of the **a**-substituent (Figure 57e,f). Thus, the small macrocycle **1**[50, 300, 301] was threaded at the substituent **c** of the allene (*M*)-**3** using an active template Cu-mediated alkyne-azide cycloaddition (AT-CuAAC)[53,54,302] reaction to generate mono-(*M*)-**2** and mono-(*P*)-**2** in excellent yields after removal of the protecting group (PG) (Figure 58a and see Experimental Section Chapter 3.3., Section 5.3.2). The presence of a bipyridine group in the macrocycle in combination with the triazole in the thread at substituent **c** opens the possibility of controlling the helical sense of poly-(*M*)-**1** and poly-(*P*)-**1** by playing with the pirouetting of the wheel respect to the substituent **c** (Figure 58b,c). Based on previous reports by Goldup and co-workers,[55, 300, 301, 303, 304] we expected the bipyridine-triazole cavity to adopt a preferred co-conformation in which the wheel is stabilized in a particular position due to the presence of an H–bond between the bipyridine N–donors and the triazole C–H. Comparison of the ^{1}H NMR spectra of the rotaxane [mono-(*M*)-**2**] and the corresponding thread [mono-(*M*)-**1**] revealed that the triazole proton resonance appears at high ppm in the former, presumably due to H-bonding between the triazole and bipyridine unit (8.89 and 7.32, respectively, see Experimental Section Chapter 3.3., Figure S15). Single-crystal X-ray diffraction (SCXRD) analysis of rotaxane mono-(*M*)-**2** corroborated the relative orientation of macrocycle and thread, showing an H-bond that stabilizes a specific geometry (Figure 58b and see Experimental Section Chapter 3.3., Figure S16).

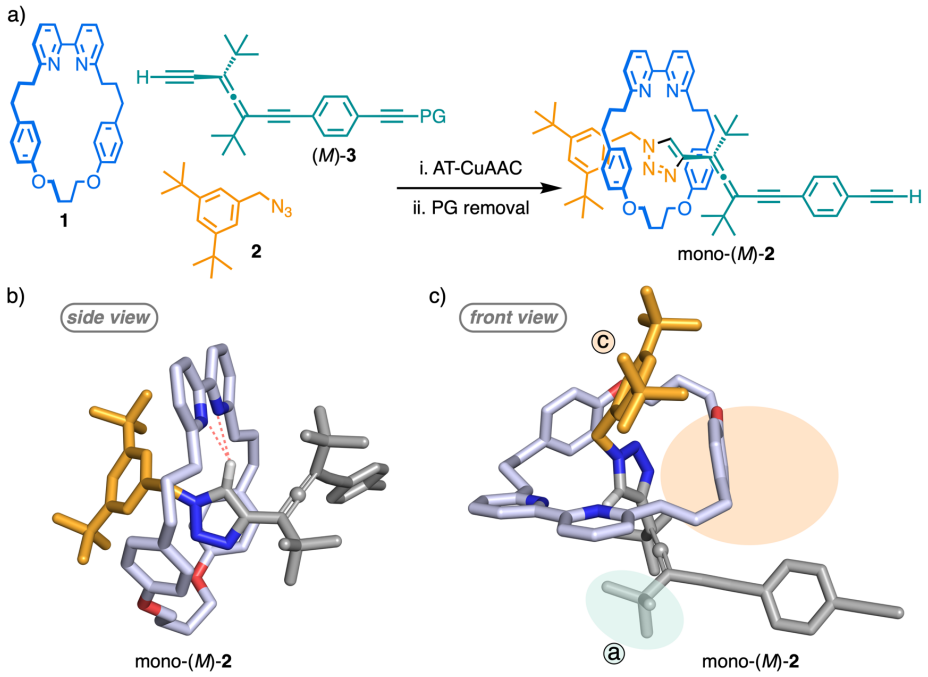

Figure 58. (a) Synthesis of mono-(*M*)-**2** using the AT-CuAAC reaction (PG = TIPS). (b) SCXRD structure of mono-(*M*)-**2**. (c) SCXRD structure of mono-(*M*)-**2** highlighting the region occupied by the macrocycle in the pendant group.

To analyze the structure of mono-(*M*)-**2** in solution, ROESY NMR spectra were measured in $CDCl_3$. From these studies, characteristic long-distance ROE peaks were found that agree with the structure observed in the crystal structure (Figure 58c and see Experimental Section Chapter 3.3., Figures S49-S51). Interestingly, in this structure it is possible to observe how the macrocycle fills the empty space on the opposite side of the substituent **a** of the allene (Figure 58c).

Polymerization of mono-(*M*)-**2** with $[Rh(nbd)Cl]_2$ as catalyst generated poly-(*M*)-**2** in good yield (90%; Figure 59a and see Experimental Section Chapter 3.3., Table S2). ECD studies of poly-(*M*)-**2** in different solvents shows the presence of a positive Cotton band centered at 485 nm (Figure 59b and see Experimental Section Chapter 3.3., Figure S27), which indicates the adoption of a *P* screw sense excess ($ECD_{485\ nm} > 0$), opposite to the *M* helical sense obtained for poly-(*M*)-**1** ($ECD_{390\ nm} < 0$) (Figure 59b).

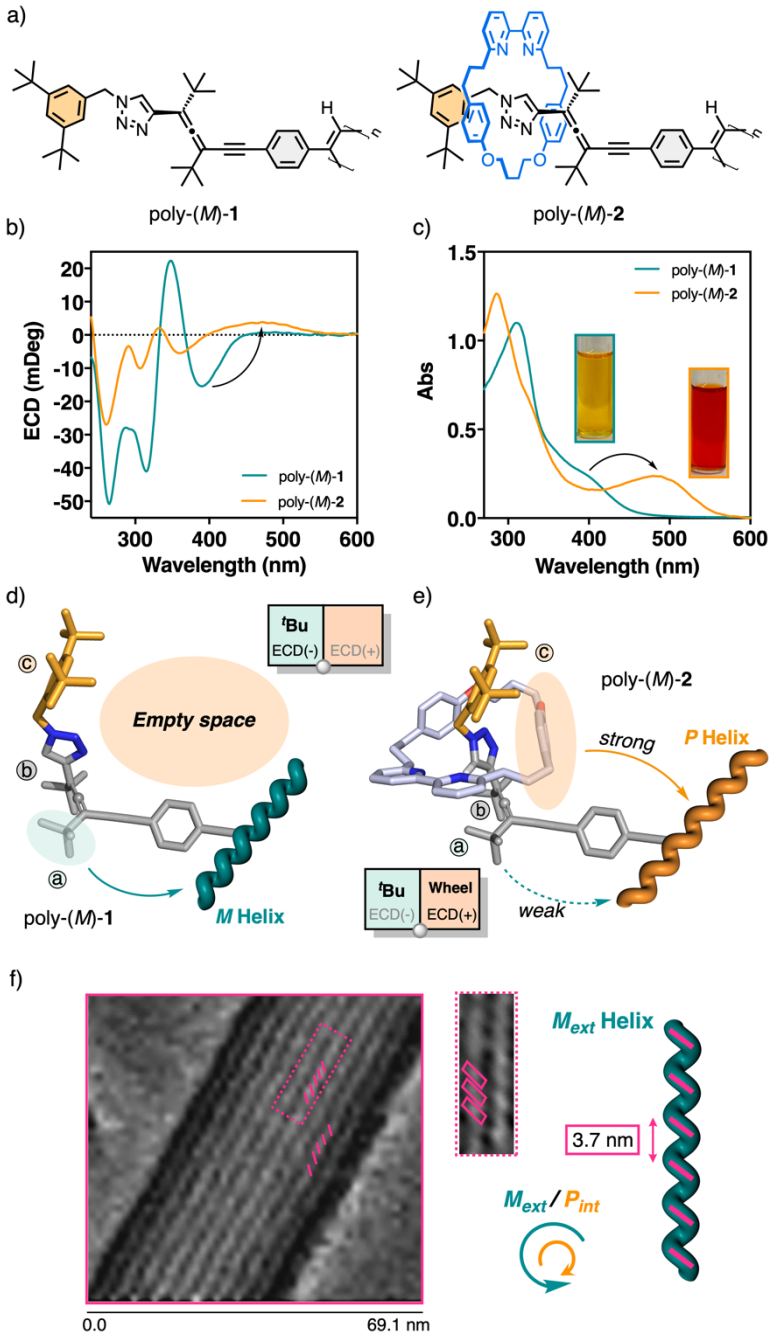

Figure 59. (a) Chemical structure of poly-(*M*)-**1** and poly-(*P*)-**2**. (b) ECD and (c) UV-vis spectra comparison between poly-(*M*)-**1** and poly-(*P*)-**2** (0.50 mM in $CHCl_3$). (d) 3D model of helix induction mechanism by tele-induction in poly-(*M*)-**1**. (e) 3D model of the substituent overpass mechanism in poly-(*M*)-**2**. (f) AFM image obtained from a poly-(*M*)-**2** monolayer.

The helix inversion observed for the polymer in the presence of the macrocycle is accompanied by a 95 nm bathochromic shift of the polyene absorption band and a yellow-to-red color change of the solution (Figure 59c). This change results from the stretching of the helical scaffold to release the steric hindrance generated in the polymer when the macrocycle threads the chiral allene used as a pendant. From a

structural point of view, in poly-(*M*)-**2** a phenoxy group of the macrocycle occupies the space on the opposite side of the *tert*-butyl group in the allene (Figures 59d,e). Hence, the bulky macrocycle is located close to the poly(phenylacetylene) and, as a result, the combination of its steric effects and its distance to the backbone makes this substituent the one with the highest helix inductor effect, surpassing the command of the *tert*-butyl group on substituent **a** (Figure 59e).

To elucidate the secondary structure of poly-(*M*)-**2**, AFM (Atomic Force Microscopy) studies were performed. Thus, 2D crystals of poly-(*M*)-**2** were obtained from a chloroform solution following Yashima's protocol[165] and employing highly oriented pyrolytic graphite (HOPG) as substrate. High resolution images revealed the presence of well-ordered monolayers. From these high-resolution images, it was possible to extract the orientation of the external helix, namely an *M* helix, and other important structural parameters, such as the helical pitch of 3.7 nm. (Figure 59f and see Experimental Section Chapter 3.3., Figure S58). These data, combined with the absorbance of the vinyl band at 485 nm in the UV-vis spectra (Figure 59c), indicate the presence of a stretched *cis-transoidal* helical scaffold, wherein the internal and external helices rotate in opposite directions. The positive Cotton band in the ECD spectrum suggests an internal *P* helix consistent with an *M* external helix, as revealed by AFM (Figures 59b,f).

Next, the dynamic behavior of mono-(*M*)-**2** in solution was analyzed using a solution of a protic acid, such as formic acid (HCOOH), as an external stimulus. Thus, protonation of the bipyridine group should induce a rotation of the wheel with respect to the chiral axis which is further stabilized by H-bonding to the triazole N–donors in the thread (Figure 60a and see Experimental Section Chapter 3.3., Section 5.3.10.1.1.). ECD studies shown that this wheel rotation produces a slight variation in the ECD spectra upon acid addition, which consists mainly in a reduction of the ECD intensity accompanied by an hypsochromic shifting of the ECD bands (Figure 60b) produced by the protonation of the bipyridine group. UV-vis studies showed the expected variations in the UV-vis bands corresponding to the bipyridine (Figure 60c), in line with previously reported systems exhibiting analogous supramolecular interactions.[305,306] ROESY studies showed the presence of characteristic long-distance ROE peaks that are in good agreement with the proposed wheel rotation (see Experimental Section Chapter 3.3., Figures S52-S54).

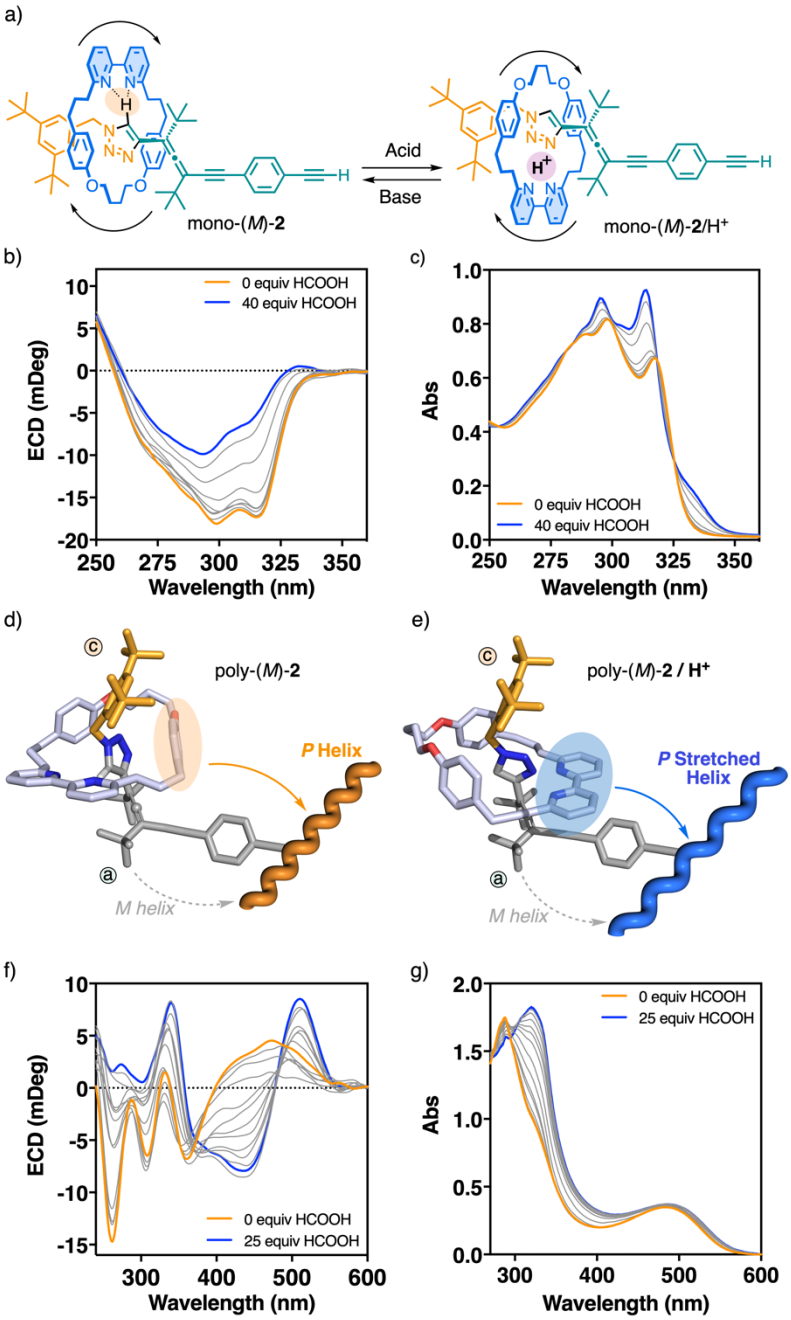

Figure 60. (a) Effect of an external stimulus (acid/base) on the orientation of the wheel in mono-(*M*)-**2**. (b) Change of the ECD and (c) UV-vis spectra of mono-(*M*)-**2** (0.25 mM in $CHCl_3$) upon addition of HCOOH (0.11 M, 0.22 M, and 0.87 M in $CHCl_3$). (d) 3D model of helix induction mechanism in poly-(*M*)-**2** and for poly-(*M*)-**2** after titration with HCOOH. (f) Change of the ECD and (c) UV-vis spectra of poly-(*M*)-**2** (0.50 mM in $CHCl_3$) upon addition of HCOOH (0.11 M, 0.22 M, and 0.87 M in $CHCl_3$). Blue line: ECD and UV-vis signal at the saturation value of HCOOH.

The same studies were carried out for the corresponding polymer. Thus, a solution of poly-(*M*)-**2** in $CHCl_3$ was titrated with formic acid resulting in the elongation of the helix inferred from the bathochromic shift of the polyene band in both the ECD and UV-vis

spectra (Figures 60f,g and see Experimental Section Chapter 3.3., Section 5.3.10.1.1.). This effect is explained by the relocation of the bipyridine group to the position previously occupied by the phenoxy group, resulting from the rotation of the wheel triggered by the acidic media. Given the larger size of the bipyridine compared to the phenoxy group, the polymer backbone is stretched to reduce the steric hindrance induced by this group (Figures 60d,e). Consequently, the rotation of the wheel places another substituent of the macrocycle close to the backbone and at the opposite side of the **a**-substituent of the allene. As a result, a substituent overpass effect is triggered due to the larger size of the bipyridine group and the shorter distance to the polyene backbone compared to the *tert*-butyl group. This elongation effect of the polymer backbone is fully reversible, and the initial state is recovered by neutralizing the acid with Et_3N (see Experimental Section Chapter 3.3., Figure S32). Analogous results were also obtained for the enantiomers mono-(*P*)-**2** poly-(*P*)-**2** (see Experimental Section Chapter 3.3., Figures S33 and S34).Titration experiments with acid were also performed with the non-interlocked analogues (mono-(*M*)-**1** and poly-(*M*)-**1**) but no relevant structural changes were observed, indicating that the macrocycle is key to modulate the elongation of the polymer (see Experimental Section Chapter 3.3., Figures S42-S45).

To further demonstrate that the control over wheel pirouetting allows modulation of the helical scaffold, we studied the response of mono-(*M*)-**2** to metal-ion binding. We selected Cu(I) in light of its high affinity to the bipyridine N–donors in sterically crowded AT-CuAAC-derived products (Figure 61a).[300] A solution of mono-(*M*)-**2** in $CHCl_3$ was titrated with $[Cu(CH_3CN)_4]BF_4$ in CH_3CN (see Experimental Section Chapter 3.3., Section 5.3.10.1.2.). ECD and UV-vis spectra (Figure 61b,c) revealed changes consistent with the coordination of the metal ion[306] to the rotaxane that were further confirmed by NMR studies (Figure 61a and see Experimental Section Chapter 3.3., Figure S47). ROESY NMR studies of the mono-(*M*)-**2**/Cu(I) complex showed the presence of characteristic long-distance ROE peaks that suggests the rotation of the wheel relative to the thread. However, in this case, the resulting orientation of the wheel is different to the one promoted by the acidic media. In the mono-(*M*)-**2**/Cu(I) complex, the fragment of the macrocycle located closer to the phenylacetylene group (PA), i.e. the phenoxy group, is oriented over the **a**-substituent of the allene moiety (Figure

61e and see Experimental Section Chapter 3.3., Figures S55-S57), whereas in the mono-(*M*)-**2**/$\mathbf{H}^+$ complex, the macrocycle moiety located closer to the PA group was placed opposite to the **a**-substituent (Figure 60e).

Similar ECD and UV-vis experiments were carried out for poly-(*M*)-**2**, which showed a bathochromic shift of the polyene band after complexation with Cu(I). This fact indicates an elongation of the PPA helix, which is also accompanied by a helix inversion as inferred from ECD, giving at the vinylic region Cotton bands with opposite sign for poly-(*M*)-**2** and poly-(*M*)-**2**/Cu(I) complex (poly-(*M*)-**2** $ECD_{500\ nm} > 0$, *P* helix; poly-(*M*)-**2**/Cu(I) $ECD_{500\ nm} < 0$, *M* helix) (Figures 61f,g).

The reversibility of the process was demonstrated by removing the metal ions through the addition of a resin metal scavenger to the solution, which was then easily removed by filtration (see Experimental Section Chapter 3.3., Figure S38). ECD titrations with other metal ions of different coordination preferences [Ag(I), Cd(II), Zn(II)] did not lead to any change in the ECD spectra (see Experimental Section Chapter 3.3., Figure S41), suggesting that the complex formation in the polymer pendants is disfavored in these cases. AFM studies on a 2D crystal of poly-(*M*)-**2** obtained from a chloroform solution titrated with 1 equiv of Cu(I) showed an external *P* helix for the polymer after complexation (Figure 61h and see Experimental Section Chapter 3.3., Figure S59), confirming the helix inversion.

Identical studies were carried out for mono-(*P*)-**2** poly-(*P*)-**2**, which show similar results but with opposite sign of the Cotton bands due to their enantiomeric relationship (see Experimental Section Chapter 3.3., Figures S39 and S40).

Titration experiments with Cu(I) were also performed with the non-interlocked analogues [mono-(*M*)-**1** and poly-(*M*)-**1**] but no structural changes were observed, indicating that the macrocycle is key to modulate the elongation of the polymer (see Experimental Section Chapter 3.3., Figures S42-S45).

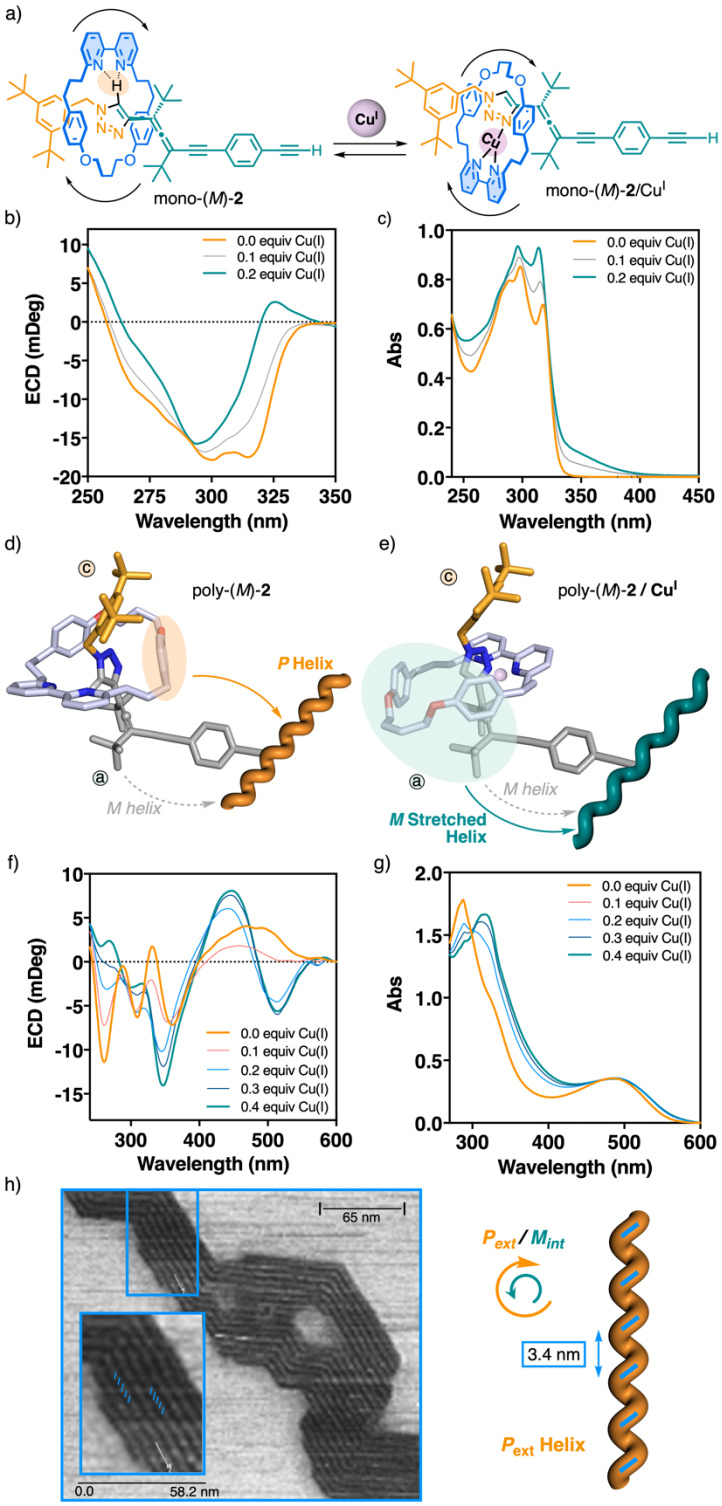

Figure 61. (a) Effect of an external stimulus Cu(I) on the orientation of the wheel in mono-(*M*)-**2**. (b) Change of the ECD and (c) UV-vis spectra of mono-(*M*)-**2** (0.25 mM in $CHCl_3$) upon addition of $[Cu(CH_3CN)_4]BF_4$ (15.89 mM in CH_3CN). (d) 3D model of helix induction mechanism in poly-(*M*)-**2** and for poly-(*M*)-**2** after titration with Cu(I). (f) Change of the ECD and (c) UV-vis spectra of poly-(*M*)-**2** (0.50 mM in $CHCl_3$) upon addition of $[Cu(CH_3CN)_4]BF_4$ (15.89 mM in CH_3CN). Green line: ECD and UV-vis signal at the saturation value of Cu(I).

Interestingly, the wheel rotation produced in poly-(*M*)-**2** after complexation with H^+ and Cu(I) to form poly-(*M*)-**2**/ H^+ and poly-(*M*)-**2**/Cu(I) complexes, induces opposite screw sense in the polymer, although the functional groups of the macrocycle and the chiral axis involved in the complex are the same— *P* helix, poly-(*M*)-**2**/H^+; *M* helix, poly-(*M*)-**2**/Cu(I)— (Figure 62). This helix inversion is attributed to the different size and coordination preferences of the host cation [H^+ and Cu(I)], which produce slight structural differences in both complexes, enough to induce opposite helical senses in the polymer. Thus, whereas in the poly-(*M*)-**2**/Cu(I) complex the two N–donors of the bipyridine are involved in the stabilization of the complex, in the case of the poly-(*M*)-**2**/H^+ complex a single N of the bipyridine is involved in the supramolecular interaction with the H^+. As a result, in the poly-(*M*)-**2**/Cu(I) complex, the fragment of the macrocycle placed closer to the PPA backbone is oriented over the **a**-substituent of the allene moiety and induces an *M* helix in the polymer (Figure 62 and see Experimental Section Chapter 3.3., Figures S55-S57). However, in the poly-(*M*)-**2**/H^+ complex, the macrocycle moiety located closer to the PPA backbone is placed opposite to the **a**-substituent inducing a *P* helix in the polymer (Figure 62).

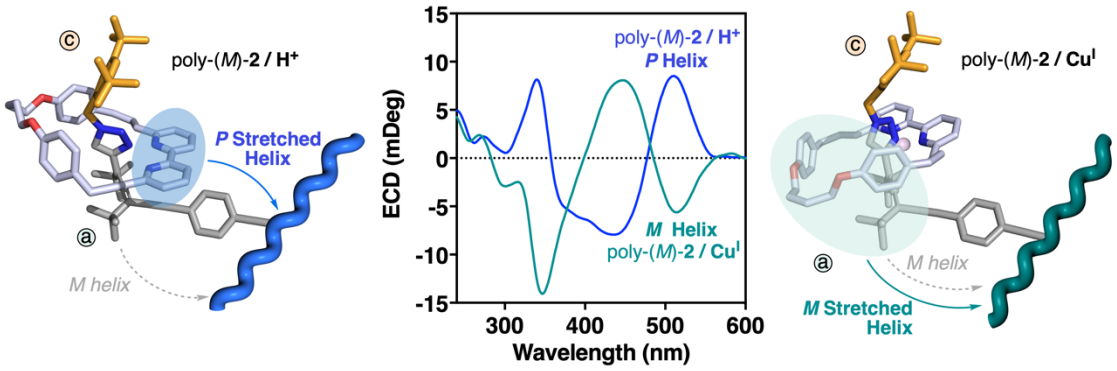

Figure 62. Comparison of the ECD spectra obtained for poly-(*M*)-**2**/H^+ and poly-(*M*)-**2**/Cu(I) and 3D model of both polymers describing the effect of the different wheel positions on the helical scaffold.

3.3.3. Conclusion

In conclusion, we have developed a novel macromolecular gear by combining dynamic mechanically interlocked molecules, i.e., rotaxanes, and dynamic helical polymers, i.e., poly(phenylacetylene)s. To this end, a chiral rotaxane consisting of a chiral thread and an achiral macrocycle was designed. A chiral allene with axial chirality and restricted conformational composition was chosen as the chiral thread and combined

with a small macrocycle. The activation/deactivation of supramolecular interactions between the wheel and the thread allows the pirouetting of the wheel with respect to the chiral axis to create a sophisticated multi-switching system. As a result, different steric effects from the macrocycle and the chiral allene are produced, altering the elongation and/or the helical sense of the polymer (Figure 63). These findings open new horizons in the conformational communication and information transmission mechanisms, where the interplay between molecular machines, chirality, supramolecular chemistry, and polymers can give rise to new mechanisms of helical induction within complex structures. Moreover, the control of these complex macromolecular gears through conformational control at different levels sheds light on the understanding of how information may be effectively transmitted across different levels of complexity.

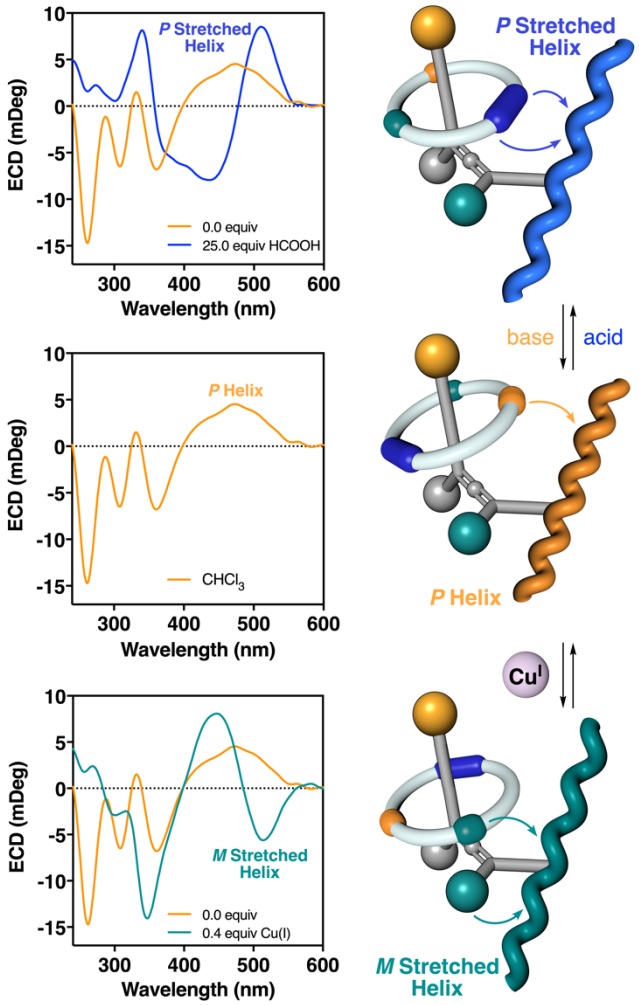

Figure 63. Macromolecular gear consisting in a dynamic chiral helical polymer (PPA) bearing a chiral rotaxane as pendant with controlled conformational composition.

3.3.4. Future Directions

In light of the results discussed above regarding the strong influence of the orientation of the wheel threaded to a chiral allene pendant on the helical conformation of a polyacetylene, future work will focus on controlling both pirouetting and shuttling of the relative position of the covalent sub-components within the mechanically interlocked pendant group. This approach aims to control the relative position of the wheel and explore the resulting changes in properties within the macromolecular system. This will provide a better understanding of how information can be efficiently transferred across different levels of complexity to generate novel molecular devices and machines. To achieve this objective, we have proposed a novel approach based on our previous system, which now incorporates two binding sites in the thread for the wheel (Figure 64).

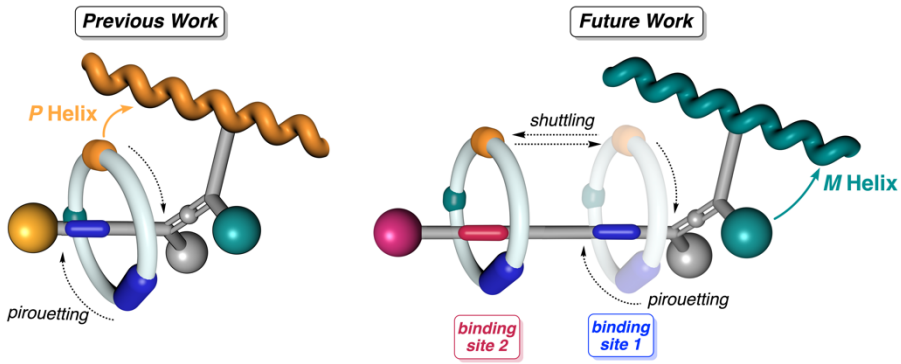

Figure 64. Comparison between previous work where the macromolecular helical structural changes commanded by the different positions of the wheel in a rotaxane with a chiral axis used as pendant, whereas future approach controlling co-conformation in a rotaxane molecular shuttle using changes in the preference for two binding sites.

Therefore, we envisioned two new rotaxanes that differ from the previous example in the achiral stopper unit **2** by incorporating an additional binding site with different functionality (Figure 65). To this end, a benzylic azide substrate **4** was selected as this derivative introduces at the benzylic position two protons with sufficient acidity to promote the shuttling of the wheel toward this new position, establishing a hydrogen bond between the N-donors of the bipyridine and the benzylic protons. On the other hand, we also selected a phenylurea azide substrate **5** since the urea group is known to be a good H-bond donor, particularly with molecules containing hydrogen bond acceptors such as the bipyridine group.[307] Hence, macrocycle **1** was threaded at the allene (*M*)-**3** with substrates **4**/**5**, using the same protocol as for mono-(*M*)-**2** (AT-CuAAC reaction) to

generate mono-(*M*)-**3** and mono-(*M*)-**4** in good yields after protecting group (PG) removal (total yield of both steps: 72% and 66%, respectively).

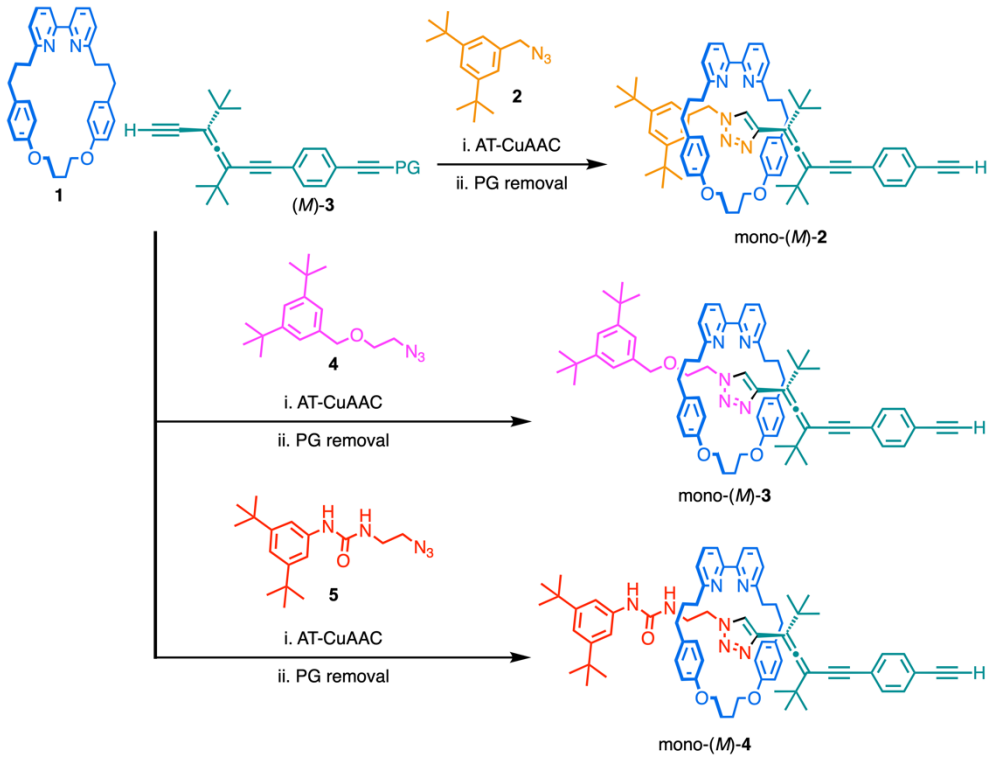

Figure 65. Synthesis of rotaxanes mono-(*M*)-**2**, mono-(*M*)-**3**, mono-(*M*)-**4**.

Comparison of the ^{1}H NMR spectra of the rotaxanes mono-(*M*)-**2**, mono-(*M*)-**3,** and mono-(*M*)-**4** revealed that the triazole proton resonance occurs at high ppm in the former (8.87 ppm), presumably due to H-bonding between the triazole and bipyridine moieties, whereas in mono-(*M*)-**3** and mono-(*M*)-**4** the triazole proton resonance shifts upfield (8.68 and 8.18 ppm, respectively), suggesting different relative arrangements of the subcomponents within the rotaxane, i.e. wheel shuttling leading to different co-conformations.

Polymerization of mono-(*M*)-**3** and mono-(*M*)-**4** with $[Rh(nbd)Cl]_2$ as catalyst generated poly-(*M*)-**3** and poly-(*M*)-**4** in good yields (90% and 85%, respectively). Comparison of the ECD studies of the abovementioned polymers in different solvents shows an excess of the *P* screw sense ($ECD_{485\ nm} > 0$), accompanied by a decrease in the intensity in the positive Cotton band centered at 485 nm the for polymers poly-(*M*)-**3** and poly-(*M*)-**4** (Figure 66). This decrease suggests a lesser effect of the wheel on the helicity due to the greater freedom of movement on the threads with two binding sites.

These preliminary studies are encouraging in terms of the possibility of selectively modulating both the pirouetting and shuttling of the wheel within a helical polymer. Stimulus-response studies in this direction are currently ongoing.

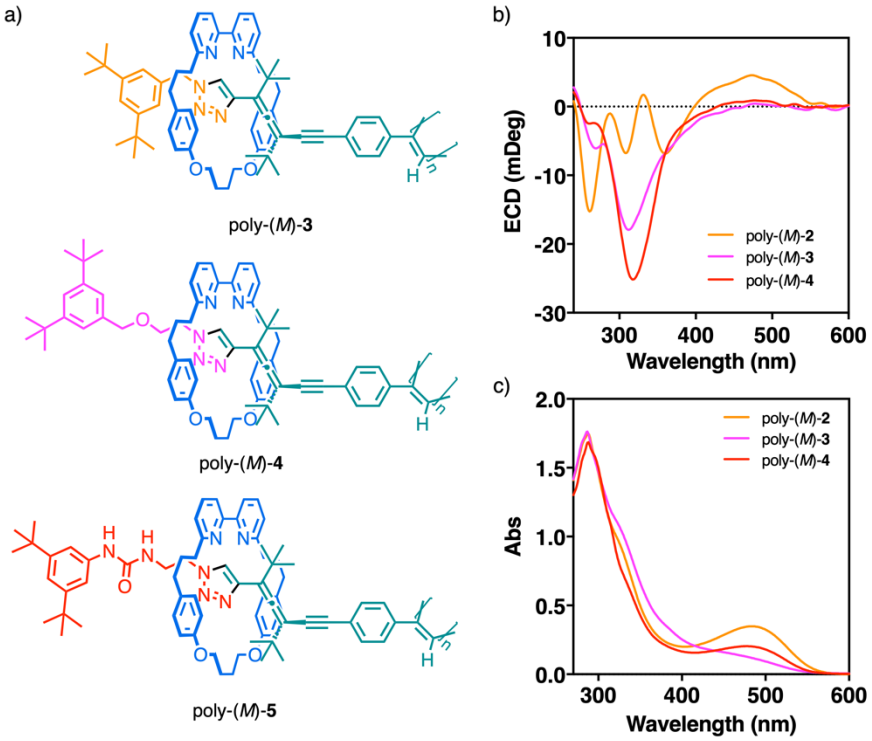

Figure 66. (a) Chemical structure of the polymers **3 – 5** and their corresponding (b) ECD and (c) UV-vis spectra (0.50 mM in $CHCl_3$).

Finally, we are also exploring the diastereoselective synthesis of the mechanical bond formation since axially chiral stereogenic elements have not been previously reported or explicitly highlighted.[48] Goldup and coworkers demonstrated that, with appropriately designed substrates, the AT-CuAAC reaction can diastereoselectively form the mechanical bond, suggesting that covalent stereochemistry and incipient mechanical stereogenic moiety interact to affect the kinetics of available diastereomeric AT-CuAAC pathways. This approach is of utmost importance as it has enabled the stereoselective synthesis of mechanically planar chiral catenanes and rotaxanes in recent years.[304, 308-311]

Inspired from these results, the asymmetric macrocycle **6** designed by Goldup's group[301] was threaded onto the allene (*M*)-**3** using the AT-CuAAC reaction (Figure 67). The resulting rotaxane mono-(*M*)-**5** was prepared with excellent diastereoselectivity (96:04 as judged by ^{1}H NMR analysis of the crude reaction products). However, the low

conversion (30%) indicates that the reaction conditions need to be optimized. Efforts in this direction are underway to improve efficiency and yield.

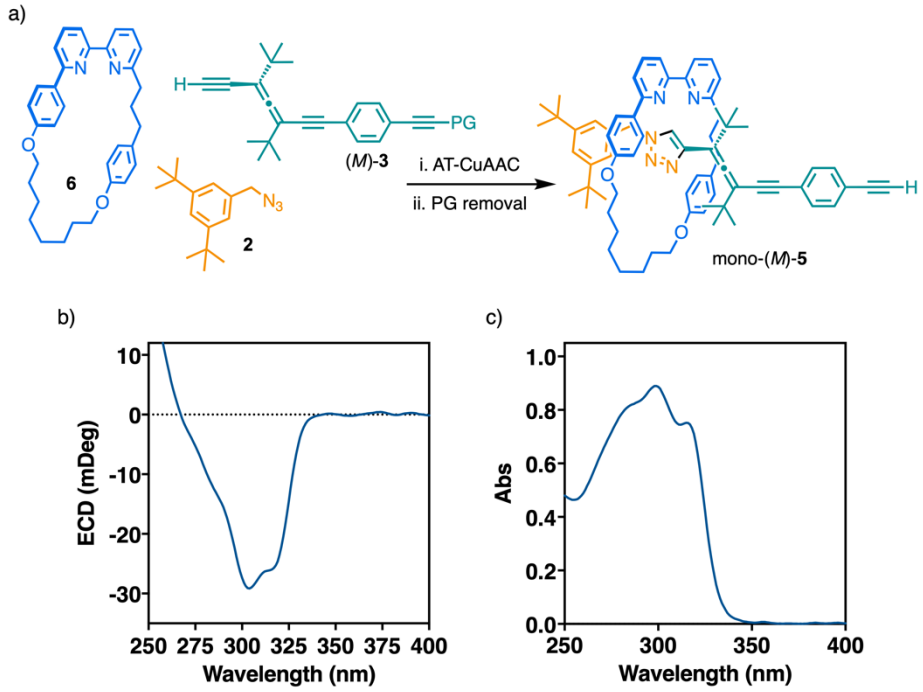

Figure 67. (a) Synthesis of mono-(*M*)-**5** using the AT-CuAAC reaction (PG = TIPS). (b) ECD and (c) UV-vis spectra of mono-(*M*)-**5** (0.25 mM in $CHCl_3$).

Future work will incorporate such mechanically interlocked systems into helical polymers. We anticipate that these preliminary results will enable the creation of multi-chiral helical structures containing three axial sources: the mechanically chiral molecules, the chiral allene, and the inherent helical chirality of the helix.

3.4. Axially-Chiral Allene-Based Supramolecular Polymers

Abstract: *P* or *M* single molecule supramolecular fibers can be obtained during the self-assembly of axially chiral allenes, which place its four substituents in two perpendicular planes. This specific spatial distribution, combined with the rigidity of the allene, makes it a great candidate for creating chiral building blocks with potential self-assembling properties. Therefore, we designed a chiral allene with two *tert*-butyl groups in different planes and opposite directions to provide stability to the building block. In the remaining two positions of the allene, π-extended and planar ethylene phenylene moieties substituted at the *para*-position of the aromatic ring with an ethylene diamide bearing a gallic wedge with paraffinic chains were introduced to favor the self-assembly of the axially chiral allene. Aggregation studies in MCH through different spectroscopic techniques such as UV-vis, ECD, IR, or NMR, in addition to Atomic Force Microscopy (AFM) studies and computational studies, revealed the formation of single-molecule chiral fibers through a cooperative mechanism. This species evolves towards the formation of larger fibers obtained by self-assembly of the single molecules. In these aggregates, an axial-to-axial helical induction mechanism emerges to generate the chiral fibers, whose handedness depends on the axial chirality of the allene: *P*-allene, *M*-aggregate; *M*-allene, *P*-aggregate.

3.4.1. Precedents

Inspired by nature, scientists have developed new types of artificial self-assembling systems, giving rise to the so-called supramolecular polymers. These macromolecular structures, that are held together through a delicate balance of non-covalent interactions (e.g., hydrogen bond, π-stacking, metal coordination, or metal-metal interactions, among others), have attracted the attention of the scientific community not only for their self-assembly processes but also for their potential applications.[98, 312-318]

The building blocks for the construction of such entities usually rely on flat aromatic cores such as benzene tricarboxamides (BTAs),[206,212,319-324] perileneimides,[325-333] bodipys,[334-339] porphyrins,[340-346] oligophenyleneethynylenes (OPEs)[20,347-350] or metal complexes,[351-358] among others. These units are endowed with either paraffinic or glycolated side chains that ensure solubility of the supramolecular polymer in the desired aggregating media. The introduction of chirality in the above-mentioned side chains generally promotes the adoption of supramolecular helical scaffolds,[3,95,96,359] allowing their application in tasks such as asymmetric catalysis,[360,364] spin-filtering materials,[365-367] chiroptical switches[267] or stimuli-responsive systems.[180] The asymmetry induction classically relies on the introduction of point chirality in the abovementioned solubilizing peripheral chains,[219,368] although other important mechanisms have been explored.[3,95,96,180,267,359] An interesting example is the copolymerization of achiral units with chiral analogues —the chiral units command a specific handedness into the achiral ones following the Sergeants and Soldiers (SaS) effect—[369-374] or copolymerization of scalemic mixtures where the enantioenriched unit commands the handedness of the system following the so-called Majority Rules (MR) effect.[375-382] Other approaches consisting of irradiation with circularly polarized (CP) light[383-387]or the use of chiral solvents[388-391]have also emerged as successful strategies for the construction of preferred-handed helices.[3,95,96,180,267,359] More recently, the use of non-planar intrinsically chiral building blocks —like cyclophanes,[392-396] biaryls,[218,219] helicenes[220,397-400] or subphtalocyanines[401,402]— emerged as a more ambitious strategy to develop chiral supramolecular architectures.[403] Surprisingly, among the above-mentioned manifold of chiral building blocks, axially chiral allenes have not been studied so far,[24] even though they have been successfully applied for the construction of functional chiral materials such as polymers,[35,279,299,404] cyclophanes,[34,405,406] supramolecular capsules[36] or

catenanes.[37] Allenes place the four substituents in two perpendicular planes and it might seem that the supramolecular self-assembly of these building blocks is not possible. However, we have recently observed that chiral allenes can be used as pendant groups in helical polymers such as poly(phenylacetylene)s (PPAs), where the helical macromolecular structure is fixed by supramolecular interactions between pendants along the structure. Hence, we envisioned that chiral allenes can be used in the preparation of helical supramolecular aggregates as a source of axial chirality, and where their self-assembly can be favored by the introduction of aggregating moieties based on ethylene diamides bearing a gallic wedge with paraffinic chains, which might favor their self-assembly in low polar media (Figure 68a). Thus, chiral allene (*P*)-**1** (Figures 68b,c) was designed bearing two *tert*-butyl groups in two perpendicular planes of the allene, along with two dendritic aggregation moieties based on ethylene diamides bearing a gallic wedge with paraffinic chains.

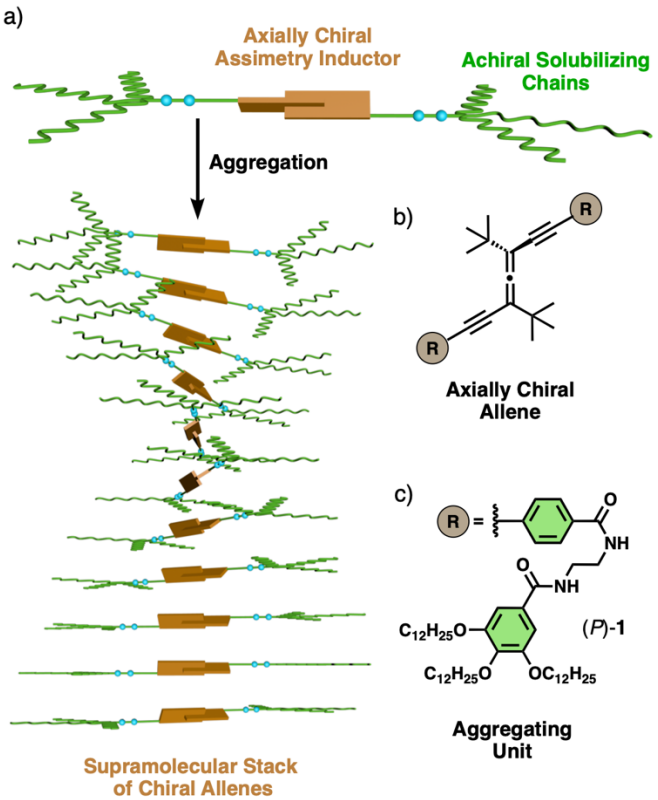

Figure 68. (a) Schematic illustration of an axially chiral extended allene and its potential supramolecular polymerization into a helical aggregate. Chemical structures of the molecules employed in this work composed by (b) an axially chiral allene unit endowed with (c) an aggregating unit.

3.4.2. Discussion

Therefore, (*P*)-**1** and (*M*)-**1** were synthesized following the synthetic protocol described in the Experimental Section Chapter 3.4. (see section 5.4.2).[279,299] Next, its self-assembly ability was investigated by a set of spectroscopic techniques in a good (Chloroform, $CHCl_3$) and a bad solvent (methylcyclohexane, MCH) to stabilize molecularly dissolved and aggregated states, respectively. For instance, comparison of IR spectra of (*P*)-**1** in $CHCl_3$ and MCH supports the formation of a chiral aggregate in the latter solvent through the self-assembly of (*P*)-**1** directed by a 4-fold array of hydrogen bonds (Figure 69c).

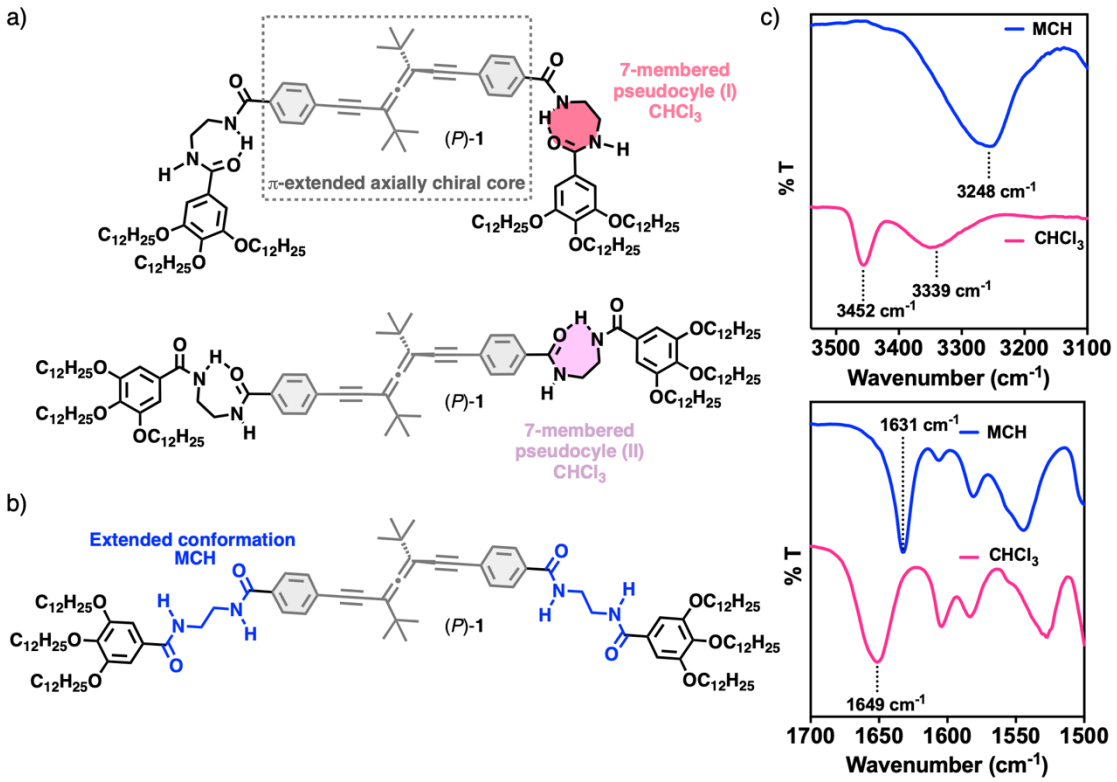

Figure 69. Structure of (*P*)-**1** with the ethylenediamide bridge forming (a) the two possible 7-membered pseudocycles or (b) the extended conformation that promoted effective aggregation. (c) IR spectra of (*P*)-**1** in $CHCl_3$ and MCH (1 mM) confirming the presence of the abovementioned structures.

Thus, while in $CHCl_3$ the stretching band of the amide and the NH appear centered at 1649 cm^{-1} (amide), and at 3452 (NH) and 3339 cm^{-1} (NH), indicative of the presence of molecularly dissolved species bestowing 7-membered hydrogen bonded pseudocycles (i.e., metastable species, Figure 69a,c), in MCH, these bands are shifted towards lower frequencies. The amide band appears now at 1631 cm^{-1}

($\Delta\upsilon$= 18 cm^{-1}), whereas the NH bands merge into one centered at 3248 cm^{-1}, ($\Delta\upsilon$= 204 and 91 cm^{-1}), suggesting a 4-fold arragement of hydrogen bonds (Figure 69c).[328,407] VT ^{1}H-NMR experiments of (*P*)-**1** in $CDCl_3$, supports the formation of 7-membered pseudocyles stabilized by intramolecular hydrogen bonds due to a concomitant deshielding of the amide protons with increasing temperature while the other signals of the molecule remain virtually unaltered (Figure 70).

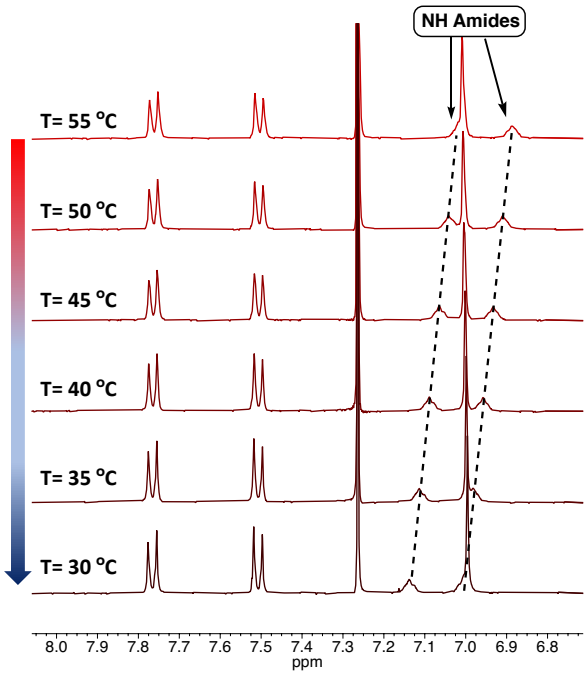

Figure 70. VT-^{1}H NMR studies of (*P*)-**1** ($CDCl_3$, 500 MHz).

On the other hand, UV-vis experiments of (*P*)-**1** in $CHCl_3$ (10μM) show a UV-vis spectrum with a small shoulder at 350 nm followed by three consecutive maxima of similar intensity centered at 318, 301, and 275 nm (Figure 71a). In contrast, in MCH (10 μM), the UV-vis spectrum shows a two-fold increase in the initial shoulder (λ = 350 nm), followed by a hypochromic effect in the band centered at 318 nm and a blue shift accompanied with an hyperchromic effect in the second band, now centered at 298 nm. Moreover, an overall increase in the remaining absorption spectra was also observed when compared to the spectra in $CHCl_3$ (Figure 71a). These changes in the UV-vis studies of (*P*)-**1** in $CHCl_3$ and MCH are consistent with the formation of an aggregate in MCH. Comparison of ECD studies in both solvents corroborates the formation of a chiral aggregate in MCH. Thus, while the ECD spectrum of (*P*)-**1** in $CHCl_3$ (10 μM) shows two positive maxima at 330 and 304 nm followed by a zero-crossing point at λ = 287 nm and a negative band centered at λ = 273 nm (Figure 71b),

a dramatic change is found when the ECD spectra is measured in MCH. First, an increase in magnitude of the overall ECD spectrum is observed, which is indicative of the formation of a supramolecular chiral aggregate. Second, an inversion of the first Cotton band, now centered at λ = 323 nm, indicates the formation of an *M* chiral aggregate. This first Cotton band is followed by a zero-crossing point at λ = 318 nm, a positive band at 298 nm followed zero-crossing point at λ = 279 nm and negative band at λ = 266 nm (Figure 71b).

Similar results were obtained for (*M*)-**1** in $CHCl_3$ and MCH, the enantiomeric form of (*P*)-**1**. In this case, opposite signs of the ECD bands are obtained due to its mirror image relationship (see Experimental Section Chapter 3.4., Figure S3a).

To decipher the supramolecular polymerization mechanism of (*P*)-**1**, VT-ECD experiments were conducted. Therefore, heating-cooling ECD curves of a solution of (*P*)-**1** in MCH (10 μM) monitored at λ = 323 nm were carried out at 0.1 K·min^{-1} and at different concentrations (Figure 71d) showing in all cases non-sigmoidal curves, indicative of a cooperative supramolecular polymerization process.[317] Moreover, negligible thermal hysteresis was found along the above mentioned heating-cooling cycles at 0.1 K·min^{-1}, indicating a supramolecular polymerization process that is under thermodynamically control (Figure 71c). Following the one component model developed by Meijer and coworkers,[408,409] the full set of thermodynamic parameters as well as the cooperativity value σ were obtained, confirming the cooperative nature of the supramolecular polymerization process (Table 1).

Table 1. Thermodynamic parameters of the supramolecular polymerization process of (*P*)-**1**.

ΔH_e (kJ·mol^{-1})	ΔS (kJ·mol^{-1}·K^{-1})	ΔH_n (kJ·mol^{-1})	T_e (K)[a]	σ[b]
-150	-0.37	-141.6	334, 336, 338	3.42·10^{-2}

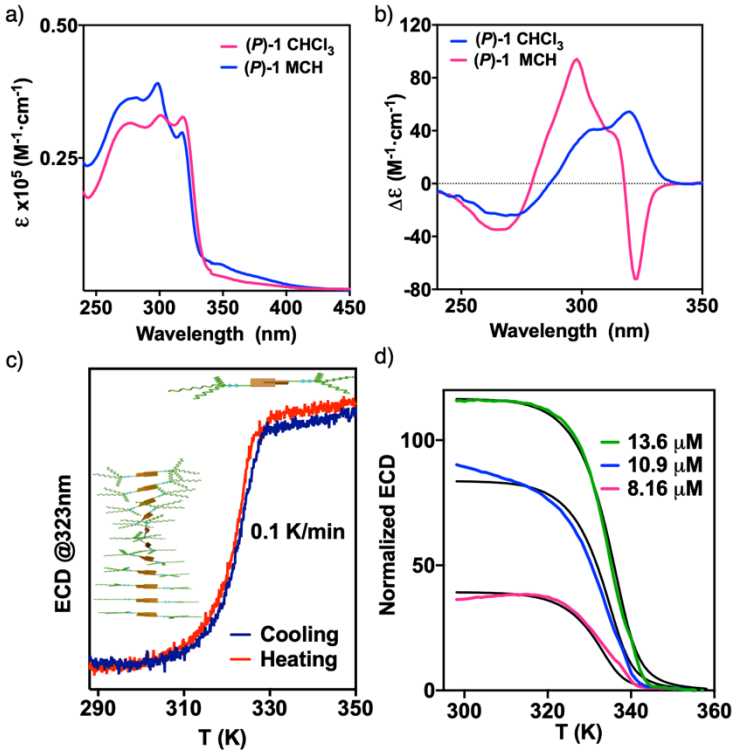

Figure 71. (a) UV-vis and (b) ECD and spectra of monomeric and aggregated states of (*P*)-**1** (10 μM). (c) Heating cooling cycle showing negligible hysteresis (λ = 323 nm, 0.1 K·min^{-1}, MCH). (d) Aggregation plots and cooperative fit curves at different concentrations to obtain the thermodynamic parameters of 1 depicted in Table 1 (λ = 323 nm, 0.1 K·min^{-1}, MCH).

Next, atomic force microscopy (AFM) studies were carried out to analyze the morphology of the aggregates. Thus, 10 μL of a 10 μM MCH solution of (*P*)-**1** were spin coated onto highly oriented pyrolytic graphite (HOPG). High-resolution AFM images revealed the presence of single molecule fibers that coexist with larger fiber like aggregates obtained by parallel packing of the single molecule fibers (Figure 72). Thus, the self-assembly of (*P*)-**1** first generated individual *M* oriented fiber-like aggregates with average height of 1 nm, helical pitch of 5 nm, width of 7 nm and packing angle of 55º. These individual helices bundle together through interdigitation of the long alkyl chains to generate longer and thicker fibbers with lengths up to 2 microns, average width of 20 nm and 2 nm in height (Figure 72 and see Experimental Section Chapter 3.4., Figures S4-S8).

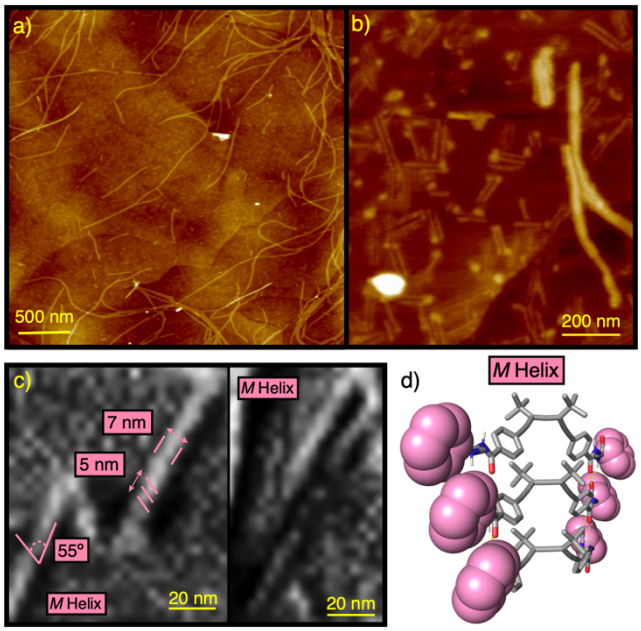

Figure 72. AFM images of (*P*)-**1** deposited onto HOPG showing fibber-like aggregates. (a) Large scale AFM image showing the presence of bundled fibbers. (b) Zoom showing the presence of unimolecular fibber-like aggregates. (c) Zoom highlighting the presence of supramolecular *M* helices for (*P*)-**1** and (d) side view of (*P*)-**1** trimer optimized by DFT (B3LYP/6-31G**). Phenyl rings of the gallic moiety have been marked as pink spheres to clarify the (*M*)-handedness of the supramolecular aggregate.

Finally, to obtain an approximated secondary structure of the helical aggregate theoretical calculations were performed. To do that, an initial screening using Grimme's extended semiempirical tight-binding method (GFN2-xTB)[326,410] for (*P*)-**1**was chosen to optimize the geometry of monomers and aggregates (n = 1-8). These studies revealed that the most stable aggregate has an extended ethylene diamide conformation (Figures 69b,c), that generates an effective 4-fold hydrogen bond supramolecular array with the upper and lower units (Figure 73b and see Experimental Section Chapter 3.4., Figure S9). Alternative conformations, presenting a 7-membered pseudocycle on the ethylene diamide bridge (Figure 69a,b), produce the formation of stable dimeric/trimeric structures, which could not effectively grow into larger aggregates due to the formation of structural defects, hindering an effective one-dimensional supramolecular polymerization process (see Experimental Section Chapter 3.4., Figures S9-S14 and Tables S1 and S2). To validate the presence of a cooperative mechanism the strategy reported by Ortí and Sánchez[326] for supramolecular polymerization processes was applied. To do that, a 16-mer was built and optimized using GFN2-xTB, followed by extraction of upper and lower terminal building blocks to obtain oligomers with decreasing size (n = 12, 10, 8, 6, 4, 2) to avoid terminal effects,[372,411] whose energies were further extracted by single-point energy

calculations.[327,410,216,412] The binding energy per increasing pair of molecules ($\Delta E_{bind, n-1}$) was estimated from the single-point energy calculations of the oligomers (See SI for details), revealing an exponential decay in the energy binding, which indicates of a cooperative supramolecular polymerization process (Figure 73a and see Experimental Section Chapter 3.4., Figure S15), fully consistent with the experimental data (Figures 70d,e and Table 1). Furthermore, Density Functional Theory (DFT) calculations employing the B3LYP method and the 6-31G** basis set were performed on monomers, dimers, trimers, and tetramers of the extended structures to validate and refine their geometry. These studies revealed that (*P*)-**1** aggregates describing a supramolecular *M* helix determined by the *P* axial chirality of the allene. Next, theoretical ECD calculations, time-dependent density functional theory (TD-DFT) was used together with a CAM-B3LYP density functional and 6-31G** basis set, were performed on the optimized structures for the monomer and oligomers (n = 2-4) (see Experimental Section Chapter 3.4., Figures S16-20).[334] The simulated ECD spectra are in good agreement with the experimental ones, describing the bisignate pattern (+/-) observed for the monomer and the (-/+/-) ECD pattern obtained in the aggregate (Figures 73c,d).

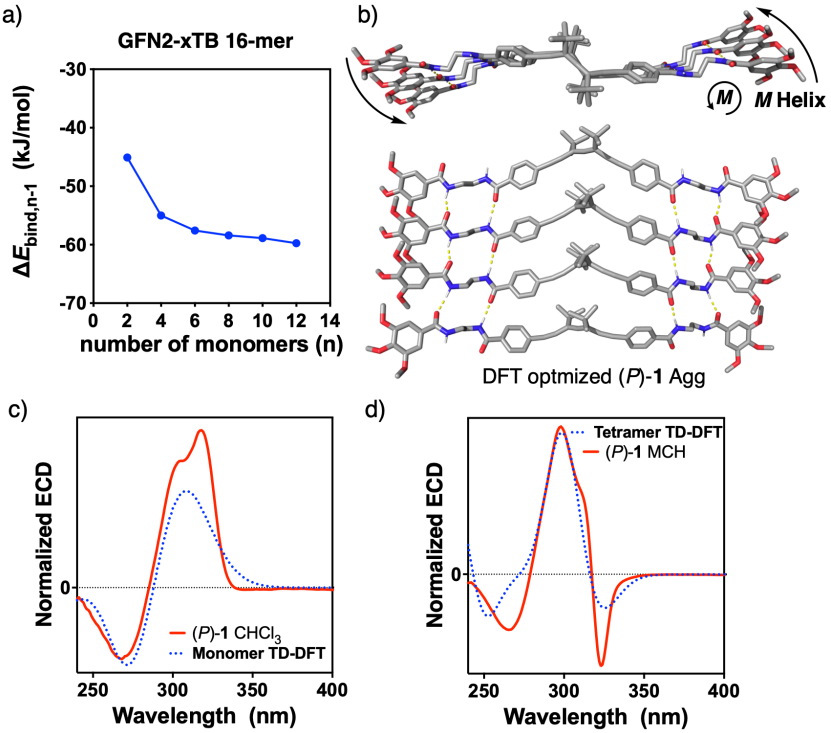

Figure 73. (a) Energy binding calculated with single points of oligomers from an optimized 16-mer in GFN2-xTB. (b) Top and side views of (*P*)-**1** aggregates optimized by DFT (B3LYP/6-31G**). Comparison of the ECD experimental ($CHCl_3$ and MCH) vs calculated spectra for (c) (*P*)-**1** monomer and the corresponding (d) tetramer optimized by DFT (B3LYP/6-31G**).

3.4.3. Conclusion

In conclusion, we have demonstrated that chiral allenes, possessing axial chirality and where its four substituents are distributed in two perpendicular planes, are suitable building blocks for the development of supramolecular polymers. In this case, we have designed and synthetized a (*P*)- and (*M*)-axially-chiral building block consisting in a chiral allene used as central part of the building block. As substituents of the chiral allene we chose two *tert*-butyl groups in different planes and opposite directions to provide stability to the allene. In the other two substituents of the allene, two π-extended and planar ethylene phenylene moieties substituted at the *para*- position of the aromatic ring with an ethylene diamide bearing a gallic wedge with paraffinic chains, were introduced to favor the self-assembly of the allene through extra π-π, H-bond and Van der Waals interactions.

Aggregation studies (UV-vis, ECD, IR, NMR, AFM and computational studies) in MCH reveal the formation of single molecule helical fibers whose chirality opposes the axial chirality of the allene— (*P*)-allene*,* (*M*)-aggregate; (*M*)-allene*,* (*P*)-aggregate—. Parallel self-assembly and interdigitation of single molecule fibers, generate larger fiber-like aggregates. In these aggregates, the chirality of the fiber is dictated by the axial chirality of the allene used as a central core of the building block. Remarkably, these results show that although *a priori* the allene does not have a planar and extended structure to facilitate its self-assembly, its derivatization with functional groups with potential π-π, H-bond and other supramolecular interactions through self-assembly, results in the spontaneous aggregation into fibrillar structures. As a result, this work deals with an interesting axial-to-axial supramolecular helix induction mechanisms through self-assembly, which allows a better understanding about the different pathways of transmission of information at different levels of complexity. Thus, this work opens a new horizon in the design of chiral supramolecular materials and the study of novel helix induction mechanisms, increasing the diversity of the chiral building blocks and therefore the properties of the aggregate associated to the building block.

Chapter 4. Conclusions

Chapter 4. Conclusions

This Doctoral Thesis has focused on the development of novel helical polymers based on axially chiral allenes as a source of chirality. Properly substituted allenes have proved to be an enticing option for obtaining chiral compounds of greater complexity.

The first example of a helical polymer containing allenes as chiral inductors is described in Chapter 3.1. We have demonstrated that modified PPA bearing allenes as pendants, termed PAEPAs, behave as quasi-static helical polymers due to the conformationally restricted pendant groups. Notably, these PAEPAs can be transformed into dynamic helical polymers through the on/off activation of supramolecular interactions. Thus, changes in the relative size of substituents in such conformationally restricted pendants relative to the polymer backbone can alter the command that governs the helical sense. This new dynamic axial-to-helical communication mechanism is demonstrated by studying the supramolecular interaction between the hydroxy group of a remote allenic substituent with secondary or tertiary amines, resulting in helix inversion due to the activation/deactivation of such interactions that modify the relative bulkiness of the dominant substituents. This dynamic axial-to-helical mechanism was demonstrated by 14N-NMR and by acetylation of the hydroxy group, demonstrating the role of the alcohol/amine interaction in the helix inversion process.

These results encouraged us to search for novel ways to induce helix sense preferences in helical polymers based on allene inductors to create a macromolecular helical switch. Chapter 3.2. describes a different approach in which the introduction of a flexible arm as an achiral side chain in one of the allene substituents allows dynamic control of the helix induction command. When the arm is stretched, the helix induction command remains with the closer allene substituent, whereas when the arm is bent, this substituent overrides the order given by the substituent as it approaches the backbone and thus commands the helical sense of the PPA. As a result, a helix inversion mechanism based on the conformational control of a flexible arm without changing the relative spatial distribution of the chiral inducer is presented. Furthermore, we found that multi-chiral helical structures containing five axial motifs can be prepared by combining rigid, extended, and axially chiral allenes with helical polymers such as PPAs.

In Chapter 3.3., a sophisticated macromolecular gear is described based on the combination of mechanically interlocked molecules (i.e., rotaxane) and dynamic helical polymers (i.e., PPAs). To this end, a chiral rotaxane consisting of a chiral thread and an achiral macrocycle was designed. A chiral allene with axial chirality and restricted conformational composition was chosen as the chiral thread and combined with a small macrocycle, acting as a wheel. Changes of supramolecular interactions between the wheel and the thread allows the wheel to be rotated with respect to the chiral axis to create a sophisticated multi-switching system. As a result, different steric effects from the macrocycle and the chiral allene are produced, altering the elongation and/or the helical sense of the polymer. Future work will focus on controlling both rotation and shuttling of the relative position of the covalent sub-components within the mechanically interlocked pendant group.

These findings regarding the control of these complex macromolecular gears by conformational control at different levels shed light on the understanding of how information may be effectively transmitted across different levels of complexity.

Finally, as described in Chapter 3.4., we have shown that chiral allenes are also suitable building blocks for the design of supramolecular polymers. These chiral molecules have a rigid three-dimensional structure that places their substituents in two perpendicular planes, preventing easy self-assembly. However, we have designed an allene functionalized with two π-extended and planar ethylene-phenylene moieties, substituted at the para position of the aromatic ring with an ethylenediamide bearing a gallic wedge with paraffinic chains, which favors aggregation through π-π, H-bond, and Van der Waals interactions. Aggregation studies in MCH revealed the formation of single-molecule helical fibers whose chirality is opposite to the axial chirality of the allene — (*P*)-allene, (*M*)-aggregate; (*M*)-allene, (*P*)-aggregate—. Parallel self-assembly and interdigitation of single-molecule fibers produce larger fiber-like aggregates. In these aggregates, the chirality of the fiber is dictated by the axial chirality of the allene used as the central core of the building block. As a result, this work deals with an interesting mechanism of axial-to-axial supramolecular helix induction by self-assembly. Therefore, it opens a new horizon in the design of chiral supramolecular materials, increasing the diversity of chiral building blocks and, thereby, the properties of the aggregate associated with the building block.

Chapter 5. Methodology and Experimental Section

5.1. Experimental Section and Methodology Chapter 3.1.

5.1.1. Materials and Methods

Reactions were conducted in dry solvents under argon unless otherwise stated. Et_3N was freshly distilled from CaH_2 under argon atmosphere. $[Rh(nbd)Cl]_2$ was obtained from Sigma-Aldrich (96%). All other chemicals were purchased from Sigma-Aldrich, Acros Organics, Alfa Aesar, Fluorochem, TCI Chemicals or Abcr and they were used as received.

The abbreviation "rt" refers to reactions carried out at a temperature between 21-25 ˚C. Reaction mixtures were stirred using Teflon-coated magnetic stir bars. Thin layer chromatography (TLC) was carried out on pre-coated silica gel F254 plates with visualization under UV light or by dipping the plate into solutions of phosphomolybdic acid or potassium permanganate solutions followed by heating. Column chromatography was performed on silica gel (40-60 μm) unless otherwise stated.

NMR experiments have been recorded in a Bruker spectromer (^{1}H frequency 300 mHz).

^{14}N-NMR experiments in a Bruker DRX-500 spectrometer (^{14}N frequency 36.12 mHz).

ECD measurements were done in a Jasco-720 and UV spectra were registered in a Jasco V-630 with a 1 mm quartz cuvette at rt. The amount of polymer used is indicated in the corresponding section.

VT-ECD were measured in a Jasco-1100 with a 1 mm quartz cuvette.

Optical rotation was measured in a Jasco-P2000 with a 1 cm quartz cuvette at rt (c = 10 mg·mL^{-1}, $CHCl_3$).

Raman spectra were carried out in a Reinshaw confocal Raman spectrometer (Invia Reflex model) equipped with two lasers (diode laser 785 nm and Ar laser 514 nm).

CSP-HPLC experiments were carried out in a Waters System equipped with a Phenomenex Lux 5 μm i-Amilose-1 column. The amount of monomer used was 0.5 mg·mL^{-1} and the mixture hexane:isopropanol (9:1) was used as eluent (flow rate: 0.5 mL·min^{-1}). Enantiomers (*P*)-**DEA** and (*M*)-**DEA** were resolved by semipreparative HPLC

using the CSP Chiralpak® IA (Diacel Chemical Industries Ltd.). Elution was performed with a mixture of Hexane:^{i}PrOH 99.2:0.8 at a flow of 3.5 mL·min^{-1}. Under these conditions, 100 μL of a solution of (±)-**DEA** in Hexane (15 mg·mL^{-1}) was injected.

GPC studies were carried out in a Waters Alliance 2695 HPLC with a UV-2489 detector (Waters) mns equipped with Phenomenex GPC columns (103 Å, 104 Å and 105 Å). The amount of polymer used was 0.5 mg·mL^{-1}. THF was used as eluent (flow rate: 1 mL·min^{-1}) and as inner standard, polystyrene narrow standards (PSS) were used.

DSC traces were obtained in a DSC Q200 Tzero Technology (TA Instruments, New Castle, UK), equipped with a refrigerated cooling system RCS90 (TA Instruments, New Castle, UK), using a Tzero low-mass aluminium pan.

TGA traces were obtained in a TGA Q5000 (TA Instruments, New Castle, UK) using a platinum pan.

AFM measurements were performed in a Multimode V Scanning Probe Microscope (Veeco Instruments) in air at rt, with standard silicon cantilevers and supersharp cantilevers in tapping mode using 12 μm and 1 μm scanners. Nanoscope processing software and WSxM 4.0 Beta 1.0 [4] (Nanotec Electrónica, S.L.) was used for image analysis. All measurements were performed at CACTI (University of Vigo, Spain).

PyMOL was used as a molecular visualization system.

All computations were performed with Gaussian-16 (G16RevC.01).[413]

5.1.2. Synthesis of Monomers

*(P)-**DEA** and (M)-**DEA***

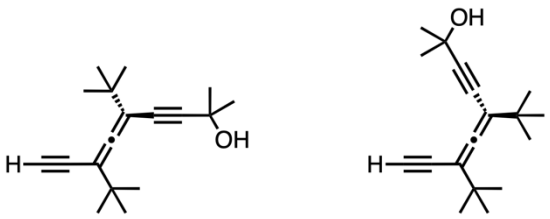

Compounds (*P*)-**DEA** and (*M*)-**DEA** were synthesized according to reported procedures (Scheme 1).[251]

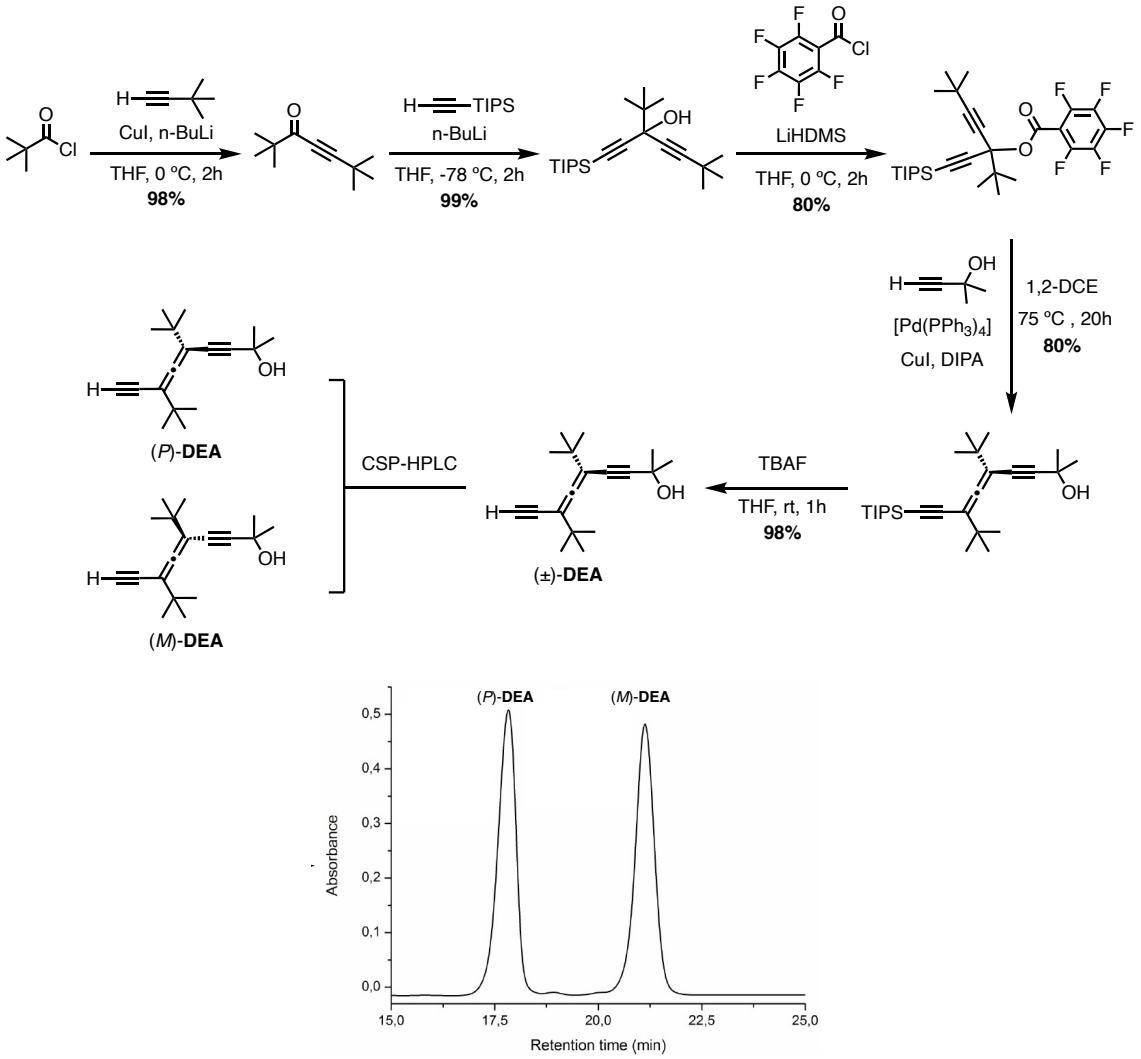

Scheme 1. Synthetic route to enantiomerically pure **DEA**, (*P*)-**DEA** and (*M*)-**DEA**, and the chromatogram of their enantiomeric resolution by HPLC.

*Di-tert-butyl-2-methyl-9-(4-((trimethylsilyl)ethynyl)phenyl)nona-5,6-dien-3,8-diyn-2-ol (**1a**)*

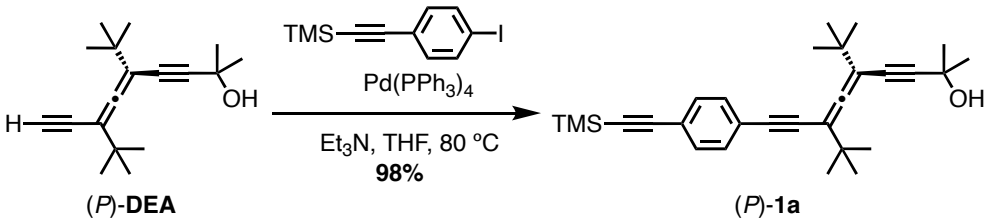

(*P*)-**DEA** (*P*)-**1a**

In a flamed Schlenk tube, ((4-iodophenyl)ethynyl)trimethylsilane (110 mol%, 0.383 mmol, 115 mg) and [$Pd(PPh_3)_4$] (5 mol%, 0.017 mmol, 21 mg) were placed. The yellow solution was bubbled with Ar and then a solution of (±)-**DEA**[S1] (100 mol%, 0.348 mmol, 90 mg) in a mixture of Et_3N (1 mL) and THF (3 mL) was added *via* cannula. The reaction mixture was stirred at 80 °C for 20 h. The reaction mixture was washed first with sat. aq NH_4Cl solution, distilled water and then with sat. aq NaCl solution. The aqueous phases were combined and extracted with DCM (3 x 10 mL). The combined organic phases were dried over anhyd Na_2SO_4. Evaporation *in vacuo* and purification by flash chromatography on silica gel (hexane: EtAcO (9:1) afforded (±)-**1a** (113 mg, 98%) as a yellow oil.

Enantiopure compounds (*P*)-**1a** and (*M*)-**1a** were obtained from (*P*)-**DEA** and (*M*)-**DEA** respectively, by applying the same protocol as for (±)-**1a**.

Molecular Formula: $C_{29}H_{38}OSi$**. MW:** 430.71 **g/mol.**

^{1}H-NMR (300 MHz, $CDCl_3$, 298K) *δ:* 7.38 (m, 4H), 1.56 (s, 6H), 1.19 (s, 9H), 1.15 (s, 9H), 0.25 (s, 8H).

^{13}C-NMR (75 MHz, $CDCl_3$, 298K) *δ:* 211.7, 132.1, 131.5, 124.1, 122.9, 105.1, 103.6, 103.2, 97.7, 96.4, 92.5, 85.7, 76.1, 66.1, 36.0, 35.9, 31.9, 0.3.

HRMS (ESI$^+$): *m/z* calcd. for $C_{29}H_{38}OSi$ 430.2692; found 431.2758 $[M+H]^+$.

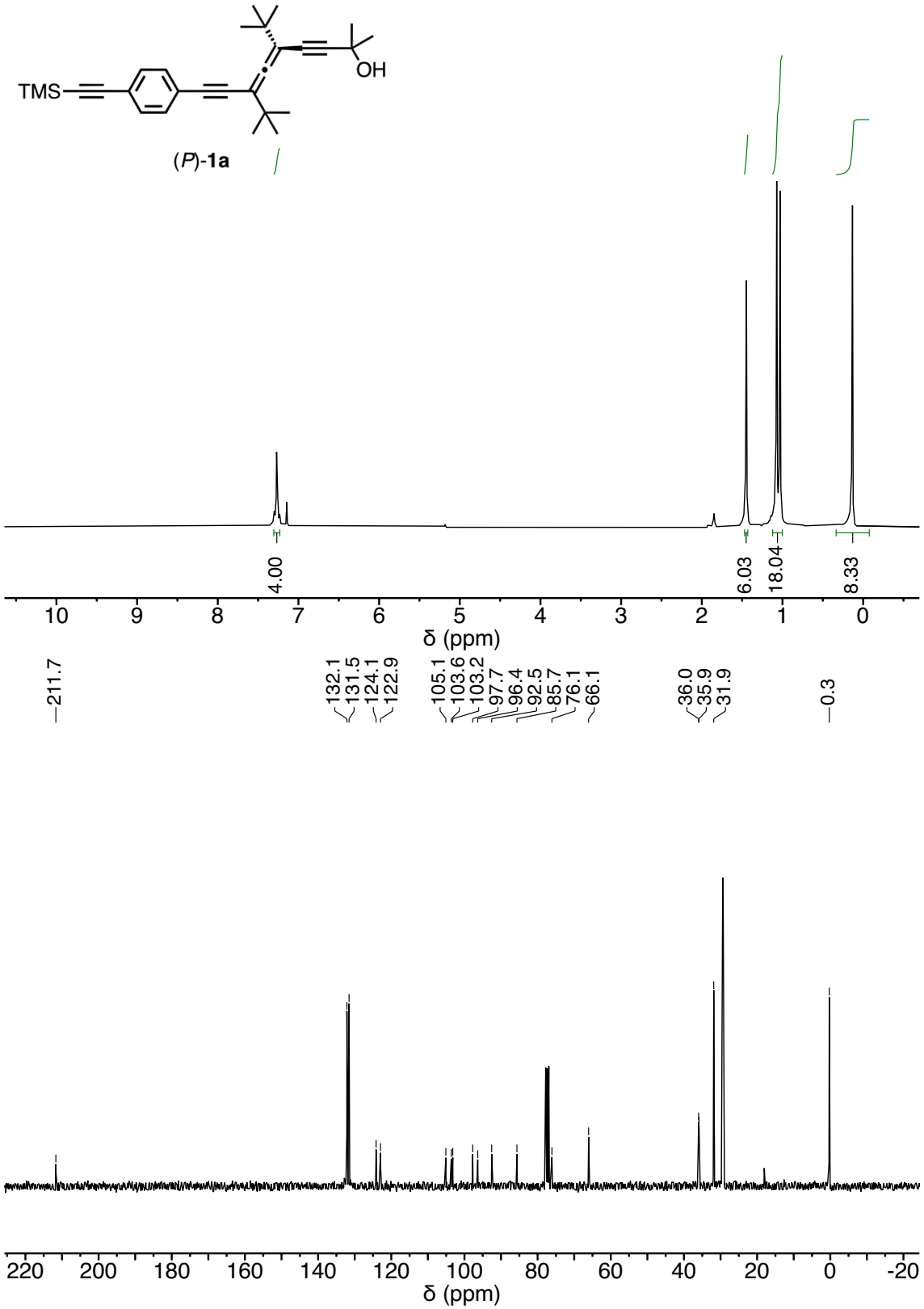

Figure S1. ^{1}H-NMR and ^{13}C-NMR of (*P*)-**1a** in $CDCl_3$.

*Di-tert-butyl-9-(4-ethynylphenyl)-2-methylnona-5,6-dien-3,8-diyn-2-ol (**1**)*

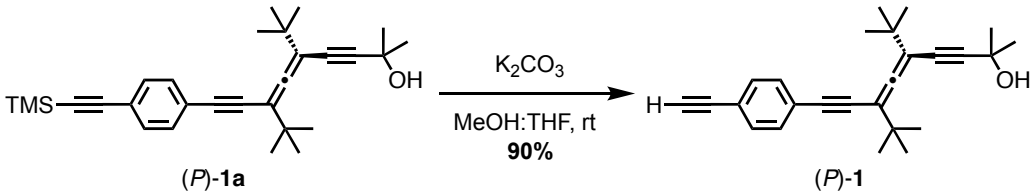

To a solution of (±)-**1a** (100 mol%, 0.548 mmol, 236 mg) in a mixture of THF:MeOH (1:1, 5 mL), K_2CO_3 (150 mol%, 0.825 mmol, 114 mg) was added at rt. After 15 min, the mixture was quenched with distilled water (40 mL) and then the aqueous phase was extracted with DCM (3 x 10 mL). The combined organic phases were dried over anhyd Na_2SO_4. Evaporation *in vacuo* and purification by flash chromatography on silica gel (hexane: EtAcO (8:2) afforded (±)-**1** (160 mg, 90%) as a yellow oil.

Enantiopure compounds (*P*)-**1** and (*M*)-**1** were obtained from (*P*)-**1a** and (*M*)-**1a** respectively, by applying the same protocol as for (±)-**1**.

For (*P*)-**1**, $[\alpha]_D^{20}$= +300 (*c*= 10 mg·mL^{-1}, $CHCl_3$). For (*M*)-**1**, $[\alpha]_D^{20}$= -336 (*c*= 10 mg·mL^{-1}, $CHCl_3$).

Molecular Formula: $C_{26}H_{30}O$. **MW:** 358.53 **g/mol.**

^{1}H-NMR (300 MHz, $CDCl_3$) δ 7.41 (m, 4H), 3.16 (s, 1H), 2.04 (s, 1H), 1.56 (s, 6H), 1.19 (s, 9H), 1.15 (s, 9H).

^{13}C-NMR (75 MHz, $CDCl_3$) δ 211.5, 132.1, 131.4, 124.4, 121.7, 103.4, 103.0, 97.6, 92.1, 85.6, 83.5, 78.9, 75.9, 65.9, 35.8, 35.7, 31.7, 29.2, 29.1.

HRMS (ESI$^+$): *m/z* calcd. for $C_{26}H_{30}O$ 358.2297; found 381.2189 $[M+Na]^+$.

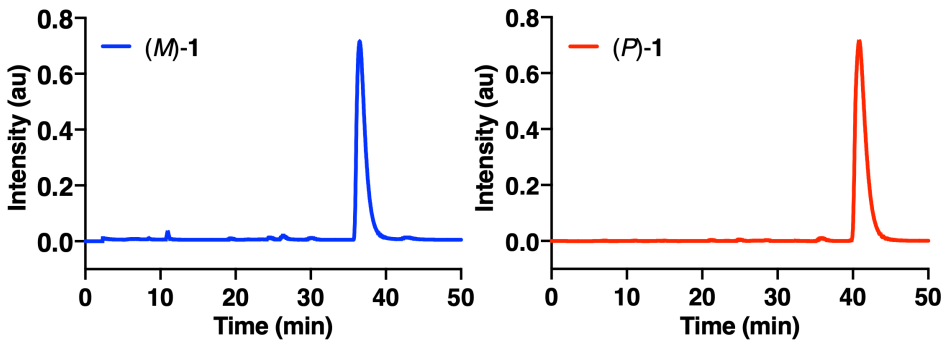

Figure S2. Chiral HPLC traces for (*M*)-**1** and (*P*)-**1** respectively (ee> 98%).

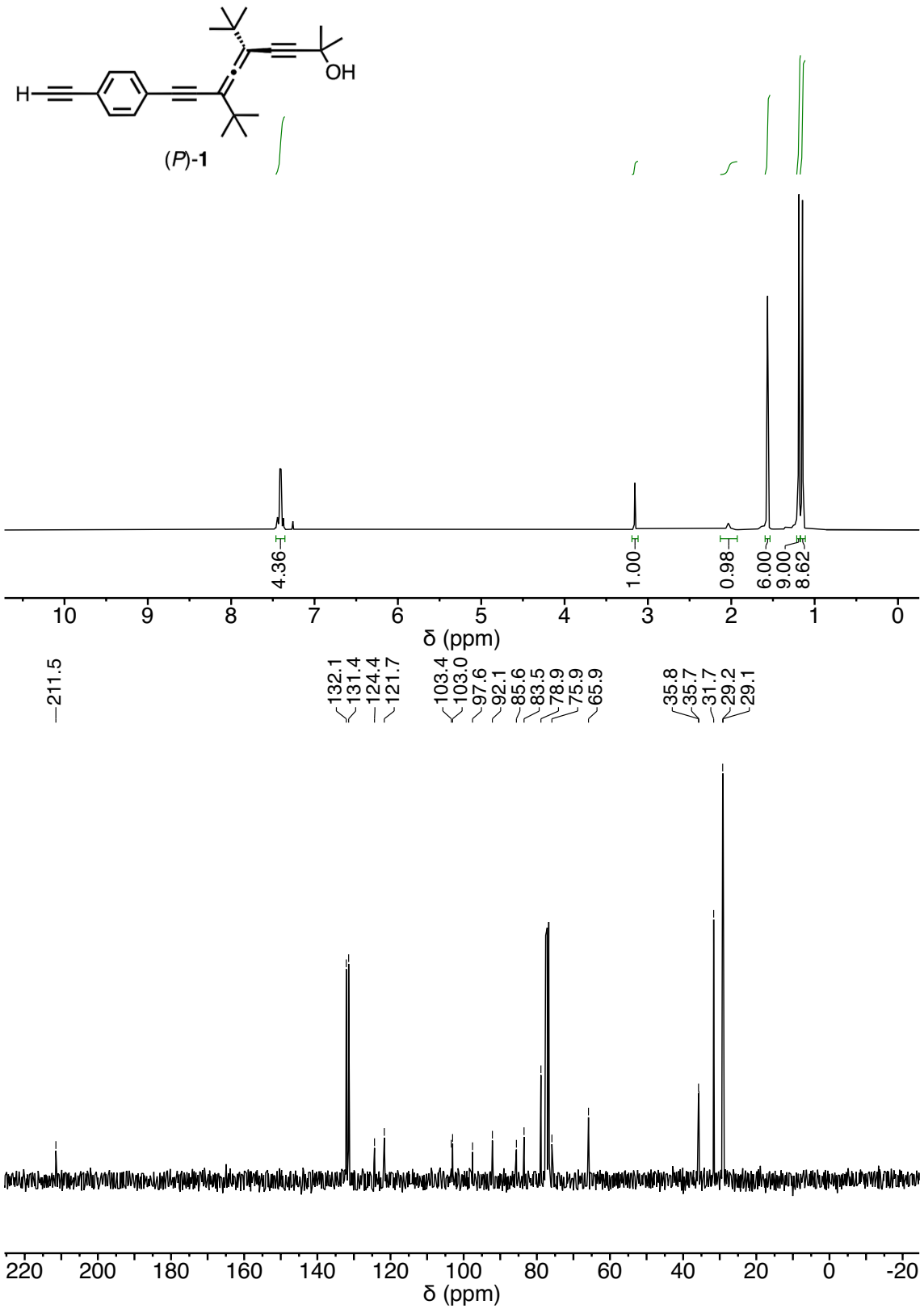

Figure S3. ^{1}H-NMR and ^{13}C-NMR of (*P*)-**1** in $CDCl_3$.

*5,7-di-tert-butyl-2-methyl-9-(4-((trimethylsilyl)ethynyl)phenyl)nona-5,6-dien-3,8-diyn-2-yl acetate (**2a**)*

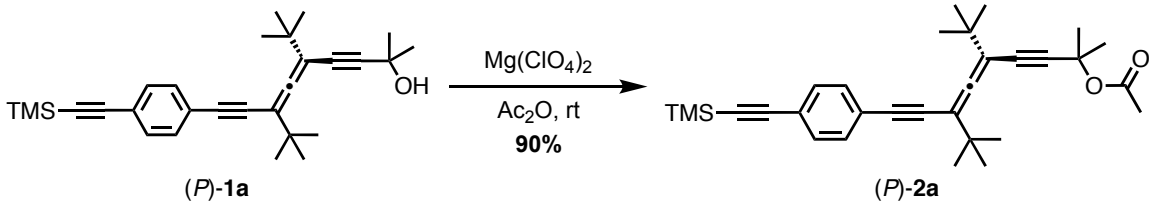

(*P*)-**1a** (*P*)-**2a**

(*P*)-**1a** (100 mol%, 0.300 mmol, 130 mg) was slowly added to a solution of $Mg(ClO_4)_2$ (20 mol%, 0.006 mmol, 1 mg) in Ac_2O (0.5 mL) at rt with stirring. After additional stirring for 1 h, the mixture was diluted with a 0.1 M solution of $NaHCO_3$ and extracted several times with Et_2O. After drying over anhyd Na_2SO_4 and filtration, the solvent was evaporated. Then, purification by flash chromatography on silica gel (hexane: EtAcO (9.5:0.5) afforded (*P*)-**2a** (127 mg, 90%) as a yellow oil.

Molecular Formula: $C_{31}H_{40}O_2Si$. **MW:** 472.74 **g/mol.**

^{1}H-NMR (300 MHz, $CDCl_3$) δ 7.39 (m, 4H), 2.01 (s, 3H), 1.70 (s, 6H), 1.19 (s, 9H), 1.15 (s, 9H), 0.25 (s, 9H).

^{13}C-NMR (75 MHz, $CDCl_3$) δ 211.5, 169.3, 131.9, 131.4, 124.0, 122.7, 104.9, 103.3, 103.2, 96.2, 94.0, 92.3, 85.6, 77.9, 72.8, 35.9, 35.8, 29.2, 29.1, 22.1.

HRMS (ESI$^+$): *m/z* calcd. for $C_{31}H_{40}O_2Si$ 472.2798; found 472.2799 $[M+H]^+$.

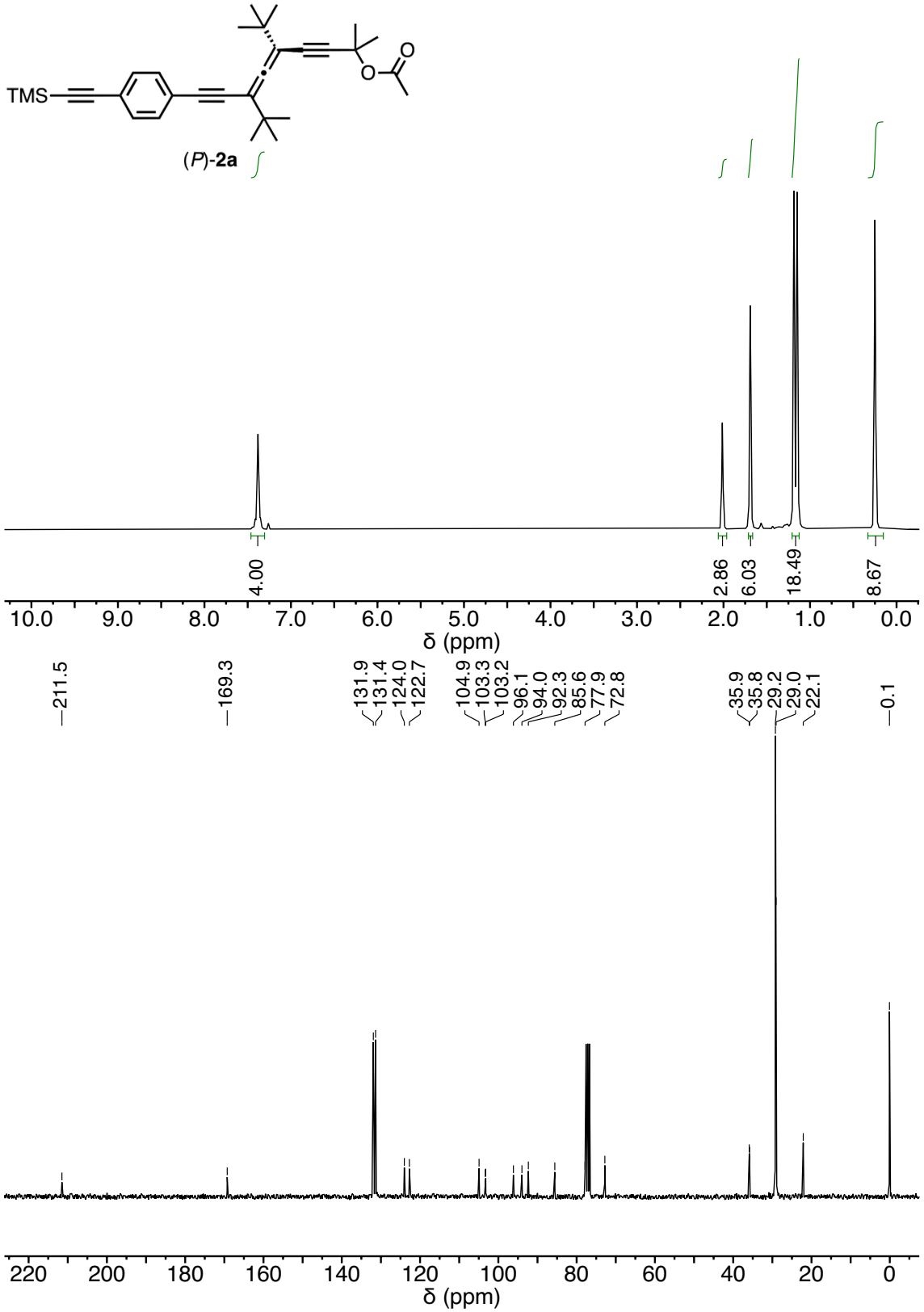

Figure S4. ^{1}H-NMR and ^{13}C-NMR of (*P*)- **2a** in $CDCl_3$.

*5,7-di-tert-butyl-9-(4-ethynylphenyl)-2-methylnona-5,6-dien-3,8-diyn-2-yl acetate (**2**)*

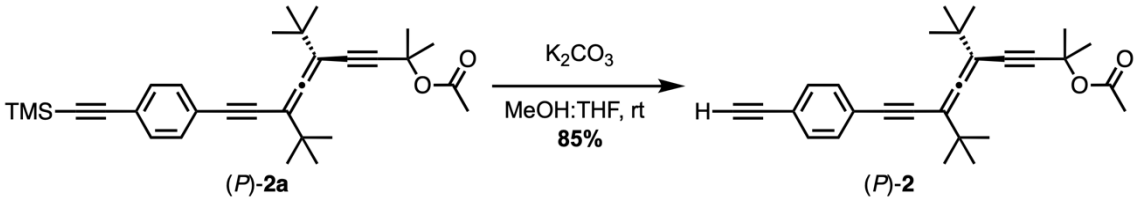

To a solution of (*P*)**-2a** (100 mol%, 0.260 mmol, 122 mg) in a mixture of THF:MeOH (1:1, 10 mL), K_2CO_3 (150 mol%, 0.390 mmol, 54 mg) was added at rt. After 2 h, the mixture was quenched with distilled water (40 mL) and then the aqueous phase was extracted with DCM (3 x 10 mL). The combined organic phases were dried over anhyd Na_2SO_4. Evaporation *in vacuo* and purification by flash chromatography on silica gel (hexane: EtAcO (9.5:0.5) afforded (*P*)**-2** (89 mg, 85%) as a yellow oil.

For (*P*)**-2**, $[\alpha]_D^{20}$= +298 (*c* = 10 mg·mL^{-1}, $CHCl_3$).

Molecular Formula: $C_{28}H_{32}O_2$. **MW:** 400.56 **g/mol.**

^{1}H-NMR (300 MHz, $CDCl_3$) δ 7.42 (m, 4H), 3.15 (s, 1H), 2.02 (s, 3H), 1.69 (s, 6H), 1.19 (s, 9H), 1.15 (s, 9H)

^{13}C-NMR (75 MHz, $CDCl_3$) δ 211.5, 169.3, 132.1, 131.5, 124.4, 121.7, 103.3, 94.0, 92.1, 85.7, 83.5, 78.8, 77.8, 72.8, 35.9, 35.8, 29.2, 29.0, 22.1.

HRMS (ESI$^+$): *m/z* calcd. for $C_{28}H_{32}O_2$ 400.2402; found 401.2422 $[M+H]^+$.

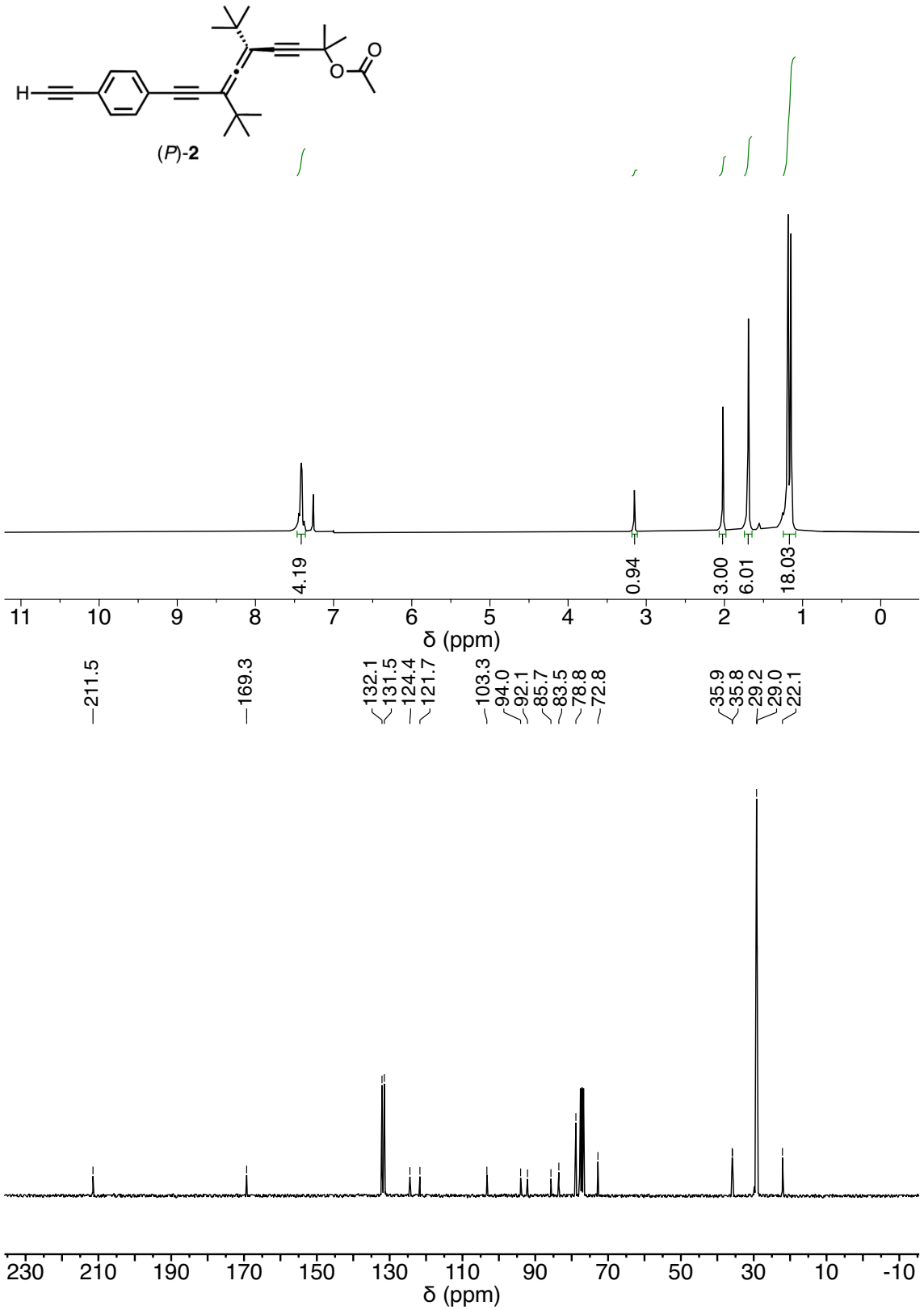

Figure S5. ^{1}H-NMR and ^{13}C-NMR of (*P*)-**2** in $CDCl_3$.

5.1.3. Synthesis of polymers

5.1.3.1. General procedure for polymerization

The reaction flask (sealed ampoule) was dried under vacuum and argon flushed for three times before a solution of the corresponding monomer in THF was added *via* cannula. Then, triethylamine was added dropwise *via* syringe. A solution of rhodium norbornadiene chloride dimer, $[Rh(nbd)Cl]_2$, in THF was added under stirring at rt. The reaction mixture was stirred at rt overnight. Then, the resulting polymer was diluted in DCM and precipitated in a large amount of hexane:diethyl ether (3:1) for **1** and MeOH for **2**, centrifuged (twice), reprecipitated in hexane and centrifuged again (Table S1).

Table S1. Calculated amounts for the synthesis of the polymers poly-(±)-**1**, poly-(*P*)-**1**, poly-(*M*)-**1**, poly-(*P*)-**1**-**OAc**.

Monomer	Mass (mg)	THF (μL)	Et_3N (μL)	Catalyst (mg)	Yield (%)
(±)-**1**	70	500	4	1	97
(*P*)-**1**	70	500	4	1	98
(*M*)-**1**	60	400	3	1	95
(*P*)-**2**	50	300	3	1	85

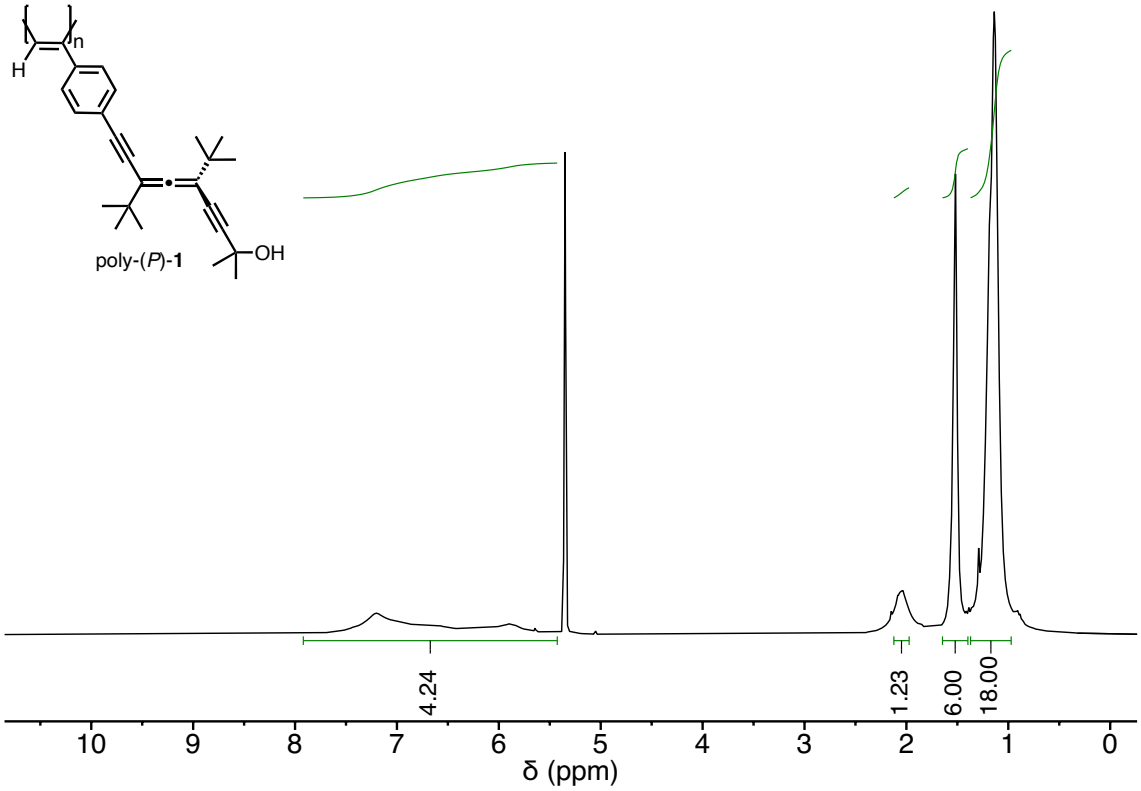

Figure S6. ^{1}H-NMR of poly-(*P*)-**1** in CD_2Cl_2.

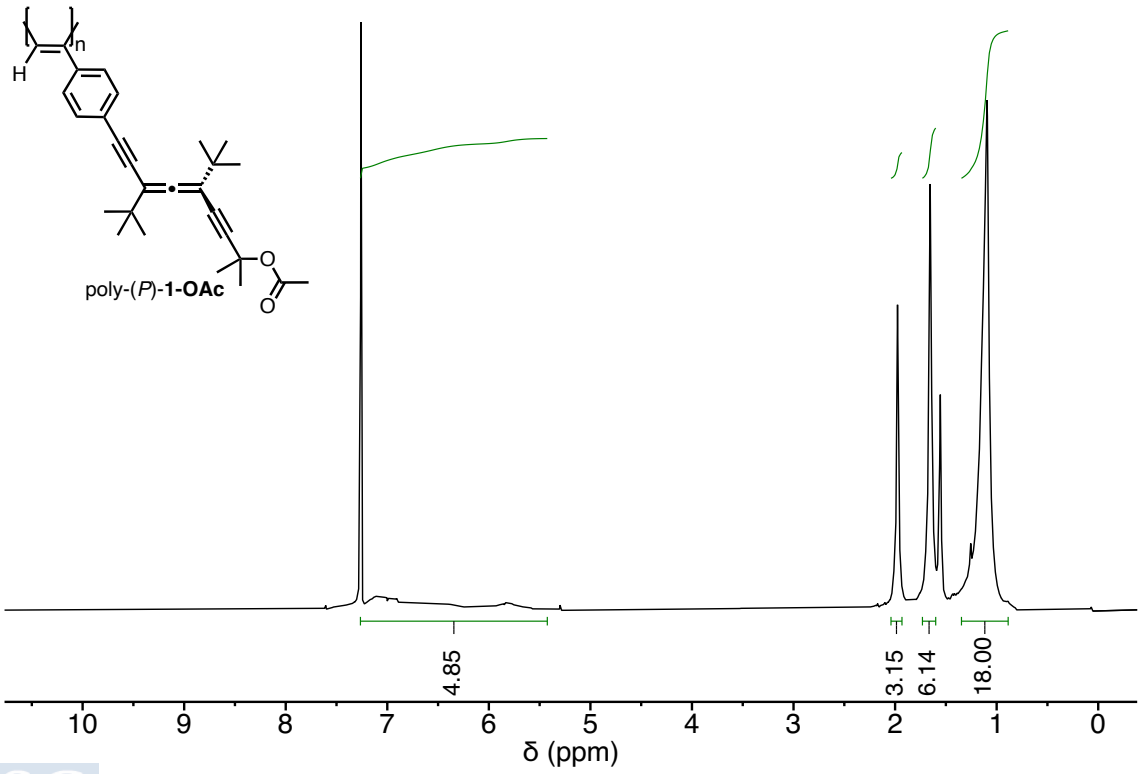

Figure S7. ^{1}H-NMR of poly-(*P*)-**1-OAc** in $CDCl_3$.

5.1.4. GPC studies

The molecular weights were estimated by GPC using THF (flow rate: 1.0 mL·min^{-1}) as eluent and polystyrene narrow standards (PSS) as calibrants.

Table S1. GPC data for the synthesized polymers.

Polymer	Mn (Daltons)	Mw (Daltons)	Mz (Daltons)	DP	Đ (Daltons)
poly-(*P*)-**1**	406868	577604	738592	1134	1.42
poly-(*M*)-**1**	498800	716625	936211	1391	1.44
poly-(*P*)-**1-OAc**	739376	101155	124190	1845	1.37

5.1.5. Raman experiments

The bands observed by Raman resonance confirmed the former configuration. The peak at highest wavelength corresponds to the C=C bond stretching and overlaps with that of the phenyl ring. The band at 1334 cm^{-1} arises from the *cis* C-C bond coupled with the single bond connecting the main chain and the phenyl ring. The peak at lowest wavelength (957 cm^{-1} for poly-(*P*)-**1** and 950 cm^{-1} poly-(*P*)-**1-OAc** corresponds to the C-H bond of the *cis* form. The disappearance of the alkyne peak (ca. 2111 cm^{-1}) also confirms the formation of the polymer.

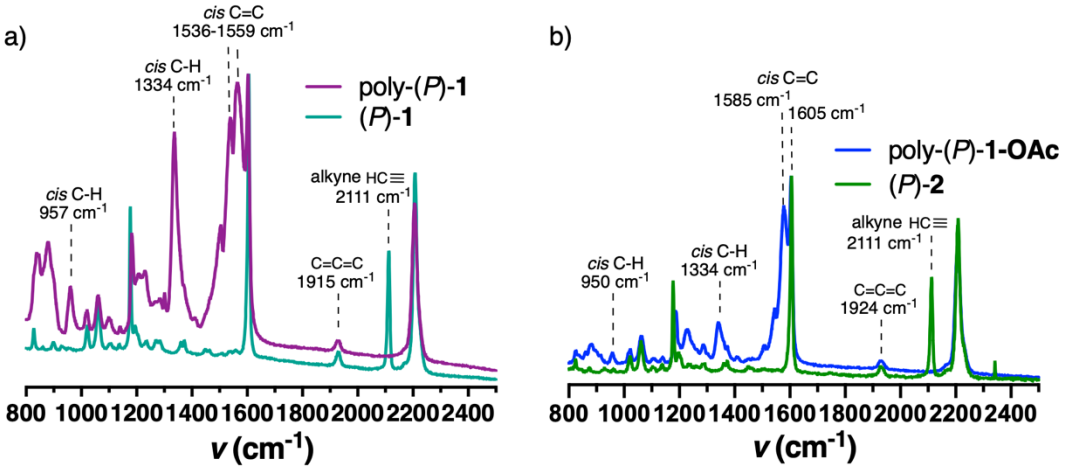

Figure S8. (a) Raman spectra of (*P*)-**1** and poly-(*P*)-**1**. (b) Raman spectra of (*P*)-**2** and poly-(*P*)-**1-OAc**.

5.1.6. Thermal studies

5.1.6.1. DSC studies

DSC experiments have been used to determine the configuration of the polymer skeleton in poly(phenylacetylene)s due to the different thermogram pattern for a *cis*-cisoidal (*c*-*c*) or a *cis*-transoidal (*c*-*t*) polyene backbone.[150,196] Hence, the geometry of the polymers were determined by DSC. According to a general protocol, the polymers were heated in an aluminum pan up to 400 °C (heating rate: 10 °C.min^{-1}). The thermogram for poly-(*P*)-**1** shows a typical *c*-*t* trace with an exothermal peak (102 °C), correspondent to a *c*-*c* transition and a final isomerization to *t*-*t* (185 °C) (Figure S9a). On the other hand, the thermogram of poly-(*P*)-**1-OAc** also shows a typical *c*-*t* trace with an exothermic peak (110 °C), corresponding to a *c*-*c* transition and a final isomerization at *t*-*t* (188 °C) (Figure S9b).

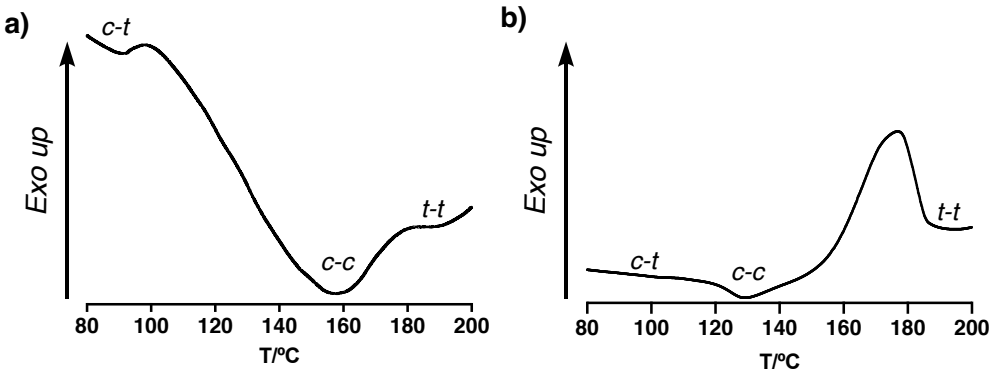

Figure S9. DSC study for (a) poly-(*P*)-**1** and (b) poly-(*P*)-**1**-**OAc**.

5.1.6.2. TGA studies

The thermal stability was evaluated by TGA. As a general protocol, the polymer sample was placed in a platinum pan and heated from 40°C to 800°C (heating rate: 10 °C.min^{-1}). Poly-(*P*)-**1** starts to degrade at 280 °C (Figure S10a) and poly-(*P*)-**1-OAc** starts to degrade at 240 °C (Figure S10b).

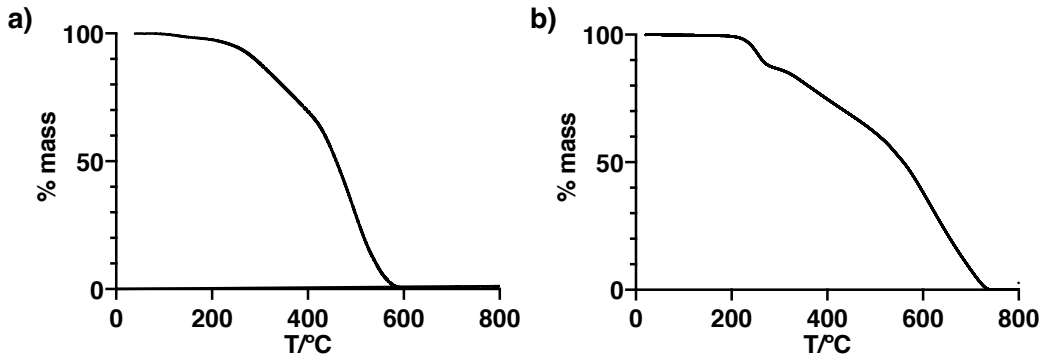

Figure S10. TGA thermograms for poly-(*P*)-**1** and poly-(*P*)-**1**-**OAc**.

5.1.7. Dynamic behaviour

5.1.7.1. Analysis in different solvents

ECD spectra of poly-(±)-**1** was measured to check the null ECD signal (Figure S11).

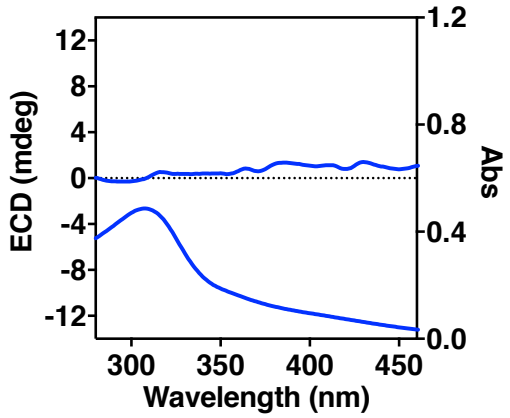

Figure S11. ECD and UV-vis spectra of poly-(±)-**1** in CHCl3 (0.3 mM).

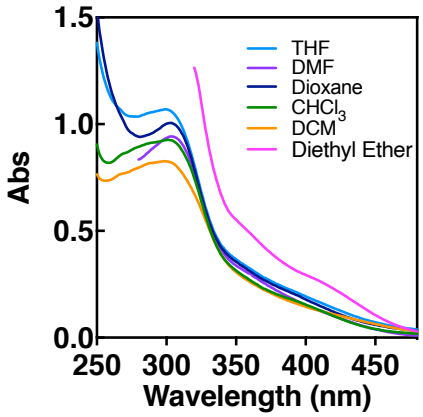

Figure S12. UV-vis spectra for poly-(*P*)-**1** in different solvents (0.5 mM).

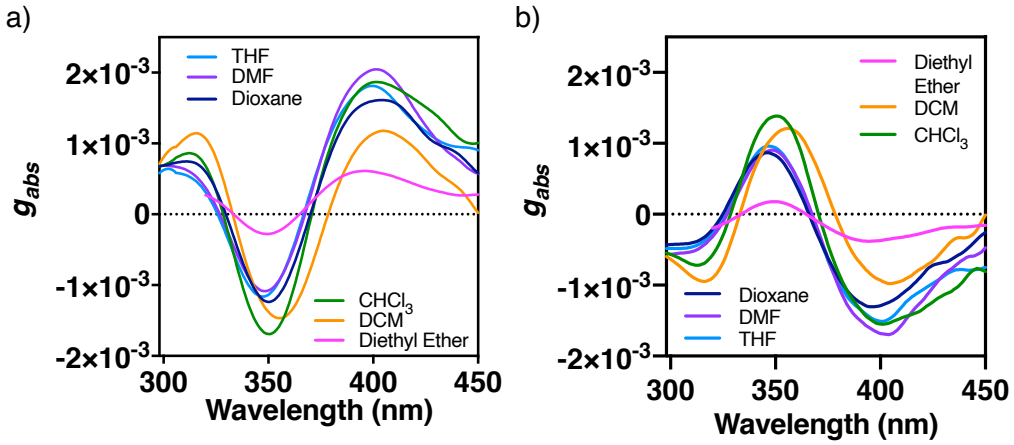

Figure S13. g_{abs} representation of (a) poly-(*P*)-**1** and (b) poly-(*M*)-**1** in different solvents.

5.1.7.2. Comparison of poly-(*P*)-1 and poly-(*M*)-1

ECD spectra of poly-(*P*)-**1** and poly-(*M*)-**1** in $CHCl_3$ (0.3 mM) show the same ECD pattern with opposite sign (Figure S14).

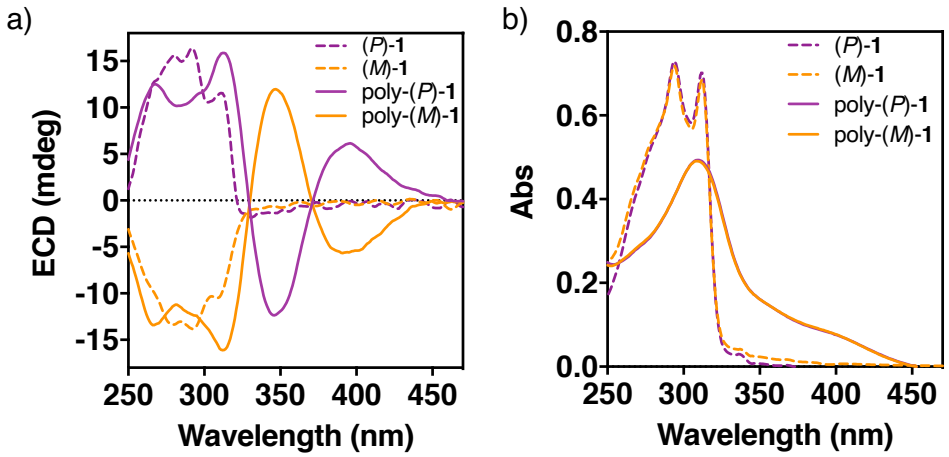

Figure S14. (a) ECD and (b) UV-vis spectra of (*P*)-**1**, (*M*)-**1**, poly-(*P*)-**1** and poly-(*M*)-**1** in $CHCl_3$ (0.3 mM).

5.1.7.3. ECD studies in amines as solvents

Poly-(*P*)-**1** was tested in amines as solvents (0.3 mM). If secondary amines are used as solvents, helix inversion takes place (Figure S15b); whereas the helical sense remains the same in primary amines as solvents (Figure S15a).

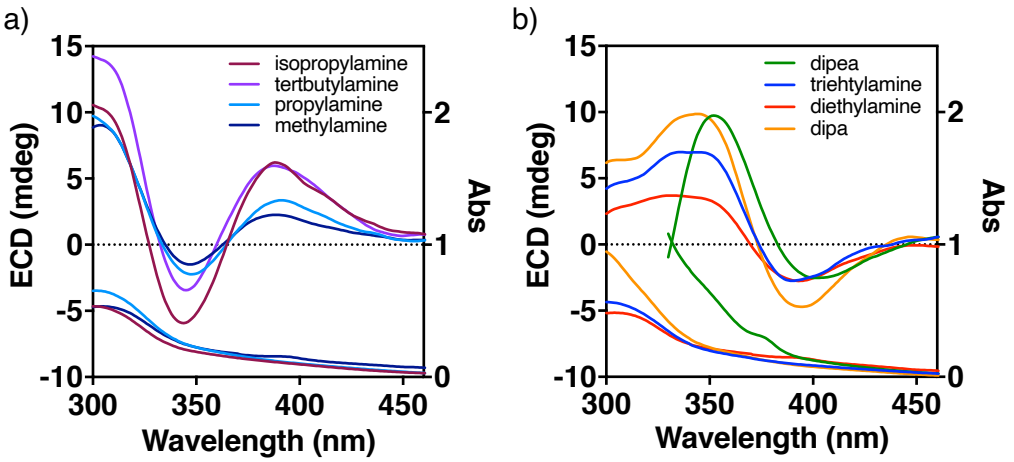

Figure S15. (a) ECD and (b) UV-vis spectra of poly-(*P*)-**1** in different amines as solvents (0.3 mM).

5.1.8. Response to external stimuli

5.1.8.1. Interaction with amines of poly-(*P*)-1

5.1.8.1.1. Titration experiments with amines

Poly-(*P*)-**1** was titrated with different primary, secondary and tertiary amines. To do so, poly-(*P*)-**1** was dissolved in diethyl ether (1 mM) and additions of the correspondent pure amine were made to the polymer solution (Figure S16, S17). The polymer shows a chiral inversion in presence of secondary or tertiary amine at the vinylic region. Interestingly, the saturation point is reached with a lower number of equivalents than with the other amines for diethylamine (Et_2NH), suggesting a more effective interaction (Figure S16b and S17b). That is, the interaction between these species and the PAEPA results in a new environment at the pendant that generates a helical inversion in the PAEPA.

Moreover, the helix inversion induced in poly-(*P*)-**1** by supramolecular interaction with amines is a reversible process. After carrying up a workup with aqueous media of the polymer solution in presence of amines (aqueous phase was extracted with diethyl ether (3 x 5 mL), it is possible to recover the initial state (Figure S18).

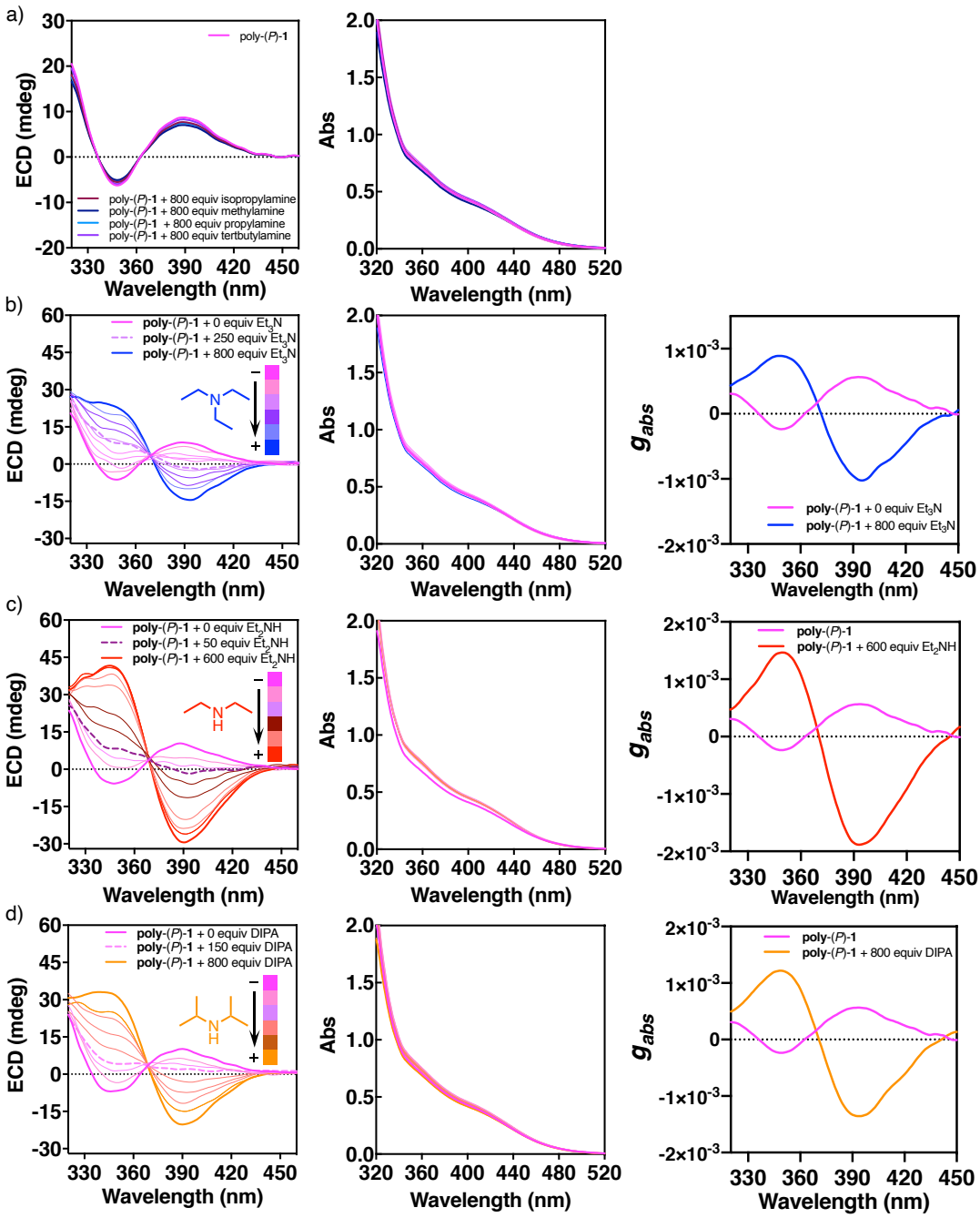

Figure S16. Titrations with amines by ECD and UV-vis of poly-(*P*)-**1** in diethyl ether (1mM) and g_{abs} representation for (b) a tertiary amine and for (c), (d) secondary amines.

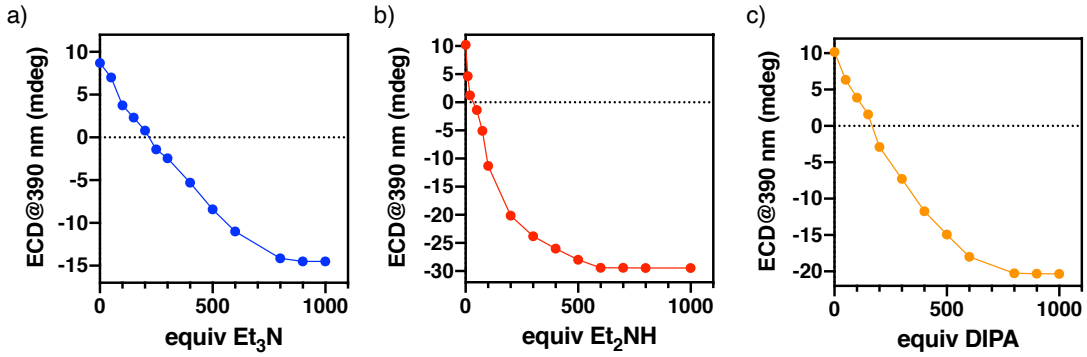

Figure S17. ECD saturation curves for the titration of poly-(*P*)-**1** in diethyl ether (1 mM) with (a) triethylamine, (b) diethylamine and (c) diisopropylamine at 390 nm.

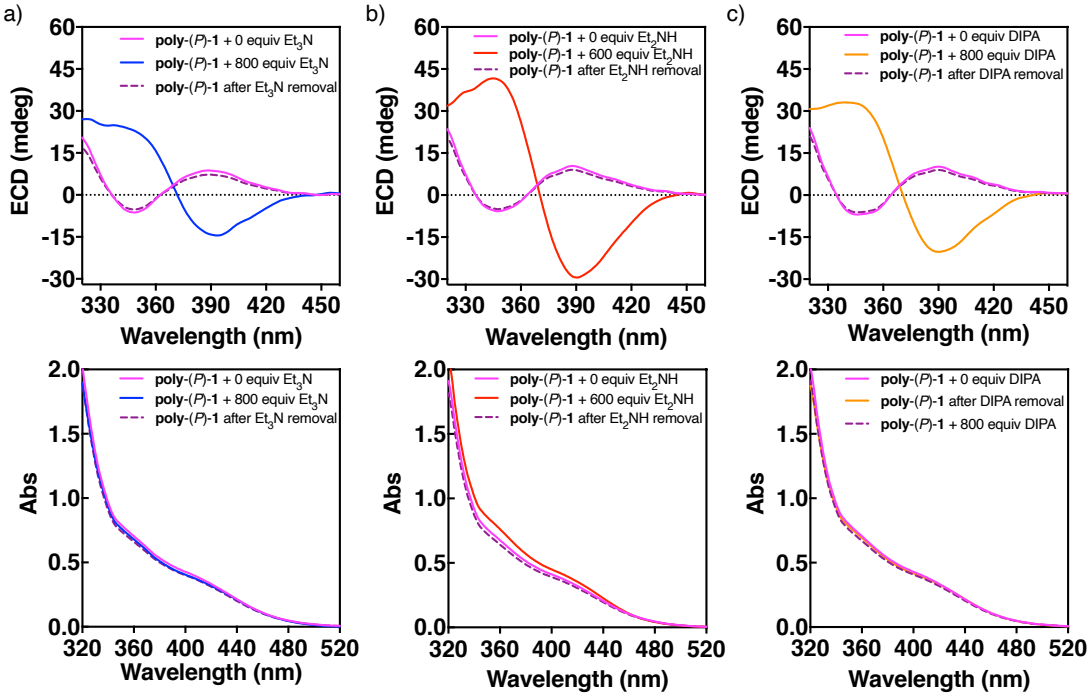

Figure S18. ECD and UV-vis studies of the reversibility of the helical inversion process of poly-(*P*)-**1** after amine removal (0.5 mM in diethyl ether).

5.1.9. ECD studies for poly-(*M*)-1

Poly-(*M*)-**1** was also tested in amines as solvents (0.5 mM). Again, as previously observed for the *P* enantiomer, if primary amines are used as solvents, helix inversion does not take place even if used as a solvent (Figure S19); whereas helix inversion takes place after titration with tertiary and secondary amines (Figure S20).

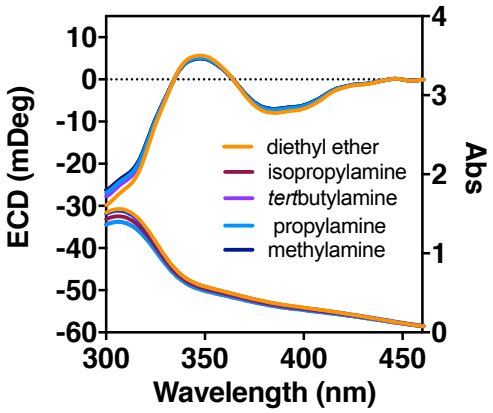

Figure S19. ECD and UV-vis experiments of poly-(*M*)-**1** in diethyl ether and primary amines as solvents (0.5 mM).

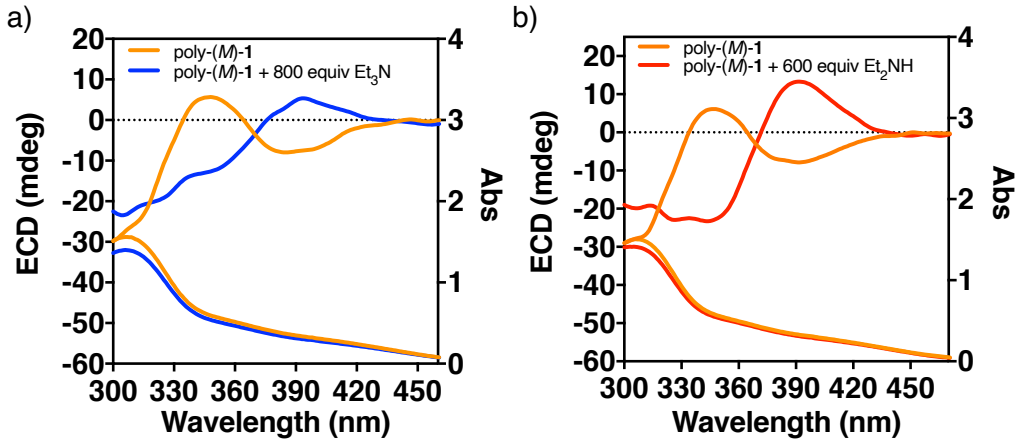

Figure S20. Titrations with (a) Et_3N and (b) Et_2NH by ECD and UV-vis of poly-(*M*)-**1** in diethyl ether (0.5 mM).

5.1.10. ECD studies for poly-(*P*)-1-OAc

Poly-(*P*)-**1-OAc** was tested in different solvents (0.5 mM), showing the same ECD pattern in all cases (Figure S21).

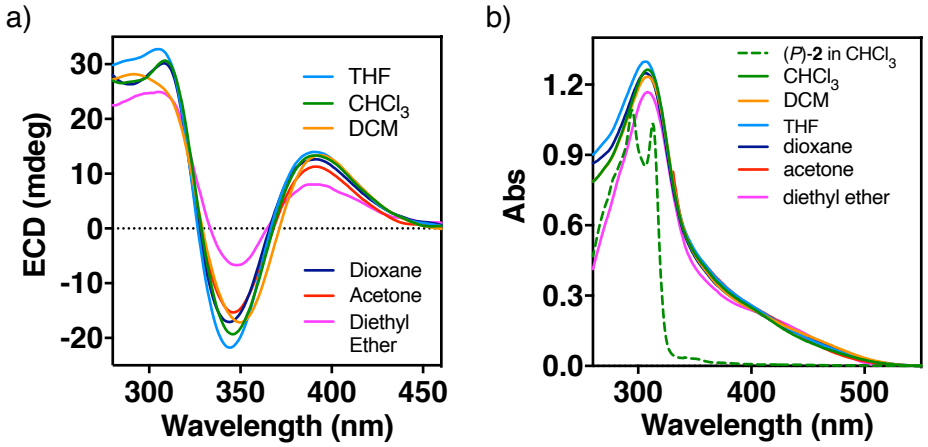

Figure S21. (a) ECD and (b) UV-vis experiments of poly-(*P*)-**1-OAc** in different solvents (0.5 mM).

5.1.10.1. ECD studies in amines as solvent

Titrations with amines by ECD and UV-vis of poly-(*P*)-**1-OAc** in diethyl ether were carried out to study the behaviour of this polymer (Figure S22). However, in this case, addition of pure amines (primary, secondary, or tertiary) to a diethyl ether solution of poly-(*P*)-**1-OAc** does not produce any change in the screw sense preference of this polymer, even after full addition of amine as solvent, due to the lack of interactions between the amines and this PAEPA (Figure 6c).

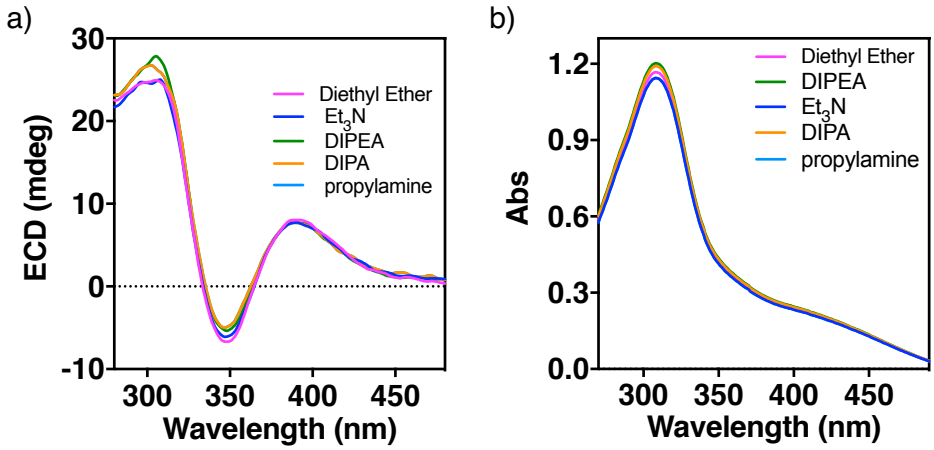

Figure S22. (a) ECD spectra and (b) UV-vis of poly-(*P*)-**1**-**OAc** after addition of 800 equiv of the corresponding amine in diethyl ether (0.5 mM).

5.1.11. ^{14}N-NMR experiments

To confirm the interaction between the amine and the hydroxyl group of the polymer via hydrogen bonding, ^{14}N-NMR experiments were carried out. A thin wall NMR tube and a capillary tube with $CDCl_3$ as deuterated solvent were used to carry out the experiment in diethyl ether no deuterated as solvent. So, ^{14}N-NMR spectra of a solution of each of the amines studied in diethyl ether (0.004 mmol of amine in 0.5 mL of diethyl ether) were recorded. Then, we performed the ^{14}N-NMR experiments of the corresponding polymer solution in diethyl ether (8 mM) after the addition of 1 equiv (0.004 mmol) of each amine.

A shifting towards higher frequencies ($\Delta\delta$=289.9 ppm) is observed for the N of the amine in a poly-(*P*)-**1**/primary amine mixture in a 1/1 mol/mol ratio (Figure S23). Therefore, although the primary amine is attached to the PAEPA, the bulkiness at the N center of primary amines is not enough to overcome the effect of the proximal *tert*-butyl group and produce a handedness inversion. The same shifting towards higher frequencies was observed when tertiary ($\Delta\delta$=265.8 ppm, Figure S24) and secondary ($\Delta\delta$=232.8 ppm, Figure S25) amines were added, which suggest again the interaction between the polymer hydroxy group and amines. Whereas, for poly-(*P*)-**1**-**OAc** the N peak of the amines does not suffer any shifting after the addition of amine ($\Delta\delta$=0 ppm, Figure S26).

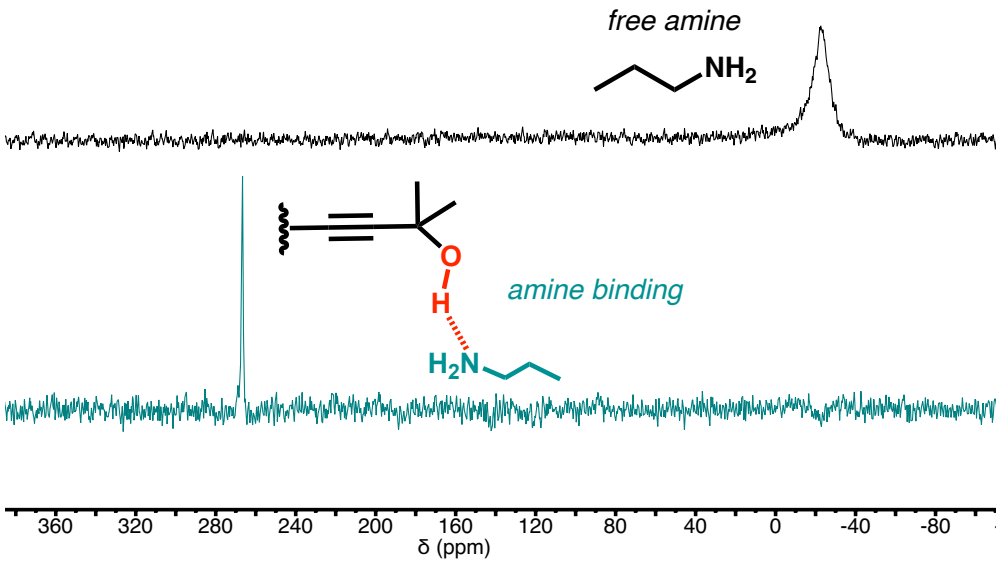

Figure S23. ^{14}N-NMR spectra of propylamine in diethyl ether (8 mM) (black) and ^{14}N-NMR spectra of poly-(*P*)-**1** in diethyl ether (8 mM) in presence of 1 equiv of propylamine (green).

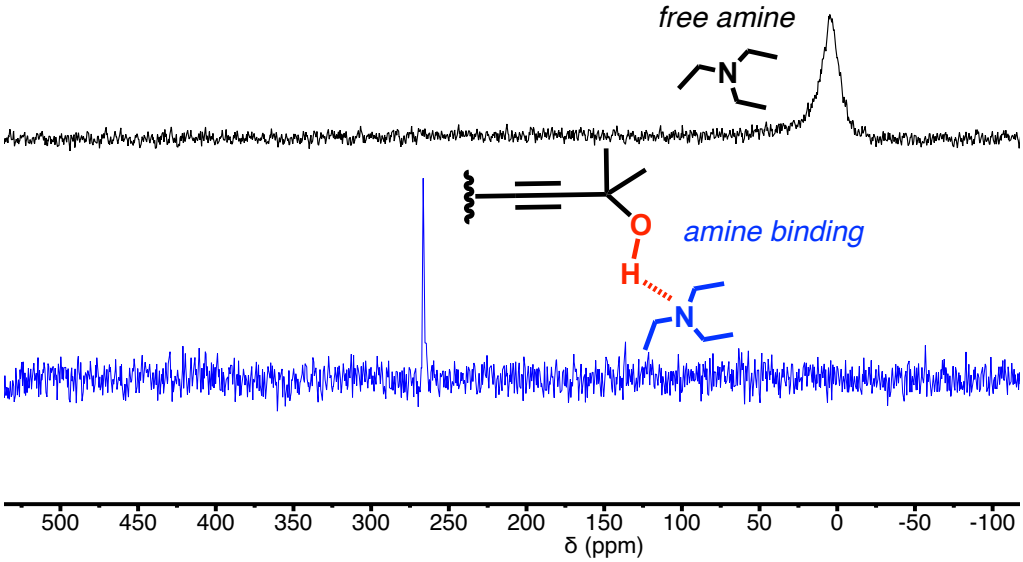

Figure S24. ^{14}N-NMR spectra of triethylamine in diethyl ether (8 mM) (black) and ^{14}N-NMR spectra of poly-(*P*)-**1** in diethyl ether (8 mM) in presence of 1 equiv of triethylamine (blue).

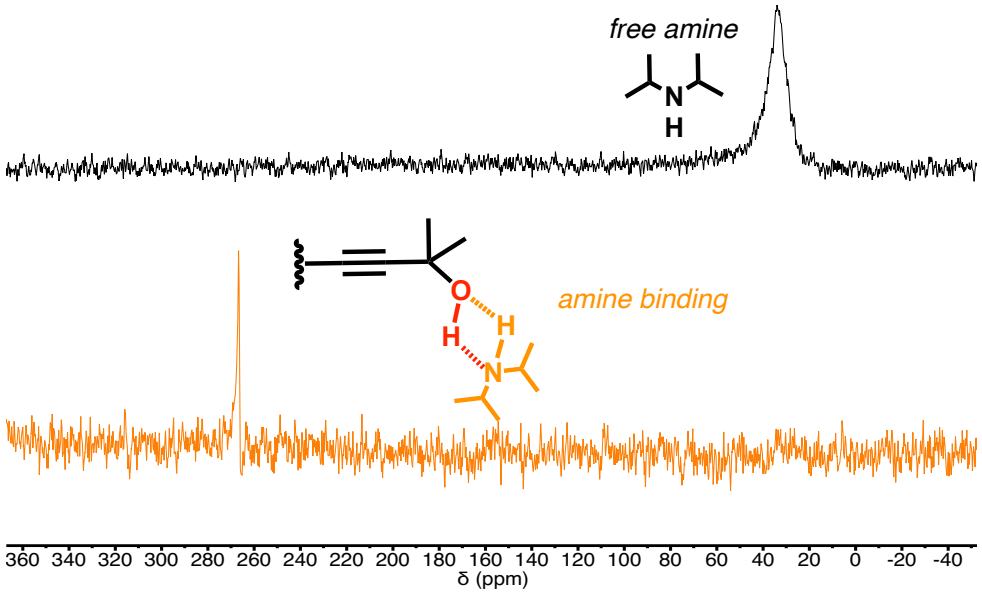

Figure S25. ^{14}N-NMR spectra of diisopropylamine in diethyl ether (8 mM) (black) and ^{14}N-NMR spectra of poly-(*P*)-**1** in diethyl ether (8 mM) in presence of 1 equiv of diisopropylamine (orange).

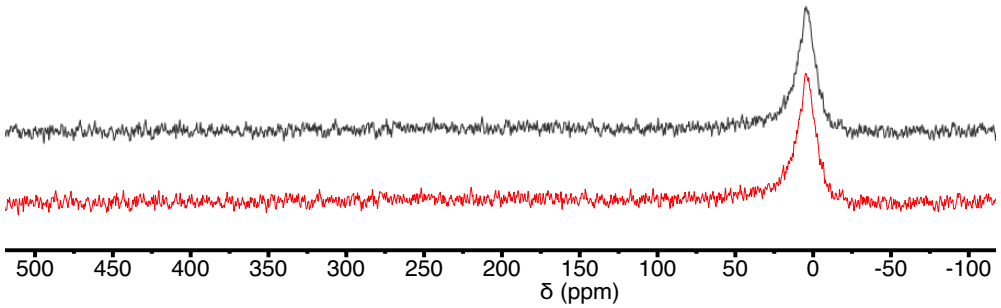

Figure S26. ^{14}N-NMR spectra of triethylamine in diethyl ether (8 mM) (black) and ^{14}N-NMR spectra of poly-(*P*)-**1**-**OAc** in diethyl ether (8 mM) in presence of 1 equiv of triethylamine (red).

5.1.12. VT-ECD Experiments

VT-ECD studies for poly-(*P*)-**1** (0.5 mM in (a) dioxane and (b) Et_3N show a quasi-static behavior of the polymer, with a slightly diminished when increasing the temperature (Figure S27), so the screw sense excess of the helical polymer cannot be altered by temperature changes. This fact is due to the static axial chirality of the allene pendant group, whose consecutive double bonds prevent any conformational change at this group.

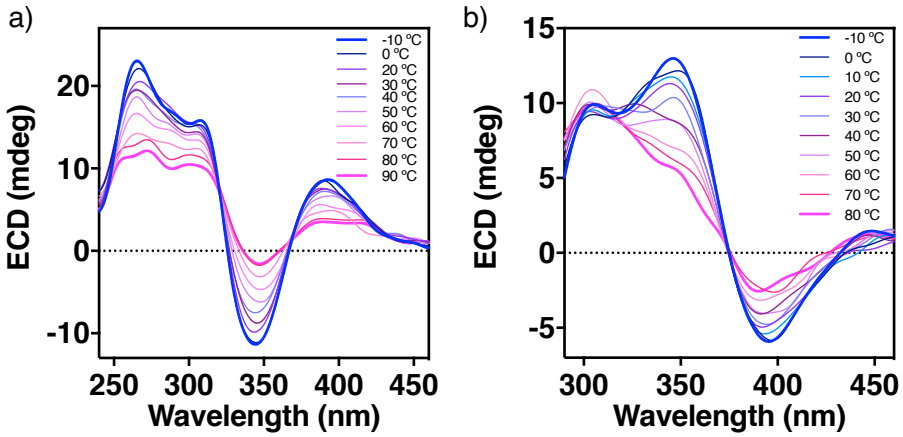

Figure S27. VT-ECD studies for poly-(*P*)-**1** in (a) dioxane (0.5 mM) and (b) Et_3N (0.5 mM, heating rate 10 $^oC.min^{-1}$).

5.1.13. Effect of polymer length

Comparative stimuli-responsive ECD studies of a short oligomer of (*P*)-**1** (Mn= 4504 Daltons, DP=12, Đ= 1.03 Daltons), prepared according to the reported method,[135] show that the length of the polymer does not affect its dynamic helical properties (Figure S28-S30).

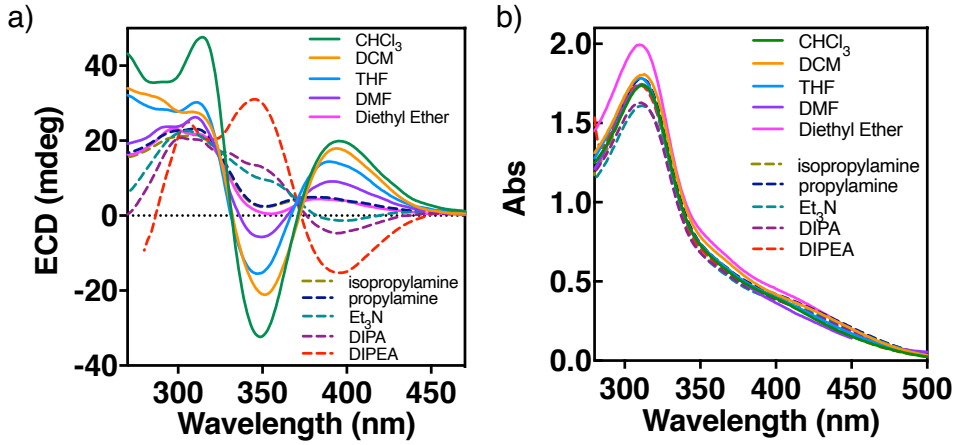

Figure S28. (a) ECD and (b) UV-vis studies of a short oligomer of (*P*)-**1** (Mn= 4504 Daltons) in different solvents (1 mM).

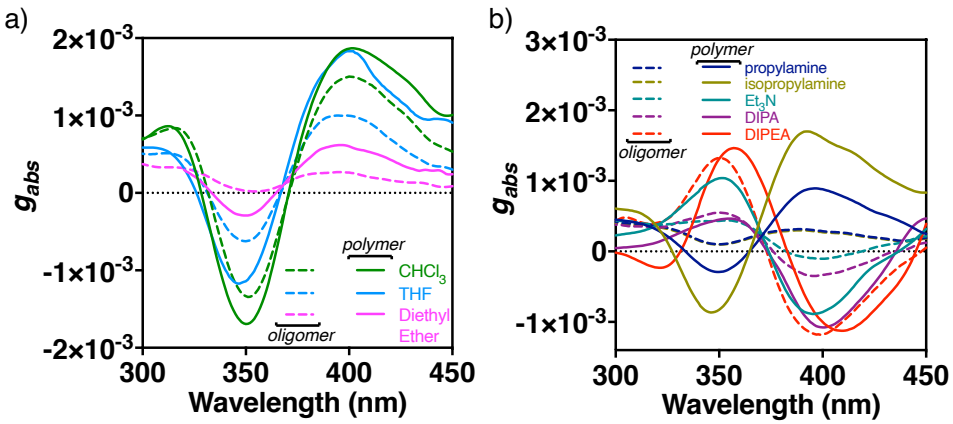

Figure S29. Comparative representation of g_{abs} for poly-(*P*)-**1** (plain lines) and short oligomer of (*P*)-**1** (Mn= 4504 Daltons) (dashed lines) in (a) different solvents and (b) amines as solvents.

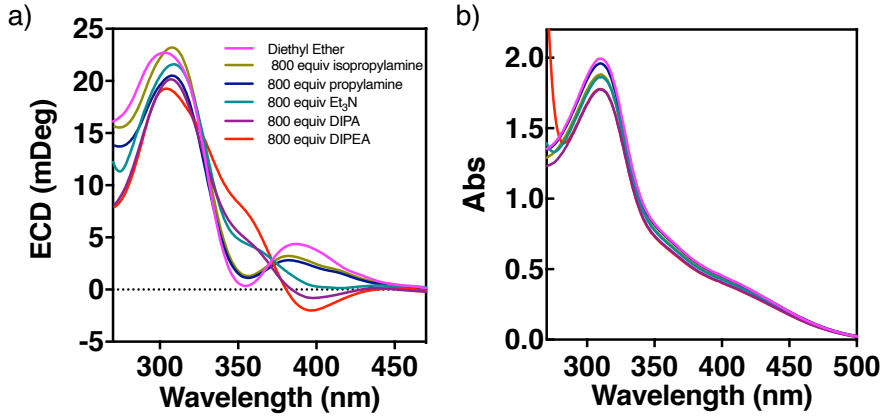

Figure S30. Titrations with amines by (a) ECD and (b) UV-vis of a short oligomer of (*P*)-**1** in diethyl ether (1mM).

5.1.14. AFM measurements for poly-(*P*)-1

a)

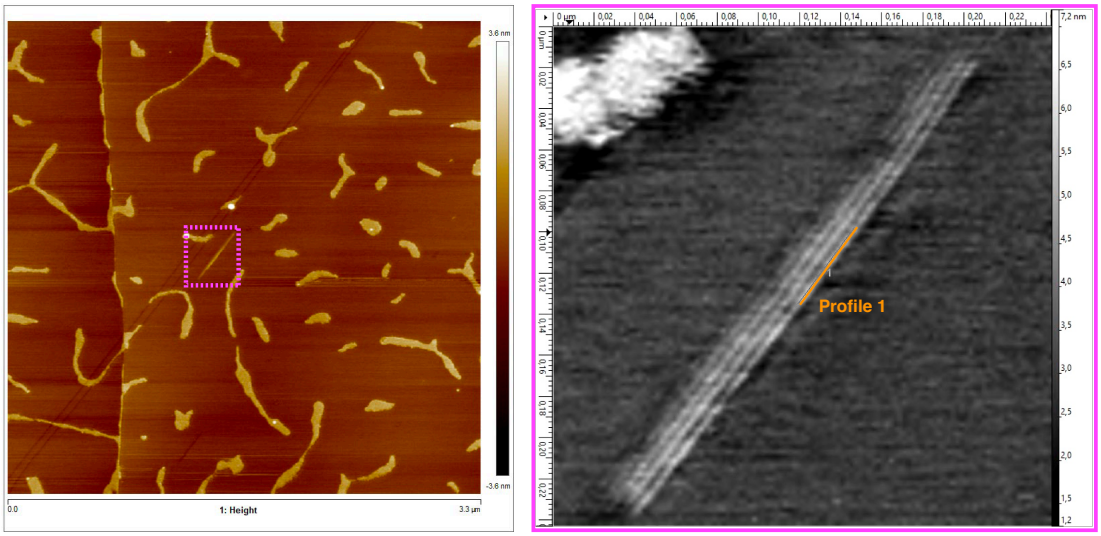

b)

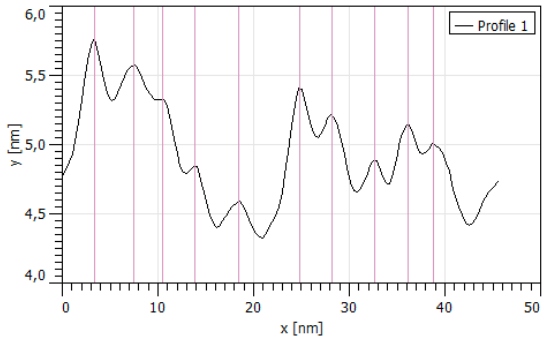

Points	X [nm]	Y [nm]	Length [nm]
	3,34	5,766	
	7,47	5,584	4,12
	10,54	5,336	3,07
	13,88	4,850	3,34
	18,46	4,597	4,58
	24,85	5,410	6,39
	28,14	5,222	3,29
	32,70	4,891	4,56
	36,12	5,151	3,42
	38,76	5,011	2,64

Figure S31. (a) AFM image for poly-(*P*)-**1** and zoomed area or the highlighted region. (b) Graphic depicting the helical pitch profile measured in the indicated area.

5.1.15. Theoretical calculations

All computations were performed with Gaussian-16 (G16RevC.01).[413]

Considering the difficulties to carry out ECD theoretical calculations on large polymers, representative oligomers were used. Hence, in the case of poly-(*P*)-**1**, an oligomer with n= 9 —where n denotes the number of monomeric repeating units (mru)— was employed. The number of monomer units was selected considering the results of previous studies,[157,158,185] where we evaluated the spectra for a series of poly(phenylacetylene) (PPA) oligomers obtained through systematic increase of monomer units and concluded that 8-10 monomers were enough to describe the n+2 polymer ECD spectra. The starting structure of poly-(*P*)-**1** was built through adjustment

to the experimental data obtained from structural techniques, such as AFM, DSC and UV-Vis spectroscopy, defining the four different dihedral angles needed to build up the helical scaffold (ω_1, ω_2, ω_3 and ω_4; see Figure S32). The oligomer geometry was optimized using the DFT method[414] together with the B3LYP functional[415] and the 3-21G basis set.[255] Frequency calculations on the optimized geometry revealed no imaginary frequencies, indicating that the calculated structure corresponds at least to local minima on the potential energy surface.

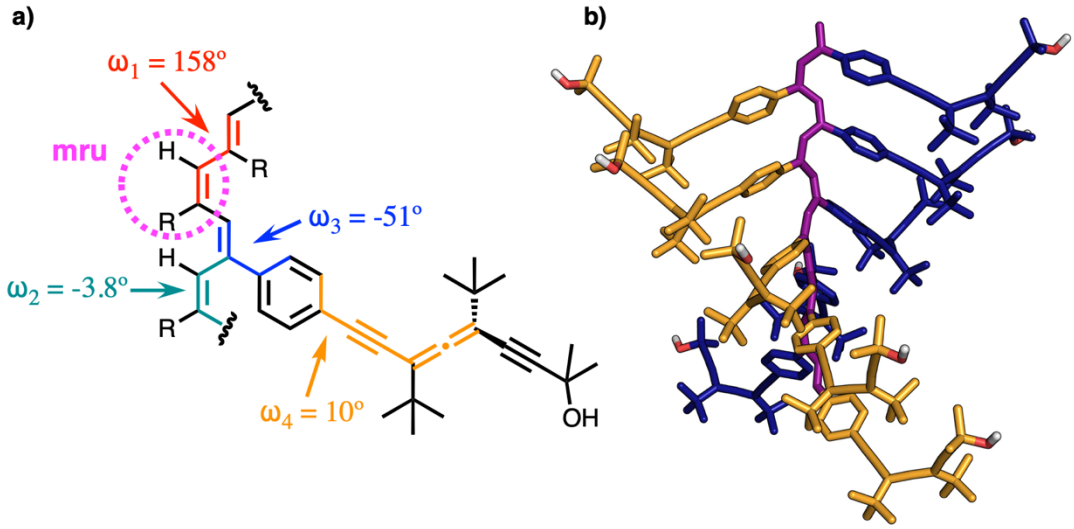

Figure S32. (a) Main dihedral angles involved in the helical structure of PAEPAs and derivatives and the corresponding values obtained for the optimized structure. (b) 3D model of the optimized n= 9 oligomer structure.

The ECD computational methodology was selected according to the size of polymers under investigation. Taking this into account, to evaluate the theoretical spectra time dependent density functional theory (TD-DFT),[253] in combination with the rCAM-B3LYP functional[254] and the 3-21G basis set,[255] have been used. By using the optimized structure (Figure S32), the ECD calculations were performed including 90 excitation energies. The full width at half height (FWHM) was fixed to 20.0 nm and the ECD were plotted with Gaussian curves. For an efficient comparison and considering the tendency of the TD-DFT method to overestimate the excitation energies, the wavelength and intensity at the maximum/minimum Cotton effect correspondent to the polyene backbone in the theoretical spectra were adjusted to the experimental spectra. Employing the same correction factors, the lambdas were shifted, and the intensities rescaled. The resulting ECD spectra is in good agreement with the experimental ones (Figure S33).

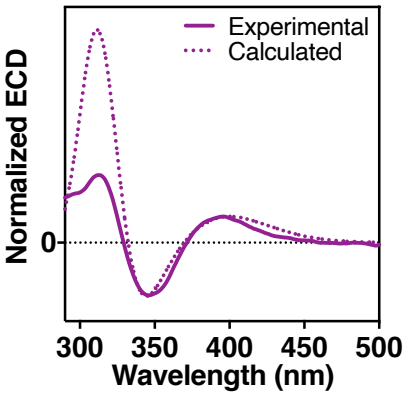

Figure S33. TD-DFT (CAM-B3LYP)/3-21G ECD spectrum for poly-(*P*)-**1** *vs.* ECD experimental spectra of poly-(*P*)-**1** in $CHCl_3$.

5.2. Experimental Section and Methodology Chapter 3.2.

5.2.1. Materials and Methods

Reactions were conducted in dry solvents under argon unless otherwise stated. Et_3N was freshly distilled from CaH_2 under argon atmosphere. $[Rh(nbd)Cl]_2$ was purchased from Sigma-Aldrich (96%). All other chemicals were purchased from Sigma-Aldrich, Acros Organics, Alfa Aesar, Fluorochem, TCI Chemicals or Abcr and they were used as received.

The abbreviation "rt" refers to reactions carried out at a temperature between 21-25 ˚C. Reaction mixtures were stirred using Teflon-coated magnetic stir bars. Thin layer chromatography (TLC) was carried out on pre-coated silica gel F254 plates with visualization under UV light or by dipping the plate into solutions of phosphomolybdic acid or potassium permanganate solutions followed by heating. Column chromatography was performed on silica gel (40-60 μm) unless otherwise stated.

NMR experiments were recorded in a Bruker spectromer (^{1}H frequency 300 mHz).

STD NMR and NOESY NMR experiments were measured at 278 K in a Bruker NEO-750 spectrometer (^{1}H frequency 750 mHz).

ECD measurements were done in a Jasco-720 and UV-vis spectra were registered in a Jasco V-750 with a 1 mm quartz cuvette. VT-ECD were measured in a Jasco-1100. The amount of polymer used is indicated in the corresponding section.

ATR/FT-IR spectra were recorded in a Perkin Elmer FT-IR ATR Spectrum Two.

Optical rotation was measured in a Jasco-P2000 with a 1 cm quartz cuvette at rt (c = 10 mg·mL^{-1}, $CHCl_3$).

Raman spectra were carried out in a Reinshaw confocal Raman spectrometer (Invia Reflexmodel) equipped with two lasers (diode laser 785 nm and Ar laser 514 nm).

CSP-HPLC experiments were carried out in a Waters System equipped with a Phenomenex Lux 5 μm i-Amilose-1 column. The amount of monomer used was 0.5

mg·mL^{-1} and the mixture hexane:isopropanol (9:1) was used as eluent (flow rate: 0.5 mL·min^{-1}).

GPC studies were carried out in a Waters Alliance 2695 HPLC with a UV-2489 detector (Waters) mns equipped with Phenomenex GPC columns (103 Å, 104 Å and 105 Å). The amount of polymer used was 0.5 mg·mL^{-1}. THF was used as eluent (flow rate: 1 mL·min^{-1}) and as inner standard, polystyrene narrow standards (PSS) were used.

DSC traces were obtained in a DSC Q200 Tzero Technology (TA Instruments, New Castle, UK), equipped with a refrigerated cooling system RCS90 (TA Instruments, New Castle, UK), using a Tzero low-mass aluminum pan.

TGA traces were obtained in a TGA Q5000 (TA Instruments, New Castle, UK) using a platinium pan.

AFM measurements were performed in a Multimode V Scanning Probe Microscope (Veeco Instruments) in air at rt, with standard silicon cantilevers and supersharp cantilevers in tapping mode using 12 μm and 1 μm scanners. Nanoscope processing software and WSxM 4.0 Beta 1.0 [4] (Nanotec Electrónica, S.L.) was used for image analysis. All measurements were performed at CACTI (University of Vigo, Spain).

PyMOL was used as a molecular visualization system.

All computations were performed with Gaussian-16 (G16RevC.01).[413]

5.2.2. Synthesis of Monomers

*Di-tert-butyl-2-methyl-9-(4-((trimethylsilyl)ethynyl)phenyl)nona-5,6-dien-3,8-diyn-2-ol (**S1**)*

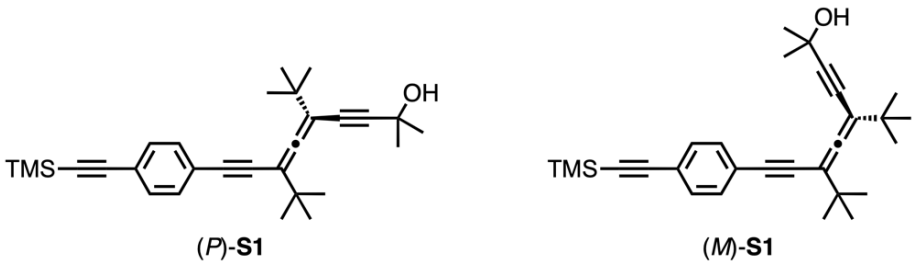

(*P*)-**S1** (*M*)-**S1**

Compounds (*P*)-**S1** and (*M*)-**S1** were prepared according to the procedure described in Experimental Section Chapter 3.1.[279]

Molecular Formula: $C_{29}H_{38}OSi$**. MW:** 430.71 **g/mol.**

^{1}H-NMR (300 MHz, $CDCl_3$, 298K) *δ:* 7.38 (m, 4H), 1.56 (s, 6H), 1.19 (s, 9H), 1.15 (s, 9H), 0.25 (s, 8H).

^{13}C-NMR (75 MHz, $CDCl_3$, 298K) *δ:* 211.7, 132.1, 131.5, 124.1, 122.9, 105.1, 103.6, 103.2, 97.7, 96.4, 92.5, 85.7, 76.1, 66.1, 36.0, 35.9, 31.9, 0.3.

HRMS (ESI$^+$): *m/z* calcd. for $C_{29}H_{38}OSi$ 430.2692; found 431.2758 $[M+H]^+$.

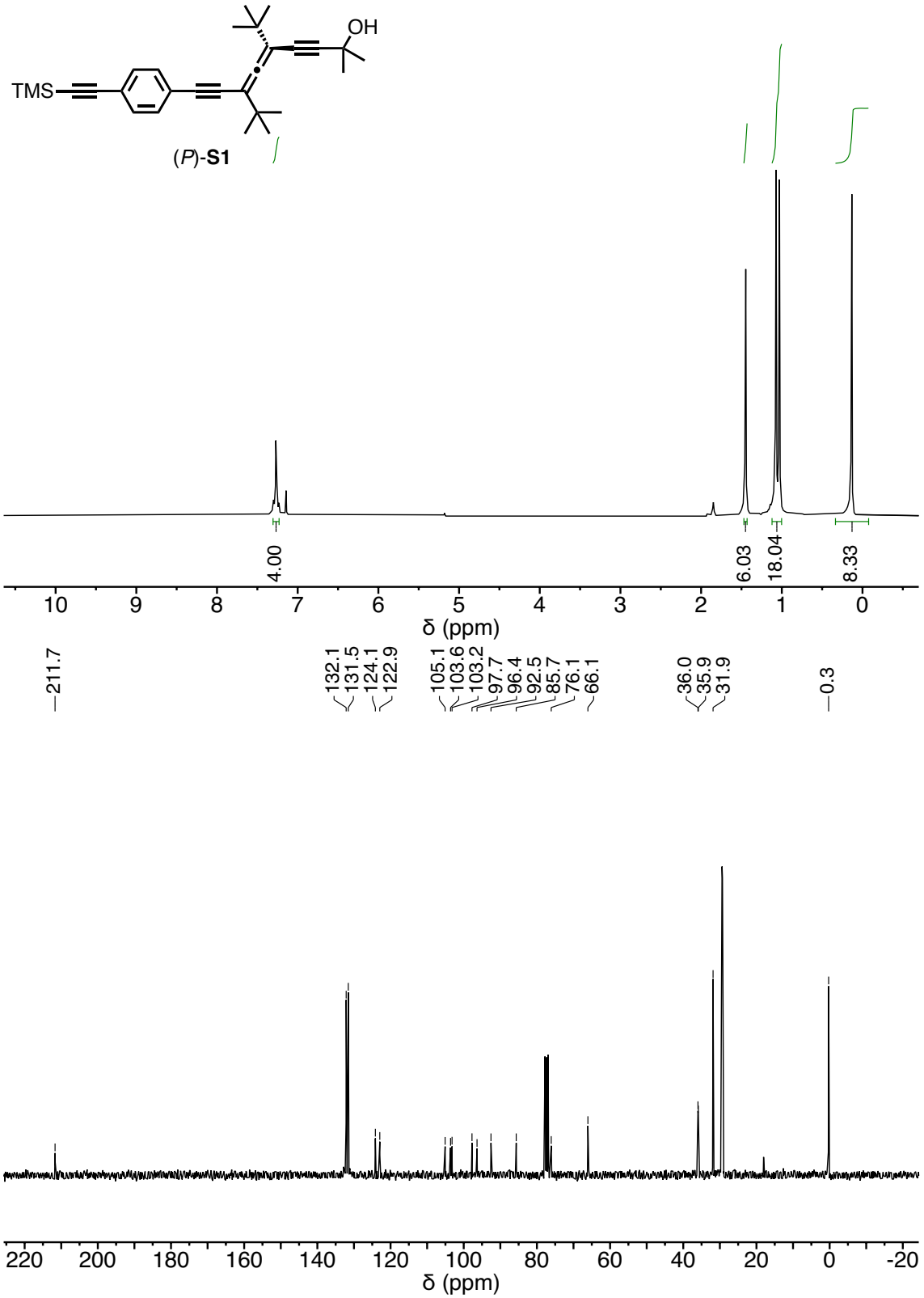

Figure S1. ^{1}H-NMR and ^{13}C-NMR of (*P*)-**S1** in $CDCl_3$.

*N-(5,7-di-tert-butyl-2-methyl-9-(4-((trimethylsilyl)ethynyl)phenyl)nona-5,6-dien-3,8-diyn-2-yl)-4 methylbenzenesulfonamide (**S2**)*

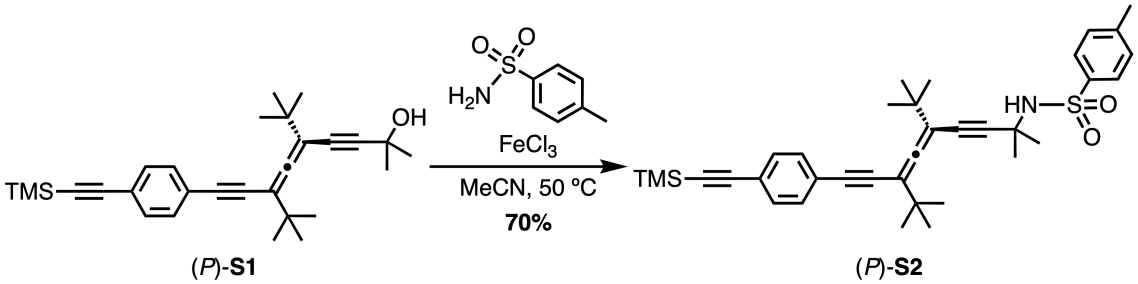

Propargylic alcohol (*P*)-**S1** (100 mol%, 0.313 mmol, 135 mg), *p*-toluenesulfonamide (300 mol%, 0.940 mmol, 161 mg), 650 μL CH_3CN and $FeCl_3$ (5 mol%, 0.016 mmol, 3mg) were successively added to a 5-mL flask, and the reaction mixture was stirred at 50°C overnight. Upon completion, the solvent was concentrated under reduced pressure, and then the residue was purified by silica gel column chromatography (Hexane:EtOAc (8.5:1.5)) to afford (*P*)-**S2** as a yellow oil (128 mg, 70%).

Molecular Formula: $C_{36}H_{45}NO_2SSi$**. MW:** 583.91 **g/mol.**

^{1}H-NMR (300 MHz, CD_3CN, 298K) *δ:* 7.73(d, 2H), 7.45 – 7.38 (m, 4H), 7.32 (d, 2H), 5.88 (s, 1H), 2.31 (s, 3H), 1.52 (s, 3H), 1.49 (s, 3H), 1.16 (s, 9H), 1.01 (s, 9H), 0.22 (s, 9H).

^{13}C-NMR (75 MHz, CD_3CN, 298K) *δ:* 212.1, 144.00 140.8, 132.8, 132.4, 130.4, 128.0, 124.5, 123.8, 105.3, 104.3, 97.3, 96.7, 93.1, 86.1, 77.0, 51.4, 36.4, 36.3, 31.8, 31.5, 29.3, 29.1, 21.6, -0.1.

HRMS (ESI$^+$): *m/z* calcd. for $C_{36}H_{45}NO_2SSi$ 583.2940; found 584.3013 $[M+H]^+$.

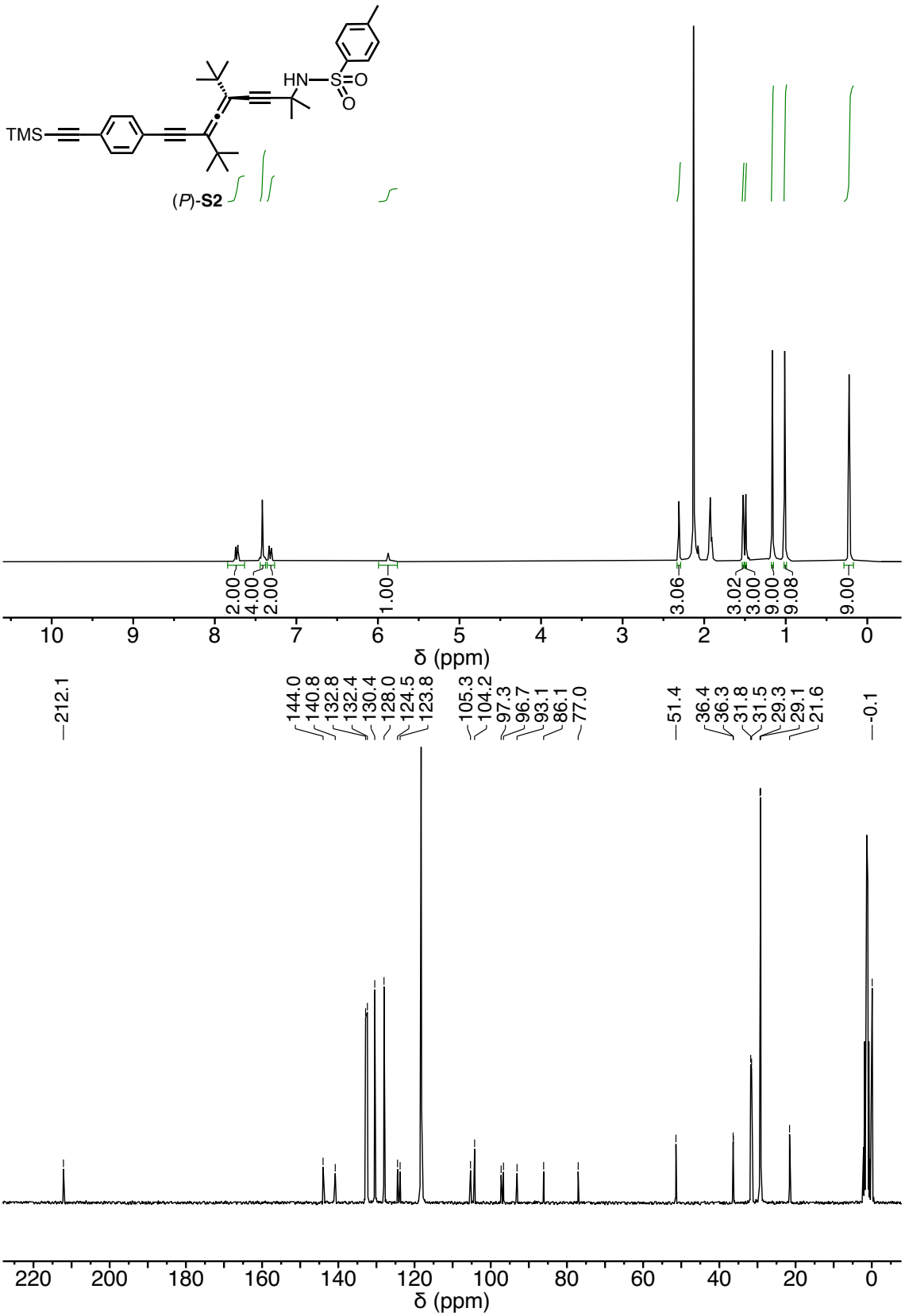

Figure S2. ^{1}H-NMR and ^{13}C-NMR of (*P*)-**S2** in CD_3CN.

*(P)-Di-tert-butyl-9-(4-ethynylphenyl)-2-methylnona-5,6-dien-3,8-diyn-2-ol (mono-(P)-**1**)*

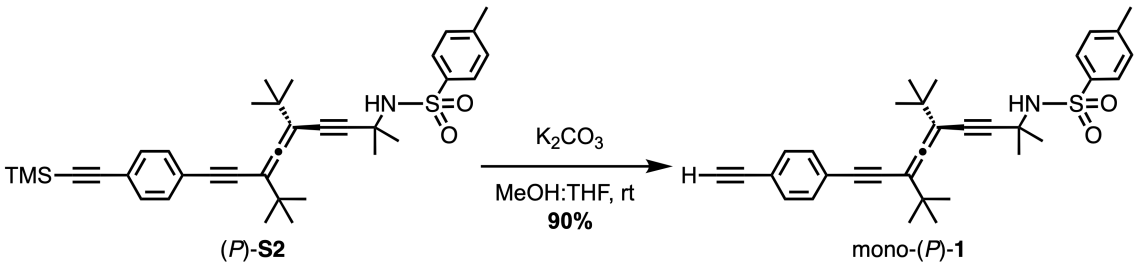

(*P*)-**S2** mono-(*P*)-**1**

To a solution of (*P*)-**S2** (100 mol%, 0.197 mmol, 115 mg) in a mixture of THF:MeOH (1:1, 4 mL), K_2CO_3 (300 mol%, 0.591 mmol, 82 mg) was added at rt. After 30 min, the mixture was quenched with distilled water (20 mL) and then the aqueous phase was extracted with DCM (3 x 10 mL). The combined organic phases were dried over anhydrous Na_2SO_4. Evaporation *in vacuo* and purification by flash chromatography on silica gel (hexane: EtAcO (8.5:1.5) afforded mono-(*P*)-**1** (91 mg, 90%) as a yellow oil.

For mono-(*P*)-**1**, $[\alpha]_D^{20}$= +302 (*c* = 10 mg·mL^{-1}, $CHCl_3$)

Molecular Formula: $C_{33}H_{37}NO_2S$. **MW:** 511.72 **g/mol.**

^{1}H-NMR (300 MHz, CD_3CN) δ 7.74 (d, 2H), 7.49 – 7.43 (m, 4H), 7.33 (d, 2H), 5.86 (s, 1H), 3.50 (s, 1H), 2.31 (s, 3H), 1.52 (s, 3H), 1.49 (s, 3H), 1.17 (s, 9H), 1.03 (s, 9H).

^{13}C-NMR (75 MHz, CD_3CN) δ 212.1, 144.0, 140.8, 133.1, 132.4, 130.4, 128.0, 124.7, 122.9, 104.3, 104.2, 96.7, 93.0, 86.1, 83.7, 80.8, 77.0, 51.4, 36.4, 36.3, 31.8, 31.5, 29.3, 29.1, 21.6.

HRMS (ESI$^+$): *m/z* calcd. for $C_{33}H_{37}NO_2S$ 511.2545; found 512.2623 $[M+H]^+$.

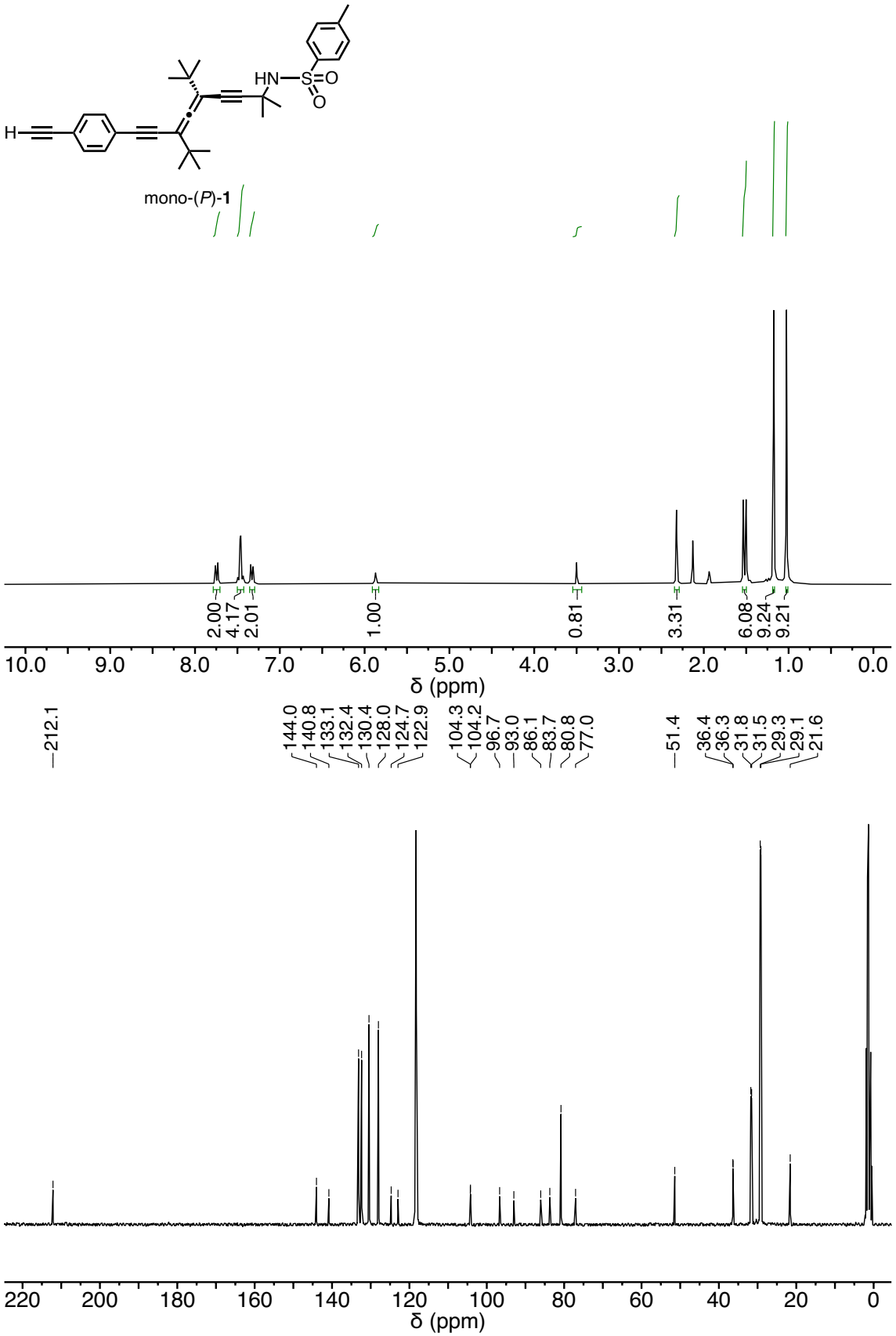

Figure S3. ^{1}H-NMR and ^{13}C-NMR of mono-(*P*)-**1** in CD_3CN.

*(M)-Di-tert-butyl-9-(4-ethynylphenyl)-2-methylnona-5,6-dien-3,8-diyn-2-ol (mono-(M)-**1**)*

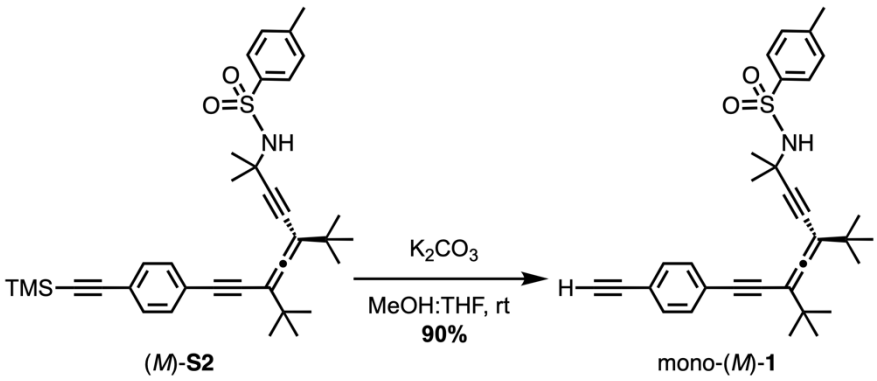

Enantiomer mono-(*M*)**-1** was obtained from (*M*)**-S2** by applying the same protocol as for mono-(*P*)**-1**. For mono-(*M*)-**1** $[\alpha]_D^{20}$= -316 (*c* = 10 mg·mL^{-1}, $CHCl_3$).

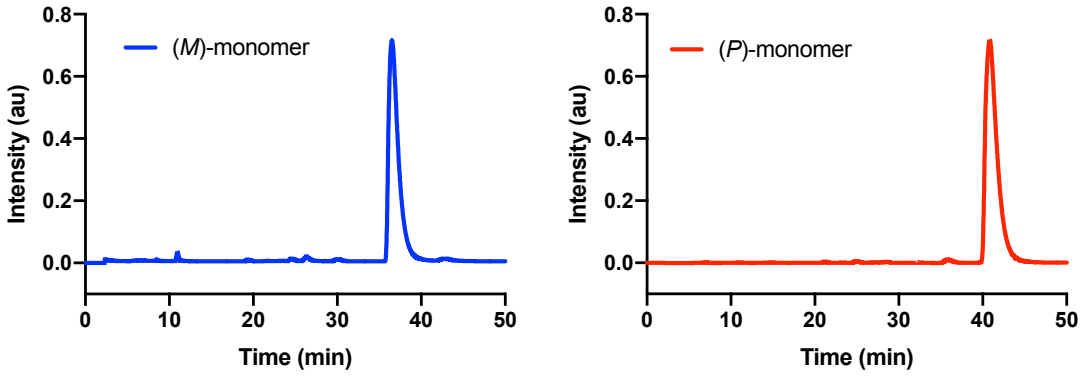

Figure S4. Chiral HPLC traces for mono-(*M*)-**1** and mono-(*P*)-**1** respectively (ee > 98%).

*(P)-N-(5,7-di-tert-butyl-9-(4-ethynylphenyl)-2-methylnona-5,6-dien-3,8-diyn-2-yl)-N,4-dimethylbenzenesulfonamide (mono-(P)-**2**)*

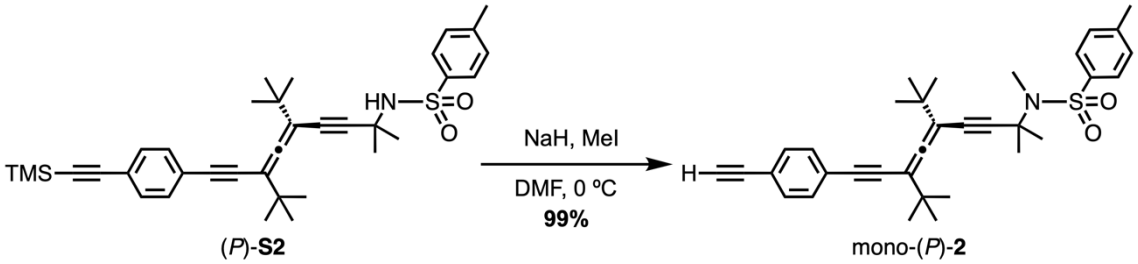

(*P*)-**S2** mono-(*P*)-**2**

A pre-cooled solution (0 °C) of (*P*)-**S2** (100 mol%, 0.103 mmol, 60 mg) in dry DMF (1 mL) was treated with NaH (powder moistened with oil, 55–65%) (220 mol%, 0.226 mmol, 9 mg). After 45 min, MeI (2000 mol%, 2.060 mmol, 0.1 mL) was added. The resulting mixture was stirred for 10 min at 0 °C. The reaction mixture was quenched with sat. aq. NH_4Cl (10 mL) and then the aqueous phase was extracted with DCM (3 x 10 mL). The combined organic phases were washed with 5% aq. LiCl, dried over anhydrous Na_2SO_4. Evaporation *in vacuo* and purification by flash chromatography on silica gel (hexane: EtAcO (9:1) afforded mono-(*P*)-**2** (54 mg, 99%) as a yellow oil.

For mono-(*P*)-**2**, $[\alpha]_D^{20}$= +322 (*c* = 10 mg·mL^{-1}, $CHCl_3$)

Molecular Formula: $C_{34}H_{39}NO_2S$. **MW:** 525.75 **g/mol.**

^{1}H-NMR (300 MHz, CD_3CN) δ 7.70 (d, 2H), 7.49 – 7.40 (m, 4H), 7.33 (d, 2H), 3.49 (s, 1H), 3.01 (s, 3H), 2.33 (s, 3H), 1.64 (s, 3H), 1.62 (s, 3H), 1.16 (s, 9H), 1.03 (s, 9H).

^{13}C-NMR (75 MHz, CD_3CN) δ 212.2, 144.4, 139.5, 133.1, 132.3, 130.6, 128.2, 124.7, 122.9, 104.3, 104.2, 96.2, 93.0, 85.9, 83.7, 80.8, 77.9, 56.9, 36.4, 36.2, 34.5, 30.6, 30.6, 29.3, 29.1, 21.5.

HRMS (ESI$^+$): *m/z* calcd. for $C_{34}H_{39}NO_2S$ 525.2702; found 548.2595 $[M+Na]^+$.

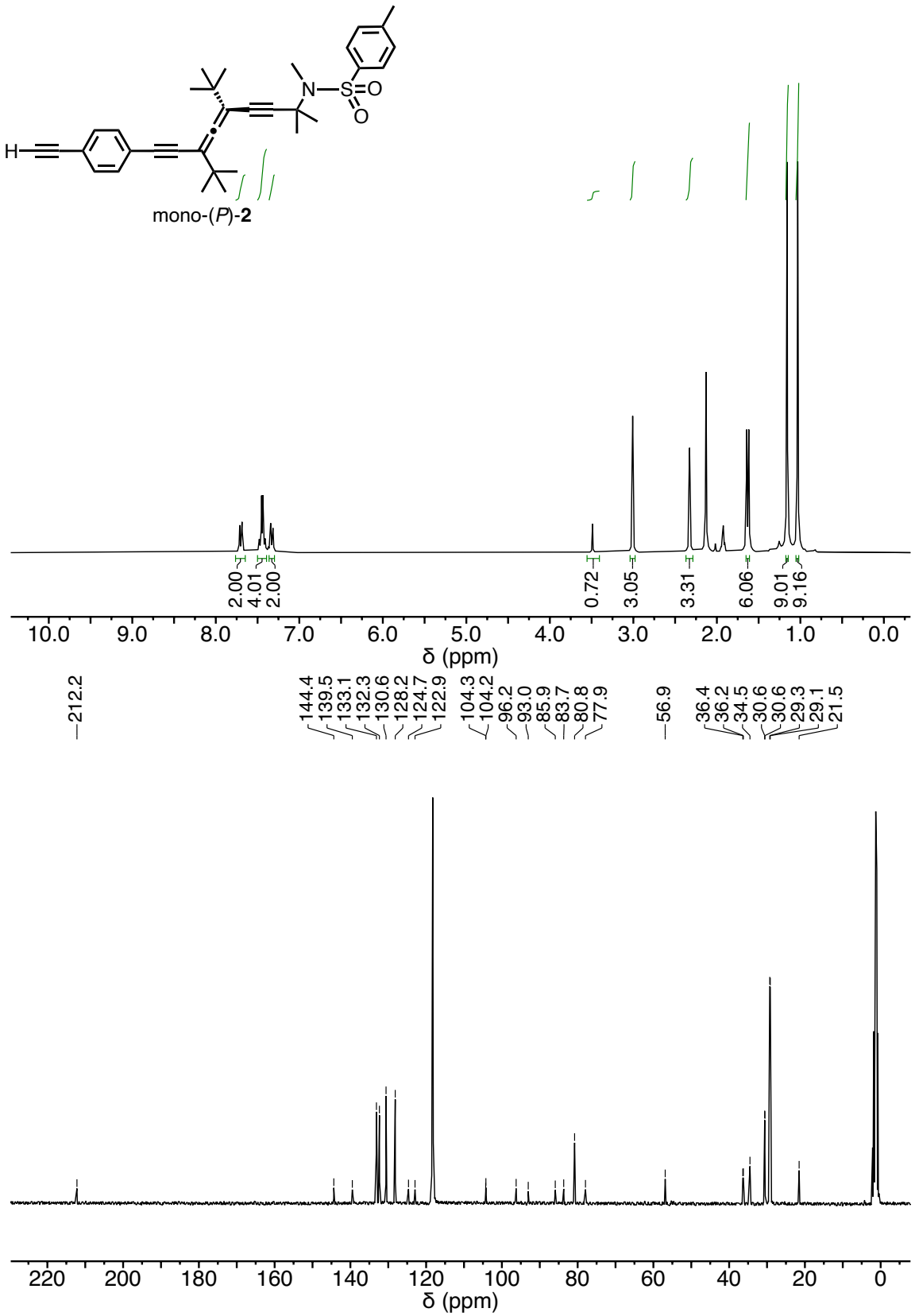

Figure S5. ^{1}H-NMR and ^{13}C-NMR of mono-(*P*)-**2** in CD_3CN.

5.2.3. Synthesis of polymers

5.2.3.1. General procedure for polymerization

The reaction flask (sealed ampoule) was dried under vacuum and argon flushed for three times before a solution of monomer in THF was added *via* cannula. Then, triethylamine was added dropwise *via* syringe. A solution of rhodium norbornadiene chloride dimer, $[Rh(nbd)Cl]_2$, in THF was added under stirring at rt. The reaction mixture was stirred at rt overnight. Then, the resulting polymer was diluted in DCM and precipitated in a large amount of MeOH, centrifuged (2 times), reprecipitated in hexane and centrifuged again (Table S1).

Table S1. Calculated amounts for the synthesis of the polymers poly-(*P*)-**1** and poly-(*M*)-**1**.

Monomer	Mass (mg)	THF (μL)	Et_3N (μL)	Catalyst (mg)	Yield (%)
mono-(*P*)-**1**	67	300	4	1	85
mono-(*M*)-**1**	50	200	3	1	83
mono-(*P*)-**2**	50	200	3	1	88

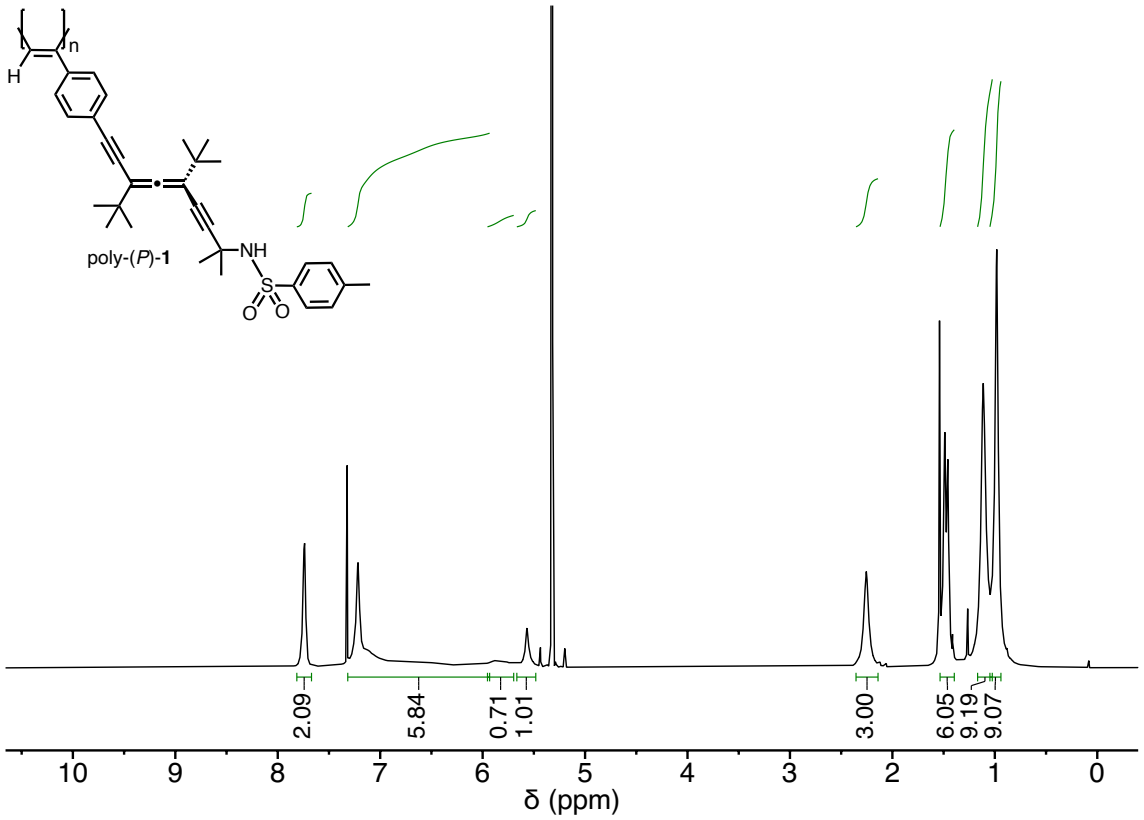

Figure S6. ^{1}H-NMR of poly-(*P*)-**1** in CD_2Cl_2.

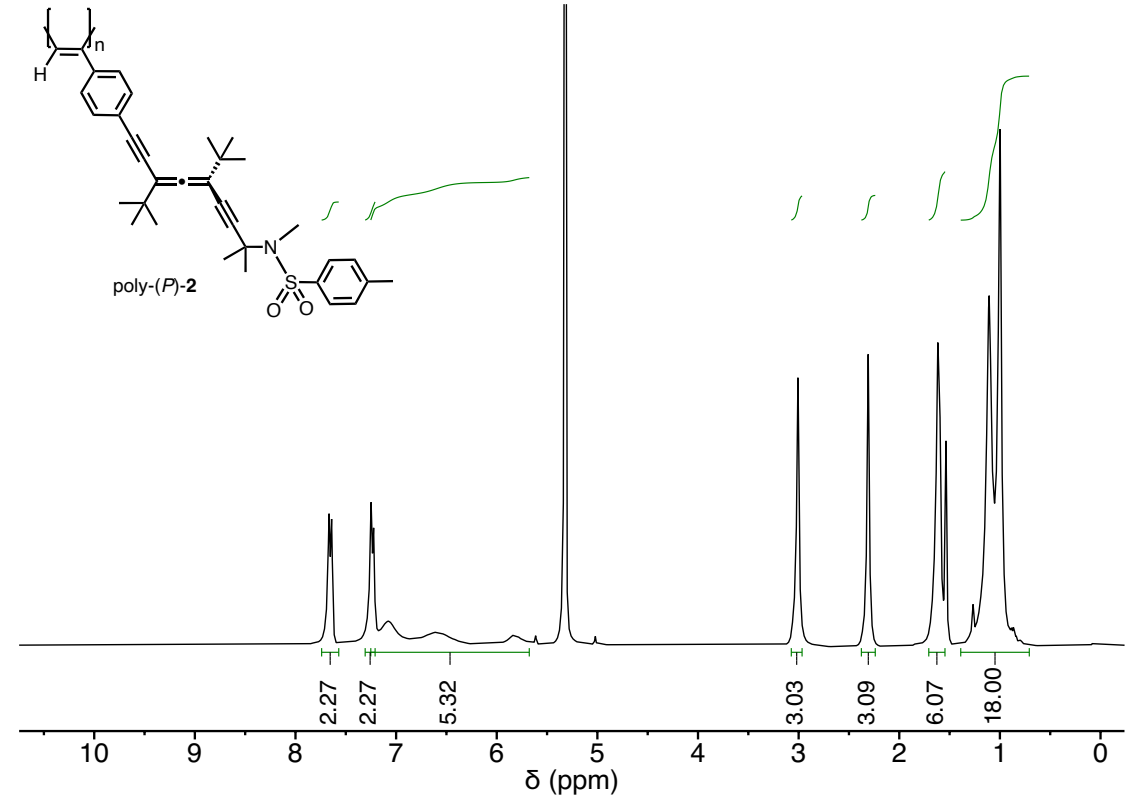

Figure S7. ^{1}H-NMR of poly-(*P*)-**2** in CD_2Cl_2.

5.2.4. GPC Studies

The molecular weight was estimated by GPC using THF (flow rate: 1.0 mL·min^{-1}) as eluent and polystyrene narrow standards (PSS) as calibrants.

Table S2. GPC data for the synthesized polymers.

Polymer	Mn (Daltons)	Mw (Daltons)	Mz (Daltons)	Đ (Daltons)
poly-(*P*)-**1**	121887	182669	2303938	1.37
poly-(*M*)-**1**	97854	121555	160857	1.24
poly-(*P*)-**2**	166513	204953	240085	1.23

5.2.5. Raman Experiments

The bands observed by Raman resonance confirmed the former configuration. The peak at highest wavelength corresponds to the C=C bond stretching and overlaps with that of the phenyl ring. The band at 1334 cm^{-1} arises from the *cis* C-C bond coupled with the single bond connecting the main chain and the phenyl ring. The peak at lowest wavelength (915 cm^{-1}) corresponds to the C-H bond of the *cis* form. The disappearance of the alkyne peak (ca. 2106 cm^{-1}) also confirms the formation of the polymer.

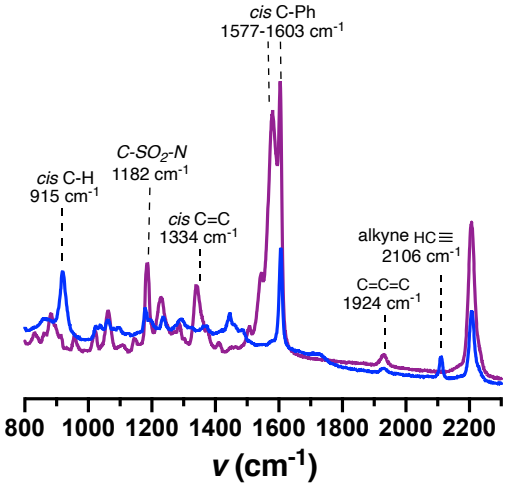

Figure S8. Raman spectra of mono-(*P*)-**1** and poly-(*P*)-**1**.

5.2.6. Thermal Studies

5.2.6.1. DSC Studies

DSC experiments have been used to determine the configuration of the polymer skeleton in poly(phenylacetylene)s due to the different thermogram pattern for a *cis*-cisoidal (*c*-*c*) or a *cis*-transoidal (*c*-*t*) polyene backbone.[150,196] Hence, the geometry of the polymer was determined by DSC. According to a general protocol, the polymer was placed in an aluminum pan up to 400 °C (heating rate: 10 °C·min^{-1}). The thermogram for poly-(*P*)-**1** shows a typical *c*-*t* trace with an exothermal peak, at 102 °C and 185 °C respectively, correspondent to a *c*-*c* transition and a final isomerization to *t*-*t* (Figure S9).

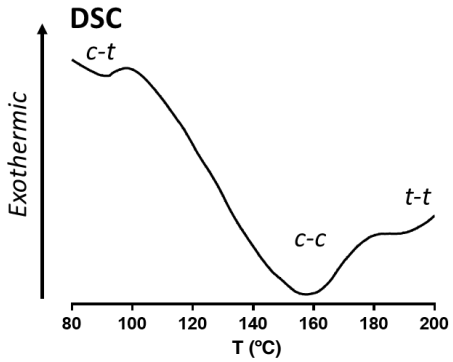

Figure S9. DSC study for poly-(*P*)-**1**.

5.2.6.2. TGA studies

The thermal stability was evaluated by TGA. As a general protocol, the polymer sample was placed in a platinum pan and heated from 40°C to 800°C (heating rate: 10 °C·min^{-1}). Poly-(*P*)-**1** starts to degrade at 280 °C (Figure S10).

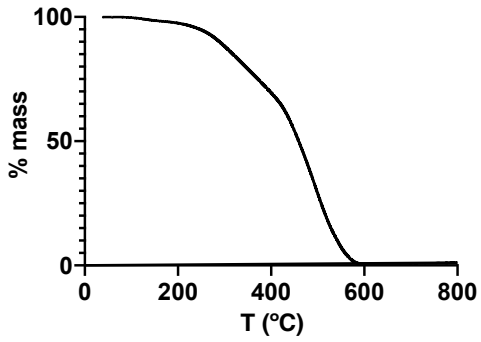

Figure S10. TGA thermogram for poly-(*P*)-**1**.

5.2.7. ECD Studies of mono-(*M*)-1

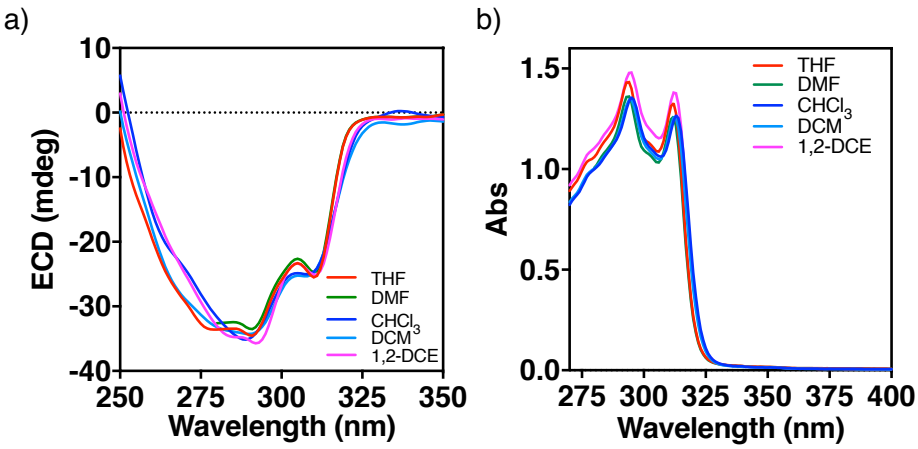

Figure S11. a) ECD spectra and (b) UV-vis of mono-(*M*)-**1** in different solvents (0.8 mM).

5.2.8. Studies of the effect of Lewis base and non-Lewis base solvents on the conformation of mono-(*P*)-1 by NMR

*^{1}H-NMR studies of mono-(P)-**1** in non-Lewis base and Lewis base solvents*

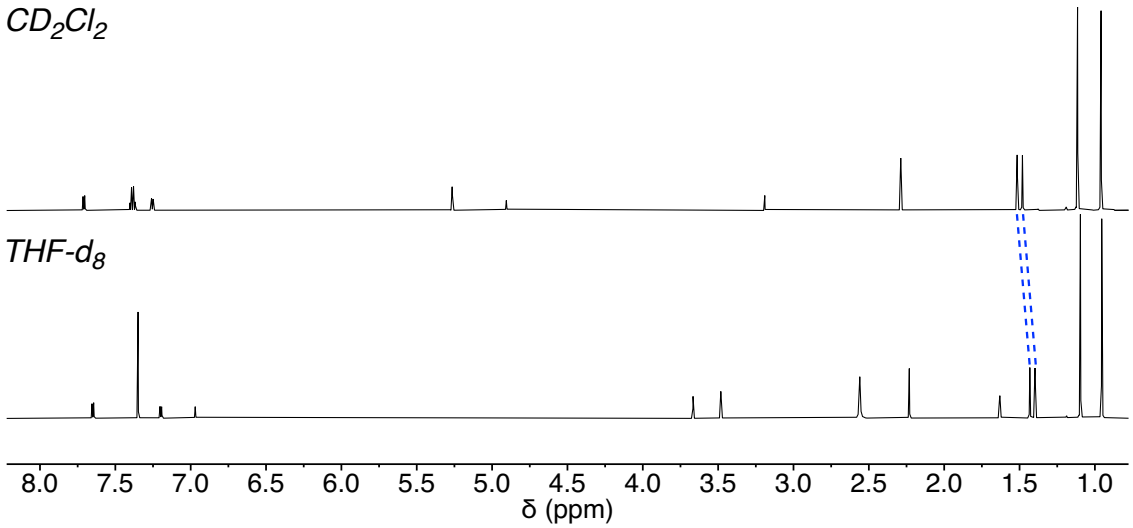

Figure S12. ^{1}H-NMR (750 MHz) of mono-(*P*)-**1** in CD_2Cl_2 (top) and THF-d_8 (below).

*NOESY-NMR studies of mono-(P)-**1** in Lewis base and non-Lewis base solvents*

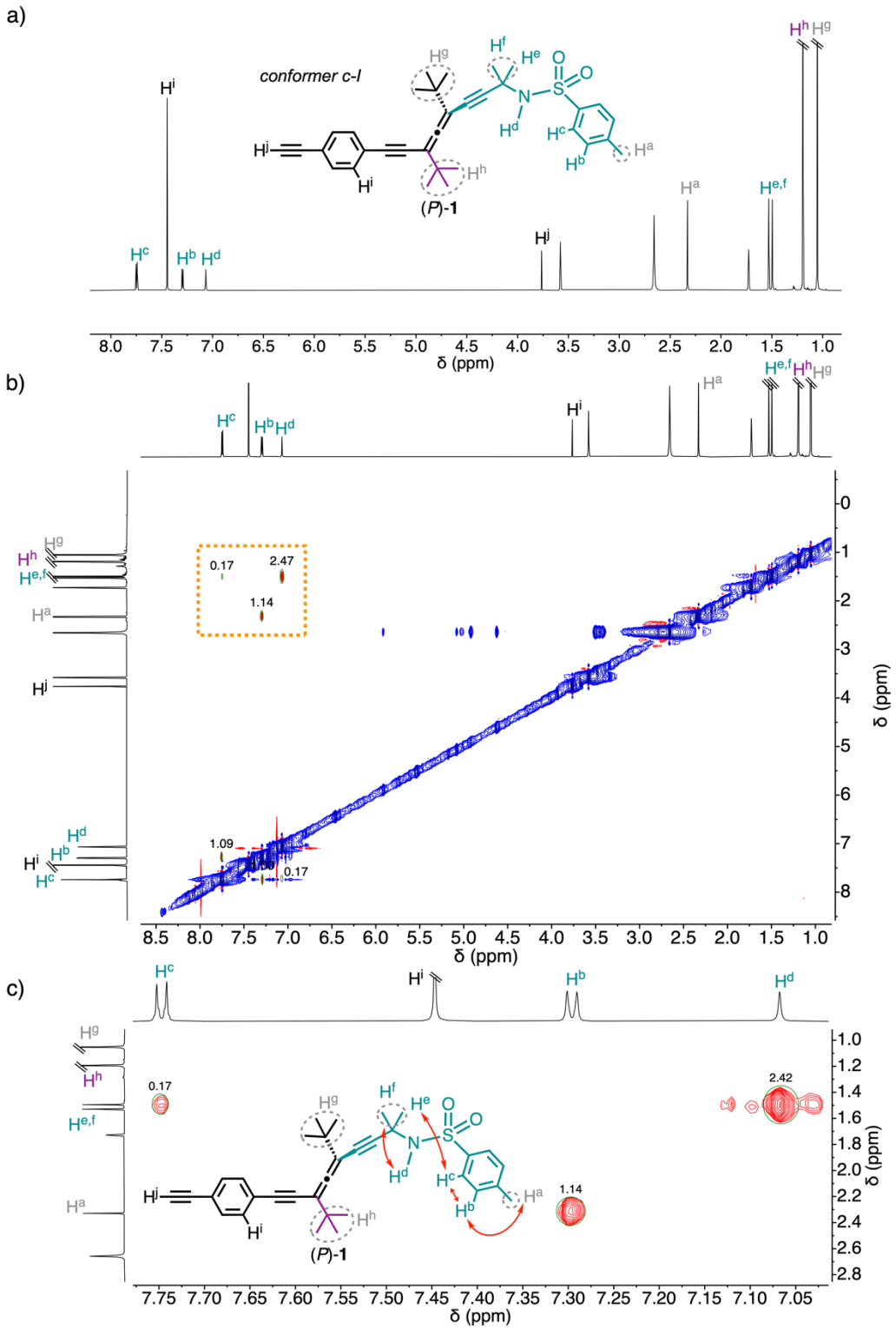

Figure S13. (a) ^{1}H-NMR of mono-(*P*)-1 and (b) NOESY and (c) NOESY zoomed area (THF-d_8, 278 K, 750 MHz).

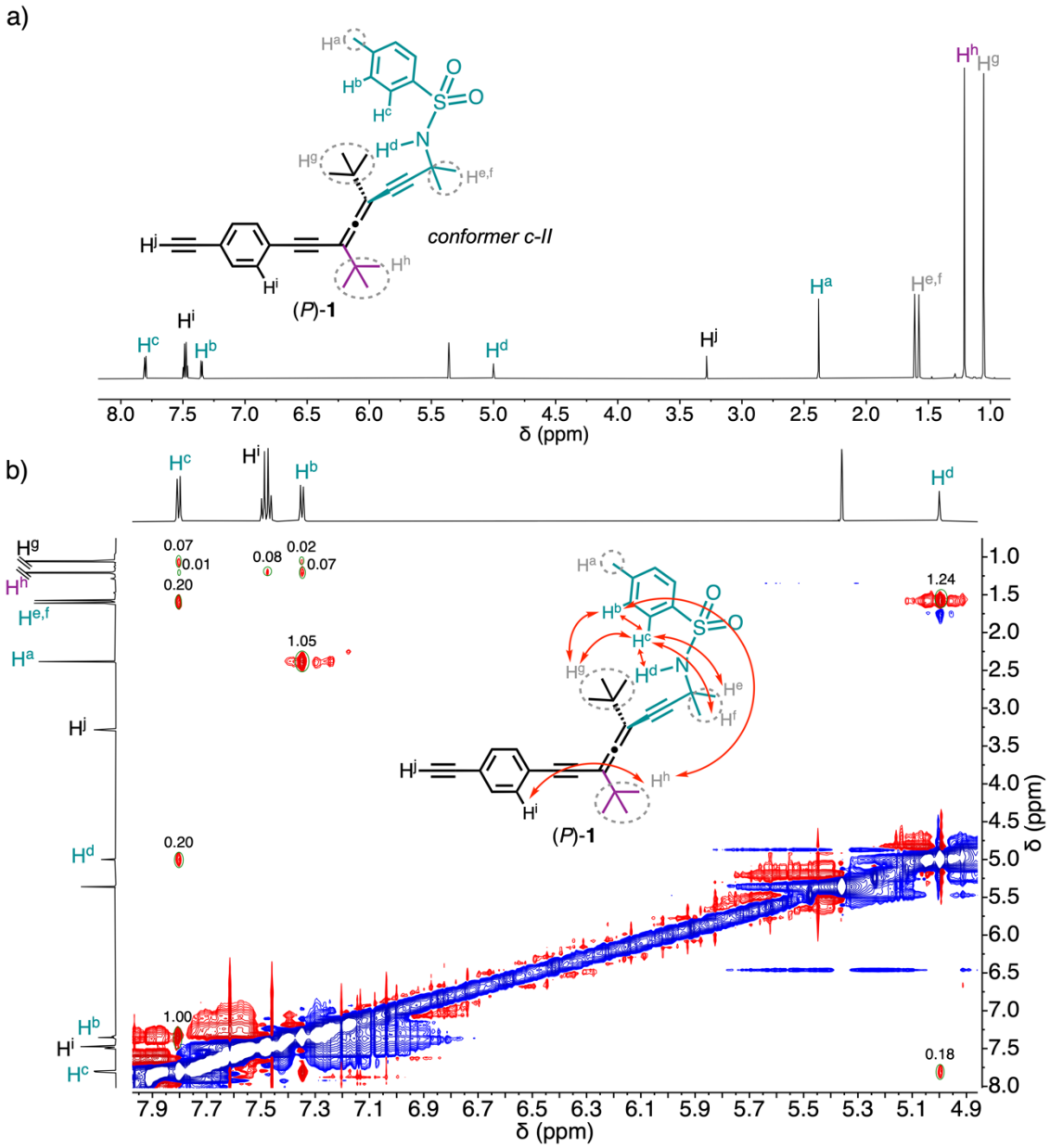

Figure S14. (a) ^{1}H-NMR of mono-(*P*)-**1** and (b) NOESY (CD_2Cl_2, 278 K, 750 MHz).

From these studies it was possible to obtain the distance between the anilide proton with the two methyl groups (Equation 1) of the carbon linked to the sulfonamide group (H^{d}-$H^{e,f}$), in addition to the distance of these two methyl groups with the *p*-tolyl group ($H^{e,f}$-H^{c}). Thus, in Lewis base solvent, the *p*-tolyl-sulfonamide group is oriented opposite to the alkyne group (Figure S13, conformer c-I), whereas in non-Lewis base solvents, a bended conformation is generated placing the *p*-tolyl-sulfonamide group closer to the alkyne (Figure S14, conformer c-II).

$$\frac{I_{AB}}{I_{CD}} = \frac{(d_{CD})^6}{(d_{AB})^6}$$

Equation 1. Relationship between interproton distance and NOESY intensities.

Table S3. Interproton distance from NOESY intensities.

Distance (Å)	H^a-H^b	H^c-$H^{e,f}$	H^d-$H^{e,f}$	H^d-H^c	H^b-H^g	H^c-H^g
conformer c-I	2.60	4.08	2.68	3.5	6.41	3.98
conformer c-II	2.60	4.2	2.69	3.4	-	-

5.2.9. ECD Studies of polymers

5.2.9.1. ECD Studies of poly-(*P*)-1

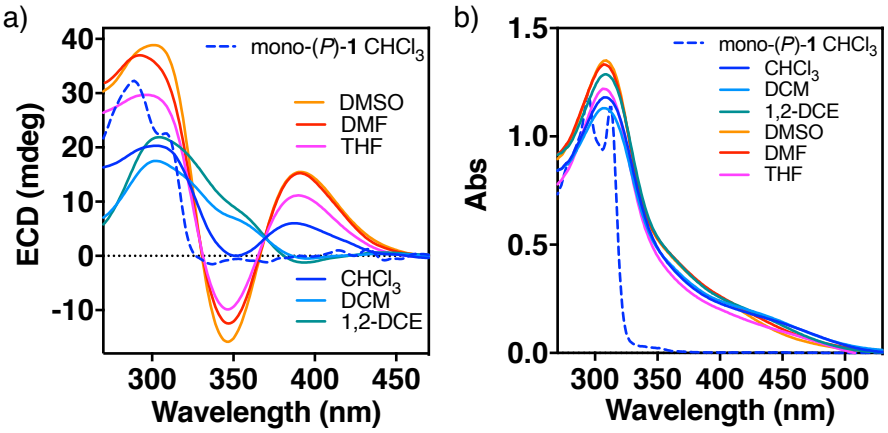

Figure S15. (a) ECD spectra and (b) UV-vis of mono-(*P*)-**1** in $CHCl_3$ and poly-(*P*)-**1** in different solvents (0.8 mM).

5.2.9.2. ECD Studies of poly-(*M*)-1

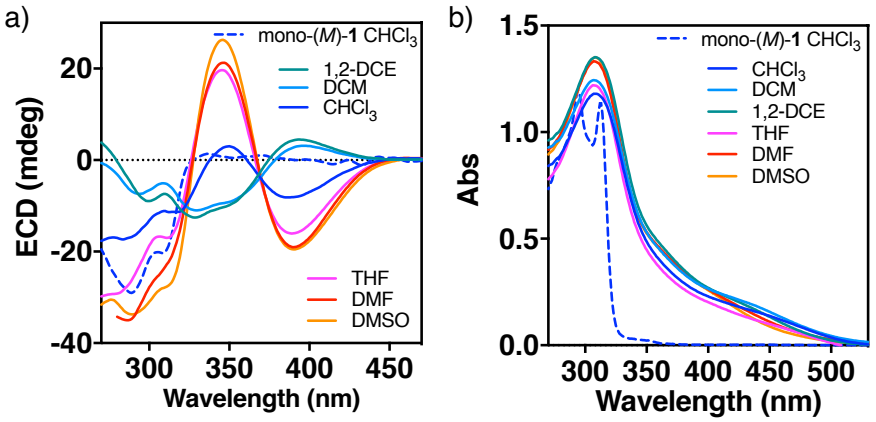

Figure S16. (a) ECD spectra and (b) UV-vis of mono-(*M*)-**1** in $CHCl_3$ and poly-(*M*)-**1** in different solvents (0.8 mM).

5.2.9.3. Comparison of (*P*)- and (*M*)-enantiomers

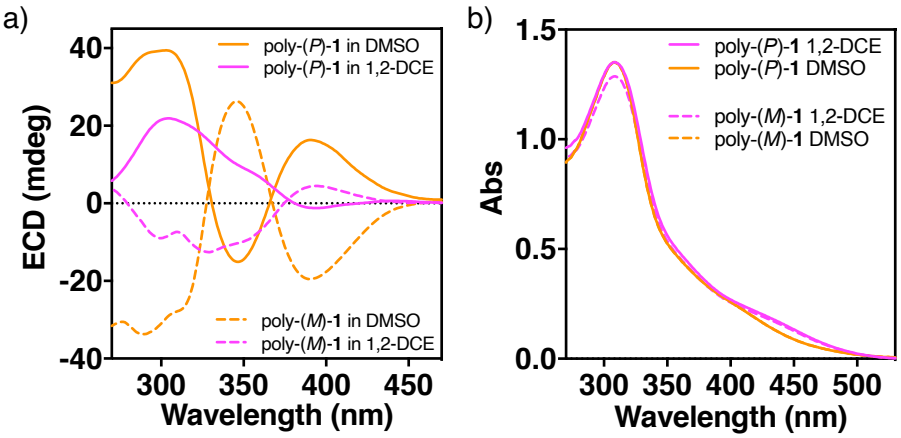

Figure S17. (a) ECD and (b) UV-vis spectra comparison of poly-(*P*)-**1** and poly-(*M*)-**1** in different solvents (0.8 mM).

5.2.9.4. ECD Studies of poly-(*P*)-2

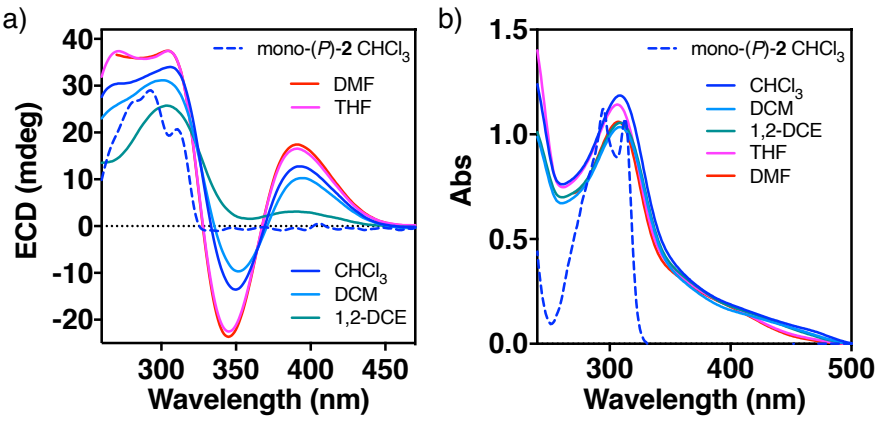

Figure S18. (a) ECD spectra and (b) UV-vis of mono-(*P*)-**2** in $CHCl_3$ and poly-(*P*)-**2** in different solvents (0.8 mM).

5.2.10. ATR/FT-IR Studies

A solution of poly-(*P*)-**1** (0.8 mM) was prepared in THF and 1,2-DCE, respectively. 20µL of these solutions were placed on a CsI cell and the solvent was removed by evaporation. FT-IR experiments show a shift towards higher frequencies at the characteristic C-SO_2-N stretching vibration in THF (Lewis base solvent) relative to the signal in 1,2-DCE (non-Lewis base solvent)(Figure S19).

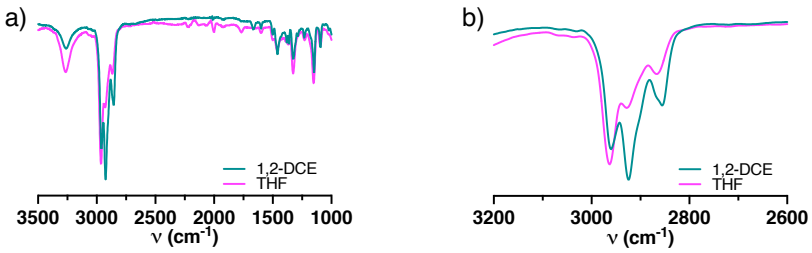

Figure S19. (a) IR spectra of a solution of poly-(*P*)-**1** in 1,2-DCE (pink line) and THF (red line) (0.8 mM) and (b) zoomed area relative to the NH of the sulfonamide group. FTIR (THF, ν, cm^{-1}): 3276 (NH); 1329,1154 (SO_2). FTIR (1,2-DCE, ν, cm^{-1}): 3245 (NH); 1321, 1146 (SO_2).

Table S4. FT-IR data of poly-1 in solution relative to the NH of the sulfonamide group.

	ν_{NH} (cm^{-1})	$\Delta\nu_{NH}$ (cm^{-1})
poly-(*P*)-**1** in THF	3276	31
poly-(*P*)-**1** in 1,2-DCE	3245	

5.2.11. Studies of the effect of Lewis base and non-Lewis base solvents on the conformation of poly-(*P*)-1 by NMR

*STD-NMR studies of the poly-(P)-**1** in Lewis base solvents and non-Lewis base solvents*

Saturation transfer difference NMR (STD-NMR) experiments were carried out at low temperature (278 K) to study the solvent-polymer interaction to have more precise information about the conformation of the pendants. The results show that, in Lewis base solvent such as THF-d_8, they present STD effects that increase with higher saturation time when the protons of the solvent are saturated. Therefore, Lewis base solvents coordinate with poly-(*P*)-**1** (Figure S20).

On the other hand, when the same experiment was carried out using a non-Lewis base solvent such as CD_2Cl_2, no STD effect was observed (Figure S21).

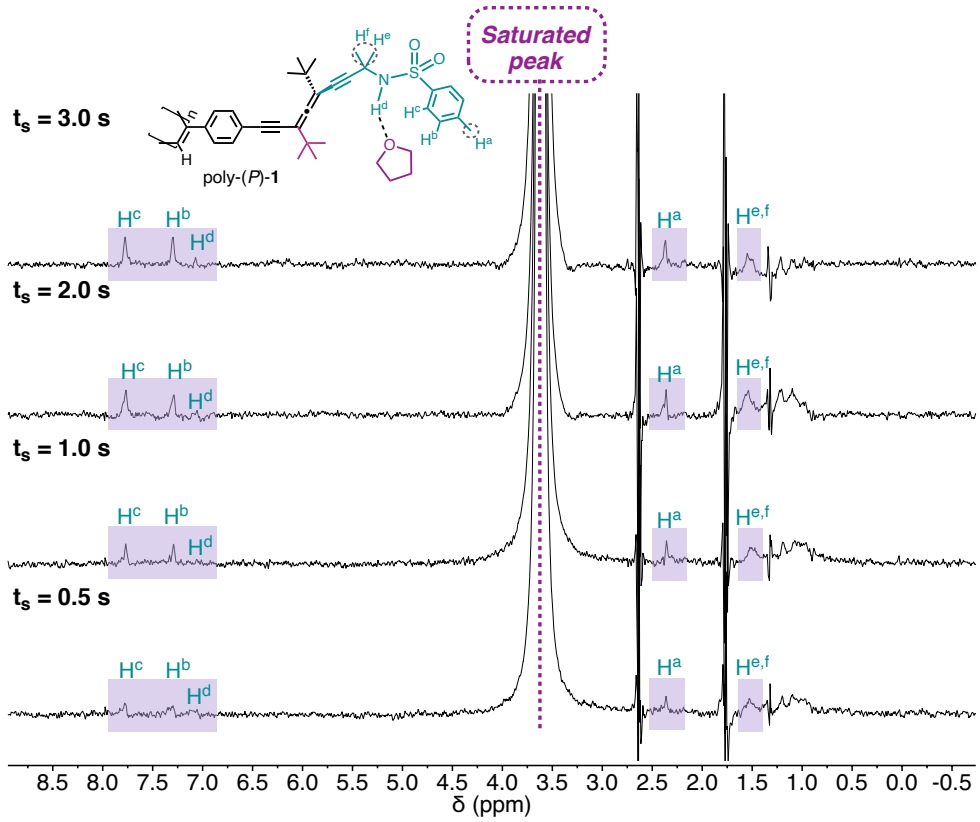

Figure S20. STD-NMR experiment of poly-(*P*)-**1** (THF-d_8, 278 K, 750 MHz). Saturated peak 3.62 ppm.

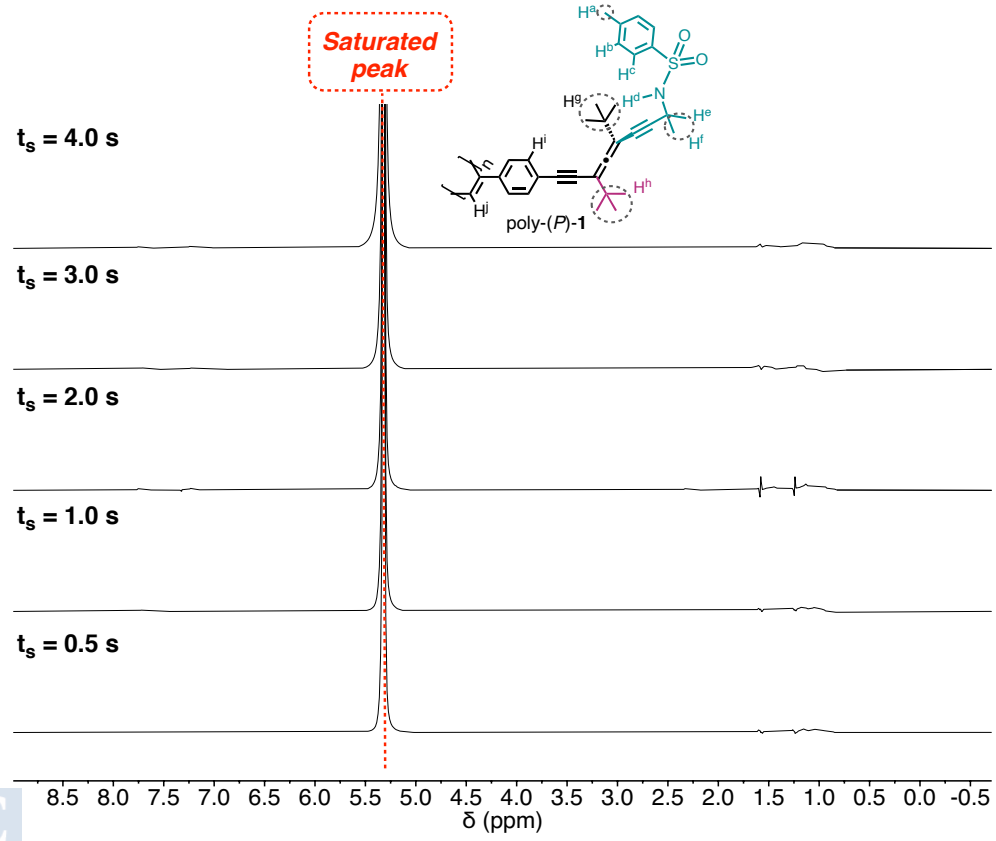

Figure S21. STD-NMR experiment of poly-(*P*)-**1** (CD_2Cl_2, 278 K, 750 MHz). Saturated peak 5.36 ppm.

*NOESY-NMR studies of the poly-(P)-**1** in Lewis base and non-Lewis base solvents*

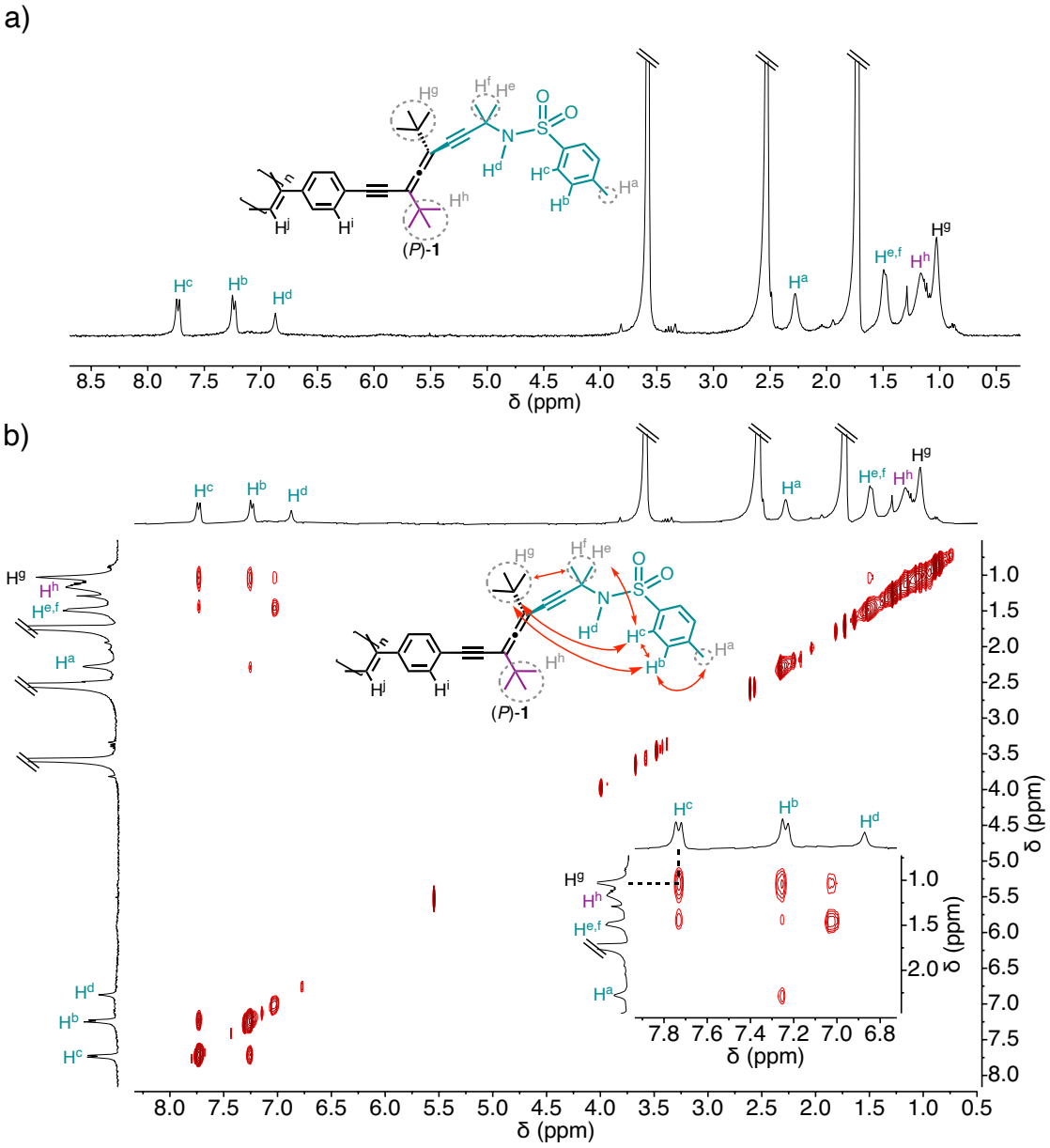

Figure S22. ^{1}H-NMR of poly-(*P*)-**1** (top) and NOESY (below) (THF-d_8, 278 K, 750 MHz).

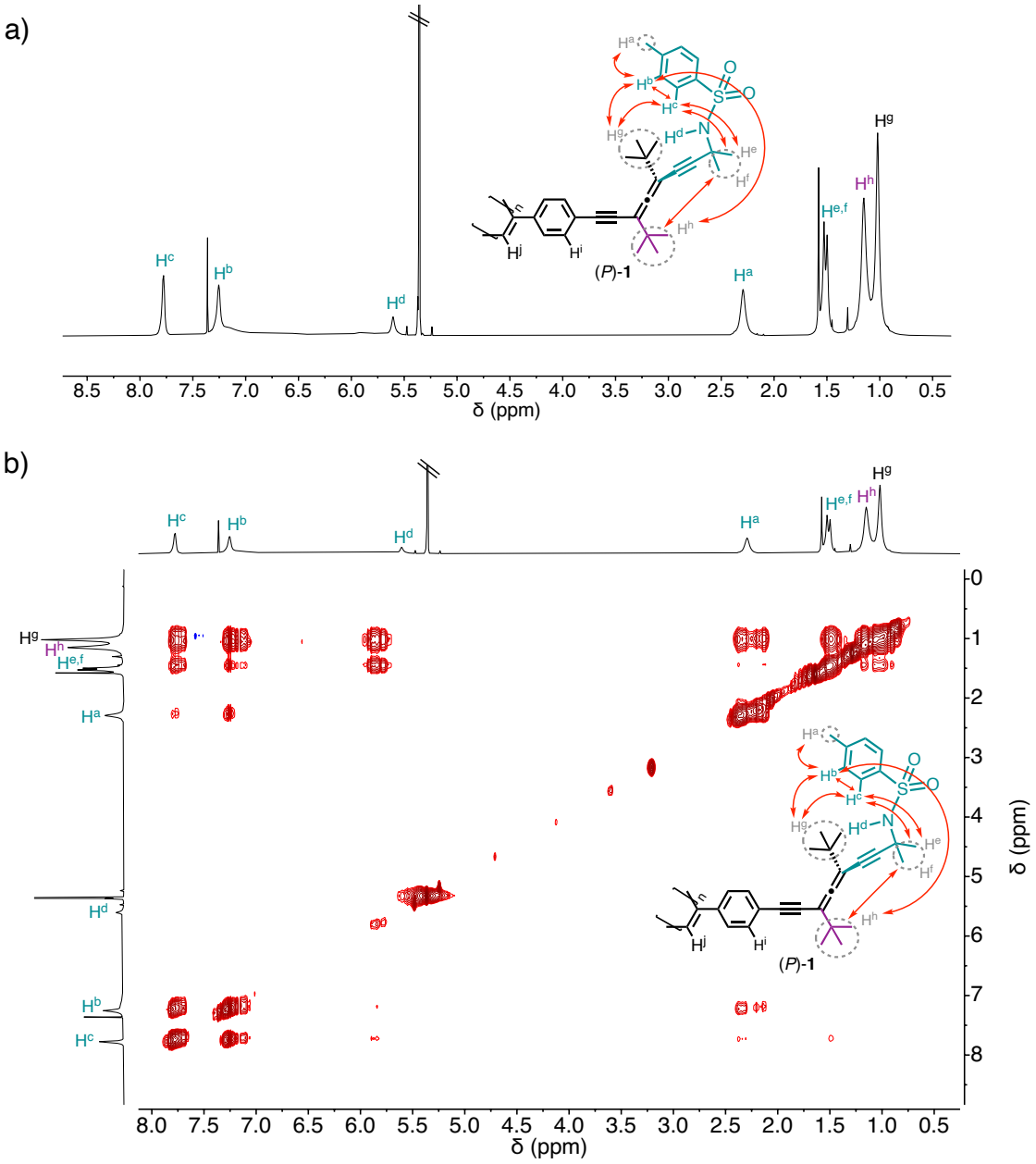

Figure S23. ^{1}H-NMR of poly-(*P*)-**1** (top) and NOESY (below) (CD_2Cl_2, 278 K, 750 MHz).

5.2.12. Low Temperature ECD Experiments

Poly-(*P*)-**1** (1.6 mM) in THF shows an increase in the ECD intensity after fast cooling (from 298 K to 268K at ≥10 K·min^{-1}). On the other hand, the ECD trace of poly-(*P*)-**1** (1.6 mM) in 1,2-DCE increases in intensity of the negative Cotton effect at 399 nm.

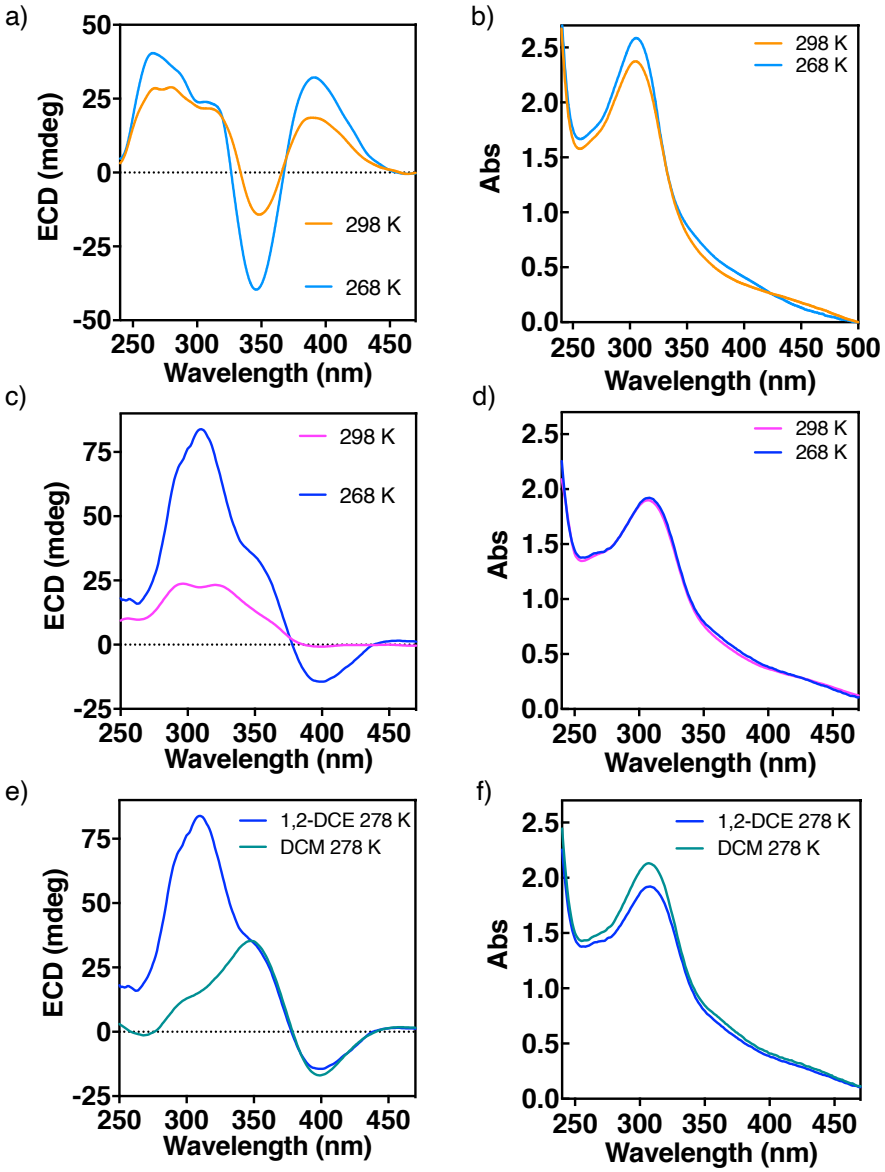

Figure S24. ECD spectra and UV-vis of poly-(*P*)-**1** (1.6 mM) at rt (298 K) and after fast cooling (at 268 K) in [(a), (b)] THF and in [(c), (d)] 1,2-DCE. (e) ECD spectra and (f) UV-vis of poly-(*P*)-**1** (1.6 mM) at 278 K in 1,2-DCE and DCM.

5.2.13. VT-ECD Experiments

5.2.13.1. VT-ECD Experiments for poly-(*P*)-1

ECD signal of poly-(*P*)-**1** solutions (1.6 mM) were monitored during slow cooling from 298 K to 268 K at 0.1 K·min^{-1} (only spectra every 5 K were plotted for clarity).

Poly-(*P*)-**1** in THF shows an increase in the ECD intensity when the temperature decreases. On the other hand, the ECD trace of poly-(*P*)-**1** in 1,2-DCE increases in intensity and takes place a bathochromic shift in the vinylic region from 400 nm to 420 nm with an increased intensity of that negative Cotton effect.

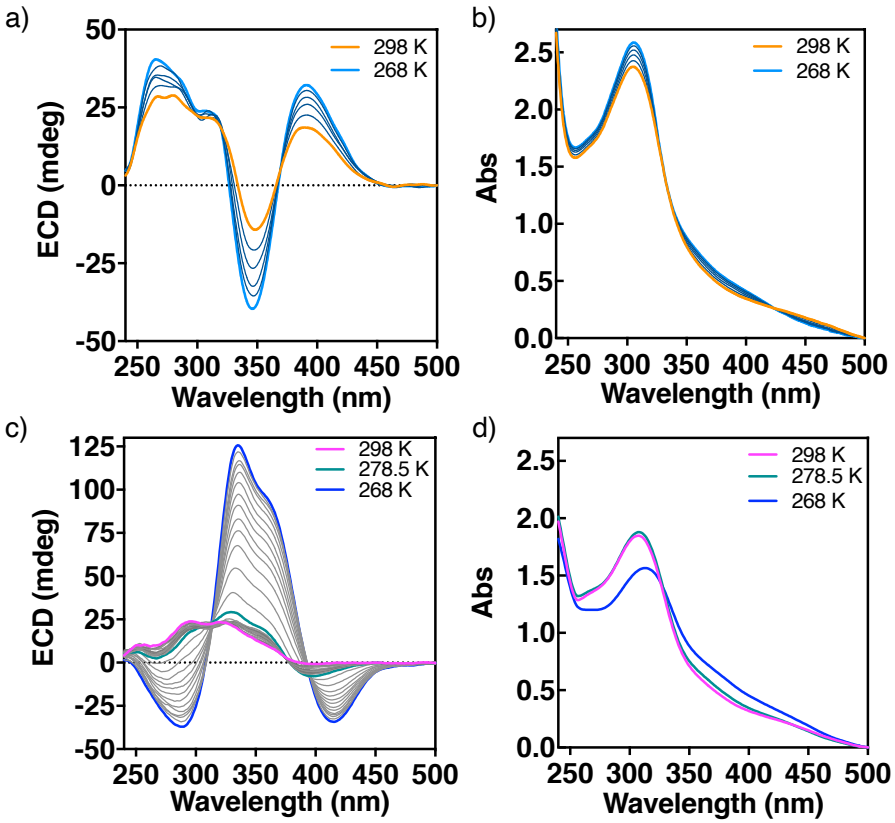

Figure S25. VT-ECD spectra and UV-vis of poly-(*P*)-**1** (1.6 mM) from 298 K to 268 K after slow cooling (0.1 K·min^{-1}) in [(a), (b)] THF and in [(c), (d)] 1,2-DCE.

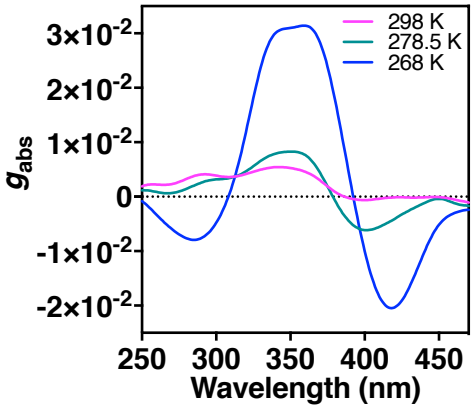

Figure S26. g_{abs} representation of poly-(*P*)-**1** (1.6 mM) from 298 K to 268 K after slow cooling (0.1 K·min^{-1}) in 1,2-DCE.

Also, several cycles of cooling-heating were carried out to corroborate the reversibility of the process (Figure S27).

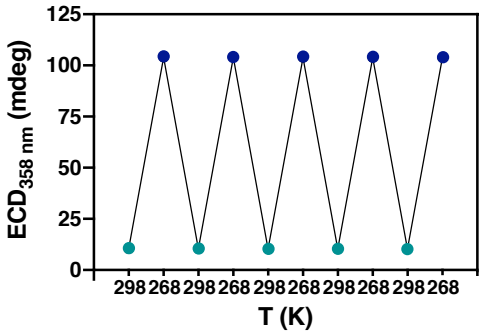

Figure S27. Temperature cycles by ECD at 358 nm.

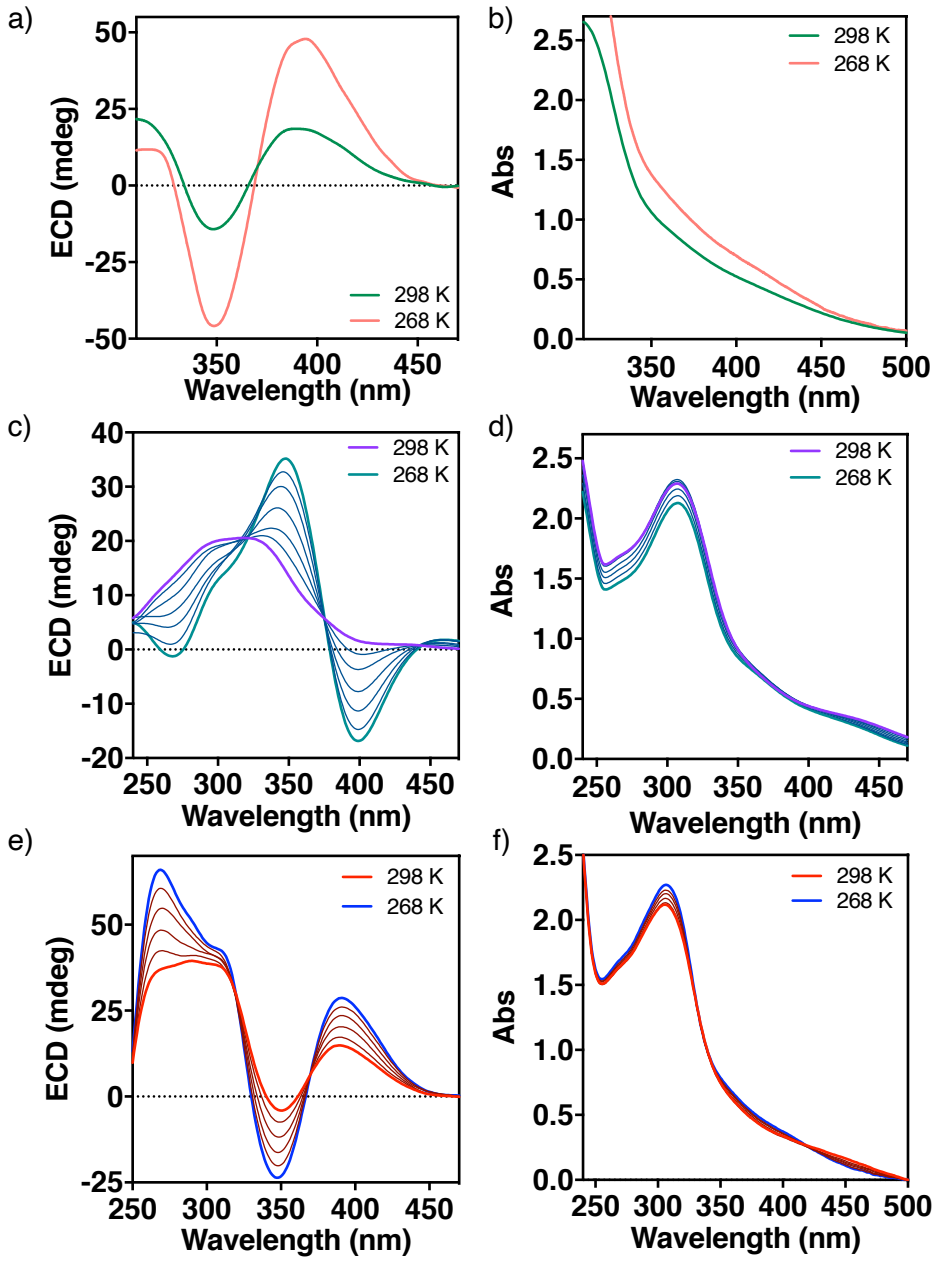

Figure S28. VT-ECD spectra and UV-vis of poly-(*P*)-**1** (1.6 mM) from 298 K to 268 K after slow cooling (0.1 K·min^{-1}) in [(a), (b)] DMF, in [(c), (d)] DCM and in [(e), (f)] $CHCl_3$.

5.2.13.2. VT-ECD Experiments for poly-(*M*)-1

VT-ECD experiments in THF and 1,2-DCE were repeated for the enantiomer poly-(*M*)-**1** and the same behaviour was observed.

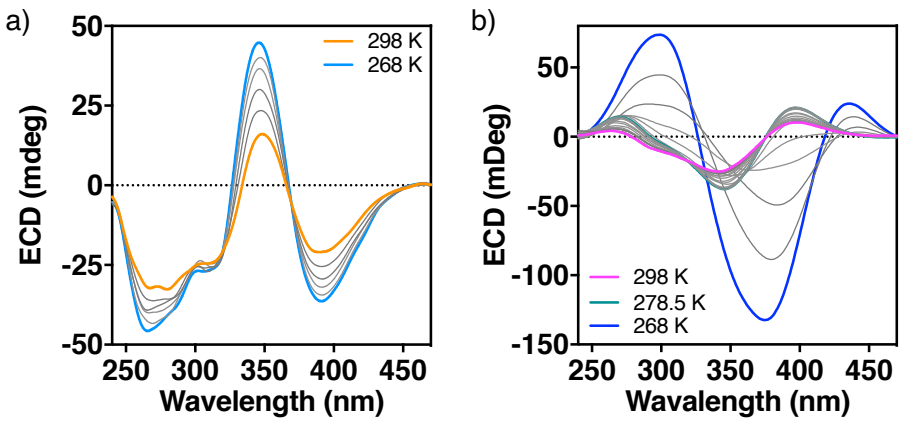

Figure S29. VT-ECD spectra of poly-(*M*)-1 (1.6 mM) from 298 K to 268 K after slow cooling (0.1 K·min^{-1}) in (a) THF and in (b) 1,2-DCE.

5.2.13.3. VT-ECD Experiments for poly-(*P*)-2

ECD signal of poly-(*P*)-**2** solutions (0.8 mM) in Lewis base solvents (Figure S30) and non-Lewis base solvents (Figure S31) were monitored during fast cooling from 298 K to 268 K at 1.0 K·min^{-1} (only spectra every 5 K were plotted for clarity).

ECD signal of poly-(*P*)-**2** solutions (0.8 mM) in Lewis base solvents (Figure S32) and non-Lewis base solvents (Figure S33) were monitored during slow cooling from 298 K to 268 K at 0.1 K·min^{-1} (only spectra every 2 K were plotted for clarity).

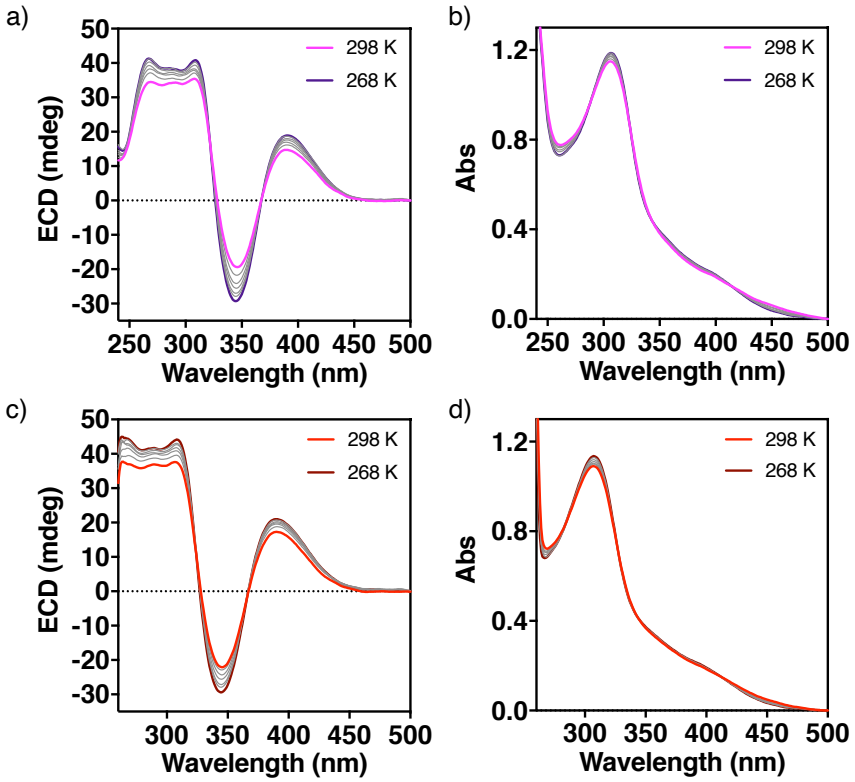

Figure S30. VT-ECD spectra and UV-vis of poly-(*P*)-**2** (0.8 mM) from 298 K to 268 K after fast cooling (1.0 K·min^{-1}) in [(a), (b)] THF and in [(c), (d)] DMF.

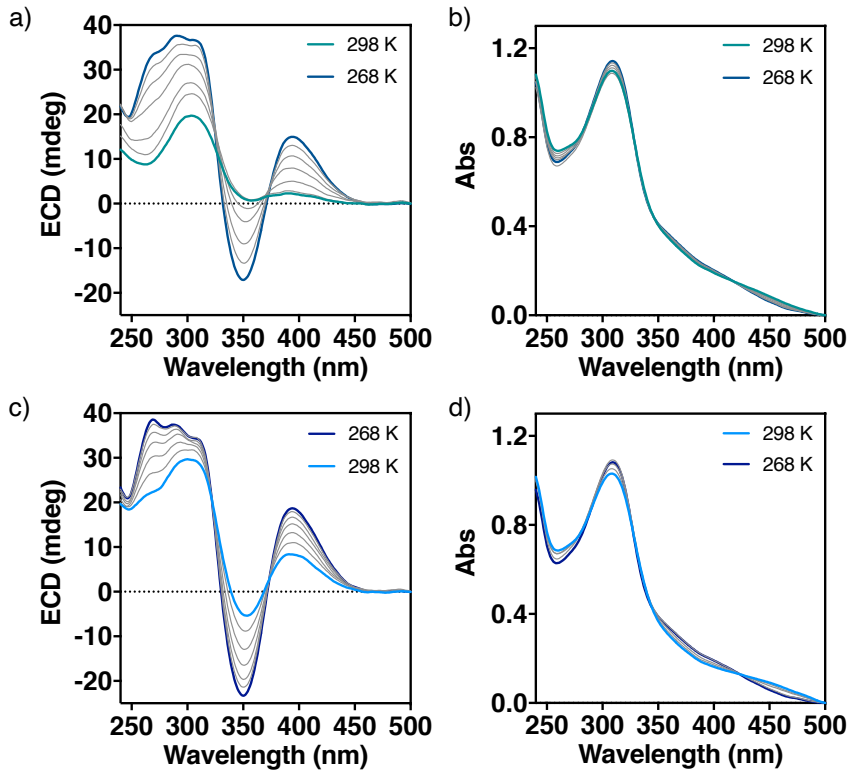

Figure S31. VT-ECD spectra and UV-vis of poly-(*P*)-**2** (0.8 mM) from 298 K to 268 K after fast cooling (1.0 K·min^{-1}) in [(a), (b)] 1,2-DCE and in [(c), (d)] DCM.

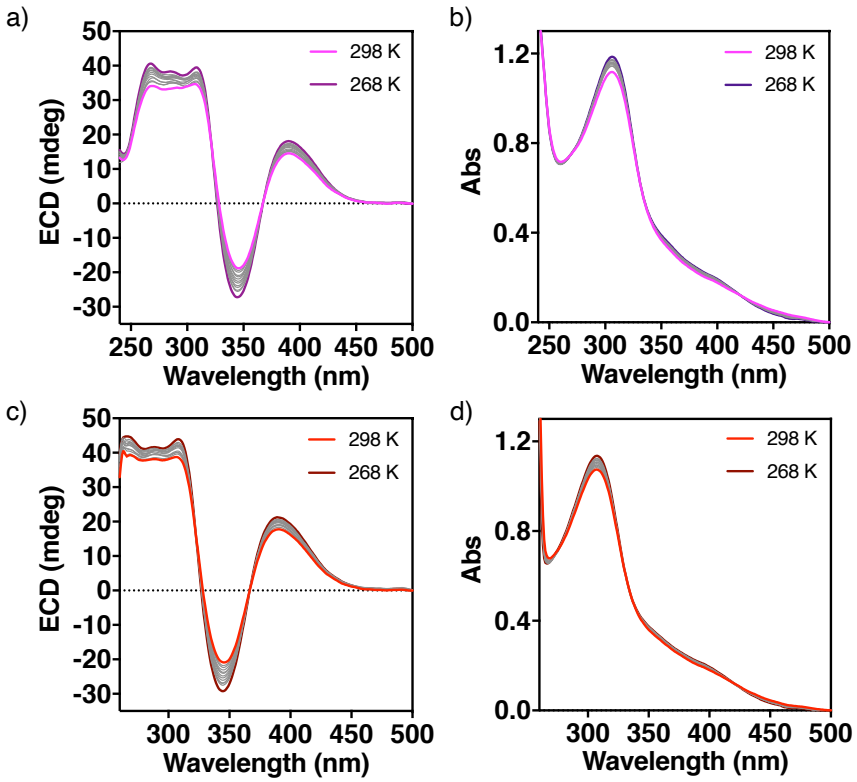

Figure S32. VT-ECD spectra and UV-vis of poly-(*P*)-**2** (0.8 mM) from 298 K to 268 K after fast cooling (1.0 K·min^{-1}) in [(a), (b)] THF and in [(a), (b)] DMF.

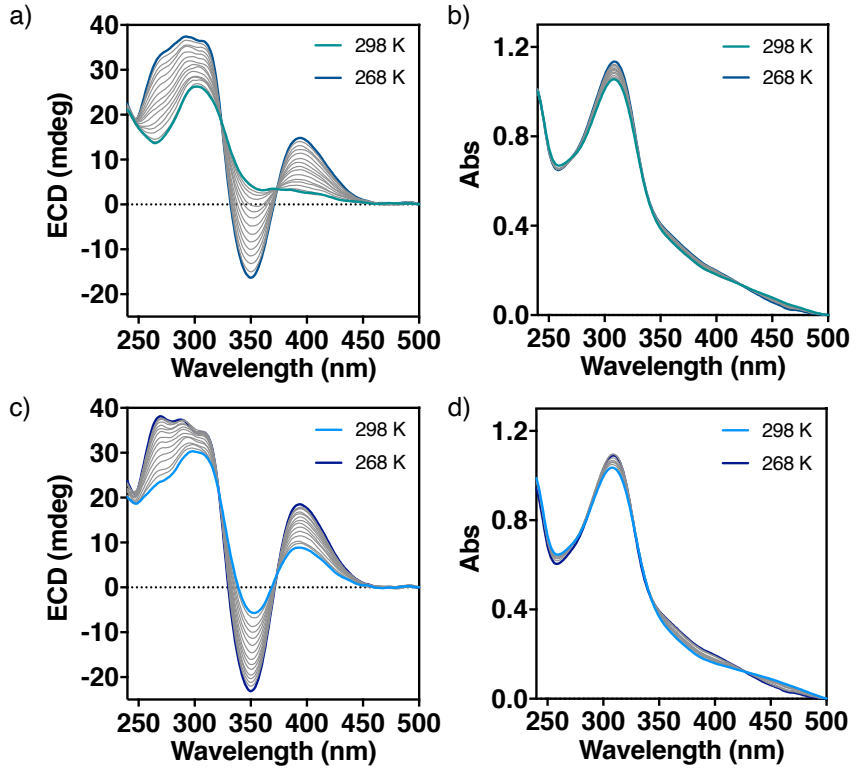

Figure S33. VT-ECD spectra and UV-vis of poly-(*P*)-**2** (0.8 mM) from 298 K to 268 K after fast cooling (1.0 K·min^{-1}) in [(a), (b)] 1,2-DCE and in [(c), (d)] DCM.

5.2.14. AFM Measurements for poly-(*P*)-1

a)

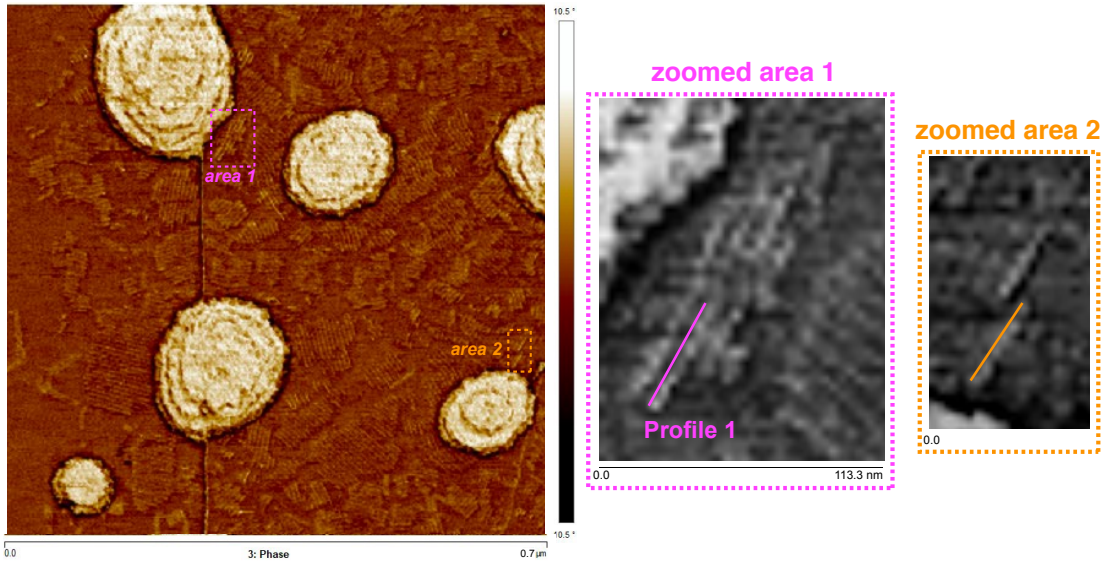

b)

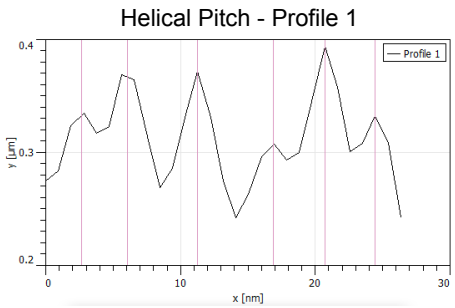

Puntos	X [nm]	Y [nm]	Longitud [nm]
	2.66	332.8	
	6.06	366.9	3.40
	11.26	370.6	5.20
	16.89	307.0	5.63
	20.72	392.8	3.84
	24.43	332.1	3.71

c)

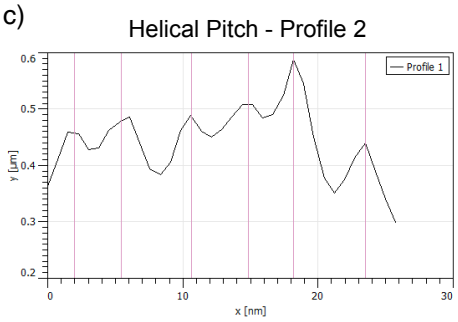

Puntos	X [nm]	Y [nm]	Longitud [nm]
	1.98	457.3	
	5.44	478.3	3.46
	10.64	487.8	5.20
	14.85	508.0	4.21
	18.19	588.3	3.34
	23.51	438.4	5.32

Figure S34. (a) AFM image for poly-(*P*)-**1** (prepared from a THF solution) and zoomed areas or the highlighted regions. (b, c) Graphics depicting the helical pitch profile measured in the indicated areas.

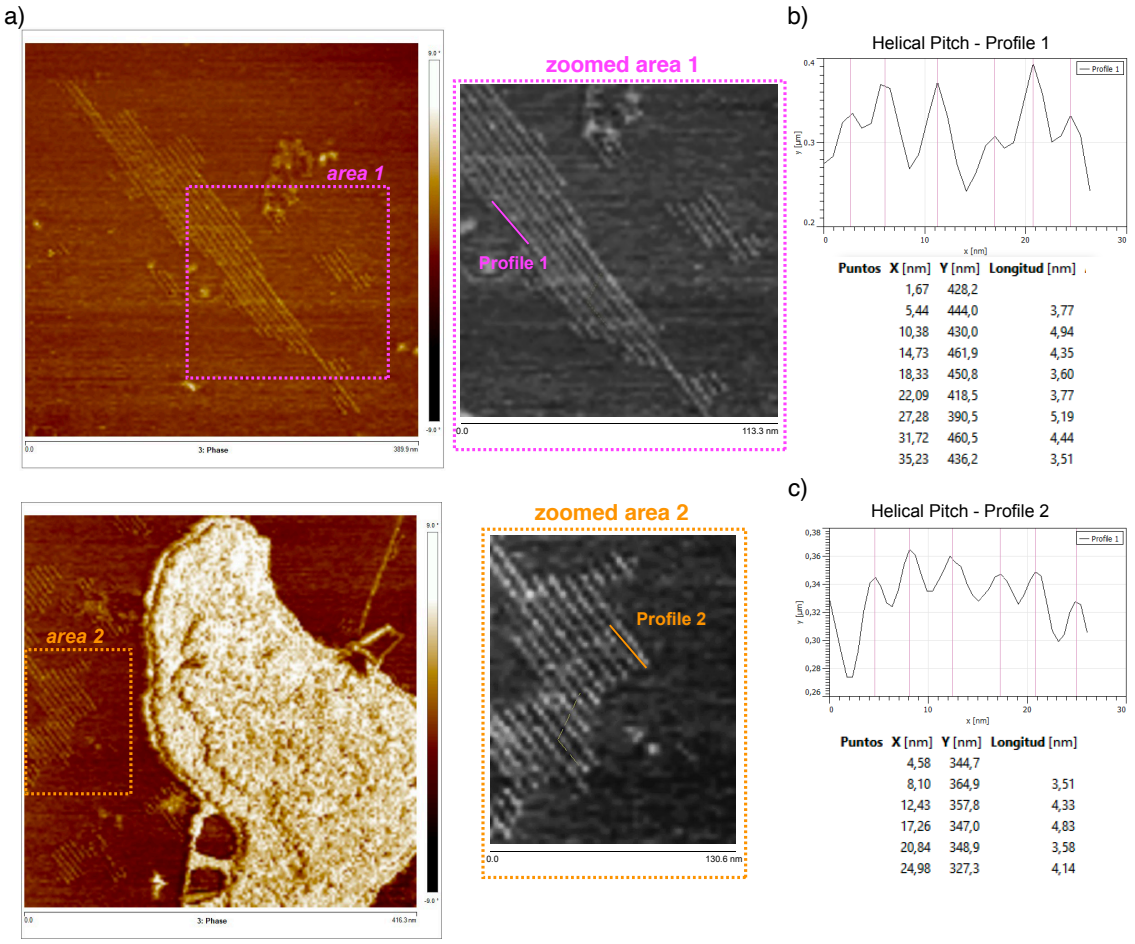

Figure S35. (a) AFM image for poly-(*P*)-**1** (prepared from a 1,2-DCE solution) and zoomed areas or the highlighted regions. (b, c) Graphics depicting the helical pitch profile measured in the indicated areas.

5.2.15. Theoretical Calculations

Considering the difficulties to carry out ECD theoretical calculations on large polymers, representative oligomers were used. So, an oligomer of poly-(*P*)-**1** with n= 9 —where n denotes the number of monomer repeating units (mru)— was employed. The number of monomer units was selected considering the results of previous studies,[157,158,185] where our group evaluated the spectra for a series of poly(phenylacetylene) (PPA) oligomers obtained through systematic increase of monomer units, and concluded that 8-10 monomers were enough to describe the n+2 polymer ECD spectra. The starting structure of poly-(*P*)-**1** was built through adjustment to the experimental data obtained from structural techniques, such as AFM, DSC and UV-vis spectroscopy, defining the four different dihedral angles needed to build up the

helical scaffold (ω_1, ω_2, ω_3 and ω_4; see Figure S36). Additionally, the pendant groups were introduced in the most stable conformation.

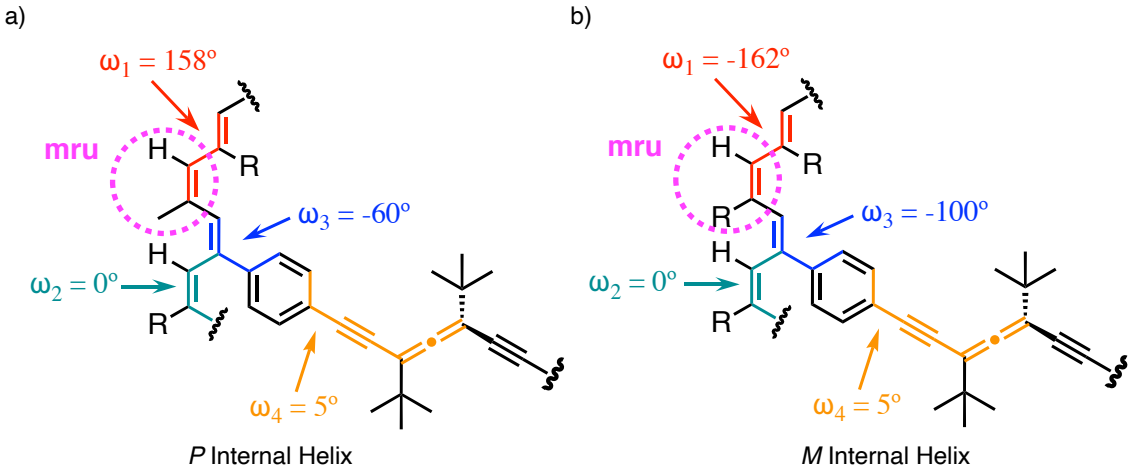

Figure S36. Main dihedral angles involved in the helical structure of PAEPAs and derivatives and the corresponding values obtained for (a) the *P* Helix and for (b) the *M* Helix.

The ECD computational methodology was selected according to the size of polymers under investigation. Taking this into account, to evaluate the theoretical spectra time dependent density functional theory (TD-DFT),[253] in combination with the CAM-B3LYP functional[254] and the 3-21G basis set,[255] have been used (including 80 excitations). All computations were performed with Gaussian-16 (G16RevC.01).[413]

The full width at half height (FWHM) was fixed to 20.0 nm and the ECD were plotted with Gaussian curves. For an efficient comparison and considering the tendency of the TD-DFT method to overestimate the excitation energies, the wavelength and intensity at the maximum/minimum Cotton effect correspondent to the polyene backbone in the theoretical spectra were adjusted to the experimental spectra. Employing the same correction factors, the lambdas were shifted, and the intensities rescaled. The resulting ECD spectra is in good agreement with the experimental ones (Figure S37, S38).

a)

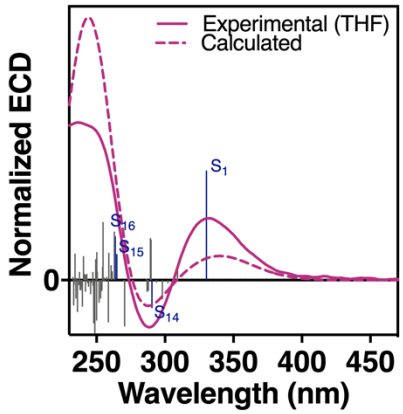

b)

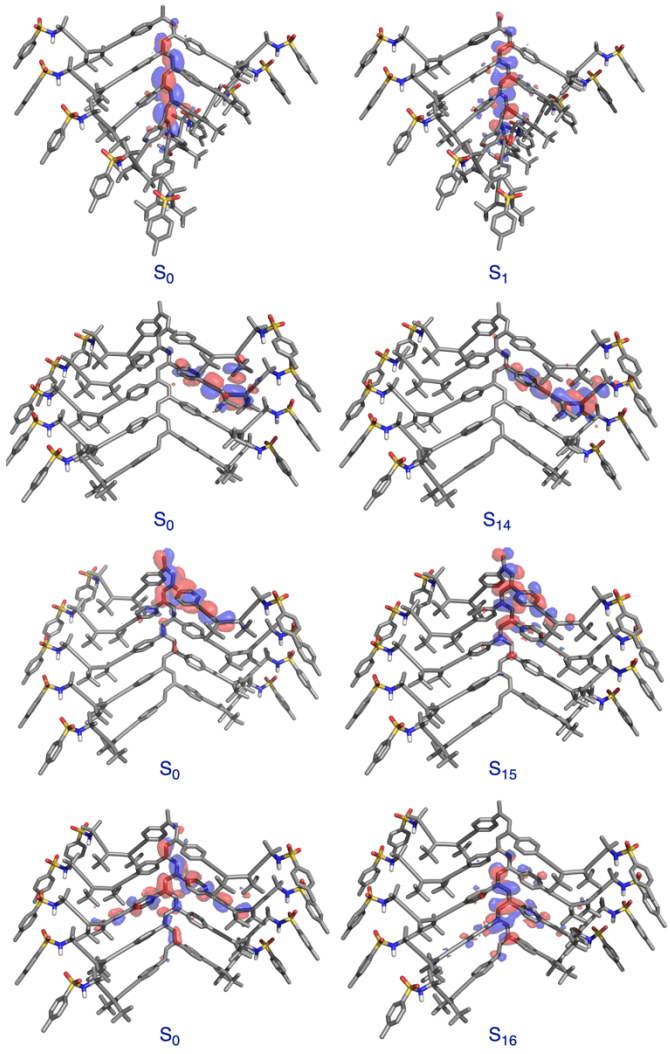

Figure S37. (a) TD-DFT (CAM-B3LYP)/3-21G ECD spectrum for poly-(*P*)-**1**, showing the excited states that contribute the most to the Cotton bands, vs. ECD experimental spectra of poly-(*P*)-**1** in THF. (b) Electron density differences with respect to the ground state for S0 to S1, S0 to S14, S0 to S15 and S0 to S16.

a)

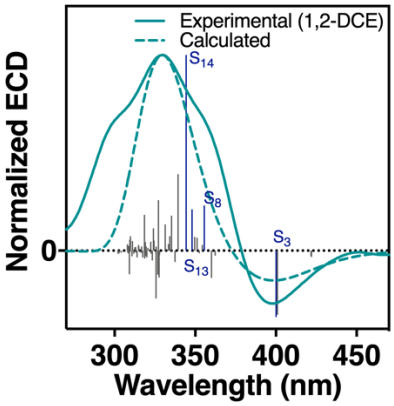

b)

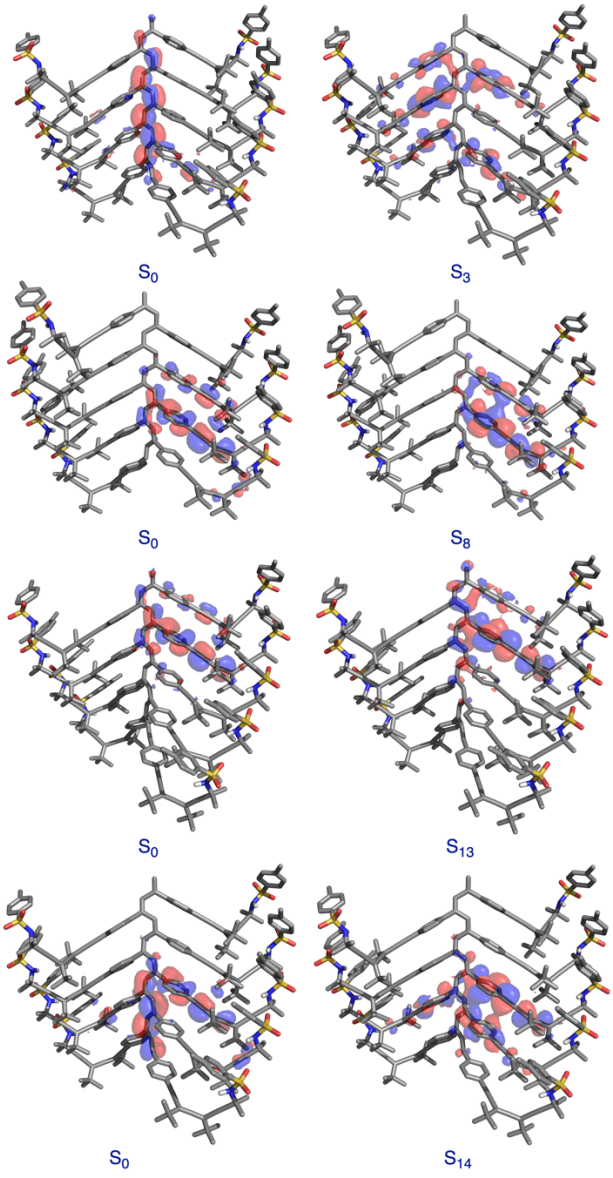

Figure S38. (a) TD-DFT (CAM-B3LYP)/3-21G ECD spectrum for poly-(*P*)-1, showing the excited states that contribute the most to the Cotton bands, vs. ECD experimental spectra of poly-(*P*)-1 in 1,2-DCE. (b) Electron density differences with respect to the ground state for S0 to S1, S0 to S8, S0 to S13 and S0 to S14.

5.2.16. ECD and UV-vis studies of poly-(*P*)-1 in presence of different anions

Solutions of the corresponding polymer (0.8 mM in anhydrous THF) and for the corresponding monomers (1.60 mM in anhydrous 1,2-DCE) were measured in the presence of tetrabutylammonium (TBA) salts derived from N_3^-, CN^-, F^- anions. TBA salts were dried for 12 h at 323 K under high vacuum. Then, these salts were dissolved in anhydrous MeCN.

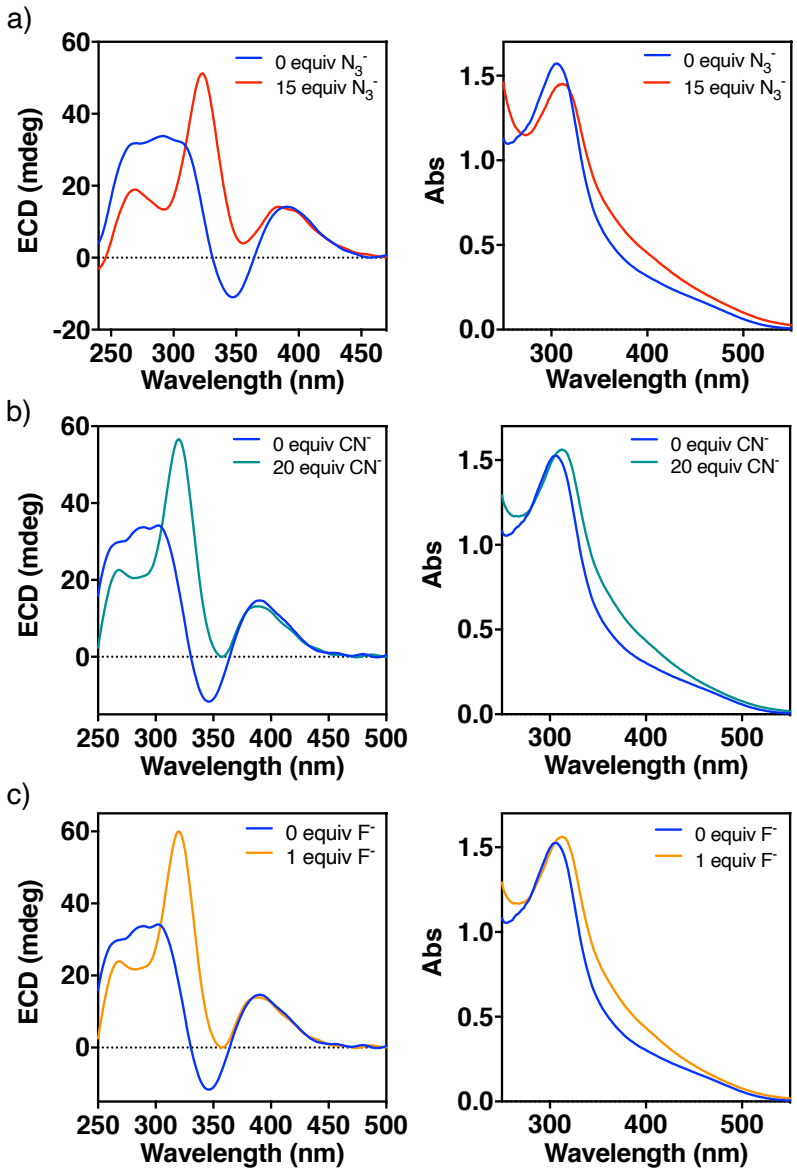

Figure S39. ECD and UV-vis spectra of poly-(*P*)-1 in THF (0.80 mM) titrated with different amounts of anions (0.35 mM in MeCN) at rt (298 K).

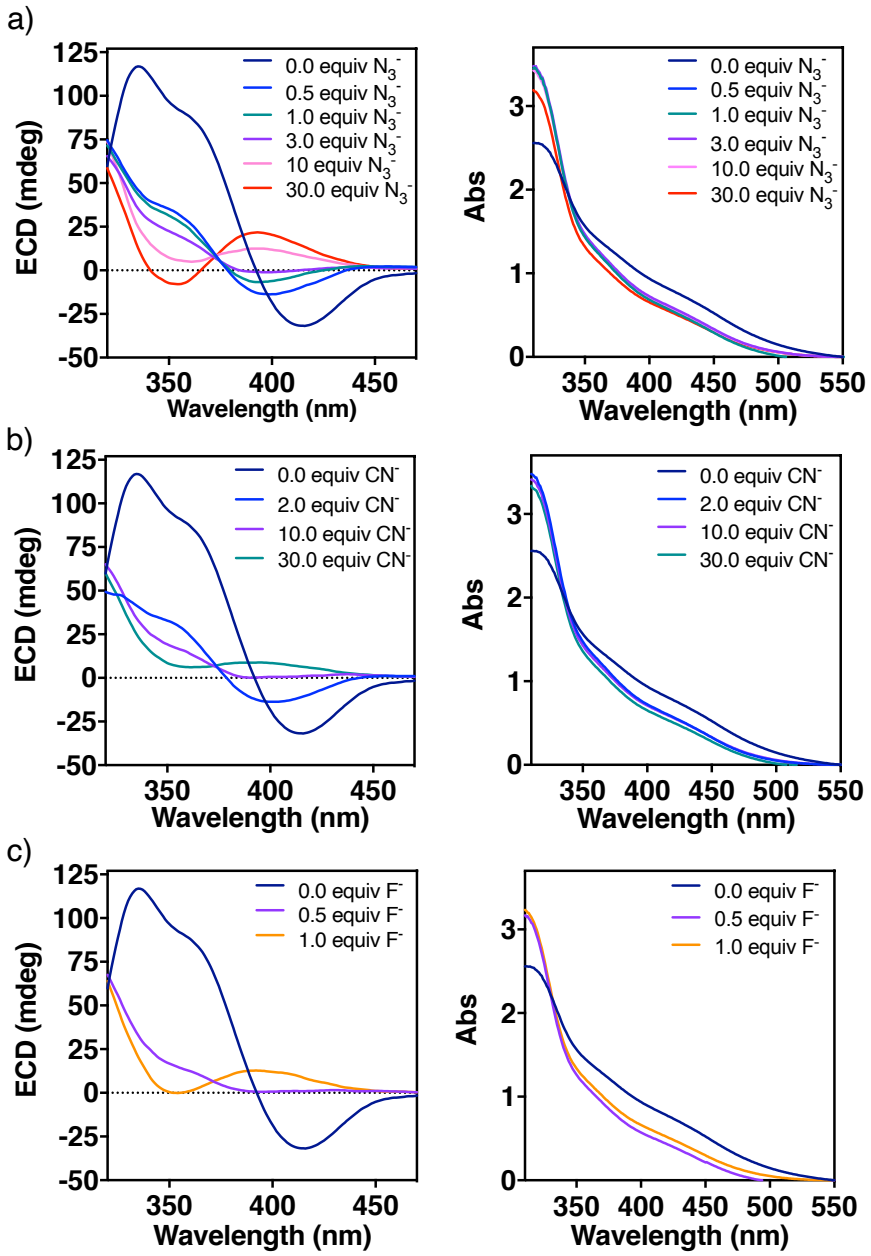

Figure S40. ECD and UV-vis spectra of poly-(*P*)-**1** in 1,2-DCE (1.60 mM) titrated with different amounts of anions (0.35 mM in MeCN) at 268 K (cooling at 0.1 K·min^{-1}).

Furthermore, the reversibility of the process was demonstrated by washing the organic solution with aqueous media to remove the anions (2 x 2mL). The resulting organic phase was dried over anhydrous Na_2SO_4 and after evaporation *in vacuo*, the sample was redissolved in 1,2-DCE (1.6 mM), recovering the original helical sense as shown by ECD (Figure S41).

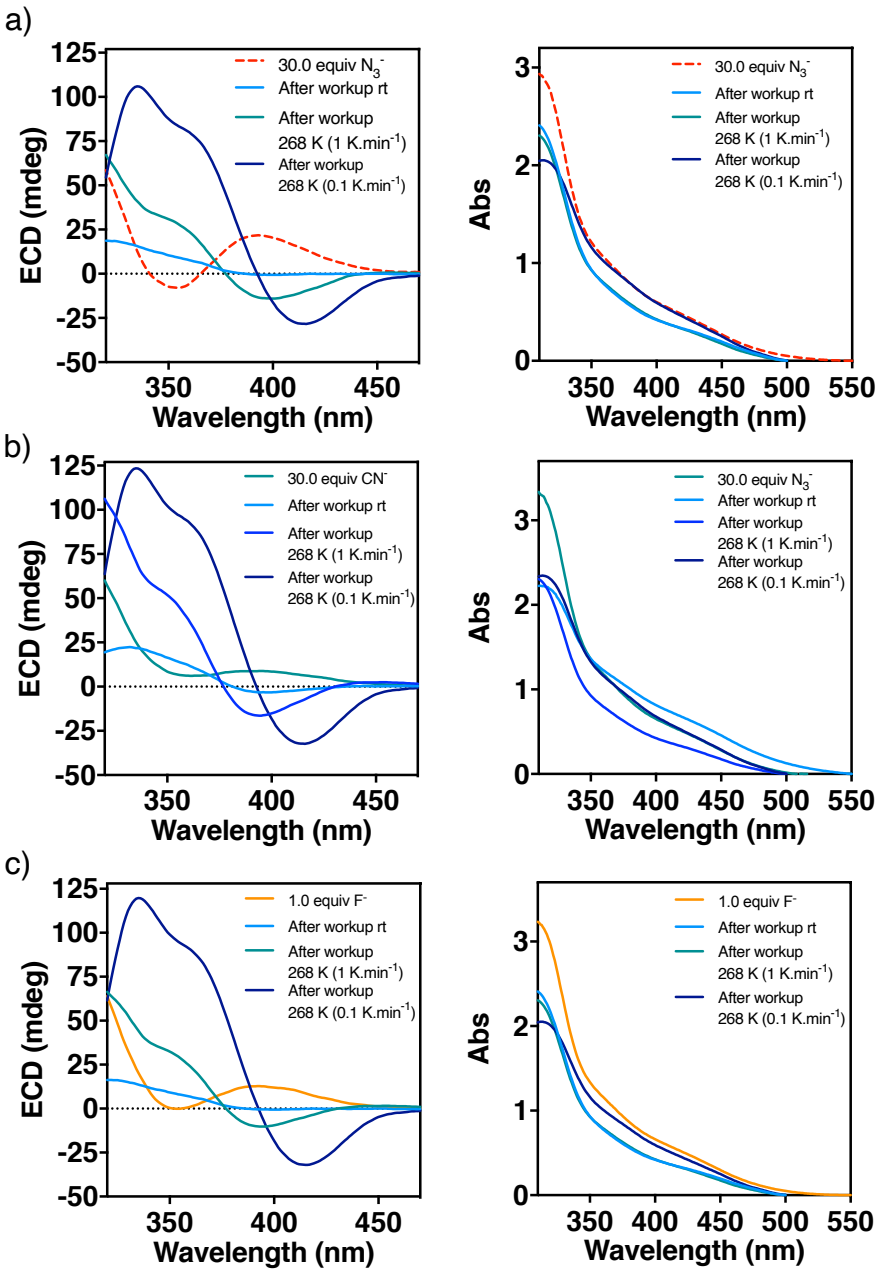

Figure S41. ECD and UV-vis spectra of poly-(*P*)-**1** in 1,2-DCE (1.60 mM) titrated with different amounts of anions (0.35 mM in MeCN) at 268 K (cooling at 0.1 K·min^{-1}) and the data after anions removal.

5.2.17. NMR Anion Titration Experiments

^{1}H NMR experiments were measure to solutions of mono-(*P*)-**1** and poly-(*P*)-**1** (5.9 mM) in THF-d_8 and in CD_2Cl_2 upon addition of tetrabutylammonium (TBA) salts derived from N_3^-, F^- anions (0.38 mM in MeCN). TBA salts were dried for 12 h at 323 K under high vacuum. Then, these salts were dissolved in anhydrous MeCN.

*NMR studies of the mono-(P)-**1** in the presence of different anions*

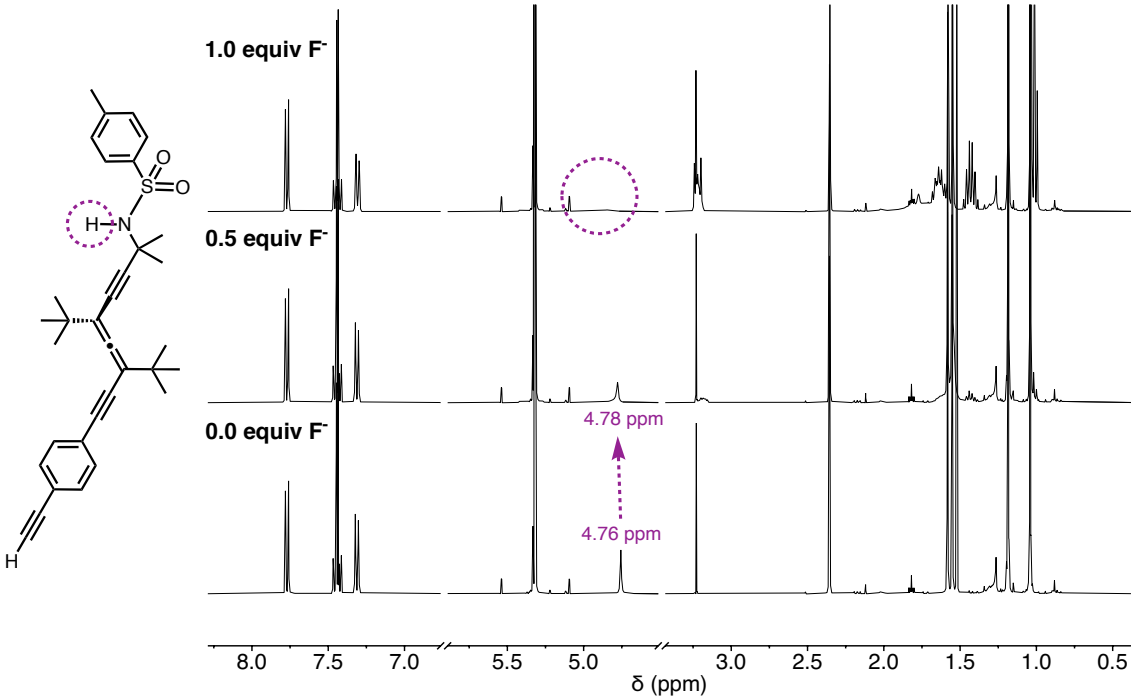

Figure S42. ^{1}H-NMR of mono-(*P*)-**1** in the presence of different amounts of TBAF (300 MHz, CD_2Cl_2).

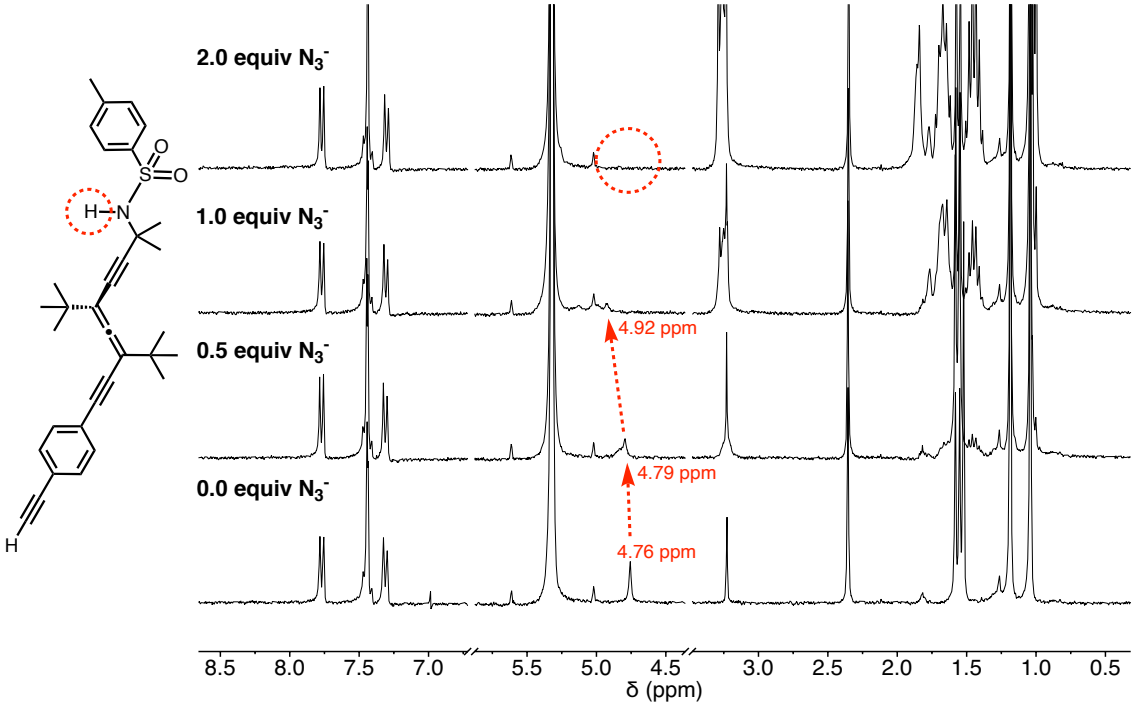

Figure S43. ^{1}H-NMR of mono-(*P*)-**1** in the presence of different amounts of $TBAN_3$ (300 MHz, CD_2Cl_2).

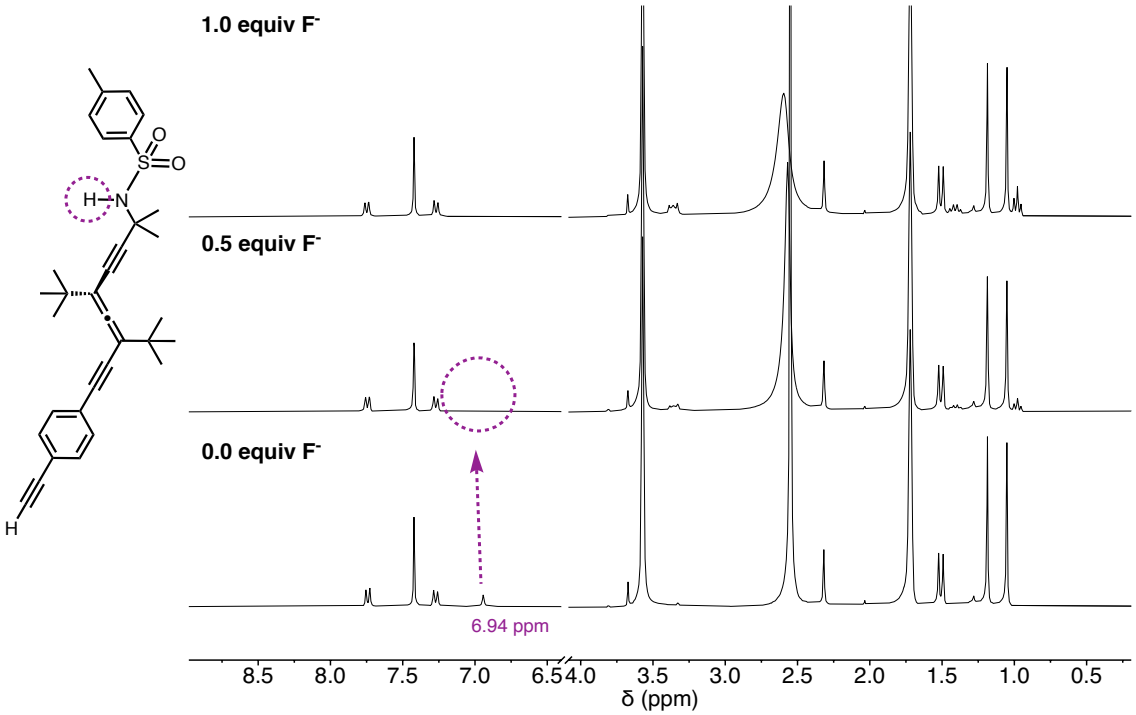

Figure S44. ^{1}H-NMR of mono-(*P*)-**1** in the presence of different amounts of TBAF (300 MHz, THF-d_8).

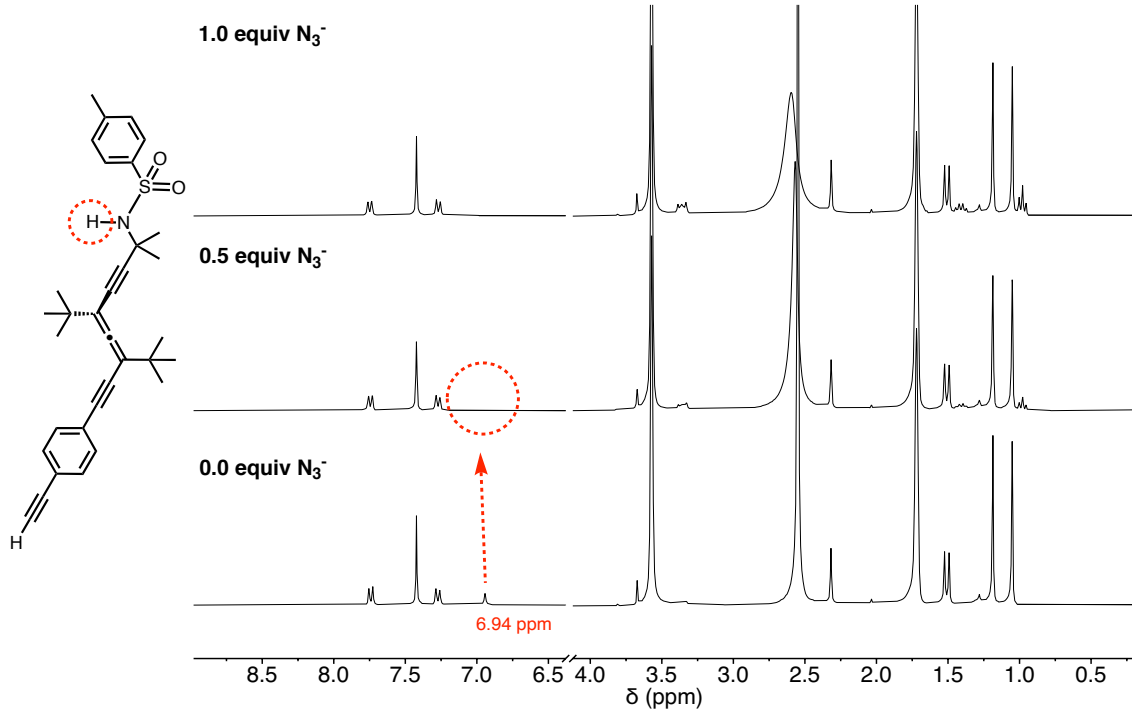

Figure S45. ^{1}H-NMR of mono-(*P*)-**1** in the presence of different amounts of $TBAN_3$ (300 MHz, THF-d_8).

*NMR studies of the poly-(P)-**1** in the presence of different anions*

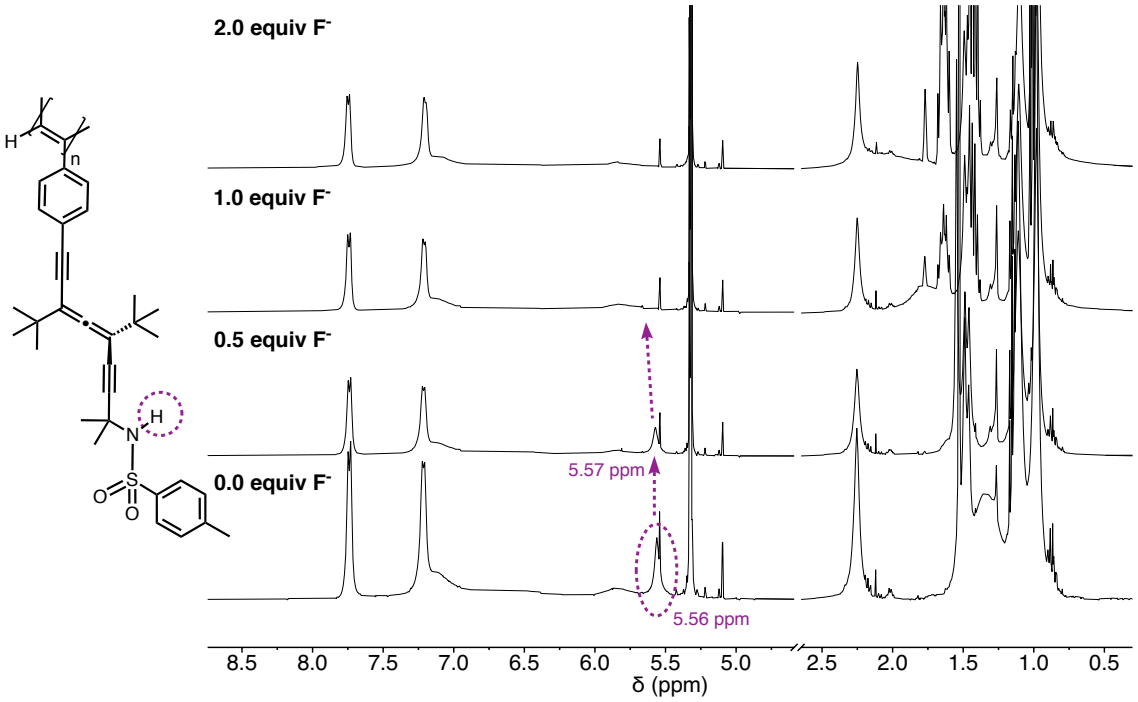

Figure S46. ^{1}H-NMR of poly-(*P*)-**1** in the presence of different amounts of TBAF (300 MHz, CD_2Cl_2).

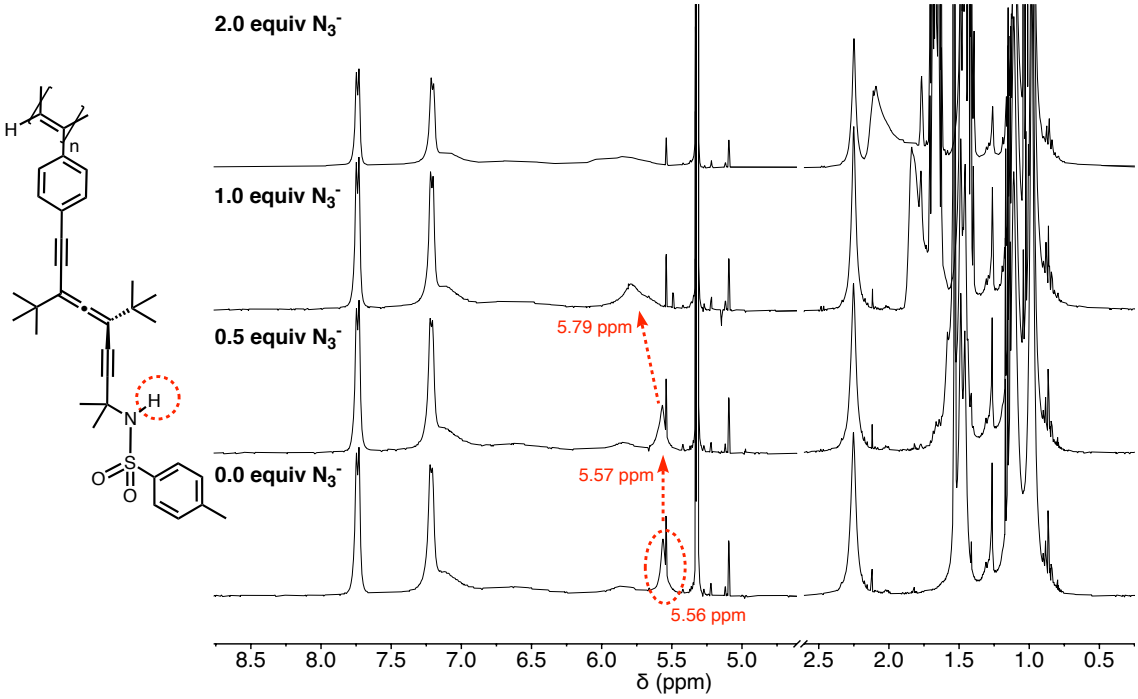

Figure S47. ^{1}H-NMR of poly-(*P*)-**1** in the presence of different amounts of $TBAN_3$ (300 MHz, CD_2Cl_2).

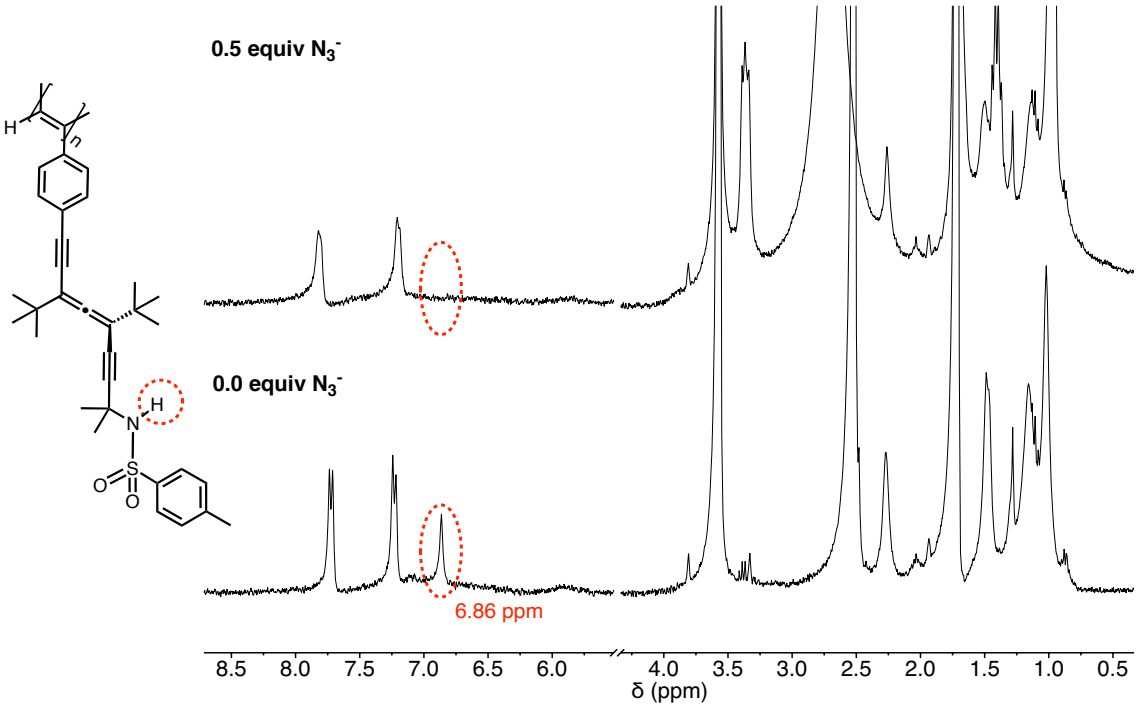

Figure S48. ^{1}H-NMR of poly-(*P*)-**1** in the presence of different amounts of $TBAN_3$ (300 MHz, THF-d_8).

5.3. Experimental Section and Methodology Chapter 3.3.

5.3.1. Materials and Methods

Reactions were conducted in dry solvents under argon unless otherwise stated. Et_3N was freshly distilled from CaH_2 under argon atmosphere. $[Rh(nbd)Cl]_2$ was purchased from Sigma-Aldrich (96%). All other chemicals were purchased from Sigma-Aldrich, Acros Organics, Alfa Aesar, Fluorochem, TCI Chemicals or Abcr and they were used as received.

The abbreviation "rt" refers to reactions carried out at a temperature between 21-25 ˚C. Reaction mixtures were stirred using Teflon-coated magnetic stir bars. Thin layer chromatography (TLC) was carried out on pre-coated silica gel F254 plates with visualization under UV light or by dipping the plate into solutions of phosphomolybdic acid or potassium permanganate solutions followed by heating. Column chromatography was performed on silica gel (40-60 μm) unless otherwise stated.

NMR experiments have been recorded in a Bruker spectromer (^{1}H frequency 300 mHz or 500 mHz). NMR titration experiments have been recorded in a Varian 300 spectromer (^{1}H frequency 300 mHz).

^{1}H ROESY NMR experiments have been measured at 278 K in a Bruker NEO-750 spectrometer (^{1}H frequency 750 mHz).

ECD measurements were done in a Jasco-720 and UV-vis spectra were registered in a Jasco V-630 with a 1 mm quartz cuvette. The amount of polymer used is indicated in the corresponding section.

Optical rotation was measured in a Jasco-P2000 with a 1 cm quartz cuvette at rt (c = 10 mg·mL^{-1}, $CHCl_3$).

Enantiomers (*P*)-**DEA** and (*M*)-**DEA** were resolved by semipreparative HPLC using the CSP Chiralpak® IA (Diacel Chemical Industries Ltd.). Elution was performed with a mixture of Hexane:^{i}PrOH 99.2:0.8 at a flow of 3.5 mL·min^{-1}. Under these conditions, 100 μL of a solution of (±)-**DEA** in Hexane (15 mg·mL^{-1}) was injected.

Raman spectra were carried out in a Reinshaw confocal Raman spectrometer (Invia Reflex model) equipped with two lasers (diode laser 785 nm and Ar laser 514 nm).

GPC studies were carried out in a Waters Alliance 2695 HPLC with a UV-2489 detector (Waters) mns equipped with Phenomenex GPC columns (103 Å, 104 Å and 105 Å). The amount of polymer used was 0.5 $mg \cdot mL^{-1}$. THF was used as eluent (flow rate: 1 $mL \cdot min^{-1}$) and as inner standard, polystyrene narrow standards (PSS) were used.

DSC traces were obtained in a DSC Q200 Tzero Technology (TA Instruments, New Castle, UK), equipped with a refrigerated cooling system RCS90 (TA Instruments, New Castle, UK), using a Tzero low-mass aluminum pan.

TGA traces were obtained in a TGA Q5000 (TA Instruments, New Castle, UK) using a platinium pan.

AFM measurements were performed in a Multimode V Scanning Probe Microscope (Veeco Instruments) in air at rt, with standard silicon cantilevers and supersharp cantilevers in tapping mode using 12 μm and 1 μm scanners. Nanoscope processing software and WSxM 4.0 Beta 1.0 [4] (Nanotec Electrónica, S.L.) was used for image analysis. All measurements were performed at CACTI (University of Vigo, Spain).

PyMOL was used as a molecular visualization system.

5.3.2. Synthesis of Monomers

The following compounds were synthesized according to literature procedures: (*P*)-**DEA** and (*M*)-**DEA**,[251] **1**,[55] **2**[300].

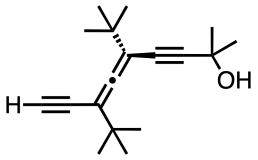

(*P*)-**DEA**

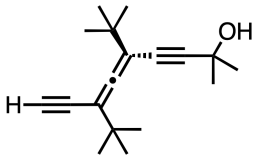

(*M*)-**DEA**

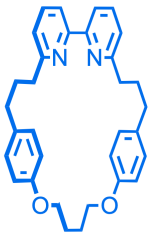

1

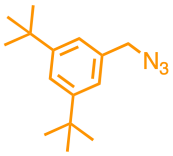

2

Di-tert-butyl-2-methyl-9-(4-((trimethylsilyl)ethynyl)phenyl)nona-5,6-dien-3,8-diyn-2-ol

(S1)

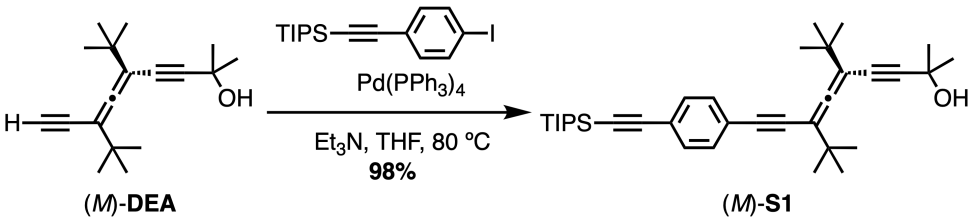

(*M*)-**DEA** (*M*)-**S1**

In a flamed Schlenk tube, ((4-iodophenyl)ethynyl)triisopropylsilane (110 mol%, 1.280 mmol, 492 mg), [$Pd(PPh_3)_4$] (10 mol%, 0.016 mmol, 18 mg), CuI (1 mol%, 0.002 mmol, 1 mg) were placed. The yellow solution was bubbled with Ar and then a solution of (*M*)-**DEA**[S1] (100 mol%, 1.160 mmol, 300 mg) in a mixture of Et_3N (2 mL) and THF (1 mL) was added *via* cannula. The reaction mixture was stirred at 80 °C for 16 h. The reaction mixture was washed first with sat. aq NH_4Cl solution, distilled water and then with sat. aq NaCl solution. The aqueous phases were combined and extracted with DCM (3 x 10 mL). The combined organic phases were dried over anhyd Na_2SO_4. Evaporation *in vacuo* and purification by flash chromatography on silica gel (hexane: EtAcO (9:1) afforded (*M*)-**S1** (591 mg, 98%) as a yellow oil.

Compounds (±)-**S1** and enantiopure (*P*)-**S1** were obtained from (±)-**DEA** and (*P*)-**DEA** respectively, by applying the same protocol as for (*M*)-**S1**.

Molecular Formula: $C_{35}H_{50}OSi$**. MW:** 514.90 **g/mol.**

^{1}H-NMR (300 MHz, $CDCl_3$, 298K) *δ:* 7.39 (m, 4H), 1.57 (s, 6H), 1.20 (s, 9H), 1.16 (s, 9H), 1.18 – 1.08 (m, 30H).

^{13}C-NMR (75 MHz, $CDCl_3$, 298K) *δ:* 211.4, 132.0, 131.3, 123.7, 123.2, 106.9, 103.4, 103.0, 97.5, 92.6, 92.4, 85.3, 75.9, 65.9, 35.8, 35.7, 31.6, 29.2, 29.1, 18.8, 11.5.

HRMS (ESI$^+$): *m/z* calcd. for $C_{35}H_{50}OSi$ 514.3631; found 515.3698 $[M+H]^+$.

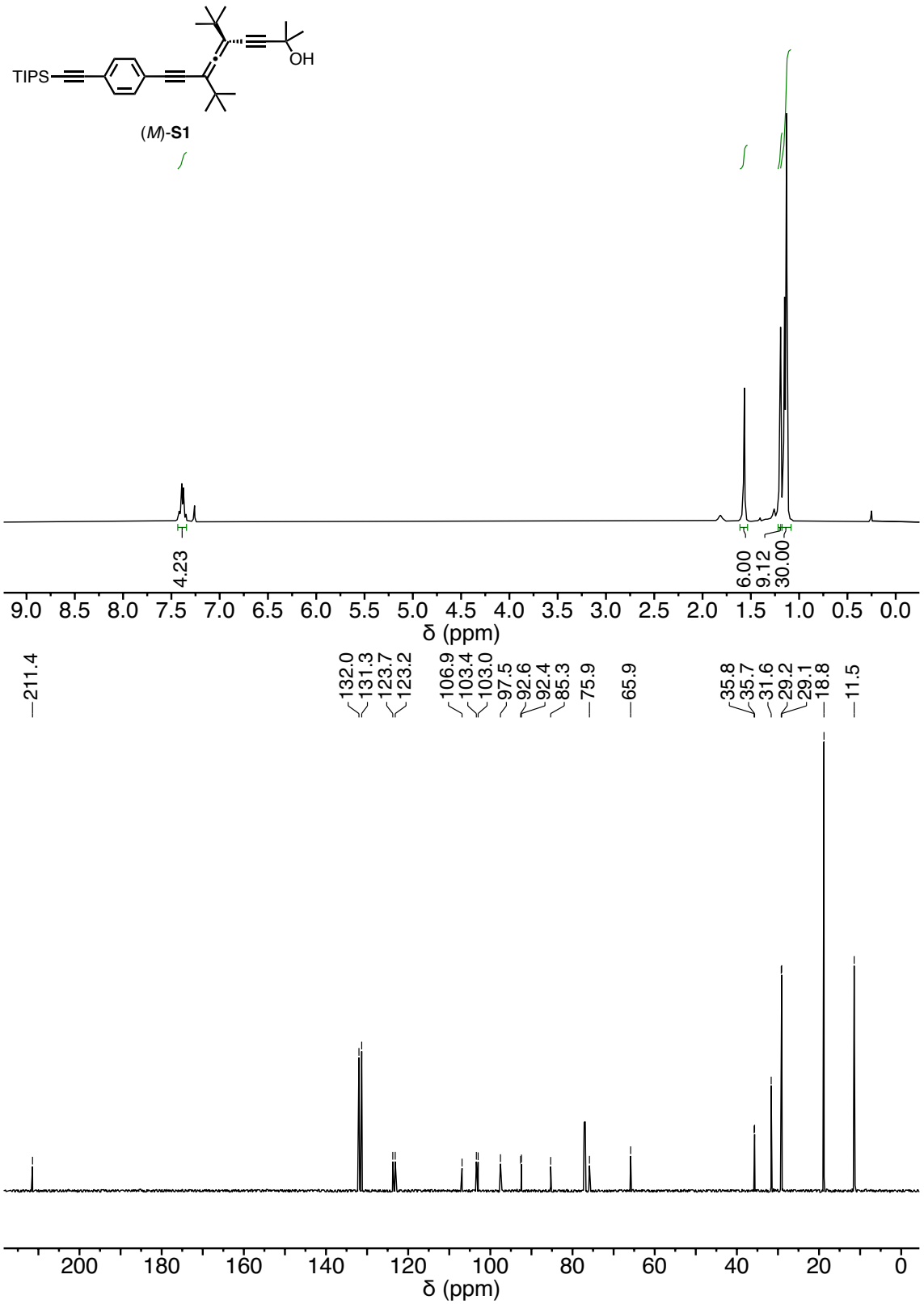

Figure S1. ^{1}H-NMR and ^{13}C-NMR of (*M*)-**S1** in $CDCl_3$.

*((4-(3,5-di-tert-butylhepta-3,4-dien-1,6-diyn-1-yl)phenyl)ethynyl)triisopropylsilane (**3**)*

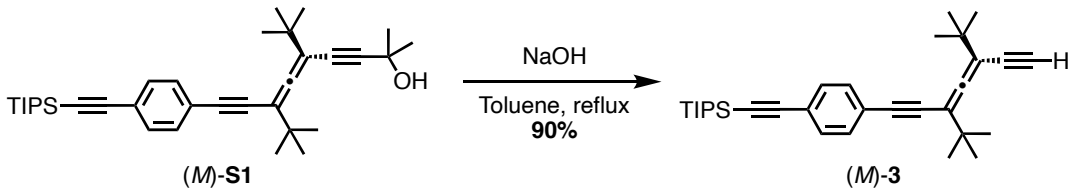

(*M*)-**S1** (*M*)-**3**

NaOH (650 mol%, 4.550 mmol, 182 mg) was pulverized, introduced in a round-bottom flask and flame-dried under vacuum and then filled with Ar. 20 mL of dried toluene were added. (*M*)-**S1** (100 mol%, 0.700 mmol, 360 mg) was dissolved in dried toluene (10 mL) and the solution was transferred to the NaOH-toluene mixture. The reaction mixture was refluxed for 2 h and then disrupted by adding distilled water. Then, the mixture was extracted with EtAcO. Evaporation *in vacuo* and purification by flash chromatography on silica gel (hexane: EtAcO (9.5:0.5) afforded (*M*)-**3** (288 mg, 90%) as a yellow oil.

Compounds (±)-**3** and enantiopure (*P*)-**3** were obtained from (±)-**S1** and (*P*)-**S1** respectively, by applying the same protocol as for (*M*)-**3**.

Molecular Formula: $C_{32}H_{44}Si$**. MW:** 456.7890 **g/mol.**

^{1}H-NMR (300 MHz, $CDCl_3$, 298K) *δ:* 7.39 (m, 4H), 3.02 (s, 1H), 1.20 (s, 9H), 1.18 (s, 9H), 1.13 (s, 21H).

^{13}C-NMR (75 MHz, $CDCl_3$, 298K) *δ:* 212.3, 132.0, 131.4, 123.7, 123.2, 106.9, 103.9, 102.6, 92.7, 84.9, 80.7, 77.6, 35.9, 35.5, 29.2, 29.0, 18.8, 11.5.

HRMS (ESI^{+}): *m/z* calcd. for $C_{32}H_{44}Si$ 456.3212; found 457.3282 $[M+H]^{+}$.

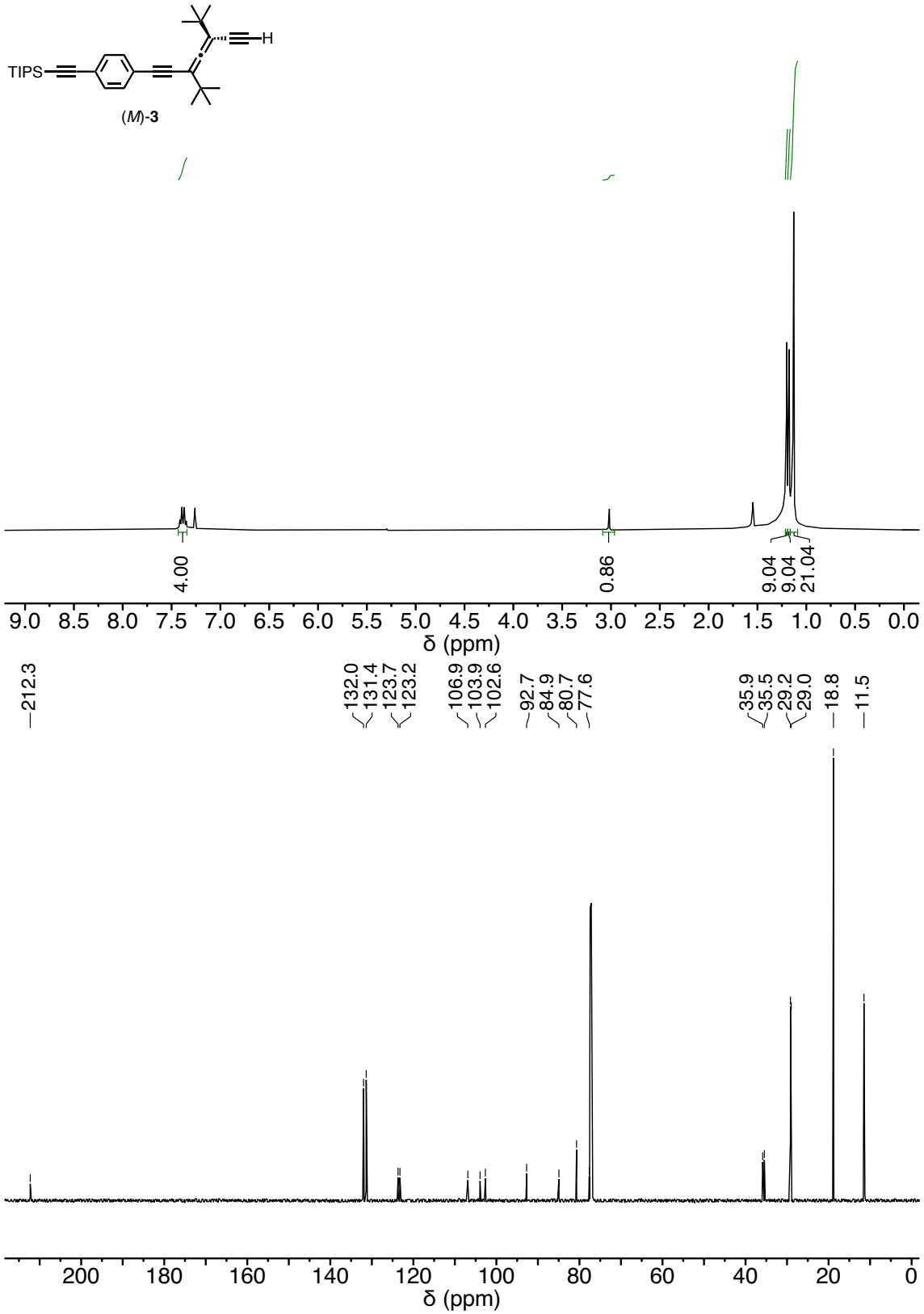

Figure S2. ^{1}H-NMR and ^{13}C-NMR of (*M*)-**3** in $CDCl_3$.

*4-(5-(tert-butyl)-2,2-dimethyl-7-(4-((triisopropylsilyl)ethynyl)phenyl)hepta-3,4-dien-6-yn-3-yl)-1-(3,5-di-tert-butylbenzyl)-1H-1,2,3-triazole (**S2**)*

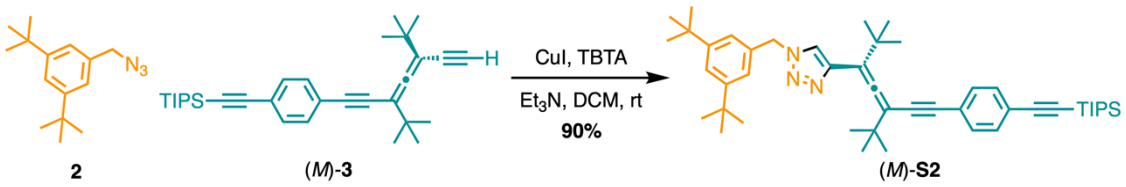

2 (*M*)-**3** (*M*)-**S2**

To **2**(100 mol%, 0.114 mmol, 28 mg), (*M*)-**3** (100 mol%, 0.114 mmol, 52 mg), CuI (6 mol%, 0.007 mmol, 1 mg) and TBTA (8 mol%, 0.009 mmol, 5 mg) in DCM (2 mL) was added Et_3N (0.1 mL) and the mixture was stirred at rt for 2h. The mixture was quenched with a saturated EDTA/NH_3 solution (10 mL) and then the aqueous phase was extracted with DCM (3 x 5 mL). The combined organic phases were dried over anhydrous Na_2SO_4. Evaporation *in vacuo* and purification by flash chromatography on silica gel (hexane: EtAcO (9:1) afforded (*M*)-**S2** (74 mg, 90%) as a yellow oil.

The same protocol was applied for (±)-**3** and (*P*)-**3** to obtain (±)-**S2** and (*P*)-**S2**, respectively.

Molecular Formula: $C_{49}H_{67}N_3Si$**. MW:** 726.18 **g/mol.**

^{1}H-NMR (500 MHz, $CDCl_3$, 298K) *δ:* 7.42 – 4.31 (m, 7H), 7.07 (m, 2H), 5.51 (s, 2H) 1.33 (s, 9H), 1.29 (s, 18H), 1.17 (s, 9H), 1.13 (s, 21H).

^{13}C-NMR (101 MHz, $CDCl_3$, 298K) *δ:* 206.9, 151.9, 144.0, 134.1, 132.0, 131.3, 123.8, 123.0, 122.7, 122.2, 109.9, 106.9, 102.7, 92.6, 91.9, 85.9, 54.6, 35.6, 35.3, 35.0, 31.5, 29.8, 29.3, 18.8, 11.5.

HRMS (ESI$^+$): *m/z* calcd. for $C_{49}H_{67}N_3Si$ 725.5104; found 726.5168 $[M+H]^+$.

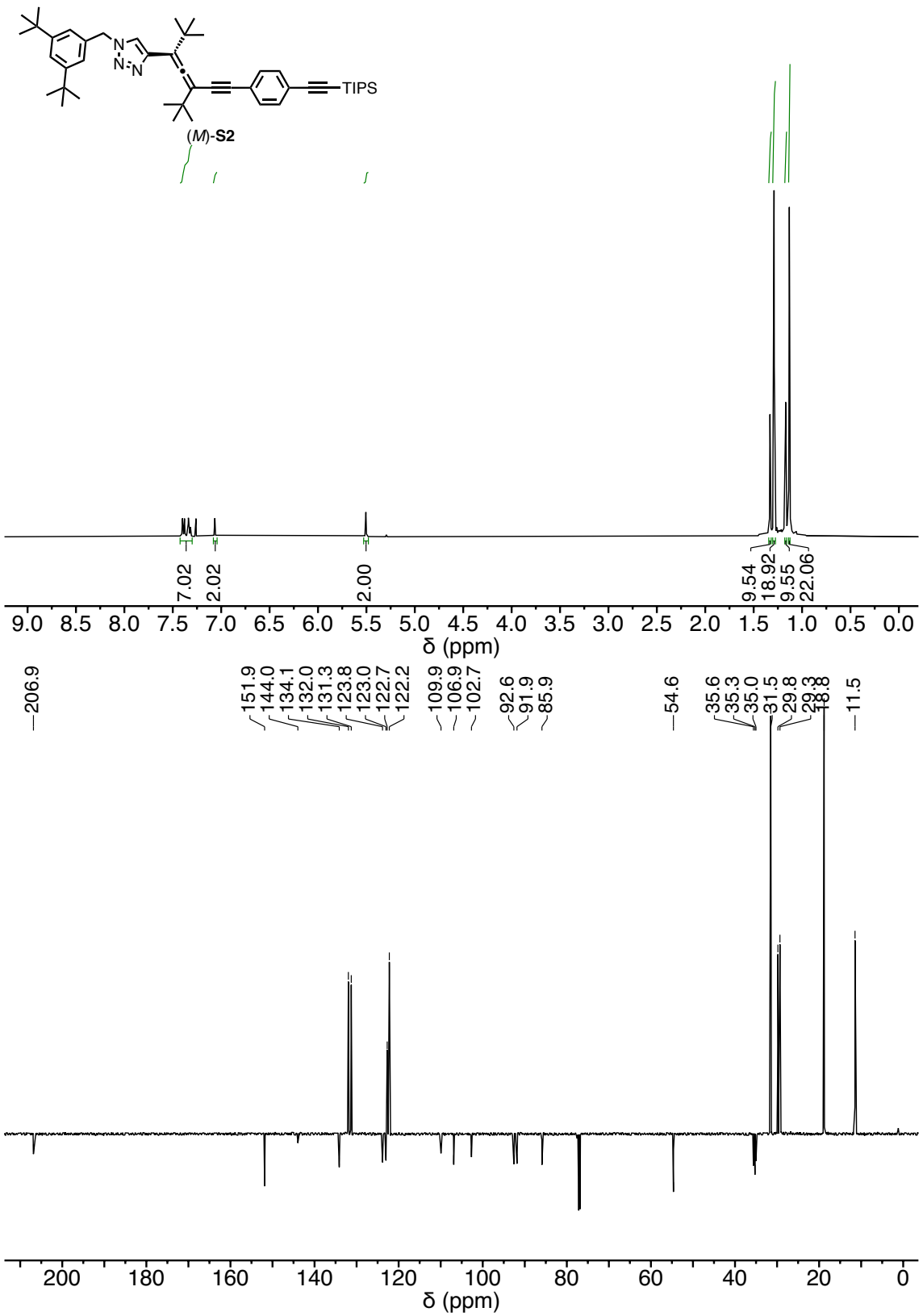

Figure S3. ^{1}H-NMR and DEPTQ-NMR of (*M*)-**S2** in $CDCl_3$.

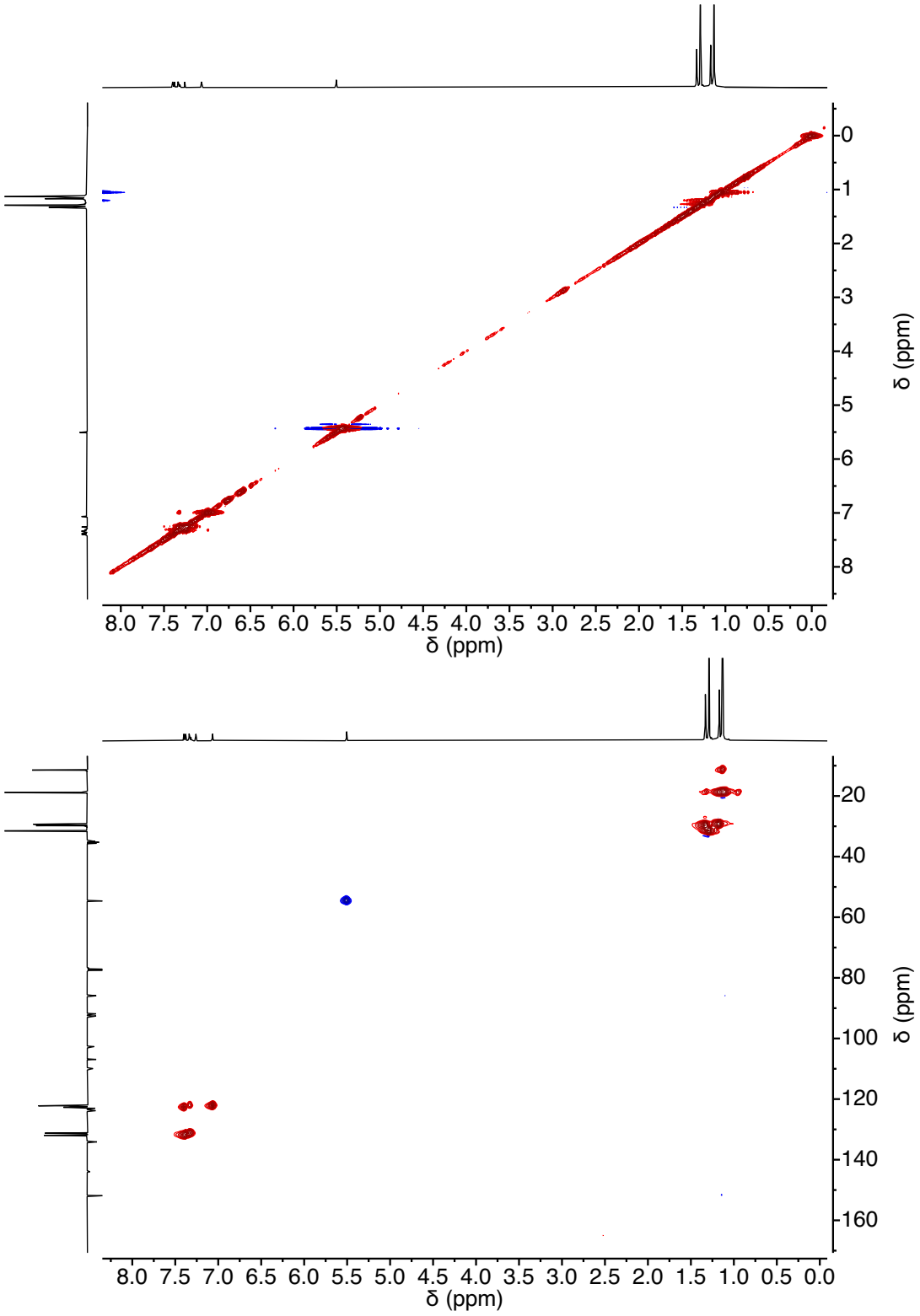

Figure S4. COSY-NMR and HSQC-NMR of (*M*)-**S2** in $CDCl_3$.

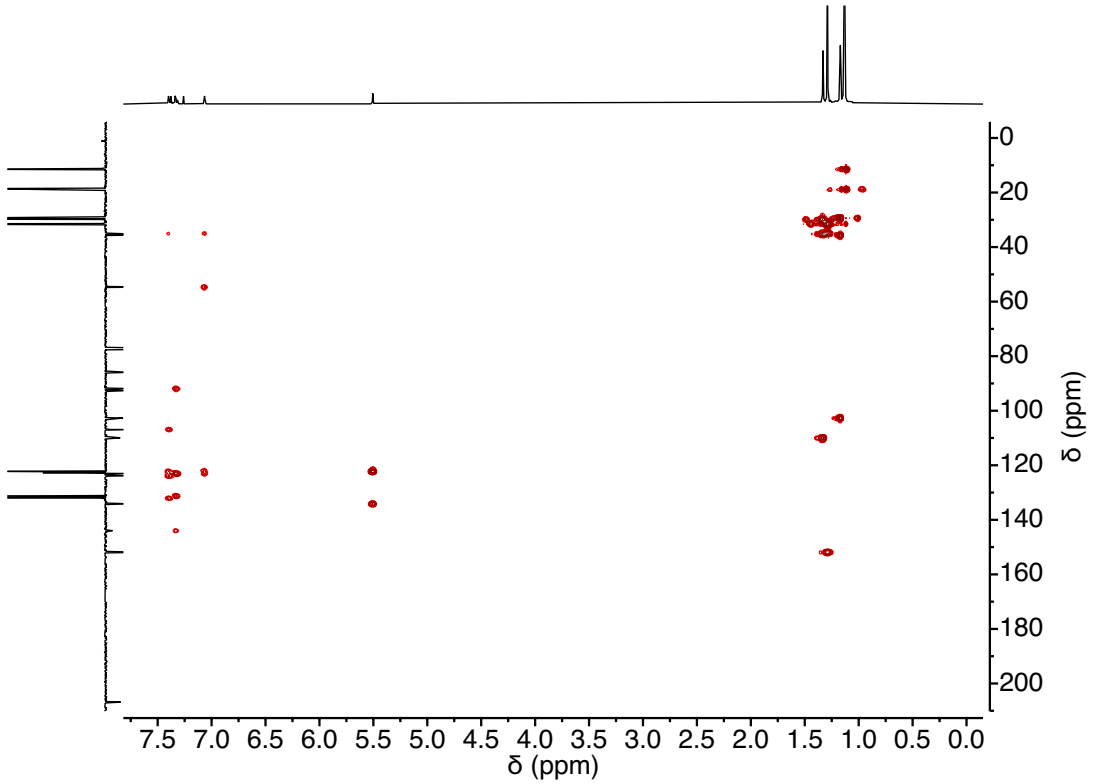

Figure S5. HMBC-NMR (*M*)-**S2** in $CDCl_3$.

*Non-interlocked monomer: mono-**1***

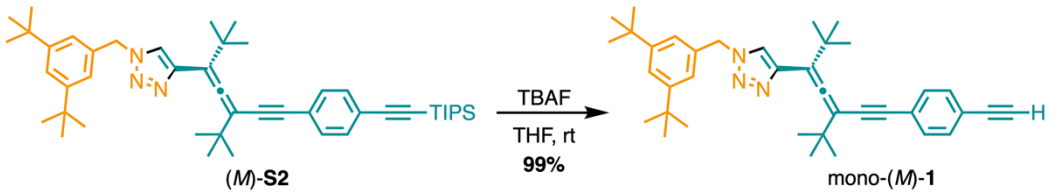

To a solution of (*M*)-**S2** (100 mol%, 0.096 mmol, 70 mg) in THF (2 mL) was added TBAF (0.1 mL) and the mixture was stirred at rt for 1h. The reaction mixture was washed first with sat. aq NH_4Cl solution (10 mL), distilled water (10 mL) and then with sat. aq NaCl solution (10 mL). The aqueous phases were combined and extracted with DCM (3 x 10 mL). The combined organic phases were dried over anhyd Na_2SO_4. Evaporation *in vacuo* and purification by flash chromatography on silica gel (hexane: EtAcO (9.5:0.5) afforded mono-(*M*)-**1** (54 mg, 99%) as a yellow oil.

The same protocol was applied for (±)-**S2** and (*P*)-**S2** to obtain mono-(±)-**1** and mono-(*P*)-**1**, respectively.

For mono-(*M*)-**1**, $[\alpha]_D^{20}$= -246 (*c* = 10 mg·mL^{-1}, $CHCl_3$); for mono-(*P*)-**1**, $[\alpha]_D^{20}$= +238 (*c* = 10 mg·mL^{-1}, $CHCl_3$).

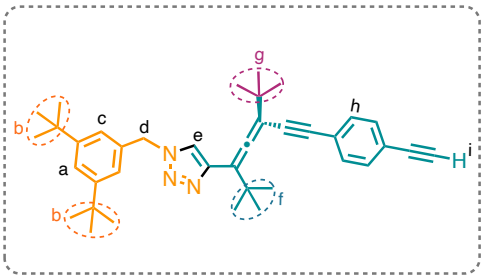

Molecular Formula: $C_{40}H_{47}N_3$**. MW:** 569.84 **g/mol.**

^{1}H-NMR (500 MHz, $CDCl_3$, 298K) *δ:* 7.42 – 7.39 (m, 3H, H_h, H_a), 7.36 – 7.34 (m, 2H, H_h), 7.32 (s, 1H, H_e), 7.06 (d, *J* = 7.4 Hz, 2H, H_c) 5.51 (s, 2H, H_d), 3.15 (s, 1H, H_i), 1.32 (s, 9H, H_f), 1.28 (s, 18H, H_b), 1.16 (s, 9H, H_g).

^{13}C-NMR (101 MHz, $CDCl_3$, 298K) *δ:* 206.9, 151.9, 143.9, 134.1, 132.1, 131.4, 124.5, 122.7, 122.2, 121.5, 110.0, 102.6, 91.6, 86.2, 83.5, 78.8, 54.6, 35.6, 35.3, 35.0, 31.5, 29.8, 29.3.

HRMS (ESI$^+$): *m/z* calcd. for $C_{40}H_{47}N_3$ 569.3770; found 592.3838 $[M+Na]^+$.

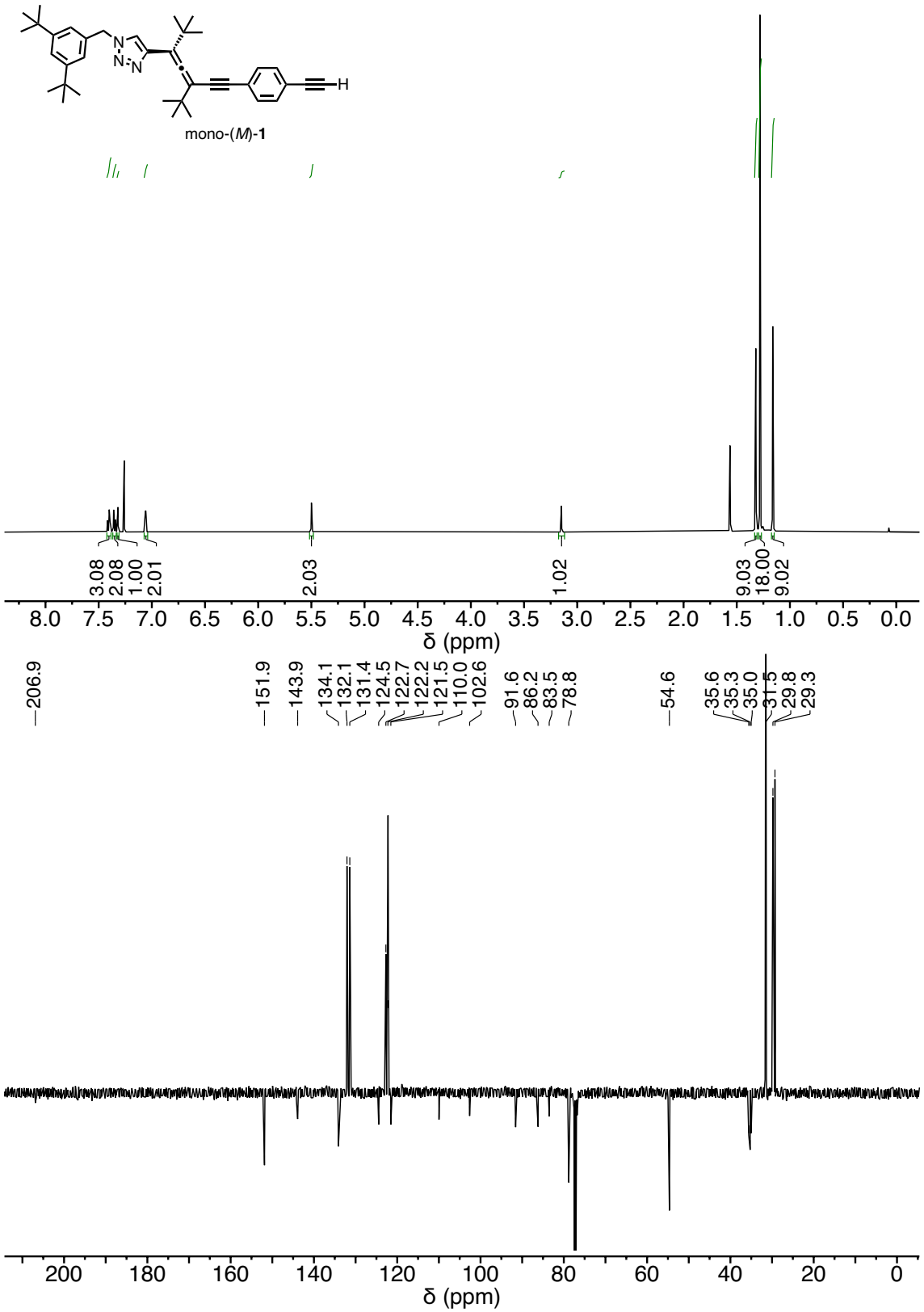

Figure S6. ^{1}H-NMR and DEPTQ-NMR of mono-(*M*)-**1** in $CDCl_3$.

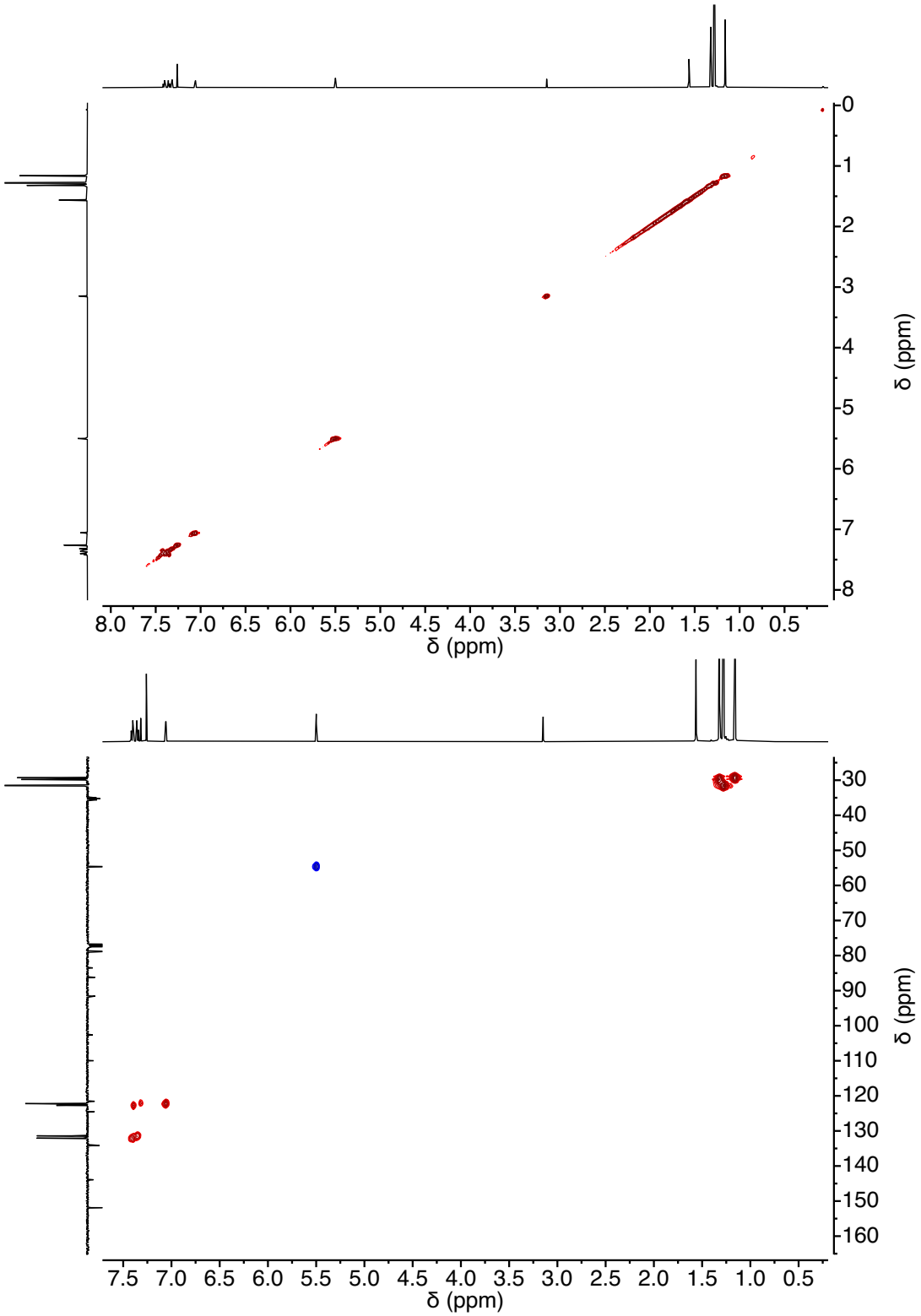

Figure S7. COSY-NMR and HSQC-NMR of mono-(*M*)-**1** in $CDCl_3$.

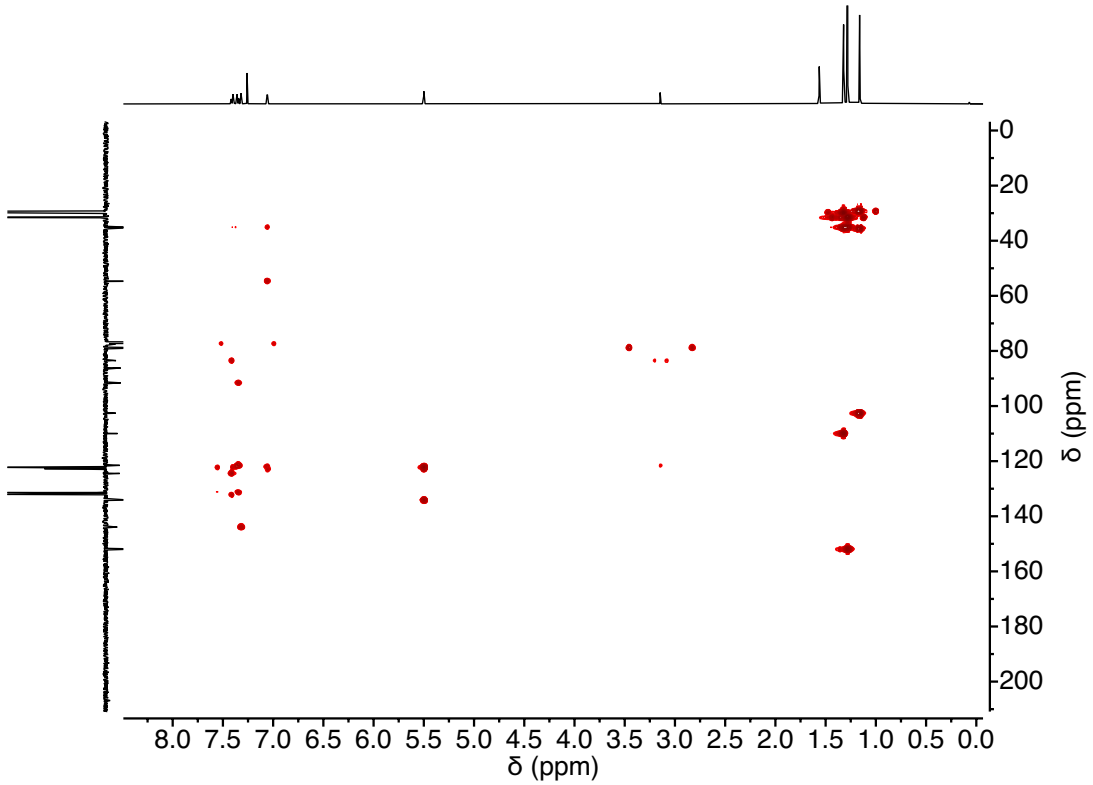

Figure S8. HMBC-NMR of mono-(*M*)-**1** in $CDCl_3$.

*Rotaxane **S3***

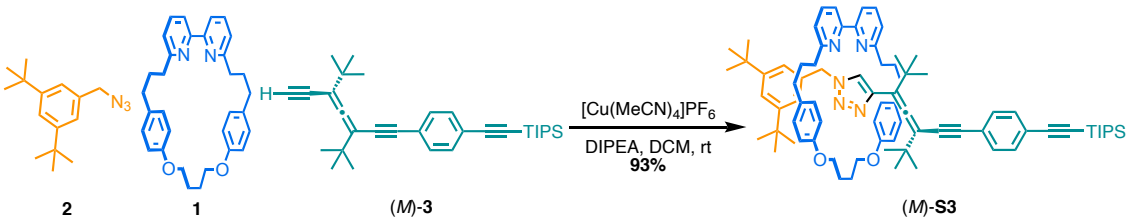

2 **1** (*M*)-**3** (*M*)-**S3**

A CEM MW vial was charge with azide **2** (150 mol%, 0.163 mmol, 40 mg), **1** (100 mol%, 0.109 mmol, 52 mg), (*M*)-**3** (150 mol%, 0.163 mmol, 75 mg), $[Cu(MeCN)_4]PF_6$ (90 mol%, 0.098 mmol, 36) and purged with N_2. DCM (2 mL) and DIPEA (400 mol%, 0.436 mmol, 80 μL) were added and the reaction was left for 4 h at rt, after which formic acid (200 mol%, 0.218 mmol, 8 μL) was added. After 4h, the reaction mixture was diluted with DCM (10 mL) and washed with a saturated EDTA/NH_3 solution (5 mL), water (5 mL) and brine (5 mL). The organic layers were dried with anhyd Na_2SO_4, filtered and concentrated. Column chromatography (0 to 10% EtOAc in Hexane) gave (*M*)-**S4** as a white solid (120 mg, 93%).

The same protocol was applied for compounds (±)-**3** and (*P*)-**3** to obtain (±)-**S3** and (*P*)-**S3**, respectively.

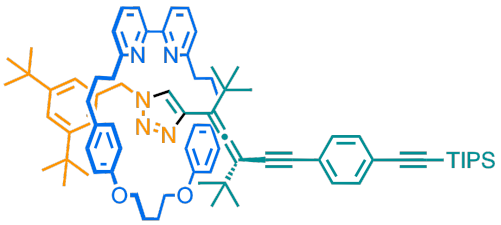

(*M*)-**S3**

Molecular Formula: $C_{79}H_{101}N_5O_2Si$**. MW:** 1180.79 **g/mol.**

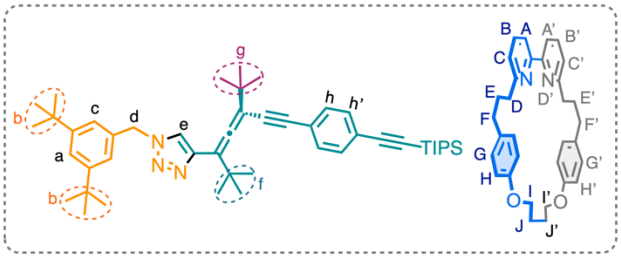

^{1}H-NMR (500 MHz, $CDCl_3$, 298K) *δ:* 8.85 (s, 1H, H_e), 7.65 (td, *J* = 7.8, 6.5 Hz, 2H, H_B), 7.49-7.44 (m, 2H, H_A), 7.41 (t, *J* = 1.9 Hz, 1H, H_a), 7.35 (m, 2H, H_h), 7.29 (m, 2H, H_h), 7.28 (m, 1H), 7.15-7.09 (m, 4H, H_C,H_c), 6.56-6.48 (m, 6H, H_G, H_H), 6.35 (m, 2H, H_H), 4.67(q, *J* = 7.4 Hz, 1H, H_I), 4.65 – 4-56 (m, 2H, H_d, H_I), 4.49 (d, *J* = 13.7 Hz, 1H, H_d), 4.16 (q, *J* = 6.9 Hz, 1H, H_I), 4.04 (td, *J* = 8.1, 5.0 Hz, 1H, H_I), 2.58 – 2.49 (m, 2H, H_D), 2.46 – 2.19 (m, 8H, H_F, H_J, H_D), 2.06 – 1.97 (m, 2H, H_J), 1.85 – 1.63 (m, 4H, H_E), 1.31 (s, 18H, H_b), 1.23 (s, 9H, H_f), 1.13 (s, 9H, H_g), 1.11 (s, 21H, H_{TIPS}).

^{13}C-NMR (101 MHz, $CDCl_3$, 298K) *δ:* 206.8, 163.2, 163.1, 157.8, 157.4, 157.3, 151.7, 150.1, 138.4, 136.7, 136.6, 134.2, 133.9, 131.9, 131.8, 131.7, 131.6, 131.1, 130.9, 128.4, 128.4, 125.4, 124.3, 122.7, 122.5, 122.1, 121.7, 121.3, 119.9, 119.7, 115.3, 114.8, 110.8, 106.8, 101.4, 92.3, 90.9, 87.4, 85.8, 66.6, 66.6, 54.5, 52.9, 37.0, 36.6, 35.2, 35.0, 34.9, 34.8, 34.8, 31.6, 31.4, 31.0, 31.0, 29.9, 29.7, 29.2, 28.6, 25.0, 18.7, 11.3.

HRMS (ESI$^+$): *m/z* calcd. for $C_{79}H_{101}N_5O_2Si$ 1179.7725; found 1180.78 $[M+H]^+$.

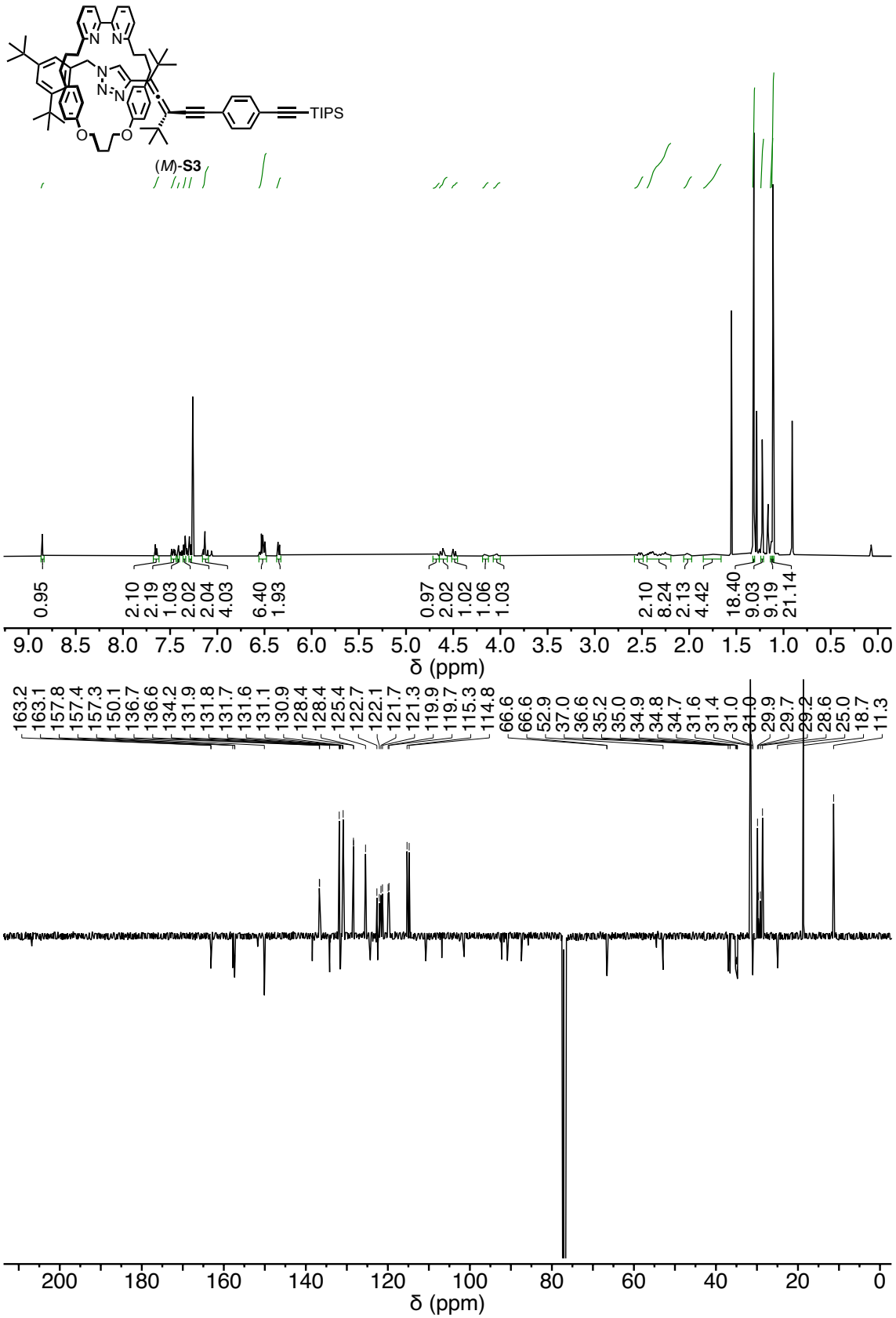

Figure S9. ^{1}H-NMR and DEPTQ-NMR of (*M*)-**S3** in $CDCl_3$.

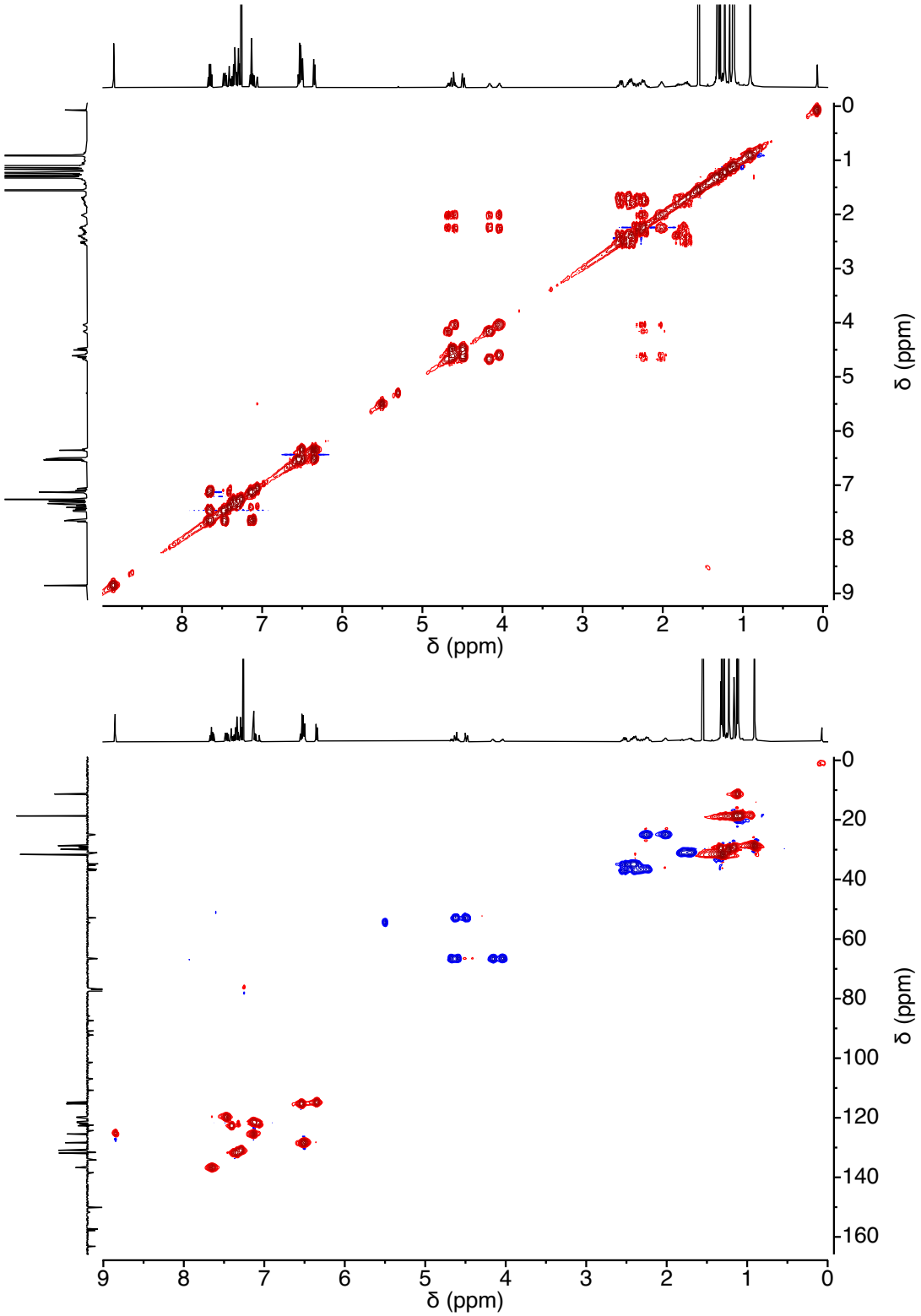

Figure S10. COSY-NMR and HSQC-NMR of (*M*)-**S3** in $CDCl_3$.

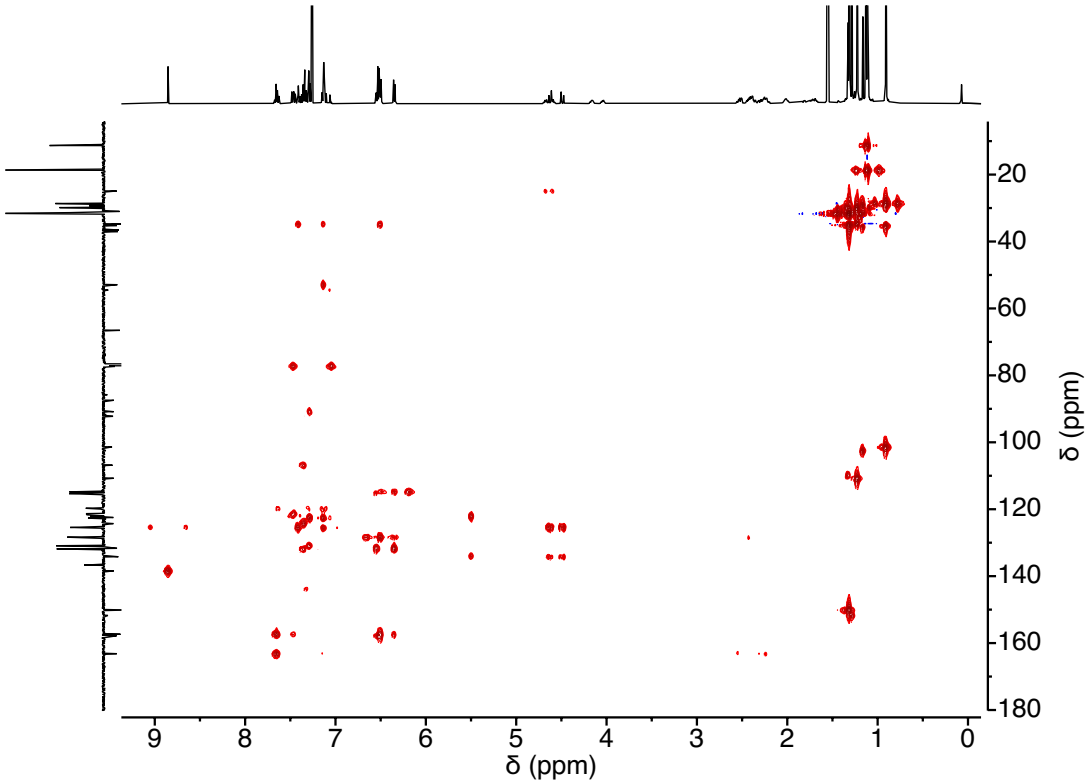

Figure S11. HMBC-NMR of (*M*)-**S3** in $CDCl_3$.

*Interlocked monomer: mono-**2***

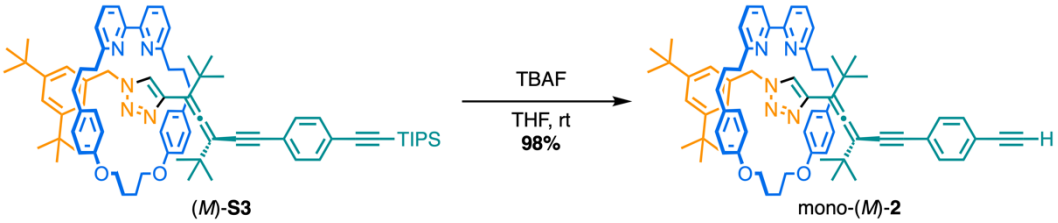

To a solution of (*M*)-**S3** (100 mol%, 0.090 mmol, 106 mg) in THF (2 mL), TBAF (100 mol%, 0.090 mmol, 0.1 mL of a 1M solution in THF) was added, and the mixture was stirred at rt for 1 h. Then the reaction mixture was treated with sat. aq. NH_4Cl solution (3 x 5 mL) and extracted with DCM (3 x 2 mL). The organic layers were dried over anhyd Na_2SO_4, filtered and concentrated. Column chromatography (0 to 10% EtOAc in Hexane) gave mono-(*M*)-**2** as a white solid (90 mg, 98%).

The same protocol was applied for compounds (±)-**S3** and (*P*)-**S3** to obtain mono-(±)-**2** and mono-(*P*)-**2**, respectively.

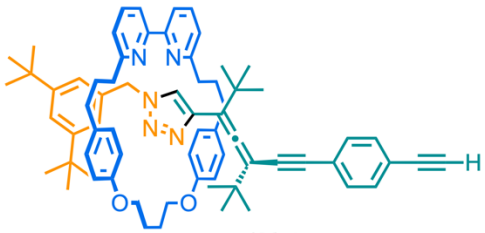

mono-(*M*)-**2**

For mono-(*P*)-**2**, $[\alpha]_D^{20}$= +157; for mono-(*M*)-**2**, $[\alpha]_D^{20}$= -158 (*c* = 10 mg·mL^{-1}, $CHCl_3$).

Molecular Formula: $C_{70}H_{81}N_5O_2$**. MW:** 1024.45 **g/mol.**

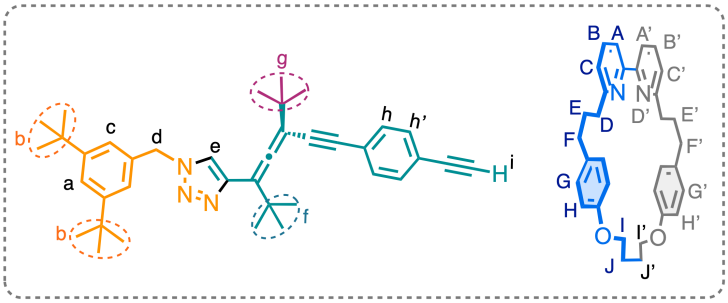

^{1}H-NMR (750 MHz, $CDCl_3$, 298K) *δ:* 8.89 (s, 1H, H_e), 7.66 (td, *J* = 7.8, 6.6 Hz, 2H, H_B, $H_{B'}$), 7.48 (d, *J* = 7.8 Hz, 1H, H_A), 7.45 (d, *J* = 7.8 Hz, 1H, $H_{A'}$), 7.41 (m, 1H, H_a), 7.37 (d, 2H, $H_{h'}$), 7.31 (d, 2H, H_h), 7.15 – 7.10 (m, 5H, H_C, $H_{C'}$, H_c), 6.55 (d, 2H, H_G), 6.51 (m, 4H, H_H, $H_{G'}$), 4.71 (q, *J* = 7.7 Hz, 1H, H_I), 4.65 – 4.61 (m, 2H, H_d, $H_{I'}$), 4.49 (d, *J* = 13.8 Hz, 1H, H_d), 4.17 (ddd, *J* = 8.7, 7.1, 5.0 Hz, 1H, H_I), 4.02 (td, J = 8.3, 5.0 Hz, 1H, $H_{I'}$), 3.14 (s, 1H, H_i), 2.55 – 2.48 (m, 2H, H_D), 2.45 – 2.39 (m, 2H, H_F), 2.38 – 2.32 (m, 2H, H_F), 2.30 – 2.23 (m ,2H, H_J), 2.16 (td, *J* = 13.8, 4.8 Hz, 1H, H_D), 2.04 – 1.97 (m, 2H, H_J), 1.84 – 1.65 (m, 4H, H_E), 1.31 (s, 18H, H_b), 1.21 (s, 9H, H_f), 0.87 (s, 9H, H_g).

^{13}C-NMR (101 MHz, $CDCl_3$, 298K) *δ:* 207.0, 163.3, 158.0, 157.5, 157.4, 150.3, 138.5, 136.9, 136.8, 134.3, 132.1, 131.8, 131.7, 131.2, 128.5, 125.6, 125.0, 122.8, 121.8, 121.5, 121.1, 120.1, 119.9, 115.5, 115.0, 111.0, 101.5, 90.7, 87.8, 83.6, 78.6, 66.8, 66.7, 53.1, 37.2, 36.7, 35.4, 35.1, 35.0, 35.0, 34.9, 31.7, 31.2, 31.1, 30.0, 28.8, 25.1, 25.0.

HRMS (ESI$^+$): *m/z* calcd. for $C_{70}H_{81}N_5O_2$ 1023.6390; found 1024.6455 $[M+H]^+$.

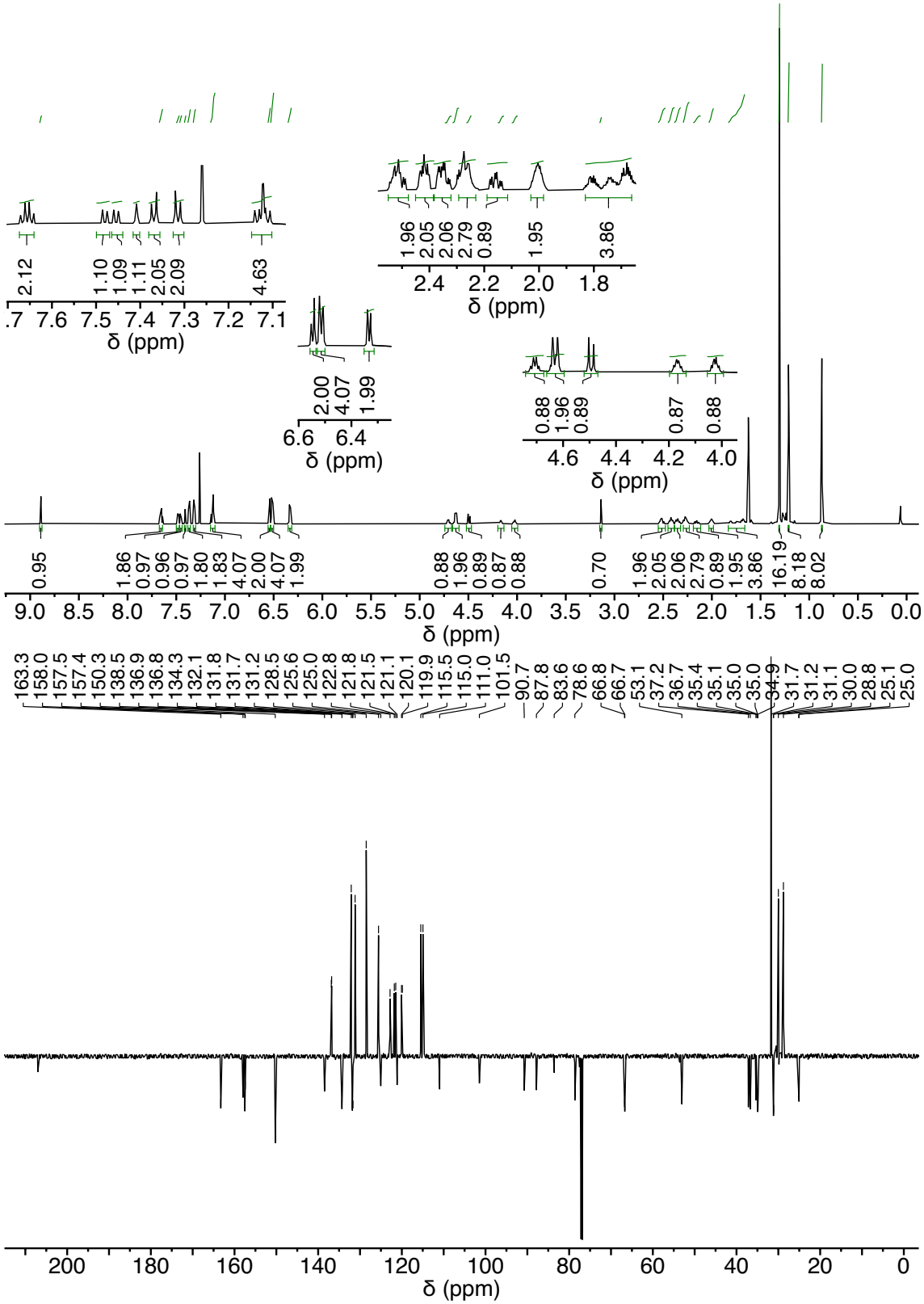

Figure S12. ^{1}H-NMR and DEPTQ-NMR of mono-(*M*)-**2** in $CDCl_3$.

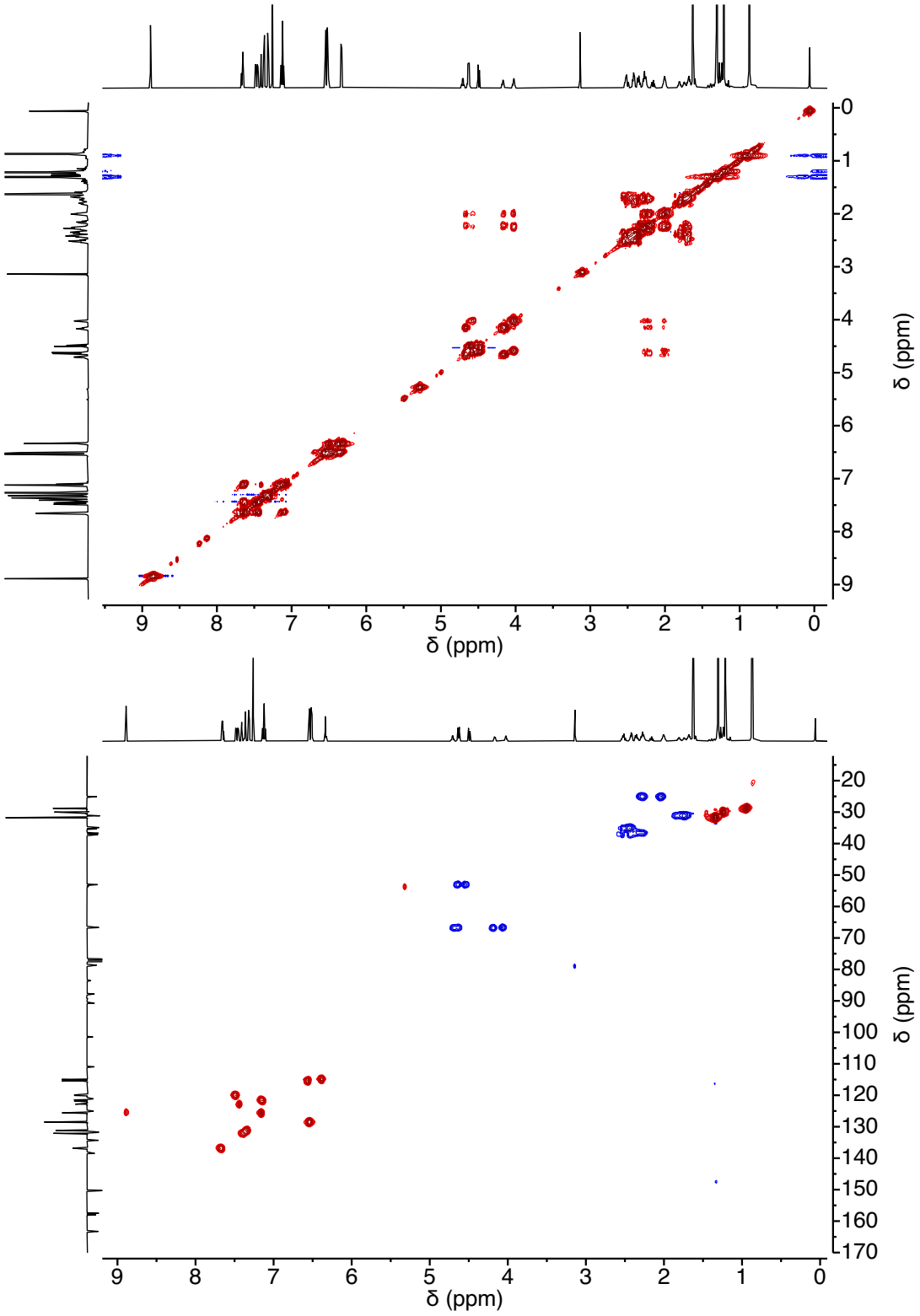

Figure S13. COSY-NMR and HSQC-NMR of mono-(*M*)-**2** in $CDCl_3$.

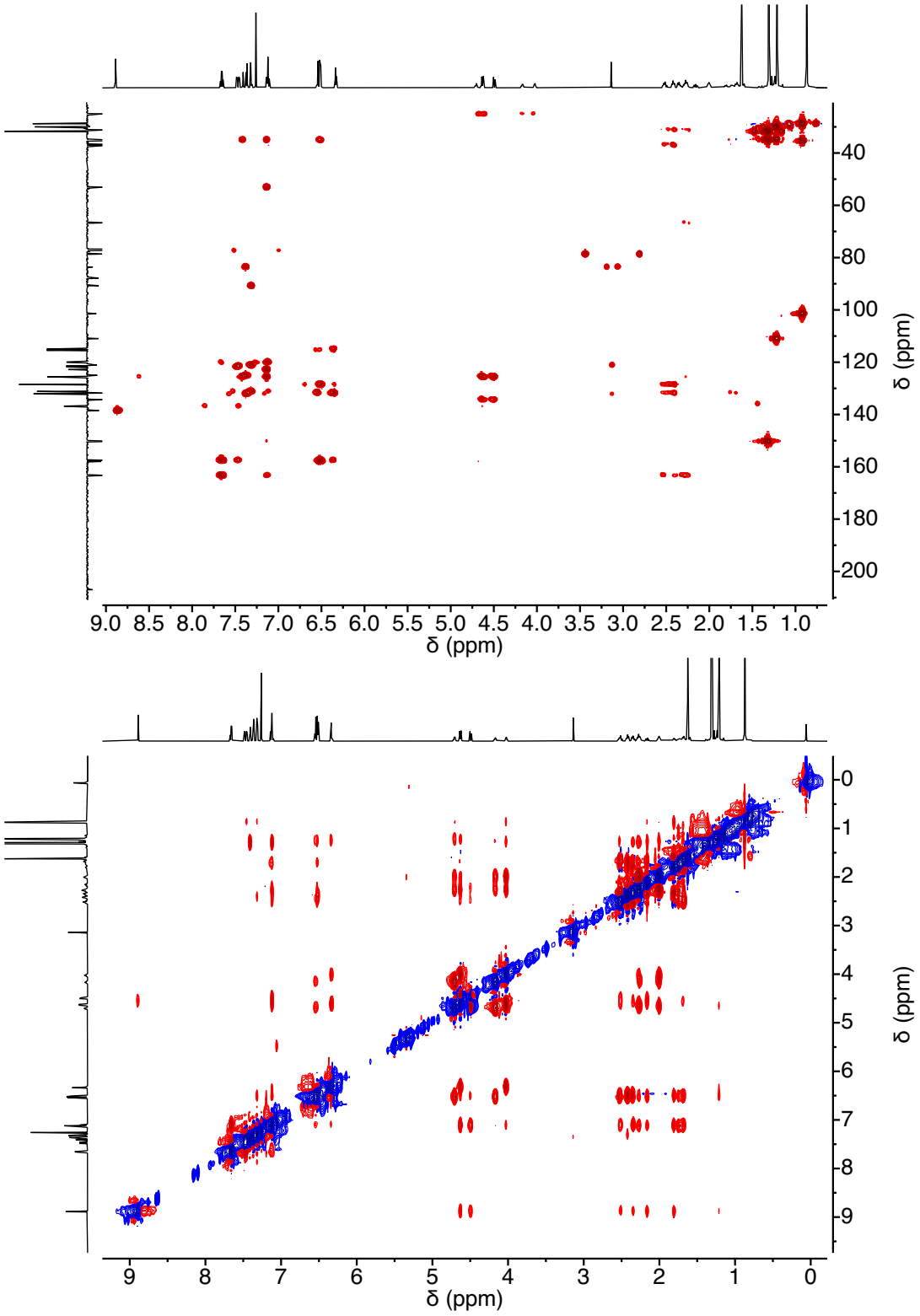

Figure S14. HMBC-NMR and ROESY-NMR of mono-(*M*)-**2** in $CDCl_3$.

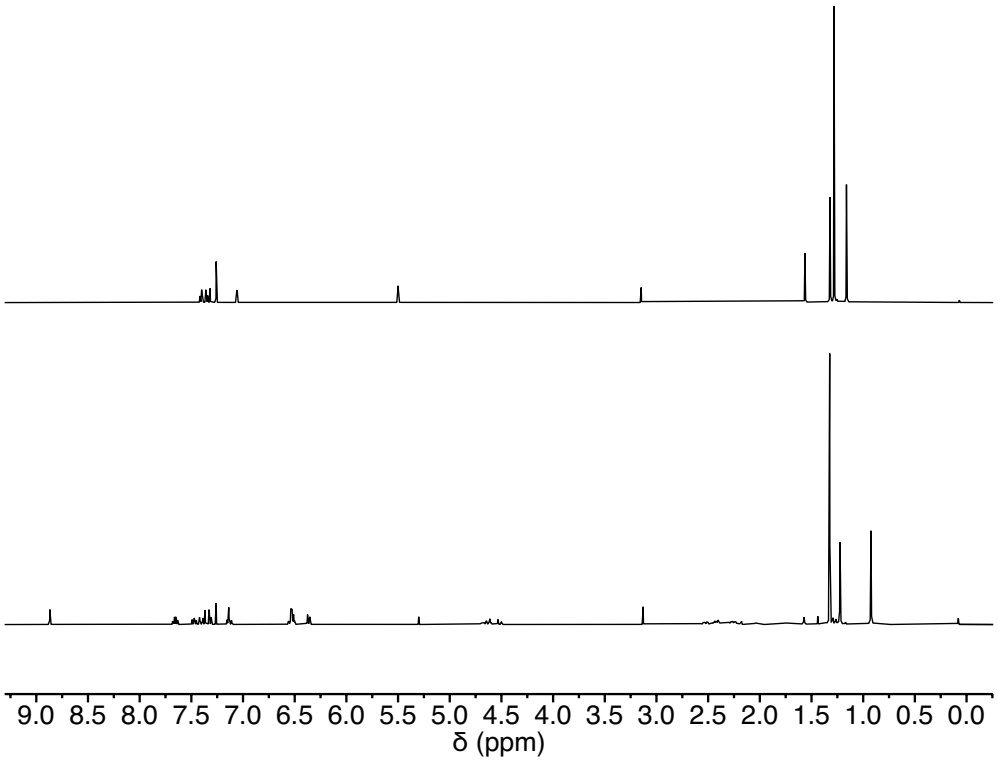

Figure S15. Stacked ^{1}H-NMR spectra (500 MHz, $CDCl_3$, 298 K) of non-interlocked monomer [mono-(*M*)-**1**] and related interlocked monomer [mono-(*M*)-**2**] revealing significant shifts in the interlocked compound.

5.3.3. SCXRD data for mono-(*M*)-2

Single crystals of mono-(*M*)-**2** were grown by slow evaporation of Heptane-DCM. A crystal was selected and mounted on a MiTeGen loop under oil and flash frozen at 100 K under a cold N2 gas stream. Xray diffraction data were collected on a Bruker X8 kappa APEX II CCD diffractometer.

Data collection: APPEX3v2022.1-1 (BRUKER AXS, 2021); cell refinement: SAINT V8.40B (Bruker AXS LLC, 2019); data reduction: SAINT V8.40B (Bruker AXS LLC, 2019); program(s) used to solve structure: SHELXT2018/2 (Sheldrick, 2015); program(s) used to refine structure: SHELXL2019/1 (Sheldrick, 2019); molecular graphics: ORTEP for Windows (Farrugia, 2012); software used to prepare material for publication: WinGX publication routines (Farrugia, 2012).

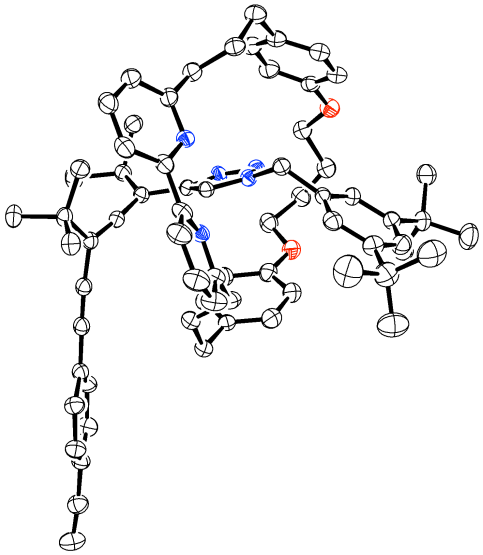

Figure S16. Ellipsoid plot of the asymmetric unit of mono-(*M*)-**2**. Ellipsoids are shown at the 50% probability level. Hydrogen atoms have been omitted for clarity.

Table S1. Crystal data and structure refinement for mono-(*M*)-**2**.

Crystal data	
Chemical formula	$C_{32}H_{34}N_2O_2 \cdot C_{38}H_{47}N_3$[+solvent]
M_r	1024.40
Crystal system, space group	Monoclinic, $P2_1$
Temperature (K)	100
a, b, c (Å)	24.9262 (9), 12.6094 (4), 29.4552 (10)
β (°)	92.814 (2)
V (Å^3)	9246.7 (5)
Z	6
Radiation type	Cu $K\alpha$
μ (mm^{-1})	0.51
Crystal size (mm)	0.28 × 0.10 × 0.04
Data collection	
Diffractometer	Bruker D8 VENTURE PHOTON III-14
Absorption correction	Multi-scan BRUKER *SADABS2016*/2
T_{min}, T_{max}	0.703, 0.864
No. of measured, independent and observed [$I > 2\sigma(I)$] reflections	112622, 26431, 19862
R_{int}	0.096
θ_{max} (°)	58.9
(sin $\theta/\lambda)_{max}$ (Å^{-1})	0.556
Refinement	
$R[F^2 > 2\sigma(F^2)]$, $wR(F^2)$, S	0.085, 0.226, 1.07
No. of reflections	26431
No. of parameters	2250
No. of restraints	1507
H-atom treatment	H-atom parameters constrained $w = 1/[\sigma^2(F_o^2) + (0.0954P)^2 + 12.3236P]$ where $P = (F_o^2 + 2F_c^2)/3$
$\Delta\rho_{max}$, $\Delta\rho_{min}$ (e Å^{-3})	0.42, −0.25
Absolute structure	Flack x determined using 6912 quotients [(I+)-(I-)]/[(I+)+(I-)] (Parsons, Flack and Wagner, Acta Cryst. B69 (2013) 249-259).
Absolute structure parameter	−0.4 (3)

5.3.4. Synthesis of polymers

5.3.4.1. General procedure for polymerization

The reaction flask (sealed ampoule) was dried under vacuum and argon flushed for three times before a solution of monomer in THF was added *via* cannula. Then, triethylamine was added dropwise *via* syringe. A solution of rhodium norbornadiene chloride dimer, $[Rh(nbd)Cl]_2$, in THF was added under stirring at rt. The reaction mixture was stirred at rt overnight. Then, the resulting polymer was diluted in DCM and precipitated in a large amount of MeOH, centrifuged, reprecipitated in MeOH and centrifuged again (Table S2).

Table S2. Calculated amounts for the synthesis of polymers poly-(±)-**1**, poly-(*M*)-**1**, poly-(*P*)-**1**, poly-(±)-**2**, poly-(*M*)-**2** and poly-(*P*)-**2**.

Monomer	Mass (mg)	THF (μL)	Et_3N (μL)	Catalyst (mg)	Yield (%)
mono-(±)-**1**	50	200	2	1	93
mono-(*M*)-**1**	70	300	3	1	95
mono-(*P*)-**1**	50	200	2	1	90
mono-(±)-**2**	55	200	2	1	88
mono-(*M*)-**2**	60	200	2	1	90
mono-(*P*)-**2**	50	200	2	1	90

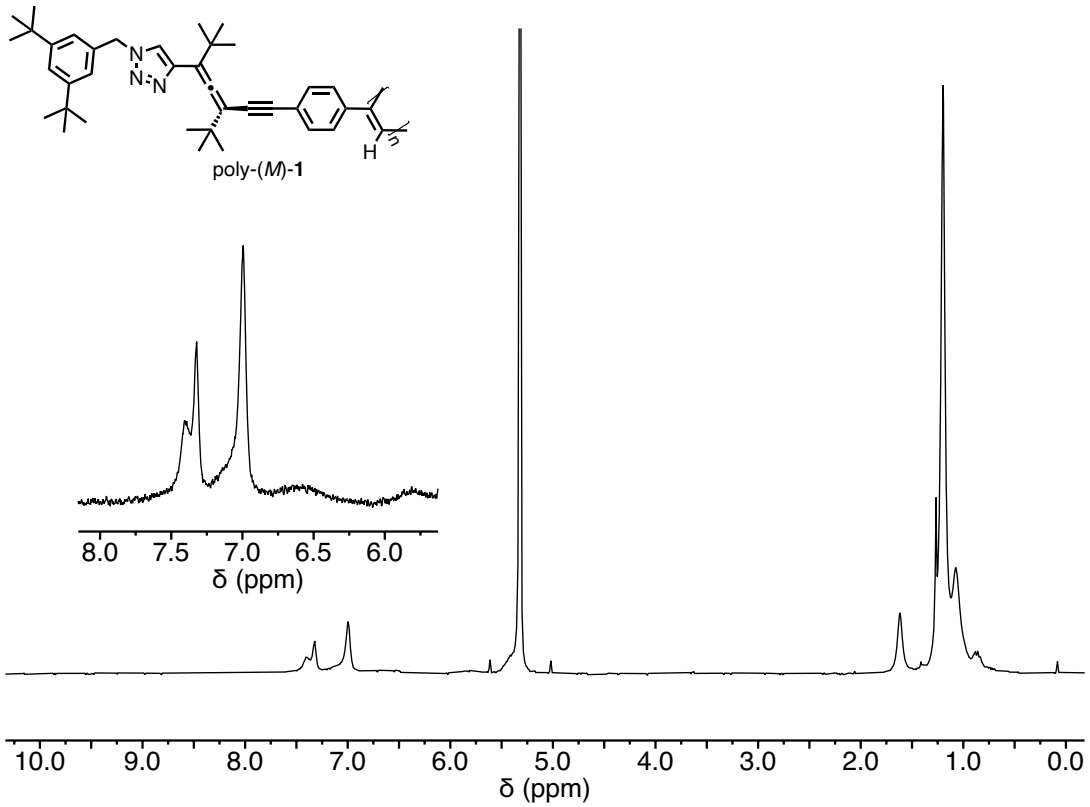

Figure S17. ^{1}H-NMR of poly-(M)-1 in CD_2Cl_2.

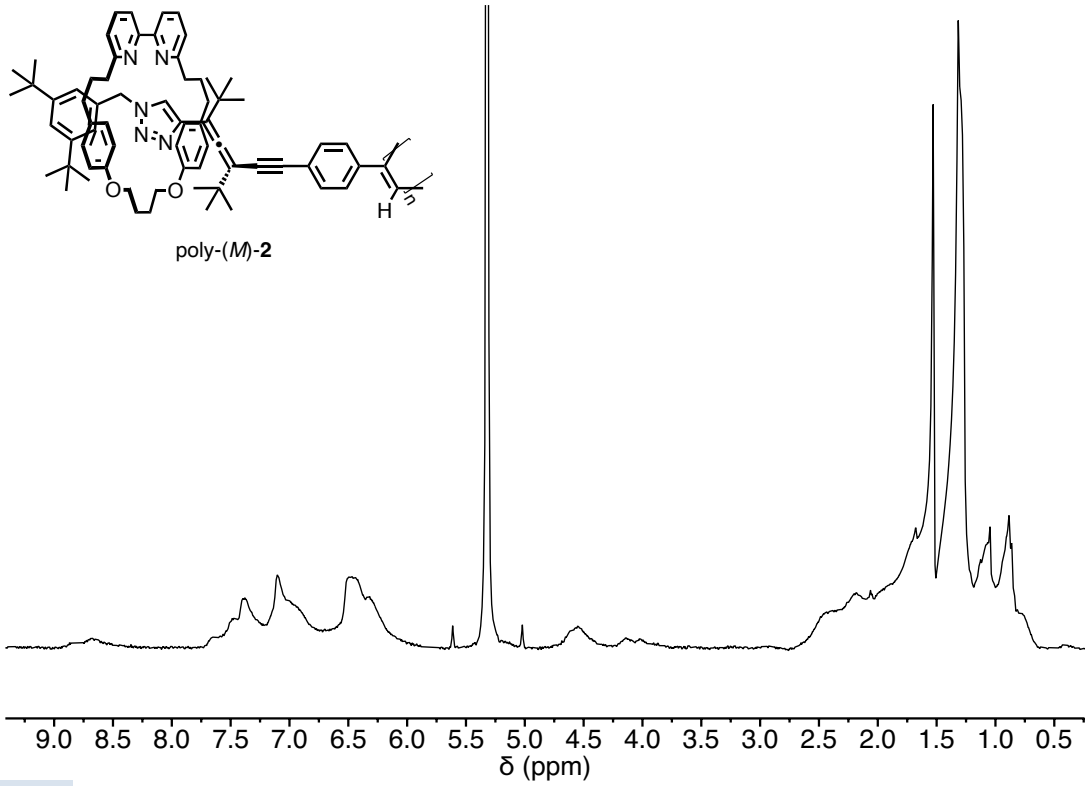

Figure S18. ^{1}H-NMR of poly-(*M*)-**2** in CD_2Cl_2.

5.3.5. GPC Studies

The molecular weight of the polymers was estimated by GPC using THF (flow rate: 1.0 mL·min^{-1}) as eluent and polystyrene narrow standards (PSS) as calibrants.

Table S3. GPC data for the synthesized polymers.

Polymer	Mn (Daltons)	Mw (Daltons)	Mz (Daltons)	Đ (Daltons)
poly-(±)-**1**	191135	285181	360055	1.49
poly-(*M*)-**1**	219704	325348	415909	1.48
poly-(*P*)-**1**	204236	289783	360974	1.42
poly-(±)-**2**	84810	109506	136580	1.29
poly-(*M*)-**2**	80330	106986	135595	1.33
poly-(*P*)-**2**	80808	106211	123501	1.31

5.3.6. Raman Experiments

The bands observed by Raman resonance confirmed the former configuration. The peak at highest wavelength corresponds to the C=C bond stretching and overlaps with that of the phenyl ring. The band at 1300-1350 cm^{-1} arises from the *cis* C-C bond coupled with the single bond connecting the main chain and the phenyl ring. The peak at lowest wavelength (920 – 970 cm^{-1}) corresponds to the C-H bond of the *cis* form. The disappearance of the alkyne peak (ca. 2100 – 2115 cm^{-1}) also confirms the formation of the polymer.

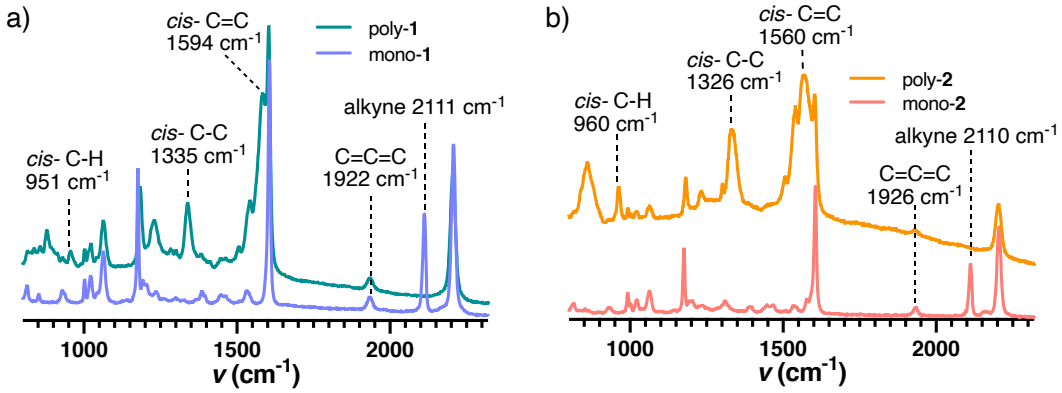

Figure S19. Raman spectra of (a) mono-**1** and poly-**1**; (b) mono-**2** and poly-**2**.

5.3.7. Thermal Studies

5.3.7.1. DSC Studies

DSC experiments have been used to determine the configuration of the polymer skeleton in poly(phenylacetylene)s due to the different thermogram pattern for a *cis*-cisoidal (*c-c*) or a *cis*-transoidal (*c-t*) polyene backbone.[150,196] Hence, the geometry of the polymer was determined by DSC. According to a general protocol, the polymer was placed in an aluminum pan up to 400 °C (heating rate: 10 °C.min^{-1}). The thermogram for poly-**1** shows a typical *c-t* trace with an exothermal peak, at 71 °C and 256 °C respectively, correspondent to a *c-c* transition and a final isomerization to *t-t* (Figure S20a). The thermogram for poly-**2** shows a *c-t* trace with an exothermal peak, at 189 °C and 321 °C respectively, correspondent to a *c-c* transition and a final isomerization to *t-t* (Figure S20b).

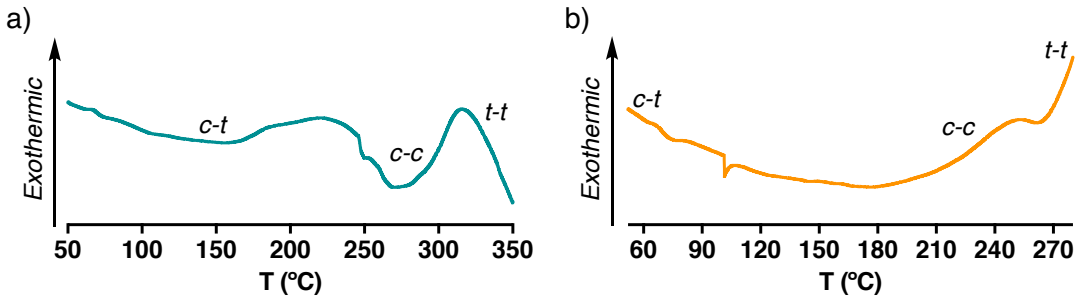

Figure S20. DSC thermogram for poly-**1** and poly-**2**.

5.3.7.2. TGA studies

The thermal stability of the synthesized polymers was evaluated by TGA. As a general protocol, the polymer sample was placed in a platinum pan and heated from 40°C to 600°C (heating rate: 10 °C·min^{-1}). Poly-**1** starts to degrade at 155 °C (Figure S21a), whereas for poly-**2** it is 300 °C(Figure S21b).

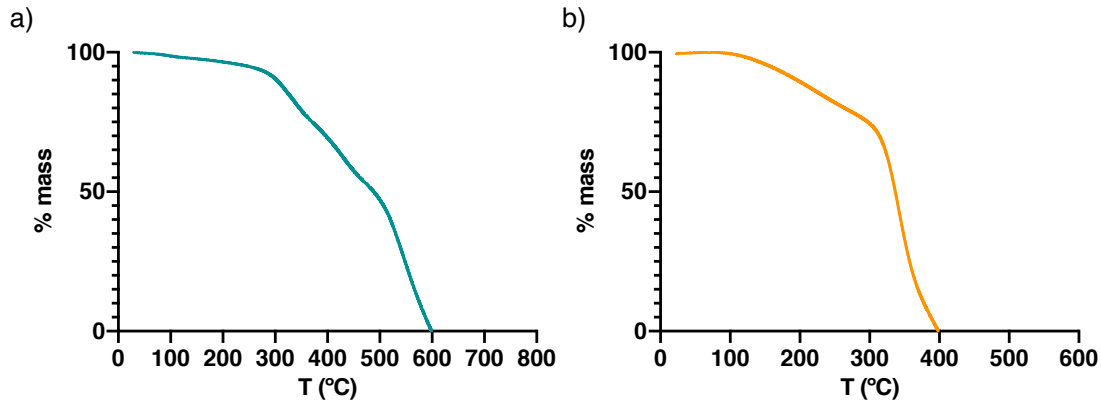

Figure S21. TGA thermogram for poly-**1** and poly-**2**.

5.3.8. ECD Studies of the monomers

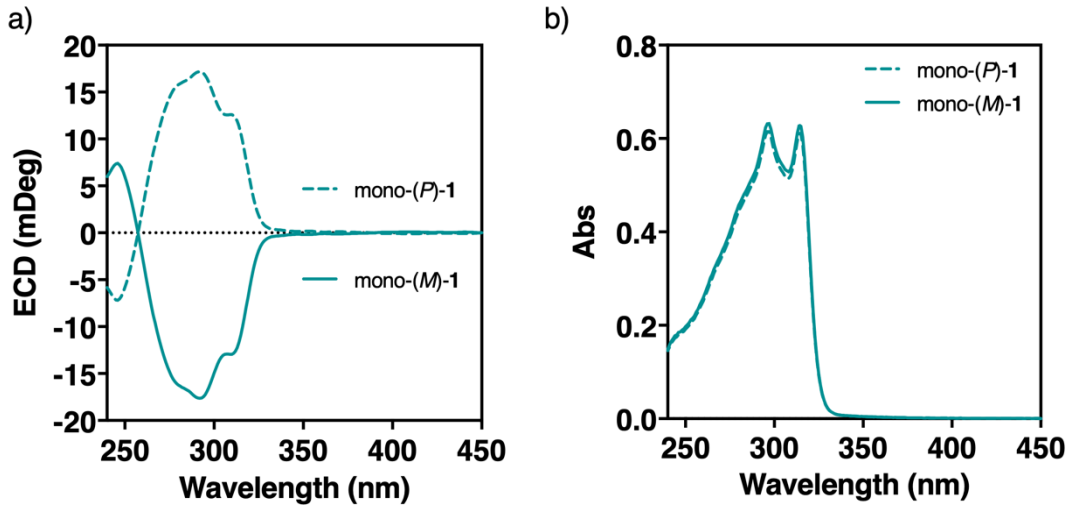

Figure S22. (a) ECD spectra and (b) UV-vis of mono-(*P*)-**1** and mono-(*M*)-**1** (0.25 mM in $CHCl_3$).

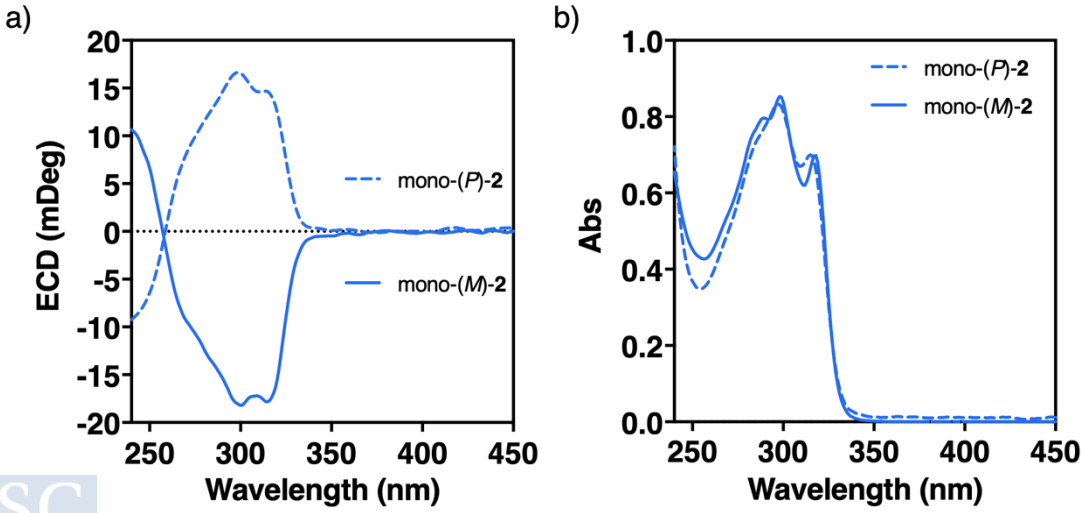

Figure S23. (a) ECD spectra and (b) UV-vis of mono-(*P*)-**2** and mono-(*M*)-**2** (0.25 mM in $CHCl_3$).

5.3.9. ECD Studies of the polymers

5.3.9.1. ECD Studies of racemic polymers: poly-(±)-1 and poly-(±)-2

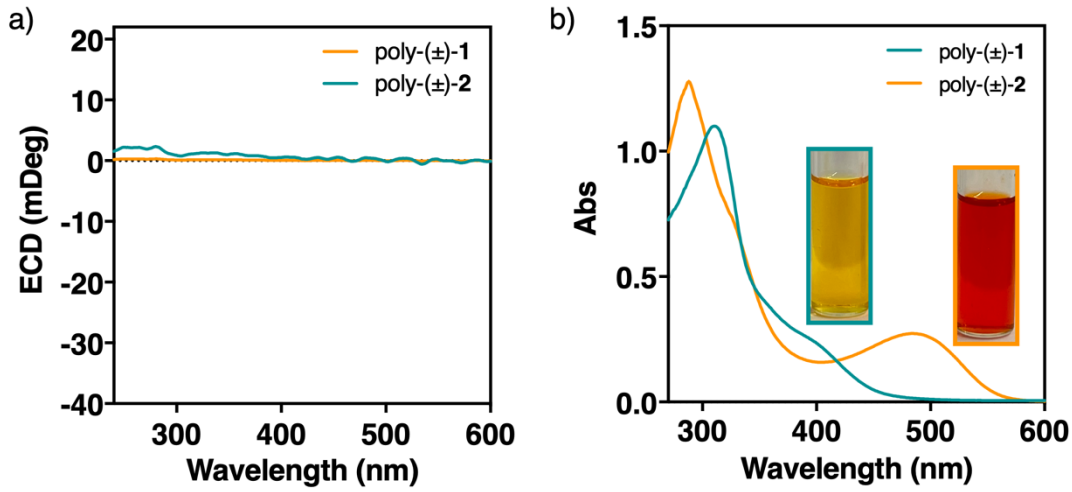

Figure S24. (a) ECD spectra and (b) UV-vis of poly-(±)-**1** and poly-(±)-**2** in $CHCl_3$ (0.5 mM).

5.3.9.2. ECD Studies of poly-(*M*)-1

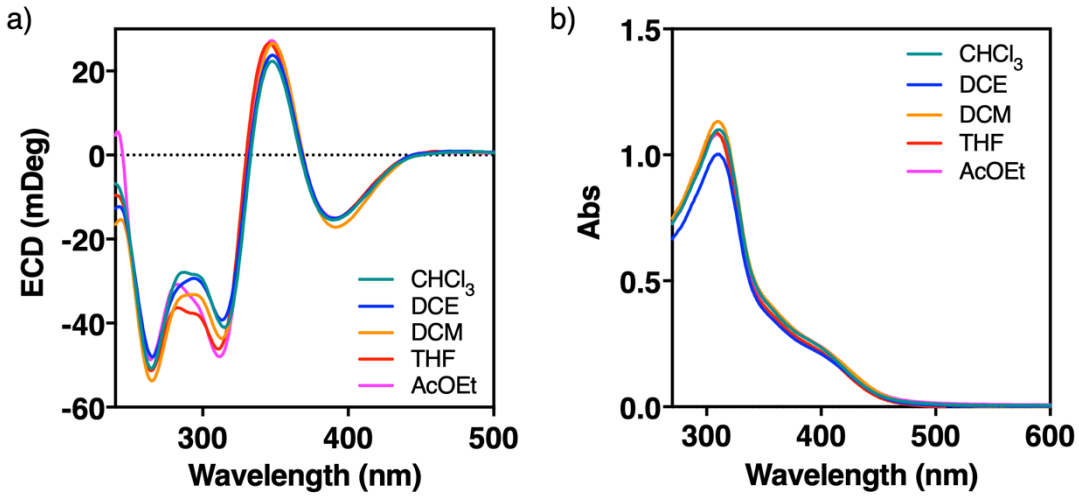

Figure S25. (a) ECD spectra and (b) UV-vis of poly-(*M*)-**1** in different solvents (0.5 mM).

5.3.9.3. ECD Studies of poly-(*P*)-1

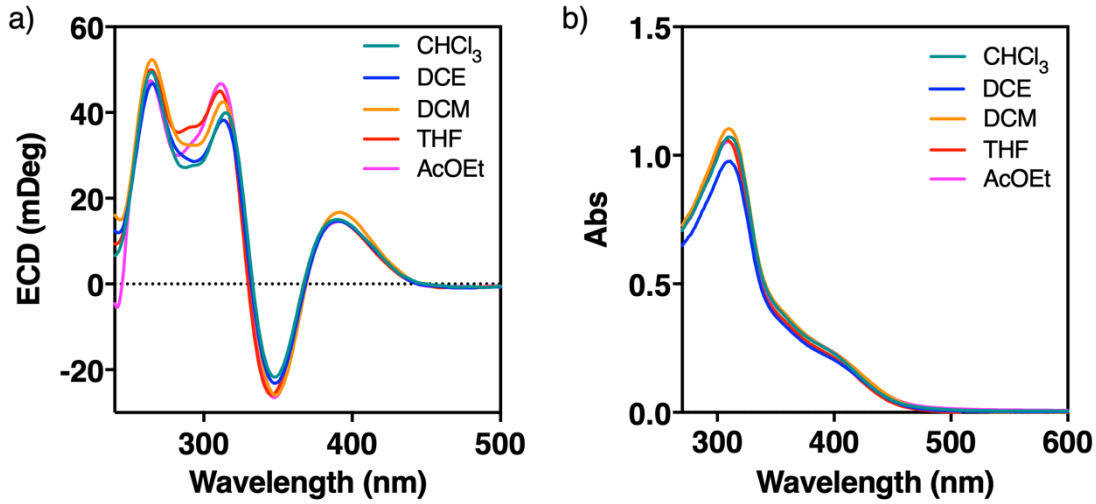

Figure S26. (a) ECD spectra and (b) UV-vis of poly-(*P*)-**1** in different solvents (0.5 mM).

5.3.9.4. ECD Studies of poly-(*M*)-2

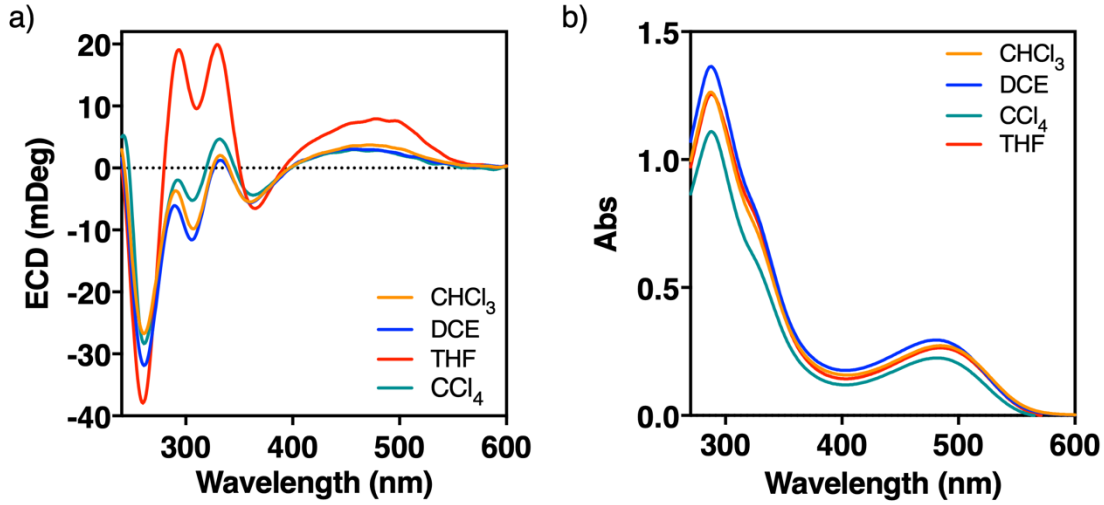

Figure S27. (a) ECD spectra and (b) UV-vis of poly-(*M*)-**2** in different solvents (0.5 mM).

5.3.9.5. ECD Studies of poly-(*P*)-2

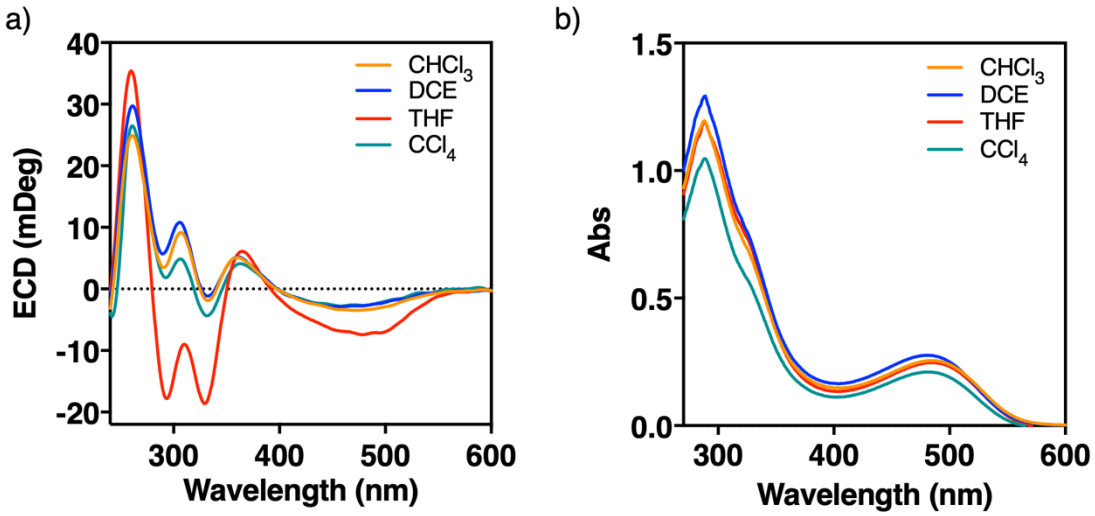

Figure S28. (a) ECD spectra and (b) UV-vis of poly-(*P*)-**2** in different solvents (0.5 mM).

5.3.10. ECD titration experiments

5.3.10.1. Titration experiments of mono-2 and poly-2

5.3.10.1.1. Titration experiments of mono-2 and poly-2 with Formic Acid

*5.3.10.1.1.1. Titration experiments of mono-(M)-**2** and poly-(M)-**2** with Formic Acid*

Mono-(*M*)-**2** was dissolved in $CHCl_3$ (0.25 mM) and different volumes of formic acid (HCOOH) solutions (0.11 M, 0.22 M, and 0.87 M in $CHCl_3$) were added. ECD and UV-vis signals were recorded after each addition of acid (Figure S29).

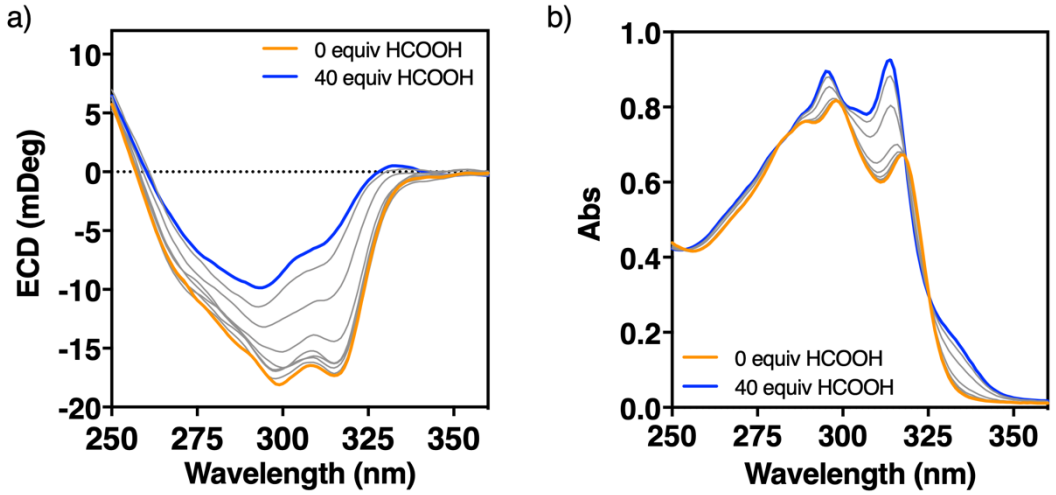

Figure S29. (a) ECD spectra and (b) UV-vis of mono-(*M*)-**2** (0.25 mM) upon addition of HCOOH in $CHCl_3$ (0.11 M, 0.22 M, and 0.87 M in $CHCl_3$). Blue line: ECD and UV-vis signal at the saturation value of HCOOH.

Poly-(*M*)-**2** was dissolved in $CHCl_3$ (0.50 mM) and different volumes of formic acid (HCOOH) solutions (0.11 M, 0.22 M, and 0.87 M in $CHCl_3$) were added. ECD and UV-vis signals were recorded after each equivalent addition of acid (Figure S30 and S31). The same conditions were used for mono-(*P*)-**2** poly-(*P*)-**2** (Figure S33 and S34, respectively).

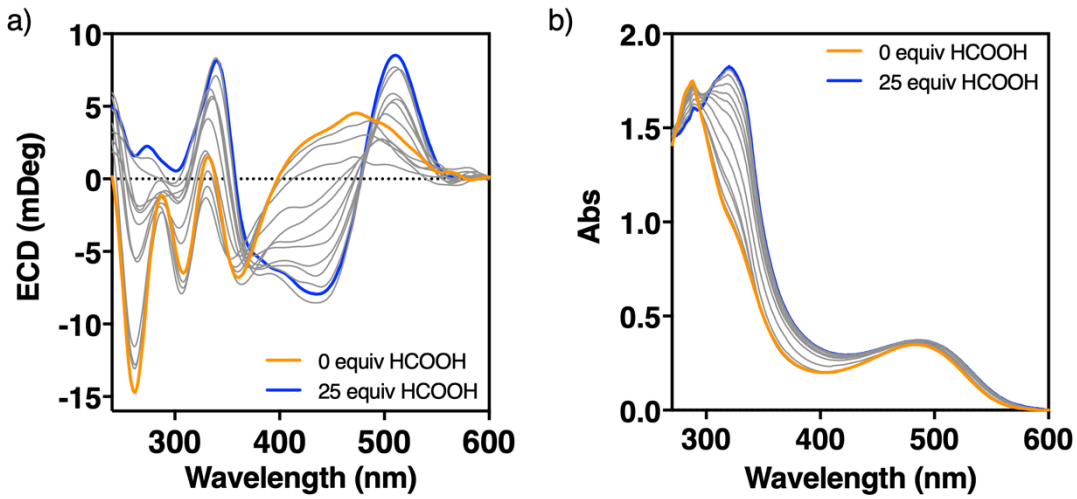

Figure S30. (a) ECD spectra and (b) UV-vis of poly-(*M*)-**2** (0.50 mM) upon addition of HCOOH in $CHCl_3$ (0.11 M, 0.22 M, and 0.87 M in $CHCl_3$). Blue line: ECD and UV-vis signal at the saturation value of HCOOH.

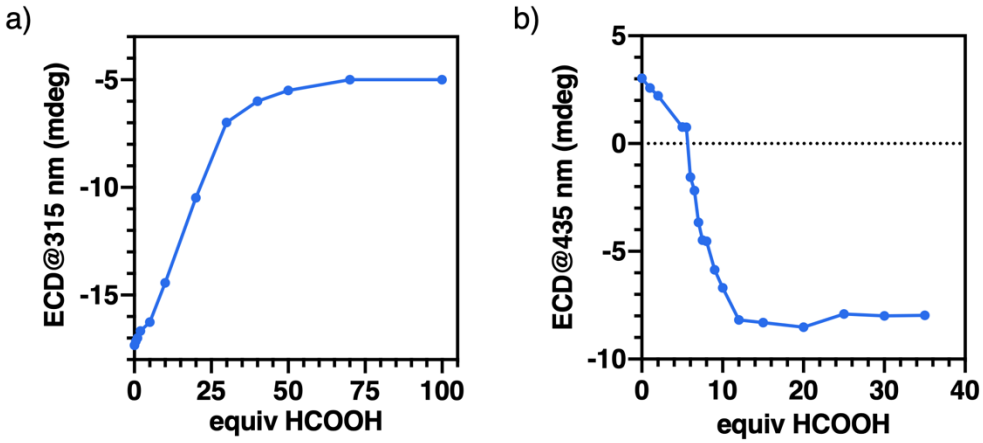

Figure S31. Saturation curves for titration in a $CHCl_3$ with HCOOH of (a) mono-(*M*)-**2** at 315nm and of (b) poly-(*M*)-**2** at 435 nm.

5.3.10.1.1.1.1. Neutralization with Et3N

A solution of Et_3N ($4.8 \cdot 10^{-4}$ M) in $CHCl_3$ was prepared. Then, small volumes of Et_3N were added to the previously acidified poly-(*M*)-**2** system until recovering original signal (red line in Figure 32).

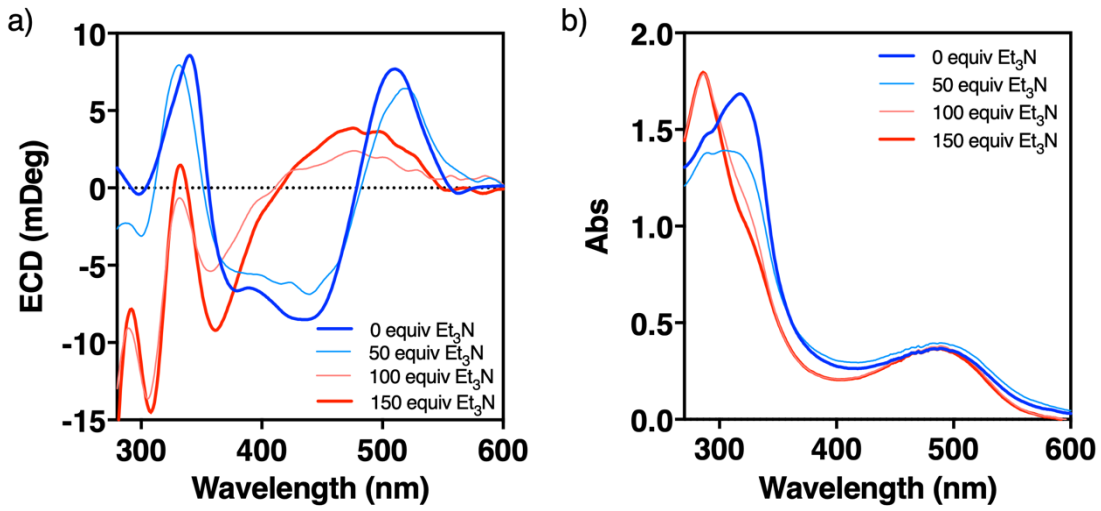

Figure S32. (a) ECD spectra and (b) UV-vis of previously acidified poly-(*M*)-**2** solution (25 equiv HCOOH to 0.50 mM polymer solution) upon addition of Et_3N in $CHCl_3$ ($4.8 \cdot 10^{-4}$ M).

*5.3.10.1.1.2. Titration experiments of mono-(P)-**2** and poly-(P)-**2** with Formic Acid*

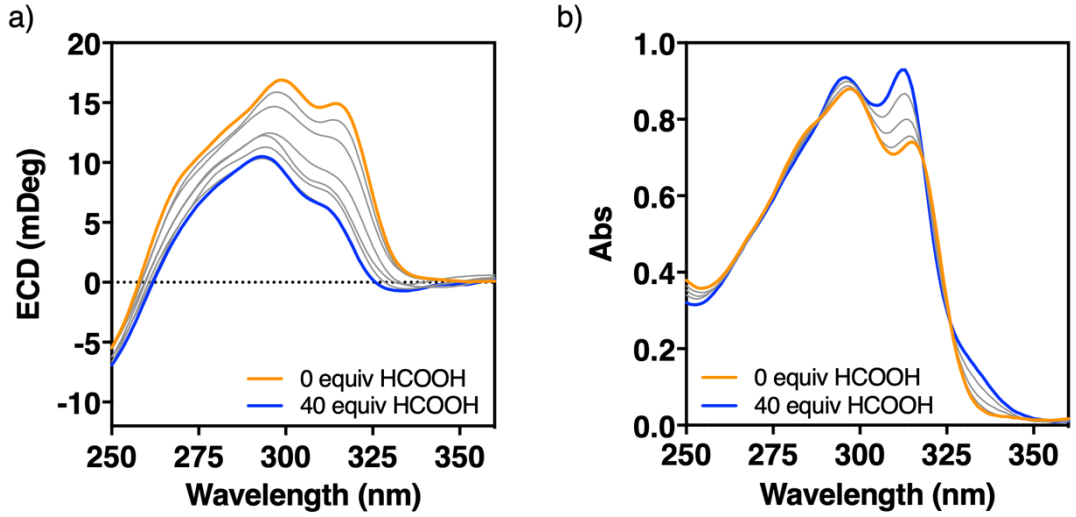

Figure S33. (a) ECD spectra and (b) UV-vis of mono-(*P*)-**2** (0.25 mM) upon addition of HCOOH in $CHCl_3$ (10.86 mM, 21.72 mM, and 86.90 mM). Blue line: ECD and UV-vis signal at the saturation value of HCOOH.

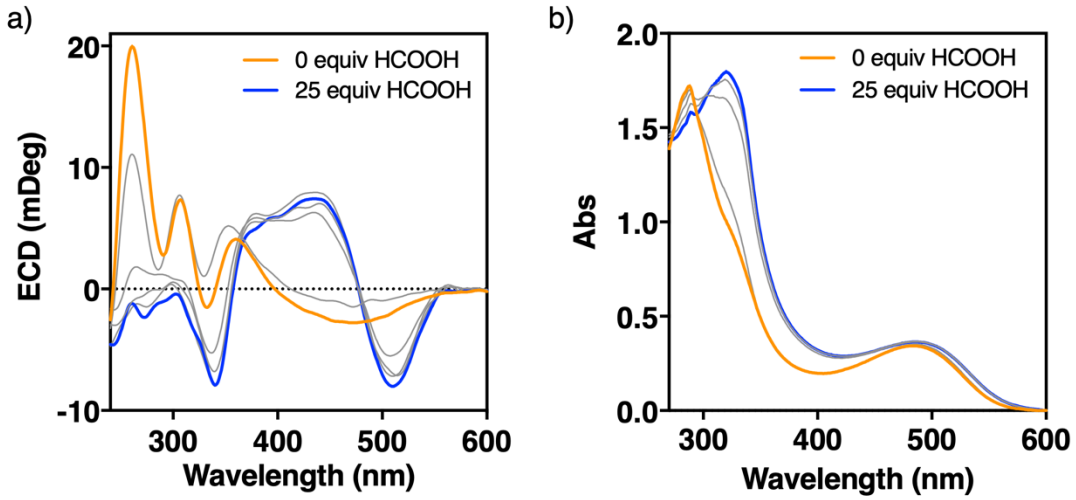

Figure S34. (a) ECD spectra and (b) UV-vis of poly-(*P*)-**2** (0.50 mM) upon addition of HCOOH in $CHCl_3$ (10.86 mM, 21.72 mM, and 86.90 mM). Blue line: ECD and UV-vis signal at the saturation value of HCOOH.

5.3.10.1.2. Titration of mono-2 and poly-2 with Metal Ions

5.3.10.1.2.1. Titration of mono-(*M*)-2 and poly-(*M*)-2 with Cu(I)

Mono-(*M*)-**2** was dissolved in $CHCl_3$ (0.25 mM) and different volumes of $[Cu(MeCN)_4]BF_4$ solution (15.89 mM in CH_3CN) were added. ECD and UV-vis signals were recorded after each addition of Cu(I) (Figure S35 and 37a).

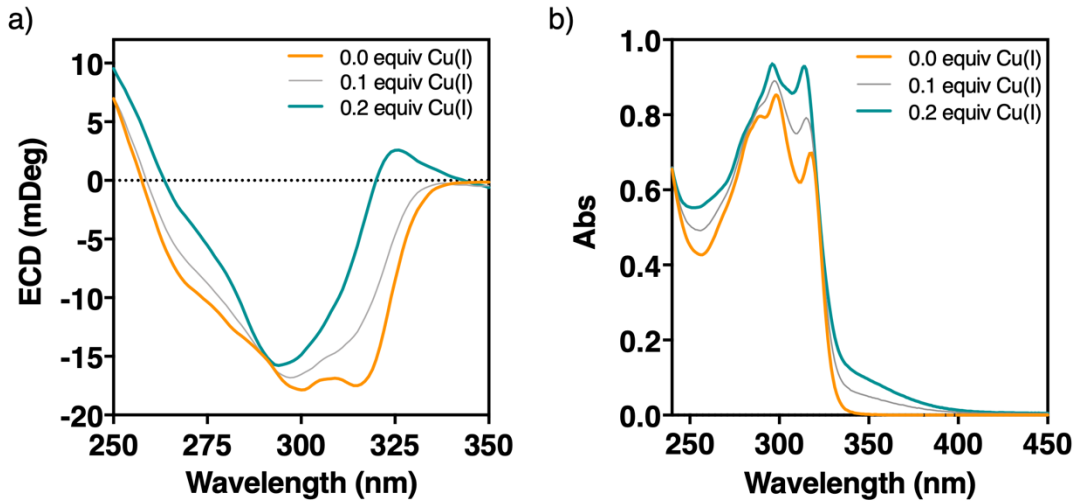

Figure S35. (a) ECD spectra and (b) UV-vis of mono-(*M*)-**2** (0.25 mM in $CHCl_3$) upon addition of $[Cu(CH_3CN)_4]BF_4$ (15.89 mM in CH_3CN). Green line: ECD and UV-vis signal at the saturation value of Cu(I).

Poly-(*M*)-**2** was dissolved in $CHCl_3$ (0.50 mM) and different volumes of $Cu(MeCN)_4BF_4$ solution (15.89 mM in CH_3CN) were added. ECD and UV-vis signals were recorded after each addition of Cu(I) (Figure S36 and S37b). The same conditions were used for mono-(*P*)-**2** poly-(*P*)-**2** (Figure S36 and S37, respectively).

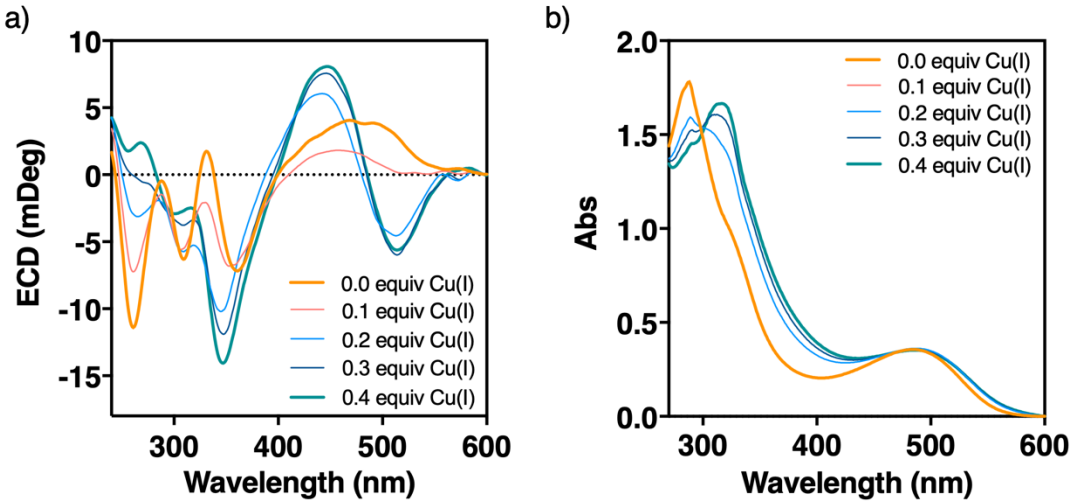

Figure S36. (a) ECD spectra and (b) UV-vis of poly-(*M*)-**1** (0.50 mM in $CHCl_3$) upon addition of $[Cu(CH_3CN)_4]BF_4$ (15.89 mM in CH_3CN). Green line: ECD and UV-vis signal at the saturation value of Cu(I).

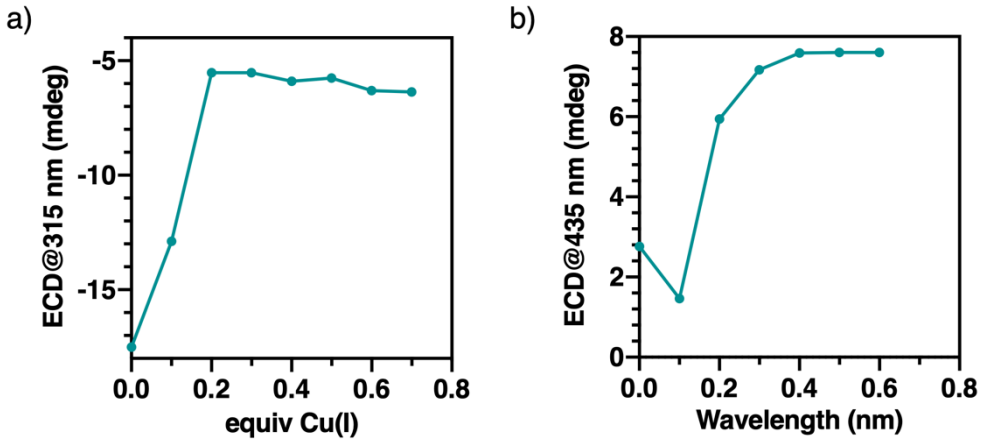

Figure S37. Saturation curves for titration in a $CHCl_3$ with Cu(I) of (a) mono-(*M*)-**1** at 315nm and of (b) poly-(*M*)-**1** at 435 nm.

5.3.10.1.2.2. Metal ion removal of poly-(*M*)-2 / Cu(I)

The metal scavenger QuadraPure™ resin was used to remove the metal ions from the previously complexed poly-(*M*)-**2** system until the original signal was recovered (red line in Figure S38). The resin was swollen in DCM for 30 minutes at room temperature prior to use. Then 10 mg of resin were added to the complexed polymer solution and the mixture was stirred at rt overnight. The resin was easily removed by filtration and the ECD and UV-vis of were recorded (Figure S38).

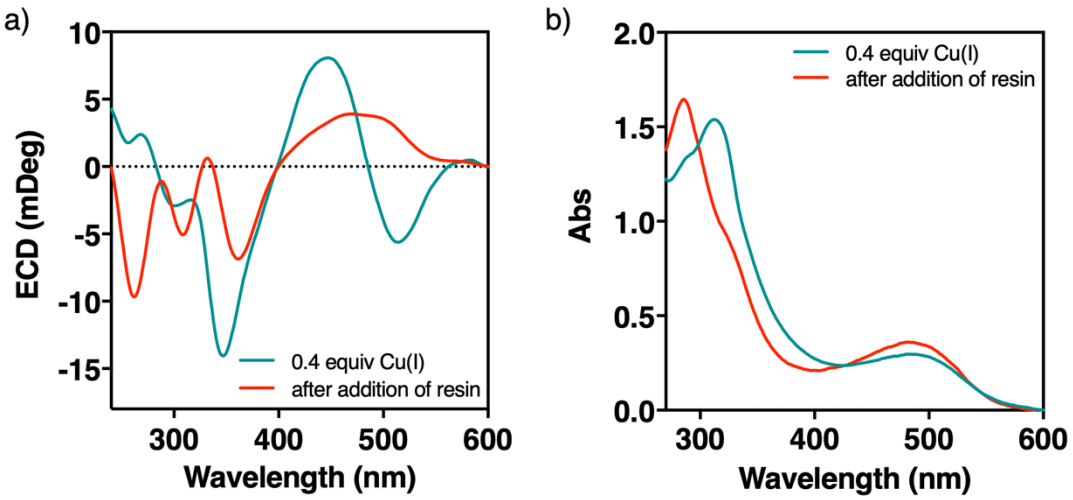

Figure S38. (a) ECD spectra and (b) UV-vis of previously Cu(I)-complexed poly-(*M*)-**2** solution (0.4 equiv of $[Cu(CH_3CN)_4]BF_4$ from 15.89 mM in CH_3CN to 0.50 mM polymer solution) and after addition of resin in $CHCl_3$.

5.3.10.1.2.2. Titration of mono-(*P*)-2 and poly-(*P*)-2 with Cu(I)

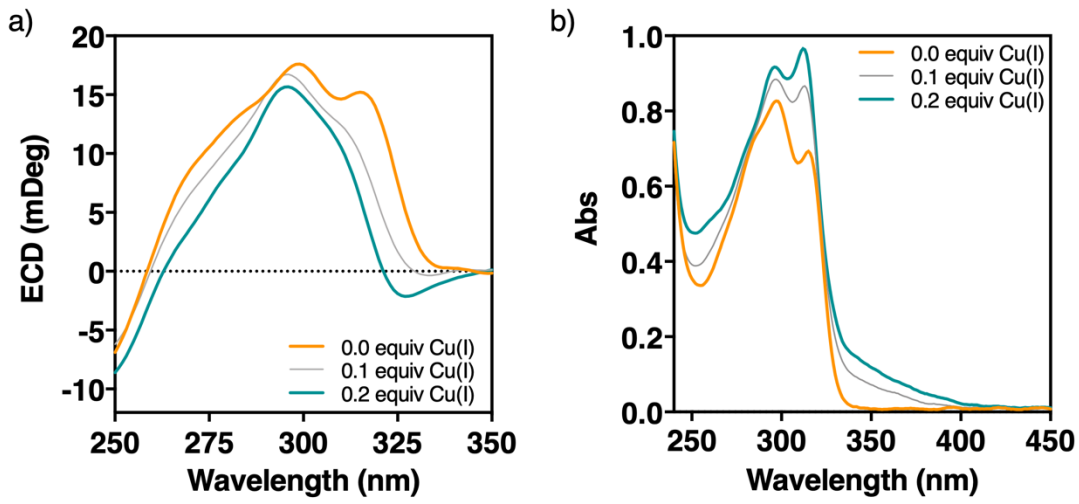

Figure S39. (a) ECD spectra and (b) UV-vis of mono-(*P*)-**2** (0.25 mM in $CHCl_3$) upon addition of $[Cu(CH_3CN)_4]BF_4$ (15.89 mM in CH_3CN). Green line: ECD and UV-vis signal at the saturation value of Cu(I).

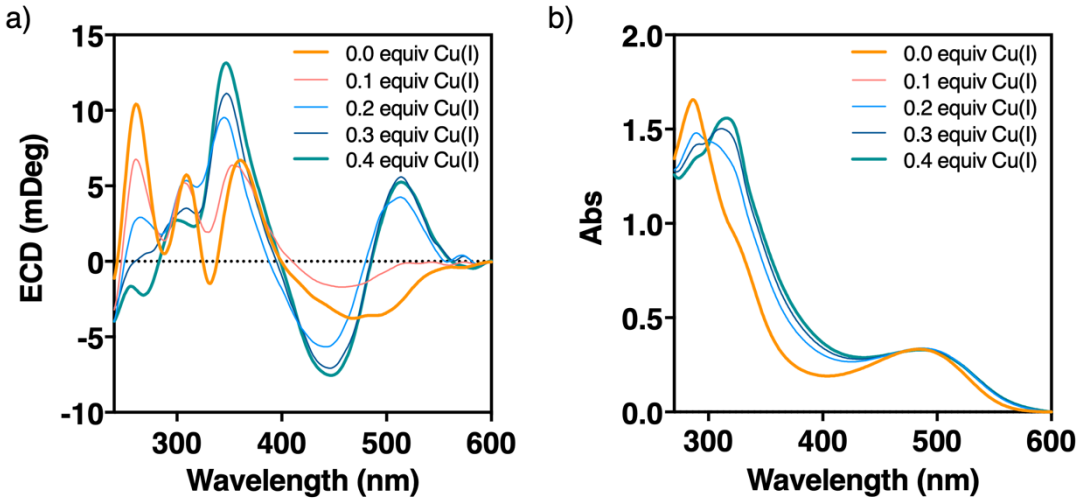

Figure S40. (a) ECD spectra and (b) UV-vis of poly-(*P*)-**2** (0.50 mM in $CHCl_3$) upon addition of $[Cu(CH_3CN)_4]BF_4$ in CH_3CN (15.89 mM). Green line: ECD and UV-vis signal at the saturation value of Cu(I).

5.3.10.1.2.3. Titration of poly-(*M*)-2 with several metal ions

Solutions of poly-(*M*)-**2** (0.50 mM in THF) were titrated with different metal ClO_4^- salts solutions (16 mM in CH_3CN).

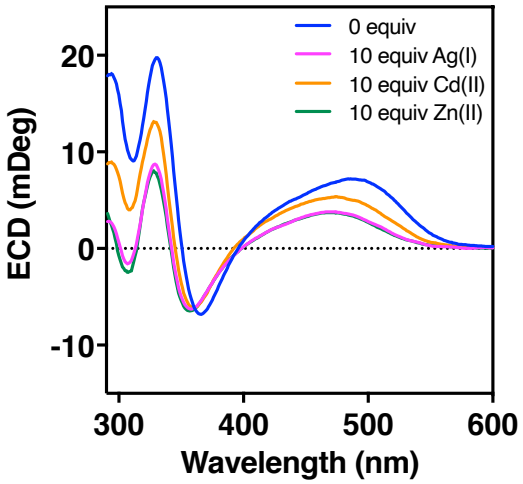

Figure S41. ECD spectra of poly-(*M*)-**2** (0.50 mM in THF) after titration with different metal ClO_4^- salts.

5.3.10.2 Titration experiments of mono-1 and poly-1

For mono-**1** and poly-**1**, conditions similar to those mentioned above for mono-**2** and poly-**2** were used.

5.3.10.2.1. Titration experiments of mono-1 and poly-1 with Formic Acid

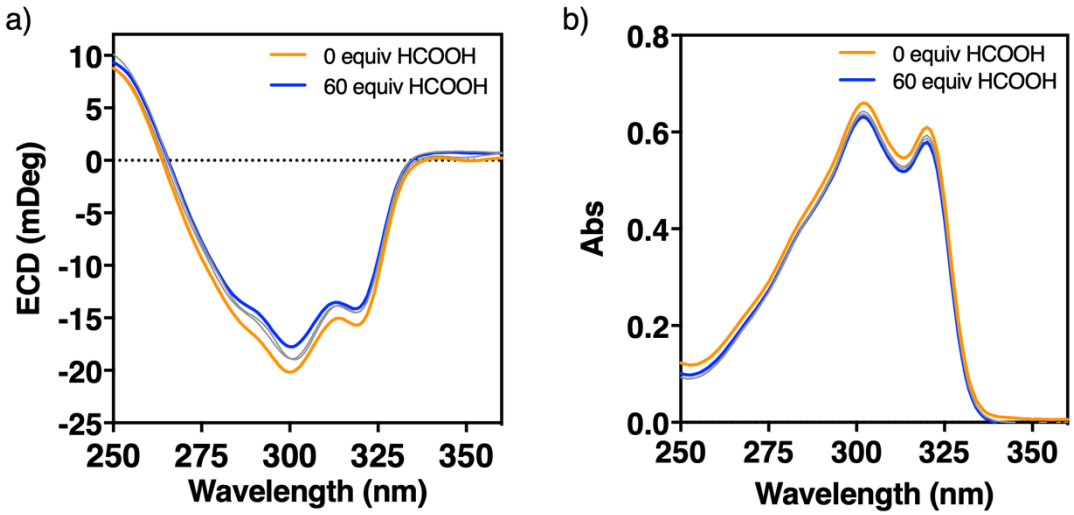

Figure S42. (a) ECD spectra and (b) UV-vis of mono-(*M*)-**1** (0.25 mM) upon addition of formic acid in $CHCl_3$ (0.43 M). Blue line: ECD and UV-vis signal at the saturation value of HCOOH.

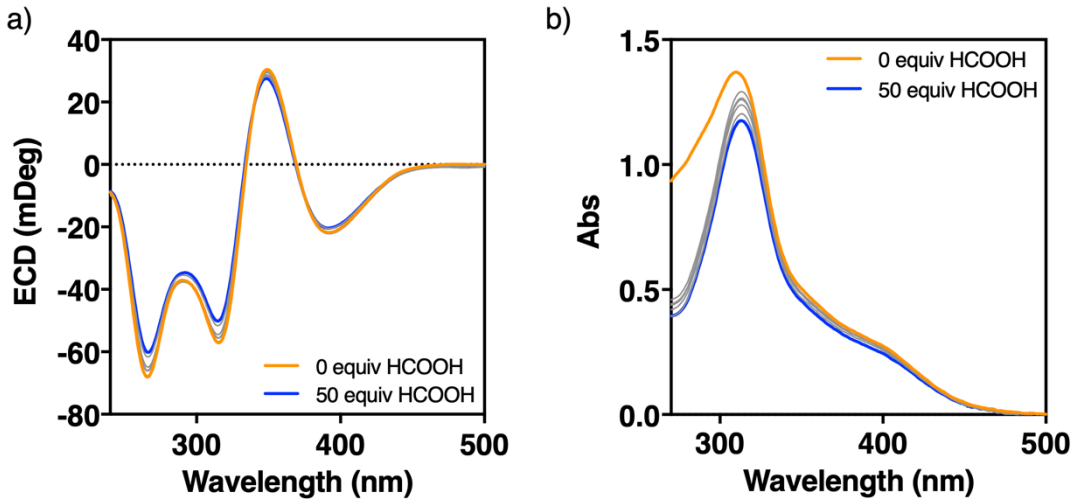

Figure S43. (a) ECD spectra and (b) UV-vis of poly-(*M*)-**1** (0.50 mM) upon addition of HCOOH in $CHCl_3$ (0.43 M). Blue line: ECD and UV-vis signal at the saturation value of HCOOH.

5.3.10.2.2. Titration experiments of mono-1 and poly-1 with Cu(I)

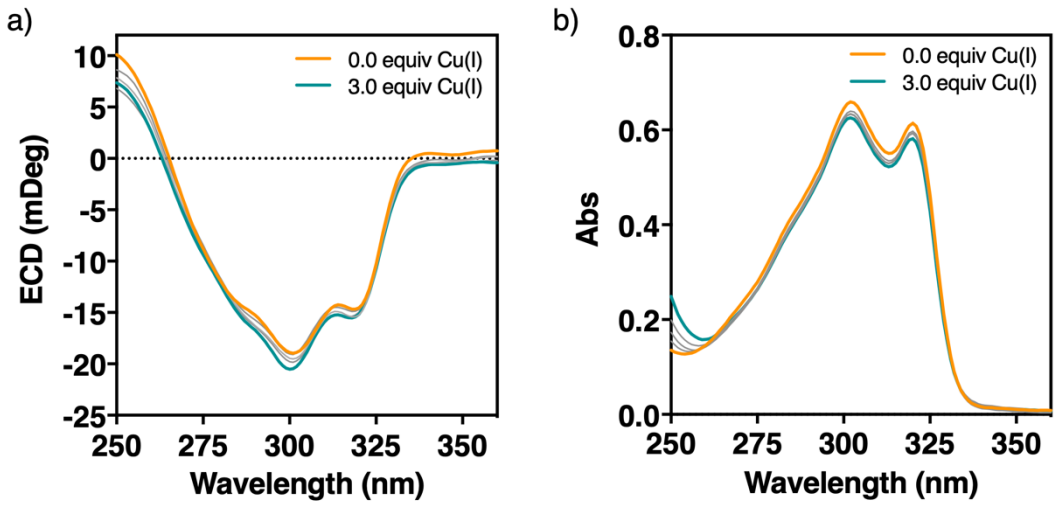

Figure S44. (a) ECD spectra and (b) UV-vis of mono-(*M*)-**1** (0.25 mM) upon addition of $[Cu(CH_3CN)_4]BF_4$ in CH_3CN (15.89 mM). Green line: ECD and UV-vis signal at the saturation value of Cu(I).

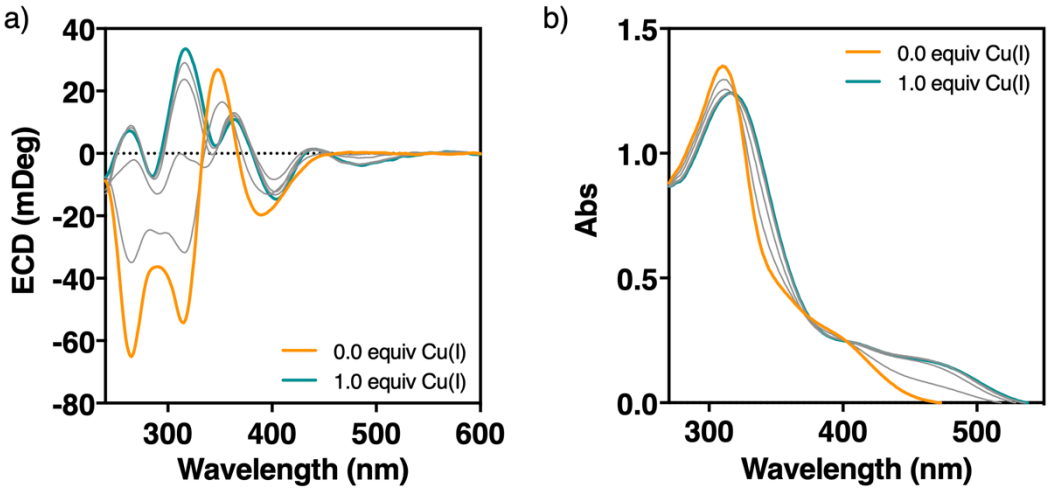

Figure S45. (a) ECD spectra and (b) UV-vis of poly-(*M*)-**1** (0.50 mM) upon addition of $[Cu(CH_3CN)_4]BF_4$ in CH_3CN (15.89 mM). Green line: ECD and UV-vis signal at the saturation value of Cu(I).

5.3.11. NMR Titrations Experiments

5.3.11.1. NMR titration experiments of the mono-(*M*)-2 with Formic Acid

^{1}H NMR experiments were measure to solutions of mono-(*M*)-**2** (11.71 mM) in $CDCl_3$ upon directly addition of Formic Acid solution (1.09 M in $CDCl_3$).

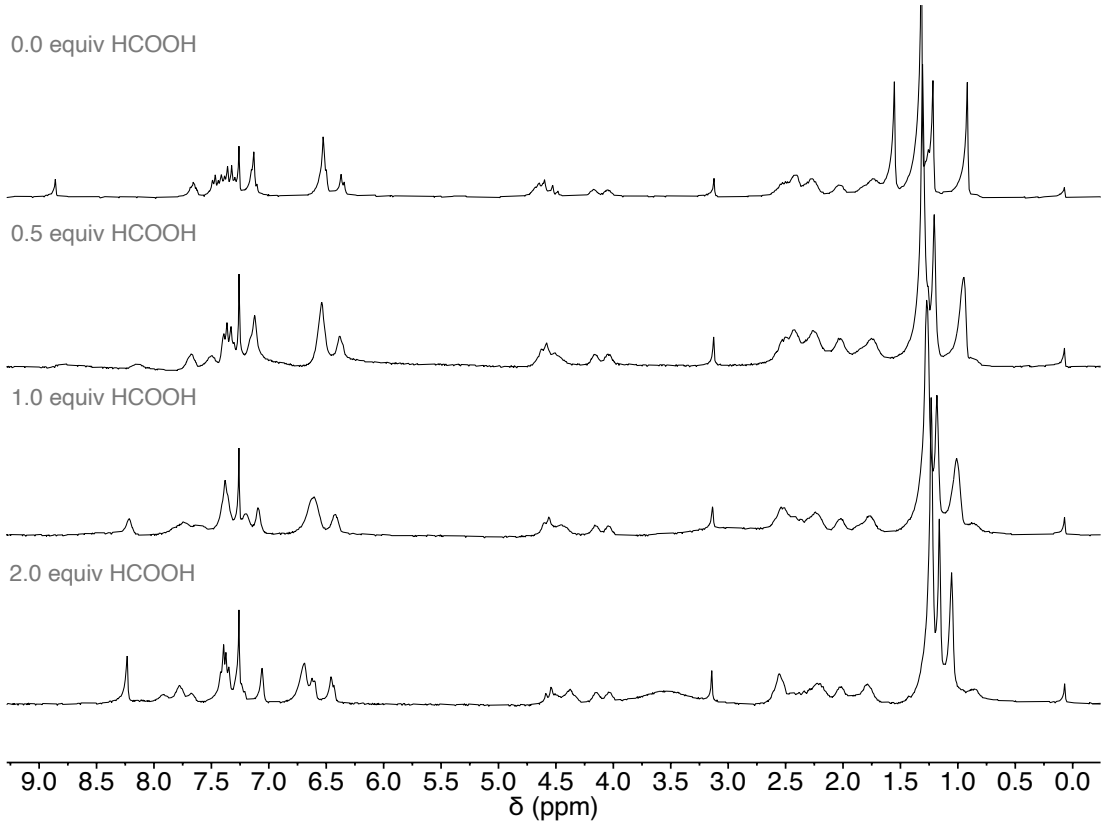

Figure S46. ^{1}H-NMR of mono-(*M*)-**2** in the presence of different amounts of formic acid (HCOOH) ($CDCl_3$, 293 K, 300 MHz).

5.3.11.2. NMR titration experiments of the mono-(*M*)-2 with Cu(I)

^{1}H NMR experiments were measure to solutions of mono-(*M*)-**2** (11.71 mM) in $CDCl_3$ upon addition of tetrakis(acetonitrile)copper(I) tetrafluoroborate solution (123.34 mM in CD_3CN). Tetrakis(acetonitrile)copper(I) tetrafluoroborate (97%) was solved in anhyd CD_3CN and directly added to the NMR tube.

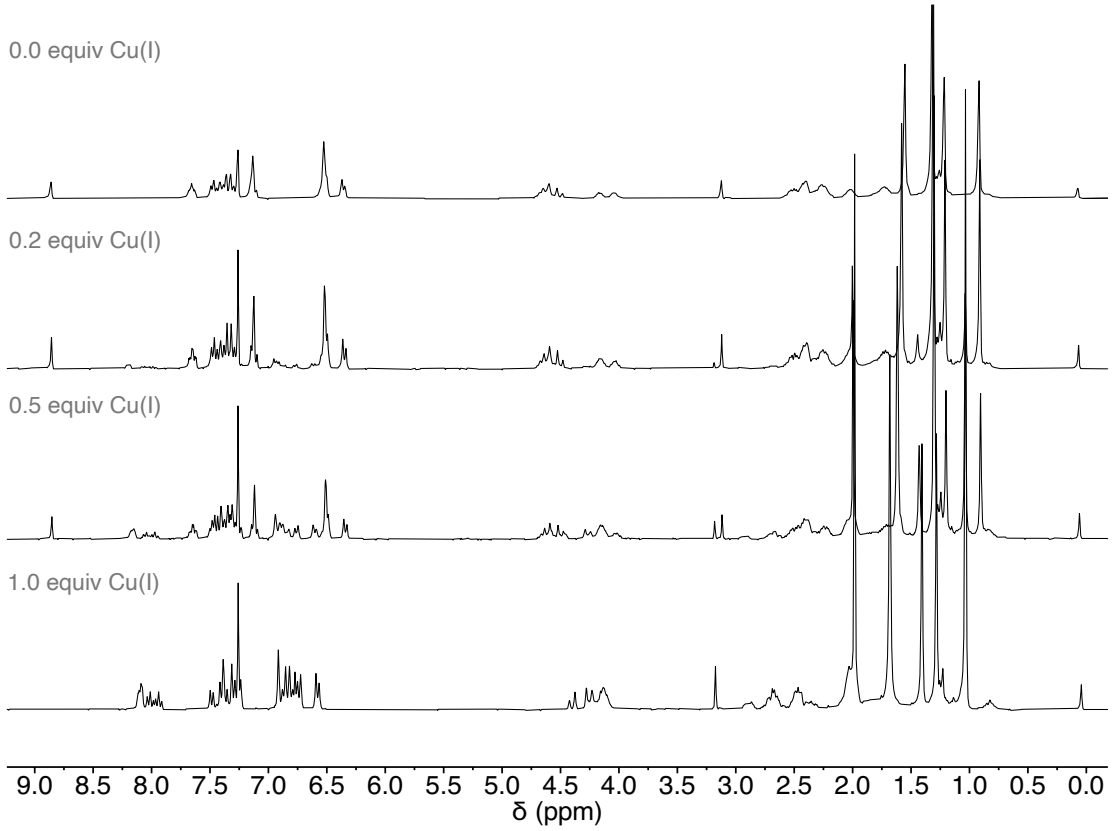

Figure S47. ^{1}H-NMR of mono-(*M*)-**2** in the presence of different amounts of Cu(I) ($CDCl_3$, 293 K, 300 MHz).

5.3.12. ROESY NMR Experiments

ROESY NMR spectra were run both before and after Cu(I) and Formic Acid titration of mono-(*M*)-**2** to evaluate the rotation of the macrocycle around the thread as the signals were significantly shifted after titration experiments (Figure S48). Cu(I) titration was performed by the addition of tetrakis(acetonitrile)copper(I) tetrafluoroborate solution (123.34 mM in CD_3CN). Formic Acid titration was carried out by the addition of an acid solution (1.09 M in $CDCl_3$). The experiments were performed at a low temperature (278 K) to favor the equilibrium shifted towards the most stable conformer in each case. The most relevant ROESY NMR cross-peaks are highlighted in the spectra and with red arrows in the monomer structure.

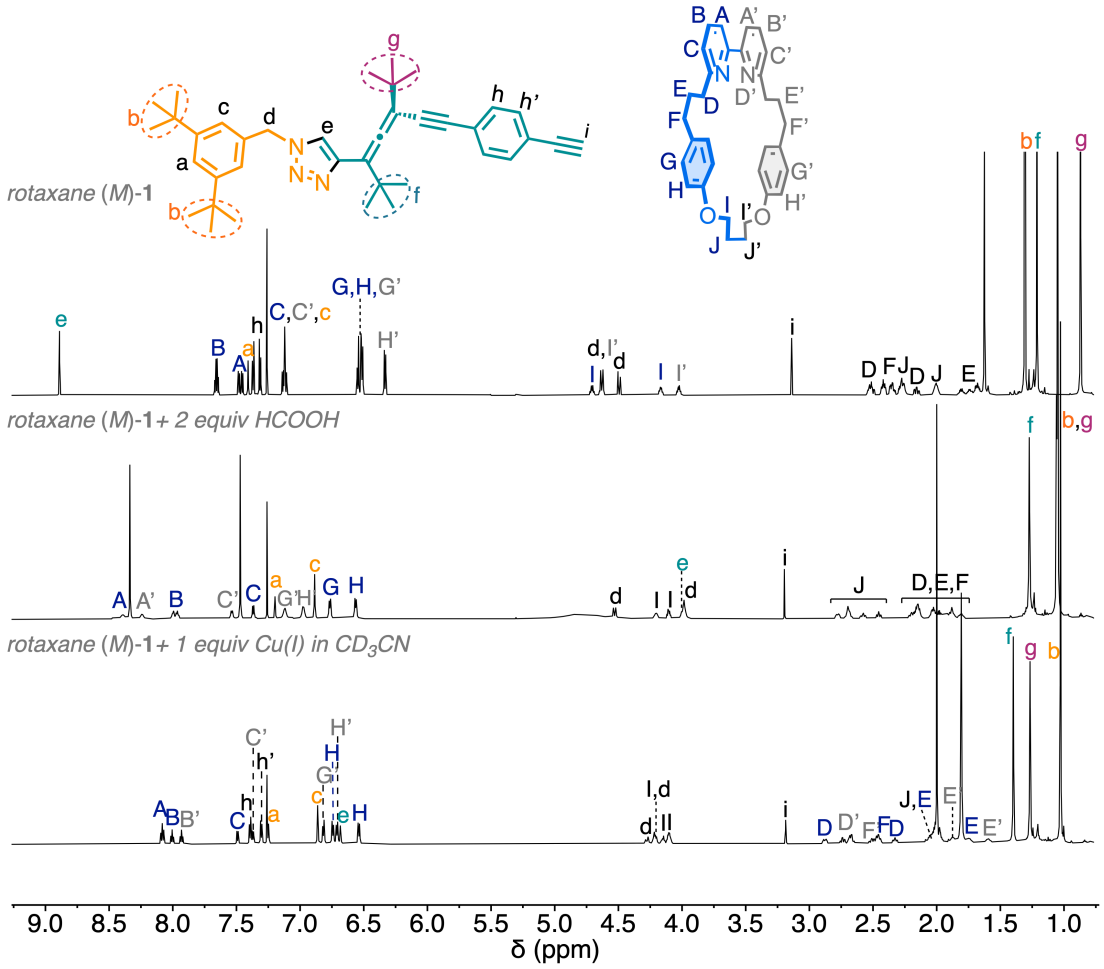

Figure S48. ^{1}H-NMR of mono-(*M*)-**2** (top), after titration with formic acid (middle) and with Cu(I) (below) ($CDCl_3$, 278 K, 750 MHz).

5.3.12.1. ROESY NMR Experiments of mono-(*M*)-2

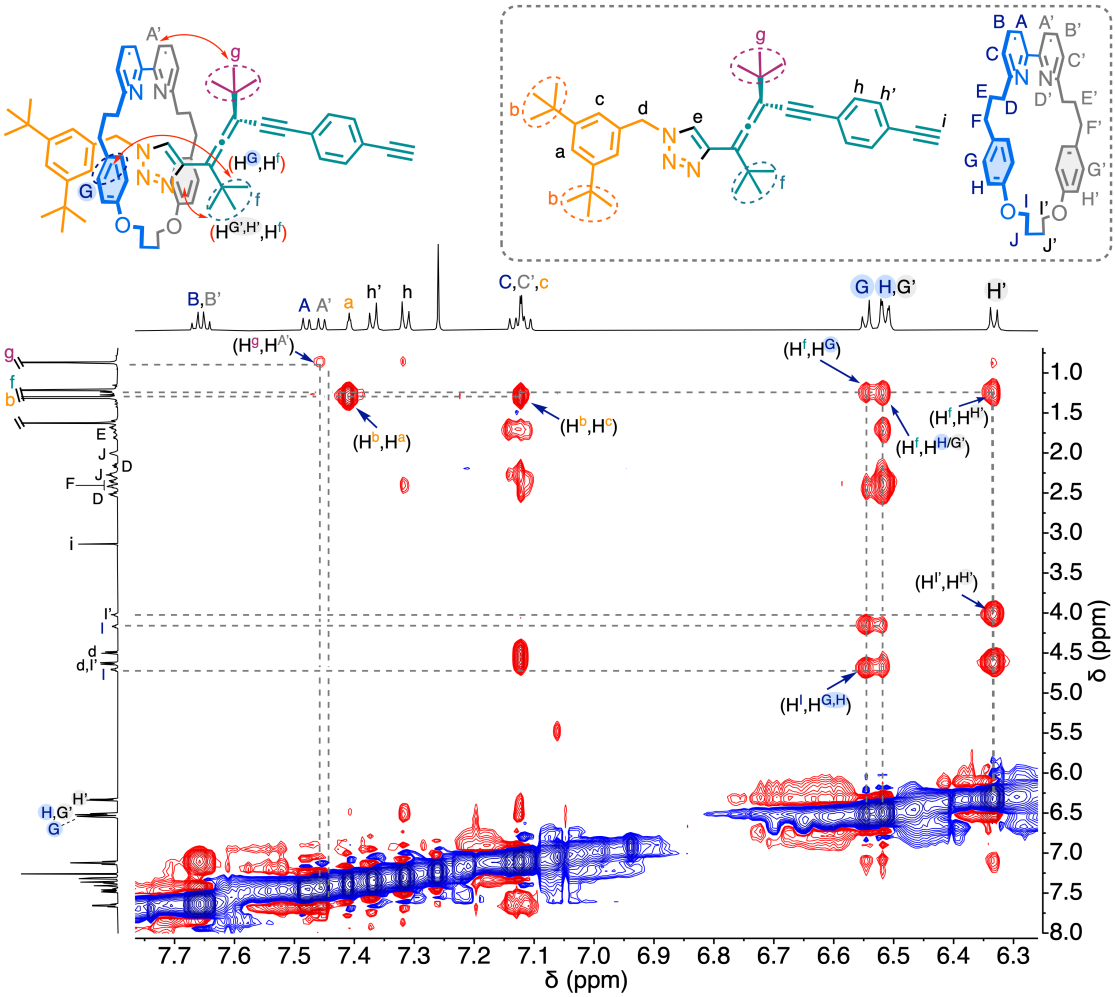

Figure S49. ^{1}H ROESY NMR of mono-(*M*)-**2**, zoomed area (7.8 – 6.2 ppm) ($CDCl_3$, 278 K, 750 MHz).

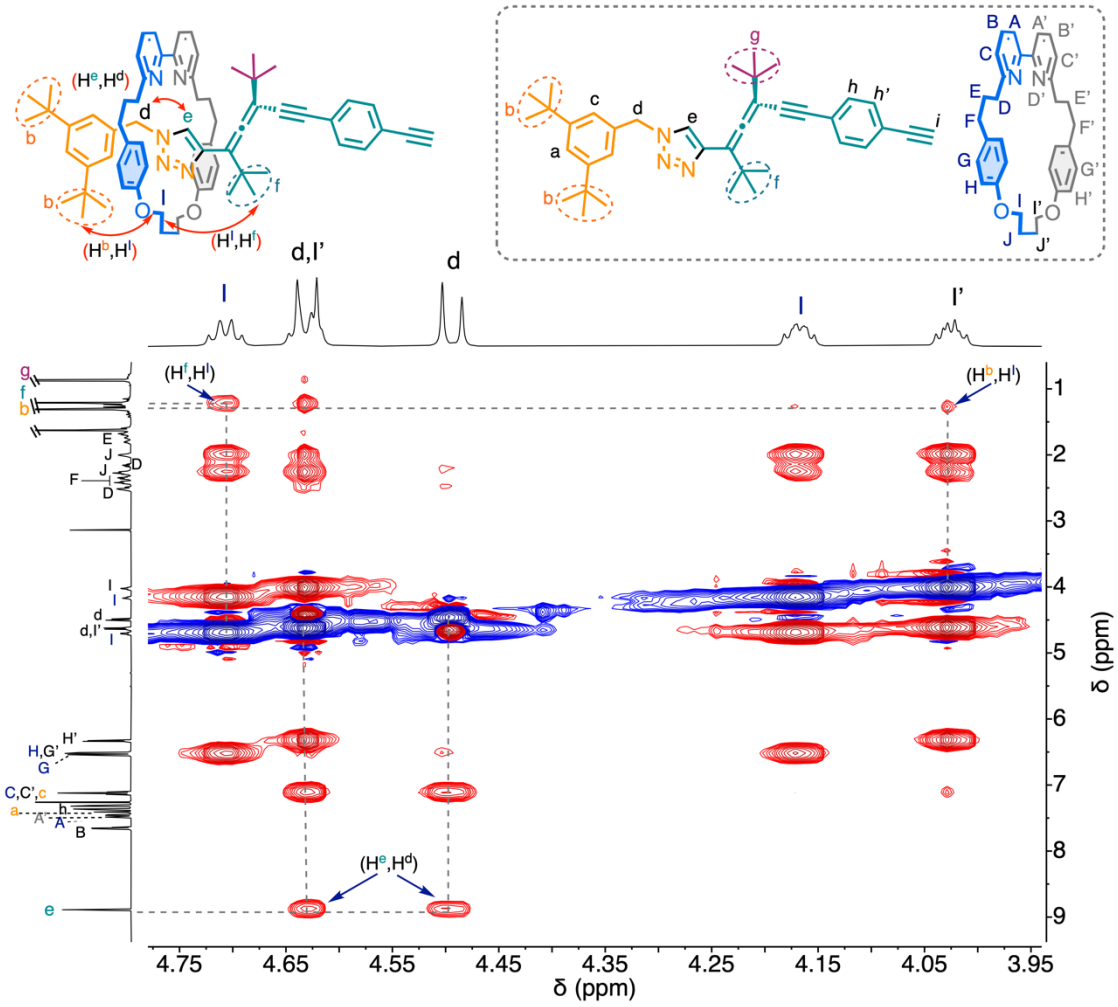

Figure S50. ^{1}H ROESY NMR of mono-(*M*)-**2**, zoomed area (4.8 – 3.9 ppm) ($CDCl_3$, 278 K, 750 MHz).

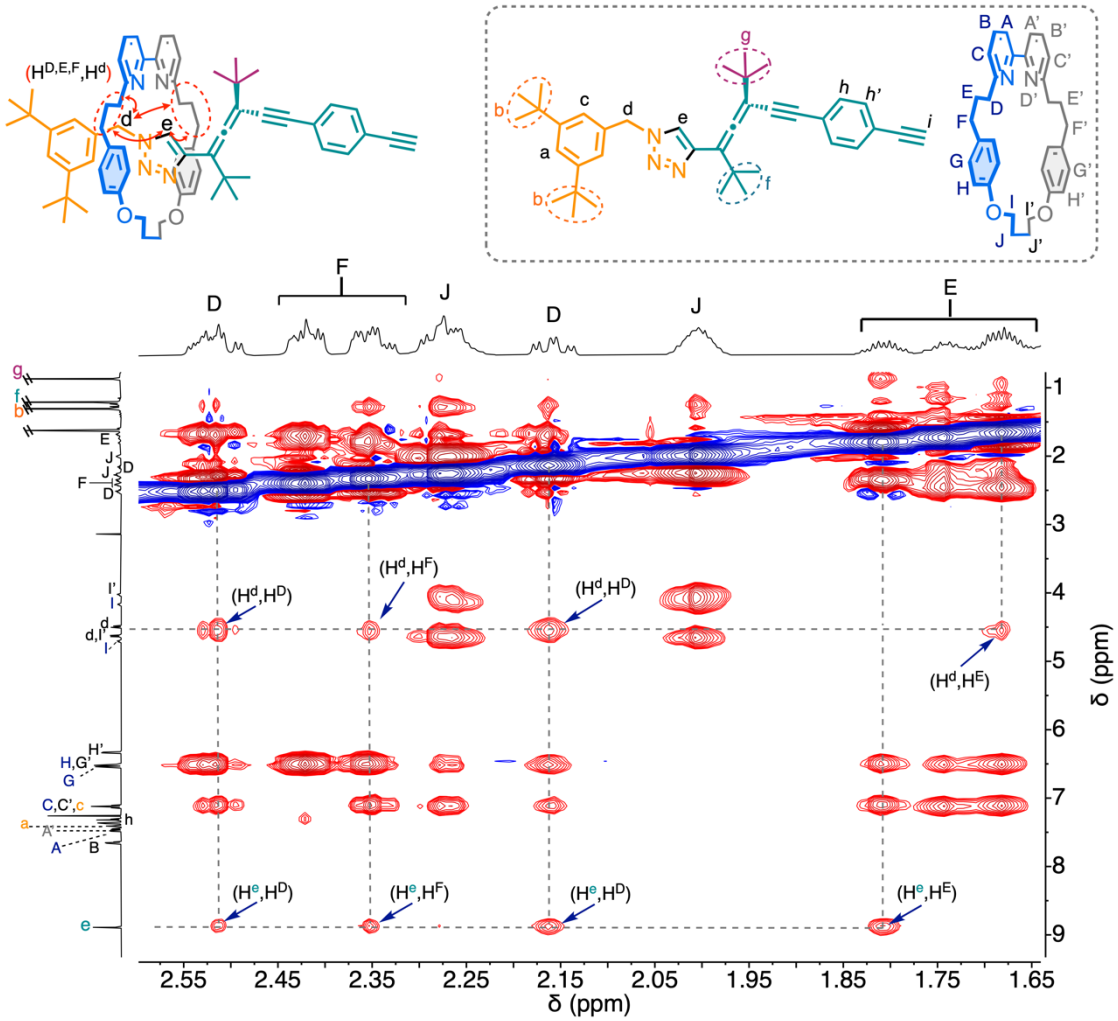

Figure S51. ^{1}H ROESY NMR of mono-(*M*)-**2**, zoomed area (2.6 – 1.6 ppm) ($CDCl_3$, 278 K, 750 MHz).

5.3.12.2. ROESY NMR Experiments of mono-(*M*)-2 after Formic Acid titration

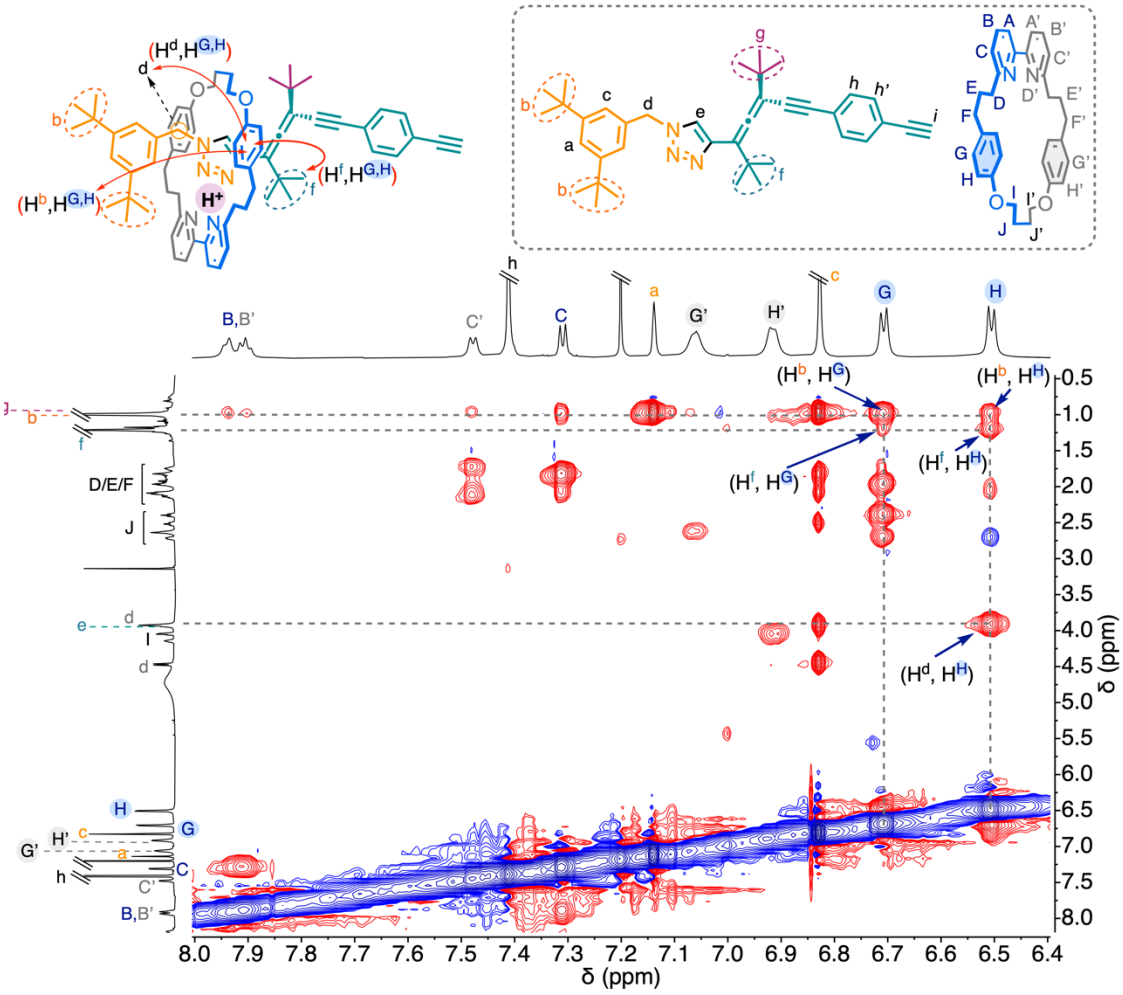

Figure S52. ^{1}H ROESY NMR of mono-(*M*)-**2** after addition of 2 equiv of HCOOH (1.09 M in $CDCl_3$), zoomed area 1 (8.0 – 6.4 ppm) ($CDCl_3$, 278 K, 750 MHz).

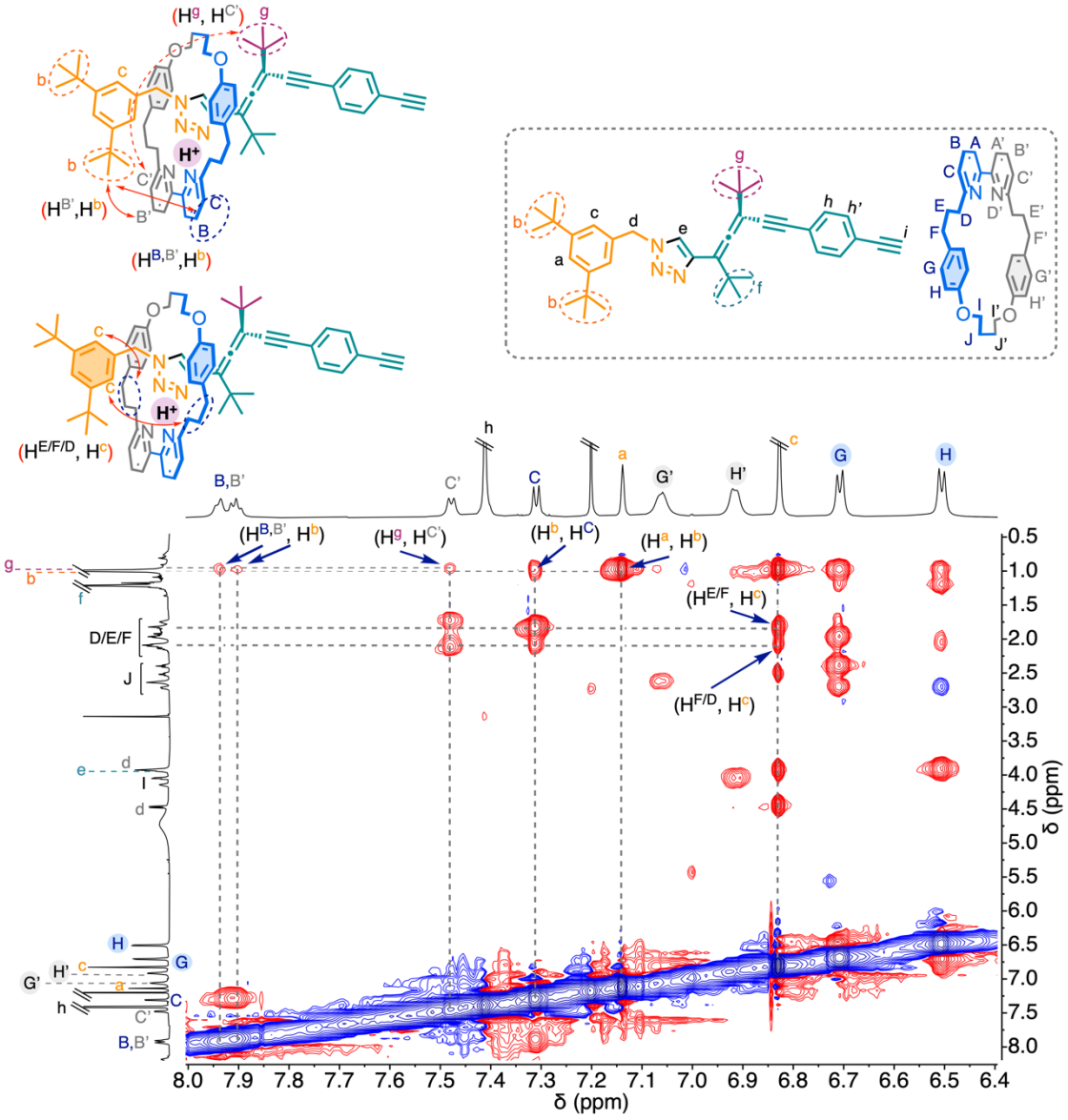

Figure S53. ^{1}H ROESY NMR of mono-(*M*)-**2** after addition of 2 equiv of HCOOH (1.09 M in $CDCl_3$), zoomed area 2 (8.0 – 6.4 ppm) ($CDCl_3$, 278 K, 750 MHz).

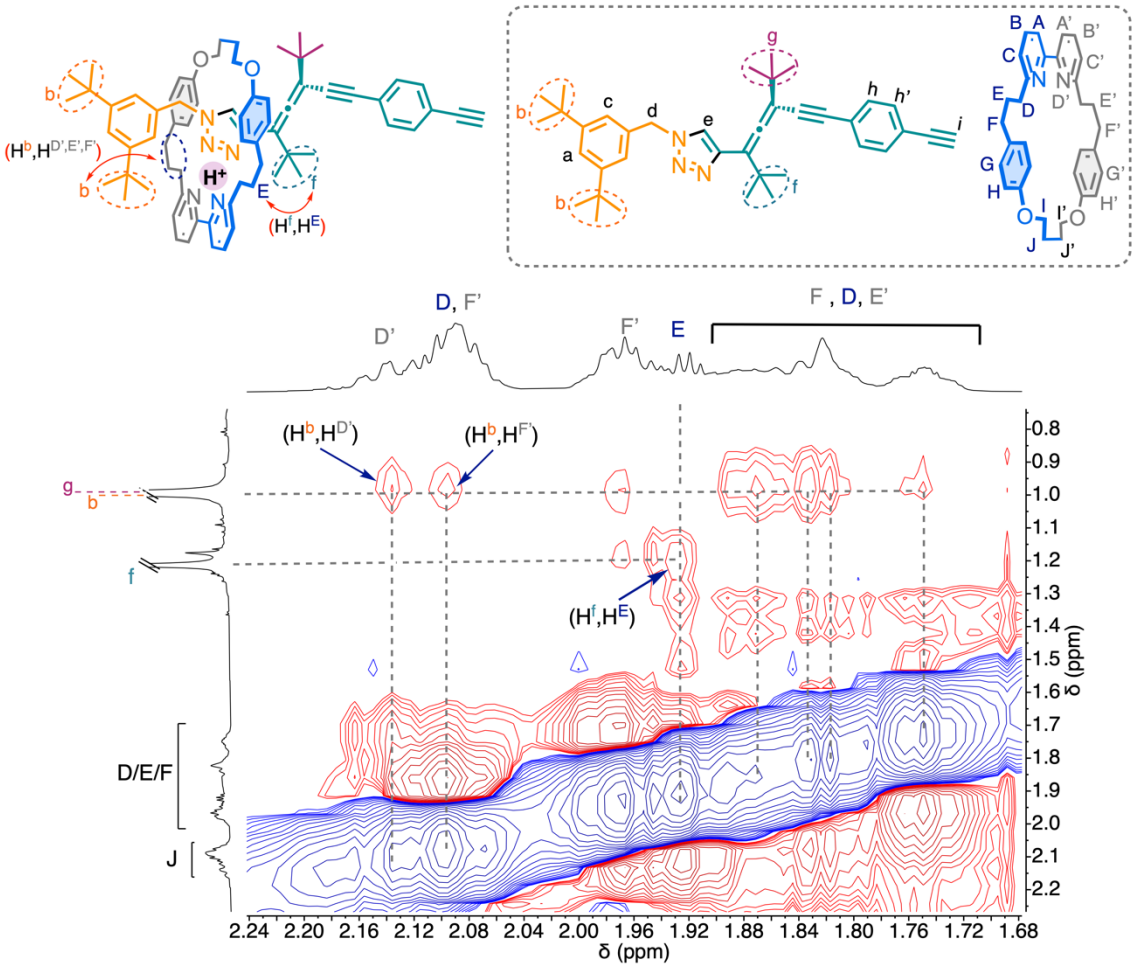

Figure S54. ^{1}H ROESY NMR of mono-(*M*)-**2** after addition of 2 equiv of HCOOH (1.09 M in $CDCl_3$), zoomed area 2 (2.2 – 1.7 ppm) ($CDCl_3$, 278 K, 750 MHz).

5.3.12.3. ROESY NMR Experiments of mono-(*M*)-2 after Cu(I) titration

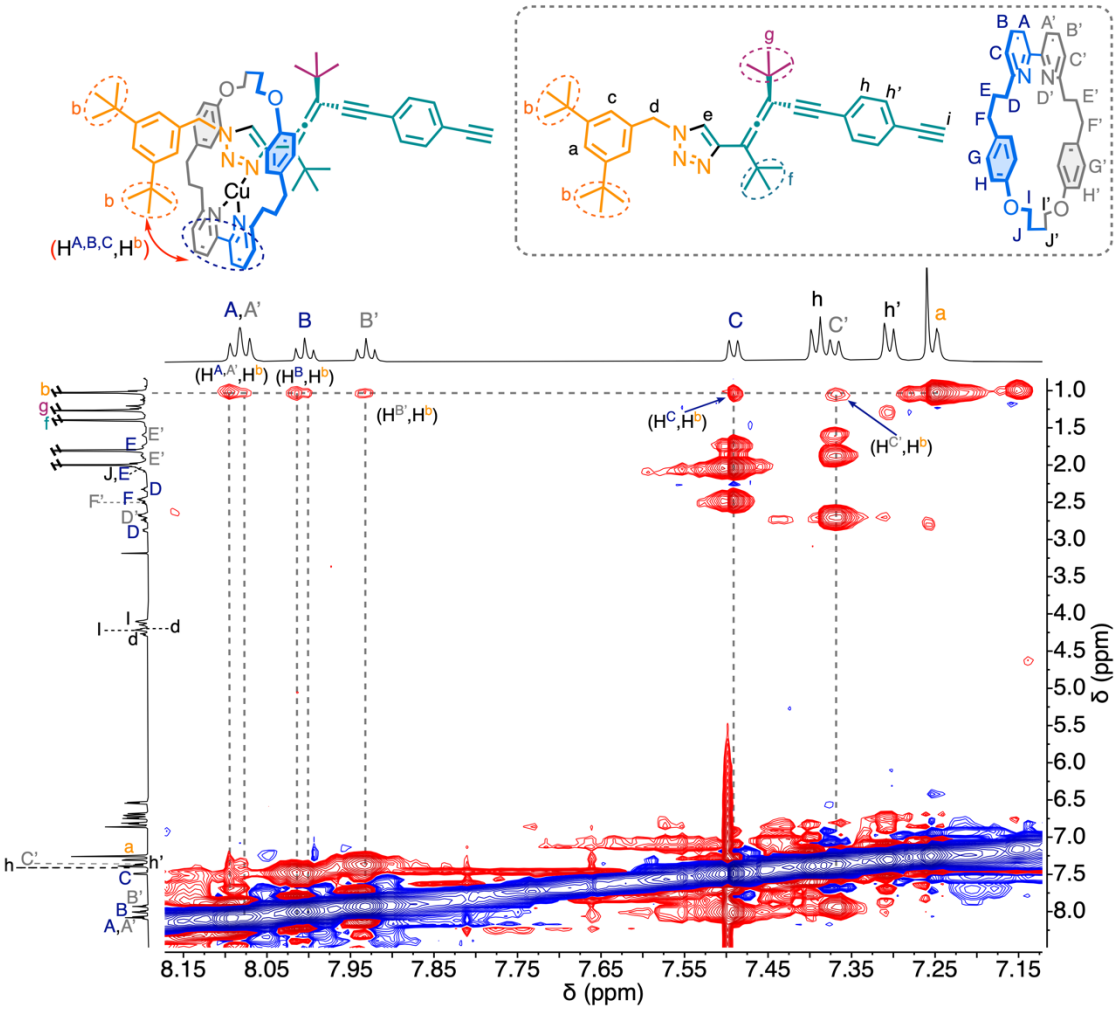

Figure S55. ^{1}H ROESY NMR of mono-(*M*)-**2** after addition of 1 equiv of $[Cu(CH_3CN)_4]BF_4$ solution (123.34 mM in CD_3CN), zoomed area (8.2 – 7.1 ppm) ($CDCl_3$, 278 K, 750 MHz).

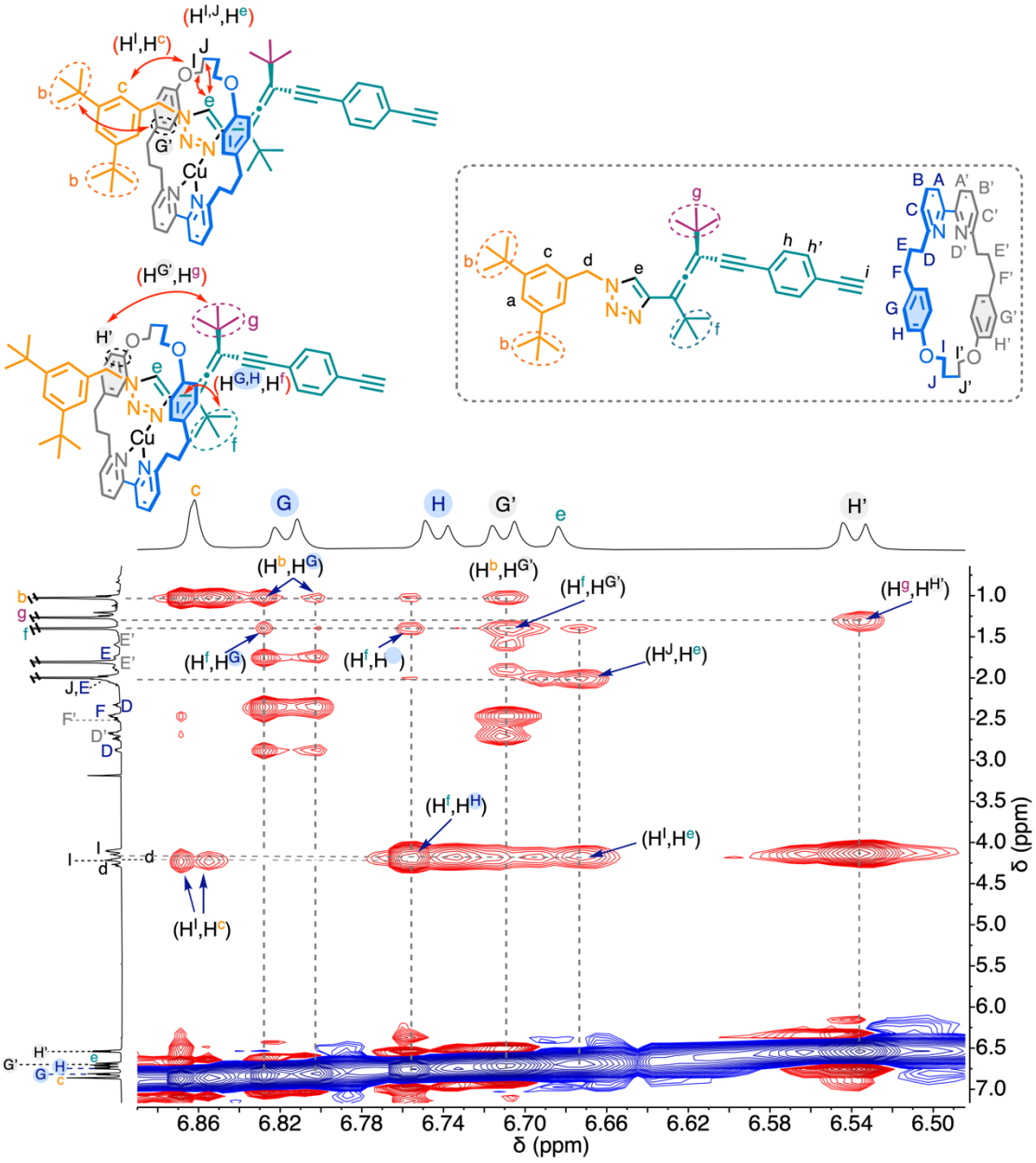

Figure S56. ^{1}H ROESY NMR of mono-(*M*)-**2** after addition of 1 equiv of $[Cu(CH_3CN)_4]BF_4$ solution (123.34 mM in CD_3CN), zoomed area (6.9 – 6.4 ppm) ($CDCl_3$, 278 K, 750 MHz).

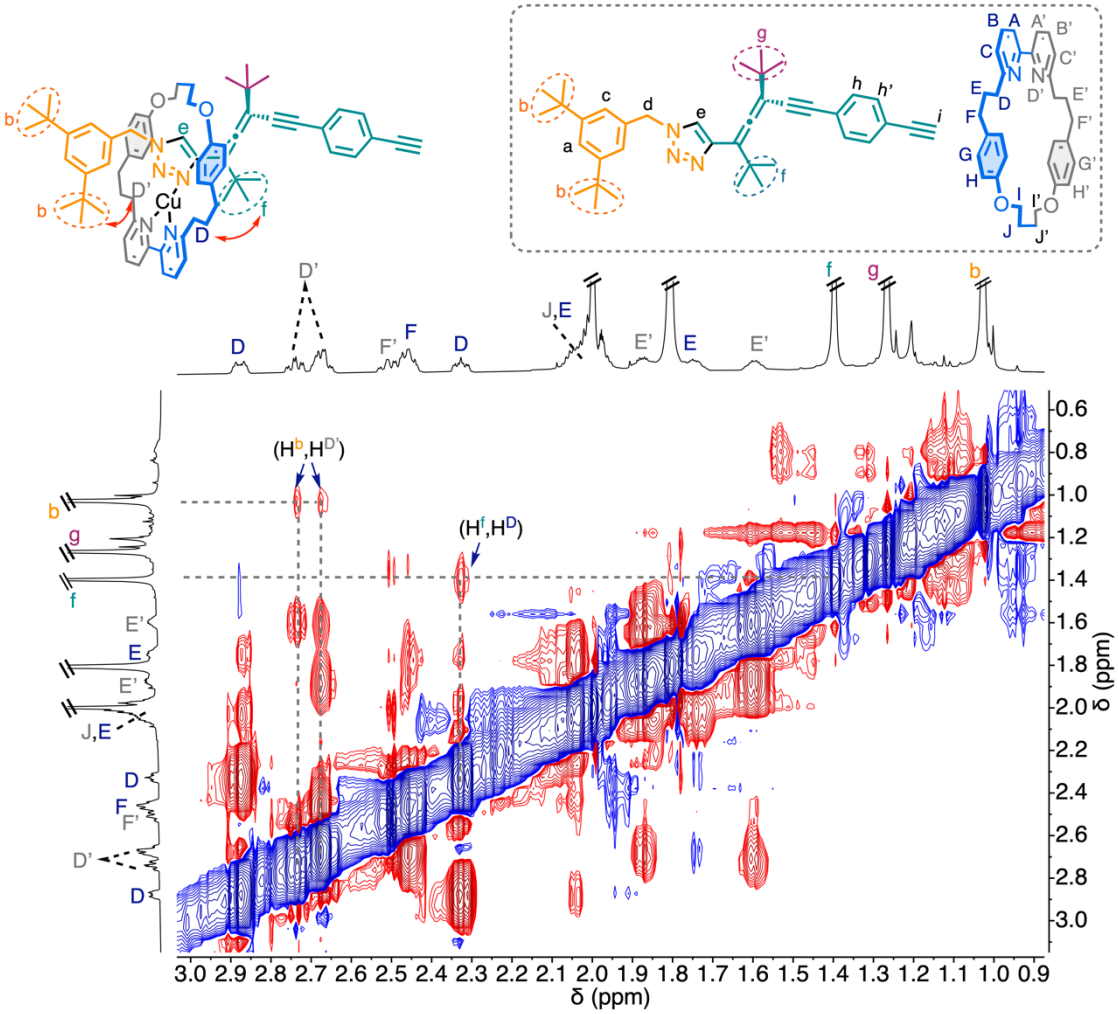

Figure S57. ^{1}H ROESY NMR of mono-(*M*)-**1** after addition of 1 equiv of $[Cu(CH_3CN)_4]BF_4$ solution (123.34 mM in CD_3CN), zoomed area (3.0 – 0.9 ppm) ($CDCl_3$, 278 K, 750 MHz).

5.3.13. AFM Measurements for poly-(*M*)-2

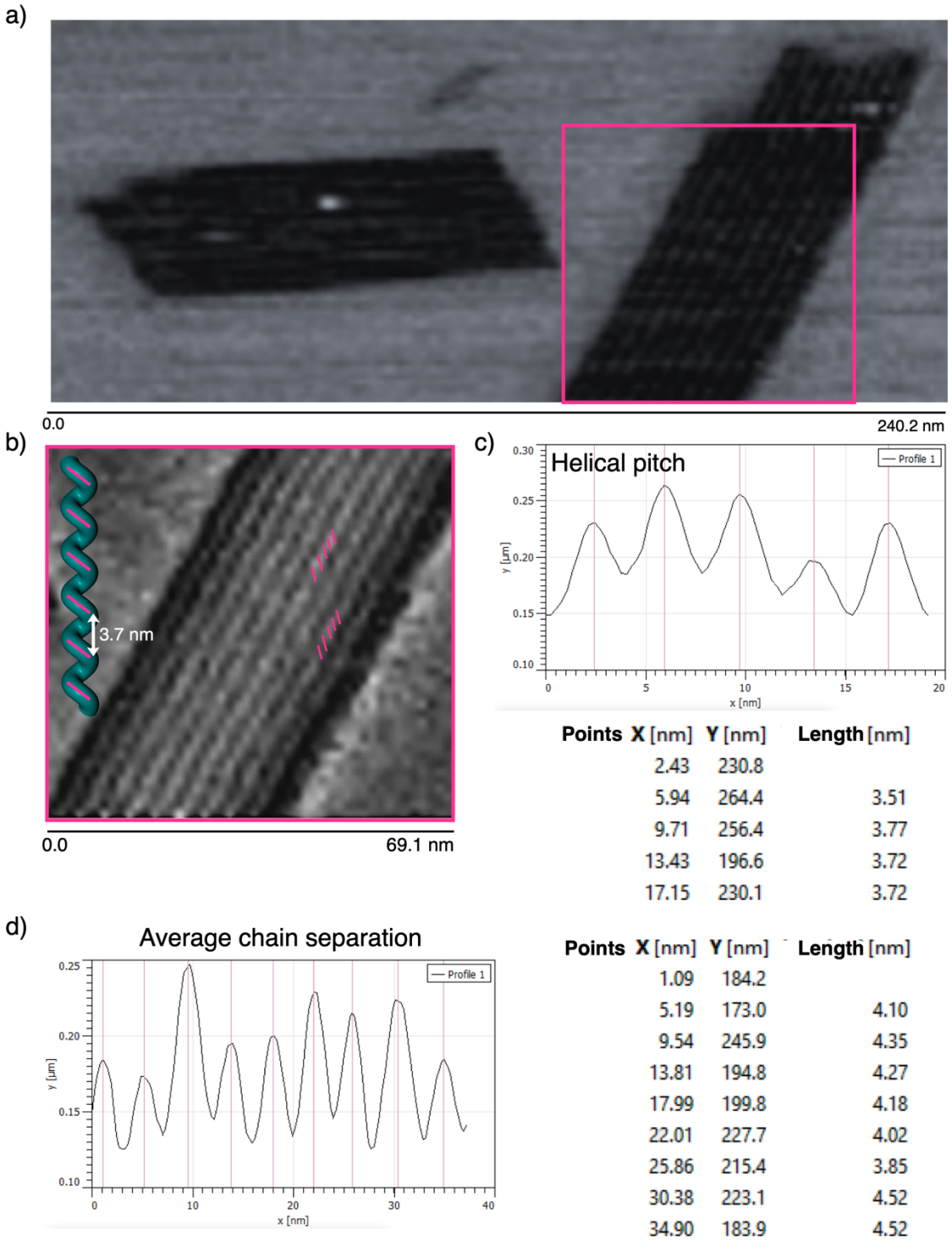

Points	X [nm]	Y [nm]	Length [nm]
	2.43	230.8	
	5.94	264.4	3.51
	9.71	256.4	3.77
	13.43	196.6	3.72
	17.15	230.1	3.72

Points	X [nm]	Y [nm]	Length [nm]
	1.09	184.2	
	5.19	173.0	4.10
	9.54	245.9	4.35
	13.81	194.8	4.27
	17.99	199.8	4.18
	22.01	227.7	4.02
	25.86	215.4	3.85
	30.38	223.1	4.52
	34.90	183.9	4.52

Figure S58. (a) AFM image for poly-(*M*)-**1** (prepared from a $CHCl_3$ solution) zoomed area. (b, c) Graphics depicting the helical pitch profile measured in the indicated area: helical pitch and average chain separation.

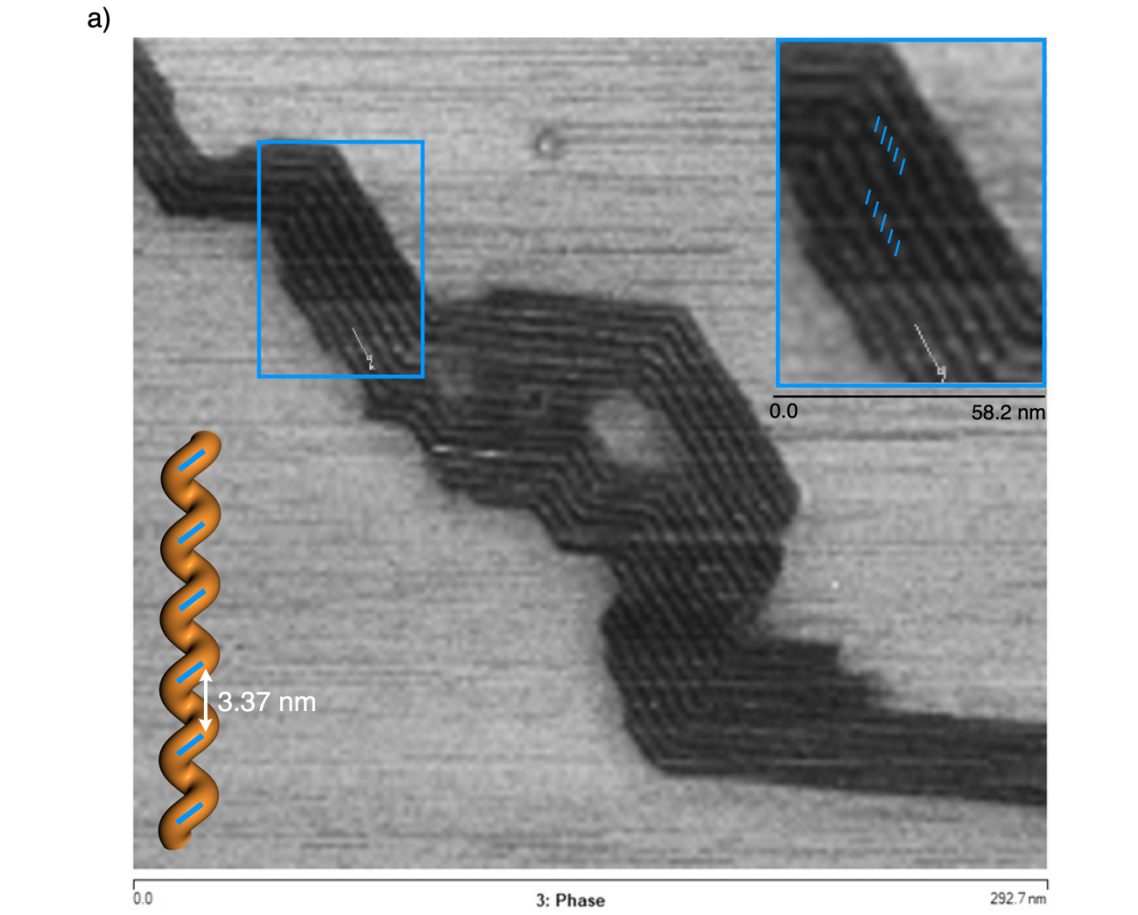

Points	X [nm]	Y [nm]	Length [nm]
	0.46	258.1	
	4.08	320.2	3.62
	7.52	405.7	3.43
	10.73	271.4	3.22
	13.95	245.7	3.22

Points	X [nm]	Y [nm]	Length [nm]
	1.67	214.3	
	6.28	247.0	4.60
	10.63	208.7	4.35
	14.90	176.3	4.27
	20.00	192.5	5.10
	23.85	201.1	3.85
	28.54	173.6	4.69

Figure S59. (a) AFM image for poly-(*M*)-**1**/Cu(I) (prepared from a solution of poly-(*M*)-**1** titrated with 1.0 equiv of Cu(I) and (b) zoomed area. (c, d) Graphics depicting the helical pitch profile measured in the indicated area: helical pitch and average chain separation.

5.4. Experimental Section and Methodology Chapter 3.4.

5.4.1. Materials and Methods

Reactions were conducted in dry solvents under argon unless otherwise stated. Et_3N was freshly distilled from CaH_2 under argon atmosphere. All chemicals were purchased from Sigma-Aldrich, Acros Organics, Alfa Aesar, Fluorochem, TCI Chemicals or Abcr and they were used as received.

The abbreviation "rt" refers to reactions carried out at a temperature between 21-25 ˚C. Reaction mixtures were stirred using Teflon-coated magnetic stir bars. Thin layer chromatography (TLC) was carried out on pre-coated silica gel F254 plates with visualization under UV light or by dipping the plate into solutions of phosphomolybdic acid or potassium permanganate solutions followed by heating. Column chromatography was performed on silica gel (40-60 µm) unless otherwise stated.

NMR experiments have been recorded in a Bruker spectromer (^{1}H frequency 300 MHz or 500MHz).

ECD measurements were done in a Jasco-720 and UV-vis studies were registered in a Jasco V-630 with a 1 mm quartz cuvette. The amount of polymer used is indicated in the corresponding section.

VT-ECD were measured in a Jasco-1100 with a 1 mm quartz cuvette.

Optical rotation was measured in a Jasco-P2000.

Enantiomers (*P*)-**DEA** and (*M*)-**DEA** were resolved by semipreparative HPLC using the CSP Chiralpak® IA (Diacel Chemical Industries Ltd.). Elution was performed with a mixture of Hexane:^{i}PrOH 99.2:0.8 at a flow of 3.5 mL·min^{-1}. Under these conditions, 100 μL of a solution of (±)-**DEA** in Hexane (15 mg·mL^{-1}) was injected.

GPC purification was performed on JAI LaboACE 5060 apparatus eluting in $CHCl_3$ at 10 mL·min^{-1} rate.

IR spectra were recorded in a Perkin-Elmer Spectrum Two apparatus using a cell equipped with BaF_2 lens and a Teflon spacer generating a 150 μm path length.

AFM measurements were performed in a Multimode V Scanning Probe Microscope (Veeco Instruments) in air at rt, with standard silicon cantilevers and supersharp cantilevers in tapping mode using 12 μm and 1 μm scanners. Nanoscope processing software and WSxM 4.0 Beta 1.0 [4] (Nanotec Electrónica, S.L.) was used for image analysis. All measurements were performed at CACTI (University of Vigo, Spain).

PyMOL was used as a molecular visualization system.

All computations were carried out using Gaussian-16 (G16RevC.01).[413]

5.4.2. Synthesis of Monomers

Enantiopure compounds (*P*)-**DEA**/(*M*)-**DEA**[251]and 3,4,5-tris(dodecyloxy)-*N*-(2-(4-iodobenzamido)ethyl)benzamide[416] were synthesized according to reported procedures (see Experimental Chapter 1 for enantiopure **DEA**).

*3,5-di-tert-butylhepta-3,4-dien-1,6-diyne (**S1**)*

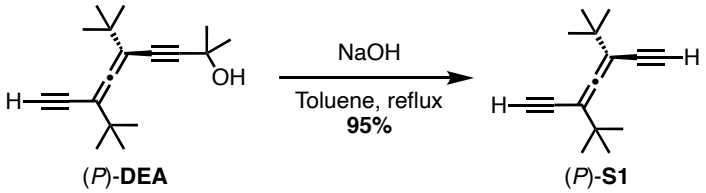

(*P*)-**DEA** (*P*)-**S1**

NaOH (650 mol%, 27.300 mmol, 1 g) was pulverized, introduced in a round-bottom flask and flame-dried under vacuum and then filled with Ar. 15 mL of dried toluene were added. (*P*)-**DEA** (100 mol%, 0.420 mmol, 150 mg) was dissolved in dried toluene (5 mL) and the solution was transferred to the NaOH-toluene mixture. The reaction mixture was refluxed for 2 h and then disrupted by adding distilled water. Then, the mixture was extracted with EtAcO. Evaporation *in vacuo* and purification by flash chromatography on silica gel (hexane: EtAcO (9.5:0.5) afforded (*P*)-**S1** (80 mg, 95%) as a yellow oil.

The corresponding enantiomer, (*M*)-**S1**, was obtained from (*M*)-**DEA**, by applying the same protocol as for (*P*)-**S1**.

Molecular Formula: $C_{15}H_{20}$**. MW:** 200.33 **g/mol.**

^{1}H-NMR (300 MHz, $CDCl_3$, 298K) *δ:* 2.99 (s, 2H), 1.15 (s, 18H)

^{13}C-NMR (75 MHz, $CDCl_3$, 298K) *δ:* 212.6, 102.8, 80.8, 80.7, 35.4, 28.9.

HRMS (ESI$^+$): *m/z* calcd. for $C_{15}H_{20}$ 200.1565; found 201.1075 $[M+H]^+$.

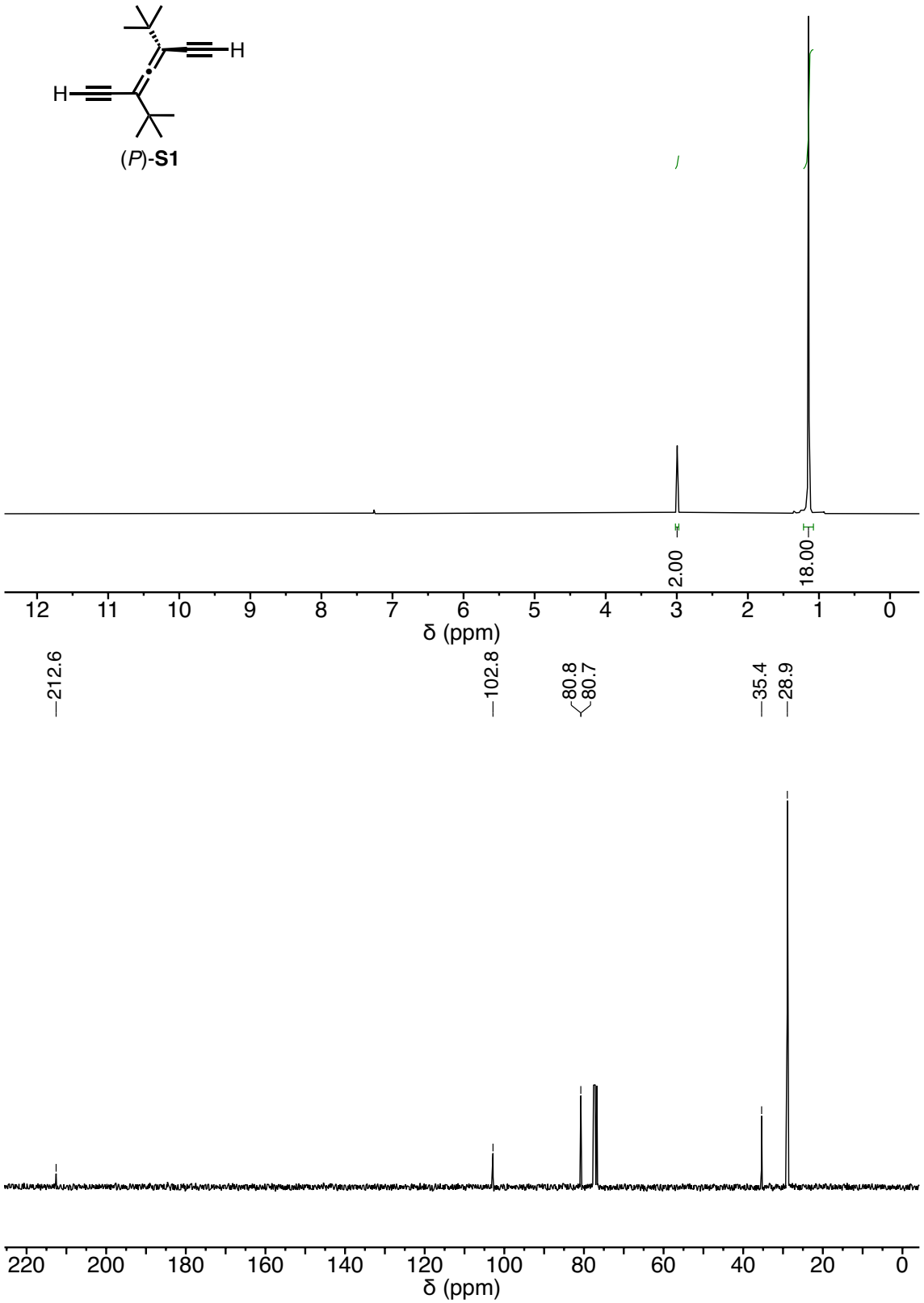

Figure S1. ^{1}H-NMR and ^{13}C-NMR of (*P*)-**S1** in $CDCl_3$.

*N,N'-(((4,4'-(3,5-di-tert-butylhepta-3,4-dien-1,6-diyne-1,7-diyl)bis(benzoyl))bis(azanediyl))bis(ethane-2,1-diyl))bis(3,4,5-tris(dodecyloxy)benzamide) (**1**)*

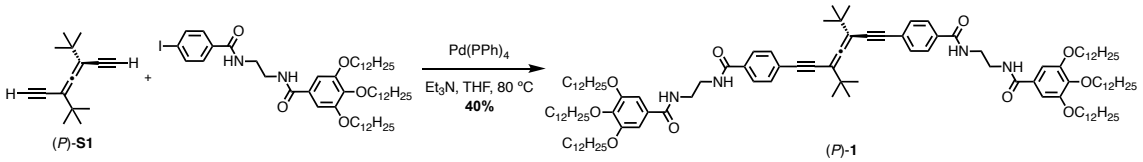

In a flame dried sealed tube 3,4,5-tris(dodecyloxy)-*N*-(2-(4-iodobenzamido)ethyl)benzamide (220 mol%, 0.300 mmol, 284 mg) and (*P*)-**DEA** (100 mol%,0.130 mmol, 25 mg) were dissolved in 5 mL of degassed mixture of THF:Et_3N (1:1). $Pd(PPh_3)_4$ (20 mol%, 0.020 mmol, 20 mg) was added to the mixture and the mixture was refluxed overnight. The solvent was evaporated at reduced pressure and the crude was purified by chromatographic column using DCM:MeOH (95:5) as eluent. The fractions containing the desired product were evaporated and the obtained solid was further purified by recycling GPC obtaining (*P*)-**1** (57 mg, 40 %).

Similar protocol was applied for the corresponding enantiomer, (*M*)-**S1**, leading to (*M*)-**1**.

For (*P*)-**1**, $[\alpha]_D^{20}$= +146 (*c* = 2.5 mg·mL^{-1}, $CHCl_3$). For (*M*)-**1**, $[\alpha]_D^{20}$= -143 (*c* = 2.5 mg·mL^{-1}, $CHCl_3$).

Molecular Formula: $C_{119}H_{192}N_4O_{10}$. **MW:** 1838.86 **g/mol.**

^{1}H-NMR (300 MHz, $CDCl_3$) δ 7.78 (dd, *J* = 8.3, 4.1 Hz, 2H), 7.49 (d, *J* = 8.2 Hz, 2H), 7.38 (t, *J* = 5.0 Hz, 1H), 7.26 (d, *J* = 9.6 Hz, 1H), 7.02 (s, 2H), 3.98 (q, *J* = 6.2 Hz, 6H), 3.70 – 3.63 (m, 4H), 1.78 (dd, *J* = 10.3, 4.5 Hz, 4H), 1.75 – 1.69 (m, 3H), 1.47 – 1.43 (m, 6H), 1.37 – 1.21 (m, 67H), 0.87 (td, *J* = 7.0, 1.9 Hz, 9H).

^{13}C-NMR (75 MHz, $CDCl_3$) δ 212.3, 168.9, 168.1, 153.3, 141.4, 133.0, 131.7, 128.8, 127.3, 127.2, 105.8, 103.8, 92.3, 85.9, 73.6, 69.4, 41.2, 36.0, 32.1, 30.5, 29.9, 29.8, 29.8, 29.7, 29.6, 29.5, 29.5, 29.3, 29.2, 26.3, 26.2, 22.8, 14.2.

HRMS (ESI$^+$): *m/z* calcd. for $C_{119}H_{192}N_4O_{10}$ 1838.863 ; found 1861.329 $[M+Na]^+$.

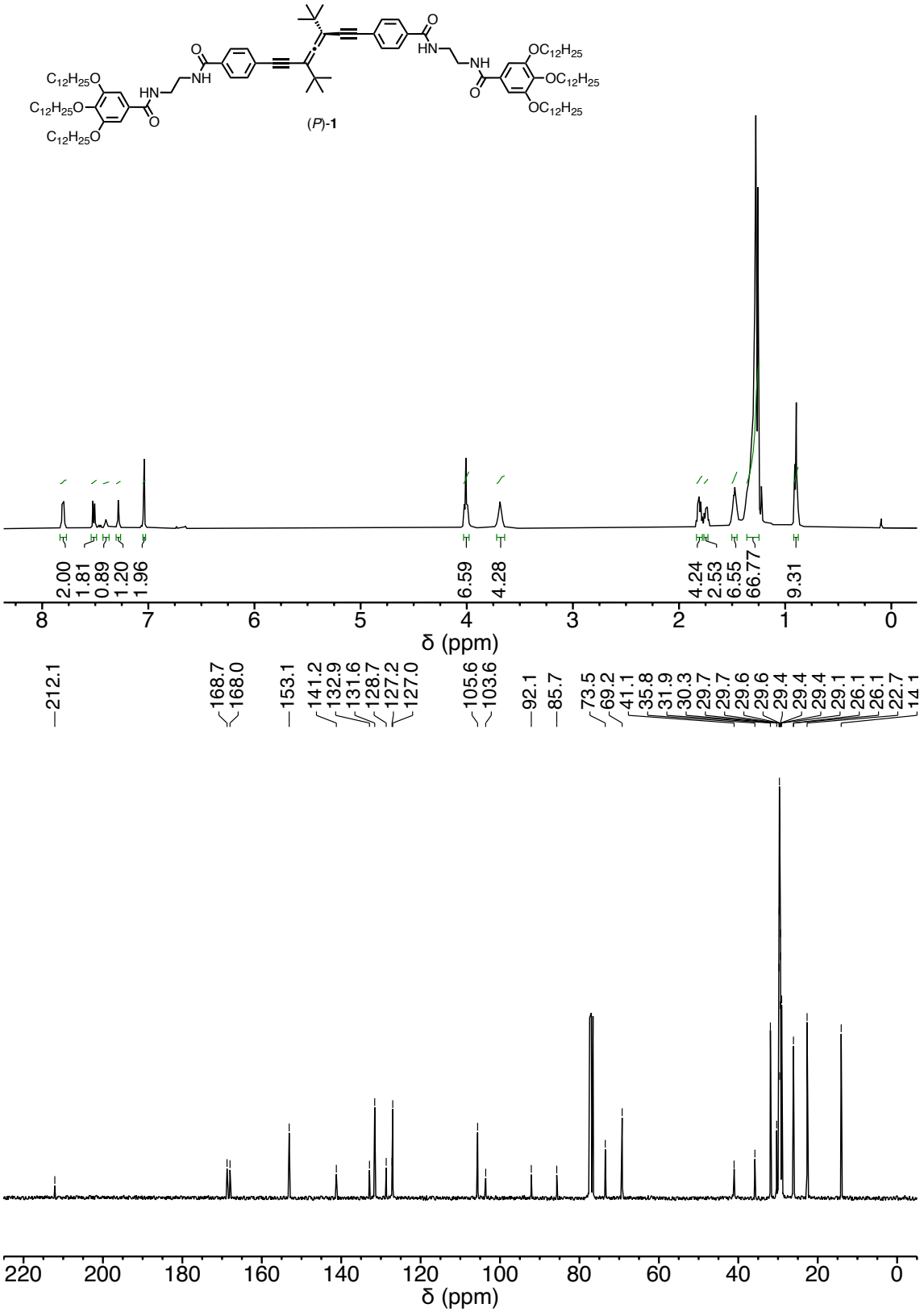

Figure S2. ^{1}H-NMR and ^{13}C-NMR of (*P*)-**1** in $CDCl_3$.

5.4.3. Aggregation Studies

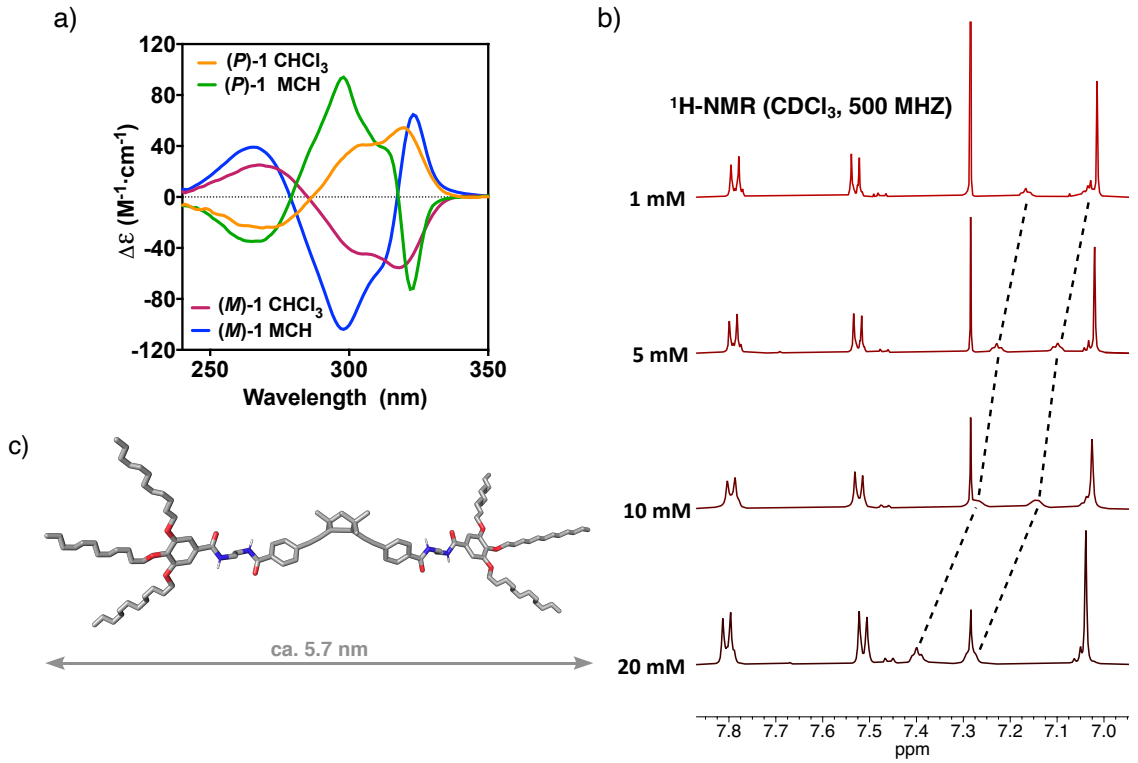

Figure S3. (a) Comparison of the ECD spectra of both (*P*)- and (*M*)-**1** in molecularly dissolved ($CHCl_3$) and aggregated states (MCH). (b) Concentration dependent ^1H NMR experiments of derivative **1** ($CDCl_3$, 500 MHz). (c) Estimated molecular size of a model of (*P*)-**1**.

5.4.4. AFM Measurements

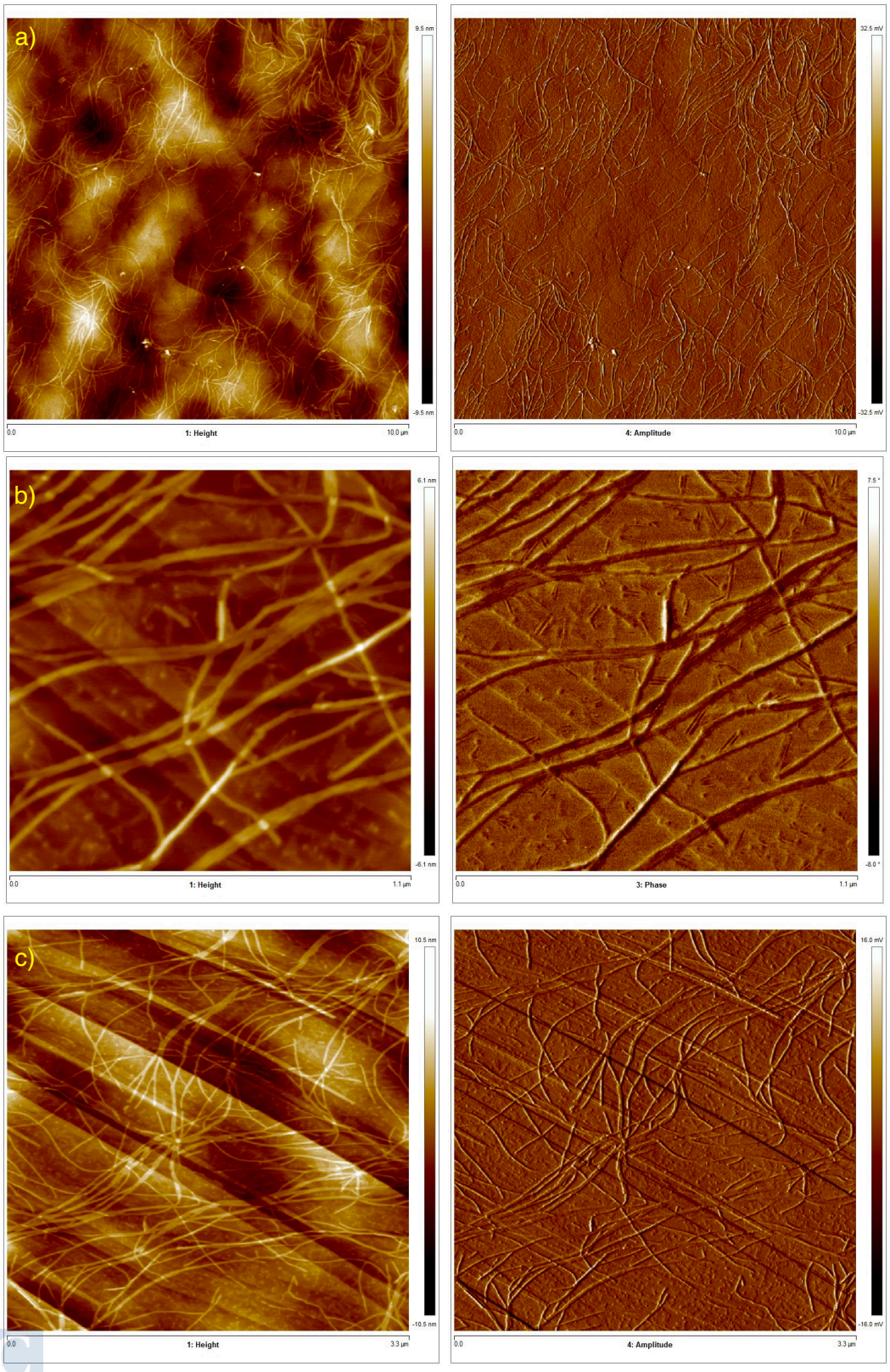

Figure S4. Additional AFM images of (*P*)-**1**.

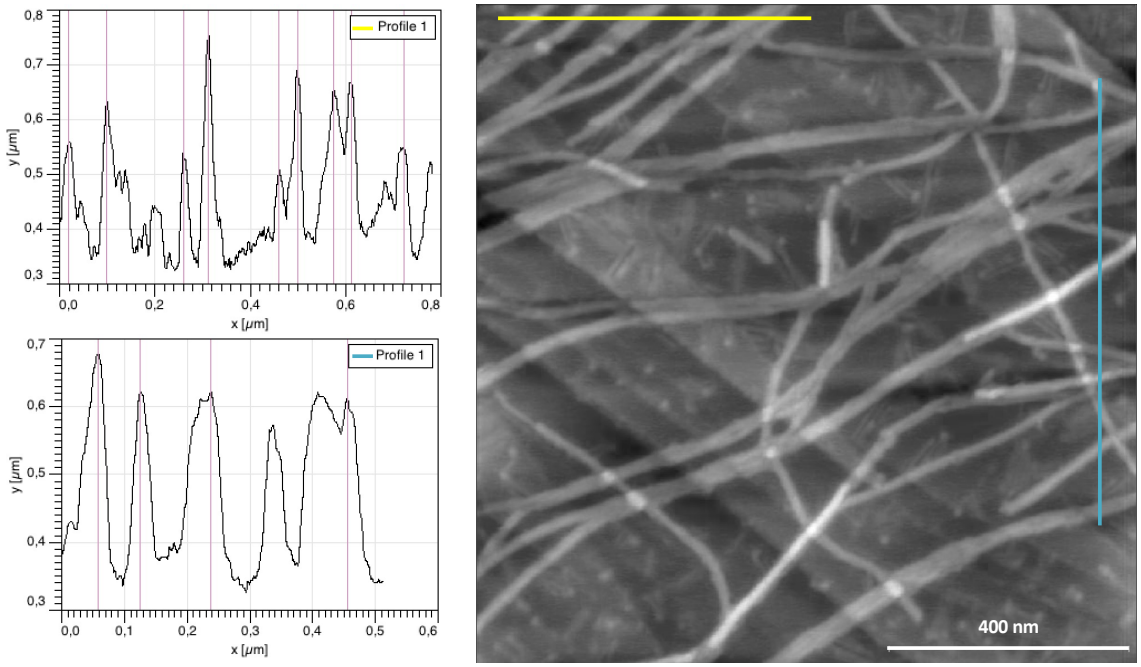

Figure S5. Additional AFM images of (*P*)-**1**.

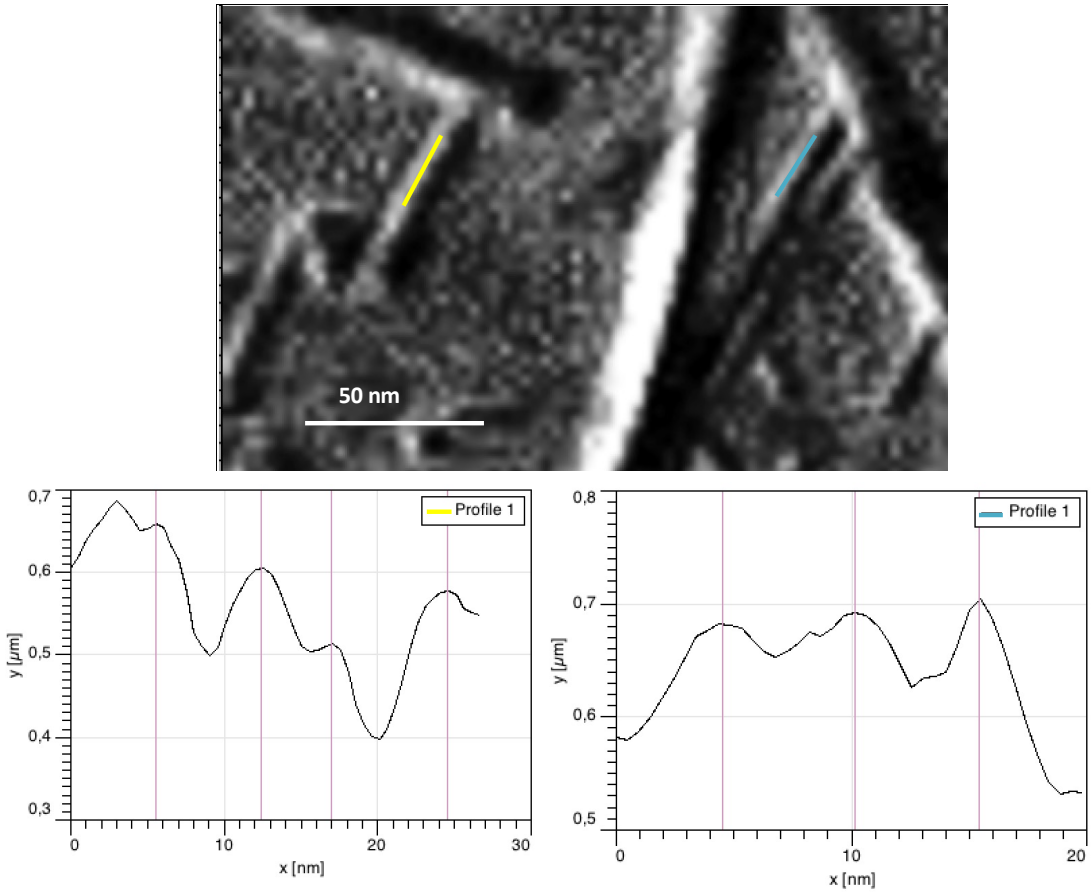

Figure S6. AFM images of (*P*)-**1** and profiles showing the helical pitch of the fibber.

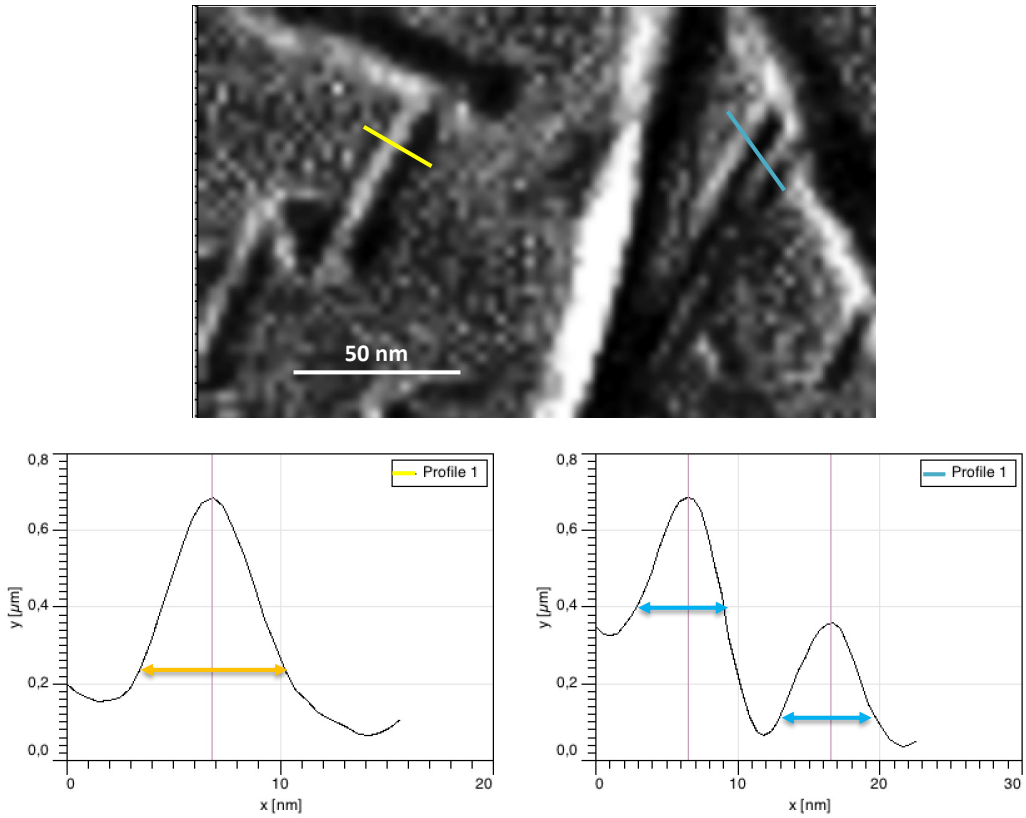

Figure S7. AFM images of (*P*)-**1** and profiles showing the width of the helical fibbers.

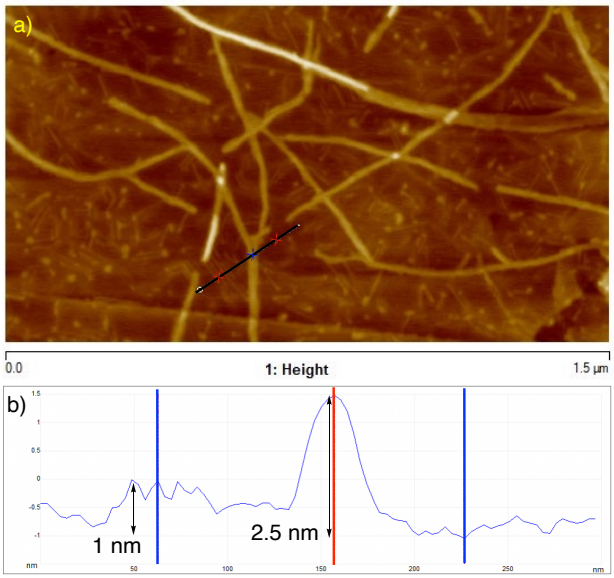

Figure S8. AFM images of (*P*)-**1** and height profiles showing of the helical fibbers.

5.4.5. Theoretical Calculations

The conformational space of a simplified monomeric unit of (*P*)-**1**, where peripheral dodecyloxy side chains are substituted by a methyl group, were planned as different possible conformations that can aggregate without esteric hinderance of the alquilic chains as (*P*)-**1a**, (*P*)-**1b**, (*P*)-**1c** and (*P*)-**1d**. Theoretical calculations were performed by means of the xTB 6.6.0 program package.[417] Full geometry optimizations were carried out at the cost-effective semiempirical GFN2-xTB level of theory, method which is based on a Hamiltonian similar to the well-known DFTB3, with a minimal valence basis set centered on atoms (STO-mG), and includes the density-dependent D4 dispersion correction.[418] Figures S7-10 show the optimized geometries computed for monomers and for aggregates (*P*)-**1a**, (*P*)-**1b**, (*P*)-**1c** and (*P*)-**1d** of increasing size (from the monomer to the 8-mer).To have a more realistic description of the structure a relative stability of the conformers of (*P*)-**1**, we have used the bigger aggregates (n=3-8) to compare the energies. The most stable aggregate and those prone to promote the supramolecular self-assembly was obtained as the most stable structure (*P*)-**1a** (Figures S13, S14 and Table S1, S2). Conformers (*P*)-**1c** and (*P*)-**1d** were discarded because the supramolecular growing is unfavourable due to the formation of defects on the polymer between monomers (Figure S13). Dimer (*P*)-**1a** was then used to build up a supramolecular hexadecamer (16-mer) constituted by sixteen (*P*)-**1a** monomers stacked up in a helical arrangement. The minimum- energy structure of the 16-mer was calculated at the GFN2-xTB level. To shed light on the polymerization mechanism operating in the self-assembling process, single-point GFN2-xTB level calculations were performed for ((*P*)-**1**)*n* oligomers of increasing length (*n* = 2–12) extracted from the central part of the previously-optimized 16-mer to mitigate undesirable terminal effects due to the lack of periodic boundary conditions. The binding energy per interacting molecular pair ($\Delta E_{\text{bind},n\text{-}1}$) was computed using the following equation:

$$\Delta E_{bind,n-1} = \frac{E_{stack} - n.E_{monomer}}{n-1}$$

where *E*stack is the total energy of the stacked ((*P*)-**1a**)*n* aggregate bearing *n* monomeric units and E_{monomer} is the energy calculated for the monomer. Theoretical calculations reveal that $\Delta E_{\text{bind},n\text{-}1}$ decreases with the oligomer size (Figure S15), which is indicative of a cooperative supramolecular polymerization mechanism.

DFT calculations were also performed on the different conformations of the dimer, trimer and tetramer species of (*P*)-**1a** through the Gaussian-16.C01 suite of programs.[413] Geometry optimizations and frequency (no negative frequencies) energy calculations were carried out by means of the popular hybrid B3LYP functional[418] and the double-zeta Pople's 6- 31G** basis set,[419] and including the Grimme's D3 dispersion correction.[420] After, time-dependent DFT (TD-DFT) calculations (CAM-B3LYP/6-31G**) on monomer, dimer, trimer and tetramer to obtain the ECD spectra (Figures S16-S18). The ECD of the opposite helical sense model of (*P*)-**1** trimer the was also computed showing opposite first cotton effect (Figure S20). Also, the Natural transition orbital (NTOs) where computed for the first excitations of the monomer corresponding to the exciton coupling of the Allene and phenyl groups core (Figures S19).

MODELS were done in Avogadro 1.2.0[421] and the optimized structures in pymol 2.5.2.

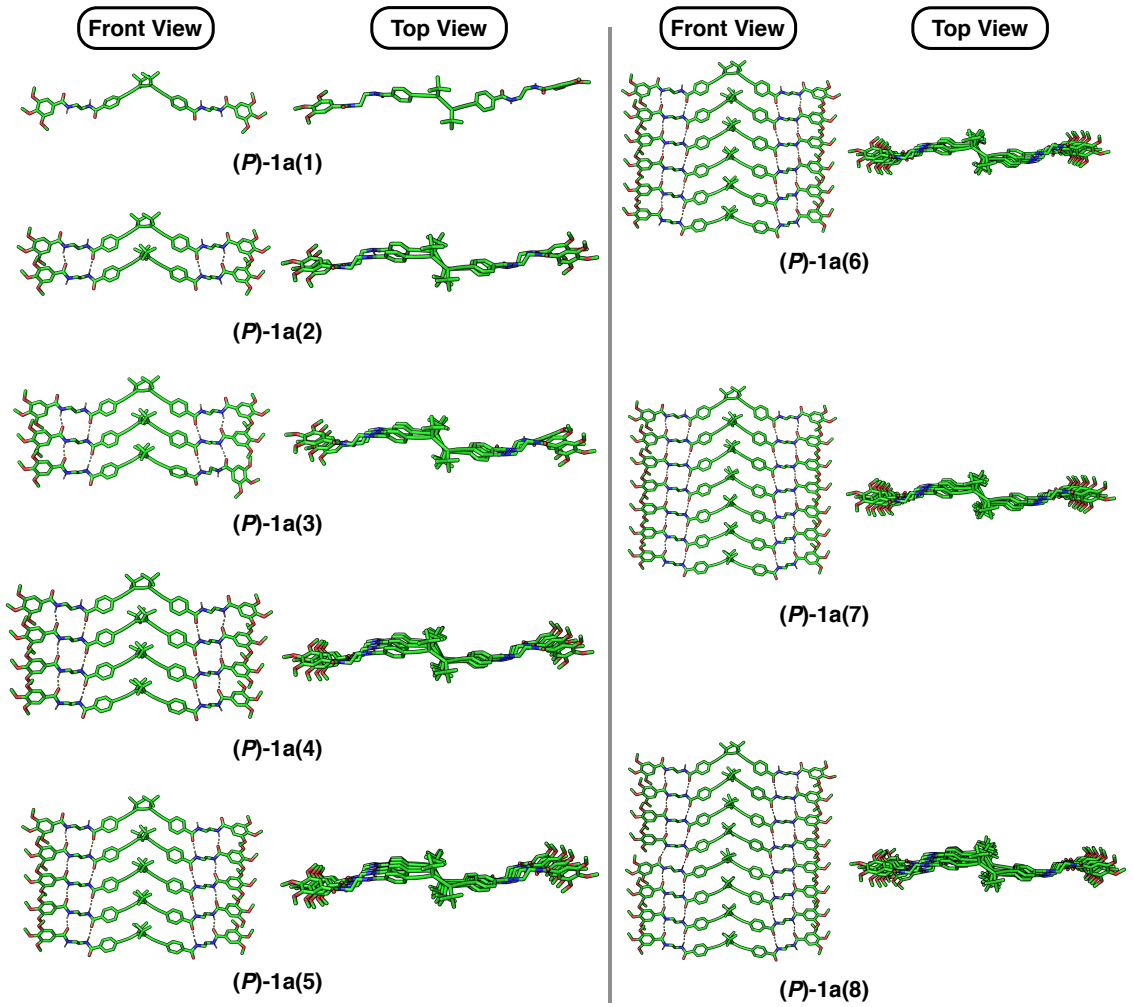

Figure S9. Minimum-energy structures computed at the GFN2-xTB level for the most stable conformers of monomer (1), dimer (2), trimer (3), tetramer (4), pentamer (5), hexamer (6), heptamer (7) and octamer (8) for (*P*)-**1a**.

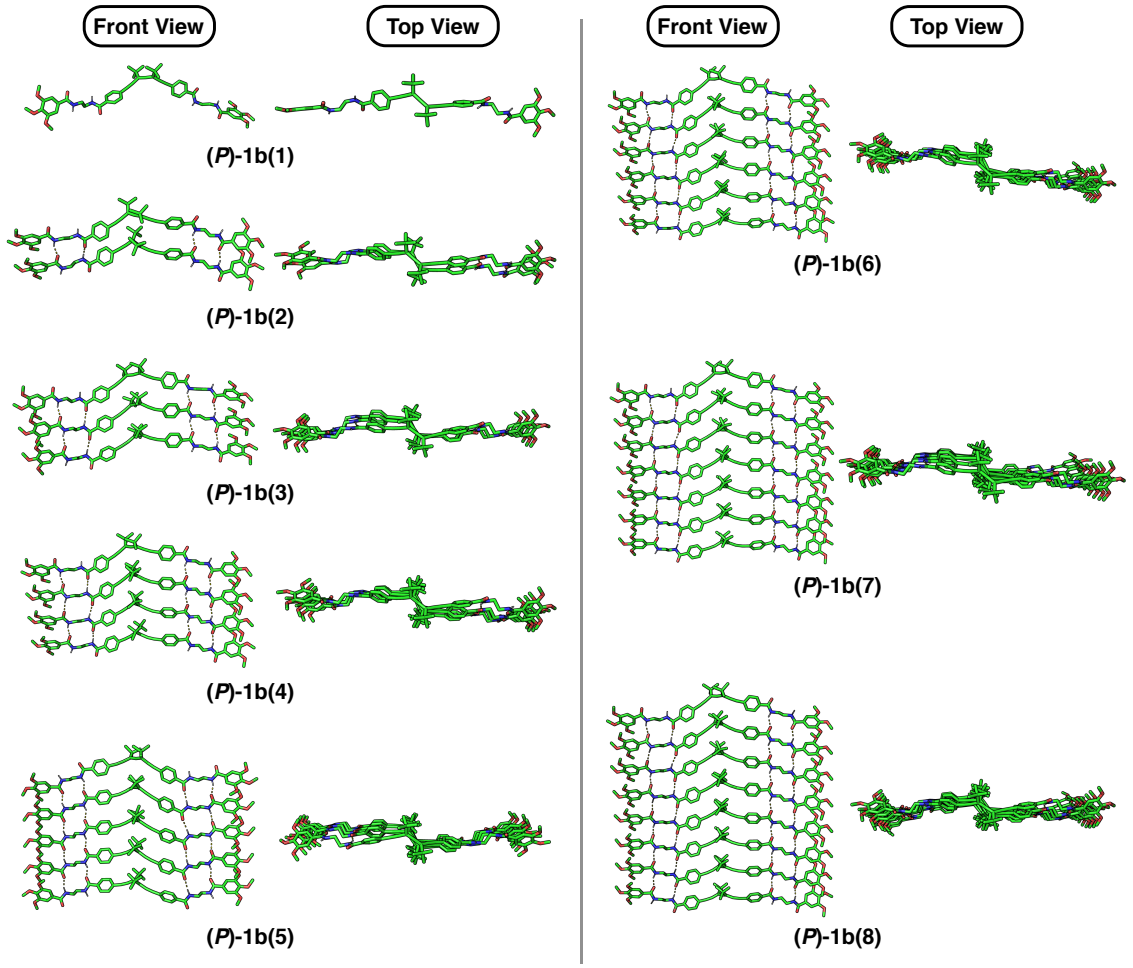

Figure S10. Minimum-energy structures computed at the GFN2-xTB level for the most stable conformers of monomer (1), dimer (2), trimer (3), tetramer (4), pentamer (5), hexamer (6), heptamer (7) and octamer (8) for (*P*)-**1b**.

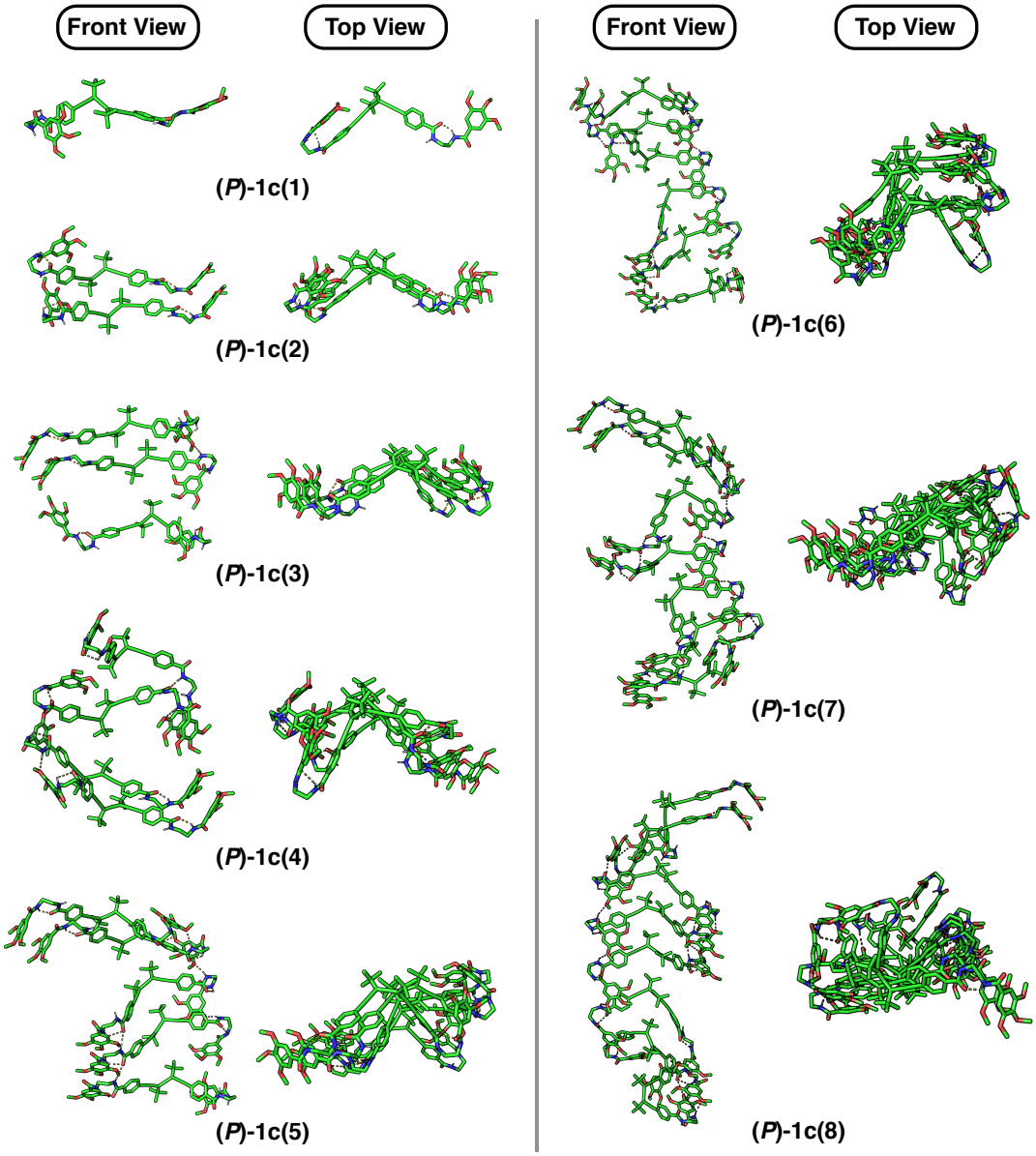

Figure S11. Minimum-energy structures computed at the GFN2-xTB level for the most stable conformers of monomer (1), dimer (2), trimer (3), tetramer (4), pentamer (5), hexamer (6), heptamer (7) and octamer (8) for (*P*)-**1c**.

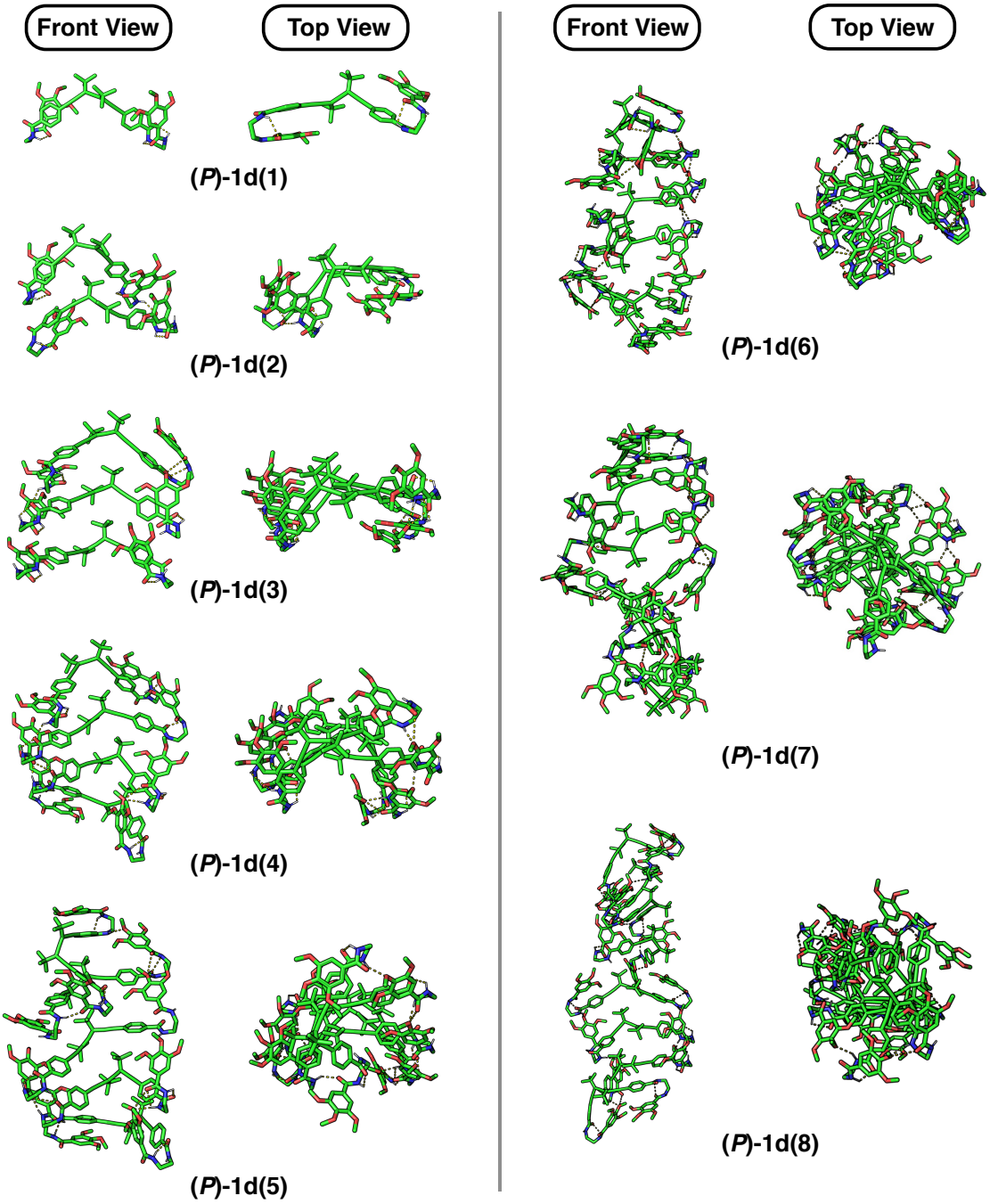

Figure S12. Minimum-energy structures computed at the GFN2-xTB level for the most stable conformers of monomer (1), dimer (2), trimer (3), tetramer (4), pentamer (5), hexamer (6), heptamer (7) and octamer (8) for (*P*)-**1d**.

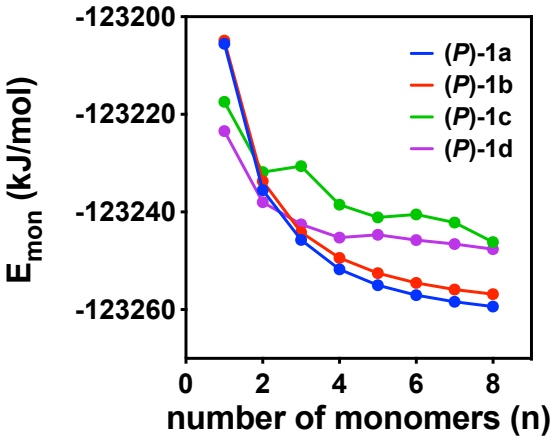

Figure S13. Minimum-energy computed at the GFN2-xTB level per monomer unit **.**

Table S1. Energy (kJ·mol^{-1}) per monomer unit relative to the extended conformer for the most stable structures of monomer (1), dimer (2), trimer (3), tetramer (4), pentamer (5), hexamer (6), heptamer (7) and octamer (8) for (*P*)-**1a**, (*P*)-**1b**, (*P*)-**1c**, (*P*)-**1d**.

Number of monomers (n)	E_{mon} (*P*)-**1a**(n)	E_{mon} (*P*)-**1b**(n)	E_{mon} (*P*)-**1c**(n)	E_{mon} (*P*)-**1d**(n)
1	-123205.6	-123204.9	-123217.4	-123223.4
2	-123235.5	-123233.7	-123231.8	-123238.0
3	-123245.7	-123244.2	-123230.6	-123242.6
4	-123251.7	-123249.4	-123238.5	-123245.2
5	-123255.0	-123252.5	-123241.1	-123244.7
6	-123257.0	-123254.5	-123240.5	-123245.8
7	-123258.4	-123255.9	-123242.2	-123246.6
8	-123259.4	-123256.8	-123246.2	-123247.6

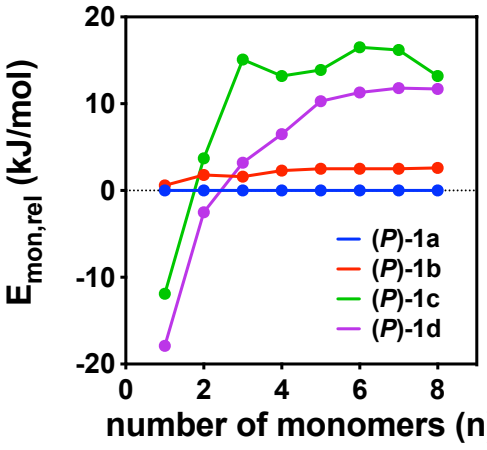

Figure S14. Minimum-energy computed at the GFN2-xTB level per monomer unit.

Table S2. Energy (kJ·mol^{-1}) per monomer unit relative to the extended conformer for the most stable structures of monomer (1), dimer (2), trimer (3), tetramer (4), pentamer (5), hexamer (6), heptamer (7) and octamer (8) for (*P*)-**1a**, (*P*)-**1b**, (*P*)-**1c,** (*P*)-**1d**.

Number of monomers (n)	$E_{mon,rel}$ (*P*)-**1a**(n)	$E_{mon,rel}$ (*P*)-**1b**(n)	$E_{mon,rel}$ (*P*)-**1c**(n)	$E_{mon,rel}$ (*P*)-**1d**(n)
1	0.0	0.6	-11.9	-17.9
2	0.0	1.8	3.7	-2.5
3	0.0	1.6	15.1	3.2
4	0.0	2.3	13.2	6.5
5	0.0	2.5	13.9	10.3
6	0.0	2.5	16.5	11.3
7	0.0	2.5	16.2	11.8
8	0.0	2.6	13.2	11.7

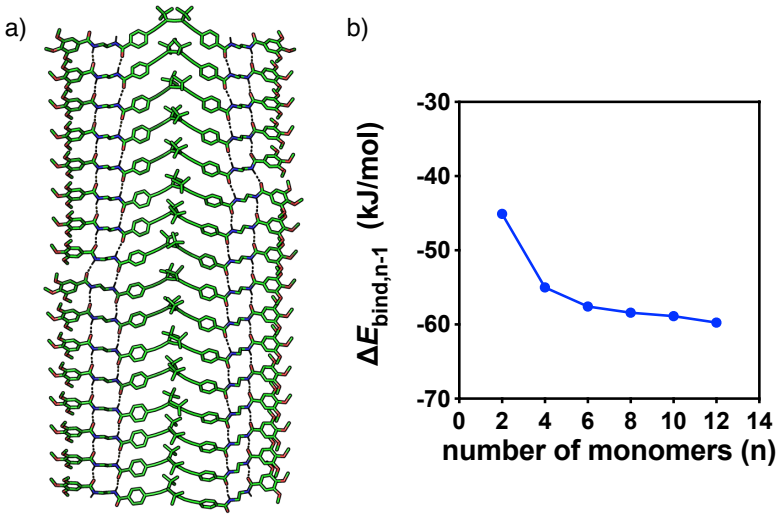

Figure S15. (a) Minimum-energy structure computed at the GFN2-xTB level for the most stable conformer hexadecamer of (*P*)-**1a**. (b) Stabilization energy per interacting pair (ΔE_{bind},*n*–1) as the number of monomers (*n*) in the [(*P*)-**1a**]n aggregate increases.

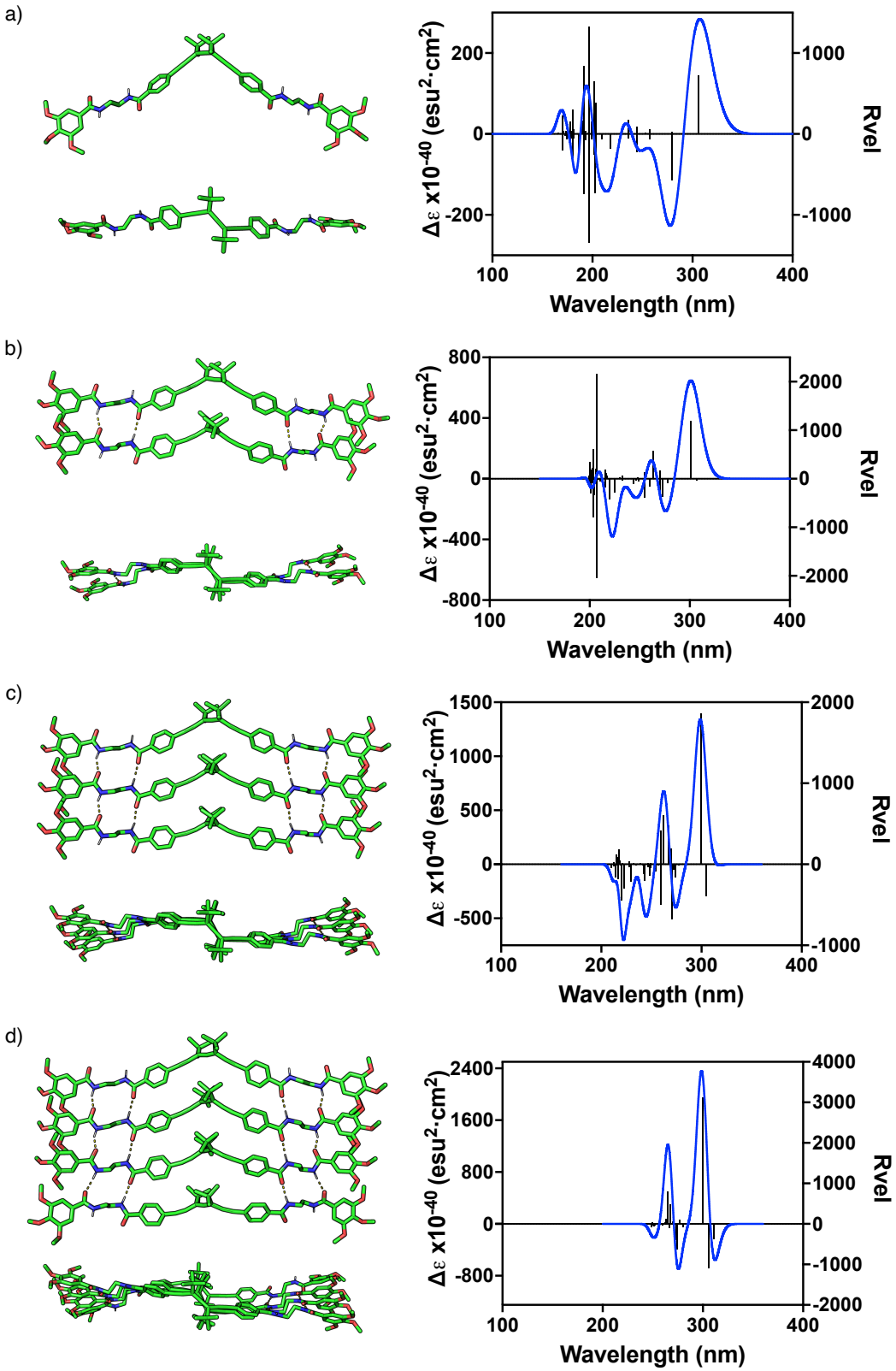

Figure S16. DFT (B3LYP/6-31G**) Minimum-energy structure for the most stable conformer and the simulated ECD from TD-DFT (CAM-B3LYP/6-31G**) of (*P*)-**1a** for the (a) monomer FWHM= 0.200 ev, (b) dimer FWHM= 0.150 ev, (c) trimer FWHM= 0.100 ev and (d) tetramer FWHM= 0.090 ev.

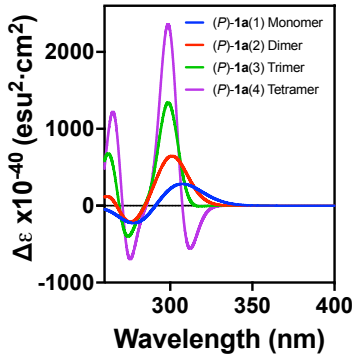

Figure S17. Comparison of the ECD from TD-DFT (CAM-B3LYP/6-31G**) of (*P*)-**1a** for monomer FWHM= 0.200 ev, dimer FWHM= 0.150 ev, trimer FWHM= 0.100 ev and tetramer FWHM= 0.090 ev.

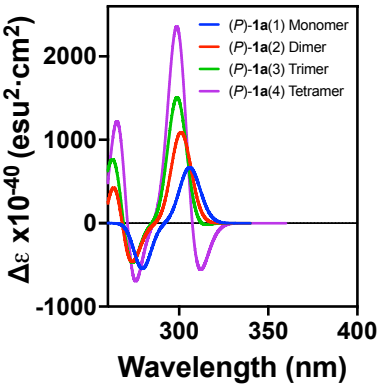

Figure S18. Comparison of the ECD from TD-DFT (CAM-B3LYP/6-31G**) of (*P*)-**1a** for monomer, dimer, trimer and tetramer with FWHM= 0.090 ev.

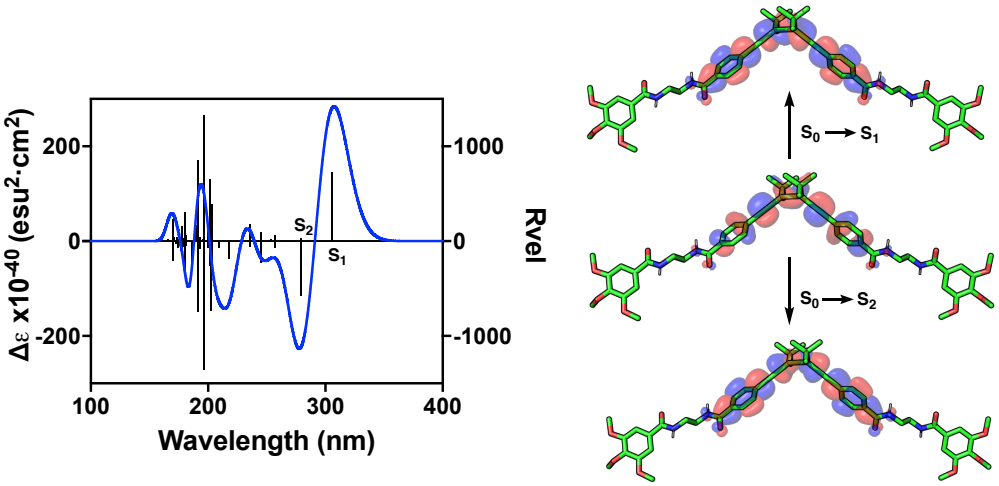

Figure S19. Natural Transition Orbitals HOMO to LUMO of the first and second excitations calculated by TD-DFT in monomer (*P*)-**1a** optimized by DFT.

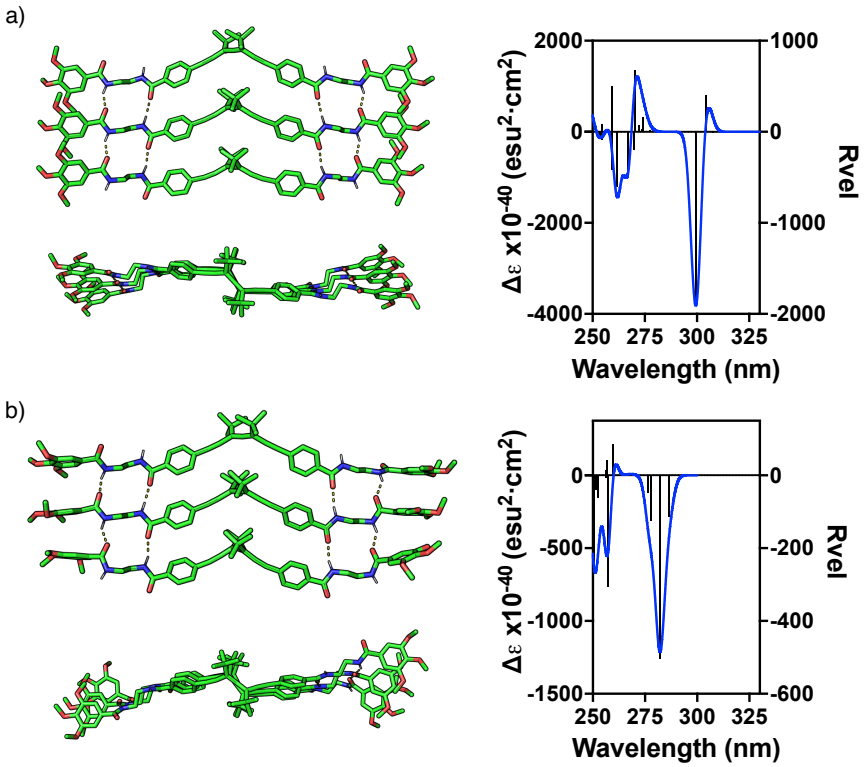

Figure S20. (a) DFT (B3LYP/6-31G**) minimum-energy structure for the most stable conformer and the simulated ECD from TD-DFT (CAM-B3LYP/6-31G**) of (*P*)-**1a** for the trimer. (b) Model of the opposite helical sense not optimizable in DFT with the corresponding simulated ECD calculated by TD-DFT (CAM-B3LYP/6-31G**).

Chapter 6. Bibliography

[1] L. Pauling; R. B. Corey, H. R. Branson, *Proc. Natl. Acad. Sci.* **1951**, *37*, 205–211.

[2] J. D. Watson, F. H. C. Crick, *Nature* **1953**, *171*, 737–738.

[3] Y. Dorca, E. E. Greciano, J. S. Valera, R. Gómez, L. Sánchez, *Chem. Eur. J.* **2019**, *25*, 5848–5864.

[4] W. W. C.Topley, G. S. Wilson, L. H. Collier, A. Balows, M. Sussman, *Topley & Wilson's Microbiology and Microbial Infections: Systematic Bacteriology*; A Hodder Arnold Publication: Arnold, **1998**.

[5] J. R. Schnell, J. J. Chou, *Nature* **2008**, *451*, 591–595.

[6] B. Alberts, A. Johnson, J. Lewis, D. Morgan, M. Raff, K. Roberts, P. Walter, *Molecular Biology of the Cell*, 6th ed.; Garland Science: New York, **2014**.

[7] W. Saenger, *Principles of Nucleic Acid Structure*, 1st ed.; Springer-Verlag: New York, **1984**, p 556.

[8] G. E. Schulz, R. H. Schrimer, *Principles of Protein Structure*, 1st ed.; Springer-Verlag: New York, **1979**.

[9] L. Pasteur, *Ann. Chim. Phys. Sér*. **1848**, *24*, 442–459.

[10] J. Gal, *Nat. Chem.* **2017**, *9*, 604–605.

[11] J. H. Van't Hoff , *Arch. Need. Sci. Exactes Nat*. **1874**, *9*, 445–454.

[12] J. A. Le Bel, *Bull. Soc. Chim. Fr.* **1874**, *22*, 337.

[13] G. A. Hembury, V. V. Borovkov, Y. Inoue, *Chem. Rev.* **2008**, *108*, 1–73.

[14] J. D. Carroll, *Chirality* **2009**, *21*, 354–358.

[15] R. R. Julian, S. Myung, D. E. Clemmer, *J. Phys. Chem. B* **2005**, *109*, 440–444.

[16] E. Eliel, S. H. Wilen, L. Mander, *Stereochemistry of Organic Compounds*, John Wiley and Sons, Inc., New York, **1994**.

[17] R. S. Cahn, C. Ingold, V. Prelog, *Angew. Chem. Int. Ed. Engl.* **1966**, *5*, 385–415.

[18] P. L. Privalov, C. Crane-Robinson, *Prog. Biophys. Mol. Biol.* **2018**, *135*, 30–48.

[19] V. V. Vu, J. A. Hangasky, T. C. Detomasi, S. J. W. Henry, S. T. Ngo, E. A. Span, M. A. Marletta, *J. Biol. Chem* **2019**, *294*, 12157–12166.

[20] Z. Fernández, B. Fernández, E. Quiñoá, F. Freire, *Angew. Chem. Int. Ed*. **2021**, *60*, 9919–9924.

[21] R. Rodríguez, E. Quiñoá, R. Riguera, F. Freire, *J. Am. Chem. Soc*. **2016**, *138*, 9620–9628.

[22] G. P. Moss, P. A. S. Smith, D. Tavernier, *Pure Appl. Chem*. **1995**, *67*, 1307–1375.

[23] V. Prelog, G. Helmchen, *Angew. Chem. Int. Ed. Engl*. **1982**, *21*, 567–583.

[24] P. Rivera-Fuentes, F. Diederich, *Angew. Chem. Int. Ed.* **2012**, *51*, 2818–2828.

[25] N. Krause, A. Hoffmann-Röder, *Tetrahedron* **2004**, *60*, 11671–11694.

[26] A. H. Alberts, H. Wynberg, *J. Chem. Soc., Chem. Commun*. **1988**, 748–749.

[27] T. Lange, J. D. van Loon, R. R. Tykwinski, M. Schreiber, F. Diederich, *Synthesis* **1996**, 537–550.

[28] R. C. Livingston, L. R. Cox, V. Gramlich, F. Diederich, *Angew. Chem. Int. Ed*. **2001**, *40*, 2334–2337.

[29] J. L. Alonso-Gómez, P. Schanen, P. Rivera-Fuentes, P. Seiler, F. Diederich, *Chem. Eur. J.* **2008**, *14*, 10564–10568.

[30] R. Livingston, L. R. Cox, S. Odermatt, F. Diederich, *Helv. Chim. Acta* **2002**, *85*, 3052–3077.

[31] J. L. Alonso-Gómez, P. Rivera-Fuentes, N. Harada, N. Berova, F. Diederich, *Angew. Chem. Int. Ed*. **2009**, *48*, 5545–5548.

[32] S. Castro-Fernández, I. R. Lahoz, A. L. Llamas-Saiz, J. L. Alonso-Gómez, M.-M. Cid, A. Navarro-Vázquez, *Org. Lett.* **2014**, *16*, 1136–1139.

[33] S. Castro-Fernández, J. Álvarez-García, L. García-Río, C. Silva-López, M. M. Cid, *Org. Lett.* **2019**, *21*, 5898–5902.

[34] S. Míguez-Lago, B. D. Gliemann, M. Kivala, M. M. Cid, *Chem. Eur. J.* **2021**, *27*,13352–13357.

[35] P. Rivera-Fuentes, J. L. Alonso-Gómez, A. G. Petrovic, F. Santoro, N. Harada, N. Berova, F. Diederich, *Angew. Chem. Int. Ed.* **2010**, *49*, 2247–2250.

[36] O. Gidron, M. Ebert, N. Trapp, F. Diederich, *Angew. Chem. Int. Ed.* **2014**, *53*, 13614–13618.

[37] O. Gidron, M. Jirásek, N. Trapp, M.-O. Ebert, X. Zhang, F. Diederich, *J. Am. Chem. Soc*. **2015**, *137*, 12502–12505.

[38] C. Gropp, N. Trapp, F. Diederich, *Angew. Chem. Int. Ed.* **2016**, *55*, 14444–14449.

[39] C. Gropp, S. Fischer, T. Husch, N. Trapp, E. M. Carreira, F. Diederich, *J. Am. Chem. Soc*. **2020**, *142*, 4749–4755.

[40] R. López, C. Palomo, *Angew. Chem. Int. Ed.* **2022**, *61*, e202113504.

[41] K. E. Malterud, T. Anthonsen, J. Hjortås, *Tetrahedron Lett.* **1976**, *17*, 3069–3072.

[42] P. J. Pye, K. Rossen, R. A. Reamer, N. N. Tsou, R. P. Volante, P. J. Reider, *J. Am. Chem. Soc*. **1997**, *119*, 6207–6208.

[43] J. C. Ruble, H. A. Latham, G. C. Fu, *J. Am. Chem. Soc*. **1997**, *119*, 1492–1493.

[44] M. Cakici, Z.-G. Gu, M. Nieger, J. Bürck, L. Heinke, S. Bräse, *Chem. Commun.* **2015**, *51*, 4796–4798.

[45] C. J. Bruns, J. F. Stoddart, *The Nature of the Mechanical Bond: From Molecules to Machines*; J. Wiley and Sons: Hoboken, NJ, **2016.**

[46] J. Niemeyer, N. Pairault, *Synlett* **2018**, *29*, 689–698.

[47] R. J. Bordoli, S. M. Goldup, *J. Am. Chem. Soc.* **2014**, *136*, 4817–4820.

[48] E. M. G. Jamieson, F. Modicom, S. M. Goldup, *Chem. Soc. Rev*. **2018**, *47*, 5266–5311.

[49] A. H. G. David, R. Casares, J. M. Cuerva, A. G. Campaña, V. Blanco, *J. Am. Chem. Soc.* **2019**, *141*, 18064–18074.

[50] J. E. M. Lewis, P. D. Beer, S. J. Loeb, S. M. Goldup, *Chem. Soc. Rev*. **2017**, *46*, 2577–2591.

[51] C. O. Dietrich-Buchecker, J. P. Sauvage, J. P. Kintzinger, *Tetrahedron Letters* **1983**, *24*, 5095–5098.

[52] P. R. Ashton, T. T. Goodnow, A. E. Kaifer, M. V. Reddington, A. M. Z. Slawin, N. Spencer, J. F. Stoddart, C. Vicent, D. J. Williams, *Angew. Chem. Int. Ed. Engl*. **1989**, *28*, 1396–1399.

[53] J. D. Crowley, S. M. Goldup, A.-L. Lee, D. A. Leigh, R. T. McBurney, *Chem. Soc. Rev*. **2009**, *38*, 1530.

[54] M. Denis, S. M. Goldup, *Nat. Rev. Chem*. **2017**, *1*, 0061.

[55] J. E. M. Lewis, R. J. Bordoli, M. Denis, C. J. Fletcher, M. Galli, E. A. Neal, E. M. Rochette, S. M. Goldup, *Chem. Sci.* **2016**, *7*, 3154–3161.

[56] E. R. Kay, D. A. Leigh, F. Zerbetto, *Angew. Chem. Int. Ed*. **2007**, *46*, 72–191.

[57] P. Luisi, *Self-organization. In The Emergence of Life: From Chemical Origins to Synthetic Biology*; Cambridge: Cambridge University Press, **2006**, 85–111.

[58] K. Kinbara, T. Aida, *Chem. Rev*. **2005**, *105*, 1377–1400.

[59] P. C. Knipe, S. Thompson, A. D. Hamilton, *Chem. Sci*. **2015**, *6*, 1630–1639.

[60] Y. Yu, M. Nakano, T. Ikeda, *Nature* **2003**, *425*, 145.

[61] R. Klajn, *Chem. Soc. Rev*. **2014**, *43*, 148–184.

[62] I. Jones, P. Knipe, T. Michaelos, S. Thompson, A. Hamilton, *Molecules* **2014**, *19*, 11316–11332.

[63] B. M. Neilson, C. W. Bielawski, *ACS Catal*. **2013**, *3*, 1874–1885.

[64] X. Su, S. Voskian, R. P. Hughes, I. Aprahamian, *Angew. Chem. Int. Ed*. **2013**, *125*, 10934–10939.

[65] Y. B. Zheng, B. Kiraly, T. J. Huang, *Nanomedicine* **2010**, *5*, 1309–1312.

[66] S. Paliwal, S. Geib, C. S. Wilcox, *J. Am. Chem. Soc*. **1994**, *116*, 4497–4498.

[67] L. Yang, C. Adam, G. S. Nichol, S. L. Cockroft, *Nat. Chem.* **2013**, *5*, 1006–1010.

[68] J. F. Stoddart, *Angew. Chem. Int. Ed*. **2014**, *53*, 11102–11104.

[69] A. Caballero, F. Zapata, P. D. Beer, *Coord. Chem. Rev*. **2013**, *257*, 2434–2455.

[70] D. Dattler, G. Fuks, J. Heiser, E. Moulin, A. Perrot, X. Yao, N. Giuseppone, *Chem. Rev*. **2019**, *120*, 310–433.

[71] S. Erbas-Cakmak, D. A. Leigh, C. T. McTernan, A. L. Nussbaumer, *Chem. Rev*. **2015**, *115*, 10081–10206.

[72] C. Pezzato, C. Cheng, J. F. Stoddart, R. D. Astumian, *Chem. Soc. Rev*. **2017**, *46*, 5491–5507.

[73] L. Zhang, V. Marcos, D. A. Leigh, *Proc. Natl. Acad. Sci. U.S.A*. **2018**, *115*, 9397–9404.

[74] A. W. Heard, S. M. Goldup, *ACS Cent. Sci*. **2020**, *6*, 117–128.

[75] J. D. Badjić, V. Balzani, A. Credi, S. Silvi, J. F. Stoddart, *Science* **2004**, *303*, 1845–1849.

[76] J. D. Badjić, C. M. Ronconi, J. F. Stoddart, V. Balzani, S. Silvi, A. Credi, *J. Am. Chem. Soc.* **2006**, *128*, 1489–1499.

[77] K. Shimomura, T. Ikai, S. Kanoh, E. Yashima, K. Maeda, *Nat. Chem*. **2014**, *6*, 429–434.

[78] D. Hirose, A. Isobe, E. Quiñoá, F. Freire, K. Maeda, *J. Am. Chem. Soc*. **2019**, *141*, 8592–8598.

[79] T. Ikai, M. Ando, M. Ito, R. Ishidate, N. Suzuki, K. Maeda, E. Yashima, *J. Am. Chem. Soc*. **2021**, *143*, 12725–12735.

[80] A. Tamura, N. Yui, *Polym. J.* **2017**, *49*, 527–534.

[81] Y. Arisaka, N. Yui, *J. Mater. Chem. B* **2019**, *7*, 2123–2129.

[82] Y. Cho, J. Kim, A. Elabd, S. Choi, K. Park, T. Kwon, J. Lee, K. Char, A. Coskun, J. W. Choi, *Adv. Mater*. **2019**, *31*, 1905048.

[83] P. Ding, L. Wu, Z. Lin, C. Lou, M. Tang, X. Guo, H. Guo, Y. Wang, H. Yu, *J. Am. Chem. Soc*. **2023**, *145*, 1548–1556.

[84] T. Takata, *ACS Cent. Sci*. **2020**, *6*, 129–143.

[85] N. Hoyas Pérez, J. E. M. Lewis, *Org. Biomol. Chem*. **2020**, *18*, 6757–6780.

[86] S. Mena-Hernando, E. M. Pérez, *Chem. Soc. Rev*. **2019**, *48*, 5016–5032.

[87] J. E. Beves, B. A. Blight, C. J. Campbell, D. A. Leigh, R. T. McBurney, *Angew. Chem. Int. Ed.* **2011**, *50*, 9260–9327.

[88] J. E. M. Lewis, P. D. Beer, S. J. Loeb, S. M. Goldup, *Chem. Soc. Rev.* **2017**, *46*, 2577–2591.

[89] Y. Suzaki, S. Murata, K. Osakada, *Chem. Lett.* **2009**, *38*, 356–357.

[90] F. Ishiwari, K. Fukasawa, T. Sato, K. Nakazono, Y. Koyama, T. Takata, *Chem. Eur. J.* **2011**, *17*, 12067–12075.

[91] F. Ishiwari, K. Nakazono, Y. Koyama, T. Takata, *Chem. Commun.* **2011**, *47*, 11739–11741.

[92] E. Kervio, A. Hochgesand, U. E. Steiner, C. Richert, *Proc. Natl. Acad. Sci. U.S.A*. **2010**, *107*, 12074–12079.

[93] A. Brewer, A. P. Davis, *Nat. Chem*. **2014**, *6*, 569–574.

[94] B. Liu, C. G. Pappas, J. Ottelé, G. Schaeffer, C. Jurissek, P. F. Pieters, M. Altay, I. Marić, M. C. A. Stuart, S. Otto, *J. Am. Chem. Soc*. **2020**, *142*, 4184–4192.

[95] F. García, R. Gómez, L. Sánchez, *Chem. Soc. Rev*. **2023**, *52*, 7524–7548.

[96] E. Yashima, N. Ousaka, D. Taura, K. Shimomura, T. Ikai, K. Maeda, *Chem. Rev*. **2016**, *116*, 13752–13990.

[97] O. J. G. M. Goor, S. I. S. Hendrikse, P. Y. W.Dankers, E. W. Meijer, *Chem. Soc. Rev*. **2017**, *46*, 6621–6637.

[98] T. Aida, E. W. Meijer, S. I. Stupp, *Science* **2012**, *335*, 813–817.

[99] E. Schwartz, M. Koepf, H. J. Kitto, R. J. M. Nolte, A. E. Rowan, *Polym. Chem*. **2011**, *2*, 33–47.

[100] E. Yashima, K. Maeda, H. Iida, Y. Furusho, K. Nagai*, Chem. Rev*. **2009**, *109*, 6102–6211.

[101] J. Liu, J. W. Y. Lam, B. Z. Tang, *Chem. Rev*. **2009**, *109*, 5799–5867.

[102] B. M. Rosen, C. J. Wilson, D. A. Wilson, M. Peterca, M. R. Imam, V. Percec, *Chem. Rev.* **2009**, *109*, 6275–6540.

[103] E. Yashima, K. Maeda, Y. Furusho, *Acc. Chem. Res*. **2008**, *41*, 1166–1180.

[104] J. G. Rudick, V. Percec, *Acc. Chem. Res*. **2008**, *41*, 1641–1652.

[105] T. Nakano, Y. Okamoto, *Chem. Rev*. **2001**, *101*, 4013–4038.

[106] N. Liu, L. Zhou, Z.-Q. Wu, *Acc. Chem. Res*. **2021**, *54*, 3953–3967.

[107] Y. Nagata, R. Takeda, M. Suginome, *ACS Cent. Sci*. **2019**, *5*, 1235–1240.

[108] F. Freire, E. Quiñoá, R. Riguera, *Chem. Rev*. **2016**, *116*,1242–1271.

[109] Y. Wang, T. Harada, L. Q. Phuong, Y. Kanemitsu and T. Nakano, *Macromolecules* **2018**, *51*, 6865–6877.

[110] J. J. L. M. Cornelissen, A. E. Rowan, R. J. M. Nolte, N. A. J. M. Sommerdijk, *Chem. Rev*. **2001**, *101*, 4039–4070.

[111] G. Natta, P. Pino, P. Corradini, F. Danusso, E. Mantica, G. Mazzanti, G. J. Moraglio, *J. Am. Chem. Soc*. **1955**, *77*, 1708–1710.

[112] P. Pino, G. P. Lorenzi, *J. Am. Chem. Soc*. **1960**, *82*, 4745–4747.

[113] R. J. M. Nolte, A. J. M., Van Beijnen, W. Drenth, *J. Am. Chem. Soc*. **1974**, *96*, 5932–5933.

[114] Y. Okamoto, K. Suzuki, K. Ohta, K. Hatada, H. Yuki, *J. Am. Chem. Soc.* **1979**, *101*, 4763–4765.

[115] M. M. Green, C. Andreola, B. Munoz, M. P. Reidy, K. Zero, *J. Am. Chem. Soc.* **1988**, *110*, 4063–4065.

[116] Y. Okamoto, T. Nakano, *Chem. Rev*. **1994**, *94*, 349–372.

[117] I. Louzao, J. M. Seco, E. Quiñoá, R. Riguera, *Angew. Chem. Int. Ed*. **2010**, *122*, 1472–1475.

[118] D. Lee, Y.-J. Jin, H. Kim, N. Suzuki, M. Fujiki, T. Sakaguchi, S. K. Kim, W.-E. Lee, G. Kwak, *Macromolecules* **2012**, *45*, 5379–5386.

[119] E. Yashima, K. Maeda, Y. Okamoto, *Nature* **1999**, *399*, 449–451.

[120] M. Fujiki, *J. Organomet. Chem*. **2003**, *685*, 15–34.

[121] M. Fujiki, *Macromol. Rapid Commun*. **2001**, *22*, 539–563.

[122] A. Ohira, M. Kunitake, M. Fujiki, M. Naito, A. Saxena, *Chem. Mater*. **2004**, *16*, 3919–3923.

[123] J. W. Y. Lam, B. Z. Tang, *Acc. Chem. Res*. **2005**, *38*, 745–754.

[124] A. J. Heeger, *Rev. Mod. Phys*. **2001**, *73*, 681–700.

[125] Y. Zhou, C. Zhang, Q. Geng, L. Liu, H. Dong, T. Satoh, Y. Okamoto, *Polymer* **2017**, *131*, 17–24.

[126] S. Leiras, E. Suárez-Picado, E. Quiñoá, R. Riguera, F. Freire, *Giant* **2021**, *7*, 100068.

[127] Y. Nagata, T. Nishikawa, M. Suginome, *J. Am. Chem. Soc.* **2015**, *137*, 4070–4073.

[128] C. I. Simionescu, V. Percec, S. Dumitrescu, *J. Polym. Sci. Polym. Chem. Ed*. **1977**, *15*, 2497–2509.

[129] C. I. Simionescu, V. Percec, *Prog. Polym. Sci*. **1982**, *8*, 133–214.

[130] M. Tabata, T. Sone, Y. Sadahiro, *Macromol. Chem. Phys*. **1999**, *200*, 265–282.

[131] Y. Kishimoto; P. Eckerle, T. Miyatake, T. Ikariya, R. Noyori, *J. Am. Chem. Soc*. **1994**, *116*, 12131–12132.

[132] K. Hirao, Y. Ishii, T. Terao, Y. Kishimoto, T. Miyatake, T. Ikariya, R. Noyori, *Macromolecules* **1998**, *31*, 3405–3408.

[133] Z. Ke, S. Abe, T. Ueno, K. Morokuma, *J. Am. Chem. Soc*. **2011**, *133*, 7926–7941.

[134] N. S. L. Tan, A. B. Lowe, *Angew. Chem. Int. Ed*. **2020**, *59*, 5008–5021.

[135] T. Taniguchi, T. Yoshida, K. Echizen, K. Takayama, T. Nishimura, K. Maeda, *Angew. Chem. Int. Ed*. **2020**, *59*, 8670–8680.

[136] C. I. Simionescu, V. Percec, *J. Polym. Sci. Polym. Chem. Ed*. **1980**, *18*, 147–155.

[137] C. I. Simionescu, V. Percec, *J. Polym. Sci. B Polym. Lett. Ed*. **1979**, *17*, 421–429.

[138] A. Motoshige, Y. Mawatari, Y. Yoshida, R. Motoshige, M. Tabata, *Polym. Chem.* **2014**, *5*, 971–978.

[139] A. Motoshige, Y. Mawatari, R. Motoshige, Y. Yoshida, M. Tabata, *J. Polym. Sci., Part A: Polym. Chem*. **2013**, *51*, 5177–5183.

[140] Y. Yoshida, Y. Mawatari, A. Motoshige, R. Motoshige, T. Hiraoki, M. Wagner, K. Müllen, M. Tabata, *J. Am. Chem. Soc.* **2013**, *135*, 4110–4116.

[141] A. Misayaka, T. Sone, Y. Mawatari, S. Setauesh, K. Müllen, M. Tabata, *Macromol. Chem. Phys.* **2006**, *207*, 1938–1944.

[142] A. Miyasaka, Y. Mawatari, T. Sone, M. Tabata, *Polym. Degrad. Stab.* **2007**, *92*, 253–259.

[143] H. Shirakawa, S. Ikeda, *Polym. J*. **1971**, *2*, 231–244.

[144] T. Ito, H. Shirakawa, S. Ikeda, *J. Polym. Sci. Polym. Chem. Ed*. **1974**, *12*, 11–20.

[145] A. Motoshige, Y. Mawatari, Y. Yoshida, C. Seki, H. Matsuyama, M. Tabata, *J. Polym. Sci. A Polym. Chem.* **2012**, *50*, 3008–3015.

[146] V. Percec, M. Peterca, J. G. Rudick, E. Aqad, M. R. Imam, P. A. Heiney, *Chem. Eur. J.* **2007**, *13*, 9572–9581.

[147] V. Percec, J. G. Rudick, M. Peterca, E. Aqad, M. R. Imam, P. A. Heiney, *J. Polym. Sci. A Polym. Chem*. **2007**, *45*, 4974–4987.

[148] V. Percec, E. Aqad, M. Peterca, J. G. Rudick, L. Lemon, J. C. Ronda, B. B. De, P. A. Heiney, E. W. Meijer, *J. Am. Chem. Soc*. **2006**, *128*, 16365–16372.

[149] V. Percec, J. G. Rudick, M. Peterca, M. Wagner, M. Obata, C. M. Mitchell, W.-D. Cho, V. S. K. Balagurusamy, P. A. Heiney, *J. Am. Chem. Soc*. **2005**, *127*, 15257–15264.

[150] L. Liu, T. Namikoshi, Y. Zang, T. Aoki, S. Hadano, Y. Abe, I. Wasuzu, T. Tsutsuba, M. Teraguchi, T. Kaneko, *J. Am. Chem. Soc*. **2013**, *135*, 602–605.

[151] B. Fernández, R. Rodríguez, E. Quiñoá, R. Riguera, F. Freire, *ACS Omega* **2019**, *4*, 5233–5240.

[152] K. Nakanishi, N. Berova, P. L. Polavarapu, and R. W. Woody, *Comprehensive Chiroptical Spectroscopy, Volume 1, Instrumentation, Methodologies, and Theoretical Simulations*, Wiley-VCH Verlag GmbH & Co. KGaA, Weinheim, Germany, **2013**.

[153] S. Allenmark, J. Gawronski, *Chirality* **2008**, *20*, 606–608.

[154] P. Vollhardt, N. Schore, *Organic Chemistry: Structure and Function,* 5th ed., Omega, **2008**.

[155] G. Pescitelli, L. Di Bari, N. Berova, *Chem. Soc. Rev*. **2011**, *40*, 4603–4625.

[156] M. Wakabayashi, S. Yokojima, T. Fukaminato, K. Shiino, M. Irie, S. Nakamura, *J. Phys. Chem. A* **2014**, *118*, 5046–5057.

[157] B. Fernández, R. Rodríguez, A. Rizzo, E. Quiñoá, R. Riguera, F. Freire, *Angew. Chem. Int. Ed*. **2018**, *57*, 3666–3670.

[158] B. Fernández, R. Rodríguez, E. Quiñoá, R. Riguera, F. Freire, *ACS Omega* **2019**, *4*, 5233–5240.

[159] J. Autschbach, *Chirality* **2009**, *21*, E116-E152.

[160] J. Autschbach, L. Nitsch-Velasquez, M. Rudolph, *Top. Curr. Chem*. **2011**, *298*, 1–98.

[161] M. Kwit, M. D. Rozwadowska, J. Gawroński, A. Grajewska, *J. Org. Chem*. **2009**, *74*, 8051–8063.

[162] C. Hammond. *The Basics of Crystallography and Diffraction*, 4th ed., Oxford University Press: Oxford, UK, **2015**.

[163] E. Yashima, *Polym. J*. **2010**, *42*, 3–16.

[164] G. Binnig, C. F. Quate, Ch. Gerber, *Phys. Rev. Lett*. **1986**, *56*, 930–933.

[165] J. Kumaki, S. -I. Sakurai, E. Yashima, *Chem. Soc. Rev.* **2009**, *38*, 737–746.

[166] T. Nishimura, K. Takatani, S. -I. Sakurai, K. Maeda, E. Yashima, *Angew. Chem. Int. Ed.* **2002**, *41*, 3602–3604.

[167] S. -I. Sakurai, K. Kuroyanagi, K. Morino, M. Kunitake, E. Yashima, *Macromolecules* **2003**, *36*, 9670–9674.

[168] S. -I. Sakurai, K. Okoshi, J. Kumaki, E. Yashima, *Angew. Chem. Int. Ed.* **2006**, *118*, 1267–1270.

[169] S. -I. Sakurai, K. Okoshi, J. Kumaki, E. Yashima, *J. Am. Chem. Soc.* **2006**, *128*, 5650–5651.

[170] S. Ohsawa, S. -I. Sakurai, K. Nagai, M. Banno, K. Maeda, J. Kumaki, E. Yashima, *J. Am. Chem. Soc.* **2010**, *133*, 108–114.

[171] S. Ohsawa, S. -I. Sakurai, K. Nagai, K. Maeda, J. Kumaki, E. Yashima, *Polym. J.* **2011**, *44*, 42–50.

[172] S. Arias, R. Rodríguez, E. Quiñoá, R. Riguera, F. Freire, *J. Am. Chem. Soc.* **2018**, *140*, 667–674.

[173] F. Freire, J. M. Seco, E. Quiñoá, R. Riguera, *Angew. Chem. Int. Ed*. **2011**, *50*, 11692–11696.

[174] S. Arias, F. Freire, E. Quiñoá, R. Riguera, *Polym. Chem*. **2015**, *6*, 4725–4733.

[175] G. G. Roberts, *Langmuir-Blodgett Films*, Plenum, New York, **1990**.

[176] A. Ulman, *An Introduction to Ultrathin, Organic Films-From Langmuir-Blodgett to Self-Assembly*, 1st ed.; Academic Press: New York, **1991**.

[177] B. S. Li, J. W. Y. Lam, Z.-Q. Yu, B. Z. Tang, *Langmuir* **2012**, *28*, 5770–5774.

[178] B. S. Li, S. Z. Kang, K. K. L. Cheuk, L. Wan, L. Ling, C. Bai, B. Z. Tang, *Langmuir* **2004**, *20*, 7598–7603.

[179] R. Rodríguez, J. Ignés-Mullol, F. Sagués, E. Quiñoá, R. Riguera, F. Freire, *Nanoscale* **2016**, *8*, 3362–3367.

[180] M. Lago-Silva, M. Fernández-Míguez, R. Rodríguez, E. Quiñoá, F. Freire, *Chem. Soc. Rev*. **2024**, *53*, 793–852.

[181] E. Yashima, T. Matsushima, Y. Okamoto, *J. Am. Chem. Soc.* **1995**, *117*, 11596–11597.

[182] R. Rodríguez, E. Suárez-Picado, E. Quiñoá, R. Riguera, F. Freire, *Angew. Chem. Int. Ed*. **2020**, *59*, 8616–8622.

[183] R. Rodríguez, E. Quiñoá, R. Riguera, F. Freire, *Small*, **2019**, *15*, 1805413.

[184] J. J. L. M. Cornelissen, J. J. J. M. Donners, R. de Gelder, W. S. Graswinckel, G. A. Metselaar, A. E. Rowan, N. A. J. M. Sommerdijk, R. J. M. Nolte, *Science* **2001**, *293*, 676–680.

[185] Z. Fernández, B. Fernández, E. Quiñoá, R. Riguera, F. Freire, *Chem. Sci.* **2020**, *11*, 7182–7187.

[186] Z. Fernández, B. Fernández, E. Quiñoá, F. Freire, *J. Am. Chem. Soc*. **2021**, *143*, 20962–20969.

[187] E. Suárez-Picado, E. Quiñoá, R. Riguera, F. Freire, *Angew. Chem. Int. Ed.* **2020**, *59*, 4537–4543.

[188] R. Rodríguez, E. Rivadulla-Cendal, M. Fernández-Míguez, B. Fernández, K. Maeda, E. Quiñoá, F. Freire, *Angew. Chem. Int. Ed.* **2022**, *134*, e202209953.

[189] S. Arias, F. Freire, M. Calderón, J. Bergueiro, *Angew. Chem. Int. Ed*. **2017**, *56*, 11420–11425.

[190] S. Wang, S. Xie, H. Du, H. Zeng, J. Zhang, X. Wan, *Sci. China Chem*. **2023**, *66*, 887–895.

[191] R. Kakuchi, S. Nagata, R. Sakai, I. Otsuka, H. Nakade, T. Satoh, T. Kakuchi, *Chem. Eur. J.*, **2008**, *14*, 10259–10266.

[192] E. Yashima, K. Maeda, O. Sato, *J. Am. Chem. Soc*. **2001**, *123*, 8159–8160.

[193] K. Maeda, H. Mochizuki, M. Watanabe, E. Yashima, *J. Am. Chem. Soc*. **2006**, *128*, 7639–7650.

[194] S. Leiras, F. Freire, E. Quiñoá, R. Riguera, *Chem. Sci*. **2015**, *6*, 246–253.

[195] N. Zhu, K. Nakazono, T. Takata, *Chem. Commun*. **2016**, *52*, 3647–3649.

[196] S. Leiras, F. Freire, J. M. Seco, E. Quiñoá, R. Riguera, *Chem. Sci*. **2013**, *4*, 2735–2743.

[197] Y. Yamamoto, T. Fukushima, Y. Suna, N. Ishii, A. Saeki, S. Seki, S. Tagawa, M. Taniguchi, T. Kawai, T. Aida, *Science* **2006**, *314*, 1761–1764.

[198] Z. Álvarez, A. N. Kolberg-Edelbrock, I. R. Sasselli, J. A. Ortega, R. Qiu, Z. Syrgiannis, P. A. Mirau, F. Chen, S. M. Chin, S. Weigand, E. Kiskinis, S. I. Stupp, *Science* **2021**, *374*, 848–856.

[199] W. Zhao, J. Tropp, B. Qiao, M. Pink, J. D. Azoulay, A. H. Flood, *J. Am. Chem. Soc*. **2020**, *142*, 2579–2591.

[200] M. A. Martínez-Aguirre, Y. Li, N. Vanthuyne, L. Bouteiller, M. Raynal, *Angew. Chem. Int. Ed*. **2020**, 133, 4229–4237.

[201] O. Dumele, L. Đorđević, H. Sai, T. J. Cotey, M. H. Sangji, K. Sato, A. J. Dannenhoffer, S. I. Stupp, *J. Am. Chem. Soc*. **2022**, *144*, 3127–3136.

[202] S. Datta, Y. Kato, S. Higashiharaguchi, K. Aratsu, A. Isobe, T. Saito, D. D. Prabhu, Y. Kitamoto, M. J. Hollamby, A. J. Smith, R. Dalgliesh, N. Mahmoudi, L. Pesce, C. Perego, G. M. Pavan, S. Yagai, *Nature* **2020**, *583*, 400–405.

[203] W. H. Carothers, *Chem. Rev*. **1931**, *8*, 353–426.

[204] M. Wehner, F. Würthner, *Nat. Rev. Chem.* **2019**, *4*, 38–53.

[205] T. F. A. De Greef, M. M. J. Smulders, M. Wolffs, A. P. H. J. Schenning, R. P. Sijbesma, E. W. Meijer, *Chem. Rev.* **2009**, *109*, 5687–5754.

[206] C. Kulkarni, E. W. Meijer, A. R. A. Palmans, *Acc. Chem. Res*. **2017**, *50*, 1928–1936.

[207] B. Adelizzi, N. J. Van Zee, L. N. J. de Windt, A. R. A. Palmans, E. W. Meijer, *J. Am. Chem. Soc*. **2019**, *141*, 6110–6121.

[208] A. Arango-Restrepo, O. Arteaga, D. Barragán, J. M. Rubi, *Phys. Chem. Chem. Phys*. **2023**, *25*, 9238–9248.

[209] O. Takahashi, Y. Kohno, M. Nishio, *Chem. Rev*. **2010**, *110*, 6049–6076.

[210] C. R. Martinez, B. L. Iverson, *Chem. Sci*. **2012**, *3*, 2191–2201.

[211] M. F. J. Mabesoone, A. R. A. Palmans, E. W. Meijer, *J. Am. Chem. Soc.* **2020**, *142*, 19781–19798.

[212] S. Cantekin, T. F. A. de Greef, A. R. A. Palmans, *Chem. Soc. Rev*. **2012**, *41*, 6125–6137.

[213] M. M. J. Smulders, A. P. H. J. Schenning, E. W. Meijer, *J. Am. Chem. Soc*. **2007**, *130*, 606–611.

[214] P. J. M. Stals, J. C. Everts, R. de Bruijn, I. A. W. Filot, M. M. J. Smulders, R. Martín-Rapún, E. A. Pidko, T. F. A. de Greef, A. R. A. Palmans, E. W. Meijer, *Chem. Eur. J*. **2010**, *16*, 810–821.

[215] T. Mes, S. Cantekin, D. W. R. Balkenende, M. M. M. Frissen, M. A. J. Gillissen, B. F. M. De Waal, I. K. Voets, E. W. Meijer, A. R. A. Palmans, *Chem. Eur. J*. **2013**, *19*, 8642–8649.

[216] F. García, P. M. Viruela, E. Matesanz, E. Ortí, L. Sánchez, *Chem. Eur. J*. **2011**, *17*, 7755–7759.

[217] F. García, P. A. Korevaar, A. Verlee, E. W. Meijer, A. R. A. Palmans, L. Sánchez, *Chem. Commun*. **2013**, 49, 8674–8676.

[218] Z. Xie, V. Stepanenko, K. Radacki, F. Würthner, *Chem. Eur. J.* **2012**, *18*, 7060–7070.

[219] J. Buendía, E. E. Greciano, L. Sánchez, *J. Org. Chem*. **2015**, *80*, 12444–12452.

[220] R. Rodríguez, C. Naranjo, A. Kumar, P. Matozzo, T. K. Das, Q. Zhu, N. Vanthuyne, R. Gómez, R. Naaman, L. Sánchez, J. Crassous, *J. Am. Chem. Soc*. **2022**, *144*, 7709–7719.

[221] J. Tarrío, R. Rodríguez, B. Fernández, E. Quiñoá, F. Freire, *Angew. Chem. Int. Ed*. **2022**, *61*, e2021150.

[222] R. Sakai, E. B. Barasa, N. Sakai, S.-I. Sato, T. Satoh, T. Kakuchi, *Macromolecules* **2012**, *45*, 8221–8227.

[223] L. Xu, Y.-J. Wu, R.-T. Gao, S.-Y. Li, N. Liu, Z.-Q. Wu, *Angew. Chem. Int. Ed.* **2023**, *62*, e202217234.

[224] T. Ikai, R. Ishidate, K. Inoue, K. Kaygisiz, K. Maeda, E. Yashima, *Macromolecules* **2020**, *53*, 973–981.

[225] M. Alzubi, S. Arias, R. Rodríguez, E. Quiñoá, R. Riguera, F. Freire, *Angew. Chem. Int. Ed.* **2019**, *58*, 13365–13369.

[226] R. Rodríguez, E. Quiñoá, R. Riguera, F. Freire, *Chem. Mater*. **2018**, *30*, 2493–2497.

[227] T. Van Leeuwen, G. H. Heideman, D. Zhao, S. J. Wezenberg, B. L. Feringa, *Chem. Commun.* **2017**, *53*, 6393–6396.

[228] M. Alzubi, S. Arias, I. Louzao, E. Quiñoá, R. Riguera, F. Freire, *Chem. Commun*. **2017**, *53*, 8573–8576.

[229] K. Maeda, K. Shimomura, T. Ikai, S. Kanoh, E. Yashima, *Macromolecules* **2017**, *50*, 7801–7806.

[230] F. Wang, C. Zhou, K. Liu, J. Yan, W. Li, T. Masuda, A. Zhang, *Macromolecules* **2019**, *52,* 8631–8642.

[231] J. Bergueiro, M. Núñez-Martínez, S. Arias, E. Quiñoá, R. Riguera, F. Freire, *Nanoscale Horiz*. **2020**, *5,* 495–500.

[232] K. Cobos, R. Rodriguez, O. Domarco, B. Fernandez, E. Quiñoá, R. Riguera, F. Freire, *Macromolecules* **2020**, *53*, 3182–3193.

[233] M. Fukuda, R. Rodríguez, Z. Fernández, T. Nishimura, T. Hirose, G. Watanabe, E. Quiñoá, F. Freire, K. Maeda, *Chem. Commun.* **2019**, *55*, 7906–7909.

[234] Y. Cao, L. Ren, Y. Zhang, X. Lu, X. Zhang, J. Yan, W. Li, T. Masuda, A. Zhang, *Macromolecules* **2021**, *54*, 7621–7631.

[235] X.-H., S.-M. Kang, R.-T. Gao, Z. Chen, N. Liu, Z.-Q. Wu, *Angew. Chem. Int. Ed.* **2023**, *62*, e20230088.

[236] M. Ando, R. Ishidate, T. Ikai, K. Maeda, E. Yashima, *J. Polym. Sci. Part A* **2019**, *57*, 2481–2490.

[237] R. P. Megens, G. Roelfes, *Chem. Eur. J.* **2011**, *17*, 8514–8523.

[238] J. Shen, Y. Okamoto, *Chem. Rev.* **2016**, *116*, 1094–1138.

[239] J. Tabei, M. Shiotsuki, F. Sanda, T. Masuda, *Macromolecules* **2005**, *38*, 9448–945.

[240] V. Percec, *Polym. Bull*. **1983**, *10*, 1–7.

[241] S. -I. Sakurai, K. Okoshi, J. Kumaki, E. Yashima, *Angew. Chem. Int. Ed.* **2006**, *45*, 1245–1248.

[242] V. Percec, J. G. Rudick, M. Peterca, S. R. Staley, M. Wagner, M. Obata, C. M. Mitchell, W. -D. Cho, V. S. K. Balagurusamy, J. N. Lowe, M. Glodde, O. Weichold, K. J. Chung, N. Ghionni, S. N. Magonov, P. A. Heiney. *Chem. Eur. J.* **2006**, *12*, 5731–5746.

[243] V. Percec, J. G. Rudick, M. Wagner, M. Obata, C. M. Mitchell, W. -D. Cho, S. N. Magonov, *Macromolecules* **2006**, *39*, 7342–7351.

[244] J. G. Rudick, V. Percec, *Chem. Phys*. **2008**, *209*, 1759–1768.

[245] V. Percec, M. Obata, J. G. Rudick, B. B. De, M. Glodde, T. K. Bera, S. N. Magonov, V. S. K Balagurusamy, P. A. Heiney, *J. Polym. Sci. Part A* **2002**, *40*, 3509–3533.

[246] B. Nieto-Ortega, R. Rodríguez, S. Medina, E. Quiñoá, R. Riguera, J. Casado, F. Freire, F. J. Ramírez, *J. Phys. Chem. Lett*. **2018**, *9*, 2266–2270.

[247] S. Arias, M. Núñez-Martínez, E. Quiñoá, R. Riguera, F. Freire, *Small* **2017**, *13*, 1602398.

[248] K. Cobos, E. Quiñoá, R. Riguera, F. Freire, *J. Am. Chem. Soc.* **2018**, *140*, 12239–12246.

[249] Y. Nagata, T. Nishikawa, M. Suginome, *ACS Macro Lett*. **2016**, *5*, 519–522.

[250] Y. -Z. Ke, Y. Nagata, T. Yamada, M. Suginome, *Angew. Chem. Int. Ed.* **2015**, *54*, 9333–9337.

[251] S. Odermatt, J. L. Alonso-Gómez, P. Seiler, M. M. Cid, F. Diederich, *Angew. Chem. Int. Ed.* **2005**, *44*, 5074–5078.

[252] F. W. Goetzke, C. Gropp, A. Schwab, J. D. Etienne, C. Thilgen, F. Diederich, *Helv. Chim. Acta* **2022**, *105*, e202200130.

[253] E. Runge, E. K. U. Gross, *Phys. Rev. Lett.* **1984**, *52*, 997–1000.

[254] Y. Yanai, D. P. Tew, N. C. Handy, *Chem. Phys. Lett*. **2004**, *393*, 51–57.

[255] J. S. Binkley, J. A. Pople, W. J. Hehre, *J. Am. Chem. Soc.* **1980**, *102*, 939–947.

[256] D. S. Goodsell, *Bionanotechnology - Lessons from Nature*; Wiley-Liss: Hoboken, NJ, **2004**.

[257] G. Petsko, D. Ringe, *Protein Structure and Function*; New Science Press: London; **2004**.

[258] C. Dugave, L. Demange, *Chem. Rev*. **2003**, *103*, 2475–2532.

[259] I. Aprahamian, *ACS Cent. Sci.* **2020**, *6*, 347–358.

[260] V. Percec, J. G. Rudick, M. Peterca, P. A. Heiney, *J. Am. Chem. Soc*. **2008**, *130*, 7503–7508.

[261] D. Sluysmans, J. F. Stoddart, *Proc. Natl. Acad. Sci. U. S. A.* **2018**, *115*, 9359–9361.

[262] M. Ilčíková, J. Tkáč, P. Kasák, *Polymers* **2015**, *7*, 2344–2370.

[263] H. Sun, C. P. Kabb, M. B. Sims, B. S. Sumerlin, *Prog. Polym. Sci*. **2019**, *89*, 61–75.

[264] B. A. F. Le Bailly, J. Clayden, *Chem. Commun.* **2016**, *52*, 4852–4863.

[265] S. Kassem, A. T. L. Lee, D. A. Leigh, A. Markevicius, J. Solà, *Nat. Chem.* **2016***, 8*, 138–143.

[266] Z. M. Png, C.-G. Wang, J. C. C. Yeo, J. J. C. Lee, N. E. Surat'man, Y. L. Tan, H. Liu, P. Wang, B. H. Tan, J. W. Xu, X. J. Loh, Q. Zhu, *Mol. Syst. Des. Eng.* **2023**, *8*, 1097–1129.

[267] L. Zhang, H.-X. Wang, S. Li, M. Liu, *Chem. Soc. Rev.* **2020**, *49*, 9095–9120.

[268] G. Maxein, R. Zentel, *Macromolecules* **1995***, 28,* 8438–8440.

[269] S. Mayer, R. Zentel, *Prog. Polym. Sci.* **2001**, *26*, 1973–2013.

[270] K. Maeda, K. Morino, Y. Okamoto, T. Sato, E. Yashima, *J. Am. Chem. Soc.* **2004**, *126*, 4329–4342.

[271] T. Ikai, M. Ito, K. Oki, N. Suzuki, E. Yashima, *Angew. Chem. Int. Ed.* **2023**, *62*, e202306252.

[272] T. Ikai, M. Ito, K. Oki, N. Suzuki, E. Yashima, *Angew. Chem. Int. Ed.* **2023**, *62*, e202301127.

[273] T. Ikai, Y. Morita, T. Majima, S. Takeda, R. Ishidate, K. Oki, N. Suzuki, H. Ohtani, H. Aoi, K. Maeda, K. Okoshi, E. Yashima, *J. Am. Chem. Soc.* **2023**, *145*, 24862–24867.

[274] M. M. Green, C. Khatri, N. C. Peterson, *J. Am. Chem. Soc.* **1993**, *115***,** 4941–4942.

[275] K. Nagai, K. Maeda, Y. Takeyama, K. Sakajiri, E. Yashima, *Macromolecules* **2005**, *38*, 5444–5451.

[276] K. Maeda, M. Nozaki, K. Hashimoto, K. Shimomura, D. Hirose, T. Nishimura, G. Watanabe, E. Yashima, *J. Am. Chem. Soc*. **2020**, *142,* 7668–7682.

[277] X. Guan, S. Wang, G. Shi, J. Zhang, X. Wan, *Macromolecules* **2021**, *54*, 4592–4600.

[278] J. J. Tarrío, R. Rodríguez, J. Crassous, E. Quiñoá, F. Freire, *Angew. Chem. Int. Ed.* **2023**, *62*, e202307059.

[279] M. Lago-Silva, M. M. Cid, E. Quiñoá, F. Freire, *Angew. Chem. Int. Ed.* **2023**, *62*, e202303329.

[280] F. Rey-Tarrío, E. Quiñoá, G. Fernández, F. Freire, *Nat. Commun*. **2023**, *14*, 3348.

[281] R. Kakuchi, R. Shimada, Y. Tago, R. Sakai, T. Satoh, T. Kakuchi, *J. Polym Sci.* **2010**, *48*, 1683–1689.

[282] Y.-Q. Zhang, M. A. Öner, I. R. Lahoz, B. Cirera, C.-A. Palma, S. Castro-Fernández, S. Míguez-Lago, M. M. Cid, J. V. Barth, J. L. Alonso-Gómez, F. Klappenberger, *Chem. Commun.* **2014**, *50*, 15022–15025.

[283] H. Shirakawa, T. Ito, S. Ikeda, *Polym. J.* **1973**, *4*, 460–462.

[284] C. Reichardt, *Solvent and Solvent Effects in Organic Chemistry*; Weinheim: Wiley-VCH, **2003**.

[285] S. Molinari, Jr. R. F. Tesoriero,C. M. Ajo-Franklin, *Matter* **2021**, *4*, 3095–3120.

[286] Z. Liu, Z. Zhang, R. O. Ritchie, *Adv. Funct. Mater.* **2020**, *30*, 1908121.

[287] D. T. J. Morris, J. Clayden, *Chem. Soc. Rev.* **2023**, *52*, 2480–2496.

[288] P. A. Hargrave, *Invest. Ophthalmol. Vis. Sci.* **2001**, *42*, 3–9.

[289] G. Wei, W. Xi, R. Nussinov, B. Ma, *Chem. Rev.* **2016**, *116*, 6516–6551.

[290] E. Ramos, J. Bosch, J. L. Serrano, T. Sierra, J. Veciana, *J. Am. Chem. Soc.* **1996**, *118*, 4703–4704.

[291] I. Louzao, J. M. Seco, E. Quiñoá, R. Riguera, *Angew. Chem. Int. Ed.* **2010**, *49*, 1430–1433.

[292] K. Okoshi, S. -I. Sakurai, S. Ohsawa, J. Kumaki, E. Yashima, *Angew. Chem. Int. Ed.* **2006**, *45*, 8173–8176.

[293] T. Yamamoto, T. Yamada, Y. Nagata, M. Suginome, *J. Am. Chem. Soc.* **2010**, *132*, 7899–7901.

[294] R. Liu, F. Sanda, T. Masuda, *Macromol. Chem. Phys*. **2009**, *210*, 331–339.

[295] E. Suárez-Picado, E. Quiñoá, R. Riguera, F. Freire, *Chem. of Mater*. **2018**, *30*, 6908–6914.

[296] F. Freire, J. M. Seco, E. Quiñoá, R. Riguera, *J. Am. Chem. Soc*. **2012**, *134*, 19374–19383.

[297] T. Ikai, M. Ito, K. Oki, N. Suzuki, E. Yashima, *Angew. Chem. Int. Ed.* **2023**, *135*, DOI 10.1002/ange.202306252.

[298] L. Xu, Y. Wu, R. Gao, S. Li, N. Liu, Z. Wu, *Angew. Chem. Int. Ed.* **2023**, *62*, DOI 10.1002/anie.202217234.

[299] M. Lago-Silva, M. M. Cid, E. Quiñoá, F. Freire, *J. Am. Chem. Soc.* **2024**, *146*, 752–759.

[300] H. Lahlali, K. Jobe, M. Watkinson, S. M. Goldup, *Angew. Chem. Int. Ed.* **2011**, *50*, 4151–4155.

[301] J. E. M. Lewis, J. Winn, L. Cera, S. M. Goldup, *J. Am. Chem. Soc.* **2016**, *138*, 16329–16336.

[302] V. Aucagne, K. D. Hänni, D. A. Leigh, P. J. Lusby, D. B. Walker, *J. Am. Chem. Soc.* **2006**, *128*, 2186–2187.

[303] J. R. J. Maynard, B. Galmés, A. D. Stergiou, M. D. Symes, A. Frontera, S. M. Goldup, *Angew. Chem. Int. Ed.* **2022**, *61*, e20211596.

[304] A. de Juan, D. Lozano, A. W. Heard, M. A. Jinks, J. M. Suarez, G. J. Tizzard, S. M. Goldup, *Nat. Chem*. **2021**, *14*, 179–187.

[305] M. Denis, L. Qin, P. Turner, K. A. Jolliffe, S. M. Goldup, *Angew. Chem. Int. Ed.* **2018**, *57*, 5315–5319.

[306] M. Cirulli, A. Kaur, J. E. M. Lewis, Z. Zhang, J. A. Kitchen, S. M. Goldup, M. M. Roessler, *J. Am. Chem. Soc*. **2018**, *141*, 879–889.

[307] A. Saady, S. M. Goldup, *Chem* **2023**, *9*, 2110–2127.

[308] M. A. Jinks, A. de Juan, M. Denis, C. J. Fletcher, M. Galli, E. M. G. Jamieson, F. Modicom, Z. Zhang, S. M. Goldup, *Angew. Chem. In.t Ed.* **2018**, *57*, 14806–14810.

[309] A. W. Heard, S. M. Goldup, *Chem* **2020**, *6*, 994–1006.

[310] A. Rodríguez-Rubio, A. Savoini, F. Modicom, P. Butler, S. M. Goldup, *J. Am. Chem. Soc*. **2022**, *144*, 11927–11932.

[311] S. Zhang, A. Rodríguez-Rubio, A. Saady, G. J. Tizzard, S. M. Goldup, *Chem* **2023**, *9*, 1195–1207.

[312] L. Brunsveld, B. J. B. Folmer, E. W. Meijer, R. P. Sijbesma, *Chem. Rev*. **2001**, *101*, 4071–4098.

[313] F. Huang, O. A. Scherman, *Chem. Soc. Rev*. **2012**, *41*, 5879–5880.

[314] T. Aida, E. W. Meijer, *Isr. J. Chem.* **2020**, 60, 33–47.

[315] P. K. Hashim, J. Bergueiro, E. W. Meijer, T. Aida, *Prog. Polym. Sci.* **2020**, *105*, 101250.

[316] M. Wehner, F. Würthner, *Nat. Rev. Chem.* **2020**, *4*, 38–53.

[317] M. Hartlieb, E. D. H. Mansfield, S. Perrier, *Polym. Chem*. **2020**, *11*, 1083–1110.

[318] C. Rest, R. Kandanelli, G. Fernández, *Chem. Soc. Rev*. **2015**, *44*, 2543–2572.

[319] L. N. J. de Windt, Z. Fernández, M. Fernández-Míguez, F. Freire, A. R. A. Palmans, *Chem. Eur. J*. **2022**, *28*, e202103691.

[320] S. Cantekin, H. M. M. ten Eikelder, A. J. Markvoort, M. A. J. Veld, P. A. Korevaar, M. M. Green, A. R. A. Palmans, E. W. Meijer, *Angew. Chem. Int. Ed*. **2012**, *51*, 6426–6431.

[321] P. J. M. Stals, J. F. Haveman, R. Martín-Rapún, C. F. C. Fitié, A. R. A. Palmans, E. W. Meijer, *J. Mater. Chem*. **2009**, *19*, 124–130.

[322] R. van Hameren, A. M. van Buul, M. A. Castriciano, V. Villari, N. Micali, P. Schön, S. Speller, L. Monsú Scolaro, A. E. Rowan, J. A. A. W. Elemans, R. J. M. Nolte, *Nano Lett*. **2008**, *8*, 253–259.

[323] T.-Q. Nguyen, R. Martel, P. Avouris, M. L. Bushey, L. Brus and C. Nuckolls, *J. Am. Chem. Soc*. **2004**, *126*, 5234–5242.

[324] M. L. Bushey, A. Hwang, P. W. Stephens, C. Nuckolls, *Angew. Chem. Int. Ed*. **2002**, *41*, 2828–2831.

[325] M. L. Bushey, A. Hwang, P. W. Stephens, C. Nuckolls, *J. Am. Chem. Soc*. **2001**, *123*, 8157–8158.

[326] C. Naranjo, A. Doncel-Giménez, R. Gómez, J. Aragó, E. Ortí, L. Sánchez, *Chem. Sci.* **2023**, *14*, 9900–9909.

[327] M. A. Martínez, A. Doncel-Giménez, J. Cerdá, J. Calbo, R. Rodríguez, J. Aragó, J. Crassous, E. Ortí, L. Sánchez, *J. Am. Chem. Soc.* **2021**, *143*, 13281–13291.

[328] M. Wehner, M. I. S. Röhr, M. Bühler, V. Stepanenko, W. Wagner, F. Würthner, *J. Am. Chem. Soc.* **2019**, *141*, 6092–6107.

[329] C. Roche, H. J. Sun, P. Leowanawat, F. Araoka, B. E. Partridge, M. Peterca, D. A. Wilson, M. E. Prendergast, P. A. Heiney, R. Graf, H. W. Spiess, X. Zeng, G. Ungar, V. Percec, *Nat. Chem.* **2016**, *8*, 80–89.

[330] F. Würthner, C. R. Saha-Möller, B. Fimmel, S. Ogi, P. Leowanawat, D. Schmidt, *Chem. Rev*. **2016**, *116*, 962–1052.

[331] L. Wang, B. E. Partridge, N. Huang, J. T. Olsen, D. Sahoo, X. Zeng, G. Ungar, R. Graf, H. W. Spiess, V. Percec, *J. Am. Chem. Soc.* **2020**, *142*, 9525–9536.

[332] B. E. Partridge, L. Wang, D. Sahoo, J. T. Olsen, P. Leowanawat, C. Roche, H. Ferreira, K. J. Reilly, X. Zeng, G. Ungar, P. A. Heiney, R. Graf, H. W. Spiess, V. Percec. *J. Am. Chem. Soc.* **2019**, *141*, 15761–15766.

[333] B. E. Partridge, P. Leowanawat, E. Aqad, M. R. Imam, H.-J. Sun, M. Peterca, P. A. Heiney, R. Graf, H. W. Spiess, X. Zeng, G. Ungar, V. Percec, *J. Am. Chem. Soc.* **2015**, *137*, 5210–5224.

[334] R. M. Veedu, N. Niemeyer, N. Bäumer, K. K. Kalathil, J. Neugebauer, G. Fernández, *Angew. Chem. Int. Ed.* **2023**, *62*, e202314211.

[335] N. Bäumer, S. Ogi, L. Borsdorf, S. Yamaguchi, G. Fernández, *Chem. Commun.* **2023**, *59*, 8937–8940.

[336] B. Matarranz, S. Díaz-Cabrera, G. Ghosh, I. Carreira-Barral, B. Soberats, M. García-Valverde, R. Quesada, G. Fernandez, *Angew. Chem. Int. Ed.* **2023**, *135*, e202218555.

[337] I. Helmers, M. Saddam Hossain, N. Bäumer, P. Wesarg, B. Soberats, L. S. Shimizu, G. Fernández. *Angew. Chem. Int. Ed.* **2022**, *61*, e202200390.

[338] B. Matarranz, G. Fernandez, *Chem. Phys. Rev.* **2021***, 2*, 041304.

[339] H. Wang, Y. Zhang, Y. Chen, H. Pan, X. Ren, Z. Chen, *Angew. Chem. Int. Ed.* **2020**, *59*, 5185–5192.

[340] H. Lee, H. Park, D. Y. Ryu, W. D. Jang, *Chem. Soc. Rev.* **2023**, *52*, 1947–1974.

[341] K. V. Rao, M. F. J. Mabesoone, D. Miyajima, A. Nihonyanagi, E. W. Meijer, T. Aida, *J. Am. Chem. Soc.* **2020**, *142*, 598–605.

[342] N. Sasaki, M. F. J. Mabesoone, J. Kikkawa, T. Fukui, N. Shioya, T. Shimoaka, T. Hasegawa, H. Takagi, R. Haruki, N. Shimizu, S.-I. Adachi, E. W. Meijer, M. Takeuchi, K. Sugiyasu. *Nat. Commun.* **2020**, *11*, 3578.

[343] M. F. J. Mabesoone, A. J. Markvoort, M. Banno, T. Yamaguchi, F. Helmich, Y. Naito, E. Yashima, A. R. A. Palmans, E. W. Meijer, *J. Am. Chem. Soc.* **2018**, *140*, 7810–7819.

[344] K. V. Rao, D. Miyajima, A. Nihonyanagi, T. Aida, *Nat. Chem*. **2017**, *9*, 1133–1139.

[345] S. Ogi, K. Sugiyasu, S. Manna, S. Samitsu, M. Takeuchi, *Nat. Chem.* **2014**, *6*, 188–195.

[346] N. Sasaki, M. F. J. Mabesoone, J. Kikkawa, T. Fukui, N. Shioya, T. Shimoaka, T. Hasegawa, H. Takagi, R. Haruki, N. Shimizu, S.-I. Adachi, E. W. Meijer, M. Takeuchi, K. Sugiyasu, *Nat. Commun.* **2020**, *11*, 35780.

[347] B. Matarranz, G. Ghosh, R. Kandanelli, A. Sampedro, K. K. Kartha, G. Fernández, *Chem. Commun.* **2021**, *57*, 4890–4893.

[348] G. Das, R. Thirumalai, B. Vedhanarayanan, V. K. Praveen, A. Ajayaghosh, *Adv. Opt. Mater.* **2020**, *8*, 1–8.

[349] S. K. Albert, H. V. P. Thelu, M. Golla, N. Krishnan, S. Chaudhary, R. Varghese, *Angew. Chem. Int. Ed.* **2014**, *53*, 8352–8357.

[350] F. García, L. Sánchez, *J. Am. Chem. Soc*. **2012**, *134*, 734–742.

[351] N. Bäumer, E. Castellanos, B. Soberats, G. Fernández, *Nat. Commun.* **2023**, *14*, 1084.

[352] K. K. Kalathil, G. Fernández. *Supramolecular Coordination Complexes: Design, Synthesis, and Applications*, Edited, Elsevier Ltd. **2023**.

[353] J. Matern, Z. Fernandez, G. Fernandez, *Chem. Commun.* **2022**, *58*, 12309–12312.

[354] J. Matern, I. Maisuls, C. A. Strassert, G. Fernandez, *Angew. Chem. Int. Ed.* **2022**, *61*, e202208436.

[355] M. H. Y. Chan, V. W. W. Yam, *J. Am. Chem. Soc.* **2022**, *144*, 22805–22825.

[356] N. Bäumer, J. Matern, G. Fernandez, *Chem. Sci.* **2021***, 12*, 12248–12265.

[357] M. Y. Leung, S. Y. L. Leung, K. C. Yim, A. K. W. Chan, M. Ng, V. W. W. Yam, *J. Am. Chem. Soc.* **2019**, *141*, 19466–19478.

[358] M. H. Y. Chan, M. Ng, S. Y. L. Leung, W. H. Lam, V. W. W. Yam, *J. Am. Chem. Soc.* **2017**, *139*, 8639–8645.

[359] S. Huang, H. Yu, Q. Li, *Adv. Sci.* **2021**, *8*, 1–20.

[360] M. A. Martínez-Aguirre, Y. Li, N. Vanthuyne, L. Bouteiller, M. Raynal, *Angew. Chem. Int. Ed.* **2021**, *60*, 4183–4191.

[361] M. Raynal**,** F. Portier, P. W. N. M. van Leeuwen, L. Bouteiller, *J. Am. Chem. Soc.* **2013**, *135*, 17687–17690.

[362] A. Desmarchellier, X. Caumes, M. Raynal, A. Vidal-Ferran, P. W. N. M. van Leewen, L. Boutellier, *J. Am. Chem. Soc*. **2016**, *138*, 4908–4916.

[363] Y. Li, A. Hammoud, L. Boutellier, M. Raynal, *J. Am. Chem. Soc*. **2020**, *142*, 5676–5688.

[364] J. M. Zimbron, X. Caumes, Y. Li, C. M. Thomas, M. Raynal, L. Bouteiller, *Angew. Chem. Int. Ed.* **2017**, *56*, 14016–14019.

[365] C. Kulkarni, A. K. Mondal, T. K. Das, G. Grinbom, F. Tassinari, M. F. J. Mabesoone, E. W. Meijer, R. Naaman, *Adv. Mater.* **2020**, *32*, 1–7.

[366] Y. Sang, Q. Zhu, X. Zhou, Y. Jiang, L. Zhang, M. Liu, *Angew. Chem. Int. Ed.* **2023**, *62*, e202215867.

[367] R. Naaman, Y. Paltiel, D. H. Waldeck, *Nat. Rev. Chem*. **2019,** *3*, 250–260.

[368] S. Ghosh, X.-Q. Li, V. Stepanenko, F. Würthner, *Chem. Eur. J.* **2008**, *14*, 11343–11357.

[369] N. J. Van Zee, M. F. Mabesoone, B. Adelizzi, A. R. A. Palmans, E. W. Meijer, *J. Am. Chem Soc*. **2020**, *142*, 20191–20200.

[370] M. M. J. Smulders, I. A. W. Filot, J. M. A. Leenders, P. van der Schoot, A. R. A. Palmans, A. P. H. J. Schenning, E. W. Meijer, *J. Am. Chem. Soc*. **2010**, *132*, 611–619.

[371] E. E. Greciano, J. Calbo, J. Buendía, J. Cerdá, J. Aragó, E. Ortí, L. Sánchez, *J. Am. Chem. Soc*. **2019**, *141*, 7463–7472.

[372] Y. Dorca, R. Sánchez-Naya, J. Cerdá, J. Calbo, J. Aragó, R. Gómez, E. Ortí, L. Sánchez, *Chem. Eur. J*. **2020**, *26*, 14700–14707.

[373] T. Kim, T. Mori, T. Aida, D. Miyajima, *Chem. Sci.* **2016**, *7*, 6689–6694.

[374] S. Okuda, N. Ousaka, T. Iwata, R. Ishida, A. Urushima, N. Suzuki, S. Nagano, T. Ikai, E. Yashima, *J. Am. Chem. Soc.* **2022**, *144*, 2775–2792.

[375] J. Van Gestel, A. R. A. Palmans, B. Titulaer, J. A. J. M. Vekemans, E. W. Meijer, *J. Am. Chem. Soc.* **2005**, *127*, 5490–5494.

[376] Y. Zhao, H. Kawano, H. Yamagishi, S. Otake, Y. Itoh, H. Huang, E. W. Meijer, T. Aida, *J. Am. Chem Soc.* **2023**, *145*, 13920–13928.

[377] T. Saito, T. Kajitani, S. Yagai, *J. Am. Chem. Soc.* **2023**, *145*, 443–454.

[378] R. Ishidate, A. J. Markvoort, K. Maeda, E. Yashima, *J. Am. Chem. Soc.* **2019**, *141*, 7605–7614.

[379] A. Lohr, F. Würthner, *Angew. Chem. Int. Ed.* **2008**, *47*, 1232–1236.

[380] J. van Gestel, *J. Phys Chem. B* **2006**, *110*, 4365–4370.

[381] J. van Gestel, *Macromolecules* **2006**, *39*, 1664–1664.

[382] M. M. Green, J.-W. Park, T Sato, A. Teramoto, S. Lifson, R. B. Selinger, J. V. Selinger, *Angew. Chem. Int. Ed.* **1999**, *38*, 3138–3154.

[383] J. Kim, J. Lee, W. Y. Kim, H. Kim, S. Lee, H. C. Lee, Y. S. Lee, M. Seo, S. Y. Kim, *Nat. Commun.* **2015**, *6*, 6959.

[384] J. S. Kang, S. Kang, J. M. Suh, S. M. Park, D. K. Yoon, M. H. Lim, W. Y. Kim, M. Seo, *J. Am. Chem. Soc.* **2022**, *144*, 2657–2666.

[385] J. Hu, Y. Xie, H. Zhang, C. He, Q. Zhang, G. Zou, *Chem. Commun.* **2019**, *55*, 4953–4956.

[386] H. Wang, Y. Liu, L. Wang, B. Raktani, T. Yang, K. M. Tran, Y. Luo, J. Yu, H. Lee, H. Lee, *ACS Mater. Lett.* **2022**, *4*, 1954–1961.

[387] E. E. Greciano, R. Rodríguez, K. Maeda, L. Sánchez*, Chem. Commun.* **2020***, 56,* 2244–2247.

[388] S. Xue, P. Xing, J. Zhang, Y. Zeng and Y. Zhao, *Chem. Eur. J*. **2019**, *25*, 7426–7437.

[389] A. R. A. Palmans, J. A. J. M. Vekemans, E. E. Havinga, E. W. Meijer, *Angew. Chem. Int. Ed.* **1997**, *36*, 2648–2651.

[390] A. K. Mondal, M. D. Preuss, M. L. Ślęczkowski, T. K. Das, G. Vantomme, E. W. Meijer, R. Naaman, *J. Am. Chem. Soc.* **2021**, *143*, 7189–7195.

[391] M. L. Ślęczkowski, M. F. J. Mabesoone, P. Ślęczkowski, A. R. A. Palmans and E. W. Meijer, *Nat. Chem*. **2021**, *13*, 200–207.

[392] D. E. Fagnani, M. J. Meese, K. A. Abboud, R. K. Castellano, *Angew. Chem. Int. Ed.* **2016**, *55*, 10726–10731.

[393] W. R. Henderson, Y. D. E. Zhu, L. G. Fagnani, K. A. Abboud, R. K. Castellano, *J. Org. Chem.* **2020**, *85*, 1158–1167.

[394] W. R. Henderson, D. E. Fagnani, J. Grolms, K. A. Abboud, R. K. Castellano, *HCA* **2019**, *102*, e1900047.

[395] D. B. Korlepara, W. R. Henderson, R. K. Castellano, S. Balasubramanian. *Chem Commun.* **2019**, *55*, 3773–3776.

[396] W. R. Henderson, R. K. Castellano, *Polym. Int.* **2021**, *70*, 897–910.

[397] R. Rodríguez, C. Naranjo, A. Kumar, K. Dhbaibi, P. Matozzo, F. Camerel, N. Vanthuyne, R. Gómez, R. Naaman, L. Sánchez, J. Crassous, *Chem. Eur. J.* **2023**, *29*, DOI 10.1002/chem.202302254.

[398] K. E. S. Phillips, T. J. Katz, S. Jockusch, A. J. Lovinger, N. J. Turro, *J. Am. Chem. Soc.* **2001**, *123*, 11899–11907.

[399] T Kaseyama, S. Furumi, X. Zhang, K. Tanaka, M. Takeuchi, *Angew. Chem. Int. Ed.* **2011**, *50*, 3684–3687.

[400] J. S. Valera, R. Gómez, L. Sánchez, *Org. Lett.* **2018**, *20*, 2020–2023.

[401] J. Guilleme, M. J. Mayoral, J. Calbo, J. Aragó, P. M. Viruela, E. Ortí, T. Torres, D. González-Rodríguez, *Angew. Chem. Int. Ed.* **2015**, *54*, 2543–2547.

[402] M. J. Mayoral, J. Guilleme, J. Calbo, J. Aragó, F. Aparicio, E. Ortí**,** T. Torres**,** D. González-Rodríguez**,** *J. Am. Chem. Soc.* **2020**, *142*, 21017–21031.

[403] W. R. Henderson, R. K. Castellano, *Polym. Int.* **2020**, *70*, 897–910.

[404] R. E. Martin, F. Diederich, *Angew. Chem. Int. Ed*. **1999**, *38*, 1350–1377.

[405] M. D. Tzirakis, M. N. Alberti, H. Weissman, B. Rybtchinski, F. Diederich, *Chem. Eur. J.* **2014**, *20*, 16070–16073.

[406] I. R. Lahoz, A. Navarro-Vázquez, A. L. Llamas-Saiz, J. L. Alonso-Gómez, M. M. Cid, *Chem. Eur. J.* **2012**, *18*, 13836–13843.

[407] E. E. Greciano, S. Alsina, G. Ghosh, G. Fernández, L. Sánchez, *Small Methods*, **2020**, *4*, 1900715.

[408] H. M. M. ten Eikelder, A. J. Markvoort, T. F. A. de Greef, P. A. J. Hilbers, *J. Phys. Chem. B* **2012**, *116*, 5291–5301.

[409] A. J. Markvoort, H. M. M. ten Eikelder, P. A. J. Hilbers, T. F. A. de Greef, E. W. Meijer, *Nat. Commun.* **2011**, *2*, 509.

[410] Y. Dorca, C. Naranjo, G. Ghosh, B. Soberats, J. Calbo, E. Ortí, G. Fernández, L. Sánchez, *Chem. Sci.* **2022**, *13*, 81–89.

[411] S. Bujosa, A. Doncel-Giménez, N. Bäumer, G. Fernández, E. Ortí, A. Costa, C. Rotger, J. Aragó, B. Soberats, *Angew. Chem. Int. Ed.* **2022**, *61*, e2022133.

[412] E. E. Greciano, J. Calbo, E. Ortí, L. Sánchez, *Angew. Chem. Int. Ed.* **2020**, *59*, 17517–17524.

[413] J. M. J. Frisch, G. W. Trucks, H. B. Schlegel, G. E. Scuseria, M. A. Robb, J. R. Cheeseman, G. Scalmani, V. Barone, G. A. Petersson, H. Nakatsuji, X. Li, M. Caricato, A. V. Marenich, J. Bloino, B. G. Janesko, R. Gomperts, B. Mennucci, H. P. Hratchian, J. V. Ortiz, A. F. Izmaylov, J. L. Sonnenberg, D. Williams-Young, F. Ding, F. Lipparini, F. Egidi, J. Goings, B. Peng, A. Petrone, T. Henderson, D. Ranasinghe, V. G. Zakrzewski, J. Gao, N. Rega, G. Zheng, W. Liang, M. Hada, M. Ehara, K. Toyota, R. Fukuda, J. Hasegawa, M. Ishida, T. Nakajima, Y. Honda, O. Kitao, H. Nakai, T. Vreven, K. Throssell, J. A. Montgomery, Jr. J. E. Peralta, F. Ogliaro, M. J. Bearpark, J. J. Heyd, E. N. Brothers, K. N. Kudin, V. N: Staroverov, T. A. Keith, R. Kobayashi, J. Normand, K. Raghavachari, A. P. Rendell, J. C. Burant, S. S. Iyengar, J. Tomasi, M. Cossi, J. M. Millam, M. Klene, C. Adamo, R. Cammi, R.; J. W. Ochterski, R. L. Martin, K. Morokuma, O. Farkas, J. B. Foresman, D. J. Fox. *Gaussian, Inc. Gaussian 16, Revision C.01*. Wallingford, CT: Gaussian, Inc.; **2016**.

[414] P. Hohenberg, K. Walter, *Physical Review* **1964**, *136*, 864–871.

[415] S. Grimme, *WIREs Computational Molecular Science* **2011**, *1*, 211–228.

[416] F. Aparicio, F. García, L. Sánchez, *Chem. Eur. J.* **2013**, *19*, 3293–3248.

[417] C. Bannwarth, E. Caldeweyher, S. Ehlert, A. Hansen, P. Pracht, J. Seibert, S. Spicher, S. Grimme, *WIREs Comput Mol Sci.* **2021**, *11*, 11:e1493.

[418] A. D. Becke, *J. Chem. Phys.* **1993**, *98*, 5648–5652.

[419] V. A. Rassolov, M. A. Ratner, J. A. Pople, P. C. Redfern, L. A. Curtiss, *J. Comput. Chem.* **2001**, *22*, 976–984.

[420] S. Grimme, S. Ehrlich, L. Goerigk, *J. Comput. Chem.* **2011**, *32*, 1456–1465.

[421] M. D. Hanwell, D. E. Curtis, D. C. Lonie, T. Vandermeersch, E. Zurek, G. R. Hutchison, *J. Cheminform.* **2012**, 4.

Appendix

A.1. List of publications derived from this Doctoral Thesis and partially reproduced

1) María Lago-Silva, María Magdalena Cid, Emilio Quiñoá, Félix Freire, Dynamic Axial-to-Helical Communication Mechanism in Poly[(allenylethynylenephenylene)acetylene]s under External Stimuli, *Angew. Chem. Int. Ed.* **2023**, *62*, e202303329. DOI: 10.1002/anie.202303329.

Reproduced in: Chapter 3.1.

Quality Indexes

Impact factor: 16.6 (2022 Journal Citation Reports).

CiteScore: 26.3 (2022 Scopus).

SJR: 5.573 (2022 SJR).

Category: Chemistry, Multidisciplinary (Q1) (2022 Journal Citation Reports).

Specific contribution to the publication

M. L.-S. contributed to the experimental part (synthesis, characterization, and computational studies), the discussion of results, and the writing of the manuscript.

Authorization from the journal

This Agreement between Ms. Maria Lago Silva ("You") and John Wiley and Sons ("John Wiley and Sons") consists of your license details and the terms and conditions provided by John Wiley and Sons and Copyright Clearance Center.

License Number	5715280292437
License date	Jan 24, 2024
Licensed Content Publisher	John Wiley and Sons
Licensed Content Publication	Angewandte Chemie International Edition
Licensed Content Title	Dynamic Axial–to–Helical Communication Mechanism in Poly[(allenylethynylenephenylene)acetylene]s under External Stimuli
Licensed Content Author	Félix Freire, Emilio Quiñoá, María Magdalena Cid, et al
Licensed Content Date	Jun 12, 2023
Licensed Content Volume	62
Licensed Content Issue	29
Licensed Content Pages	7
Type of use	Dissertation/Thesis

2) María Lago-Silva, María Magdalena Cid, Emilio Quiñoá, Félix Freire, *P/M* Macromolecular Switch Based on Conformational Control Exerted by an Achiral Side Chain within an Axially Chiral Locked Pendant, *J. Am. Chem. Soc.* **2024**, *146,* 752 – 759. DOI: 10.1021/jacs.3c10766.

Reproduced in: Chapter 3.2.

Quality Indexes

Impact factor: 15.0 (2022 Journal Citation Reports).

CiteScore: 25.7 (2022 Scopus).

SJR: 5.945 (2022 SJR).

Category: Chemistry, Multidisciplinary (Q1) (2022 Journal Citation Reports).

Specific contribution to the publications

M. L.-S. contributed to the experimental part (synthesis, characterization, and computational studies), the discussion of results, and the writing of the manuscript.

Authorization from the journal

This publication is licensed under CC-BY 4.0. As it can be read in the following text for thesis and dissertation not permission is required.

Cite this: *J. Am. Chem. Soc.* 2024, 146, 1, 752−759
Publication Date: December 27, 2023
https://doi.org/10.1021/jacs.3c10766

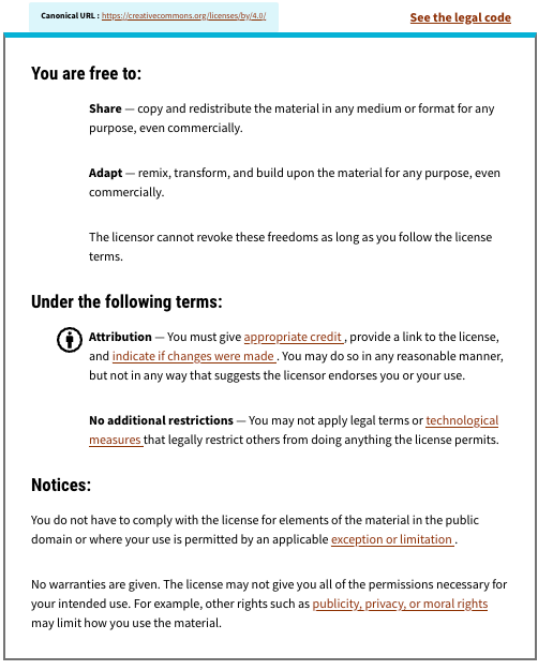

3) María Lago-Silva, Manuel Fernández-Míguez, Rafael Rodríguez, Emilio Quiñoá, Félix Freire, Stimuli-responsive synthetic helical polymers, *Chem. Soc. Rev.* **2024**, *53*, 793 – 852. DOI: 10.1039/D3CS00952A.

Quality Indexes

Impact factor: 46.2 (2022 Journal Citation Reports).

CiteScore: 81.3 (2022 Scopus).

SJR: 15.109 (2022 SJR).

Category: Chemistry (Q1) (2022 Journal Citation Reports).

Reproduced in: Chapter 1.6.1.

Specific contribution to the publications

M. L.-S. contributed to the planning and the writing of the manuscript.

Authorization from the journal

License number for the reproduction of the article: this publication is licensed under CC-BY 3.0.

Stimuli-responsive synthetic helical polymers

M. Lago-Silva, M. Fernández-Míguez, R. Rodríguez, E. Quiñoá and F. Freire, *Chem. Soc. Rev.*, 2024, **53**, 793 **DOI:** 10.1039/D3CS00952A

This article is licensed under a Creative Commons Attribution 3.0 Unported Licence. **You can use material from this article in other publications without requesting further permissions** from the RSC, provided that the correct acknowledgement is given.

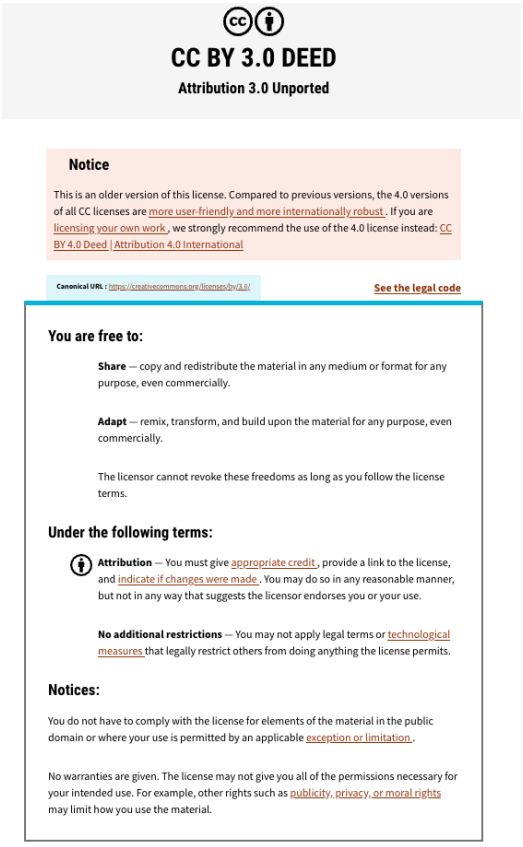

A.2. Conflict of Interest

The PhD candidate María Lago Silva declares no conflict of interest in relation to the doctoral thesis.

Santiago de Compostela, January 20th 2024.

A.3. Rights and Permissions of the images

All American Chemical Society images (ACS):

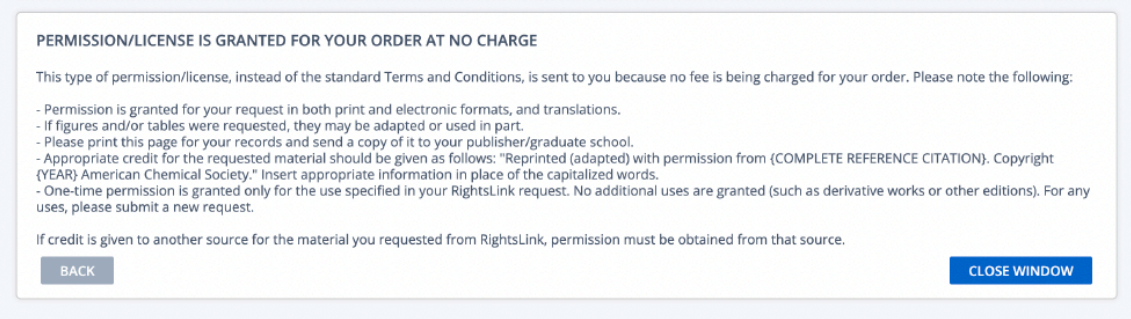
PERMISSION/LICENSE IS GRANTED FOR YOUR ORDER AT NO CHARGE

This type of permission/license, instead of the standard Terms and Conditions, is sent to you because no fee is being charged for your order. Please note the following:

- Permission is granted for your request in both print and electronic formats, and translations.
- If figures and/or tables were requested, they may be adapted or used in part.
- Please print this page for your records and send a copy of it to your publisher/graduate school.
- Appropriate credit for the requested material should be given as follows: "Reprinted (adapted) with permission from {COMPLETE REFERENCE CITATION}. Copyright {YEAR} American Chemical Society." Insert appropriate information in place of the capitalized words.
- One-time permission is granted only for the use specified in your RightsLink request. No additional uses are granted (such as derivative works or other editions). For any uses, please submit a new request.

If credit is given to another source for the material you requested from RightsLink, permission must be obtained from that source.

BACK CLOSE WINDOW

All Elsevier images:

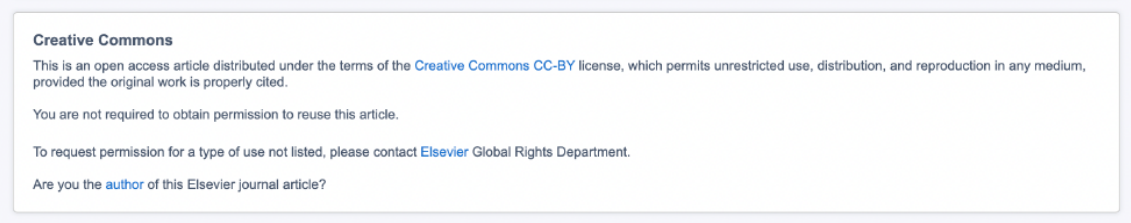
Creative Commons

This is an open access article distributed under the terms of the Creative Commons CC-BY license, which permits unrestricted use, distribution, and reproduction in any medium, provided the original work is properly cited.

You are not required to obtain permission to reuse this article.

To request permission for a type of use not listed, please contact Elsevier Global Rights Department.

Are you the author of this Elsevier journal article?

Figure 1. (d)

SPRINGER NATURE LICENSE
TERMS AND CONDITIONS

Dec 26, 2023

This Agreement between Ms. Maria Lago Silva ("You") and Springer Nature ("Springer Nature") consists of your license details and the terms and conditions provided by Springer Nature and Copyright Clearance Center.

License Number	5696590350279
License date	Dec 26, 2023
Licensed Content Publisher	Springer Nature
Licensed Content Publication	Nature
Licensed Content Title	Structure and mechanism of the M2 proton channel of influenza A virus
Licensed Content Author	Jason R. Schnell et al
Licensed Content Date	Jan 31, 2008
Type of Use	Thesis/Dissertation
Requestor type	academic/university or research institute
Format	print and electronic
Portion	figures/tables/illustrations
Number of figures/tables/illustrations	1

Figure 1. Top-right

JOHN WILEY AND SONS LICENSE
TERMS AND CONDITIONS

Dec 26, 2023

This Agreement between Ms. Maria Lago Silva ("You") and John Wiley and Sons ("John Wiley and Sons") consists of your license details and the terms and conditions provided by John Wiley and Sons and Copyright Clearance Center.

License Number	5696611473141
License date	Dec 26, 2023
Licensed Content Publisher	John Wiley and Sons
Licensed Content Publication	Angewandte Chemie International Edition
Licensed Content Title	The Competitive Aggregation Pathway of an Asymmetric Chiral Oligo(p-phenyleneethynylene) Towards the Formation of Individual P and M Supramolecular Helical Polymers
Licensed Content Author	Félix Freire, Emilio Quiñoá, Berta Fernández, et al
Licensed Content Date	Mar 18, 2021
Licensed Content Volume	60
Licensed Content Issue	18
Licensed Content Pages	6
Type of use	Dissertation/Thesis

Figure 2.

JOHN WILEY AND SONS LICENSE
TERMS AND CONDITIONS

Dec 26, 2023

This Agreement between Ms. Maria Lago Silva ("You") and John Wiley and Sons ("John Wiley and Sons") consists of your license details and the terms and conditions provided by John Wiley and Sons and Copyright Clearance Center.

License Number	5696631378855
License date	Dec 26, 2023
Licensed Content Publisher	John Wiley and Sons
Licensed Content Publication	Angewandte Chemie International Edition
Licensed Content Title	1,3-Diethynylallenes: New Modules for Three-Dimensional Acetylenic Scaffolding
Licensed Content Author	Robert C. Livingston, Liam R. Cox, Volker Gramlich, et al
Licensed Content Date	Jun 13, 2001
Licensed Content Volume	40
Licensed Content Issue	12
Licensed Content Pages	4
Type of use	Dissertation/Thesis
Requestor type	University/Academic
Format	Print and electronic

Figure 3.

JOHN WILEY AND SONS LICENSE
TERMS AND CONDITIONS

Dec 26, 2023

This Agreement between Ms. Maria Lago Silva ("You") and John Wiley and Sons ("John Wiley and Sons") consists of your license details and the terms and conditions provided by John Wiley and Sons and Copyright Clearance Center.

License Number	5696650926028
License date	Dec 26, 2023
Licensed Content Publisher	John Wiley and Sons
Licensed Content Publication	Angewandte Chemie International Edition
Licensed Content Title	Chiroptical Detection of Nonchromophoric, Achiral Guests by Enantiopure Alleno–Acetylenic Helicages
Licensed Content Author	Ori Gidron, Marc-Olivier Ebert, Nils Trapp, et al
Licensed Content Date	Nov 10, 2014
Licensed Content Volume	53
Licensed Content Issue	49
Licensed Content Pages	5
Type of use	Dissertation/Thesis
Requestor type	University/Academic
Format	Print and electronic

JOHN WILEY AND SONS LICENSE
TERMS AND CONDITIONS

Dec 26, 2023

This Agreement between Ms. Maria Lago Silva ("You") and John Wiley and Sons ("John Wiley and Sons") consists of your license details and the terms and conditions provided by John Wiley and Sons and Copyright Clearance Center.

License Number	5696650733121
License date	Dec 26, 2023
Licensed Content Publisher	John Wiley and Sons
Licensed Content Publication	Angewandte Chemie International Edition
Licensed Content Title	Alleno–Acetylenic Cage (AAC) Receptors: Chiroptical Switching and Enantioselective Complexation of trans-1,2-Dimethylcyclohexane in a Diaxial Conformation
Licensed Content Author	François Diederich, Nils Trapp, Cornelius Gropp
Licensed Content Date	Oct 14, 2016
Licensed Content Volume	55
Licensed Content Issue	46
Licensed Content Pages	6
Type of use	Dissertation/Thesis

JOHN WILEY AND SONS LICENSE
TERMS AND CONDITIONS

Dec 26, 2023

This Agreement between Ms. Maria Lago Silva ("You") and John Wiley and Sons ("John Wiley and Sons") consists of your license details and the terms and conditions provided by John Wiley and Sons and Copyright Clearance Center.

License Number	5696651224092
License date	Dec 26, 2023
Licensed Content Publisher	John Wiley and Sons
Licensed Content Publication	Chemistry - A European Journal
Licensed Content Title	A Chiral Molecular Cage Comprising Diethynylallenes and N-Heterotriangulenes for Enantioselective Recognition
Licensed Content Author	María Magdalena Cid, Milan Kivala, Bettina D. Gliemann, et al
Licensed Content Date	Aug 12, 2021
Licensed Content Volume	27
Licensed Content Issue	53
Licensed Content Pages	6
Type of use	Dissertation/Thesis
Requestor type	University/Academic

JOHN WILEY AND SONS LICENSE
TERMS AND CONDITIONS

Dec 26, 2023

This Agreement between Ms. Maria Lago Silva ("You") and John Wiley and Sons ("John Wiley and Sons") consists of your license details and the terms and conditions provided by John Wiley and Sons and Copyright Clearance Center.

License Number	5696640696433
License date	Dec 26, 2023
Licensed Content Publisher	John Wiley and Sons
Licensed Content Publication	Angewandte Chemie International Edition
Licensed Content Title	Amplification of Chirality in Monodisperse, Enantiopure Alleno–Acetylenic Oligomers
Licensed Content Author	Pablo Rivera-Fuentes, José Lorenzo Alonso-Gómez, Ana G. Petrovic, et al
Licensed Content Date	Mar 10, 2010
Licensed Content Volume	49
Licensed Content Issue	12
Licensed Content Pages	4
Type of use	Dissertation/Thesis
Requestor type	University/Academic
Format	Print and electronic

JOHN WILEY AND SONS LICENSE
TERMS AND CONDITIONS

Dec 26, 2023

This Agreement between Ms. Maria Lago Silva ("You") and John Wiley and Sons ("John Wiley and Sons") consists of your license details and the terms and conditions provided by John Wiley and Sons and Copyright Clearance Center.

License Number	5696640973470
License date	Dec 26, 2023
Licensed Content Publisher	John Wiley and Sons
Licensed Content Publication	Angewandte Chemie International Edition
Licensed Content Title	An Enantiomerically Pure Alleno–Acetylenic Macrocycle: Synthesis and Rationalization of Its Outstanding Chiroptical Response
Licensed Content Author	François Diederich, Nina Berova, Nobuyuki Harada, et al
Licensed Content Date	Jul 8, 2009
Licensed Content Volume	48
Licensed Content Issue	30
Licensed Content Pages	4
Type of use	Dissertation/Thesis

Figure 10.

JOHN WILEY AND SONS LICENSE
TERMS AND CONDITIONS

Dec 26, 2023

This Agreement between Ms. Maria Lago Silva ("You") and John Wiley and Sons ("John Wiley and Sons") consists of your license details and the terms and conditions provided by John Wiley and Sons and Copyright Clearance Center.

License Number	5696660137757
License date	Dec 26, 2023
Licensed Content Publisher	John Wiley and Sons
Licensed Content Publication	Angewandte Chemie International Edition
Licensed Content Title	Planar Chirality: A Mine for Catalysis and Structure Discovery
Licensed Content Author	Claudio Palomo, Rosa López
Licensed Content Date	Jan 27, 2022
Licensed Content Volume	61
Licensed Content Issue	13
Licensed Content Pages	12
Type of use	Dissertation/Thesis
Requestor type	University/Academic
Format	Print and electronic

Figure 13.

SPRINGER NATURE LICENSE
TERMS AND CONDITIONS

Dec 26, 2023

This Agreement between Ms. Maria Lago Silva ("You") and Springer Nature ("Springer Nature") consists of your license details and the terms and conditions provided by Springer Nature and Copyright Clearance Center.

License Number	5696660575573
License date	Dec 26, 2023
Licensed Content Publisher	Springer Nature
Licensed Content Publication	Nature Reviews Chemistry
Licensed Content Title	The active template approach to interlocked molecules
Licensed Content Author	Mathieu Denis et al
Licensed Content Date	Aug 9, 2017
Type of Use	Thesis/Dissertation
Requestor type	academic/university or research institute
Format	print and electronic
Portion	figures/tables/illustrations
Number of figures/tables/illustrations	1

Figure 14.

SPRINGER NATURE LICENSE
TERMS AND CONDITIONS

Dec 26, 2023

This Agreement between Ms. Maria Lago Silva ("You") and Springer Nature ("Springer Nature") consists of your license details and the terms and conditions provided by Springer Nature and Copyright Clearance Center.

License Number	5696660810927
License date	Dec 26, 2023
Licensed Content Publisher	Springer Nature
Licensed Content Publication	Nature Chemistry
Licensed Content Title	How much do van der Waals dispersion forces contribute to molecular recognition in solution?
Licensed Content Author	Lixu Yang et al
Licensed Content Date	Oct 20, 2013
Type of Use	Thesis/Dissertation
Requestor type	academic/university or research institute
Format	print and electronic
Portion	figures/tables/illustrations
Number of figures/tables/illustrations	1

Figure 19.

Synthetic strategies towards mechanically interlocked oligomers and polymers

N. Hoyas Pérez and J. E. M. Lewis, *Org. Biomol. Chem.*, 2020, **18**, 6757 **DOI:** 10.1039/D0OB01583K

Figure 20. (b)

CCC Marketplace

This is a License Agreement between Maria Lago Silva ("User") and Copyright Clearance Center, Inc. ("CCC") on behalf of the Rightsholder identified in the order details below. The license consists of the order details, the Marketplace Permissions General Terms and Conditions below, and any Rightsholder Terms and Conditions which are included below.

All payments must be made in full to CCC in accordance with the Marketplace Permissions General Terms and Conditions below.

Order Date	27-Dec-2023	Type of Use	Republish in a thesis/dissertation
Order License ID	1431274-1		
ISSN	1364-548X	Publisher	ROYAL SOCIETY OF CHEMISTRY
		Portion	Image/photo/illustration

LICENSED CONTENT

Publication Title	Chemical communications	Rightsholder	Royal Society of Chemistry
Article Title	Rational control of a polyacetylene helix by a pendant rotaxane switch.	Publication Type	e-Journal
		Start Page	11739
Author/Editor	Royal Society of Chemistry (Great Britain)	End Page	11741
		Issue	42
Date	01/01/1996	Volume	47
Language	English		
Country	United Kingdom of Great Britain and Northern Ireland		

REQUEST DETAILS

Portion Type	Image/photo/illustration	Distribution	Worldwide
Number of Images / Photos / Illustrations	1	Translation	Original language of publication
Format (select all that apply)	Print, Electronic	Copies for the Disabled?	No
		Minor Editing Privileges?	No
Who Will Republish the Content?	Author of requested content	Incidental Promotional Use?	No
Duration of Use	Life of current edition	Currency	EUR
Lifetime Unit Quantity	Up to 499		
Rights Requested	Main product		

NEW WORK DETAILS

Title	Covalent and Supramolecular Helical polymers based on Axially Chiral Allenes	Institution Name	University of Santiago de Compostela
		Expected Presentation Date	2024-03-22
Instructor Name	Maria Lago Silva		

Figure 26.

JOHN WILEY AND SONS LICENSE
TERMS AND CONDITIONS

Dec 27, 2023

This Agreement between Ms. Maria Lago Silva ("You") and John Wiley and Sons ("John Wiley and Sons") consists of your license details and the terms and conditions provided by John Wiley and Sons and Copyright Clearance Center.

License Number	5697090198138
License date	Dec 27, 2023
Licensed Content Publisher	John Wiley and Sons
Licensed Content Publication	Angewandte Chemie International Edition
Licensed Content Title	Facile and Versatile Synthesis of End–Functionalized Poly(phenylacetylene)s: A Multicomponent Catalytic System for Well–Controlled Living Polymerization of Phenylacetylenes
Licensed Content Author	Katsuhiro Maeda, Tatsuya Nishimura, Kokoro Takayama, et al
Licensed Content Date	Mar 19, 2020
Licensed Content Volume	59
Licensed Content Issue	22
Licensed Content Pages	11
Type of use	Dissertation/Thesis

Figure 30. (b)

JOHN WILEY AND SONS LICENSE
TERMS AND CONDITIONS

Dec 27, 2023

This Agreement between Ms. Maria Lago Silva ("You") and John Wiley and Sons ("John Wiley and Sons") consists of your license details and the terms and conditions provided by John Wiley and Sons and Copyright Clearance Center.

License Number	5697091360496
License date	Dec 27, 2023
Licensed Content Publisher	John Wiley and Sons
Licensed Content Publication	Angewandte Chemie International Edition
Licensed Content Title	A Helical Array of Pendant Fullerenes on an Optically Active Polyphenylacetylene
Licensed Content Author	Tatsuya Nishimura, Kohei Takatani, Shin–ichiro Sakurai, et al
Licensed Content Date	Oct 4, 2002
Licensed Content Volume	41
Licensed Content Issue	19
Licensed Content Pages	3
Type of use	Dissertation/Thesis
Requestor type	University/Academic
Format	Print and electronic

Figure 30. (c,d)

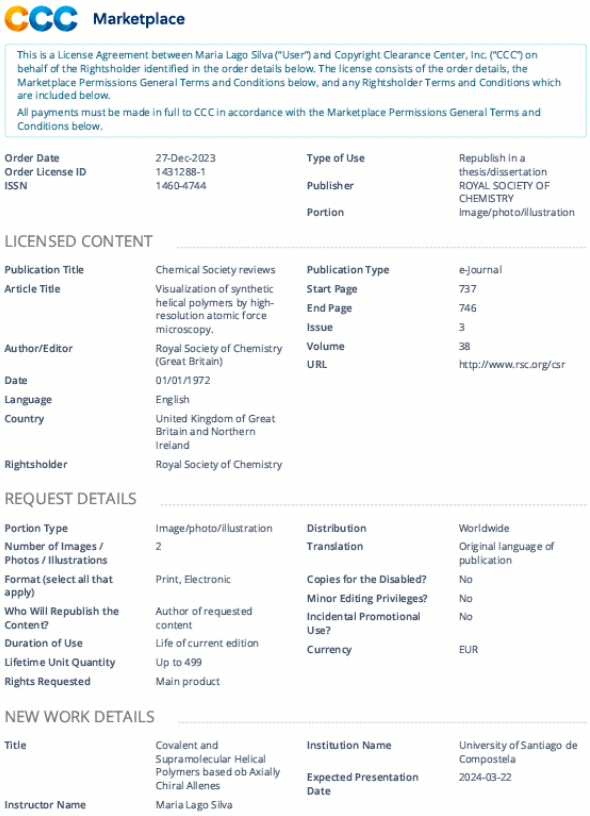

Marketplace

This is a License Agreement between Maria Lago Silva ("User") and Copyright Clearance Center, Inc. ("CCC") on behalf of the Rightsholder identified in the order details below. The license consists of the order details, the Marketplace Permissions General Terms and Conditions below, and any Rightsholder Terms and Conditions which are included below.

All payments must be made in full to CCC in accordance with the Marketplace Permissions General Terms and Conditions below.

Order Date	27-Dec-2023	Type of Use	Republish in a thesis/dissertation
Order License ID	1431288-1		
ISSN	1460-4744	Publisher	ROYAL SOCIETY OF CHEMISTRY
		Portion	Image/photo/illustration

LICENSED CONTENT

Publication Title	Chemical Society reviews	Publication Type	e-Journal
Article Title	Visualization of synthetic helical polymers by high-resolution atomic force microscopy.	Start Page	737
		End Page	746
		Issue	3
Author/Editor	Royal Society of Chemistry (Great Britain)	Volume	38
		URL	http://www.rsc.org/csr
Date	01/01/1972		
Language	English		
Country	United Kingdom of Great Britain and Northern Ireland		
Rightsholder	Royal Society of Chemistry		

REQUEST DETAILS

Portion Type	Image/photo/illustration	Distribution	Worldwide
Number of Images / Photos / Illustrations	2	Translation	Original language of publication
Format (select all that apply)	Print, Electronic	Copies for the Disabled?	No
		Minor Editing Privileges?	No
Who Will Republish the Content?	Author of requested content	Incidental Promotional Use?	No
Duration of Use	Life of current edition	Currency	EUR
Lifetime Unit Quantity	Up to 499		
Rights Requested	Main product		

NEW WORK DETAILS

Title	Covalent and Supramolecular Helical Polymers based ob Axially Chiral Allenes	Institution Name	University of Santiago de Compostela
		Expected Presentation Date	2024-03-22
Instructor Name	Maria Lago Silva		

Figure 31. (b)

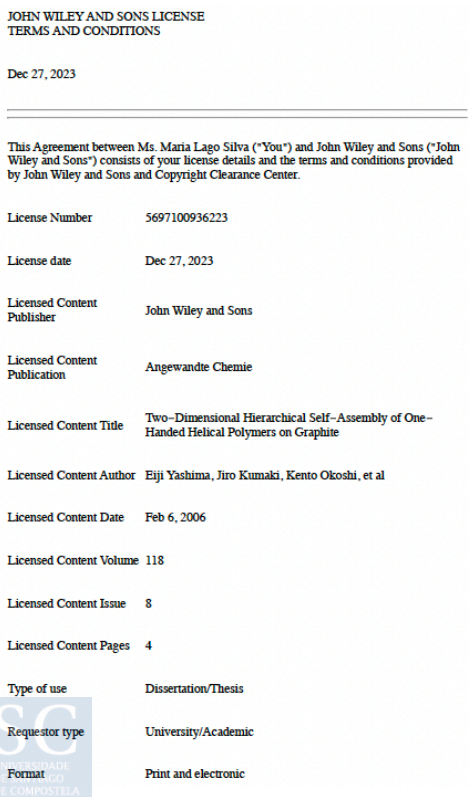

JOHN WILEY AND SONS LICENSE
TERMS AND CONDITIONS

Dec 27, 2023

This Agreement between Ms. Maria Lago Silva ("You") and John Wiley and Sons ("John Wiley and Sons") consists of your license details and the terms and conditions provided by John Wiley and Sons and Copyright Clearance Center.

License Number	5697100936223
License date	Dec 27, 2023
Licensed Content Publisher	John Wiley and Sons
Licensed Content Publication	Angewandte Chemie
Licensed Content Title	Two–Dimensional Hierarchical Self–Assembly of One–Handed Helical Polymers on Graphite
Licensed Content Author	Eiji Yashima, Jiro Kumaki, Kento Okoshi, et al
Licensed Content Date	Feb 6, 2006
Licensed Content Volume	118
Licensed Content Issue	8
Licensed Content Pages	4
Type of use	Dissertation/Thesis
Requestor type	University/Academic
Format	Print and electronic

Figures 32, 34 and 35.

Stimuli-responsive synthetic helical polymers

M. Lago-Silva, M. Fernández-Míguez, R. Rodríguez, E. Quiñoá and F. Freire, *Chem. Soc. Rev.*, 2024, **53**, 793 **DOI:** 10.1039/D3CS00952A

Figure 36. (c)

CCC Marketplace

This is a License Agreement between Maria Lago Silva ("User") and Copyright Clearance Center, Inc. ("CCC") on behalf of the Rightsholder identified in the order details below. The license consists of the order details, the Marketplace Permissions General Terms and Conditions below, and any Rightsholder Terms and Conditions which are included below.

All payments must be made in full to CCC in accordance with the Marketplace Permissions General Terms and Conditions below.

Order Date	27-Dec-2023	Type of Use	Republish in a thesis/dissertation
Order License ID	1431306-1	Publisher	ROYAL SOCIETY OF CHEMISTRY
ISSN	1364-548X	Portion	Image/photo/illustration

LICENSED CONTENT

Publication Title	Chemical communications	Rightsholder	Royal Society of Chemistry
Article Title	Reversible polyphenylacetylene helix conversion driven by a thermoresponsive rotaxane switch in the solid state.	Publication Type	e-Journal
		Start Page	3647
		End Page	3649
		Issue	18
Author/Editor	Royal Society of Chemistry (Great Britain)	Volume	52
Date	01/01/1996		
Language	English		
Country	United Kingdom of Great Britain and Northern Ireland		

REQUEST DETAILS

Portion Type	Image/photo/illustration	Distribution	Worldwide
Number of Images / Photos / Illustrations	1	Translation	Original language of publication
Format (select all that apply)	Print, Electronic	Copies for the Disabled?	No
		Minor Editing Privileges?	No
Who Will Republish the Content?	Author of requested content	Incidental Promotional Use?	No
Duration of Use	Life of current edition	Currency	EUR
Lifetime Unit Quantity	Up to 499		
Rights Requested	Main product		

NEW WORK DETAILS

Title	Covalent and Supramolecular Helical polymers based on Axially Chiral Allenes	Institution Name	University of Santiago de Compostela
		Expected Presentation Date	2024-03-22
Instructor Name	Maria Lago Silva		

Figure 37.

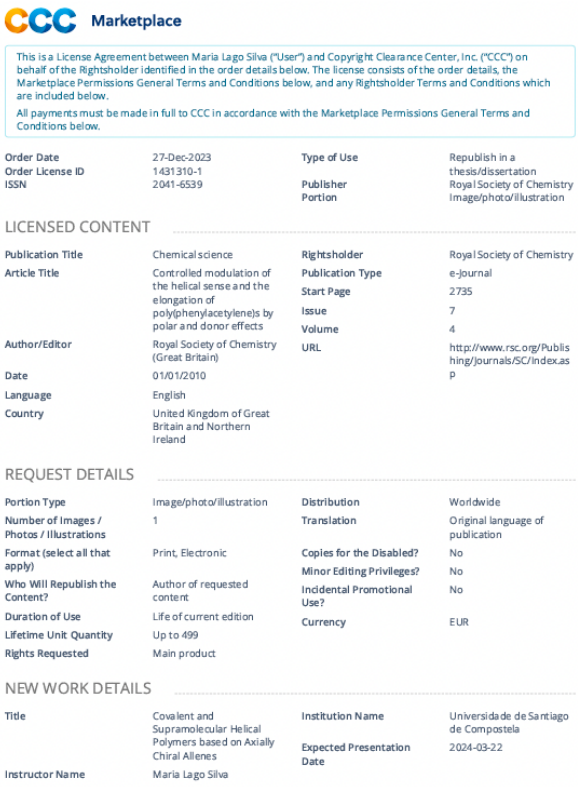

CCC Marketplace

This is a License Agreement between Maria Lago Silva ("User") and Copyright Clearance Center, Inc. ("CCC") on behalf of the Rightsholder identified in the order details below. The license consists of the order details, the Marketplace Permissions General Terms and Conditions below, and any Rightsholder Terms and Conditions which are included below.

All payments must be made in full to CCC in accordance with the Marketplace Permissions General Terms and Conditions below.

Order Date	27-Dec-2023	Type of Use	Republish in a thesis/dissertation
Order License ID	1431310-1		
ISSN	2041-6539	Publisher	Royal Society of Chemistry
		Portion	Image/photo/illustration

LICENSED CONTENT

Publication Title	Chemical science	Rightsholder	Royal Society of Chemistry
Article Title	Controlled modulation of the helical sense and the elongation of poly(phenylacetylene)s by polar and donor effects	Publication Type	e-Journal
		Start Page	2735
		Issue	7
		Volume	4
Author/Editor	Royal Society of Chemistry (Great Britain)	URL	http://www.rsc.org/Publishing/Journals/SC/Index.asp
Date	01/01/2010		
Language	English		
Country	United Kingdom of Great Britain and Northern Ireland		

REQUEST DETAILS

Portion Type	Image/photo/illustration	Distribution	Worldwide
Number of Images / Photos / Illustrations	1	Translation	Original language of publication
Format (select all that apply)	Print, Electronic	Copies for the Disabled?	No
		Minor Editing Privileges?	No
Who Will Republish the Content?	Author of requested content	Incidental Promotional Use?	No
Duration of Use	Life of current edition	Currency	EUR
Lifetime Unit Quantity	Up to 499		
Rights Requested	Main product		

NEW WORK DETAILS

Title	Covalent and Supramolecular Helical Polymers based on Axially Chiral Allenes	Institution Name	Universidade de Santiago de Compostela
		Expected Presentation Date	2024-03-22
Instructor Name	Maria Lago Silva		

Figure 41.

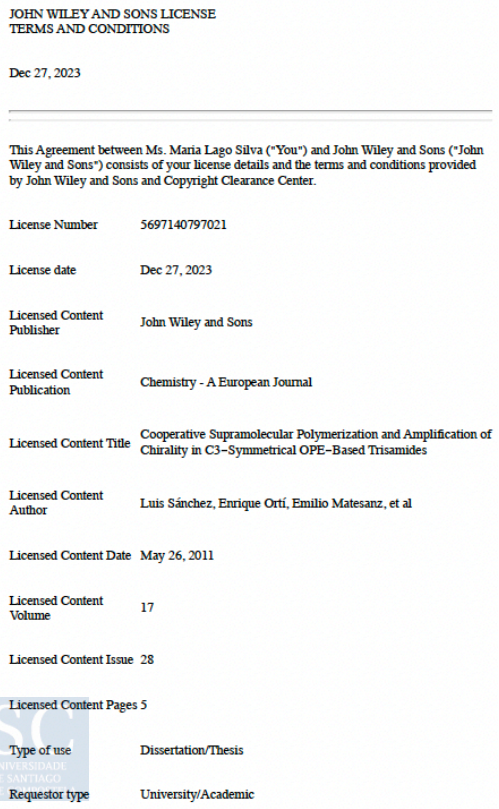

JOHN WILEY AND SONS LICENSE
TERMS AND CONDITIONS

Dec 27, 2023

This Agreement between Ms. Maria Lago Silva ("You") and John Wiley and Sons ("John Wiley and Sons") consists of your license details and the terms and conditions provided by John Wiley and Sons and Copyright Clearance Center.

License Number	5697140797021
License date	Dec 27, 2023
Licensed Content Publisher	John Wiley and Sons
Licensed Content Publication	Chemistry - A European Journal
Licensed Content Title	Cooperative Supramolecular Polymerization and Amplification of Chirality in C3–Symmetrical OPE–Based Trisamides
Licensed Content Author	Luis Sánchez, Enrique Ortí, Emilio Matesanz, et al
Licensed Content Date	May 26, 2011
Licensed Content Volume	17
Licensed Content Issue	28
Licensed Content Pages	5
Type of use	Dissertation/Thesis
Requestor type	University/Academic

A.4. Declaration of all other images

All other images in this Doctoral Thesis without the corresponding acknowledgment and proper reproduction have been personally elaborated.

Molecular switches, supramolecular chemistry, and polymers can be combined to create stimuli-responsive multi-chiral materials. Herein, novel mechanisms to modify the helical scaffold in helical systems are presented based on axially chiral allenes. The screw sense of the helical system is determined by the priority of the allenyl substituents that can be altered with respect to the backbone by external stimuli. Hence, a helix inversion occurs through a novel axial-to-helical communication mechanism, opening a new scenario for taming the helices of chiral dynamic helical polymers. These results show that complex dynamic multi-chiral materials can be obtained by polymerization of appropriate monomers that combine chirality, switching properties, and the ability to generate chiral supramolecular assemblies.